

**Proceedings of the  
17<sup>th</sup> Annual Symposium  
Imaging Network Ontario  
March 28 – 29, 2019  
DoubleTree by Hilton  
London, Ontario**

## Silver Sponsors



**GE Healthcare** Inspired to challenge the limitations of rigid coils, our AIR Technology™ Suite began as an industry-leading set of coils designed to comfortably conform to the human body. Each coil is designed to fit all patients, allowing flexibility in any direction, closely wrapping around your patient for greater visibility of hard-to-scan areas. Multiple coils can also be used together and overlapped for excellent SNR and image quality. Visit us at the booth to learn more.



The **Biomedical Imaging Research Centre** (BIRC) is a Full Partnership Centre at Western University encompassing London-wide Imaging. Partners include Schulich School of Medicine & Dentistry, Department of Medical Imaging, Lawson Health Research Institute, Robarts Research Institute and the School of Biomedical Engineering

## Bronze Sponsors



Founded in 2000, **Modus Medical Devices Inc.** develops and manufactures quality assurance tools for advanced radiotherapy and medical imaging. With over 4,900 QUASAR™ phantoms being used in more than 3,000 leading treatment centres, Modus is the partner of choice in providing accuracy and confidence to customers worldwide.



**Shelley Medical Imaging Technologies** - A leader in developing, manufacturing and distributing programmable, highly accurate & realistic CT, MRI, ultrasound, PET & SPECT compatible phantoms for medical imaging, radiation therapy and endovascular techniques.

**Products:** DCE perfusion flow phantom, respiratory tumor motion phantoms, geometric distortion phantom, physiological flow pump systems, silicone anatomical models, Doppler flow phantoms, heart motion phantoms and micro-CT QA phantoms.

---

**Table of Contents**

<b>Silver Sponsors</b>	<b>2</b>
GE Healthcare	2
The Biomedical Imaging Research Centre	2
<b>Bronze Sponsors</b>	<b>2</b>
Modus Medical Devices Inc.	2
Shelley Medical Imaging Technologies	2
<b>Welcome Letter</b>	<b>5</b>
<b>Sponsoring Consortia</b>	<b>6</b>
Development of Novel Therapies for Bone and Joint Diseases	6
Heart Failure: Prevention through Early Detection Using New Imaging Methods	6
Imaging for Cardiovascular Device Intervention (ICDI)	6
Ontario Institute for Cancer Research Imaging Program	7
NIH – NICHD Human Placenta Project	7
<b>Keynote Speakers</b>	<b>8</b>
Amber Simpson	8
Rebecca Fahrig	8
Rebecca Thornhill	9
Penny Gowland	9
<b>Scientific and Organizing Committees</b>	<b>10</b>
Scientific Committee	10
Organizing Committee	10
Abstract Reviewers	10
Oral and Poster Judges	10
<b>Program</b>	<b>11</b>
<b>Oral Presentation Abstracts</b>	<b>15</b>
Session 1: Instrumentation and Technology Development	16
Session 2: Machine Learning	23
Session 3: Cellular and Molecular Imaging	30
Session 4: New MRI Approaches	36
Session 5: Image Guided Intervention and Augmented Reality	42

Session 6: Bone and Joint Imaging	49
Session 7: Cancer Imaging	56
Session 8: Fetal, Neonatal and Pediatric Imaging	62
Session 9: Lung Imaging	68
Session 10: New Contrast Agents	74
Session 11: Neuroimaging	80
Session 12: Cardiac and Vascular Imaging	87
<b>Poster Presentation Abstracts</b>	<b>94</b>
Session 1: Instrumentation and Technology Development	95
Session 2: Machine Learning	114
Session 3: Cellular and Molecular Imaging	122
Session 4: New MRI Approaches / Magnetic Resonance Imaging	126
Session 5: Image Guided Intervention and Augmented Reality	142
Session 6: Bone and Joint Imaging	152
Session 7: Cancer Imaging	163
Session 8: Lung Imaging	170
Session 9: New Contrast Agents	174
Session 10: Neuroimaging	180
Session 11: Cardiac and Vascular Imaging	190
<b>Imaging Network Ontario Code of Conduct</b>	<b>204</b>
<b>Author Index</b>	<b>205</b>
<b>Poster Layout</b>	<b>215</b>

## Welcome Letter

Dear ImNO 2019 Attendees:

Welcome to the Imaging Network Ontario (ImNO) 2019 Symposium. This year marks our 17<sup>th</sup> annual meeting.

ImNO is an initiative created in response to a request by the Ontario Research Development Challenge Fund – now the Ontario Research Fund – for assistance in harmonizing its investments in imaging research. The establishment of ImNO provides a means of harnessing and focusing the intellectual and innovative capabilities at Ontario universities in partnerships with emerging and established medical imaging companies to create a strong and sustainable internationally competitive imaging industry based on scientific excellence in Ontario.

Since its' inception in 2003, the annual ImNO meeting has welcomed invited presentations from world-class scientists and proffered presentations from Ontario and across the county. This year, we are pleased to thank the five consortia for supporting our conference:

- Development of Novel Therapies for Bone and Joint Diseases;
- Heart Failure: Prevention through Early Detection Using New Imaging Methods;
- Imaging for Cardiovascular Device Intervention (ICDI);
- Ontario Institute for Cancer Research (OICR) Imaging Program; and
- NIH – NICHD Human Placenta Project – Hyperpolarized <sup>13</sup>C MRI of Placental Metabolic Abnormalities Resulting from the Western Diet.

For the 2019 meeting, abstracts were reviewed by an average of 3 reviewers and 167 were accepted. The ImNO 2019 Scientific Committee then assembled the final program: 4 keynote speakers, 66 oral presentations and 98 poster presentations.

In closing, we would like to acknowledge the significant contributions made by the members of the Scientific and Organizing Committees. Together they have worked very hard to bring us this year's meeting. We hope you enjoy this year's program and world-renowned keynote speakers.

Sincerely,

Ali R Khan, Charles McKenzie and Tamie Poepping  
Co-Chairs, Scientific Committee, 2019 ImNO Symposium

## Sponsoring Consortia

The Annual Meeting of Imaging Network Ontario (ImNO) promotes Canada's role as a leader in medical imaging innovation by cultivating synergy among consortia and partnerships between Ontario and other Canadian imaging entities.

The following consortia and programs supported the 2019 ImNO Symposium financially.

### Development of Novel Therapies for Bone and Joint Diseases

**Director: Dr. David Holdsworth**

**Ontario Research Fund**

Musculoskeletal disorders are the most common cause of severe long-term pain and physical disability, affecting hundreds of millions of people around the world. The economic burden is high; joint diseases cost the Ontario economy more than \$2 billion per year. To reduce this disease burden, this Ontario Research Fund Research Excellence program focuses on the "Development of Novel Therapies for Bone and Joint Diseases," including improved diagnostic imaging techniques and new approaches for image-guided therapy. A multidisciplinary team of imaging scientists, biomedical engineers, physical therapists, and orthopaedic surgeons work together on key research projects, including the development of new ways to post-process 3D MRI and CT data to guide surgery, dynamic imaging of moving joints (under load), and image-based design of "patient-specific" orthopaedic components.

### Heart Failure: Prevention through Early Detection Using New Imaging Methods

**Director: Dr. Frank Prato**

**Ontario Research Fund**

Consortium partners: Lawson Health Research Institute, Sunnybrook Research Institute and University of Ottawa Heart Institute. Ten percent of Ontarians over 60 have heart failure. One quarter will die within one year of diagnosis and almost all in ten years. Our LHRI/SRI/UOHI consortium is developing combined PET and MRI imaging methods for early diagnosis when treatment is still possible. The imaging methods developed are being commercialized and will benefit Ontario by improving the health of its citizens and creating new jobs.

### Imaging for Cardiovascular Device Intervention (ICDI)

**Director: Dr. Graham Wright**

**Ontario Research Fund**

Cardiovascular diseases have evolved from an acute killer to a chronic disease challenge. In recent years, there have been major advances in less invasive treatments, placing an emphasis on the development of imaging and tracking technologies. Focusing on electrophysiology, percutaneous procedures, and valve replacement, researchers at Sunnybrook and Robarts Research Institutes, working with local, national, and multinational diagnostic imaging and interventional device companies, are advancing the state-of-the-art in image acquisition and analysis with ultrasound, MRI, x-ray, and CT methods, including the design of visualization platforms and associated communication and control interfaces for interventional guidance, facilitating fusion and manipulation of prior and real-time imaging and device information. The ultimate goal is more effective utilization of imaging to improve outcomes for patients with chronic ischemia, complex arrhythmias, and heart failure related to structural heart diseases.

## **Ontario Institute for Cancer Research Imaging Program**

**Directors: Dr. Aaron Fenster/Dr. Martin Yaffe**

**Ontario Institute for Cancer Research**

The OICR Imaging Program accelerates the translation of research into the development of new imaging innovations for earlier cancer detection and diagnosis and treatment through four major projects: probe development and commercialization, medical imaging instrumentation and software, pathology validation, and imaging for clinical trials. The Imaging Program facilitates improved screening and treatment options for cancer patients by streamlining advances in medical imaging through the complex pipeline from discovery to clinical translation and ultimately to clinical use.

## **NIH – NICHD Human Placenta Project - Hyperpolarized <sup>13</sup>C MRI of Placental Metabolic Abnormalities Resulting from the Western Diet**

**Director: Dr. Charles McKenzie**

**NICHD**

Over 30% of all pregnancies in North America occur in women that are obese. Maternal obesity is often a result of lifelong consumption of an obesity-promoting Western Diet. Altered placental metabolism contributes to increased rates of adverse outcomes in these Western Diet exposed pregnancies, but there is currently no method available to non-invasively measure placental metabolism. The goal of this project is to develop and validate an MRI based method that can be used in human pregnancy to distinguish the placenta with normal metabolism from one where metabolic function is abnormal due to exposure to the Western Diet. Ultimately this will allow improved diagnosis and monitoring of metabolically compromised pregnancies and allow improved treatment that will reduce the rates of adverse outcomes.

## Keynote Speakers

**Thursday, March 28 at 8:40**

**Amber Simpson, PhD, Computer Scientist, Department of Surgery, Memorial Sloan Kettering**

Amber Simpson, PhD is a computer scientist at Memorial Sloan Kettering (MSK) specializing in medical image analysis and computer-aided surgery. She received a PhD in computer science from Queen's University in Kingston, Ontario, Canada. Dr. Simpson joined the MSK faculty as the first PhD in the Department of Surgery, where she leads a research lab in machine learning, biomedical data science, and medical imaging. Her current work aims to advance understanding of cancer biology through interdisciplinary integration of multimodal measurements from imaging (both radiographic and histopathologic) and tissue-based assays (next generation sequencing, atomic force microscopy, etc.). Dr. Simpson is a current recipient of an American Association of Cancer Research Career Development Award and recently received extramural funding from the National Cancer Institute.



**Thursday, March 28 at 16:55**

**Rebecca Fahrig, PhD, Vice President of Innovation, Advanced Therapies, Siemens Healthineers**

Dr. Rebecca Fahrig has spent more than 25 years in the development and application of advanced x-ray imaging techniques with the goal of improving guidance, increasing targeting accuracy, and evaluating outcomes during minimally invasive procedures. Dr. Fahrig earned her Ph.D. at the University of Western Ontario in 1999, where she joined pioneers of C-arm-based conebeam CT imaging in the Holdsworth lab. She completed a postdoctoral fellowship at Stanford University developing an x-ray/MR hybrid system. She then joined the faculty of the Department of Radiology at Stanford, where she and her team – in collaboration with national and international clinical and scientific colleagues – developed new MR-compatible hardware, x-ray detectors, image reconstruction and correction algorithms, and protocols for clinical applications with funding from industry and NIH. Dr. Fahrig is currently Vice-president of Innovations, business area Advanced Therapies, at Siemens Healthcare GmbH where she directs a group of 55 scientists designing, prototyping and testing new applications and image guidance systems. She is also Professor at the Pattern Recognition Lab, Friedrich-Alexander University in Erlangen, Germany.





**Friday, March 29 at 8:55**

**Rebecca Thornhill, PhD, Assistant Professor, Department of Radiology, University of Ottawa**

Dr Thornhill completed her M.Sc. and Ph.D. in Medical Biophysics from the University of Western Ontario, where her work focused on cardiac magnetic resonance imaging (MRI). She continued on to do postdoctoral research fellowships at McMaster University and the University of Toronto (Hospital for Sick Children). Since 2010, Dr Thornhill has been working as an Imaging Scientist in the Department of Medical Imaging at The Ottawa Hospital, with special interests in cardiac MRI as well as quantitative pattern analysis of medical images. Dr. Thornhill is an Assistant Professor in the Department of Radiology at the University of Ottawa and an Adjunct Research Professor in the Department of Systems and Computer Engineering at Carleton University.



**Friday, March 29 at 16:40**

**Penny Gowland, PhD, Professor, Physics, University of Nottingham**

Penny Gowland has worked on developing quantitative MR techniques to answer a variety of biomedical questions at the University of Nottingham for most of her career. She has particular interests in studying fetal development and placental function with MRI and the interactions of electromagnetic fields with the human body. She also has strong interests in techniques for structural and functional neuroimaging at 7T, imaging gastrointestinal function.



## Scientific and Organizing Committees

**Co-Chairs: Ali R Khan, Charles McKenzie and Tamie Poepping**

### Scientific Committee

Corey Baron	Gabor Fichtinger	Cari Whyne
Robert deKemp	David Holdsworth	Graham Wright
Maria Drangova	Anne Martel	Martin Yaffe
Aaron Fenster	Aaron Ward	

### Organizing Committee

Johanne Langford	Jean Rookwood
Carol Richardson	Janette Wallace

## Abstract Reviewers

Nishard Abdeen	Richard Frayne	Emily Lalone	Tamie Poepping
Natasha Alves-Kotzev	Stewart Gaede	Andras Lasso	Giles Santyr
Corey Baron	Nilesh Ghugre	M Louis Lauzon	Tim Scholl
Stephen Breen	Donna Goldhawk	Ting Lee	Kathleen Surry
Tim Burkhart	Maged Goubran	Chris Macgowan	Matthew Teeter
Ian Cameron	Roy Haast	James Mainprize	Jonathan Thiessen
Elvis Chen	Michael Hardisty	Anne Martel	Rebecca Thornhill
Catherine Coolen	Matthew Holden	Naomi Matsuura	Tamas Ungi
Greg Cron	David W Holdsworth	Cheryl McCreary	Glenn Wells
Robert deKemp	Michael Jurkiewicz	Charles McKenzie	Cari Whyne
Mamadou Diop	Ali R. Khan	Elka Miller	Eugene Wong
Maria Drangova	Miranda Kirby	Michael Noseworthy	Graham Wright
Aaron Fenster	Mike Kolios	Terry Peters	Yiming Xiao
Gabor Fichtinger	Manuela Kunz	Csaba Pinter	Ivan Yeung
Paula Foster			

## Oral and Poster Judges

**Coordinators: Corey Baron, Maria Drangova, Gabor Fichtinger and Anne Martel**

Aidin Arbabi	Maged Goubran	Alexei Ouriadov	Sarah Svenningsen
Robert Bartha	Penny Gowland	Grace Parraga	Ali Tavallaei
Elvis Chen	Amanda Hamilton	Terry Peters	David Tessier
Robert deKemp	William Handler	Csaba Pinter	Jonathan Thiessen
Christine Demore	Michael Hardisty	Ajay Rajaram	Aaron Ward
Savita Dhanvantari	Justin Hicks	John Ronald	Cari Whyne
Mamadou Diop	Natasja Janssen	Rojan Saghian	Eugene Wong
Rebecca Fahrig	Ryan Jones	Timothy Scholl	Graham Wright
Stewart Gaede	Jim Lacefield	Amber Simpson	Martin Yaffe
Jean Gariepy	Andras Lasso	Keith St. Lawrence	WeiWei Zhang
Neil Gelman	Angus Lau	Greg Stanisz	
Donna Goldhawk	Charles McKenzie	Kathleen Surry	

**Program**

**Day 1 - Thursday, March 28, 2019**

7:15	<b>Registration</b>	Grand Ballroom Foyer
7:15 – 8:30	<b>Poster Set-Up</b>	Grand Ballroom West
8:30 – 8:40	<b>Opening Remarks</b> Ali R Khan, Charles McKenzie & Tamie Poepping, ImNO 2019 Scientific Committee Chairs	Grand Ballroom Centre and East
	<b>Keynote Session</b> Chair: Anne Martel, Sunnybrook Research Institute	Grand Ballroom Centre and East
8:40 – 9:25	<b>Separating the Hype from the Hope in Medical Imaging AI</b> Amber Simpson, PhD, Memorial Sloan Kettering	
9:25 – 10:25	<b>Poster Session &amp; Nutrition Break</b>	Grand Ballroom West
	<b>Grand Ballroom Centre</b>	<b>Grand Ballroom East</b>
	<b>1 - Instrumentation and Technology Development</b>	<b>2 - Machine Learning</b>
	<b>Chairs:</b> Christine Démoré, Sunnybrook Research Institute Tim Scholl, Robarts Research Institute	<b>Chairs:</b> Michael Hardisty, Sunnybrook Research Institute Amber Simpson, Memorial Sloan Kettering
10:25 – 10:39	1-1 <b>Designing a Spine-Specific Ultrasound Phased Array</b> Rui Xu, University of Toronto	2-1 <b>Texture-Based Prostate Cancer Classification on MRI: How Does Inter-Class Size Mismatch Affect Measured System Performance?</b> Ryan M Alfano, Western University
10:39 – 10:53	1-2 <b>Comparing Vibrometer and Accelerometer Measurements of Gradient Field Induced Vibration in an MRI</b> Idan Nemirovsky, Western University	2-2 <b>Ventricular and Total Intracranial Vault Segmentations for Brains with Extensive Atrophy Using Three-Dimensional Convolutional Neural Networks</b> Emmanuel Edward Ntiri, Sunnybrook Research Institute
10:53 – 11:07	1-3 <b>Varying Microstructural Properties of a 3D Printed Phantom for Diffusion MRI Validation</b> Farah N Mushtaha, Robarts Research Institute	2-3 <b>Automatic High-Grade Prostate Cancer Detection on Digital Histopathology Imaging</b> Wenchao Han, Western University
11:07 – 11:21	1-4 <b>Hypoxia Standardization Phantom to Quantify Variation in Hypoxia Measurement with Positron Emission Tomography across Multiple Centres</b> Brandon Driscoll, QIPCM, TECHNA Institute, UHN	2-4 <b>Multi-Contrast Carotid Lumen-wall Segmentation using Deep Learning</b> Anna Danko, University of Calgary
11:21 – 11:35	1-5 <b>Selective Laser Melted 2D Focused Anti-Scatter Grids for Cone-beam CT</b> Santiago F Cobos, Robarts Research Institute	2-5 <b>Tissue Segmentation in Multi-Weighted Breast MRI using a Deep Learning Unet</b> Grey C Kuling, University of Toronto
11:35 – 11:49	1-6 <b>A Novel Microfluidic Device for Real-time Microscopic Imaging of Endothelial Cell Responses to Laminar and Disturbed Fluid Flow</b> Daniel Lorusso, Robarts Research Institute	2-6 <b>Vertebral Body Segmentation in CT Images using V-Net</b> Geoff Klein, University of Toronto
11:49 – 13:00	<b>Lunch</b>	Grand Ballroom Foyer

Day 1 - Thursday, March 28, 2019

	Grand Ballroom Centre	Grand Ballroom East
	<p><b>3 - Cellular and Molecular Imaging</b></p> <p><b>Chairs:</b> Jean Gariépy, Sunnybrook Research Institute Amanda Hamilton, Robarts Research Institute</p>	<p><b>4 - New MRI Approaches</b></p> <p><b>Chairs:</b> Angus Lau, Sunnybrook Research Institute Greg Stanisz, Sunnybrook Research Institute</p>
13:00 – 13:14	3-1 <b>Gas Vesicle Nanoparticles for the Photodynamic Treatment of Tumors</b> Ann Fernando, University of Toronto	4-1 <b>Clinically-Viable and Robust Measurement of Microscopic Diffusion Anisotropy</b> Nico JJ Arezza, Robarts Research Institute
13:14 – 13:28	3-2 <b>Monitoring Two Cell Populations using Iron Oxides and Perfluorocarbons with Dual 1H and 19F Magnetic Resonance Imaging at 3 Tesla</b> Olivia C Sehl, Robarts Research Institute	4-2 <b>Rapid B1+ Measurement using a Non-Steady-State Progressive Flip Angle Sequence and Parallel Imaging</b> Nadia Bragagnolo, University of Toronto
13:28 – 13:42	3-3 <b>Molecular Imaging of Hypoxia: Kinetic Analysis of Dynamic PET Data from Pancreatic Cancer</b> Fiona Li, Western University	4-3 <b>Using Low Resolution Pre-Scans and Singular Value Decomposition Derived Sensitivities to Allow for the Combination of Large Phase Datasets</b> Olivia W Stanley, Robarts Research Institute
13:42 – 13:56	3-4 <b>Tumour-Activatable Minicircles Expressing Prodrug-Suicide Gene Systems for Prostate Cancer Therapy</b> TianDuo Wang, Robarts Research Institute	4-4 <b>Validation of Simulated vs Experimentally Acquired B0 Field Maps Surrounding Metal</b> Gregory Hong, Robarts Research Institute
13:56 – 14:10	3-5 <b>In Vivo Cell Tracking via Multimodality Reporter-Based Fluorescence, Photoacoustic, and Magnetic Resonance Imaging at 3 Tesla</b> Nivin N Nyström, Robarts Research Institute	4-5 <b>Initial Comparison of RF-Induced Heating in the ASTM Phantom and a Cadaver Leg: A Pilot Study</b> Amgad Louka, Western University
14:10 – 15:15	<p><b>Poster Session &amp; Nutrition Break</b></p> <p>Grand Ballroom Centre</p> <p><b>5 - Image Guided Intervention and Augmented Reality</b></p> <p><b>Chairs:</b> Elvis Chen, Robarts Research Institute Rebecca Fahrig, Siemens Healthineers</p>	<p>Grand Ballroom West</p> <p>Grand Ballroom East</p> <p><b>6 - Bone and Joint Imaging</b></p> <p><b>Chairs:</b> Nikolas Knowles, Western University Cari Whyne, Sunnybrook Research Institute</p>
15:15 – 15:29	5-1 <b>Assessment of Intraoperative Neurosurgical Planning with the Microsoft HoloLens</b> Zachary Baum, Queen's University	6-1 <b>Differentiation of Osteoblastic and Healthy Bone Tissue in Metastatically Involved Vertebrae using Radiomic Features</b> Allison J Clement, Sunnybrook Research Institute
15:29 – 15:43	5-2 <b>Augmented Reality Guidance in Cerebrovascular Surgery using Microscopic Video Enhancement</b> Reid Vassallo, Robarts Research Institute	6-2 <b>Iterative Design of a Small-Animal Hip-Hemiarthroplasty Model for Preclinical Orthopaedic Research</b> Adam DM Paish, Robarts Research Institute
15:43 – 15:57	5-3 <b>Navigation of the iKnife for Intra-Operative Tissue Characterization in Neurosurgery</b> Mark Asselin, Queen's University	6-3 <b>Micro-CT of Kangaroo Cervical Spine: Analysis of Bone Mineral Density of C3-C7</b> Joseph U Umoh, Robarts Research Institute
15:57 – 16:11	5-4 <b>Design and Evaluation of a New Positron Emission Mammography Ultrasound-Guidance Device for Core Needle Biopsy in Breast Tumours</b> Claire K Park, Robarts Research Institute	6-4 <b>Multimodal Image-based Analysis of Ultrafast Burst Mode Laser Ablation on Articular Cartilage</b> Melissa J Prickaerts, University Health Network
16:11 – 16:25	5-5 <b>Characterizing the Accuracy and Precision of Micro-Coil Tracking in Ablation Catheters</b> Jay B Soni, Sunnybrook Research Institute	6-5 <b>Three-Dimensional Computed Tomographic Reconstruction in a Natural Weight-Bearing Stance using Ceiling-Mounted X-Ray Fluoroscopy</b> Rudy Baronette, Robarts Research Institute
16:25 – 16:39	5-6 <b>Geometrically Variable 3D Ultrasound with Mechanical Assistance for Interventional Liver Cancer Therapies</b> Derek J Gillies, Robarts Research Institute	6-6 <b>Intra-Operative Verification of the Glenoid Implant Position with Structured Light Imaging in Total Shoulder Arthroplasty</b> David Burns, Sunnybrook Research Institute
16:39 – 16:55	<b>Nutrition Break</b>	Grand Ballroom Foyer
16:55 – 17:40	<p><b>Keynote Session</b></p> <p>Chair: David Holdsworth, Robarts Research Institute</p>	Grand Ballroom Centre and East
16:55 – 17:40	<b>Integration, Intelligence and Multi-Modality Image Guidance for Procedural Therapies</b> Rebecca Fahrig, PhD, Siemens Healthineers	

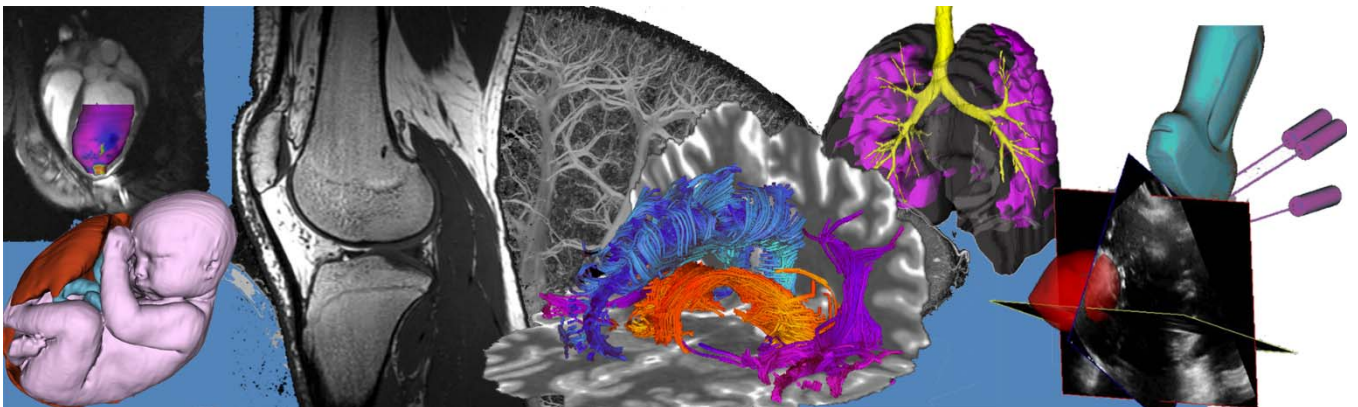
Day 2 - Friday, March 29, 2019

8:00	<b>Registration</b>	Grand Ballroom Foyer
8:00 – 8:50	<b>Poster Set-Up</b>	Grand Ballroom West
8:50 – 8:55	<b>Opening Remarks</b>	Grand Ballroom Centre and East
	Ali R Khan, Charles Mckenzie & Tamie Poepping, ImNO 2019 Scientific Committee Chairs	
	<b>Keynote Session</b>	Grand Ballroom Centre and East
	Chair: Frank Prato, Lawson Health Research Institute	
8:55 – 9:40	<b>Tissue Characterization with Cardiac Magnetic Resonance</b>	
	Rebecca Thornhill, PhD, University of Ottawa	
9:40 – 10:40	<b>Poster Session &amp; Nutrition Break</b>	Grand Ballroom West
	<b>Grand Ballroom Centre</b>	<b>Grand Ballroom East</b>
	<b>7 - Cancer Imaging</b>	<b>8 - Fetal, Neonatal and Pediatric Imaging</b>
	<b>Chairs:</b> Kathleen Surry, London Regional Cancer Program Aaron Ward, Western University	<b>Chairs:</b> Rojan Saghian, The Hospital for Sick Children Penny Gowland, University of Nottingham
10:40 – 10:54	7-1 <b>Radiomics for Detecting Recurrence After Stereotactic Ablative Radiotherapy: Sensitivity of Performance to Sample Size</b> Salma Dammak, Western University	8-1 <b>Quantifying T1 and T2* Relaxation Times of Fetal Tissues at 1.5 T</b> Simran Sethi, Western University
10:54 – 11:08	7-2 <b>Detection and Localization of Dominant Intra-prostatic Nodules with CT Perfusion</b> Dae-Myoung Yang, Robarts Research Institute	8-2 <b>Lateral Ventricle Volume Based on Posture of the Neonate Having Intraventricular Hemorrhage</b> Priyanka Roy, Robarts Research Institute
11:08 – 11:22	7-3 <b>Prostate MRI Delineated Lesion Boosting through High Dose Rate Brachytherapy Dwell Time Adjustment</b> Christopher W Smith, Western University	8-3 <b>User Friendly Fetal fMRI Image Segmentation Pipeline</b> Estee Goldberg, Western University
11:22 – 11:36	7-4 <b>Metabolic Imaging of a Renal Cell Carcinoma Patient with Brain Metastasis using Hyperpolarized <sup>13</sup>C MRI</b> Casey Y Lee, University of Toronto	8-4 <b>NNeMo (Neonatal Neuromonitor): A Non-Invasive Optical Device for Assessing the Coupling of Cerebral Blood Flow and Energy Metabolism in the Developing Brain</b> Ajay Rajaram, Western University
11:36 – 11:50	7-5 <b>Dual Bioluminescence Imaging Reveals Remarkable Tumour Self-Seeding of Spontaneous and Experimental Metastases in Mice</b> Katie M Parkins, Robarts Research Institute	8-5 <b>Identifying Lesions in Paediatric Epilepsy using Morphometric and Textural Analysis of MRI</b> Azad Aminpour, University of Ontario Institute of Technology
11:50 – 13:00	<b>Lunch</b>	Grand Ballroom Foyer
	<b>Grand Ballroom Centre</b>	<b>Grand Ballroom East</b>
	<b>9 - Lung Imaging</b>	<b>10 - New Contrast Agents</b>
	<b>Chairs:</b> Sarah Svenningsen, McMaster University Alexei Ouriadov, Western University	<b>Chairs:</b> Rebecca Sullivan, Lawson Health Research Institute Donna Goldhawk, Lawson Health Research Institute
13:00 – 13:14	9-1 <b>Novel COPD Multi-parametric Response Map Phenotypes</b> Jonathan MacNeil, Robarts Research Institute	10-1 <b>Safe Harbor Targeted CRISPR/Cas9 Tools for Molecular-Genetic Imaging of Cells in Living Subjects</b> Veronica Dubois, Robarts Research Institute
13:14 – 13:28	9-2 <b>Multi-scalar Perfusion and Ventilation Defects in Asthma</b> Alexander M Matheson, Robarts Research Institute	10-2 <b>Multimodality Organic Contrast Agents for Ultrasound and Photoacoustic Imaging</b> Yohannes Soenjaya, Sunnybrook Research Institute
13:28 – 13:42	9-3 <b>Improved Tumor Motion Estimation by Incorporating Pathophysiology in Biomechanical Model of the Lung</b> Parya Jafari, Western University	10-3 <b>Lanthanide Nanoparticles as Vascular Contrast Agents for In Vivo Dual Energy Microcomputed Tomography</b> Charmaine Cruje, Robarts Research Institute
13:42 – 13:56	9-4 <b>Is Vascular Pruning Related to MRI Ventilation Defects in Bronchiectasis and COPD patients?</b> Andrea L Barker, Robarts Research Institute	10-4 <b>Lymphatic Drainage from the Eye Quantified Non-Invasively by Photoacoustic Imaging using a Near Infrared Tracer</b> Kirsten Cardinell, Ryerson University
13:56 – 14:10	9-5 <b>Can Oscillometry Explain Differences Between <sup>3</sup>He and <sup>129</sup>Xe Ventilation Heterogeneity?</b> Rachel L Eddy, Robarts Research Institute	10-5 <b>Ultrafast Three-Dimensional Microbubble Imaging for Monitoring Nonthermal Brain Ablation</b> Ryan M Jones, Sunnybrook Research Institute

Day 2 - Friday, March 29, 2019

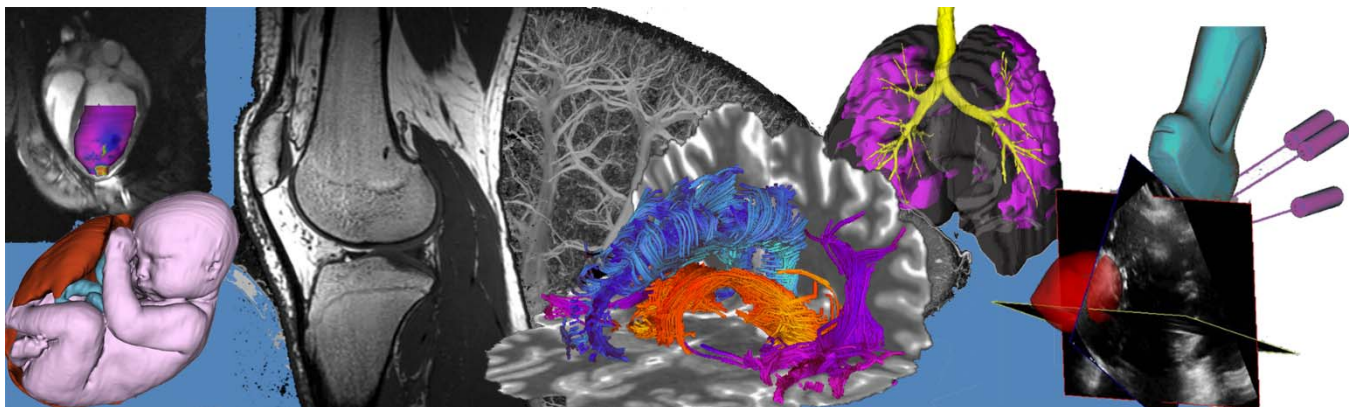
14:10 – 15:00	<b>Poster Session &amp; Nutrition Break</b>		Grand Ballroom West
	<b>Grand Ballroom Centre</b>	<b>Grand Ballroom East</b>	
	<b>11 - Neuroimaging</b>	<b>12 - Cardiac and Vascular Imaging</b>	
	<b>Chairs:</b> Aidin Arbabi, Robarts Research Institute Corey Baron, Robarts Research Institute	<b>Chairs:</b> Ali Tavallaei, Sunnybrook Research Institute Jonathan Thiessen, Lawson Health Research Institute	
15:00 – 15:14	11-1 <b>Error Analysis of a Non-Invasive Hybrid PET/MRI Method for Imaging CMRO2</b> Lucas D L Narciso, Lawson Health Research Institute	12-1 <b>Examining the Effect of Hepcidin on Cardiac Inflammation using THP-1 Monocytes and MRI</b> Praveen Sankajith B Dassanayake, Western University	
15:14 – 15:28	11-2 <b>Empirical Evaluation of A DTI Tractography Pipeline using Whole-Brain Tractograms from a White Matter Phantom</b> Stefan E Poirier, Lawson Health Research Institute	12-2 <b>Development of an Ex Vivo Porcine Model of Coarctation of the Aorta: Possible Treatment Applications with MR-Guided HIFU using Boiling Histotripsy</b> Sergio A Vega, The Hospital for Sick Children	
15:28 – 15:42	11-3 <b>Differentiating the Substantia Nigra Pars Compacta and Ventral Tegmental Area in Early-Stage Parkinson’s Disease using Structural Magnetic Resonance Imaging</b> Erind Alushaj, Western University	12-3 <b>Soft Tissue and Vascular Visualization of Iodine-Enhanced Samples via Dual-Energy Computed Tomography</b> Justin J Tse, Robarts Research Institute	
15:42 – 15:56	11-4 <b>Sub-Millimeter Blood Flow Mapping of Cortical and Hippocampal Gray Matter</b> Roy Haast, Robarts Research Institute	12-4 <b>Towards Quantifying Tissue Perfusion with Dynamic Contrast-Enhanced Near-Infrared Imaging</b> Seva Ioussoufovitch, Western University	
15:56 – 16:10	11-5 <b>Optimization of Phase Contrast for CBF Quantification by the Non-Invasive Hybrid PET/MR-approach</b> Tracy Ssali, Lawson Health Research Institute	12-5 <b>Exploring the Effects of Standard and Cooled Hemodialysis on Renal Blood Flow using CT Perfusion</b> Raanan Marants, Western University	
16:10 – 16:24	11-6 <b>Assessing the Reliability and Reproducibility of Neurobundle Extraction and Evaluation Resource, an Automated Tool for Clustering Diffusion Tractography</b> Jason Kai, Robarts Research Institute	12-6 <b>Effects of the Iron Chelator Deferiprone on Porcine Acute Myocardial Infarction and Cardiac Remodeling</b> Jill Weyers, Sunnybrook Research Institute	
16:24 – 16:40	<b>Nutrition Break</b>		Grand Ballroom Foyer
	<b>Keynote Session</b>		Grand Ballroom Centre and East
	Chair: Charles McKenzie, Western University		
16:40 – 17:25	<b>The Placental Pump</b> Penny Gowland, PhD, University of Nottingham		
17:25 – 17:45	<b>Awards and Closing Remarks</b>		Grand Ballroom Centre and East
17:45 – 18:15	<b>Poster Take Down</b>		Grand Ballroom West

# Oral Presentation Abstracts (in order of the talks)



# Oral Presentation Abstracts

## Session 1: Instrumentation and Technology Development





## Designing a Spine-Specific Ultrasound Phased Array

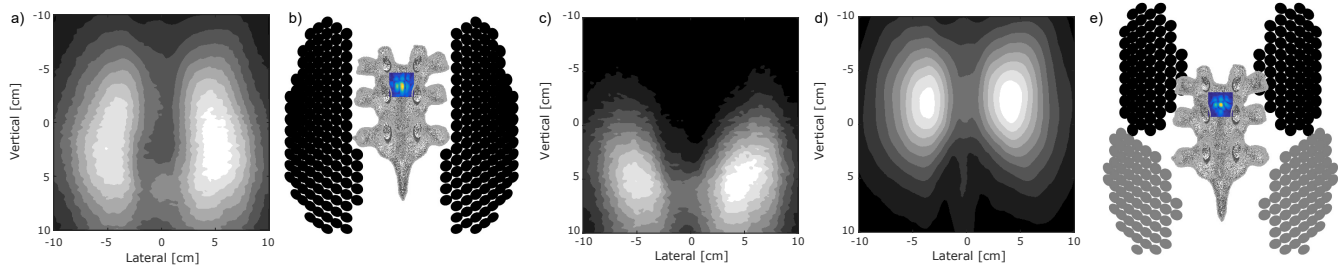
Rui Xu<sup>1,2</sup>, Meaghan O'Reilly<sup>1,2</sup>

<sup>1</sup>Medical Biophysics, University of Toronto, <sup>2</sup>Sunnybrook Research Institute, Toronto, ON, Canada

**Introduction.** Focused ultrasound is poised to transform brain therapy via non-invasive functional neurosurgery, targeted drug delivery and neuromodulation. Similar opportunities exist for the spinal cord, however, focusing ultrasound through the human spine is currently an unsolved challenge. Safe and accurate transspinal focused ultrasound requires beamforming for vertebra-induced ultrasound wavefront aberration. Given the irregularity of the spine and the consequential variability in beamforming, we believe that a phased array is best suited for transspinal-ultrasound applications. Phased arrays have been designed for many therapeutic applications, including hemispherical and conformal arrays for transskull ultrasound therapies [1, 2]. While the geometry of the skull guides the design of transskull arrays, the geometry of the spine gives less intuition to the design of a spine-specific phased array. Two viable transspinal ultrasound propagation paths exist: a paravertebral path, through the spaces between laminae, and a transvertebral path, through the laminar bone itself. We design two spine-specific phased arrays using backward ray acoustics simulation [3]; one with dedicated sub-arrays for the transvertebral and paravertebral paths, the other where each element transmission path is determined using adaptive focusing.

**Methods.** The simulation system was generated using *ex vivo* thoracic vertebrae that were degassed, placed in degassed and deionized water, then CT scanned at 0.5 mm isotropic resolution. Vertebral geometries were extracted using semi-automatic segmentation. Simulated sources were placed within the vertebral canal, spanning the height of the thoracic spine, and sound propagation was simulated via paravertebral and transvertebral paths to 10 cm x 10 cm measurement surfaces placed 10 cm posterior to the sources. The mean sound measurement surfaces were used to place 256 cylindrical elements (7.5 mm diameter), maximizing ultrasound reception and transmission for targets spanning the thoracic spinal cord. Array efficiency (focal pressure in the vertebral canal, normalized by focal pressure in water  $\times 100\%$ ) was evaluated for both arrays using forward ray acoustics simulation.

**Results.** A 2-component array was designed using the total sound pressure map (Fig. a), and an example of adaptive focusing to the vertebral canal is shown in Fig. b). The transmission path of each element in the 2-component array is determined using adaptive focusing. A 4-component array was designed using the paravertebral (Fig. c) and transvertebral (Fig. d) sound pressure maps, and an example of focusing to the vertebral canal is shown in Fig. e). The inferior components (grey elements) transmit via the paravertebral path, and the superior components (black elements) transmit via the transvertebral path. All elements are placed in locations with  $\geq 60\%$  normalized sound pressure, maximizing array sound reception and transmission efficiency. Both arrays were focused to targets spanning the height of the thoracic spinal cord. Mean  $\pm$  standard deviation in array efficiency for the 2- and 4-component arrays were  $32\% \pm 11\%$ , and  $29\% \pm 13\%$  respectively. However, maximum array efficiency (65%) was achieved with the 4-component array when the paravertebral path was clear.



Backward simulation: a) total, c) paravertebral, d) transvertebral acoustic propagation to 10 cm x 10 cm measurement surfaces 10 cm posterior to the sources. Array efficiency was evaluated with forward simulation using the b) 2-component array, and e) 4-component array (anterior views of the arrays and vertebrae with the vertebral bodies removed to view the simulated pressure profile within the canal).

**Conclusions.** Simulation shows that adaptive focusing for transspine ultrasound is more efficient than dedicated sub-arrays for the transvertebral and paravertebral paths. However, the 4-component array was more efficient when the paravertebral path was clear, suggesting that array efficiency may be further improved using a combination of multiple components that can be translated relative to one another, in addition to adaptive focusing. The development of these arrays and demonstration of safe and efficient transspine focusing capacity is a critical step to the translation of focused ultrasound spine therapy.

**References.** [1] G. Clement, J. White, and K. Hynynen, *Phys. Med. & Biol.*, vol. 45, no. 4, 2000. [2] A. Hughes and K. Hynynen, *Phys. Med. & Biol.*, vol. 62, no. 17, 2017. [3] R. Xu and M. O'Reilly, *Phys. Med. & Biol.*, vol. 63, no. 14, 2018.

## Comparing vibrometer and accelerometer measurements of gradient field induced vibration in an MRI

Idan Nemirovsky, Christine M. Wawrzyn, Daniel J. Martire, Colin M. McCurdy, William B. Handler, and Blaine A. Chronik

*The xMR Labs, Physics and Astronomy, Western University, London, ON, Canada*

**Introduction:** Measuring the eddy current induced vibration caused by time-varying gradient fields in an MRI is an essential component in determining MR compatibility of medical devices [1]. To date, laser Doppler vibrometry (LDV) is considered the gold standard method to measure such vibrations, however, it is desirable for implantable medical devices to be tested in a tissue mimicking phantom, making such optical measurements of vibration difficult. An alternative method uses an accelerometer adhered directly to the device which does not require “line-of-sight” access to the device under test. This study aims to validate the use of accelerometers for vibration testing by analyzing the displacement differences compared to an LDV in an MR environment.

**Methods:** Experiments were performed at 3T (Siemens Prisma, Robarts Research Institute, Western University) using a stainless-steel disk with a 50 mm diameter and 3 mm thickness. The disk was positioned parallel to the scanner bed on a 2.5 cm block of synthetic ballistic gelatin in a location in the bore measured to have a maximal  $\text{dB}_y/\text{dt}$  ( $X=0$ ,  $Y=+24$  cm,  $Z=+30$  cm). A coronal pulse sequence was used to generate 8 discrete tones at frequencies of 200-1500 Hz with gradient amplitudes ranging from 20-75 mT/m respectively. In addition, the disk was also exposed to a linear frequency chirp from 200 to 2000 Hz at a constant amplitude of 15 mT/m. Vibration was measured with a Laser Doppler Vibrometer (LDV; OFV-505/5000, Polytec GmbH, Germany) positioned on a tripod at the edge of the scanner bed. The laser reflected off a 45-degree mirror and focused on a 0.6-gram miniature single axis piezoelectric accelerometer (MPA; 352A21, PCB Piezotronics, USA) adhered to the edge of the disk using petro wax. Data was collected with a 12.8 kHz sampling rate for 3.2 seconds per frequency.

Displacement at each target frequency was compared by the LDV and MPA using Matlab (2018a). Data was filtered by applying zero-phase digital filtering using a bandwidth of  $\pm 50$  Hz. After filtering, the MPA data was integrated twice using Simpson’s rule (sampling rate of 10.24 kHz) to obtain dynamic displacement, then filtered again to remove any low frequency noise and buildup errors. A linear sinusoidal fit was applied to the resulting displacement signals and the amplitude and its standard deviation were obtained using a 95% confidence interval linear sinusoidal fit. The frequency sweep was discretized into linearly spaced frequencies from 200-2000 Hz and compared to the discrete frequency measurements by scaling all data to the exposure  $\text{dB}/\text{dt}$ .

**Results:** The applied signal processing method results in a maximum residual between the two measurement methods of  $1.7 \pm 0.3$   $\mu\text{m}$  at the gradient pulse frequency of 200 Hz, which corresponded to a 1.5% difference. The scaled frequency sweep measurements also matched the discrete values obtained for all frequencies.

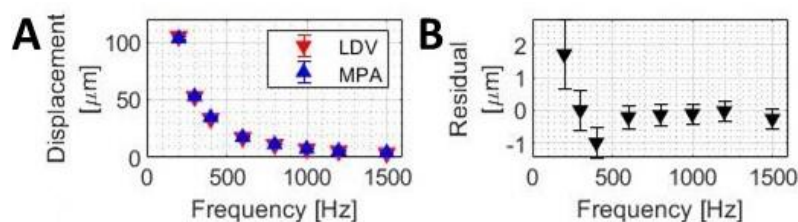


**Figure 1.** Disk displacement (A) and displacement residuals (B) measured at discrete gradient frequencies.

**Conclusions:** This study validates the use of accelerometers as a tool to measure gradient field induced vibration in an MR scanner. Displacement measurements using a miniature piezoelectric accelerometer and a laser Doppler vibrometer were found to agree to within  $1.7$   $\mu\text{m}$  in the MR system at all frequencies tested.

**References:** [1] ISO/TS 10974. Assessment of the safety of magnetic resonance imaging for patients with an active implantable medical device; 2018.

## Varying microstructural properties of a 3D printed phantom for diffusion MRI validation Farah N.

Mushtaha, Tristan K. Kuehn, John Moore, Ali R. Khan, Corey A. Baron

Robarts Research Institute, Western University, London, Canada

**Introduction.** Diffusion MRI has the potential to quantify histological features of the brain at a micrometre scale <sup>1</sup>. However, there is no “ground truth” to validate its techniques. We have recently proposed a novel phantom produced using fused deposition modeling (FDM) 3D printing with a composite material consisting of rubber-elastomeric polymer and a PVA component (PORO-LAY <sup>2</sup>). When immersed in water, the PVA dissolves, leaving behind small pores that can mimic diffusion characteristics of axons. Different printing parameters such as print-head temperature can have an effect on the microstructural properties of the phantom. In this study, we investigate how diffusion tensor MRI (DTI) derived metrics of the phantom vary with different print-head temperatures.

**Methods.** 3 phantoms were created by printing 11 mm radius cylinders with 100  $\mu\text{m}$  thick layers of parallel lines to mimic linear fibres (Fig. 1). The phantoms were produced at three different print temperatures: 215°C (low), 225°C (nominal), and 235°C (high). The phantoms were immersed in water for 168 hrs and stacked in a test tube with distilled water for imaging. Diffusion MRI was implemented at 9.4 T using 120, 60, and 20 directions at  $b=2000$ ,  $b=1000$ , and  $b=0$   $\text{s}/\text{mm}^2$  respectively,  $\text{TE}/\text{TR}=37/2500$  ms,  $\text{FOV}=200\times 200$   $\text{mm}^2$ , 0.7 mm isotropic in-plane resolution, 6 axial slices (3 mm, one per phantom), and scan time 8.5 min per each scan.

MRtrix <sup>3</sup> was used to compute DTI-derived metrics (axial diffusivity, AD; radial diffusivity, RD; fractional anisotropy, FA). To investigate phantom stability, an identical scan and analysis was performed 11 days later.

**Results.** AD and RD had a strong observed dependence on print temperature within both subsamples. RD had an almost linear relationship with the printing temperature. The repeated scan showed phantom stability within optimal and high temperatures (Fig. 2)

**Conclusion.** The strong dependence of diffusion properties of the phantoms on print-head temperature suggests that customization of diffusion properties on this phantom may be possible. The observed results from the scan performed 11 days later illustrates the strong stability of the phantoms in water over time for optimal and high temperatures. Future work should investigate the effect of other printing parameters and experiment with more complex brain-mimetic geometries.

**Acknowledgements.** This work was supported by the Canada First Research Excellence Fund, Brain Canada, and Discovery Grants from the Natural Sciences and Engineering Research Council (NSERC).

**References.** [1] Alexander D.C, *et al.* *NMR in Biomedicine*. 2017; e3841. doi:10.1002/nbm.3841. [2] Abu-Sardanah S.O, *et al.* *Proc. SPIE*. 10573, 2018. [3] Westin C, *et al.* *ISMRM '97. Vancouver Canada*, (1997, April), 1742. [4] Tournier J.-D, *et al.* *NeuroImage*. 2007; 35(4):459–1472.

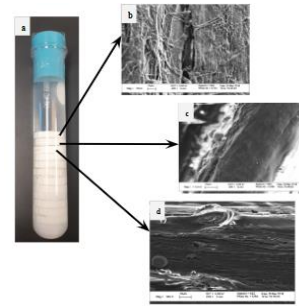


**Figure 1.** a) 12 phantoms with varying parameters in a test tube. b) SEM image of a phantom created with low print-head temperature. c) SEM image of a phantom with nominal print-head temperature. d) SEM image of a phantom with high print-head temperature.

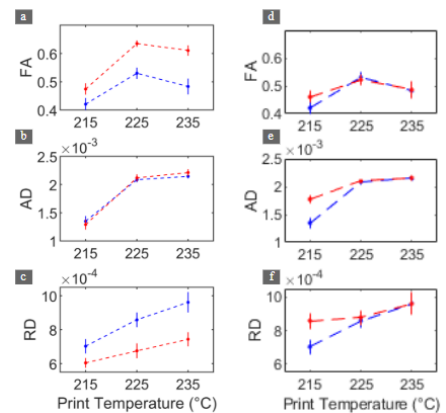


**Figure 2:** DTI-derived metrics as a function of print temperature. Error bars indicate standard deviation. In a, b and c, blue line represents values derived using 60 and 20 directions at  $b=1000$  and  $b=0$ , respectively. Red line represents values using 120 and 20 directions at  $b=2000$  and  $b=0$ , respectively. a) Fractional anisotropy vs printing temperature b) Axial diffusivity vs printing temperature. c) Radial diffusivity vs printing temperature. In d, e, and f, the blue line represents the first scan performed, and the red line represents the scan performed 11 days later. d) Fractional anisotropy vs printing temperature e) Axial diffusivity vs printing temperature. f) Radial diffusivity vs printing temperature.

## Hypoxia Standardization Phantom to Quantify Variation in Hypoxia Measurement with Positron Emission Tomography across Multiple Centres

B. Driscoll<sup>1</sup>, D. Jaffray<sup>1,2,3</sup> and I. Yeung<sup>1,2,3</sup>

(1) QIPCM, TECHNA Institute, University Health Network., Toronto, Canada (2) Radiation Medicine Program, Princess Margaret Cancer Center, Toronto, Canada (3) Dept. Radiation Oncology, University of Toronto, Toronto

**Introduction:** Detection of tumour hypoxia with positron emission tomography (PET) imaging with <sup>18</sup>F-labelled nitroimidazole-based hypoxia agents (e.g. fluorazomycin-arabinoiside [FAZA]) is a promising clinical method for stratification of patients in personalized cancer medicine. The quantification of tumour hypoxia, known as the hypoxic fraction (HF), typically relies on a count of the number of voxels above a predetermined threshold activity over the tumour. There is currently no consensus as to how the threshold is chosen and variation in scanner characteristics will affect the uptake distribution which will directly affect HF calculation. We have built a ‘Hypoxia Standardization Phantom’ to quantify the variation of HF measurements across multiple centres within the NIH Quantitative Imaging Network (QIN).

**Methods:** To simulate various levels of tumour hypoxia as well as reference regions for comparison (i.e. blood, muscle) a phantom was developed consisting of a set of two plates separated by 2mm acrylic rods of different spacing densities to create negative space to simulate different uptakes inside a phantom filled with F<sup>18</sup> and water. The hypoxia standardization phantom contains four regions; a ‘normoxic’ surrogate region (40% filled with rods) and 3 regions representing various ‘hypoxic tumour’ geometries.



Figure 1: Design and fabrication of the Hypoxia Standardization PET phantom

In order to evaluate the differences in hypoxia quantification between different scanning protocols and scanners a set of standard imaging parameters was generated and the phantom was then circulated among seven different sites (and 9 PET scanners) in North America as part of a QIN Challenge launched by our group.

**Results:** The hypoxia phantom produced a range of histograms which resemble those of clinical tumours, having both ‘normoxic’ and ‘hypoxic’ regions (Figure 2).

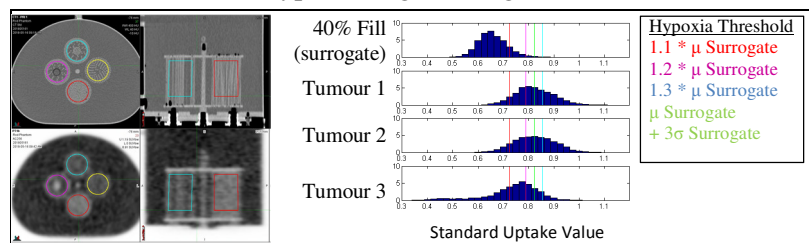
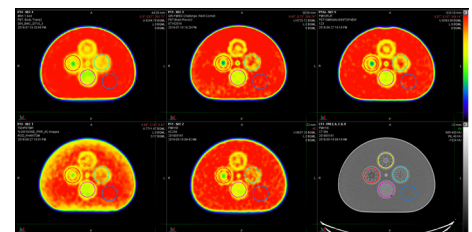


Figure 2: Hypoxia Quantification using different thresholds using the hypoxia standardization phantom.

The three simulated tumour regions produced a suitably wide range of hypoxic fractions ranging from 5 to 95% depending on the threshold tested. While the QIN challenge is still in progress, to date 5 institutions have scanned the phantom using 3 sets of reconstruction protocols (Figure 3 upper). For the same region of interest and noise based thresholding technique the range of calculated hypoxic fractions of the phantom ranged dramatically between 18.9 and 99.2 % for one region (Figure 3 lower).

**Conclusions:** The hypoxia standardization phantom created and utilized for the QIN hypoxia quantification challenge is quantitative and it simulates clinical imaging of hypoxic tumors. This phantom will be able to help quantify differences in hypoxia measurements between sites and is sensitive enough to detect significant differences in hypoxic fraction calculation even on the same scanner with different reconstruction techniques.

Using the 40% filled surrogate region, hypoxia thresholds were calculated using a range of literature values between 1.1 and 1.3 times the surrogate as well as noise based techniques ( $\mu + 3\sigma$ ).



Region	Mean HF	Max HF	Min HF	Std HF
Tumour 1	73.9%	99.2%	18.9%	21.6%
Tumour 2	66.7%	98.8%	13.8%	21.7%
Tumour 3	44.0%	73.4%	10.3%	15.2%

Figure 3: Preliminary Multi-centre results show a wide variation of hypoxic fractions across scanners and reconstruction protocols.

## Selective Laser Melted 2D Focused Anti-Scatter Grids for Cone-beam CT

Santiago F Cobos,<sup>1</sup> Hristo N Nikolov,<sup>2</sup> Steven I Pollmann,<sup>2</sup> and David W Holdsworth,<sup>1,2,3</sup>

<sup>1</sup>Department of Medical Biophysics, Western University, <sup>2</sup>Robarts Research Institute, <sup>3</sup>Department of Surgery, Western University, London, Ontario, Canada

**Introduction:** Cone-beam CT (CBCT) systems acquire clinically relevant volumetric data faster than fan-beam or multi-slice CT due to their optimized beam geometry. For such systems, scattered radiation remains as the main source of image quality degradation leading to increased noise, image artifacts, and CT number inaccuracies. Recent advances in metal additive manufacturing allow the production of highly focused anti-scatter grids (2D-ASGs) that can be used to reduce scatter intensity while preserving primary radiation transmission. Here we present the first implementation of a full-size 2D-ASG for flat-panel CBCT including grid-line artifact removal and related improvements in image quality.

**Methods:** A 245x294x10 mm 2D-ASG was manufactured from chrome-cobalt using high resolution powder-bed selective laser melting (AM400, Renishaw plc) – *Fig. 1.a*. The ASG had a square profile with a pitch of 9.09 lines/cm and 10:1 grid ratio. The nominal 0.1 mm grid septa were focused to a 732 mm x-ray source to increase primary x-ray transmission and reduced grid line shadowing at the detector. Selective laser melting allowed structural stability of the ASG with no need for additional inter-septal support. The 2D-ASG was coupled to a 0.139 mm element pitch flat-panel detector (DRX-Plus, Carestream Health) and proper alignment was confirmed by consistent grid line shadow thickness across the whole detector array. A 140 mm CBCT image quality phantom was imaged using a rotary stage and a ceiling mounted x-ray unit (Proteus XR/a, GE Medical Systems, 80kVp, 0.5mAs). Grid line artifacts were removed using a combination of traditional gain-offset corrections and spatial frequency Fourier filtering in the Radon space.<sup>1</sup> Projections were reconstructed using a Parker weighted FDK algorithm and voxels were spatially-averaged to 357x357x595  $\mu\text{m}$  to improve signal-to-noise characteristics of the volume. Finally, the phantom was imaged under the same CBCT conditions but with no 2D-ASG to compare image-quality parameters accurately and quantitatively.<sup>2</sup> No additional anti-scatter (i.e. air-gap, bowtie filtration) strategies were used to evaluate the effects in image quality caused by the 2D-ASG alone.

**Results:** The full-size 2D-ASG prototype was successfully designed and manufactured using selective laser melting. CBCT image quality improvements using the 2D-ASG included: an overall CNR increase across the volume, including low-contrast inserts inside the artifact characterization section of the QA phantom (*Fig 1.b*) and a reduction  $\sim 300$  HU of cupping artifact in axial profiles of water-filled cross sections of the phantom. (*Fig. 1.c*) Advanced imaging processing strategies to remove grid line artifacts did not affect spatial resolution (*Fig. 1.d*) or geometric accuracy of the system.

**Conclusions:** Selective laser melting can be used to manufacture highly efficient 2D focused ASGs that can be easily coupled to clinical flat-panel detectors. The implementation of ASGs in CBCT leads to reduced scatter related artifacts, improved CT number accuracy, and enhanced CNR with no increased equivalent dose to the patient. Further image quality might be achieved with a combination of scatter correction algorithms and iterative reconstruction strategies. Finally, clinical applications where other scatter removal strategies are unfeasible now might achieve superior soft-tissue visualization and quantitative capabilities.

**References:** 1. B. Münch et al., "Stripe and ring artifact removal with combined wavelet—Fourier filtering," *Optics express* **17.10**, 8567-8591 (2009) 2. Y. Du, Louise et al., "A quality assurance phantom for the performance evaluation of volumetric micro-CT systems," *Physics in Medicine and Biology* **52**, 7087-7108 (2007)

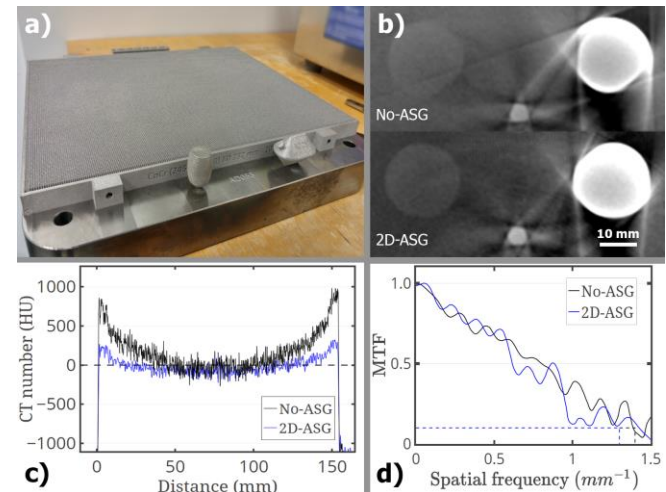


**Fig. 1:** a) Selective laser melted full-size 2D-ASG. b) Artifact characterization section of the QA phantom – CNR low contrast insert 0.6 no-ASG vs 1.9 2D-ASG. c) Uniformity of radial signal profiles across water-filled region. (d) Slanted edge MTF 10% level reached at 1.6 no-ASG; 1.4 2D-ASG.

## A novel microfluidic device for real-time microscopic imaging of endothelial cell responses to laminar and disturbed fluid flow

Daniel Lorusso, Kayla Soon, Hristo N. Nikolov, Jaques S. Milner, John R. de Bruyn, J. Geoffrey Pickering, S. Jeffrey Dixon, David W. Holdsworth, Tamie L. Poepping.

The University of Western Ontario, London, Canada

**Introduction:** Fluid shear stress is a form of mechanical stimulation that is critical to the normal functioning of vascular endothelium. Disturbed (non-laminar) fluid flow has been implicated in endothelial dysfunction, which contributes to atherosclerosis. Our goal was to observe the immediate responses of endothelial cells to disturbed flow. In this study, we developed and validated a novel microfluidic device for applying laminar and disturbed flow to live endothelial cell cultures, while ensuring compatibility with real-time optical microscopy and photometry. Using this device, we performed fluorescence imaging of changes in cytosolic calcium – a mediator involved in transducing mechanical signals in many cell types, including endothelium.

**Methods:** The microfluidic device was custom designed and fabricated from silicone polymer (PDMS) (Fig. 1 shows micrograph of device). Flow introduced through the top inlet established laminar flow within the imaging chamber. Flow through the two side inlets generated high-velocity jets that impinged on each other within the flow chamber to create disturbed flow. Fluid velocities and flow patterns were modeled with computational fluid dynamics (CFD) software and determined experimentally by imaging at high speed with a laser-illuminated micro-particle image velocimetry (micro-PIV) system. To investigate the calcium responses, human aortic or human umbilical vein endothelial cells were seeded into the device, loaded with fluorescent calcium probe fura-2 and monitored by fluorescence ratio imaging.

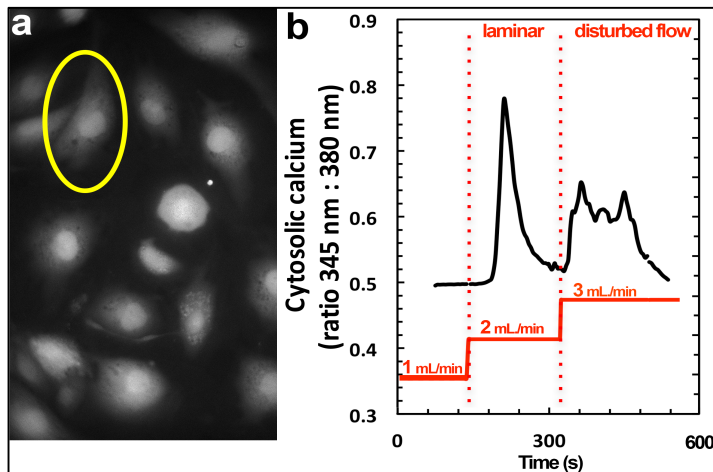
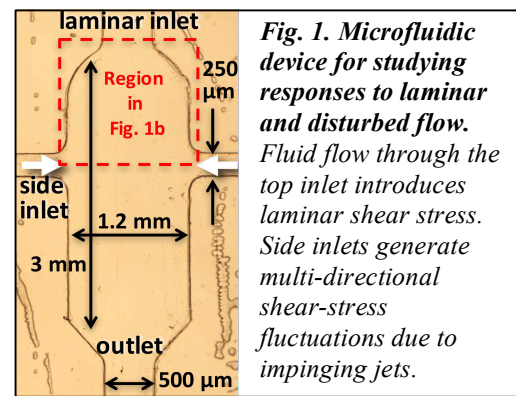


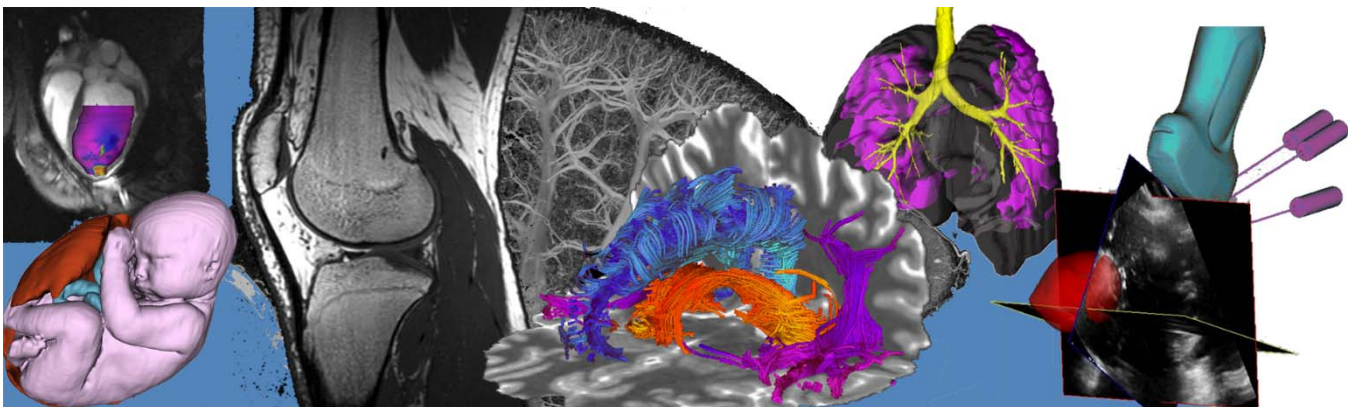
**Fig. 2. Cytosolic calcium in single human aortic endothelial cell subjected to laminar and disturbed flow.** (a) Fluorescence image of cells loaded with fura-2. (b) Time course of cytosolic calcium in single cell (indicated in a), stimulated with laminar flow at 1 or 2 mL/min and disturbed flow at 3 mL/min.

**Results:** Using CFD modeling and micro-PIV, velocity maps were generated for our device and used to calculate wall shear stress vectors for both laminar and disturbed flow. In preliminary studies, cytosolic calcium transients in endothelial cells were observed in response to changes in laminar and disturbed flow. Cells loaded with fura-2 were imaged with the flow chamber (Fig. 2a). All cells were first subjected to an initial laminar flow stimulus, which induced a transient elevation of calcium in most cells. Subsequently, changes in laminar flow from 1 to 2 mL/min (inlet flow rates) induced transient elevation of calcium (Fig. 2b, left). In contrast, a change from laminar to disturbed flow (2 to 3 mL/min) induced a more sustained elevation of calcium (Fig. 2b, right).

**Conclusions:** We have developed and validated a microfluidic device capable of – for the first time – delivering clinically relevant laminar and multi-directional disturbed flow to live-cells during real-time imaging. This device is compatible with a wide-range of microscopy techniques. Our preliminary studies suggest that endothelial cells may display distinct cytosolic calcium responses to changes in laminar and disturbed flow.

# Oral Presentation Abstracts

## Session 2: Machine Learning



## Texture-Based Prostate Cancer Classification on MRI: How Does Inter-Class Size Mismatch Affect Measured System Performance?

R. Alfano<sup>1,2,8</sup>, D. Soetemans<sup>1</sup>, G. S. Bauman<sup>2,6</sup>, M. Gaed<sup>3,4</sup>, M. Moussa<sup>4</sup>, J. A. Gomez<sup>4</sup>, J.L. Chin<sup>5,6</sup>, S. Pautler<sup>5,6</sup>, A. D. Ward<sup>1,2,6,8</sup>

1. Baines Imaging Research Laboratory, 2. Department of Medical Biophysics 3. Robarts Research Institute, Depts. of 4. Pathology and Laboratory Medicine, 5. Surgery, 6. Oncology, 7. Biomedical Engineering Graduate Program 8. Lawson Health Research Institute, London, Ontario, Canada

**Introduction:** Prostate cancer (PCa) is one of the most prevalent cancers in men. Diagnosis depends on a transrectal ultrasound (TRUS)-guided biopsy, which has a high false negative rate and is confounded by sparse sampling. Multi-parametric magnetic resonance imaging (mpMRI) maps the prostate in 3D, but has inter-observer variability in lesion localization and scoring. Computer-aided diagnosis (CAD) systems have been developed as a potential solution and have been shown to boost diagnostic accuracy. In our previous work towards classification of malignant vs. benign regions on mpMRI, healthy tissue was manually delineated by approximately matching the size and shape of the tumour on the contralateral side of the prostate [1]. In this project, we aim to investigate the performance of a CAD model trained on regions generated without any selection or spatial bias. Furthermore, we wish to interrogate the effect of inter-class area mismatch and how it affects overall system performance.

**Methods:** We used a prostatectomy cohort of 61 patients with T2-weighted MRIs and apparent diffusion coefficient (ADC) maps. Genitourinary pathologist-verified contours of malignant regions of interest (ROIs) on histology were mapped to the mpMRI using our previously developed registration pipeline [2]. Healthy tissue was generated through the development of an unbiased, automated, iterative sampling algorithm. In each ROI, we extracted 22 first and 33 second order texture features. We trained a logistic linear classifier (LOGLC), support vector machine (SVC), k-nearest neighbour (KNN) and random forest classifier (RFC) using 1-10 features from forward feature selection, for a total of 40 different classifiers. We performed 4-fold and leave-one-patient-out (LOO) cross validation and reported the misclassification rate (MCR), false positive rate (FPR), and false negative rate (FNR) for the classifier with the highest area under the receiver operating characteristic curve (AUC) for both the peripheral zone (PZ) and central gland (CG). Furthermore, healthy tissue was eroded radially by  $\sim 0.3\text{mm}$  (1 px.) iteratively and system performance was plotted against the number of erosions.

**Results:** Error metrics depicting system performance are shown in Figure 1. The highest AUCs recorded in the PZ and CG were 0.80 and 0.82 respectively for LOO cross validation. In a 4-fold cross validation analysis of malignant vs. benign tissue with healthy tissue eroded iteratively the PZ and CG models displayed a bias as the area difference between healthy ROIs and malignant ROIs grew larger (Fig. 2). Qualitatively, our systems correctly identified all benign and malignant regions with the primary focus being of Gleason 3+4 in the PZ (Fig. 3a-c) and Gleason 3 in the CG (Fig. 3d-f).

**Conclusions:** A computer aided diagnosis system for classifying prostate lesions on mpMRI classified malignant vs. benign regions with  $\text{AUC} \geq 0.8$  within the PZ and CG. Although no lesion size features were used, mean system performance artificially increased as a function of size differences between malignant and benign regions, suggesting the importance of size matching when conducting radiomics studies using texture features.

**References:** [1] R. Alfano SPIE, 10575, 2018. [2] E. Gibson IJROBP 96(1), 188-196, 2016

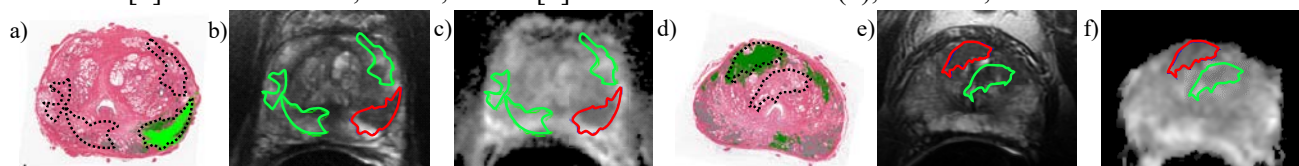


Figure 3: Visual representations of region-based classification. Regions outlined with red indicate true positive lesions and green indicate true negative lesions. Regions coloured in light green and dark green represent pathologist-based contours of Gleason Grade 3+4 and Gleason Grade 3 respectively. From left to right we have a (a) whole mount histology section, (b) T2W image, and (c) ADC map for one patient, and a (d) whole mount histology section, (e) T2W image, and (f) ADC map for a different patient in our dataset.

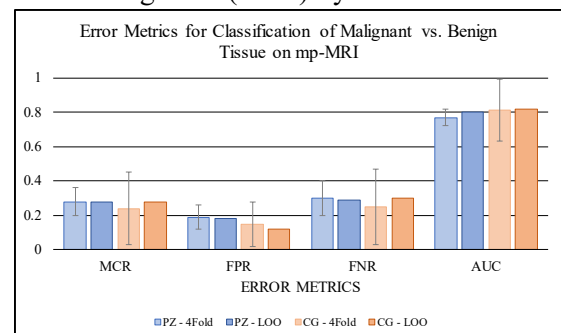


Figure 1: Error metrics for classification of malignant vs. benign tissue for 4-fold and leave-one-patient-out cross validation.

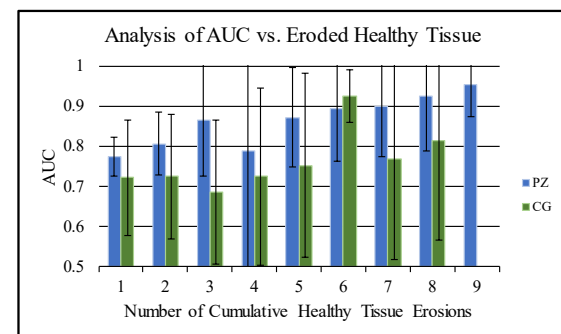


Figure 2: Plot of AUC for classification of malignant vs. benign tissue as a function of cumulative healthy tissue erosions. At each stage in the erosion, 40 classifiers are trained in 4-fold cross validation and the classifier with the highest AUC was reported.



## Ventricular and total intracranial vault segmentations for brains with extensive atrophy using three-dimensional convolutional neural networks

Ntiri E E\*, Goubran M\*, Holmes M, Akhavan H, Adamo S, Ramirez J, Gao F, Ozzoude M, Scott C, Smith E, MacIntosh B, Dowlatshahi D, Lawrence-Dewar J, Kwan D, Marras C, Lang T, Symons S, Bartha R, Strother S, Moody A, Swartz R, Black SE *Sunnybrook Research Institute, Hurvitz Brain Sciences Program, Toronto, ON, Canada*

\*These authors contributed equally to this work

**Introduction:** Differential rates of atrophy in the ventricles and total intracranial vault (TIV) can be used as biomarkers of cognitive decline in dementia. We developed 3D convolutional neural networks (CNNs) to segment the ventricles and TIV using multi-contrast inputs.

**Methods:** A total of 540 subjects from the ONDRI and CAIN studies were recruited for training and validation of the ventricular and TIV segmentation algorithms. We implemented a U-net architecture that utilizes both contracting and expanding pathways with pooling and upsampling operators, respectively [1]. Our networks were validated against established state-of-the-art techniques on a separate test set of 50 subjects. The TIV segmentation was compared against the Brain Extraction Tool (BET), Multi-cONrast brain STRipping (MONSTR), and Deep Extraction, using the Dice similarity coefficient and volume correlations. The ventricular model’s performance was compared against Freesurfer’s segmentation.

**Results:** Our networks had the highest volume correlations ( $r=0.99$ ,  $p>0.0001$ ) and Dice similarity ( $d > 0.9$ ) with ground truth for TIV (Fig. 1 & 2) and ventricular segmentation (Fig. 3 & 4). The segmentations produced by the networks were robust against vascular and neurodegenerative changes, including the presence of strokes and white matter hyperintensities. Our networks successfully segmented the ventricles and TIV after the addition of noise and downsampling to assess performance against potential clinical-grade datasets.

**Conclusions:** Our 3D CNN has potential to be used to study structural biomarkers in patients with significant atrophy. Future studies will involve training the models on other datasets with more variant disease groups and testing on larger cohorts.

### References:

[1] Ronneberger, O., Fischer, P., Brox, T., 2015. U-Net: Convolutional Networks for Biomedical Image Segmentation, in: Lecture Notes in Computer Science. pp. 234–241.

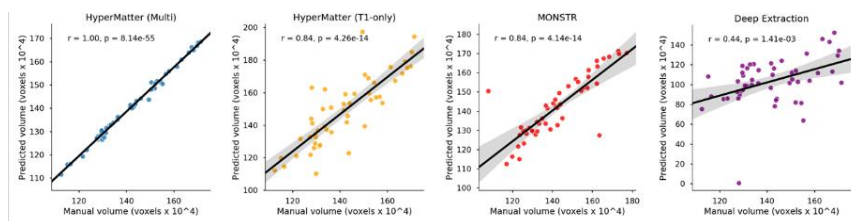


Fig. 1 Correlations between the manually segmented TIV volumes and volumes generated through model predictions. Pearson R. correlation coefficients and p-values are shown for each test.

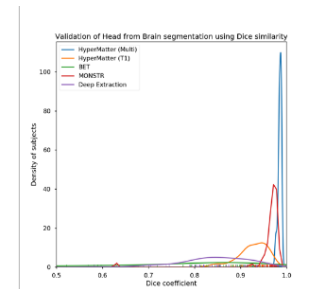


Fig. 2 Distribution of Dice coefficients between manual TIV labels and models

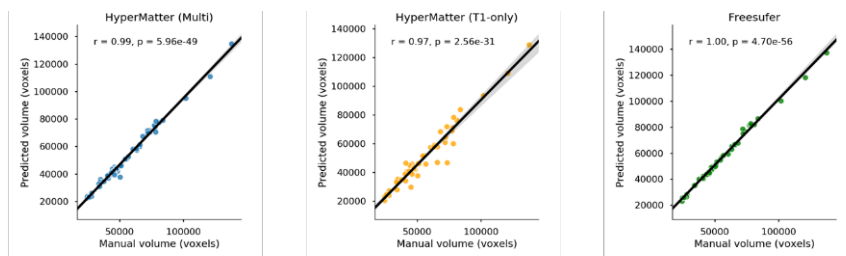


Fig 3. Correlations between the manually segmented ventricular volumes and volumes generated for each model. Pearson R. correlation coefficients and p-values are shown for each model.

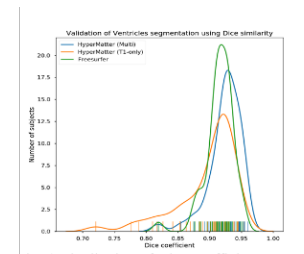


Fig. 4 Distribution of Dice coefficients between manual ventricular labels and models

**Automatic High-Grade Prostate Cancer Detection on Digital Histopathology Imaging**

W. Han<sup>1,2,6</sup>, C. Johnson<sup>1</sup>, M. Gaed<sup>3</sup>, J. A. Gomez<sup>5</sup>, M. Moussa<sup>5</sup>, J. L. Chin<sup>4,5</sup>, S.E. Pautler<sup>4,5</sup>, G. Bauman<sup>2,5</sup>,  
A. D. Ward<sup>1,2,5,6</sup> (research supervisor)

<sup>1</sup>Baines Imaging Research Laboratory, London Regional Cancer Program; Depts. of <sup>2</sup>Medical Biophysics, <sup>3</sup>Pathology, <sup>4</sup>Surgery, <sup>5</sup>Oncology, Western University; <sup>6</sup>Lawson Health Research Institute, London, Canada

**Introduction:** Automatic high-grade cancer detection on radical prostatectomy specimens can benefit pathological assessment for prognosis and post-surgery treatment decision making. There is an unmet need for such a system that is sufficiently fast and parallelizable so as to be integrated into the clinical pathology workflow, and is validated using whole-slide images.

**Methods:** 299 mid-gland whole-mount slide images (WSIs) were obtained from 71 radical prostatectomy patients. The surgically removed prostates were sectioned at  $4\mu\text{m}$ , stained with hematoxylin and eosin (H&E) and scanned at 20X ( $0.5\mu\text{m}/\text{pixel}$ ). Computations were conducted independently on  $480\mu\text{m} \times 480\mu\text{m}$  sub-images covering each WSI completely. 13 WSIs from 3 patients were used for system tuning and a separate 68 patient data set comprising 1,248,503  $480\mu\text{m} \times 480\mu\text{m}$  sub-images across 286 whole-slide images (WSIs) was used for validation. Computation proceeded as follows. (1) Automatic labeling of each tissue component as nucleus, lumen, and stroma/other using our previously developed methods. (2) Extracting 13 (for cancer detection) or 37 (for cancer grading) top-ranked first- and second-order statistical features from labeled tissue component sub-images. (3) Classifying (a) cancerous vs. non-cancerous (b) high-grade vs. low-grade (Gleason Grade (G) 4 vs. G3, G4 and G5 vs. G3, and G4- or G5-involved [e.g. G4+5, G4+3] vs. G3) sub-images using supervised machine learning with three different classifiers (Fisher classifier, Logistic classifier [Loglc], and support vector machine [SVM] classifier). (4) Combining cancer classification and grading, where a tumour has to be correctly detected and graded as high vs. low-grade to be considered as true positive and true negative respectively. (5) Validating the system against expert-drawn contours via leave-one-patient-out cross-validation. All relevant ROIs were used throughout all WSIs, and error metrics were calculated on a per-tumour basis, with correct detection of high-grade cancer meaning that at least one ROI in the tumour has been correctly classified as high grade.

**Results:** Fig.1 (bottom) shows the manual contours with a colour code indicating which lesions were correctly detected and classified. The best observed performance metrics for high-grade cancer detection are shown in Fig. 2. The system had error rates of 19.4%, 19.5%, 23.4% for G4, G4 and G5, G4 and G5 with mixed grades, respectively. Note the higher FNR in the mixed grade experiment. More than 50% of the false negatives are G3+4 tumours with size less than or equal to  $0.23\text{ mm}^2$ , which is negligible compared to Epstein's  $0.2\text{ cm}^3$  volume threshold for clinical significance (area of  $34\text{ mm}^2$ ). The processing time with an un-optimized, non-parallel, predominantly Matlab based implementation is approximately 25 mins/WSI for mid-gland prostate tissue sections.

**Conclusion:** In general, our system demonstrated good performance in high-grade cancer detection on mid-gland prostate WSIs, and was validated on a large dataset.

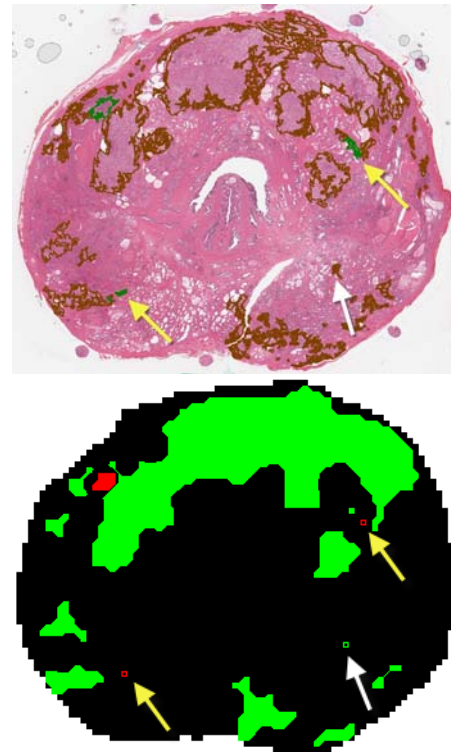


**Fig. 1:** WSI (top) and map showing tumour classifications (bottom). Colour contours (top) are the expert-drawn reference standard (brown and green indicate low and high-grade, respectively). Green and red labels (bottom) mean low and high-grade, respectively. Filled regions are true positives and non-filled regions are false negatives. The yellow and white arrows indicate missed high and low-grade tumours.

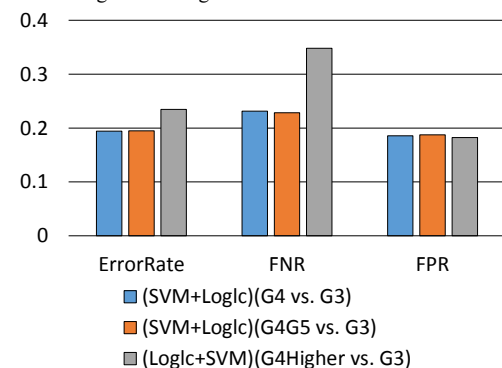


**Fig. 2:** Performance metrics. (A+B) indicates classifier A was used for detection and B for grading.

# Multi-Contrast Carotid Lumen-wall Segmentation Using Deep Learning

Anna Danko,<sup>1-3</sup> Roberto Souza,<sup>2-3</sup> Richard Frayne<sup>1-3</sup>

<sup>1</sup>Medical Sciences Graduate Program, <sup>2</sup>Clinical Neurosciences and Radiology, Hotchkiss Brain Institute, University of Calgary, Calgary, Canada; <sup>3</sup>Seaman Family MR Research Centre, Foothills Medical Centre, Calgary, Canada

**Introduction:** Multi-contrast magnetic resonance (MR) imaging has been recommended for its potential in carotid artery imaging research as it can resolve several plaque components and provide evidence of possible increased stroke risk.[1] However, the standard measure of evaluating stroke risk is still carotid luminal stenosis, despite acknowledgement that it alone is an insufficient indicator.[2] Automatic segmentation would facilitate the use of vessel wall features in patient assessment. We propose a deep-learning carotid vessel wall segmentation model, and demonstrate its effectiveness on multi-contrast MR images.

**Methods:** Data was collected from 26 atherosclerosis patients imaged locally as part of the AIM-HIGH MR substudy. [3] One AIM-HIGH patient was excluded from training to act as a test subject. Three additional test images, acquired with a DANTECube sequence, were obtained from an ongoing local study (CARDIS). AIM-HIGH data included four contrasts: T1- (with and without contrast agent), T2- and PDW-weighting (T1W, CET, T2W, and PDW, respectively). AIM-HIGH segmentations were provided by the Vascular Imaging Laboratory (Seattle, WA) [3] and include the lumen and outer wall of either the left or right carotid artery (common carotid, bifurcation point, internal carotid artery). Each slice was divided into five patches, and data augmentation techniques were applied during training.[4] Corresponding slices from different image contrasts were treated as independent images by our network. Data was trained on a U-Net.[4]

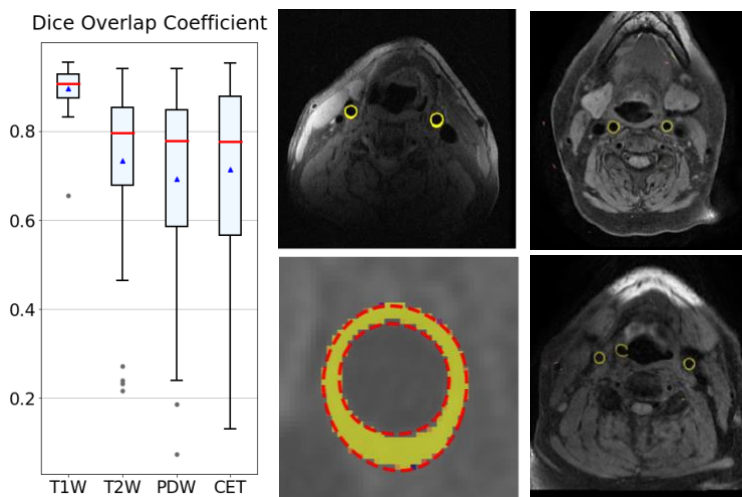


Fig 1. Left: Dice scores between AIM-HIGH test subject scans from different image contrasts. Middle: an AIM-HIGH T1-weighted image, overlaid with a segmentation generated by our model. Below, our model's output (yellow) is compared with the ground truth (red). Right: predicted carotid segmentations on two CARDIS subjects.

CARDIS images contained more false positives, but had promising results on select slices, suggesting the network was learning some features that are not image contrast- or domain- specific. We are currently investigating additional experiments using multi-contrast images, using adversarial networks.[6] The goal is to develop a segmentation tool trained on AIM-HIGH data that can produce high-quality carotid artery segmentation on CARDIS images, without retraining. We acknowledge that domain-invariant segmentation is primarily useful for features which are salient across all contrasts, such as the vessel wall. However, whether the goal is measuring stenosis or identifying plaque composition, vessel wall segmentation remains an unavoidable precursor, and therefore would benefit those applications.

**References:** [1] Saba, L., *et al.*, *AJNR* 2018; **39**: E9-E31; [2] Au, K. *et al.*, *Arthritis Rheum*, 2011; **63**: 2078-90; [3] Zhao, X.Q., *et al.*, *Am J Cardiol* 2014; **114**:1412-1419; [4] Ronneberger *et al.* CoRR 2015 absL/1505.04597 [5] Francois C, *et al.* Keras 2015, <https://keras.io>; [6] E. Tzeng *et al.*, *Proc CVPR IEEE* 2017:2962-2971

## Tissue Segmentation in Multi-Weighted Breast MRI using a Deep Learning Unet

Gregory Kuling<sup>1</sup>, Homa Fashandi<sup>2</sup>, YingLi Lu<sup>2</sup>, Hongbo Wu<sup>1</sup>, and Anne L. Martel<sup>1,2</sup> <sup>1</sup>Department of Medical Biophysics, University of Toronto, Toronto, Ontario M4N 3M5, Canada <sup>2</sup>Physical Sciences, Sunnybrook Research Institute, Toronto, Ontario M4N 3M5, Canada

**Introduction:** Since the 1990s, the mortality rate of breast cancer has dramatically dropped due to screening programs that catch abnormalities at an early stage, resulting in more abundant treatment options [1]. Women of high risk (HR) are screened in Ontario using mammography and magnetic resonance imaging (MRI), and a large database of HR patient scans have been collected at Sunnybrook Research Institute. We hypothesize that this database of nearly 10 thousand scans can be exploited to predict cancer risk more accurately based on previously researched risk indicators, and by developing new indicators using machine learning and artificial intelligence. This will benefit HR women immensely, relieving stress and costs of the health care system for HR women of low risk, and informing higher risk women to try preventative measures, such as chemo-prevention as well as other options. In recent years, there has been a resurgence of interest in risk prediction based on breast density (BD) and background parenchymal enhancement (BPE) observed in MRI. BD is defined as the ratio of fibroglandular tissue (FGT) volume to the total breast volume, while BPE is an enhancement pattern observed in healthy FGT during dynamic contrast enhanced MRI (DCE-MRI). These indicators have risk predictions based on discrete qualitative categories, therefore there is a need for risk prediction based on an accurate continuous quantification of BD and BPE. [2] We present here, a machine learning algorithm for quantifying BD and BPE based on the segmentation of FGT and fat tissue in DCE-MRI of the Breast. The UNet [3] algorithm has been very efficient at segmenting images based on supervised training.

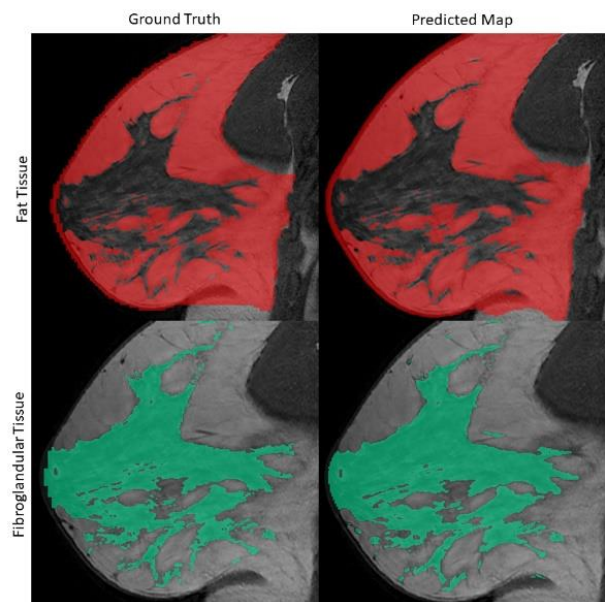
**Method:** We performed a classical machine learning experiment using a hyperparameter grid search (Table) with 98 patient scans split into train/validation/test sets. This algorithm utilizes 2D T1w images with and without fat suppression (FS and WOFS) of the breast acquired in the sagittal plane. To segment the breast, we manually segmented the breast tissue from the breast-air boundary and the chest wall-breast boundary using ITK-SNAP. Within the breast mask we used a combination of thresholding techniques, and k-Means clustering algorithms with the T1w FS and T1w WOFS data to determine the FGT ground truth. The loss function was defined as the sum of Dice Similarity Coefficients (DSC) of the three classes [4] subtracted from the number of classes.

**Results and Discussion:** Performance was measured using the DSC, where the algorithm achieved an average DSC  $\pm$  one standard deviation for FGT and fat tissue of  $0.83 \pm 0.23$  and  $0.95 \pm 0.16$ , respectively. The figure shows the results of the Unet performance on sagittal slices. Using this algorithm, we plan to quantify BD and BPE on a continuous scale and evaluate risk prediction models using our quantification. We then will continue to use machine learning to learn new indicators from our database to better predict a HR woman's risk of developing breast cancer in the near future.

**Conclusion:** We have presented segmentation results using a deep Unet model to segment FGT in breast MRI.

**References:** [1] Tabar, Lazlo, et al. "Reduction in mortality..." *The Lancet* (1985). [2] Amir, Eitan, et al. "Assessing women at high risk of breast..." *JNCI*. (2010). [3] Ronneberger, Olaf, et al. "U-net: Convolutional networks..." *In. Con. on MICCAI* (2015). [4] Zou, Kelly H., et al. "Statistical validation of image seg..." *Acad. rad.* (2004).

Hyperparameter	Domain
Image Weighting	T1w WOFS, T1w FS, 2channel
Network depth	[5,6,7]
Dilation Rate	[1,2]
Drop Out	[0, 0.25, 0.5]
Optimizer	ADAM, SGD with Nesterov
Learning Rate	[1e-2, 1e-6]



## Vertebral Body Segmentation in CT Images using V-Net

Geoff Klein<sup>1,2</sup>, Michael Hardisty<sup>1</sup>, Arjun Sahgal<sup>3</sup>, Cari Whyne<sup>1</sup>, Anne Martel<sup>1,2</sup>

<sup>1</sup>Physical Sciences, Sunnybrook Research Institute, Toronto, Ontario, Canada

<sup>2</sup>Department of Medical Biophysics, Toronto, Ontario, Canada

<sup>3</sup>Department of Radiation Oncology, University of Toronto, Toronto, Ontario, Canada

**Introduction:** Approximately two-thirds of cancer patients will develop bone metastases with the spine being the most common site for breast, prostate, lung and renal cancer patients [1]. These metastases can mimic osteoblastic and osteolytic cells causing uncontrollable bone remodelling in their local regions, and in severe cases lead to vertebral compression fracture (VCF) [1]. Predicting the occurrence of VCF is difficult due to variations in size, shape, and location of metastases as well as variation of vertebral body size [2]. Previous investigations in predicting VCF occurring with Computed Tomography (CT) showed correlations between the relative volumes of the trabecular centrum and osteolytic tumours [3]. This required segmentations of the trabecular centrum from metastatic vertebrae, which has been shown to be difficult for fully-automated methods due to tumour involvement and complexity of the 3D vertebral body shape [3][4]. Currently, segmentations are obtained using a semi-automated 3D deformable atlas registration and level set method, which achieved a  $89.28 \pm 2.42\%$  concurrency when compared against expert manual segmentations [5]. The work presented here investigated a fully automated method to segment the trabecular centrum from both metastatic and healthy vertebra using Convolutional Neural Networks (CNN), specifically a V-Net [6]. The V-Net is a 3D variant of the successful U-Net [7], but with utilization of skip-connections. This allows for more contextual information to be passed through the different levels of the network without the addition of extra parameters.

**Methods:** Training data was collected from CT scans from the Odette Cancer Center at Sunnybrook Hospital and consisted of a mixture of T4-L5 healthy and metastatic vertebrae from 16 patients scanned at 4-month intervals. Training and validation consisted of 551 (527 metastatic, 24 healthy) and 137 (129 metastatic, 8 healthy) vertebrae, respectively. Spatial transformations were applied randomly to the training data to augment the training data set. Images were also resampled to  $0.5 \times 0.5 \times 1.25 \text{ mm}^3$  to a  $128 \times 128 \times 64$  grid. The V-Net was run for 200-epochs on 3 NVIDIA Titan Xp Graphics Processing Units (GPU). Layer depths of {2, 3, 4, 5, 6} were investigated with base number of filter of {8, 16, 32}. However, the 32 base number of filters was not possible for layer depth of 6 due to memory constraints.

**Results:** V-Net segmentation predictions for all configurations were compared to manually corrected segmentation results of the semi-automated approach. The top performing model was the layer depth of 5 and base number of filters of 32 configuration, achieving a  $92 \pm 3\%$  for both average dice score coefficient (DSC) and concurrency. Predictions were achieved in 0.35 seconds using a single NVIDIA Titan Xp GPU.

**Conclusion:** An accurate and fully automated model for segmenting the trabecular centrum of metastatic vertebral bodies has been achieved with a V-Net. It was able to more segment the trabecular centrum with greater concurrency and  $\sim 100$  times faster than the current semi-automated method. Future work for this project will look at using this V-Net to segment the vertebral bone as well as the osteoblastic and osteolytic tumours for the vertebral bodies. This would allow for potential way to automatically predict VCF occurring for patients.

**References:** [1] Maccauro, G. *et al. Int. J. Surg. Oncol.* **2011**, 107969 (2011). [2] Rose, P. S. *et al. J. Clin. Oncol.* **27**, 5075–5079 (2009). [3] Thibault, I. *et al. Int. J. Radiat. Oncol. Biol. Phys.* **97**, 75–81 (2017). [4] Ghosh, S., Alomari, R. S., Chaudhary, V. & Dhillon, G. *SPIE Med. Imaging Conf.* **3**, 796303-796303–9 (2011). [5] Hardisty, M., Gordon, L., Agarwal, P., Skrinikas, T. & Whyne, C. *Med. Phys.* **34**, 3127–3134 (2007). [6] Milletari, F., Navab, N. & Ahmadi, S. A. V-Net: *Proceedings - 2016 4th International Conference on 3D Vision, 3DV* (2016). [7] Ronneberger, O., P.Fischer & Brox, T. *MICCAI* **9351**, 234–241 (2015).

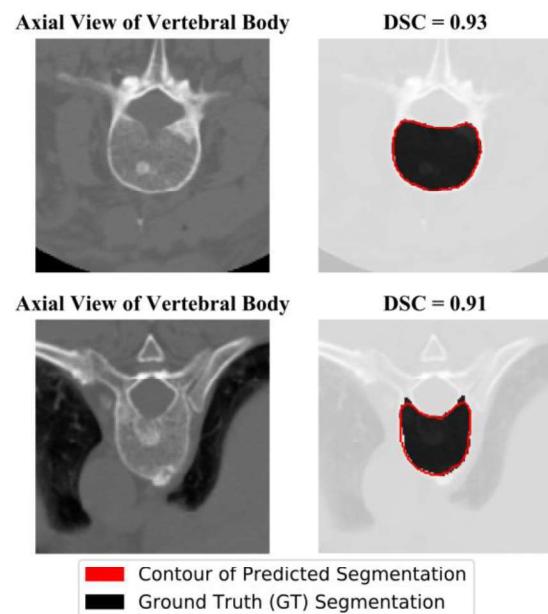
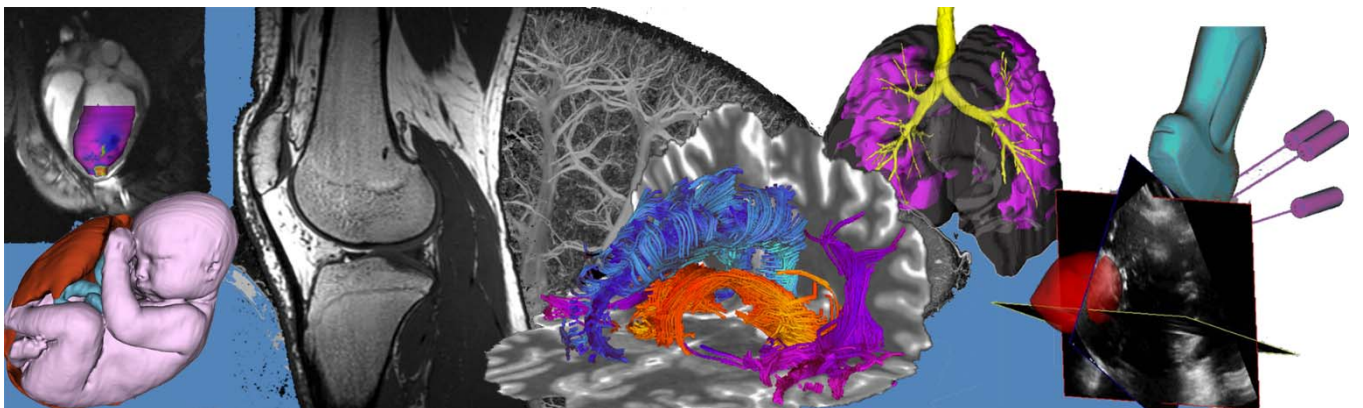


Figure 1: Axial slices of vertebral bodies and associated ground truth and predicted segmentations for two examples. DSC comparing predicted and ground truth

# Oral Presentation Abstracts

## Session 3: Cellular and Molecular Imaging



## Gas Vesicle Nanoparticles for the Photodynamic Treatment of Tumors

Ann Fernando<sup>1,2</sup> and Jean Gariépy\*<sup>1,2,3</sup>

<sup>1</sup> Department of Pharmaceutical Sciences, University of Toronto, Toronto, Ontario, Canada <sup>2</sup>  
Sunnybrook Research Institute, Toronto, Ontario, Canada

<sup>3</sup> Department of Medical Biophysics, University of Toronto, Toronto, Ontario, Canada

**Introduction:** For photodynamic imaging (PDI) and photodynamic therapy (PDT), the use of the free photosensitizer chlorin e6 (Ce6) for cancer treatment is constrained by poor aqueous solubility and low tumor accumulation (Yen et al. 2012). Although Ce6 can inhibit tumor growth in the presence of red light due to production of toxic reactive singlet oxygen, such limitations can reduce therapeutic outcome. Gas vesicles (GVs) are proteinaceous nanoparticles that are intracellularly expressed by halophilic archaea and bacteria to relocate cells to the surface of ponds (Walsby 1994). Being on the order of 300 nm, coupling Ce6 to GV s may enhance tumor delivery by way of the enhanced permeability and retention effect (Matsumura and Maeda 1986). Furthermore, GV s have been demonstrated to have versatile roles as imaging agents for ultrasound and MRI (Shapiro et al 2014; Bulte 2018). Conjugation of Ce6 to GV s will also enable imaging by light creating a novel theragnostic Ce6 conjugated GV (Ce6-GV). Here, our overall objective is to assess the potential of chlorin e6-GV s in killing cancer cells.

**Methods:** We have purified GV s and covalently grafted Ce6 onto their surface using carbodiimide chemistry. We used amino-acid hydrolysis to quantify Ce6 loading on GV s and performed confocal microscopy and flow cytometry to assess cellular uptake. We used MTT assay to evaluate *in vitro* biocompatibility and toxicity relative to free Ce6 and assessed reactive oxygen species formation using 2',7'-dichlorodihydrofluorescein diacetate as a probe.

**Results:** By dynamic light scattering and transmission electron microscopy we observed Ce6-GV s to have a size of ~340-400 nm with ~80,000 molecules of Ce6 per GV. We observed cellular uptake of Ce6 GV s in human cancer cells by confocal microscopy and flow cytometry (MCF-7, FaDu-GFP). Ce6-GV s were found to be ten –times more cytotoxic towards cancer cells in the presence of red light than free Ce6 and produced reactive oxygen species upon light exposure.

**Conclusion:** We have developed and characterized Ce6 conjugated GV s and demonstrated their potential as agents for image-guided photodynamic therapy.

### References:

Bulte, Jeff W. M. “Gas Vesicles as Collapsible MRI Contrast Agents.” *Nature Materials*, vol. 17, no. 5, 2018, pp. 386–387., doi:10.1038/s41563-018-0073-x.

Matsumura, Y, and H Maeda. “A New Concept for Macromolecular Therapeutics in Cancer Chemotherapy: Mechanism of Tumoritropic Accumulation of Proteins and the Antitumor Agent Smancs.” *Cancer Research.*, U.S. National Library of Medicine, Dec. 1986, www.ncbi.nlm.nih.gov/pubmed/2946403.

Shapiro, Mikhail G. “Gas Vesicles: Acoustic Biomolecules for Ultrasound Imaging.” *The Journal of the Acoustical Society of America*, vol. 141, no. 5, 2017, pp. 3953–3953., doi:10.1121/1.4988979.

Walsby, A. “Gas Vesicles.” *Microbiol Rev.* 1994; vol 58 No 1, pp 94- 144.

Yen, Tran Thi Hai, et al. “Comparative Studies in Vivo of Free and Liposomal Forms of Photosensitizer on a Base of Hydrophilic Derivative of Chlorin e6.” *Journal of Drug Delivery Science and Technology*, vol. 22, no. 4, 2012, pp. 291–294., doi:10.1016/s1773-2247(12)50048-1.

**Monitoring two cell populations using iron oxides and perfluorocarbons  
with dual  $^1\text{H}$  and  $^{19}\text{F}$  magnetic resonance imaging at 3 Tesla**

Olivia C. Sehl<sup>\*1,2</sup>, Ashley V. Makela<sup>1,2</sup>, Amanda M. Hamilton<sup>1</sup>, and Paula J. Foster<sup>1,2</sup>

<sup>1</sup>Robarts Research Institute, The University of Western Ontario, London, Ontario, Canada

<sup>2</sup>The Department of Medical Biophysics, The University of Western Ontario, London, Ontario, Canada

**Introduction** Mesenchymal stem cells (MSCs) have shown promising results as a cellular therapeutic<sup>1-4</sup>. MSCs play an important role in modulating inflammation within the local microenvironment through secretion of trophic factors<sup>1</sup>. Unfortunately, this therapeutic potential is often limited due to stem cell death, in response to the stresses of administration and inadequate access to nutrients. Cytokines released by the apoptotic stem cells attract macrophages to the implant site to trigger an immune response by the host. Ultimately, the resulting influx of immune cells is great enough to trigger stem-cell rejection<sup>2,3</sup>. Fundamental questions regarding the fate of cells after MSC transplantation remain unanswered. To implement successful cell-based therapies, methods must be developed to allow long-term monitoring of transplanted cells and infiltrating macrophages *in vivo*. Cellular MRI has proven to be an effective technique for non-invasive and longitudinal tracking of cells<sup>2-6</sup>. To date, most cellular MRI has been performed with either iron oxides or perfluorocarbons (PFC). In this study we explored the ability to label, detect, and quantify two cell types (MSC and macrophages) simultaneously using dual iron (Fe) and fluorine-19 ( $^{19}\text{F}$ ) based MRI cell tracking in a model of stem cell rejection. This is the first study to utilize PFC to indicate inflammation associated with iron labeled stem cells and to track this over time. This is also the first study to demonstrate the ability to image macrophage infiltration *in vivo* using  $^{19}\text{F}$  on a clinical (3T) MRI system.

**Methods** Mouse mesenchymal stem cells (mMSCs) were labeled with 100 $\mu\text{g}$  Fe/mL ferumoxytol, an ultrasmall superparamagnetic iron oxide (USPIO), following protocol by Thu *et al.*<sup>7</sup>.  $1 \times 10^6$  labeled ( $n=5$  mice) or unlabeled ( $n=3$  mice) mMSCs were implanted in the right hind limb muscle of C57Bl/6 mice. Immediately after, each mouse was administered 200 $\mu\text{L}$  120 mg/mL PFC intravenously (iv) via the tail vein for *in situ* labeling of phagocytic macrophages. 24 hours later, both  $^1\text{H}$  and  $^{19}\text{F}$  images were acquired on a 3T clinical scanner using a 4.31cm dual-tuned surface coil and a 3D balanced steady state free precession (bSSFP) sequence<sup>6</sup> (day 1). Imaging was repeated on day 12 to investigate temporal changes in iron-associated signal voids and  $^{19}\text{F}$  signal. Regions of signal void due to mMSC were delineated manually and void volume calculated. The number of  $^{19}\text{F}$  spins was quantified by comparison of  $^{19}\text{F}$  signal in the region of interest to  $^{19}\text{F}$  signal in reference tubes. A student's t-test was completed to compare void volume at day 1 and 12,  $^{19}\text{F}$  signal between mice injected with unlabeled or iron labeled mMSCs, and also between day 1 and 12.

**Results** We have shown that it is possible to detect both implanted mMSCs and infiltrating macrophages in the same mouse during the same scanning session (as shown in **Figure 1**). On day 1 regions of signal void were detected in  $^1\text{H}$  MRI of all mice which received iron-labeled mMSCs. There were no signal voids found in  $^1\text{H}$  MRI of mice injected with unlabeled mMSCs. The signal void created by iron positive MSCs declines by 64% by day 12, likely due to MSC death. PFC-labeled macrophages accumulate near the MSCs within 24 hours, as an immune reaction. The  $^{19}\text{F}$  signal persists and rises by 25% over 12 days, indicating the increased infiltration of immune cells. No differences in  $^{19}\text{F}$  signal were found between mice with iron labeled or unlabeled mMSCs.

**Conclusions**  $^1\text{H}$  and  $^{19}\text{F}$  MRI can be used in conjunction to noninvasively monitor the fate two cell populations *in vivo*. We propose that this cellular imaging technique could be used to detect the infiltration of macrophages at transplant sites to identify cell rejection and contribute to other *in vivo* cell tracking applications.

1. Meirelles, S.L., *et al.* (2009). *Frontiers in bioscience (Landmark edition)*, 14, 4281-4298.
2. Gaudet, J. M., *et al.* (2017). *Magnetic resonance in medicine*, 78(2), 713-720.
3. Hitchens, T. K., *et al.* (2011). *Magnetic resonance in medicine*, 65(4), 1144-1153.
4. Makela, A. V., *et al.* (2016). *Topics in Magnetic Resonance Imaging*, 25(5), 177-186.
5. Hitchens, T. K., *et al.* (2015). *Magnetic resonance in medicine*, 73(1), 367-375.
6. Makela *et al.* (2018). *Magn Reson Mater Phy*, 80(3).
7. Thu, M. S., *et al.* (2012). *Nature medicine*, 18(3), 463.

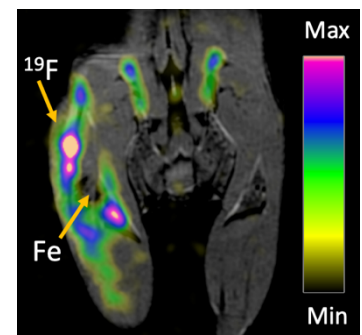


**Figure 1:** Coronal bSSFP MRI of mouse hind limbs on day 1. The right limb contains iron labeled mMSCs (Fe) and surrounding immune cells. The color bar denotes the number of  $^{19}\text{F}$  spins associated with infiltrating immune cells. Maximum signal is peach colored.



## Molecular imaging of hypoxia: kinetic analysis of dynamic PET data from pancreatic cancer

Fiona Li<sup>1,2</sup>, Edward Taylor<sup>3,4</sup>, Ivan Yeung<sup>3,4</sup>, David Jaffray<sup>3,4</sup>, David W. Hedley<sup>3,4</sup>, Ting-Yim Lee<sup>1,2</sup>

<sup>1</sup>Department of Medical Biophysics, Western University, London, Canada; <sup>2</sup>Lawson Health Research Institute and Robarts Research Institute, London, Canada; <sup>3</sup>Department of Medical Biophysics, University of Toronto, Canada; <sup>4</sup>Princess Margaret Cancer Centre, University Health Network, Toronto, Canada

### Introduction:

Pancreatic cancer is a fatal cancer with low survival rate due to prevalent hypoxia, which contributes significantly to its resistance to chemo- and radiotherapy. Hypoxia can be imaged non-invasively using the nitroimidazole analog, <sup>18</sup>F labeled (<sup>18</sup>F-FAZA), which is thought to bind irreversibly to macromolecules and proteins following reduction of the nitro group under conditions of reduced oxygen level. The aim of this study is to investigate if PET imaging with <sup>18</sup>F-FAZA can detect hypoxia in pancreatic cancer.

### Method:

Twenty patients with pancreatic ductal adenocarcinoma underwent <sup>18</sup>F-FAZA PET imaging at University Health Network in Toronto. Dynamic scans of the pancreas were done over 60 mins starting with injection of <sup>18</sup>F-FAZA. Tumors in 20 and normal tissue in 14 patients were contoured manually by radiologists. Due to pancreatic atrophy, normal tissue could not be contoured in 5 patients. The dynamic tissue time activity curves (TACs) were analysed using two model independent graphical analyses – Patlak and Logan plot for irreversible and reversible binding of <sup>18</sup>F-FAZA respectively, and using the standard two tissue compartment models (S2TCM) as well as our developed kinetics model, the flow modified two-tissue compartment model (F2TCM). While the S2TCM treats blood vessels as a compartment, the F2TCM incorporate the mean transit time through blood vessels, which could significantly affect the estimation of model parameters. Using multivariate logistic regression with backward elimination, the optimal parameter set for distinguishing normal tissue from hypoxic pancreatic tumor was determined.

### Result:

Graphical analysis showed that the tracer was reversibly bound and the distribution volume determined by Logan plot correlated with the volumes determined by S2TCM and F2TCM with  $R^2 = 0.83$  and  $0.93$  respectively. According to the Akaike Information Criteria (AIC), F2TCM fitted TACs from both normal and cancerous pancreatic tissue better than S2TCM. The root mean square (RMS) deviation between the fitted and measured TAC was also lower for F2TCM than S2TCM. Logistic regression determined that two F2TCM parameters- distribution volume (DV) and dissociation rate constant ( $k_4$ ) could classify normal from hypoxic pancreatic cancerous tissue with sensitivity and specificity of 85% and 71% respectively.

### Discussion:

Contrary to the accepted notion that <sup>18</sup>F-FAZA is irreversibly bound to macromolecules in hypoxic tissue<sup>1</sup>, both graphical and kinetic analysis revealed the binding is reversible. The proposed mechanism is that the reduced <sup>18</sup>F-FAZA metabolite (amino-FAZA) is conjugated to glutathione (amino-FAZA-GS) which is usually trapped in cells due to its hydrophilicity<sup>2</sup>, however, in the presence of elevated multidrug resistance protein (MRP-1) in pancreatic tumor, amino-FAZA-GS can be ‘pumped’ out of the cells<sup>3</sup> leading to radioactivity washout or reversible binding.

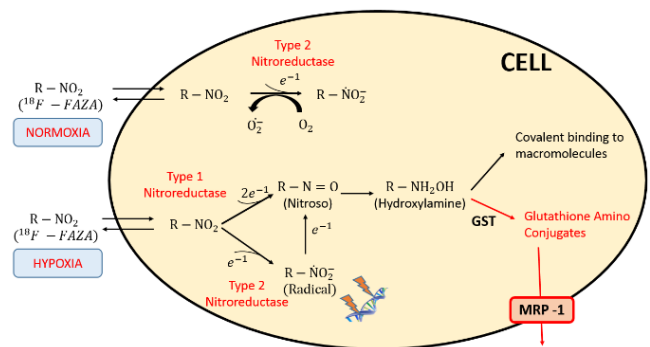
Besides enabling normal pancreatic tissue to be distinguished from cancerous one, kinetic modeling of TACs allows evaluation of the dissociation (washout) rate constant ( $k_4$ ) which can be associated with MRP-1 activity, while the binding rate constant ( $k_3$ ) can be associated with nitroreductase and glutathione activity.

### References:

<sup>1</sup>J Nucl Med. 2005; 46:106-13; <sup>2</sup>Sci Rep. 2015;5:16802; <sup>3</sup>Ann Nucl Med. 2017;31:596-604.

### Acknowledgement:

<sup>18</sup>F-FAZA was supplied by CPDC, Hamilton, Canada.



## Tumour-activatable minicircles expressing prodrug-suicide gene systems for prostate cancer therapy

TianDuo Wang<sup>1,2</sup>, Yuanxin Chen<sup>1</sup>, John. A. Ronald<sup>1,2,3</sup>

1. Robarts Research Institute – Imaging; 2. Department of Medical Biophysics, University of Western Ontario;  
3. Lawson Health Research Institute, London, ON, Canada.

**INTRODUCTION:** Gene therapy, the introduction of foreign genetic material into biological systems, is a popular approach for cancer treatment. One challenge in this strategy is off-target effects due to non-specific expression of cytotoxic genes in normal tissues. Improving the delivery and cancer specificity of gene vectors is an important step towards clinical acceptance of cancer gene therapy. Our group has previously developed non-viral gene vectors called tumour-activatable minicircles<sup>1</sup> (TA-MCs), shortened plasmids that possess superior potency and safety profiles<sup>2</sup>. These MCs used the tumour-specific survivin promoter<sup>3</sup> (pSurv) to mediate transcription of an exogenous blood biomarker in prostate cancer (PCa) cells but not healthy cells. Due to higher pSurv activity in more aggressive PCa cells, TA-MCs were able to titrate biomarker output to tumour aggression. We posited that the same system can be used for tumour-targeted cytotoxicity, where therapeutic effects are enhanced in more aggressive PCa. Hence, in this work, we describe TA-MCs that express the fusion protein cytosine deaminase uracil phosphoribosyl transferase (CD), an established cancer suicide gene that acts by converting the prodrug 5-fluorocytosine (5-FC) to the tumour-toxic 5-fluorouridine monophosphate (5-FUMP)<sup>4</sup>. Our goal is to explore these CD-expressing TA-MCs as therapeutic agents for PCa in cells and mice.

**METHODS:** We first constructed parental plasmids, precursors to minicircles, that expressed CD downstream of pSurv. TA-MCs were then made from these parental plasmids using a previously described production system<sup>5</sup>. Next, we validated these TA-MCs via transfection of high-survivin PC3MLN4 PCa cells engineered to express firefly luciferase (Fluc) as a marker of cell viability using bioluminescence imaging (BLI). One day after transfection, 5-FC was added to wells and BLI was performed using the IVIS (PerkinElmer). We then assessed these TA-MCs in nude mice bearing subcutaneous PC3MLN4 tumours of ~150 mm<sup>3</sup>. TA-MCs complexed with a polyethylenimine transfection agent was injected intratumourally into one mouse, while a control mouse received PBS. Both mice received daily intraperitoneal injections of 5-FC and tumour burden was assessed using BLI.

**RESULTS:** PC3MLN4 cells transfected with TA-MCs and treated with 5-FC dramatically reduced proliferation (Fig. 1B and C). In the absence of MCs and/or 5-FC, PCa cells were able to proliferate normally, showing significantly higher BLI signal than cells treated with both MC and 5-FC. Initial pilot data of 1 mouse showed that prostate tumour treated with both TA-MCs and 5-FC grew slower than untreated tumour until endpoint (Fig. 1D).

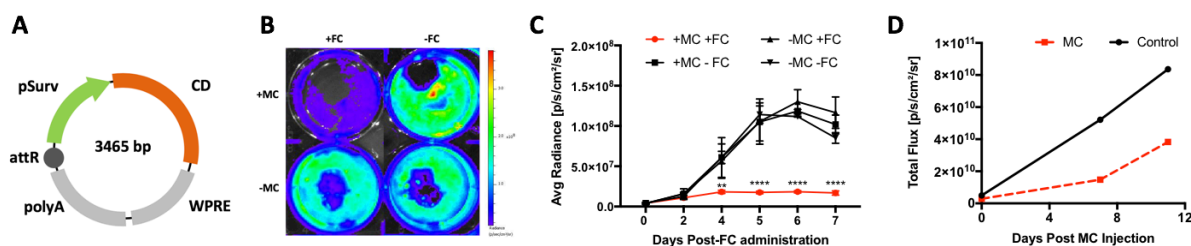


**Figure 1.** (A) Vector map of TA-MC. (B) BLI of Fluc+ PC3MLN4 cells in 6-well plate on day 6 after transfection with TA-MCs with (C) quantification (n=3). (D) BLI signal from mice with PC3MLN4 tumours post-MC injection and administration of 5-FC (n=1). Data are presented as mean ± SD. \*\*, p<0.01, \*\*\*\*, p<0.0001.

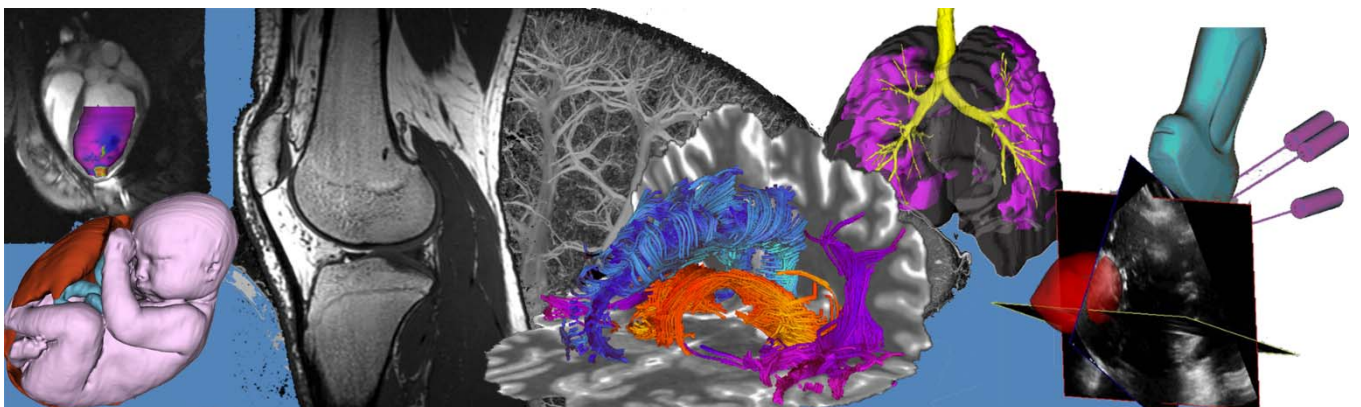
**DISCUSSION:** We have shown here that in PCa cells, cytotoxicity can be controlled due to requiring both prodrug and converting enzyme, with minimal negative effects to cells in the presence of only one component. In conjunction with a tumour-specific promoter, our suicide gene system could reduce off-target effects. Carrying this system on non-viral MCs, an emerging vector for effective gene delivery, also increases the clinical potential of this agent. *In vivo* pilot studies are promising and we are currently expanding this cohort and evaluating different MC and prodrug dosing. We are also currently investigating these TA-MCs on low-survivin expressing PCa to validate whether therapeutic effect is dependent on tumour aggressiveness. We envision adding a reporter gene to these TA-MCs to create a theragnostic platform for aggressive prostate cancer detection and therapy.

**REFERENCES:** [1] Ronald J. et al., PNAS, 2015, 112(10): 3068–3073. [2] Chen Z. et al., Mol Ther, 2003, 8(3): 495–500. [3] Shariat S. et al., Cancer, 2004, 100(4): 751–757. [4] Koyama F. et al., Nat Am, 2000, 7(7): 1015–1022. [5] Kay M. et al., Nat Biotechnol, 2010, 28(12): 1287–1289.



# Oral Presentation Abstracts

## Session 4: New MRI Approaches



## Clinically-viable and robust measurement of microscopic diffusion anisotropy

Nico J. J. Arezza<sup>1,2</sup>, Aidin Arbabi<sup>2</sup>, and Corey A. Baron<sup>1,2</sup>

<sup>1</sup>Department of Medical Biophysics, Schulich School of Medicine and Dentistry, Western University

<sup>2</sup>Centre for Functional and Metabolic Mapping, Robarts Research Institute, Western University

**Introduction:** Diffusion MRI gives insight into neuron microstructure via metrics such as fractional anisotropy (FA), which describes the degree of diffusion anisotropy within tissue but cannot distinguish between neuron integrity and fiber orientation coherence. In contrast, the more recently defined microscopic diffusion anisotropy ( $\mu A$ ) is sensitive to diffusion anisotropy independent of neuron fiber orientation<sup>1</sup>. To date, most *in vivo* demonstrations of  $\mu A$  have been time-consuming or low-SNR. Here, we demonstrate a new isotropic diffusion encoding scheme and  $\mu A$  protocol on a 7T MRI that requires only 3 minutes for high-SNR full-brain imaging.

**Methods:** Data was collected from a relapsing-remitting multiple sclerosis (MS) patient, abiding by ethics board guidelines, on a 7T head-only MRI system (80mT/m strength and 350T/m/s slew rate) using 7, 15, and 30 linear encodings at  $b=100\text{s/mm}^2$ ,  $1000\text{s/mm}^2$ , and  $2200\text{s/mm}^2$ , respectively. The same number of isotropic encodings were acquired at each  $b$ -value. The other parameters were: TE/TR=99/6000ms, FOV=196x196mm<sup>2</sup> with 2mm resolution, 36 slices (4mm thickness), and 10.5-minute total scan time. Post-processing included denoising<sup>2</sup> and eddy current correction with FSL<sup>3</sup>. To encode isotropic diffusion, we developed an efficient method that utilizes trapezoidal gradients (Fig. 1). To assess the feasibility of a rapid (3 minute) clinical scan, the data was subsampled to 15 linear and 15 isotropic acquisitions (both at  $b=2200\text{s/mm}^2$ ) before computing  $\mu A^2$  via<sup>4</sup>:  $\mu A^2 = b^{-2}[\ln(S_{linear}) - \ln(S_{isotropic})]$ , where  $S_{linear}$  and  $S_{isotropic}$  are the powder averages of the linear and isotropic scans, respectively. The 15 linear  $b = 1000 \text{ s/mm}^2$  scans were used to compute FA maps for comparison, and a dual-inversion recovery (DIR) scan was performed on the patient to identify MS lesions that result from neuron degradation and demyelination. Some of the data was not used.

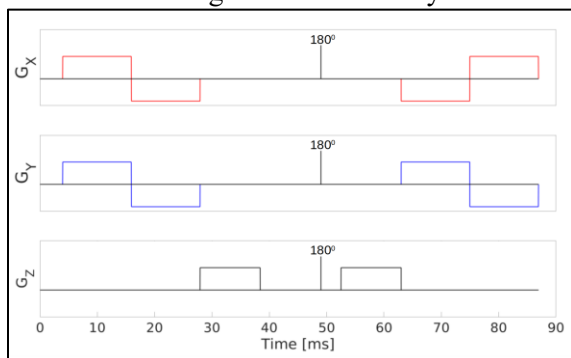


Fig. 1. Schematic representation of the isotropic diffusion encoding.

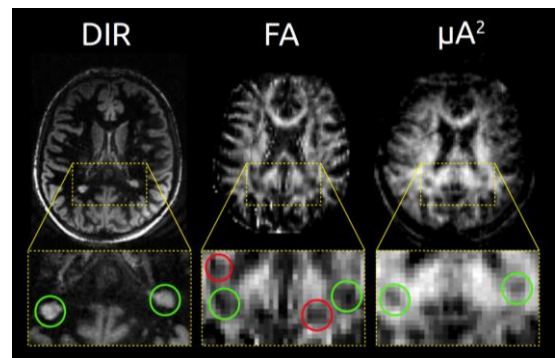


Fig. 2. DIR, FA, and  $\mu A^2$  images from a patient with MS.

**Results:** DIR, FA, and  $\mu A^2$  images from the MS patient are shown in Fig. 2. Hyperintense white matter lesions on the DIR image correspond to hypointensities in the FA and  $\mu A^2$  images, showing that both metrics are sensitive to MS lesions (green circles in Fig. 2). However, hypointense regions are observed in the FA map that do not correspond to lesions in DIR, which could result from crossing neuron fibers (red circles in Fig. 2);  $\mu A^2$  thus showed improved specificity over FA to MS lesions.

**Conclusions:** The sensitivity of  $\mu A^2$  to MS lesions is comparable to recent work using double diffusion encoding at 3T by Yang et al<sup>5</sup>. Here, the higher gradient and field strengths and our unique isotropic encoding scheme reduced the required TE (thus increasing SNR), reduced scan time, increased brain coverage, and improved in-plane resolution. The subsampled data used to generate the images in Fig. 2 would only require a scan time of 3 minutes, demonstrating high feasibility for clinical  $\mu A$  imaging. At TE=99ms, the SNR advantages of 7T over 3T were modest and similar image quality may be feasible at 3T with 80mT/m gradients. Previous methods to compute  $\mu A$  *in vivo* using isotropic encoding have involved fitting the diffusion-weighted signal to a constrained model<sup>6</sup>. The approach used here has less stringent acquisition requirements and can be rapidly computed with no need for tuning or regularization, which is essential for practical clinical use.

**References:** <sup>1</sup>Shemesh, N et al. *Magn Reson Med* 75 (2016). <sup>2</sup>Veraart, J et al. *Neuroimage* 142 (2016). <sup>3</sup>Andersson, JLR et al. *Neuroimage* 125 (2016). <sup>4</sup>Ianus, A et al. *Magn Reson Med* 78 (2017). <sup>5</sup>Yang, G et al. *Magn Reson Med* 80 (2018). <sup>6</sup>Szczepankiewicz F et al. *Neuroimage* 142 (2016).

**Acknowledgements:** Canada First Research Excellence Fund to BrainsCAN, Ontario Graduate Scholarships, NSERC Discovery Grant, Western Medical and Health Science Review Board Seed Grant

## Rapid $B_1+$ Measurement using a Non-Steady-State Progressive Flip Angle Sequence and Parallel Imaging

Nadia D. Bragagnolo<sup>1,2</sup>, Benjamin J. Geraghty<sup>1,2</sup>, Casey Y. Lee<sup>1,2</sup>, and Charles H. Cunningham<sup>1,2</sup>

<sup>1</sup>Medical Biophysics, University of Toronto, <sup>2</sup>Physical Sciences, Sunnybrook Research Institute, Toronto, ON, Canada.

**Introduction:** Hyperpolarized  $^{13}\text{C}$  MRI often suffers from an inhomogeneous  $B_1+$  transmit field, as it requires the use of a secondary transmit coil system within the proton-only body coil. This inhomogeneous field leads to varying flip angles, which makes the image signals difficult to interpret. There are several methods for measuring the spatial distribution of the  $B_1$  field for a given transmit coil, such as the double angle<sup>1</sup> and Bloch-Siegert<sup>2</sup> methods. However, applying these methods during *in vivo*  $^{13}\text{C}$  scans is infeasible due to timing constraints. Moreover, using a pre-measured  $B_1+$  map from a phantom to minimize variation in *in vivo* scans is prone to error, because the field distribution may change as coil loading and positioning changes. To account for changes in the  $B_1+$  distribution from coil loading, some form of  $B_1+$  calibration is often performed using a  $^{13}\text{C}$  phantom placed near the region of interest. However, this calibration becomes challenging in large field-of-view applications, as there is a distribution of  $B_1+$  fields within the large target region. In this work, a method that rapidly obtains several  $B_1+$  measurements from an array of  $^{13}\text{C}$  phantoms is proposed.

**Methods:** A transmit profile of a “clamshell”  $^{13}\text{C}$  volume transmitter (GE Healthcare, Cleveland, OH)<sup>3</sup> was measured using the double angle method with a target angle of  $60^\circ$  (Fig. 1). This transmit profile gives  $B_1+(x,y,z)$ , a spatial map of the transverse component of the  $B_1$  field. A short TR pulse-acquire sequence with linearly increasing flip angles was designed to simultaneously excite four small phantoms distributed across the elements of an 8-channel receiver coil (Fig. 2). With TR = 175 ms and 50 iterations, the total scan time is 9 s. The signal evolution from the train of excitations for each phantom was fitted to a non-steady state model of the signal equation to determine the  $B_1+$  at each location. These  $B_1+$  values are discrete samples of the  $B_1+(x',y',z')$  field, the  $B_1+$  field that is unique to each subject's positioning in the scanner. From large field-of-view localizer images showing the four phantoms and fiducials placed on the transmitter, a set of vectors describing the location of the phantoms can be defined. These vectors are used to affine transform the pre-computed  $B_1+(x,y,z)$  map to fit the four  $B_1+(x',y',z')$  measurements, compensating for any loading effects. The transformed pre-computed  $B_1+(x,y,z)$  map is then used to determine a correction factor for each slice in the region of interest.

**Results:** The  $B_1+$  map in Figure 1 shows a large variability in the  $B_1+$  field, which supports the need for a method that can determine a correction factor for each slice in large field-of-view images. The rapid  $B_1+$  measurement sequence has been tested on a  $^{13}\text{C}$ -urea phantom during calibration for human scans ( $n=10$ ), showing that this method is capable of computing the  $B_1+$  field accurately within  $\pm 1\mu\text{T}$ . The feasibility of using this technique to simultaneously acquire  $B_1+$  measurements of four phantoms across an 8-channel receive coil is demonstrated (Fig. 3). A model to transform the  $B_1+(x,y,z)$  map to fit the  $B_1+(x',y',z')$  measurements is being developed.

**Conclusion:** A method to acquire rapid (9 s)  $B_1+$  field measurements *in vivo* has been demonstrated. The method shown here can be used to minimize the variability in flip angle due to inhomogeneous  $B_1+$  in large field-of-view images; for example, those containing both the thoracic and upper abdominal cavities.

### References:

1. Hornak *et al.* (1988) Magn Reson Med.
2. Sacolick *et al.* (2010) Magn Reson Med.
3. Tropp *et al.* (2011) J Magn Reson.

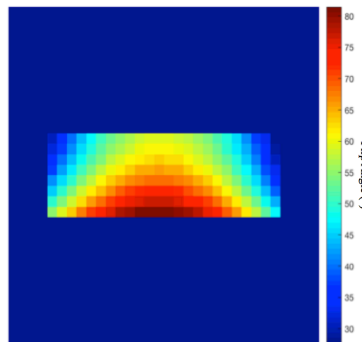


Fig. 1. The pre-computed  $B_1+(x,y,z)$  map. The transmit coil is at the bottom of the phantom.

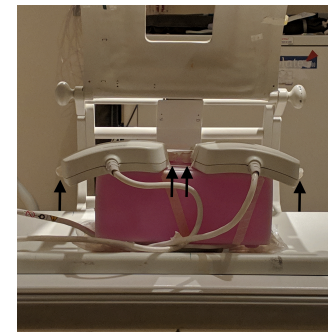


Fig 2. Coil setup for  $B_1+$  map, with arrows showing the  $^{13}\text{C}$  phantoms on the receiver coils.

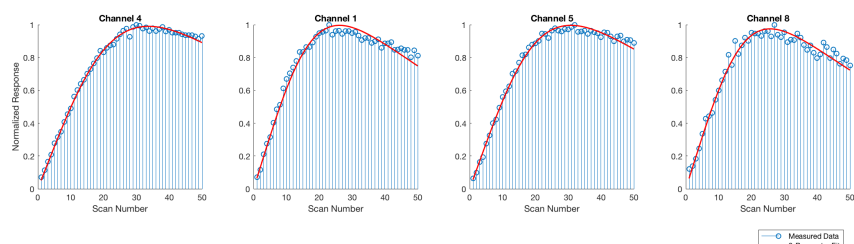


Fig. 3. Normalized signal profiles of  $^{13}\text{C}$ -urea phantoms obtained simultaneously across an 8-channel receive coil using the progressive flip angle technique.

## Using low resolution pre-scans and singular value decomposition derived sensitivities to allow for the combination of large phase datasets

Olivia W Stanley<sup>1</sup>, Ravi S Menon<sup>1</sup>, L Martyn Klassen<sup>1</sup>

Centre for Functional and Metabolic Mapping, Robarts Research Institute, London, ON

**Introduction:** Interest in the contrasts available from phase images has increased in recent years<sup>1,2</sup>, parallel to the development of multi-channel radio frequency (RF) arrays for accelerated imaging. Using RF arrays for phase imaging with suboptimal combination will lead to destructive interference and poor image quality. Existing phase methods commonly rely on a post-acquisition combination of multiple images, for example, singular value decomposition (SVD) combination<sup>3</sup>. SVD combination utilizes a set of images to find the relative sensitivities for an RF array, phase aligns the images using those sensitivities, and combines the images using a complex sum. This post-acquisition operation is time consuming and conventionally done voxel-wise leading to high computational costs. However, it is possible to use the SVD of a low-resolution prescan to determine the relative sensitivities and align the phase of a larger image set in real time while the imaging is being completed. This is achieved through our proposed fitted SVD sensitivities method that uses a low resolution SVD and solid harmonic interpolation to provide computationally efficient, phase sensitive, coil combination.

**Methods:** The prescan used to derive relative sensitivity estimates via SVD was a 10 image 8mm isotropic prescan and is routinely collected as part of the  $B_1^+$  shimming protocol. Once calculated, these relative sensitivity estimates were corrected for shared signal using a weighted combination of the sensitivities. This was done to ensure that the sensitivities did not contain extraneous phase from other sources (e.g.  $B_0$  and  $B_1^+$ ) or phase singularities common to all sensitivities. Relative sensitivities were fit to the solid harmonics using an iterative least squares fitting algorithm. This algorithm removes a common complex scaling term every iteration in order to move the sensitivities closer to the solid harmonic solution and improve interpolation. These fits can be stored as coefficients of solid harmonics and permit interpolation of relative sensitivities to any image size and geometry. This interpolation can be used to align the phases of the receiver channels in subsequent acquisitions for improved phase sensitive combination. This method is more computationally efficient than performing SVD combination on every image set collected.

All images were collected on the Siemens Magnetom 7T head-only MRI system located at the Centre for Functional and Metabolic Mapping. Human data was collected with the approval of the University of Western Ontario Research Ethics Board. First, a symmetric whole head coil with 32 receive channels<sup>4</sup> was used to collect both the  $B_1^+$  shimming set and gradient echo data (1mm resolution). Second an asymmetric coil with 32 receive channels targeting the occipital parietal region<sup>5</sup> was used to collect  $B_1^+$  shimming data and EPI data (2mm resolution). The efficacy of the method was evaluated using visual inspection from singularities after the phase images were unwrapped<sup>6</sup> and comparing the quality ratio across the brain<sup>7</sup>. The quality ratio is the ratio of the combined image magnitude to the SVD combined image and represents signal loss due to destructive interference.

**Results:** This method successfully removes the phase singularity caused by direct complex sum combination (Figure 1) and the quality ratio across the brain is  $0.94 \pm 0.09$  (mean  $\pm$  standard deviation). The combined phase of the asymmetric coil showed no singularities and had a quality ratio of  $0.94 \pm 0.17$  across the brain.

**Discussion:** This method allows for a phase sensitive combination to be used for multiple scans during an imaging session. It is computationally efficient, requires minimal computer storage, and is fully automated. This method performs well in both symmetric and asymmetrical coils. Using solid harmonic fitting to interpolate SVD derived relative coil sensitivities from a prescan can align the phases of any data obtained during the remainder of an imaging session. This allows for phase-based contrasts to be routinely collected on the MRI system.

### References:

1. Fan et al. J. Cereb. Blood Flow Metab. 2015
2. Reichenbach et al. Clin. Neuroradiol. 2015
3. Walsh et al. Magn. Reson. Med. 2000
4. Gilbert et al. ISMRM 2015
5. Gilbert et al. ISMRM 2017
6. Abdul-Rahman et al. Appl. Opt. 2007
7. Robinson et al. NMR Biomed. 201

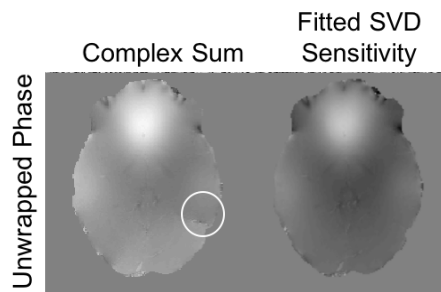


Figure 1 - Unwrapped gradient echo phase images for complex sum and the fitted SVD sensitivities method. Note the resolution of the phase singularity (white circle).

**Validation of simulated vs. experimentally acquired B<sub>0</sub> field maps surrounding metal**Gregory Hong,<sup>1,2,3</sup> Junmin Liu,<sup>1</sup> David W Holdsworth,<sup>1,2,3</sup> Maria Drangova<sup>1,2,3</sup>

Development of Novel Therapies for Bone and Joint Diseases Consortium

<sup>1</sup>Robarts Research Institute, <sup>2</sup>Western Bone and Joint Institute, <sup>3</sup>Department of Medical Biophysics, Western University, London, Ontario, Canada

**Introduction:** Orthopedic implants are known to be the source of large field inhomogeneity in MRI, leading to artifacts that obscure relevant soft-tissue information in the proximity of the implant. The deterministic nature of these susceptibility artifacts has led to novel and exciting applications of simulated field maps for object localization<sup>1</sup> and susceptibility estimation.<sup>2</sup> These techniques hinge on the ability to calculate spatially accurate field maps and compare them to experimental data; however, these experiments may suffer from inaccurate co-registration between the simulated and scanned field maps, making quantitative validation of the underlying simulation challenging. We present the evaluation of a novel 3D printed phantom, which allows for generation of geometrically robust regions of interest to quantitatively compare an experimentally acquired field map to its simulation. We demonstrate the utility of the phantom by comparing a scanned field map of two titanium rods surrounded by the grid to a simulation in 3D.

**Methods**

*Phantom Design:* The phantom design is a modification of a previously presented grid phantom<sup>3</sup> consisting of 4.5 mm spherical marker and 0.8 mm supporting walls 3D printed in PLA. Marker spheres placed along the perimeter of the phantom generate a bounding box, within which metal objects can be placed. This experiment configured the phantom with two titanium rods (6.4 mm diameter) held by clips 26 mm apart in the center of the phantom. The phantom was submerged in a CuSO<sub>4</sub> solution and evacuated of air.

*Imaging:* Experimental B<sub>0</sub> field maps were calculated from the difference in phase accumulation between two gradient-echo scans at 3T (8-channel head coil; 256x128x128; 1 mm isotropic voxels; TE = 3, 3.5 ms; TR = 15 ms; 15° flip angle) resulting in field maps with ±1 kHz bandwidth. To avoid the need for shimming, a field map without the grid was generated with the same parameters and subtracted from the phantom acquisition. Through morphological erosion of the thin supporting walls, the centroids of the marker beads were calculated, providing fiducial points that define the boundary of a volume of interest (VOI) of 91x91x130 mm. (Figure 1, yellow)

*Simulation and analysis:* A Fourier-based simulation<sup>1</sup> was used to calculate the field map surrounding the titanium rods, in the configuration of the physical phantom (parallel, 26 mm apart) with an assigned titanium susceptibility  $\chi = 182$  ppm.<sup>4</sup> The simulated volume was co-registered with the scanned VOI by placing the center of the simulation volume at the center of the VOI. To demonstrate the agreement between simulation and experiment, the field maps of two 65 mm line profiles that transect both rods placed ±39 mm from the central axial slice (Figure 1, cyan) were examined.

**Results:** Figure 2 shows a quantitative comparison between simulated and scanned field maps using the lines shown in Figure 1. The symmetric nature of the fields generated by two rods in this configuration yields line profiles that should be identical. The large noise spikes caused by lack of signal from the metal rod line up well with the zero-masked simulation rod, with a small distortion likely due to gradient warping. The slight left to right asymmetry in both A and B is indicative of a small misalignment (relative to B<sub>0</sub>) between the phantom and simulated geometry.

**Conclusions:** Simulated field maps play an important role in the testing and development of metal artifact reduction techniques and are beginning to be applied directly in novel ways. However, the high susceptibility of metal creates a field inhomogeneity that is highly sensitive to object geometry and orientation that is difficult to ascertain without reference geometry. The presented phantom is easily customized and provides a means of accurate 3D registration between simulated and experimental field maps. Future research will make use of this design with more complex implants to better characterize the field perturbations they generate, with the aim of incorporating this knowledge into metal artifact reduction.

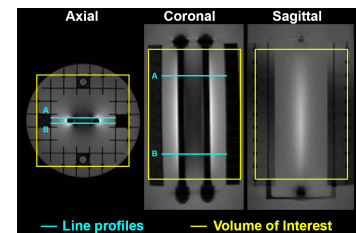
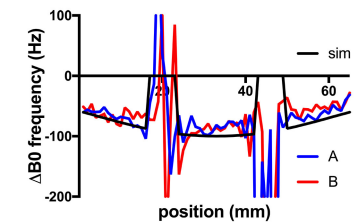


Figure 1: VOI and line profile locations

Figure 2: B<sub>0</sub> simulation (with metal mask) vs scanned line profiles

1. Zijlstra, F. et al. MRM, doi:10.1002/mrm.26556 (2016). 2. Shi, X. et al. MRM, doi:10.1002/mrm.26313 (2016). 3. Hong, G. et al. ISMRM (Honolulu, 2017). 4. Schenck, J. F. Med. Phys. 23, 815-850, doi:10.1118/1.597854 (1996).



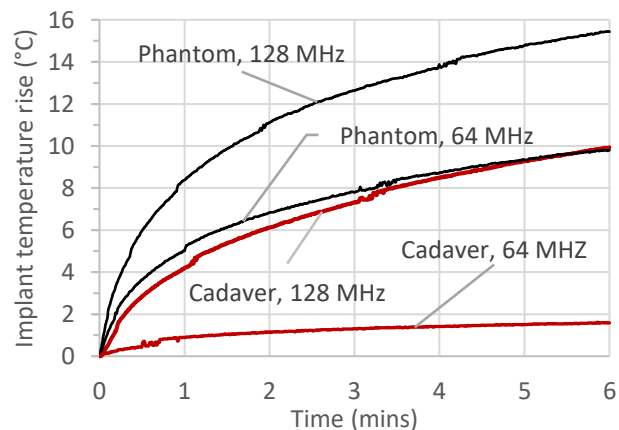
**Initial comparison of RF-induced heating in the ASTM phantom and a cadaver leg: a pilot study**A. Louka<sup>1,2</sup>, K. Wawrzyn<sup>1</sup>, A. Getgood<sup>3</sup>, T. Burkhart<sup>4</sup>, W.B. Handler<sup>1</sup>, B.A. Chronik<sup>1,2</sup><sup>1</sup>The xMR Labs, Department of Physics & Astronomy, Western University, London, Ontario, Canada;<sup>2</sup>Department of Medical Biophysics, Western University, London, Ontario, Canada<sup>3</sup>Fowler Kennedy Sports Medicine Clinic, Western University, London, Ontario, Canada.<sup>4</sup>Lawson Health Research Institute, London, Ontario, Canada.

**Introduction:** The current standard for measurement of RF-induced heating for implanted devices is described in ASTM International F2182-11a<sup>1</sup>. An implant under test is placed in a standardized rectangular phantom filled with gelled saline and exposed to RF fields for a period of 15 minutes. The temperature rise ( $\Delta T$ ) over this period, scaled to calorimetry-determined whole-body SAR (WBSAR), is used for MR-conditional labeling of the device. In a separate measurement, peak device  $\Delta T$  for a standard 10-cm Titanium rod after six minutes of RF exposure is used to calculate the Local SAR (LSAR) at the test location. The ASTM phantom is used because it represents a highly conservative situation (i.e. higher than expected heating) both in terms of the geometry and the material used. Results, and therefore labeling, obtained from tests using the ASTM phantom result in implants that exceed safety thresholds by a large margin. It is important to continue to investigate the nature and extent of the safety margin in these tests. Here we present a pilot cadaveric study at both 64 and 128 MHz, investigating the relationship between heating of a standard device (10-cm Ti rod) placed within the ASTM phantom versus a cadaveric leg. We hypothesize that the heating will be significantly reduced in the cadaver as compared to the ASTM phantom.

**Methods:** All RF-heating tests were performed on the Medical Implant Test Systems (MITS) 1.5 & 3.0, which are laboratory RF exposure platforms that operate at frequencies of 64 MHz & 128 MHz respectively. The implant used was the 10 cm titanium rod described above. Temperature probes were placed centered in pre-drilled 1 mm holes, centered 1 mm from each end of the rod. The phantom was filled with HEC gel, to a depth of 9-cm, and the implant was placed 3 cm from the side and at a depth of 32mm. A fresh-from-frozen cadaveric leg specimen was obtained and the implant was fixed to the anterolateral surface of the distal femur using zip ties. LSAR at 64 and 128 MHz was calculated by dividing peak device temperature after 6 minutes of RF exposure ( $\Delta T_{360s}$ ) by 1.3 or 1.45, respectively<sup>1</sup>. Calorimetry measurements for the MITS 1.5 & 3.0 systems indicated WBSAR values of 2.94 ( $\pm 0.12$ ) and 2.83 ( $\pm 0.15$ ) W/kg respectively. Calculated LSAR values were normalized to a WBSAR value of 2 W/kg via a linear interpolation.

**Results:** At 64 MHz and 128 MHz, implant  $\Delta T_{360s}$  in the cadaver was 1.57 and 9.87 °C, and normalized implant SAR was calculated as 0.82 and 4.81 W/Kg, respectively. In the phantom, implant  $\Delta T_{360s}$  was 9.81 and 15.4 °C, and normalized implant SAR was calculated as 5.13 and 7.51 W/kg at 64 and 128 MHz, respectively. Figure 1 (right) shows the implant heating in the cadaver and the phantom at both frequencies.

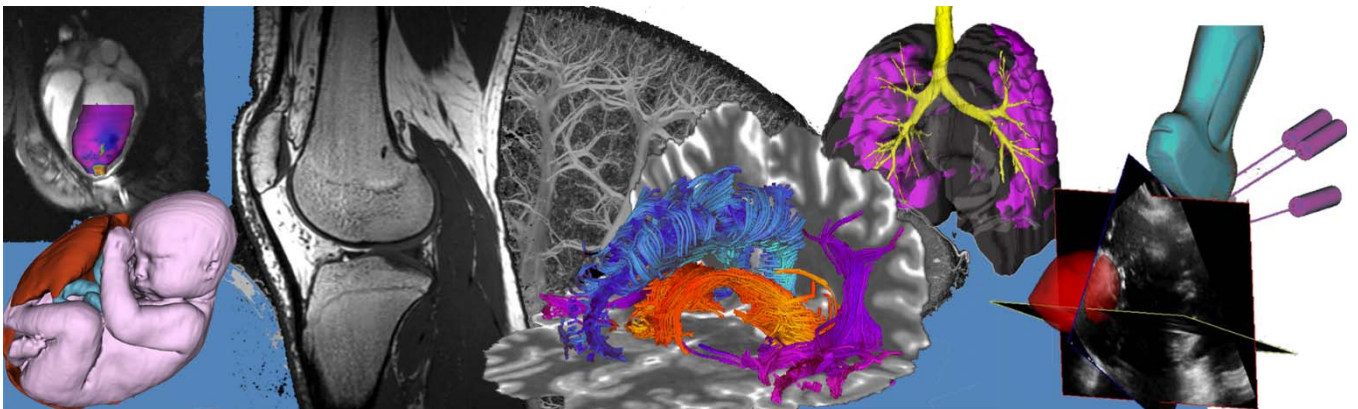
**Conclusions:** The reduction in device heating is attributed to the differences in geometry and electrical properties between the cadaver and the gel phantom. It is possible the difference in heating reduction between frequencies could be due to positioning errors within the systems. Poor visualization of the implant within the cadaver may have resulted in higher SAR exposure (i.e. device was closer to an RF hotspot), compared to the gel phantom. Nonetheless, these results suggest that margin between heating in the ASTM phantom and heating in-vivo could easily be a factor of 2-3 if not more. The cadaver is in a sense a perfect “geometrical representation” of the in-vivo situation; however, it is completely non-functional. It is possible that a simple geometry phantom, similar to the ASTM phantom, could be developed that introduced an approximation of in-vivo function (i.e. perfusion). Determining the margins between device heating results as a function of geometry and function is an important avenue for future work in our program.



1. ASTM F2182-11a, ASTM International, West Conshohocken, PA, 2011, [www.astm.org](http://www.astm.org)

# Oral Presentation Abstracts

## Session 5: Image Guided Intervention and Augmented Reality



## Assessment of intraoperative neurosurgical planning with the Microsoft HoloLens

Zachary Baum<sup>1</sup>, S. Ryan<sup>1</sup>, E. Rae<sup>1</sup>, A. Lasso<sup>1</sup>, T. Ungi<sup>1,2</sup>, R. Levy<sup>2</sup>, G. Fichtinger<sup>1,2</sup>

1. Laboratory for Percutaneous Surgery, Queen's University, Kingston, Canada
2. Department of Surgery, Queen's University School of Medicine, Kingston, Canada

**INTRODUCTION:** Neurosurgical lesions are inherently difficult to visualize due to their potentially complex shapes, which can be hidden within the skull or spinal canal [1]. Augmented reality (AR) is a technology in which computer-generated images are blended with a user's view of the real world. This technology enables the wearer to look 'inside' patients in 3D, in real time. We seek to assess whether the use of AR can aid in denoting surgical targets through an intraoperative performance comparison.

**METHODS:** An Institutional Research Ethics Board approved prospective cohort study was performed. Enrollment and consent were obtained from each patient subject, trainee (medical student, surgery resident), and neurosurgeon participant.

A surgical planning system was developed using the Microsoft HoloLens. Patient subject computerized tomography or magnetic resonance imaging was used to create 3D models of the patient's skin surface, brain, and intra-cortical lesion. Patient models are loaded to our system and brought into the operating room where participants must denote a surgical access point and trajectory with a conventional "anatomical" method and with our AR system. The conventional method allows use of only the patient's pre-operative images for reference to complete the task. Our AR method allows use of our system to view holographic models of the anatomy 'inside' the patient to complete the task (Fig. 1).

The denoted surgical access point and trajectory was compared to the gold-standard defined using a commercial surgical navigation system. The comparison was based on distance between participant access point and gold-standard access point (distance to access point), distance between participant trajectory and the lesion's center (distance to lesion), angle between participant trajectory and gold-standard trajectory (angle to access point), and angle between participant trajectory and trajectory between participant access point and the lesion's center (angle to lesion) (Fig. 2). Results are presented as mean [minimum-maximum].

**RESULTS:** Fifteen intraoperative assessments were completed. A one-tailed Mann-Whitney U Test for independent unpaired samples demonstrated significant reductions in distance to access point (33 [13-68] vs. 21 [2-44] mm,  $p=0.031$ ), distance to lesion (19 [5-49] vs. 13 [1-43] mm,  $p=0.037$ ), and angle to lesion (29 [4-67] vs. 17 [1-53] deg.,  $p=0.015$ ) for trainees ( $n=15$ ) using the AR system compared to the conventional approach. While mean angle to access point also decreased (37 [9-84] vs. 29 [11-57] deg.,  $p=0.44$ ) for trainees, the decrease was not significant. Neurosurgeon ( $n=15$ ) mean distance to access point (13 [5-28] vs. 10 [4-21] mm,  $p=0.18$ ) and mean distance to lesion (11 [4-20] vs. 10 [3-20] mm,  $p=0.17$ ) were not significantly lower using the AR system. Mean angle to access point (18 [3-28] vs. 18 [2-35] deg.) and mean angle to lesion (13 [5-27] vs. 13 [3-36] deg.) had no decrease.

**CONCLUSION:** A surgical planning system was developed using the Microsoft HoloLens to assess use of AR for denoting surgical targets intraoperatively. Overall, mean trainee performance was improved by the AR system, and neurosurgeon performance was largely unaffected by the AR system.

**REFERENCES:** [1] Meola *et al.*, *Neurosurgical Review*, 2017.



**Figure 1.** Neurosurgeon using the HoloLens to denote the surgical access point and trajectory.

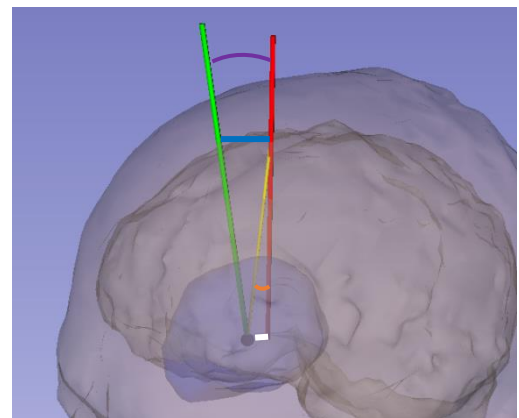


**Figure 2.** 3D models of surface anatomy, brain, and lesion from one case in our study.

*Black point* shows lesion center of mass; *green line* shows gold-standard access point and trajectory; *red line* shows participant access point and trajectory; *yellow line* shows trajectory from participant access point to lesion's center; *blue line* shows distance to access point; *white line* shows distance to lesion; *purple arc* shows angle to access point; *orange arc* shows angle to lesion.

**Augmented reality guidance in cerebrovascular surgery using microscopic video enhancement**R. Vassallo\*<sup>1,2</sup>, H. Kasuya<sup>3</sup>, B.W.Y. Lo<sup>4</sup>, T. Peters<sup>1,2</sup>, Y. Xiao<sup>1</sup><sup>1</sup>Robarts Research Institute, <sup>2</sup>School of Biomedical Engineering, Western University, London, Canada<sup>3</sup>Department of Neurosurgery, Tokyo Women's Medical University Medical Centre East, Tokyo, Japan<sup>4</sup>Montreal Neurological Hospital, Montreal, Canada

**Introduction:** Cerebrovascular surgery repairs abnormalities of blood vessels in the brain including aneurysms and arteriovenous malformations (AVMs). During surgical treatment, it is crucial to identify the direction of blood flow, as clipping the wrong vascular branch can result in severe complications. However, it is almost impossible to differentiate feeding from draining vessels visually and these procedures have a 31% complication rate [1]. Current standard practice highlights blood flow by injecting fluorescent dye observable through routinely used surgical microscopes. However, this fails to provide continuous hemodynamic updates and further complicates surgical workflows. The injected dye may also have adverse effects on patients' health. New solutions have been proposed, but they may risk rupturing fragile vessels or suffer from inaccurate real-time vessel identification. Therefore, a new contactless and robust method with minimal interruption of the surgical workflow is desired.

**Methods:** Five to ten second videos were obtained retrospectively from two cerebrovascular surgeries: one AVM and one aneurysm. The operating surgeon for these cases documented which vessels were bringing blood towards and away from the abnormal region, creating the ground truth. These short videos underwent enhancement methods [2] to reveal blood vessel pulsation patterns previously invisible to the unaided eye. The intensity fluctuations of each pixel were transformed into the frequency domain and analyzed on a pixel-by-pixel basis. To characterize the spectrum of each pixel, two metrics were used: spectral power and spectral entropy. Colourmaps of these metrics were created and overlaid onto the view of the surgical microscope's video feed, shown in **Fig. 1**. To create the AR display, the pixel-wise colourmap was combined with a frame from the original video using a novel multiplication-based image-fusion strategy.

**Results:** This method was validated by comparing the vessel identity (feeder or drainer) suggested by the colourmaps to the ground truth provided by the operating surgeon. These identities matched the ground truths in this proof-of-concept study. Overall, it can be seen in **Fig. 1** that the feeding arteries have a higher spectral power and lower spectral entropy than the draining vessels, representing stronger and more rhythmic pulsation patterns. Additionally, based on the preliminary experience of the clinicians involved in this project, image multiplication was preferable to the more common alpha-blending technique to combine images. It allows for a more natural fusion of the colourmap with the tissue textures without weakening its colour representation.

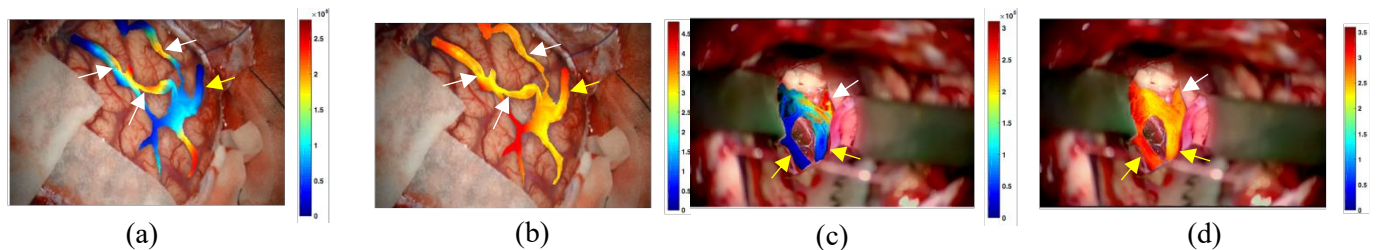


**Figure 1:** AR views with feeding vessels denoted with white arrows and draining vessels with yellow: (a) spectral power and (b) spectral entropy of AVM; (c) spectral power and (d) spectral entropy of aneurysm.

**Conclusions:** The preliminary results suggest that our proposed technique can identify feeding and draining vessels during cerebrovascular surgery. As a contactless method, it can provide continuous intraoperative hemodynamic information to the clinician, without disrupting the standard clinical workflow or injecting chemicals into the patient's body. This may lead to a safer and more informed surgical practice, and address the limitations in previously proposed solutions to this guidance problem. Future studies with more clinical cases, simulation, and animal models will further validate our method and provide better insights for the meaning of the observed vessel pulsation patterns.

**References:** [1] S. M. Michalak, et al., "Incidence and Predictors of Complications and Mortality in Cerebrovascular Surgery: National Trends From 2007 to 2012," *Neurosurgery*, 2016.; [2] H.-Y. Wu, et al., "Eulerian video magnification for revealing subtle changes in the world," *ACM T Graphics*, 2012.

## Navigation of the iKnife for intra-operative tissue characterization in neurosurgery

Mark Asselin<sup>1</sup>, Martin Kaufmann<sup>1</sup>, Natasja Janssen<sup>1</sup>, Julia Wiercigroch<sup>1</sup>, Kyle Sunderland<sup>1</sup>, Tamas Ungi<sup>1</sup>,  
Andras Lasso<sup>1</sup>, John Rudan<sup>2</sup>, Gabor Fichtinger<sup>1,2</sup>

<sup>1</sup>Laboratory for Percutaneous Surgery, School of Computing, Queen's University, Kingston, Canada

<sup>2</sup>Department of Surgery, School of Medicine, Queen's University, Kingston, Canada

**INTRODUCTION:** During tumor resection the goal is to remove the entirety of the tumor and the minimum of healthy surrounding tissue. In neuro-oncological surgery, the consequences of resecting surrounding healthy tissue are particularly severe, including loss of motor function or permanent neurological damage. With current methods, the surgeon has no real-time analysis of the tissue being dissected. The iKnife, a mass spectrometry based molecular resolution margin probe can provide surgeons this analysis. Researchers at Imperial College have shown that the iKnife has a sensitivity of 97.7% and specificity of 96.5% when classifying electrocautery smoke from tumor and healthy tissue across several tumor types [1]. However, the iKnife can only indicate the class of the tissue being cauterized and does not provide the surgeon critical information about where in the anatomy and the pre-operative imaging this tissue reading is from. In this paper we augment the iKnife with a neurosurgery navigation platform to demonstrate the feasibility of its use as a spatially navigated margin probe.

**METHODS:** To create this system, we developed a PLUS (Public Library for UltraSound) toolkit interface for the Medtronic StealthStation – a clinical standard neurosurgery navigation platform. To simulate intra-operative tissue classification, we built a machine learned model to differentiate the mass spectral signals of the surgical smoke resulting from electrocauterization. We collected the mass spectra of smoke produced by cauterizing porcine and bovine tissues (n=48 burns each) as simulated tumor & healthy tissue, respectively. We then used Waters Corporation's Abstract Model Builder (AMX) to create a PCA/LDA model to classify these spectra. We collected an independent test set of randomized burns (n=22) from fresh porcine & bovine tissue to assess the model's performance. Then using the SlicerIGT extension of the 3D Slicer software package we integrated the tracking information from the StealthStation and the molecular classifications from the mass spectrometer. We developed a visualization of the iKnife reading which positions the reading on pre-operative imaging, and in a 3D rendering of the skull (Fig. 1). This provides a high information-content visualization of the tissue classifications to an operating surgeon.

**RESULTS:** The PCA/LDA model correctly classified every mass spectrum in our test set (n=22). The system returned an average confidence in its classification of 99.37% for porcine tissue, and 99.36% for bovine (Table 1).

**CONCLUSIONS:** We have demonstrated an intra-operative mass spectrometry based margin probe capable of producing spatially localized tissue characterization in real-time.

**ACKNOWLEDGEMENTS:** G. Fichtinger is supported as a Canada Research Chair. This work was funded, in part, by NIH/NIBIB and NIH/NIGMS (via grant 1R01EB021396-01A1 - Slicer+PLUS: Point-of-Care Ultrasound) and by CANARIE's Research Software Program.

**REFERENCES:** [1] Balog et al., "Intraoperative Tissue Identification Using Rapid Evaporative Ionization Mass Spectrometry." *Science Translational Medicine*, vol. 5, no. 194, pp. 194ra93, 2013.

**Table 1.** Average confidence of iKnife at differentiating porcine & bovine tissues.

	Confidence	
	Mean (%)	SD (%)
porcine	99.37	0.015
bovine	99.36	0.029



**Fig 1.** Left: Molecular readings spatially localized on axial MRI slice. Middle: Physical setup, including simulated tumor tissue undergoing cauterization. Right: 3D model of the skull, including spatially resolved iKnife classifications.

## Design and evaluation of a new positron emission mammography ultrasound-guidance device for core needle biopsy in breast tumours

Claire K. Park<sup>1,2</sup>, Jeffrey Bax<sup>2</sup>, Aaron Fenster<sup>1,2</sup>

<sup>1</sup>Department of Medical Biophysics, Western University, London, Ontario, Canada

<sup>2</sup>Imaging Research Laboratories, Robarts Research Institute, London, Ontario, Canada

**Consortia:** Ontario Institute for Cancer Research – Imaging Translation Program

**INTRODUCTION:** Image-guided percutaneous biopsy is crucial for diagnosis and pre-surgical planning of women with breast cancer. High-resolution breast functional imaging using positron emission mammography (PEM) demonstrates increased sensitivity for detecting breast tumours compared to conventional modalities and techniques [1]. PEM has been shown to be useful for surgical planning and is suitable to guide biopsy [2]. Thus, our aim is to extend the use of PEM imaging by integrating it with an ultrasound (US) guided interventional technique to improve sampling of breast tumours. We will first achieve this by developing a new guidance device for core needle biopsy (CNB) in breast tumours compatible with a PEM system. To be implemented, a guidance device was designed to operate between PEM detector plates. We evaluated the range of US transducer positions relative to the biopsy needle target by mathematically modelling the system using geometric constraints of the device. We hypothesize that the guidance device will accurately position the transducer relative to the biopsy needle target, allowing the relevant area to be imaged independent of breast geometry and target depth.

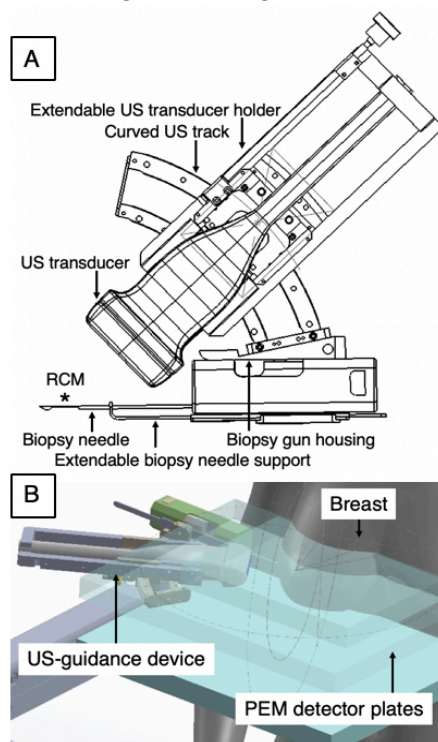


**Fig. 1:** A) Schematic illustration of the guidance device for breast biopsy. B) Relative device position to PEM detectors and breast.

regions accessed, constrained by collinearity between the transducer holder and biopsy housing.

**RESULTS:** The thickness of the device is 2.54 cm allowing in plane accessibility between detector plates for the full range of breast thicknesses seen in clinical practice [5]. The minimum and maximum target depths accessible were 1.56 cm and 5.74 cm. Targets within this range will have sufficient transducer contact for guidance. Vertical needle paths may be considered with sufficient tissue buffer, for shallow targets less than 1.56 cm in depth [4].

**CONCLUSIONS:** Based on our evaluation, the new guidance device demonstrates feasibility to be implemented on the PEM system. The device can be positioned between detector plates, in plane with the target. The design allows image-guided biopsy independent of breast geometry and target depth. Future work will examine mechanical device error and needle guidance accuracy using experimental phantoms.

**REFERENCES:** [1] Berg, WA., et al. *Breast J.* 12(1)309-23 (2006). [2] Kalinyak, JE., et al. *Breast J.* 17(2)143-51 (2011). [3] Ma, K., et al. *Med Phys.* 36(6)2118-29 (2009). [4] Newell, MS., & Mahoney, MC. *Tech Vasc Interv Radiol.* 17(1)23-31 (2013). [5] Salvagnini, E., et al. *Med Phys.* 43(9)5104-16 (2016).

# Characterizing the Accuracy and Precision of Micro-Coil Tracking in Ablation Catheters

**Authors:** Jay Soni<sup>†</sup>, Labonny Biswas<sup>†</sup>, Sebastian Ferguson<sup>†</sup>, Philippa Krahn<sup>†</sup>, M. Ali Tavallaei<sup>†</sup>, and Graham Wright<sup>†</sup>

**Institutional Affiliations:** Sunnybrook Research Institute (†)

**Introduction:** Magnetic resonance imaging (MRI) guided catheter ablations are a promising method to treat cardiac arrhythmia. MRI allows for excellent soft tissue contrast but compromises the ability to visualize the catheter. This study focuses on active tracking<sup>[1]</sup>, a method that localizes micro-coils on the catheter. We characterize the error in localizing the tip of catheter by tracking two, 3 mm long micro-coils near the distal tip of MR-compatible ablation catheters. An acceptable error tolerance for the catheter tip was determined to be  $< 6.1$  mm, by taking the typical lesion radius (7.5 mm)<sup>[3]</sup> produced by similar catheters and subtracting the minimum length of conductive tissue required for re-excitation (1.4mm)<sup>[5]</sup>; this would ensure all the target tissue is within the lesion radius.

**Methods:** Three experiments were conducted on a 1.5T MR scanner (MR450w, General Electric Healthcare, Waukesha, Wisconsin, USA). 9F MR-compatible catheters (Imricor Medical Systems, Burnsville, MN, USA) were placed in fixtures, in predetermined positions and orientations, and submerged in a polyacrylic acid (PAA) gel phantom<sup>[4]</sup> prior to scanning. The setup was scanned with high-resolution 3D FSE-XL images (512x512, 5mm slice thickness, 24 cm FOV, 24.8 ms TE, 500 ms TR, 90° flip angle) to establish the ground truth positions of the micro-coils. Data was acquired using two different active tracking sequences, implemented in RTHawk (HeartVista Inc., Menlo Park, California, USA). Tracking involved applying a non-selective RF pulse, then reading out MR data in the presence of a frequency-encoding gradient along a spatial axis. The first sequence applied the gradient along the X, Y, and Z axes while the second used Hadamard multiplexing with phase dithering<sup>[1],[6]</sup> (Table 1). For each projection, the centroid was calculated for a small window (twice the micro-coil length) around the peak to localize the coil along that projection, and correction for gradient non-linearities was applied.

**Results:** The micro-coils were tracked in 5 orientations along the X-Z plane near isocenter (-90°, -45°, 0°, 45°, 90°) with 0° referring to the catheter being aligned with +Z-axis, along the main magnetic field. This experiment was repeated twice (Table 2). In the third experiment, the micro-coils were tracked in 2 positions (isocenter, off-isocenter) while keeping the catheter oriented along the +Z-axis. The off-isocenter position was displaced by +149.14 mm along the X-axis and -207.33 mm along the Z-axis. The error in tip position was measured to be  $2.58 \pm 0.32$  (mm) at isocenter and  $6.20 \pm 0.75$  (mm) at off-isocenter. The Hadamard sequence data showed a larger variance for both near- and off-isocenter positions as compared to basic tracking.

**Conclusions:** The error in catheter tip position was within the acceptable error tolerance ( $< 6.1$  mm) for 5 different orientations along the X-Z plane. Placing the catheter away from isocenter increased the error to  $6.2$  mm  $\pm$  0.75 mm slightly exceeding the tolerance threshold. The error at off-isocenter appears to be due to a linear shift between measured and true positions, rather than a lack of precision, suggesting that gradient linearity could be a potential cause for the error and that gradient non-linearity correction does not fully correct for this. Future experiments will optimize the centroid algorithm to improve accuracy in tracking.

**Acknowledgments:** The authors thank the Federal Economic Development Agency of Southern Ontario and HeartVista Inc. for their support.  
 [1] Dumoulin et al., MRM 1993;29 [2] Daniels et al., MRI 2016;34 [3] Sapp et al., J Cardiovasc Electrophysiol 2006;17 [4] ASTM F2182-02a, ASTM International, 2002 [5] Ranjan et al., Circ Arrhythm Electrophysiol 2011;4 [6] Dumoulin et al., MRM 2010;63

Parameters	Basic active tracking	Hadamard-multiplexing with phase-field dithering
Flip angle	5°	5°
Pixels	512	256
FOV (cm)	60	30
Repetition time (ms)	14.268	4.136
Tracking rate (fps)	23.4	20.1
Spatial resolution (mm)	1.17	1.17

**Table 1:** Active tracking sequence parameters used to localize micro-coils

Experiments	Error in tip position: mean $\pm$ 2 SD (in mm)				
	-90°	-45°	0°	45°	90°
1	3.10 $\pm$ 0.70	2.33 $\pm$ 0.75	2.73 $\pm$ 0.53	2.71 $\pm$ 0.73	3.50 $\pm$ 0.50
2	1.92 $\pm$ 0.48	2.48 $\pm$ 0.48	2.91 $\pm$ 0.87	3.10 $\pm$ 0.77	3.90 $\pm$ 0.44

**Table 2:** Error in tip position as measured from two micro-coils over five orientations along the X-Z plane at near isocenter position

## Geometrically Variable 3D Ultrasound with Mechanical Assistance for Interventional Liver Cancer Therapies

Derek J Gillies<sup>1,2</sup>, Jeffery Bax<sup>2</sup>, Kevin Barker<sup>2</sup>, Lori Gardi<sup>2</sup>, David Tessier<sup>2</sup>, Nirmal Kakani<sup>3</sup>, Aaron Fenster<sup>1,2</sup>

<sup>1</sup>Department of Medical Biophysics, <sup>2</sup>Robarts Research Institute, Western University, London, Ontario, Canada; <sup>3</sup>Department of Radiology, Manchester Royal Infirmary, Manchester, UK;

**Introduction:** Liver cancer is the second and sixth most frequent cause of cancer mortality worldwide in men and women, respectively. Conventional curative therapies include transplantation and resection and currently report 5-year survival rates of about 40% with traumatic hospitalization experiences for approximately 26% of liver resection patients and 33% of liver transplant patients. These experiences include serious complications like organ rejection that lead to long patient recovery times. Minimally invasive percutaneous techniques, such as radiofrequency ablation, offer alternative therapy options with lower complication rates and shorter recovery times, but these procedures have high local cancer recurrence rates due to insufficient or inaccurate local tumour ablation. Minimally invasive techniques typically use x-ray computed tomography images for planning and two-dimensional (2D) ultrasound (US) for intraoperative guidance of applicator insertion(s) into the tumour(s). Poor ablation coverage has been associated with 2D US guidance, leading to variability in applicator targeting and placement accuracy. Thus, we have developed a novel intraoperative three-dimensional (3D) US imaging and guidance system with the goal of improving placement and verification of therapy applicators during focal liver tumour ablation therapies.

**Methods:** A three-motor mechanical mover was designed to provide geometrically adjustable linear, tilt, and hybrid geometries for variable 3D US fields-of-view. 3D-printed holders can be designed for any clinically available 2D US transducer and attached to this mover to intraoperatively guide therapy applicator insertions. This mover is held by a counterbalanced mechanically encoded tracking system mounted to a cart that features foot-released electromagnetic brakes for ease-of-use in the operating room. Verification of the three-motor mover was first performed using optical tracking with a mounted stylus to confirm mechanical motions of the scanner. Image reconstruction was assessed using a string phantom with known dimensions and manually measured to validate geometric accuracy. Preliminary 3D US images were acquired of a volunteer's liver to assess clinical applicability.

**Results:** Optical tracking using the stylus resulted in mean linear and angular motion differences of 0.21 mm (0.20%) and 0.23° (0.52%), respectively. Image reconstruction of the string phantom resulted in mean linear errors <3% on the string phantom. Human volunteer images were able to visualize the portal vein bifurcation, gallbladder, and kidney, which are clinically relevant anatomy.

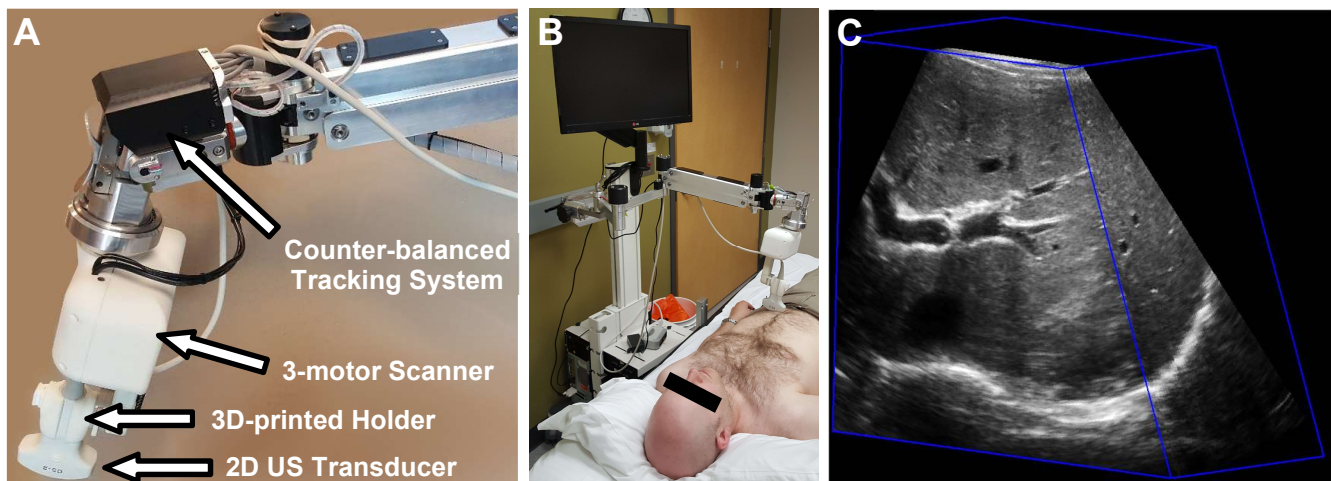


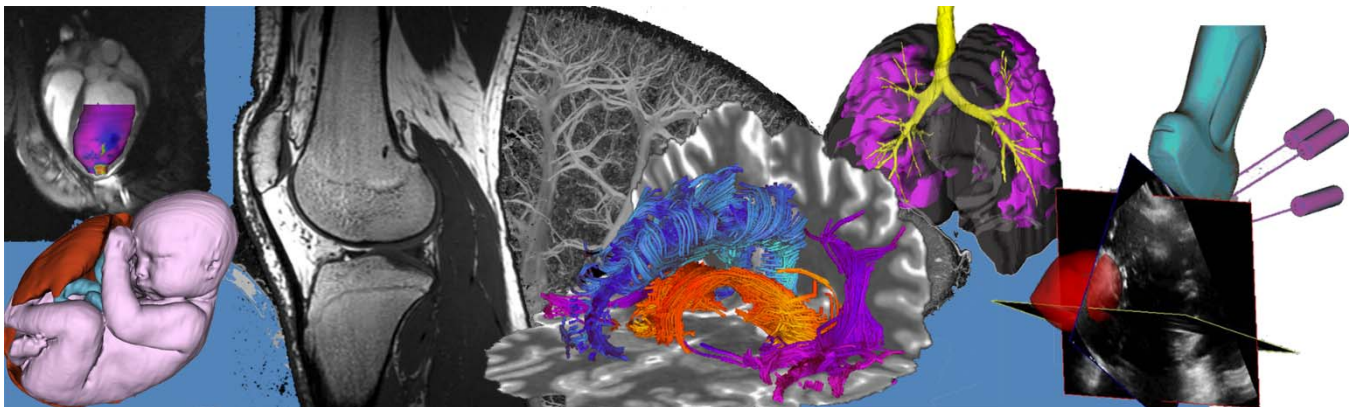
**Figure 1.** Mechanical wrist view (A), proposed clinical use (B), and a 3D US liver image using the proposed mechanically assisted 3D US system

**Conclusions:** The proposed three-motor mover assembly was shown to reconstruct images accurately and allows for variable scan geometries to accommodate clinical anatomical variations. The mechanically assisted 3D US system was able to image clinically relevant anatomy and current work is focused on quantifying the tracking system encoder accuracy prior to a simulated image-guided phantom procedure.



# Oral Presentation Abstracts

## Session 6: Bone and Joint Imaging



## Differentiation of Osteoblastic and Healthy Bone Tissue in Metastatically Involved Vertebrae using Radiomic Features

Allison Clement<sup>1,2</sup>, Cari Whyne<sup>1,4</sup>, Margarete Akens<sup>2,3</sup>, Albert Yee<sup>1,4</sup>, Michael Hardisty<sup>1</sup>, Phoenix Wilkie<sup>1</sup>

<sup>1</sup>Sunnybrook Research Institute, Toronto, Canada <sup>2</sup>Institute of Biomedical and Biomaterials Engineering, University of Toronto, Canada <sup>3</sup>Department of Surgery, University of Toronto, Canada <sup>4</sup>Techna Institute, Toronto, Canada <sup>5</sup>Department of Medical Biophysics, University of Toronto, Canada

**Introduction:** Quantification of metastatic involvement of the spine is important for assessing disease progression and treatment response. Quantification is challenging as tumours may appear as osteolytic (bone resorbing), osteoblastic (bone forming) or mixed. Metastasis affects bone deposition and quality, which can be visualized as a change in trabecular bone texture in micro-computed tomography ( $\mu$ CT) imaging. This investigation aims to develop an automated method to segment osteoblastic lesions in  $\mu$ CT images from a preclinical model of metastatic vertebrae using radiomic-based feature extraction from medical images. We hypothesize that radiomics will be sensitive to changes in osteoblastic lesion bone texture and that these changes will be useful for automating osteoblastic segmentation.

**Methods:** Osteoblastic metastases were generated via intracardiac injection of human ZR-75-1 breast cancer cells into a preclinical athymic rat model (n=3). Four months post inoculation, ex-vivo  $\mu$ CT images (34 $\mu$ m,  $\mu$ CT100, Scanco) were acquired of third lumbar vertebra (L3).

The trabecular bone within each vertebra was isolated using an atlas and level-set based approach. Pyradiomics was used to calculate 3D image features at each voxel location within the trabecular bone. Manual segmentations of lesions were verified by ground truth segmentations confirmed by histology.

Osteoblastic lesions isolation was done by thresholding of individual Radiomic feature maps. Segmentation accuracy (Dice Similarity Coefficient (DSC)) of osteoblastic tissue was evaluated on randomly selected axial and sagittal 2D slices from L3 vertebrae (n=6). A Random Forest Classifier was used to combine multiple feature maps. Randomly selected axial and sagittal from 2D slices from L3 vertebrae were used for input training data (n=6) and test data (n=3). DSC was used to compare osteoblastic manual segmentation with generated random forest predictions.

**Results:** The radiomic based features that best segmented osteoblastic tissue while optimizing computational time were derived from the Neighbouring Gray Tone Difference Matrix (NGTDM). Measures of coarseness yielded the best agreement with the manual segmentations (DSC=70 $\pm$ 7%) followed by contrast, strength and complexity (DSC=65 $\pm$ 13%, 54 $\pm$ 28%, and 48 $\pm$ 26%, respectively). These features were combined using machine learning based classification to improve segmentation performance. Random Forest classification was found to predict accurate results for segmentation of input training data (n=6, DSC=99 $\pm$ .2%). Test data predictions, example seen in Figure 1, were found to have a decreased predictive accuracy (n=3, DSC=55 $\pm$ 19%), likely due to the minimal amount of training data.

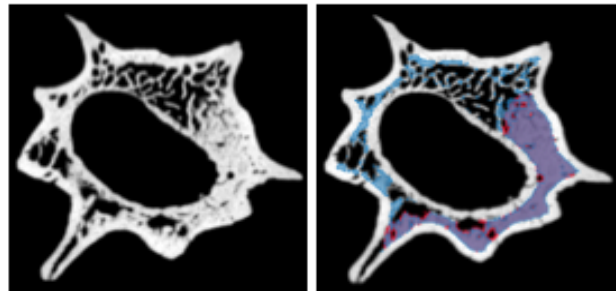


**Figure 1:** Test data slice. Left is  $\mu$ CT Scan, Right Blue indicates segmentation predictions, Red indicating the manual segmentation and Purple showing the overlap.

**Conclusion:** This pilot study using a radiomic based approach demonstrates the utility of the NGTDM features for segmentation of vertebral osteoblastic lesions. In future work, we will incorporate increased amounts of training data as well as explore segmentation in three dimensions toward improving automated quantification of osteoblastic metastasis for evaluation of new and existing treatments.

## Iterative Design of a Small-Animal Hip-Hemiarthroplasty Model for Preclinical Orthopaedic Research

Adam. D.M. Paish<sup>1,2</sup>, Hristo N. Nikolov<sup>1,2</sup>, Emily A. Truscott<sup>2</sup>, Alexander O. El Warrak<sup>4</sup>, Ian D. Welch<sup>5</sup>,  
Matthew G. Teeter<sup>1,2,6</sup>, Douglas D. Naudie<sup>2,6</sup>, David W. Holdsworth<sup>1,2,6</sup>

<sup>1</sup>Robarts Research Institute, London ON, <sup>2</sup>Western University, London ON, <sup>4</sup>VCA Hospitals, Concord NH, <sup>5</sup>University of British Columbia, Vancouver BC, <sup>6</sup>London Health Sciences Centre, London ON

**Introduction:** As new innovations are developed to improve the longevity of joint replacement components, preclinical testing is necessary in the early stages of research into areas such as osseointegration, metal-cartilage wear and peri-prosthetic joint infection. Large-animal studies have traditionally been used to test load-bearing components, but are expensive, requiring that animals be housed in special facilities. In contrast, a small-animal model, such as the rat, has several advantages, including lower cost and broad use across the basic sciences. However, load-bearing implants are difficult to manufacture in the sizes required for small-animal testing. Fortunately, this barrier can be overcome by combining micro-CT imaging to create custom rat hip implants, and additive manufacturing (3D metal-printing) to permit rapid prototyping and iterative implant design. Thus, our objectives are to create and optimize a rat 3D-printed hip hemi-arthroplasty system and to develop a surgical approach that will allow for *in vivo* testing of functional implants in a preclinical small-animal model.

**Methods:** A database of n=25 micro-CT volumes (154 $\mu$ m 80kVp, 50mA, 16s, *eXplore Locus Ultra*, GE Medical) of male Sprague-Dawley rats (390-610g) were analyzed to guide the creation a femoral implant template in computer-aided design software (*Solidworks*, Dassault Systemes). Several variants were created, including collared and collarless designs, and in a range of sizes to accommodate rats of various weights. Initial prototypes were 3D-printed in 316L stainless steel (no pores), with subsequent iterations printed in F75 cobalt-chrome (500 $\mu$ m pores) (*AM 125*, *AM 400*, Renishaw plc). N=5 live Sprague-Dawley rats (430-900g) received implants via either an anterior approach (AA) (n=3) or posterior approach (PA) (n=2), in order to compare muscle preservation and ease of installation between the two approaches. Micro-CT imaging (120kVp, 20mA, 16s) and X-ray fluoroscopy (60Hz) were performed post-operatively and at 1, 3, 6, 9 and 12 weeks to evaluate gait and component positioning within the bone.

**Results:** Implantation was achieved in all cases, and each animal was observed to ambulate on its affected limb post-operatively and at 3 weeks via fluoroscopy. The first rat (900g, 316L, AA), was kept for 11 months post-implantation, with no evidence of implant failure. Imaging of the second rat (500g, 316L, AA) revealed evidence of implant subsidence at three weeks. The third rat (750g, F75, AA) experienced a hairline fracture intraoperatively, which became non-union at its 9-week time point. The fourth rat (500g, F75, PA) has currently had no complications at 9-weeks. The fifth rat (430g, 316L, PA) experienced implant rotation at 6 weeks.

**Conclusions:** We report the first hip hemi-arthroplasties in a rat using custom 3D-printed implants. The PA afforded better access to install implants and required less aggressive muscle retraction and release, and will be used in future surgeries. The F75 implant with pores may facilitate better primary and secondary fixation, and will be used at the design template for future implants, including a set in Ti6Al4V titanium alloy. This model provides a low-cost preclinical platform for investigating the bone-metal and metal-cartilage interfaces. Future work will include a peri-prosthetic infection study using bioluminescence imaging to evaluate bacterial growth around components, before and after treatment with antimicrobial agents.

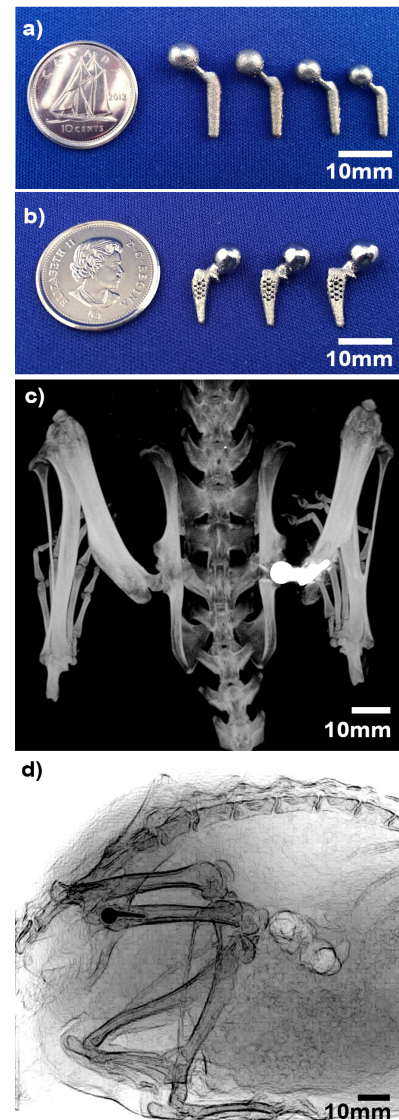


Fig 1: Custom rat implant set in (a) 316L SS and (b) F75 Co-Cr; (c) Maximum intensity projection of a rat at 3 weeks post-implantation, and; (d) fluoroscopic image of a rat with an implant *in situ*.

**Micro-CT of Kangaroo Cervical Spine: Analysis of Bone Mineral Density of C3 – C7**Joseph U. Umoh<sup>1</sup>, Helium Mak<sup>2</sup>, Wankei Wan<sup>2</sup>, and David W. Holdsworth<sup>1,3</sup>

Development of Novel Therapies for Bone and Joint Diseases Consortium

<sup>1</sup>Preclinical Imaging Research Centre, Robarts Research Institute, <sup>2</sup>Depts. of Chemical and Biochemical Engineering, <sup>3</sup>Depts. of Medical Biophysics and Surgery, Western University, London, ON, Canada

**Introduction:** The cervical spine supports the head, allows movement of the neck, and protects the spinal cord from injury. Changes in the bone mineral density (BMD) of the cervical vertebrae can indicate changes in the strength of these bones in response to loading. Characterization of BMD within the cervical vertebrae can improve our understanding of the biomechanics of the cervical vertebra and susceptibility to injury. The kangaroo has recently been investigated as a model of human thoracic spine,<sup>1</sup> based on its pseudo-biped nature and relatively easy availability. The purpose of this study is to quantify and characterize the BMD and geometry of the kangaroo cervical vertebrae C3 – C7, using micro-computed tomography (micro-CT).

**Methods:** Five kangaroo cervical spines were used in this study. Micro-CT imaging was used to acquire image data of the spines (Fig. 1). They were imaged on the same micro-CT scanner (GE Locus Ultra), with the same scan protocol (x-ray tube voltage 80 kV, tube current 55 mA, 1000 projections, exposure time 16 s) and the same reconstruction parameters (154  $\mu\text{m}$  3D image voxels). Each of the cervical vertebrae (Fig. 2) was segmented to create an isosurface of geometry. Using the image data of the vertebrae, water, and our bone-mimicking phantom (SB3), we computed BMD (expressed as mg hydroxyapatite [HA] per  $\text{cm}^3$ ) as previously described<sup>2</sup>. Density of the bone equivalent of the hydroxyapatite in the SB3 used to compute the BMD was 1.073  $\text{g}/\text{cm}^3$ .

**Results:** The mean BMD of the vertebrae (Fig. 3) appears to decrease from C3 towards C5 and also decrease from C7 towards C5. Repeated measures ANOVA shows that the BMD of the cervical vertebrae (C3 - C7) is significantly different ( $P < 0.05$ ,  $R^2 = 0.02$ ).

**Conclusions:** This study presents estimates of the BMD of the kangaroo cervical vertebrae C3 – C7. Within this sample population, BMD appears to reach a minimum at C5. Knowledge of the bone mineral density and geometric shape of the kangaroo cervical spine will help to guide future *ex vivo* and *in vivo* studies of spine biomechanics, using the kangaroo model.

**References:** [1] Balasubramanian *et al.* *Eur Spine J.* 2016; 25: 4140-4154. [2] Beaucage, K.L., Pollmann, S.I., Sims, S.M., Dixon, S.J., and Holdsworth, D.W. *Bone Reports* 2016; 70-80.



**Figure 1:** Micro-CT, isosurface-rendered image of a kangaroo cervical spine, showing C3 – C7, together with the reference T1.



**Figure 2:** Micro-CT image of a kangaroo C4 showing the anterior view (top), posterior view (middle) and superior view (bottom).

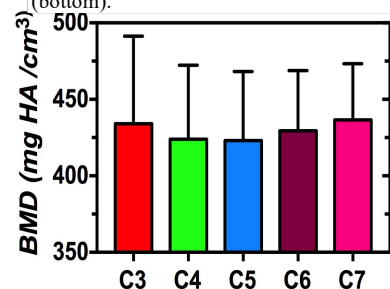


**Figure 3:** Estimates of the mean BMD of the kangaroo cervical vertebrae. Error bars are standard deviation.

### **Multimodal Image-based Analysis of Ultrafast Burst Mode Laser Ablation on Articular Cartilage**

Melissa Prickaerts<sup>1,2</sup>, Kailas Cassidy<sup>1</sup>, Tom Dzelzainis<sup>3</sup>, Sabrina Hammouti<sup>3</sup>, Elena Dybner<sup>1</sup>, Cameron Romanet<sup>1</sup>, Ahmad Golaraei<sup>3,4,5</sup>, Faiyza Alam<sup>3</sup>, Valentin Demidov<sup>2,4</sup>, Ömer Ilday<sup>6,7,8</sup>, Hamit Kalaycıoğlu<sup>6,7</sup>, Seydi Yavas<sup>9</sup>, I. Alex Vitkin<sup>2,4,10</sup>, Virginijus Barzda<sup>3,5</sup>, Lothar Lilge<sup>2,4</sup>, Robin Marjoribanks<sup>3</sup>, Margarete Akens<sup>1,2,11</sup>

<sup>1</sup>Techna Institute, UHN, <sup>2</sup>Department of Medical Biophysics, University of Toronto, <sup>3</sup>Department of Physics, University of Toronto, <sup>4</sup>Princess Margaret Cancer Centre, UHN, <sup>5</sup>Department of Chemical and Physical Sciences, University of Toronto Mississauga, <sup>6</sup>UNAM, National Nanotechnology Research Center, Bilkent University, Ankara, Turkey, <sup>7</sup>Department of Physics, Bilkent University, Ankara, Turkey, <sup>8</sup>Department of Electrical and Electronics Engineering, Bilkent University, Ankara, Turkey, <sup>9</sup>Lumos Laser, Istanbul, Turkey, <sup>10</sup>Department of Radiation Oncology, University of Toronto, <sup>11</sup>Department of Surgery, University of Toronto

**Purpose:** Osteoarthritis significantly decreases millions of patients' quality of life. Tissue grafting can correct large areas of damaged joint cartilage and become permanently incorporated into the body. This can prevent or delay more invasive joint replacement surgery, decreasing the risk of multiple replacement surgeries of the same joint. Ultrafast burst-mode lasers are a promising surgical tool that could allow for minimally invasive procedures yielding precise custom-cut osteochondral grafts and recipient beds, with minimal collateral tissue damage. Multimodal imaging approaches are necessary to determine unintended consequences of laser ablation on cells and extracellular matrix components. This work seeks to ascertain the optimal conditions for tissue ablation rates while facilitating rapid integration of the graft.

**Methods:** Articular cartilage explants were harvested from femoral condyles of healthy Yorkshire pigs. The explants were partially ablated with an ultrafast burst-mode ytterbium fibre laser (1037nm wavelength, 350fs pulse duration, 60 pulses per burst, 7µm spot diameter). Damage was compared to mechanical modification using a surgical drill bit (straight shank with four flutes) and a 3mm biopsy punch, which are used commonly in joint surgeries. Modified cartilage was stained with a live/dead fluorescence-based assay, and confocal microscopy was used to generate series of cross sections (Z-stacks) depicting cell viability around ablation craters. Imaris software generated 3D models from these Z-stacks, and cell death margins were quantified. Histological tissue sections, stained with hematoxylin and eosin (H&E) and safranin-O (SO), were analysed using HALO machine learning software. Algorithms were tuned to identify regions with differences in cellular structure and proteoglycan content. Change of collagen fibril organization within the extracellular matrix was evaluated using polarization-resolved second harmonic generation (PR-SHG) imaging. Scanning electron microscopy (SEM) enabled examination of cut face topographies. Measured cross-sectional areas and user-programmed laser scanning speeds provided the different material removal rates. Optical coherence tomography (OCT) and a MATLAB script allowed for calculations of bulk material removed.

**Results:** Cartilage tissue was ablated in custom geometries up to 0.25 mm<sup>2</sup> with an estimated maximum removal rate of 8.25 x 10<sup>-3</sup> mm<sup>3</sup>/J. Laser ablation resulted in significantly less cellular damage versus mechanically drilled holes and biopsy punch removal, (1-way ANOVA, p<0.01; Tukey, p<0.01), while HALO analysis revealed changes in tissue structure and proteoglycan content immediately surrounding removal sites. Damage varied significantly between methods (H&E and SO: 1-way ANOVA, p<0.01) with the surgical drill producing significantly larger regions of damage (Tukey, p<0.01). PR-SHG imaging showed changes in collagen organization (ratio of in-plane vs. out-of-plane fibrils increased), and a decrease in fibril counts, suggesting structural changes to collagen fibrils, adjacent to both sites of ablation and mechanical removal. The damage boundaries corresponded directly to those measured in histological sections. SEM images of ablated graft beds depicted precise edges and smooth walls.

**Conclusions:** Unlike mechanical methods, ultrafast burst-mode laser ablation produces minimal levels of collateral tissue damage while allowing for graft customization. Ongoing investigations seek the optimal parameters for laser ablation of musculoskeletal tissues. Use of multiple complementary 2D and 3D imaging modalities provides information about laser ablation outcomes in the studied 3D tissues. This work highlights potential clinical benefits of using an ultrafast burst-mode laser as an orthopaedic tool.

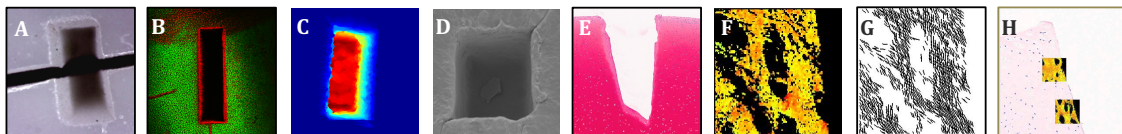


**Figure 1. Effects of Laser Ablation on Cartilage** A) Brightfield images of cut. B) Confocal microscopy image of a live/dead fluorescent assay that labelled damaged cells red and live cells green. C) Calculation of the ablated tissue volume using OCT imaging and a MATLAB script. Volume = 0.251 mm<sup>3</sup>. Blue to green to red indicates greater depth. D) SEM image of cut face. E) SO staining indicates relative proteoglycan content. F) Susceptibility ratios are fit for each pixel in area analysed by PR-SHG, green to yellow to red indicates a higher ratio. G) Projections of the in-out plane fibrils determined by PR-SHG. H) PR-SHG analysis mapped to H&E stained tissue

### Three-dimensional computed tomographic reconstruction in a natural weight-bearing stance using ceiling-mounted x-ray fluoroscopy

Rudolphe J Baronette<sup>1,2,3</sup>, Steven I Pollmann<sup>2</sup>, Matthew G Teeter<sup>1,3,4,5</sup>, David W Holdsworth<sup>1,2,3,4</sup>

<sup>1</sup>Western Bone and Joint Institute

<sup>2</sup>Imaging Research Laboratories, Robarts Research Institute

Depts. of Medical Biophysics<sup>3</sup> and Surgery,<sup>4</sup> Western University

<sup>5</sup>Lawson Health Research Institute, London ON, Canada

**Introduction:** Weight-bearing 3D images for investigation of various musculoskeletal diseases have become a recent focus in the medical imaging community. Previous research demonstrated significant differences between non-weight-bearing and weight-bearing conditions in the lower extremity. Recent advances have developed ceiling-mounted flat-panel cone-beam computed tomography (CBCT) scanners to evaluate the lower extremity while weight-bearing. These systems provide superior weight-bearing information about the lower extremity, but may deviate from a perfect trajectory during rotation thus requiring image corrections prior to reconstruction. The objective of this study was to characterize imperfections during rotation of a flat-panel ceiling-mounted x-ray fluoroscopy system, implement image-based corrections, and validate accuracy of reconstructed image volumes.

**Methods:** Image acquisitions were performed using a ceiling-mounted single-plane x-ray fluoroscopy system, shown in **Figure 1a** (Adora RF, Nordisk Røntgen Teknik A/S, Denmark), equipped with a flat-panel detector (CXDI-50RF, Canon) that has a 2688 x 2208 image matrix over a nominal 43 x 35 cm field of view. All projection images were acquired using the 2 x 2 binning mode, resulting in a 1344 x 1104 matrix with 320  $\mu$ m pixel size. Image reconstruction requires seven steps that include: (1) characterization of the flat-panel detector to determine a logarithmic or linear response to x-ray exposures, (2) correction for pixel-to-pixel variations through application of a bright and dark image, (3) recording gantry position at each x-ray exposure with a custom-designed x-ray detector to encode the gantry position, (4) characterization of gantry motion during rotation using a 3D printed calibration cube, (5) application of image-based corrections based on characterization of gantry motion, (6) back-projection of image data to produce 3D image reconstructions, and (7) verification of image quality parameters including: geometric accuracy, image noise, linearity, spatial resolution, and uniformity. A cadaveric knee (**Figure 1b**) was also used to evaluate image quality. Resulting image volumes (27 cm length, 32 cm diameter) were reconstructed with an isotropic voxel spacing of 0.25 mm.

**Results:** Overall, the ceiling-mounted gantry displays significant, but exceptionally reproducible imperfections in gantry motion during image acquisitions within a day, as well as over a year. Reproducibility of gantry motion in the x-plane was high, with standard deviations of 2.47 pixels (0.79 mm). The system uniformity (calculated as the average difference in signal intensity values between the peripheral and central regions) was 31 HU, shown in **Figure 1c**.

**Conclusion:** We demonstrated for the first time that a ceiling-mounted single-plane x-ray fluoroscopy system can generate accurate CBCT reconstructions using image-based corrections for highly reproducible imperfections in gantry motion. The ceiling-mounted x-ray fluoroscopy system allows for a larger FOV, compared to current CBCT scanners.

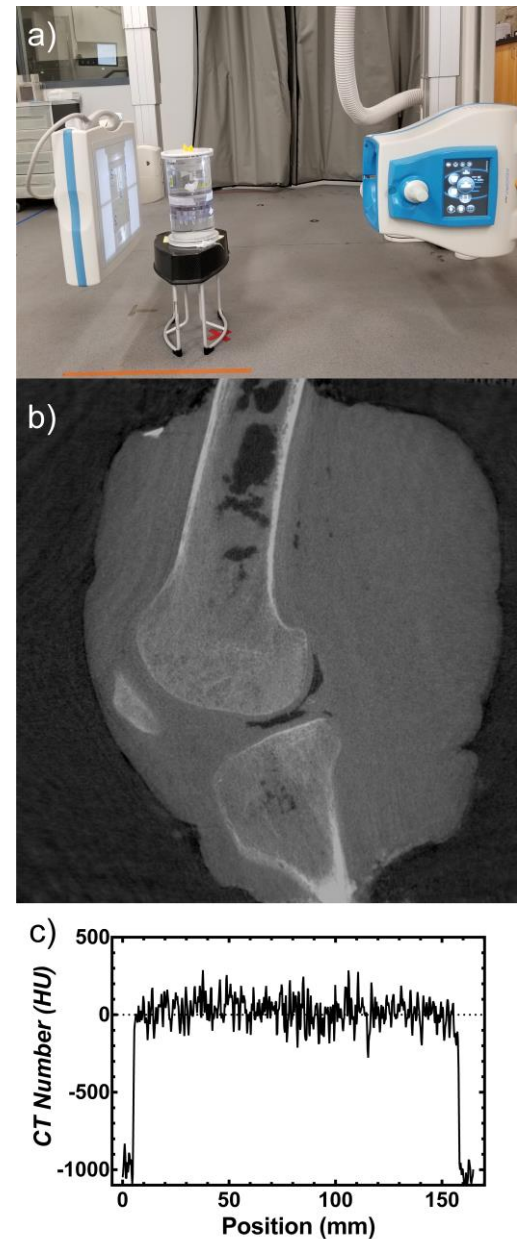


**Fig. 1:** (a) photo of the Adora RF x-ray fluoroscopy system; (b) reconstructed sagittal slices with an artefact correction; and (c) image uniformity shown as a line profile in an area of uniform density.

## Intra-Operative Verification of the Glenoid Implant Position with Structured Light Imaging in Total Shoulder Arthroplasty

David Burns<sup>1,3</sup>, Robin Richards<sup>2,3</sup>, Cari Whyne<sup>1</sup>

<sup>1</sup>Sunnybrook Research Institute, Toronto, Ontario, Canada.

<sup>2</sup>Sunnybrook Health Sciences Centre, Toronto, Ontario, Canada.

<sup>3</sup>University of Toronto, Division of Orthopaedic Surgery, Toronto, Ontario, Canada.

**Introductions:** Positioning of the glenoid component is one of the most challenging steps in total shoulder arthroplasty. Prosthetic longevity and functional outcomes are considered highly dependent on accurate positioning. Currently, there are no adequate means to verify the position of the glenoid component intra-operatively which is a significant impediment to accurate positioning. We describe and evaluate Bullseye, a novel intra-operative imaging system that utilizes a hand-held structured light sensor and computer vision algorithms to verify the 3D position of the glenoid vault guide pin prior to preparation of the glenoid for component implantation.

**Methods:** The Bullseye system was evaluated for measuring the position of the glenoid vault guide pin on 10 Sawbone and 6 cadaveric procedures. Pre-operative CT scans were obtained for each scapula. The glenoid vault of the scapulae were instrumented with a 3.2 mm threaded guide pin. The Bullseye optical tracker was positioned over the guide pin against the glenoid articular surface. A single optical color surface image of the surgical field was obtained using a hand-held structured light sensor, capturing the optical tracker and the glenoid surface. The position of the glenoid guide pin with respect to the scapula was registered from the pre-operative CT scan and the intra-operative optical surface image. The accuracy of the Bullseye system for measuring the glenoid vault guide pin position was validated against a post-operative CT scan in terms of start-point offset and angular trajectory of the guide pin.

**Results:** All 16 imaging procedures were carried out successfully. For the sawbone procedures, the Bullseye glenoid vault guide pin position measurement was accurate to  $0.37 \pm 0.28$  mm for the start point, and  $0.92 \pm 0.40$  degrees for the trajectory. For the cadaveric procedures, the accuracy was  $0.54 \pm 0.49$  mm for start-point, and  $1.72 \pm 0.95$  degrees for trajectory.

**Conclusions:** Optical surface structured light imaging can be used to accurately evaluate the 3D position of the glenoid vault guide pin for total shoulder arthroplasty in-vitro and ex-vivo. The Bullseye imaging system permits shoulder surgeons to verify and readjust the glenoid vault guide pin as necessary to achieve accurate implantation of the glenoid component in total shoulder arthroplasty. Future work will involve Phase 1 validation of the Bullseye system in the setting of a clinical trial, and demonstration of improved glenoid component positioning outcomes with its use.

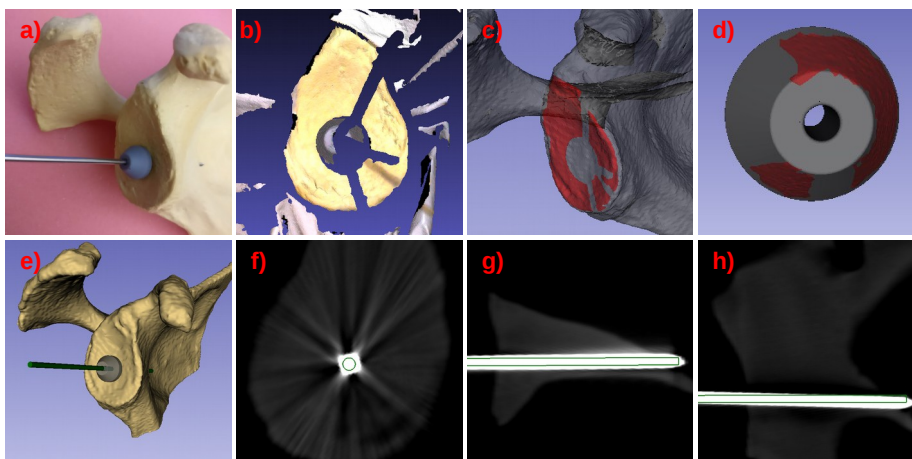
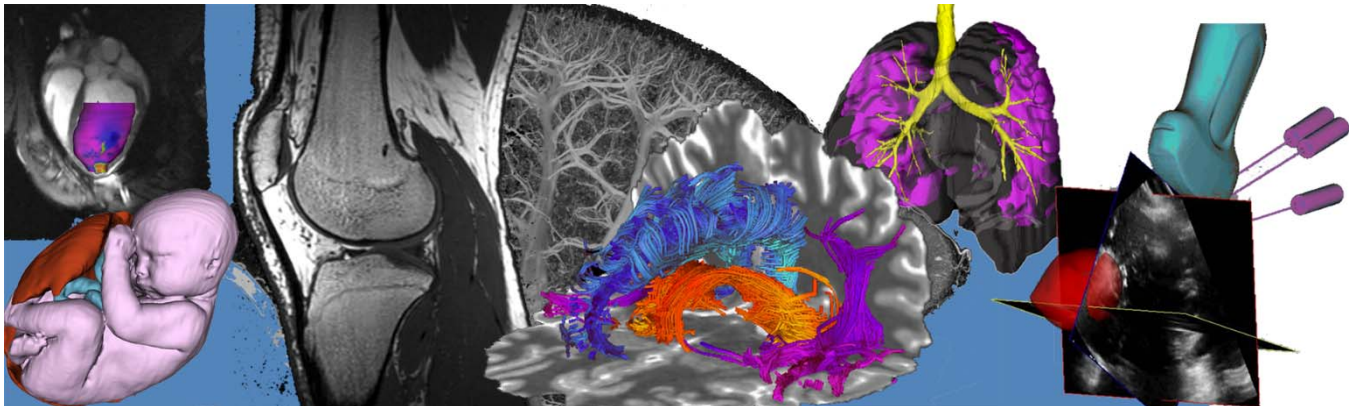


**Figure 1:** a) Optical fiducial on sawbone scapula, b) structured light image of the scapula and optical fiducial, c) registration of optical glenoid surface image to CT data, d) registration of optical fiducial image to its computer model, e) 3D model of registered fiducial and predicted guidepin position, f-h) predicted (green) and actual guidepin position for sagittal, axial, and coronal planes.

# Oral Presentation Abstracts

## Session 7: Cancer Imaging





## Radiomics for detecting recurrence after stereotactic ablative radiotherapy: sensitivity of performance to sample size

Salma Dammak<sup>1</sup>, David Palma<sup>1</sup>, Sarah Mattonen<sup>2</sup>, Suresh Senan<sup>3</sup>, Aaron D. Ward<sup>1</sup>

<sup>1</sup>The University of Western Ontario, <sup>2</sup>Stanford University, <sup>3</sup>VU University Medical Center

**Introduction:** Stereotactic ablative radiotherapy (SABR) is a guideline-recommended treatment option for patients with Stage I non-small cell lung cancer who are inoperable [1]. This treatment, however, has a high likelihood of introducing a type of benign radiation-induced lung injury (RILI) that can be difficult to differentiate from disease recurrence on follow-up computed tomography (CT) scans. We have previously shown that radiomics coupled with machine learning [2] can differentiate RILI from recurrence in the 2–5 month period post-SABR with an area under the receiver operating characteristic curve (AUC) of 0.77 (n=81) [ImNO 2018]. Our primary objective was to conduct a simulation study measuring whether system performance plateaus as the n=81 sample size was approached, which would suggest a sufficiently large data set. Our secondary objective was to measure whether different classifiers provided similar performance, suggesting suitability of our selected features for this problem.

**Methods:** This study was approved by our institutional human subjects research ethics board. We obtained contrast-enhanced follow up CT scans taken 2-5 months post-SABR from 81 patients matched at 1 recurrence:2 RILI. We analysed two regions of interest (ROIs): the consolidative (red in Figure 1) and peri-consolidative (blue in Figure 1) regions, which were contoured using our semi-automated algorithm [3]. From these regions, we extracted a total of 127 features, which we reduced to 10 features using supervised forward feature selection with seven different classifiers, obtaining seven sets of 10 features. The same features were then used in leave-one-out to investigate which were best at separating RILI from recurrence using 1 to 10 features. Using the resulting AUC metric, we determined the four best performing combinations of features and classifiers (highest AUC) when using 81 patients. For those four systems, we performed a drop-out experiment where three patients (2 RILI:1 recurrence) were removed from the data set consecutively until the sample size reached 21 patients, and feature selection then classification were repeated for the shrunken dataset using the same parameters. We measured AUC, classification error, false positive rate (FPR), and false negative rate (FNR) as the number of patients was reduced across the four different systems. Then, we calculated the mean and standard deviation across all systems for the different numbers of patients.

**Results:** The top four performing systems with 81 patients all used two features selected by the trainable automatic radial basis Support Vector Classifier (SVC). The two mostly commonly selected features by this classifier were the gray level standard deviation in the consolidative, and gray level uniformity in the pre-consolidative. The systems used the following four classifiers: nu-type SVC, linear Bayes normal classifier (LDC), trainable logistic linear classifier (loglc), and combined Adaboost and nu-type SVC. The average and standard deviation (whiskers) across the four classifiers are plotted in Figure 2. As seen in Figure 2, average performance improved for AUC and FNR, and the performance between the classifiers became less variable when more data are added.

**Conclusions:** Performing a drop-out experiment confirmed that performance becomes better and more stable with an increasing data set size. However, the performance metrics do not appear to plateau, suggesting that a larger sample is required to obtain optimal performance using a radiomics-based system for this problem. Three out of the four classifiers chosen when using the full set of patients are linear, suggesting that the data are consistently linearly separable in feature space, using the selected features.

### References:

1. Ettinger DS *et al.*, NCCN. 2017.
2. Mattonen SA *et al.*, Int J Radiat Oncol Biol Phys., 2016; 94(5):1121-8.
3. Mattonen SA *et al.*, J Med Imaging (Bellingham), 2015:2(4):041010.

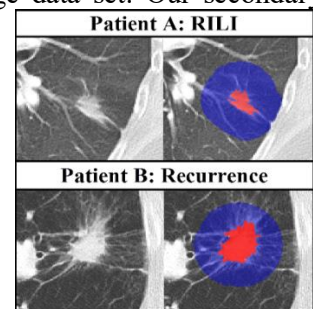


**Figure 1:** Original (left) and contoured (right) two patients' CT scans A with RILI and B with recurrence

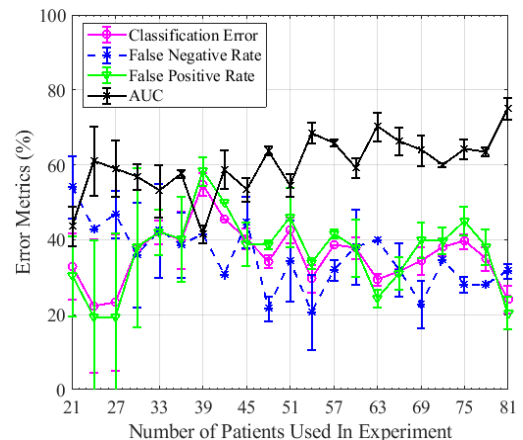


**Figure 2:** Mean  $\pm$  std of error metrics across four different classifiers, versus the sample size.

## Detection and Localization of Dominant Intra-prostatic Nodules with CT Perfusion

Dae-Myoung Yang<sup>1,3,4</sup>, Glenn Bauman<sup>2,4,5</sup>, Joseph Chin<sup>2,5</sup>, Stephen Pautler<sup>2,4</sup> and Ting-Yim Lee<sup>1,2,3,4</sup>

<sup>1</sup>Department of Medical Biophysics, <sup>2</sup>Oncology, and <sup>3</sup>Robarts Research Institute, The University of Western Ontario, <sup>4</sup>Lawson Health Research Institute and <sup>5</sup>London Regional Cancer Program, London Health Sciences Centre, London, Ontario

**Introduction.** IGPC-2, a prospective clinical study, at our institution investigates detecting and predicting the grade of prostate cancer (PCa) using multimodal imaging including CT perfusion (CTP). CTP is a quantitative functional imaging modality that is well suited to investigate tissue hemodynamics (delivery and permeation of endothelial barrier). Localized prostate cancer on an individual patient basis is characterized by a dominant focus of cancer in the gland (Dominant intraprostatic lesion/DIL) that is thought to drive the overall aggressiveness of the disease for that man. Strategies to identify and selectively target the DIL are being investigated. The goal of this study is to investigate whether CTP-derived functional parameters can detect and localize DIL.

**Methods.** Patients with histologically confirmed PCa underwent CTP to quantitatively map BF (blood flow), BV (blood volume), MTT (mean transit time), PS (vessel permeability surface product) and t0 (contrast arrival delay) in the whole prostate (Figure 1). Since free-breathing was allowed during CTP scanning, non-rigid image registration (GE Healthcare) of CT images was applied to minimize misalignment from breathing motion among the images before the CTP functional maps were generated. Information from prostate sextant biopsy and other imaging modalities (<sup>18</sup>F-DCFPyL PET and multiparametric MRI) were correlated to identify the location of the DIL in the prostate. A region of interest encompassing the DIL and another region within the prostate outside the DIL were outlined manually and their locations confirmed by a radiation oncologist. Difference between DIL and non-DIL CTP parameters were compared using the Wilcoxon matched pair signed rank test, and logistic regression with backward elimination was used to determine the most sensitive set of CTP parameters to distinguish DIL from benign tissue.

**Results.** Nineteen patients were evaluated with CTP. CTP showed significant differences in BF (median 66.90 vs. 48.87 mL/min/100g;  $P < 0.001$ ), BV (median 9.31 vs. 5.53 mL/100g;  $P < 0.001$ ), MTT (median 14.48 vs. 10.97 s;  $P < 0.001$ ) and PS (median 46.02 vs. 36.58 mL/min/100g;  $P < 0.001$ ) between DIL and benign tissue. Amongst these CTP parameters, BF and MTT is the most sensitive model to distinguish DIL from benign tissue – sensitivity 84.2%, specificity 84.2%, positive predictive value 84.2%, negative predictive value 84.2% and area under the curve of ROC analysis 0.93 (Figure 2).

**Conclusions.** In PCa patients studied with CTP, the combination of BF and MTT is the most sensitive parameter set associated with the DIL. As a next step, the CTP imaging will be registered to the digital histopathology images for more accurate delineation of DIL and to further validate the parameter set. The performance of the CTP parameter set will be further investigated for DIL detection and will be compared to current clinical PiRADS criteria and PET imaging.

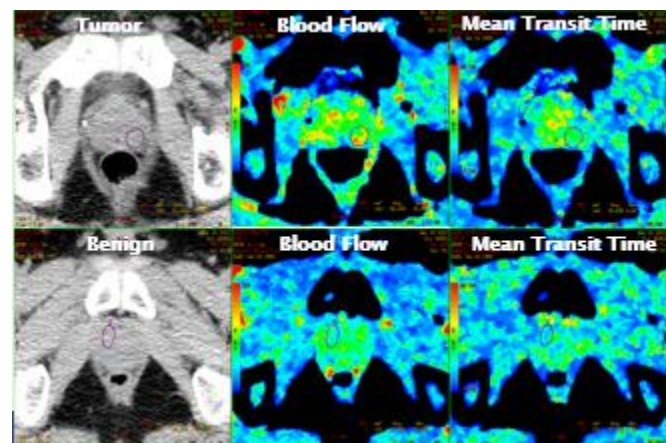


Figure 1. CTP-derived BF and MTT maps from an IGPC-2 patient

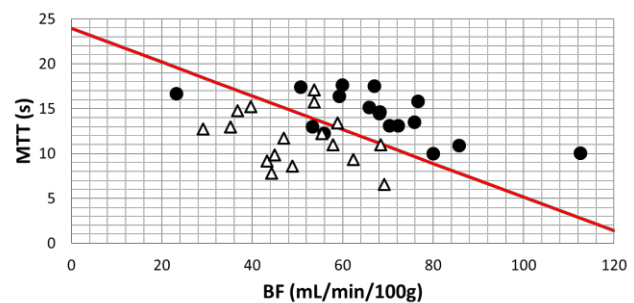


Figure 2. Logistic regression classifier of DIL and benign tissue based on CTP-derived BF and MTT. (Black circle: DIL, White triangle: Non-DIL)

## Prostate MRI delineated lesion boosting through high dose rate brachytherapy dwell time adjustment

C W Smith, BSc<sup>3</sup>, D A Hoover, PhD<sup>1,3</sup>, K Surry, PhD<sup>1,3</sup>, D D'Souza, MD<sup>1</sup>, D W. Cool, MD, PhD<sup>2</sup>, Z Kassam, MD<sup>2</sup>, M Bastian-Jordan, MD<sup>2,4</sup>, G S. Bauman, MD<sup>4</sup>, A D Ward, PhD<sup>1,3</sup>

Departments of 1. Oncology, 2. Medical Imaging and 3. Medical Biophysics, University of Western Ontario, London, Ontario, Canada; 4. Queensland Health, Brisbane, Queensland, Australia.

**Introduction:** Prostate cancer is clinically understood to be a heterogenous disease. It ranges from being indolent with chronic, slow progression, to aggressive and potentially lethal. Management of the disease is challenging because low-volume, sub-clinical disease may be diffuse, with superimposed foci of higher grade/aggressive disease, termed intraprostatic lesions (DILs), scattered throughout the gland resulting in a high false-negative rate for prostate biopsy. The standard therapeutic approach is to treat the prostate uniformly through surgical resection or radiation therapy. Evidence indicates that local recurrence often occurs at DILs. Through the utilization of magnetic resonance imaging (MRI) it has been shown that DILs can be localized and delineated. Our goal is to incorporate MRI DILs into previously performed high dose rate brachytherapy (HDR-BT) treatment plans and adjust the dwell times of the plans in order to provide superior dose to DILs. Toward that goal, in this study we address two questions: (1) by what amount can dwell time adjustments increase the dose to DILs, and (2) are the number of catheters and size of DIL important factors affecting the maximum dose to the DILs?

**Methods:** The first step to design DIL targeted HDR-BT treatment plans was to build a registration procedure to place the MRI defined DILs into the intraprocedural transrectal ultrasound (TRUS) context for HDR-BT. To do so, an iterative closest point transformation followed by a thin-plate spline transformation aligned and then deformed the MRI prostate surfaces to match the TRUS surfaces. 20 prostate cancer patients with DILs segmented on MRI were mapped to treatment plans of 19 different prostate cancer patients who underwent HDR-BT. We then designed treatment plans that maximally boosted the dose to the DIL while the dose to the whole gland was maintained and abided to dose constraints of surrounding organs at risk. The 19 HDR-BT clinical whole gland plans were used as starting points to design the DIL-boosted plans. We then adjusted the dwell times of the catheters nearest to the DIL(s) to maximally boost the dose to the DIL(s). We then calculated the boosted dose to each DIL, and a ratio of the number of catheters located within 5 mm of the surface of each DIL to the volume of the DIL to determine the significance of catheter proximity to the maximum DIL boost dose.

**Results:** In total, 38 DIL targeted HDR-BT plans were designed to provide 48 simulated DILs with a boosted dose. Of these 48 simulated DILs, prior to boosting nine would not have received the prescription dose of 15 Gy, which we deemed to be underdosed. Following the dwell time adjustment (Fig. 2), only one DIL remained underdosed, while the mean DIL dose increase was 3.32 Gy. Additionally it was observed (Fig. 3) that boost dose increased with respect to the number of catheters within 5 mm of the surface of the DIL per volume of the DIL.

**Conclusion:** This study suggests that incorporating lesion-specific dwell time adjustment into the treatment planning process will result in a clinically significant reduction in the number of potentially underdosed lesions. By reducing the likelihood of underdosing DILs, we hypothesize that the incorporation of DIL targeting via dwell time adjustment could yield a reduction of HDR-BT treatment failures and superior patient outcomes.

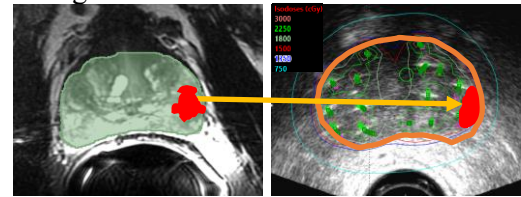


**Figure 1.** (A) T2W MRI with a DIL contour. (B) intraprocedural TRUS image, with co-registered red DIL.

### DIL Boost Dose vs Clinical Dose

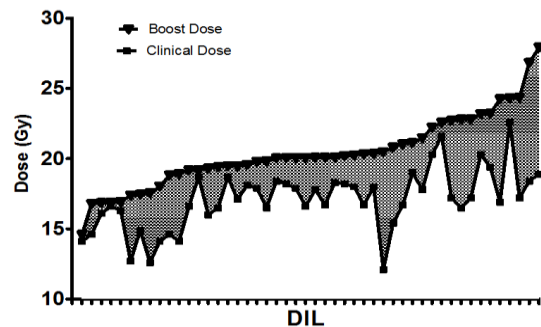


**Figure 2.** Scatter plot of the initial clinical dose and boost dose of each DIL.

### Catheter/Volume Relationship with Dose

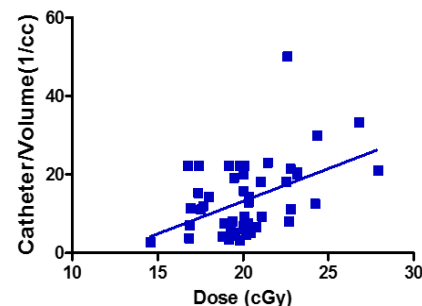


**Figure 3.** Scatter plot of the DIL dose vs. the ratio of the number of catheters within 5 mm of the DIL to DIL volume

**Metabolic Imaging of a Renal Cell Carcinoma Patient with Brain Metastasis using Hyperpolarized  $^{13}\text{C}$  MRI**Casey Y. Lee<sup>1,2</sup>, Hany Soliman<sup>3</sup>, Benjamin J. Geraghty<sup>1,2</sup>, Albert P. Chen<sup>4</sup>, Nadia D. Bragagnolo<sup>1,2</sup>, William J. Perks<sup>5</sup>, and Charles H. Cunningham<sup>1,2</sup><sup>1</sup>Medical Biophysics, University of Toronto, <sup>2</sup>Physical Sciences, Sunnybrook Research Institute, <sup>3</sup>Radiation Oncology, Sunnybrook Health Sciences Centre, <sup>4</sup>GE Healthcare Technologies, <sup>5</sup>Pharmacy, Sunnybrook Health Sciences Centre, Toronto, ON, Canada

**Introduction** Hyperpolarized (HP)  $^{13}\text{C}$  MRI is a non-invasive imaging method that can acquire images of  $[1-^{13}\text{C}]$ pyruvate and its downstream, metabolites including  $[1-^{13}\text{C}]$ lactate. It has the potential to be a powerful clinical tool in assessing tumour metastasis and to monitor response to radiation treatments, based on the known correlation between tumour lactate concentration, metastasis and radiation resistance<sup>1,2</sup>. In this study, metabolic images generated from  $[1-^{13}\text{C}]$ pyruvate and  $[1-^{13}\text{C}]$ lactate signals were acquired from a pilot study of patient with a brain metastasis. Metabolic images from 7 healthy volunteers are also acquired to characterize the background metabolic signals from healthy brain tissue.

**Methods** Written informed consent was obtained from a renal cell carcinoma patient with brain metastasis and 7 healthy volunteers. A 20-gauge intravenous catheter was inserted into the subject's forearm prior to being positioned supine and head-first in a GE MR750 3.0T MRI scanner (GE Healthcare, Waukesha, WI). The subject's head was secured upon a fixed head-coil based that could lock into either the  $^1\text{H}$  receive array or the  $^{13}\text{C}$  birdcage to minimize head motion between scans. Using the scanner's built-in body coil,  $^1\text{H}$  multi-echo reference data was acquired. A home-made birdcage  $^{13}\text{C}$  head coil placed over the subject's head was used to acquire  $^{13}\text{C}$  -signals following the injection of HP  $[1-^{13}\text{C}]$ pyruvate (0.1 mmol/kg dose at 4 mL/s followed by a 25 mL normal saline flush at 5 mL/s). The  $^{13}\text{C}$  signal was acquired with spectral-spatial excitation<sup>3</sup> of lactate/bicarbonate/pyruvate resonances (sequentially) followed by a 3D dual-echo EPI (DE-EPI) readout<sup>4</sup> (5s TR; axial; 1.5cm isotropic resolution with FOV  $24 \times 24 \times 36 \text{cm}^3$ ). The  $^{13}\text{C}$  head coil was replaced with a standard 8-channel  $^1\text{H}$  neurovascular array (Invivo Inc.) and T2-FLAIR (axial, FOV  $22 \times 22 \text{cm}^2$ , in-plane resolution  $0.6875 \times 0.982 \text{mm}^2$ , 3 mm slice thickness, TR/TE 8000/120 ms, flip angle  $111^\circ$ ) images were acquired for anatomical reference.  $^{13}\text{C}$  image reconstruction was performed offline using MATLAB R2013a. Data from the  $^1\text{H}$  multi-echo reference scan was used to correct geometric distortion artefacts from odd/even echo asymmetry, subject-dependent phase errors, and  $^{13}\text{C}$  centre frequency calibration error<sup>4</sup>. The final metabolite images were generated by summing odd/even echoes and summing individual time-resolved images over full 60s acquisition window to improve SNR. Voxel-by-voxel lactate z-scores were computed from the patient's lactate data, after removing the voxels with the signal below 15% of the maximum lactate signal.

**Results and Discussions** In the brains of healthy volunteers, high lactate was consistently observed in the regions around occipital lobe. Metabolic maps of lactate and pyruvate for the slice that contains metastasis from the patient with metastatic renal cell carcinoma shows strong lactate signals in the patient's entire cerebellar region, excluding the region of edema (surrounding the metastasis). The lactate z-score was found to be the highest ( $z = 3.4$ ) in the voxel within the metastasis. Pyruvate signal was also high within the metastasis. This patient passed away 2 months after these metabolic images were acquired due to disease progression and the metabolic profile shown here (i.e. high lactate and pyruvate signals within metastasis) may have been indicative of the progressive disease state.

**Conclusion** Hyperpolarized  $^{13}\text{C}$  brain images of a renal cell carcinoma patient showed elevated lactate signal within the metastasis, while regions of edema showed decreased lactate signal, which may be indicative of the progressive disease state of this patient.

**Acknowledgements** The authors thank Julie Green and Sumeet Sachdeva for coordinating the study, and Ruby Endre for MR technical support. Funding support from the Brain Canada and Canadian Institutes for Health Research. **References** 1. Walenta *et al.* (2000) *Cancer Res.* 2. Quennet *et al.* (2006) *Radiother Oncol.* 3. Cunningham *et al.* (2008) *JMR* 4. Geraghty *et al.* (2018) *Magn. Reson. Med.*

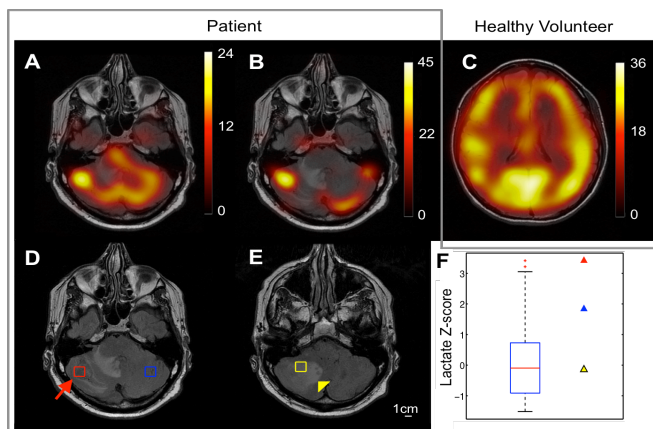


Fig. 1. (A)  $^{13}\text{C}$ -lactate and (B)  $^{13}\text{C}$ -pyruvate images from the patient with metastatic renal cell carcinoma. (C) Representative  $^{13}\text{C}$ -lactate image from a healthy volunteer. (D/E) show voxels from metastasis (red) and its contralateral side (blue), and edema (yellow). (F) The lactate z-scores from the patient's entire brain (boxplot) and the voxels shown in (D/E).

## Dual bioluminescence imaging reveals remarkable tumour self-seeding of spontaneous and experimental metastases in mice

Katie M Parkins<sup>1,2</sup>, Veronica P Dubois<sup>1,2</sup>, John J Kelly<sup>1</sup>, Yuanxin Chen<sup>1</sup>, Paula J Foster<sup>1,2</sup>, John A Ronald<sup>1,2</sup>

<sup>1</sup>Robarts Research Institute, The University of Western Ontario, London, Ontario, Canada

<sup>2</sup>The Department of Medical Biophysics, The University of Western Ontario, London, Ontario, Canada

**Introduction:** Metastasis, responsible for the majority of cancer deaths, can be defined as the spread of cancer cells from the primary tumour to distant sites in the body. Metastasis has been shown to be an inefficient process, with the primary tumour shedding a high number of cancer cells into the circulation, and very few going on to form overt metastases.<sup>1,2</sup> Previous studies have shown that molecular barriers and unfavorable survival conditions in distant organs may impede the formation of lethal metastases.<sup>3</sup> However, tumour vasculature is often considered “leaky” as a result of compromised vascular endothelial barrier function, and thus would more easily facilitate the transport of cancer cells from the circulation back into the original tumour. This concept termed “self-seeding” involves the recruitment of circulating tumour cells from the bloodstream, contributing to both primary tumour growth as well as the dissemination of cells at distant sites, and has been shown to occur in animal models of human breast, colon and melanoma cancer.<sup>4</sup> Here, we demonstrate for the first time, an *in vivo* imaging model to visualize cancer seeding in a mouse model of metastatic breast cancer using dual luciferase bioluminescence imaging (BLI).

**Methods:** Our experimental design can be seen in **Figure 1**. BALB/c mice received an injection of  $3 \times 10^5$  Renilla luciferase (RLuc) expressing parental 4T1 cells into the mammary fat pad (MFP) to generate a primary tumour. After 7 days of primary tumour growth, ultrasound guidance was used to inject  $2 \times 10^4$  firefly luciferase (FLuc) expressing, brain-seeking 4T1BR5 cells into the beating mouse heart. RLuc and FLuc BLI were performed over the next two weeks on adjacent days to evaluate the number of metastases throughout the mouse body that are composed of each cell type (RLuc v. FLuc signal). BLI was performed on an IVIS Lumina optical/x-ray system. Immunological staining was performed on tissues at endpoint to evaluate the presence of both cell types.

**Results:** On days 0 and 6 post 4T1-RLuc injection, RLuc signal was detected in the MFP as well as at some distant sites throughout the body, validating the presence of spontaneous metastases. After FLuc cells were injected into the heart, RLuc and FLuc signal patterns throughout mice indicated that FLuc and RLuc cells were migrating to the same place. On day 19, the number and location of RLuc positive metastases per mouse was quantified throughout the body and compared to the number and location of FLuc positive metastases detected on day 20. Across all mice, an average of  $10.6 \pm 2.0$  total metastases (RLuc or FLuc) were detected. The number of metastases that were both RLuc and FLuc positive ( $M = 9.8 \pm 1.9$ ) was significantly higher than the number of metastases that were either only RLuc-positive ( $M = 0.6 \pm 0.4$ ;  $p < 0.01$ ) or FLuc-positive ( $M = 0.2 \pm 0.2$ ;  $p < 0.001$ ).

**Conclusion:** Here, we demonstrate the utility of dual luciferase BLI to visualize cancer seeding in a mouse model of breast cancer metastasis. The luciferase reporter genes we used require orthogonal substrates that do not cross-react, and thus allowed us to noninvasively track two different cancer cell

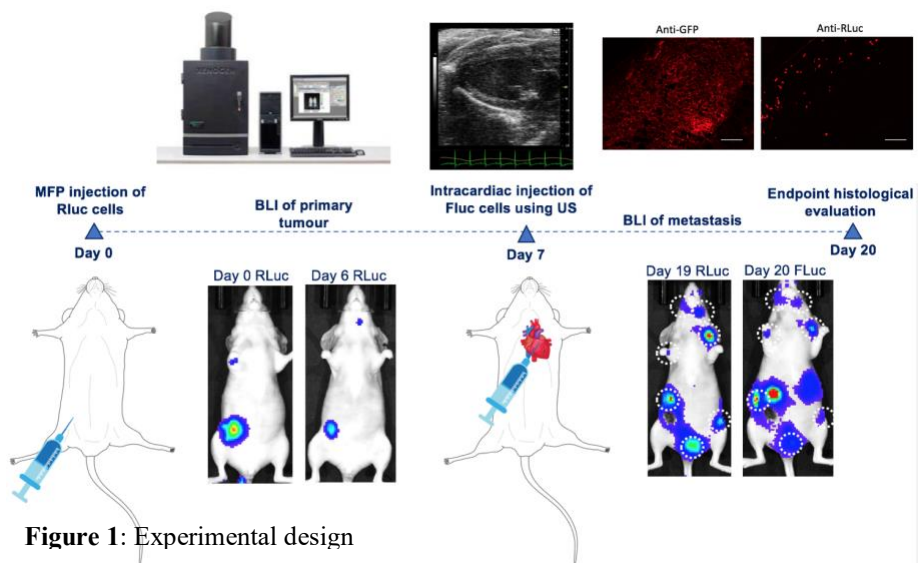
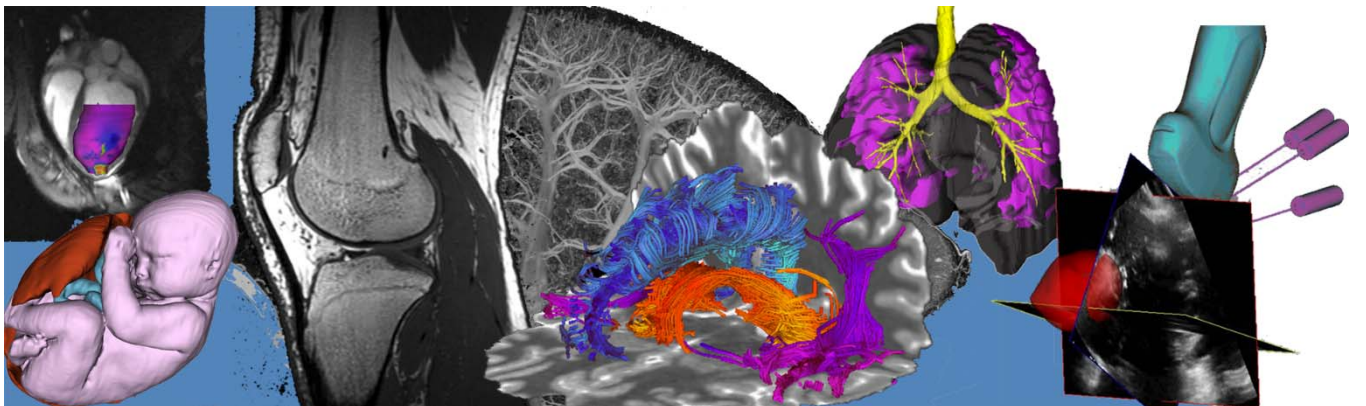


**Figure 1:** Experimental design

populations in the same animal. Remarkably, we found that circulating breast cancer cells are more likely to seed and form metastases at distant sites where spontaneous metastases have already started growing than they are to seed at new sites. Future work will look at the potential of exploiting these self-homing properties of cancer cells to use them as vehicles for self-targeted delivery of therapeutic agents to primary and metastatic tumours.

# Oral Presentation Abstracts

## Session 8: Fetal, Neonatal and Pediatric Imaging



### Quantifying $T_1$ and $T_2^*$ Relaxation Times of Fetal Tissues at 1.5 T

Simran Sethi<sup>1</sup>, Stephanie A. Giza<sup>1</sup>, Mary-Ellen E. Empey<sup>1</sup>, Barbra de Vrijer<sup>2,3</sup>, and Charles A. McKenzie<sup>1,3</sup>

<sup>1</sup>Medical Biophysics, Western University, <sup>2</sup>Obstetrics & Gynaecology, Western University, <sup>3</sup>Division of Maternal, Fetal and Newborn Health, Children's Health Research Institute, London, ON

**Introduction:** Fetal life is an important period of human development as organ systems that will sustain us throughout our life outside the womb begin to develop<sup>1-3</sup>. Acquiring accurate information about this developmental period will allow clinicians to better understand, and potentially distinguish abnormal from normal development.  $T_1$  and  $T_2^*$  relaxation times for adult organs have been previously quantified<sup>4,5</sup> because they are commonly used as a source of contrast in images<sup>6</sup>. However, these values may not be valid for the fetus due to the dramatic physiological growth occurring during gestation<sup>1-3</sup>. To the best of our knowledge, relaxation times of fetal tissues, especially as a function of gestational age (GA), have not been previously published. Quantification of relaxation times of fetal tissues will allow better optimization of image acquisition for fetal magnetic resonance imaging (MRI). Thus, the objective of this study is to quantify  $T_1$  and  $T_2^*$  relaxation times of amniotic fluid, placenta, fetal fat, fetal liver, and fetal kidney as a function of GA at 1.5 T.

**Methods:** Women with singleton pregnancies, and GA between 28 and 38 weeks were imaged in a 1.5 T MRI (GE MR450w). 3D water-fat MR (Quantitative IDEAL, TR: 9.3-9.8 ms, Field of View: 50 cm, 128x128 pixels, slice thickness: 4-6.5 mm, 42-78 slices, ARC acceleration: 2x phase 2.5x slice and 32x32 calibration lines, acquisition time: 12-28 s) images were acquired with flip angles of 6° and 20° in separate breath holds.

3D Slicer (v4.9.0-2018-05-04)<sup>6</sup> was used to place 7-mm diameter regions of interest (ROIs) in the same location of amniotic fluid, placenta, fetal subcutaneous fat, a vessel-free region of the liver, and fetal kidney cortex in the two images. Example ROI locations are shown in Figure 1.

$T_1$  values were quantified from the mean signal value in the ROIs at the two flip angles using DESPOT1 as described in Deoni et al<sup>8</sup>.  $T_2^*$  values were quantified from the high flip angle  $R_2^*$  image reconstructed by Quantitative IDEAL. Linear regression was performed to determine if the slope of  $T_1$  and  $T_2^*$  over GA for each tissue and fluid was significantly different than zero using GraphPadPrism (v7.03) ( $\alpha = 0.05$ ).

**Results:** Twenty-two women with a GA between 28 and 37 weeks participated. Sequences were repeated for three participants and no participant was excluded due to significant fetal motion. The slopes of placental  $T_1$  and  $T_2^*$ , fetal fat  $T_1$  and  $T_2^*$ , and fetal liver  $T_2^*$  as a function of GA were significantly different than zero ( $p < 0.001$ ) [Figure 2].

**Conclusions:** Placental  $T_1$  and  $T_2^*$ , fetal fat  $T_1$  and  $T_2^*$ , and fetal liver  $T_2^*$  relaxation times continuously changed between 28 and 38 weeks gestation.

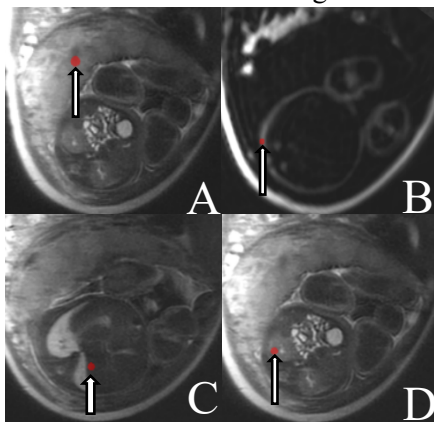


**Figure 1.** A 7-mm diameter ROI in placenta (A), fat (B), liver (C), and kidney (D).

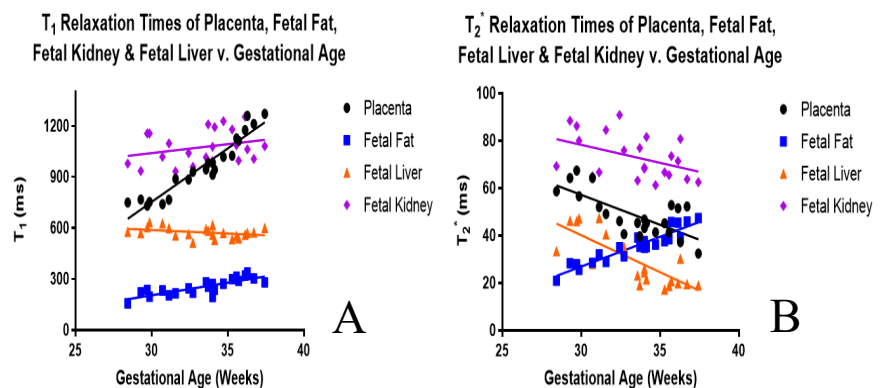


**Figure 2.**  $T_1$  (A) and  $T_2^*$  (B) relaxation times of fetal tissues as a function of gestational age.

**References:** (1) Mayer C, et al. *Ultrasound Obstet Gynecol* 2013;41(2):136-45. (2) Harding R, et al. *Fetal growth and development*. Cambridge: Cambridge University Press 2011. (3) Langman J, et al. *Langman's Medical Embryology*. Fifth ed. Baltimore: Williams & Wilkins 1985;61-125. (4) de Bazelaire CMJ, et al. *Radiology* 2004;230(3):652-59. (5) Chavhan GB, et al. *Radiographics* 2009;29(5):1433-39. (6) Nitz WR, et al. *Eur Radiol* 1999;9(6):1032-46. (7) Fedorov A, et al. *Magn Reson Imaging* 2012;30(9):1323-41. (8) Deoni SC, et al. *Magn Reson Med* 2003;49(3):515-26.

## Lateral ventricle volume based on posture of the neonate having intraventricular hemorrhage

Priyanka Roy<sup>1,2</sup>, Marcus Lo<sup>4</sup>, Aaron Fenster<sup>1,2</sup>, Soume Bhattacharya<sup>3</sup>, Roy Eagleson<sup>5</sup>, Sandrine de Ribaupierre<sup>1,3,4</sup>

<sup>1</sup> Department of Medical Biophysics, The University of Western Ontario, London, Ontario, Canada; <sup>2</sup> Robarts Imaging, University of Western Ontario, London, Ontario, Canada; <sup>3</sup> Department of Paediatrics, University of Western Ontario, London Health Sciences Centre, London, Ontario, Canada; <sup>4</sup> Department of Clinical Neurological Sciences, University of Western Ontario, London Health Sciences Centre, London, Ontario, Canada; <sup>5</sup> Department of Electrical and Computer Engineering, The University of Western Ontario, London, Ontario, Canada

**Introduction:** Despite all the advantages of obstetric care, premature birth is still a problem worldwide. In Canada 8% of babies are born premature. Intraventricular hemorrhage (IVH) occurs among 25 % of neonates who are born before 28 weeks of gestation. This can result in lifelong neurological impairment and even death if left untreated. Therefore, this condition should be properly diagnosed and treated when necessary, which is still controversial as to the exact timing. Clinician base their intervention mostly on 2D ultrasound (US) and clinical symptoms; but more recently we have shown that 3D US might be better suited. However, ventricle volumes might be dependent of the position of infant's head. Our hypothesis is that the cerebrospinal fluid (CSF) volume in the ventricle can change according to the posture of the head. A larger amount of CSF will accumulate in the lowermost ventricle while head position is right lateral or left lateral position for a long time. Thus, the ventricle tap (removal of CSF from anterior fontanel) should be from the ventricle with the larger volume to minimize risk to the neonate. Our objective is to quantify the amount of volume variations of two lateral ventricles of the neonates having IVH depending on their head postures.

**Methods:** We have developed a 3D ultrasound (3D US) system which can house a 2D probe and tilt it while the 2D ultrasound images are acquired into a computer and reconstructed into a 3D US image. The ventricle volume is measured by segmenting the ventricle by software application developed at Robarts. We are recruiting patients from the neonatal intensive care unit (NICU) at Victoria Hospital, London, Ontario, who have IVH. We usually scan the patients with our 3D US system twice per week or weekly according to the severity of IVH until the patient is discharged. For the scan we are using Philip IU 22 ultrasound machine and a curved array C8-5 MHz neonatal transducer. We are changing the postures to those babies only who are stable enough to do so. We usually scan the baby 30 min after turning to one side and then we change the posture of the same baby to the other side and scan again after 30 min.



Fig A. 3D model system

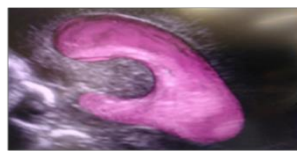


Fig B. Segmented ventricle

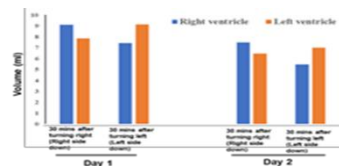


Fig C. Day 1 and Day 2 scan

**Results:** Until now we have recruited 9 patients from NICU of Victoria hospital but one patient is stable enough to do posture change experiment. The preliminary results of two scan are shown in figure. We are planning to get at least 10 patients with 5 posture change for each and we will do ANOVA analysis.

**Conclusions:** While ventricular tap can be done on either side of the ventricle, if an Ommaya is placed, then the same side is always targeted. If there is complete unrestricted flow in the system, that is not a problem, however, if the position of head influences the size of ventricles then position of the patient when tapping might be important. Sometimes desirable amount of CSF cannot be removed resulting in unequal shrinkage of the two lateral ventricles and a recurrent tap is needed. If the posture change has some effect on the volume of the lateral ventricles, neurosurgeons will be able to make their decision more accurately regarding on which posture and from which ventricle CSF should be removed for a patient.



### User Friendly Fetal fMRI Image Segmentation Pipeline

Estee Goldberg<sup>1</sup>, Charles A. McKenzie<sup>2,3</sup>, Barbra de Vrijer<sup>3,4</sup>, Roy Eagleson<sup>1,5</sup>, Sandrine de Ribaupierre<sup>1,2,3,5,6</sup>

<sup>1</sup>School of Biomedical Engineering, <sup>2</sup>Dept. Medical Biophysics, Western University; <sup>3</sup>Division of Maternal, Fetal and Newborn Health, London, ON; <sup>4</sup>Dept. of Obstetrics and Gynaecology, <sup>5</sup>Brain and Mind Institute, <sup>6</sup>Dept. of Clinical Neurological Sciences; Western University.

**Introduction:** The ability to accurately capture the growing brain *in utero* provides insight into the fetal maturation process and can constrain models to predict cognitive development. Functional MRI (fMRI) is a non-invasive method to investigate the neural correlates of brain development. Fetal MRI is challenging due to unpredictable fetal movement during the acquisition of images. Acquisitions longer in duration are more susceptible to within-sequence fetal motion. To attempt to minimize this, certain MRI sequences such as single shot fast spin echo sequences (SSFSE) or gradient echo-echo planar imaging (GE-EPI) allow images of individual slices to be acquired quickly enough to address the problem of fetal motion<sup>1</sup>. Unfortunately, this does not prevent all fetal motion, requiring a motion correction post processing step. Traditional anatomical motion correction pipelines have not been implemented and modified for fetal MRI nor do they pose the capacity to accommodate the significant amount of motion a fetus may make during image acquisition. To combat this, software algorithms have been presented in various studies that have been developed “in-house” for anatomical fetal data<sup>2-4</sup>. These algorithms are challenging to run, computationally expensive, timely in their segmentation timeframe, and challenging to create due to the unpredictable nature of fetal motion. Additionally, these algorithms can only accommodate specific ranges of motion, discarding data that has motion exceeding this range<sup>5</sup>. We hope to establish a reliable motion correction pipeline for fMRI of the fetal brain that preserves the maximum amount of fetal data by manually correcting and realigning each volume.

**Methods:** fMRI volumes were assessed for fetal motion through manual reorientation which was done for each volume using the FSL’s (v5.0.11)<sup>6</sup> FSLEyes Nudge tool<sup>7</sup> to preserve the maximum amount of data. The volumes were then co-registered to the CRL’s fetal atlas<sup>8</sup> for the correct gestational age. Brain extraction was done using FSL’s BET<sup>9</sup> and segmentation was completed using the FAST<sup>10</sup> tool (Fig.1). The same process was done for the anatomical images, which were then co-registered to the functional images.

**Results:** All of the volumes (n=672) from the six datasets were processed using this pipeline were successfully corrected for motion and were segmented. These datasets were persevered in their entirety and were used to undergo fMRI analysis.

**Conclusions:** This study suggests that by conducting primary manual orientation of the fetal brain, we are able to improve the feasibility of acquiring usable fetal fMRI datasets in their entirety. Additionally, we expect that by extending this pipeline and the use of only open-source programs to segment and extract the fetal brain, we are providing the community with a better solution to deal with fetal motion correction for fMRI.

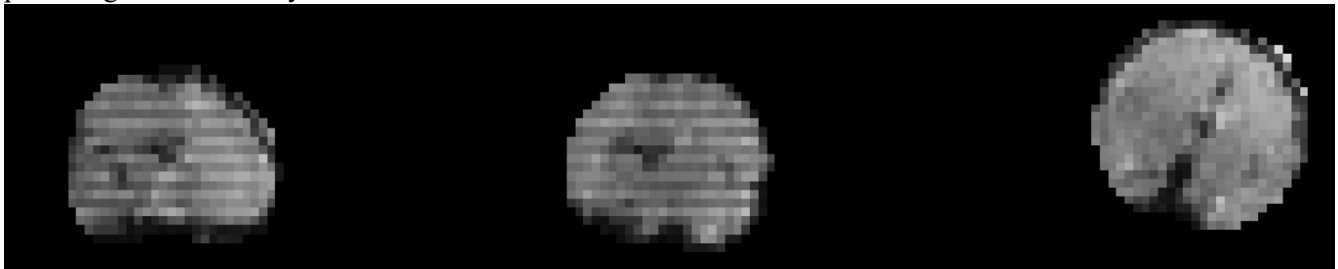


**Figure 1.** The sagittal, coronal, and axial views of an fMRI of a fetal brain whose volumes underwent the image segmentation pipeline.

#### References:

1. Levine, D. *et al. Radiology* **206**, 549–54 (1998).
2. Rousseau, F. *et al. Comput. Methods Programs Biomed.* **109**, 65–73 (2013).
3. Kainz, B. *et al. IEEE Trans. Med. Imaging* **34**, 1901–1913 (2015).
4. Kuklisova-Murgasova, M. *et al. Med. Image Anal.* **16**, 1550–64 (2012).
5. Rousseau, F. *et al. Acad. Radiol.* **13**, 1072–1081 (2006).
6. Jenkinson, M. *et al. Neuroimage* **62**, 782–790 (2012).
7. McCarthy, P. (2018).
8. Gholipour, A. *et al. Sci. Rep.* **7**, 476 (2017).
9. Smith, S. M. *Hum. Brain Mapp.* **17**, 143–155 (2002).
10. Zhang, Y. *et al. IEEE Trans. Med. Imaging* **20**, (2001).

## **NNeMo (Neonatal NeuroMonitor): A non-invasive optical device for assessing the coupling of cerebral blood flow and energy metabolism in the developing brain**

**A. Rajaram**<sup>1,2</sup>, L. Yip<sup>1,2</sup>, M. Kewin<sup>1</sup>, L. Kebaya<sup>3</sup>, V. Han<sup>3</sup>, S. Bhattacharya<sup>3</sup>, M. Diop<sup>1,2</sup>, K. St. Lawrence<sup>1,2</sup>

<sup>1</sup> Imaging Program, Lawson Health Research Institute, London, ON, Canada,

<sup>2</sup> Department of Medical Biophysics, Western University, London, ON, Canada

<sup>3</sup> Department of Neonatology, London Health Sciences Center, London, ON, Canada

**Introduction:** The human brain relies almost exclusively on oxidative metabolism, having very limited energy storage, and is therefore susceptible to injury related to impaired cerebral blood flow (CBF). This is particularly evident in preterm infants as the underdeveloped vascular system in the immature brain can lead to poor CBF control. For example, cerebral autoregulation – the ability to maintain CBF despite changes in blood pressure – is known to be impaired in this age group [1]. However, the impact of cerebrovascular dysfunction on the coupling of CBF to cerebral energy demand in the developing brain is unknown due to a lack of adequate technologies for assessing these measures in such a fragile population. The objective of this study was to develop a clinic-friendly neuromonitor capable of simultaneous measurement of CBF and energy metabolism to investigate physiological changes surrounding injury in the developing brain.

**Methods:** Optical technologies offer a safe and inexpensive approach for monitoring the brain. Broadband near-infrared spectroscopy (B-NIRS) can measure both cerebral saturation (StO<sub>2</sub>) and the redox state of cytochrome c oxidase (CCO) – a direct marker of tissue energy metabolism [2]. Diffuse correlation spectroscopy (DCS) is a newer technology that provides continuous CBF monitoring by measuring temporal intensity fluctuations caused by moving red blood cells. Combining these techniques is not trivial: NIRS and DCS utilize opposing light sources that produce cross-talk when used in conjunction. In this study we present NNeMo (Neonatal NeuroMonitor), a non-invasive optical neuromonitor developed by combining B-NIRS and DCS technology utilizing a multiplexing shuttering system (Fig 1). This portable device provides continuous monitoring of StO<sub>2</sub>, CBF, and CCO at the bedside with a temporal resolution on the order of seconds [3]. System performance was validated in an animal model of brain injury. In four newborn piglets, CBF and metabolism were independently manipulated while NNeMo monitored CBF and CCO. Cerebral energy metabolism was altered by (i) serial injections of an anesthetic (propofol) of increasing concentrations, and (ii) temporally occluding the common carotid arteries to induce ischemia. Ischemia was held over a 10-minute period, leading to CBF-driven changes in metabolism.



*Fig 1. NNeMo: optical neuromonitor*

**Results:** Utilizing optical shutters, B-NIRS and DCS techniques can be combined to obtain absolute StO<sub>2</sub>, CBF, and CCO values at a high temporal resolution. Propofol injections in piglets resulted in CBF and CCO changes proportional to the concentration injected. Carotid clamping caused an immediate drop in CBF followed shortly by a concurrent metabolic decrease. The delay was likely due to a transient increase in oxygen extraction which was quickly exhausted by larger drops in flow.

**Conclusions:** NNeMo, a unique optical technology for measuring CBF and metabolism, can provide a fundamental understanding of cerebral blood flow/metabolic coupling in the developing brain as shown within a relevant animal model. A real-time measure of CBF and metabolism at the bedside will provide clinicians with information regarding the physiological changes in the brain during early development and ultimately help improve clinical outcome with respect to reducing the incidence of preterm brain injury.

**References:** [1] Soul, J. et al. (2007) *Ped. Research* 61(4), [2] Bale, G. et al. (2016) *Biomed. Opt.* 21(9), [3] Rajaram, A. et al. (2018) *Biomed. Opt. Exp.* 9(6)

## Identifying Lesions in Paediatric Epilepsy using Morphometric and Textural Analysis of MRI

Sangeetha Kulaseharan<sup>(\*)</sup>, Azad Aminpour<sup>(\*)</sup>, Mehran Ebrahimi<sup>(\*)</sup>, and Elysa Widjaja<sup>(\*\*)</sup>

<sup>(\*)</sup> Faculty of Science, University of Ontario Institute of Technology, 2000 Simcoe Street N, Oshawa, ON, Canada, L1H 7K4

<sup>(\*\*)</sup> Diagnostic Imaging, The Hospital for Sick Children (SickKids), 555 University Avenue, Toronto, ON, Canada, M5G 1X8

### Introduction:

Pediatric epilepsy has devastating consequences on children's quality of life. Fortunately, many of them can be successfully treated by removing the lesion responsible for epilepsy. Lesions that are responsible for pediatric epilepsy include focal cortical dysplasia (FCD) and tumours. In contrast to tumours, which are readily identifiable on MRI, FCD can be subtle and may not be detectable on routine MRI. Therefore, there is a need for more advanced and objective tool for analyzing the MRI data in FCD. Image processing offers the potential to detect subtle structural changes, which may not be identifiable on visual inspection of MRI.

### Methods:

In this research, we utilized textural features along with FCD morphometric features on MRI, to improve lesion identification and detection. Fifty-four children with focal intractable epilepsy and have undergone epilepsy surgery were included in the study. Thirty-one children have subtle lesion on MRI that was suspected to be FCD (MRI-positive) and 23 children have MRI-negative focal epilepsy. Healthy controls consisted of 13 children. For morphometric features, we extracted cortical thickening and blurring at the gray-white matter interface.

The shorter distance between the white matter surface and pial surface was used to calculate cortical thickness. For gray-white matter junction blurring, we employed gradient magnitude to measure rate of change at each voxel of the interface. To detect the interface, at each voxel the neighbouring 8 voxels were examined. If at least 30% were contained in the gray matter and at least 30% were contained in the white matter, the voxel was considered to fall on the interface [1]. Textural features were assessed using Gray-Level Co-occurrence Matrices (GLCM). Symmetric GLCMs were computed with the following parameters: a distance of 3 voxels, and an intensity range of 32 gray levels such that 13 co-occurrence matrices were produced per voxel. From each generated matrix 12 textural descriptor features were computed. For each feature, the average of the 13 was taken to be the value mapped back to the initial position. Subsequently, we applied a 2-Step Naive Bayes classifier to train on morphometric, followed by textural features [1]. The following were used to measure the performance of the algorithm: 1. *subjectwise sensitivity* (the number of epilepsy subjects in which a lesion is correctly identified divided by the total number of epilepsy subjects), 2. *subjectwise specificity* (the number of controls in which no lesion is identified divided by the total number of control subjects), 3. *lesional sensitivity* (the sum of all cortical segments labeled lesional by the classifier divided by the total segments labelled lesional for all subjects), and 4. *lesional specificity* (the sum of all segments labeled non-lesional by the classifier divided by the total segments labeled non-lesional).

### Results:

The results are presented in table 1. For MRI-positive cases, T1 has the highest subjectwise sensitivity relative to T2 and FLAIR (94% vs. 90% vs. 71% respectively), and also the highest lesional sensitivity (63% vs. 60% vs. 42% respectively), but the lowest lesional specificity. Combination of all three sequences improved the performance of the algorithm, with 97% subjectwise sensitivity. For MRI-negative cases, T1 has the highest subjectwise sensitivity relative to T2 and FLAIR (48% vs. 30% vs. 39% respectively), and also the highest lesional sensitivity (31% vs. 22% vs. 28% respectively). However, T2 has the highest lesional specificity relative to T1 and FLAIR (95% vs. 94% vs. 92% respectively). Combination of all three sequences improved the performance of the algorithm, with 70% subjectwise sensitivity. The 2-Step Naive Bayes classifier correctly rejected 100% of the healthy subjects for all three sequences.

### Conclusions:

In summary, computational techniques using a 2-Step Bayesian classifier trained on morphometric and textural features can assist with detecting a lesion on MRI in children with epilepsy. By demonstrating the potential location of the abnormality, the neuroradiologists can perform a second review of these areas on MRI and correlate the changes with the epileptogenic zone as identified on video EEG and other functional imaging.

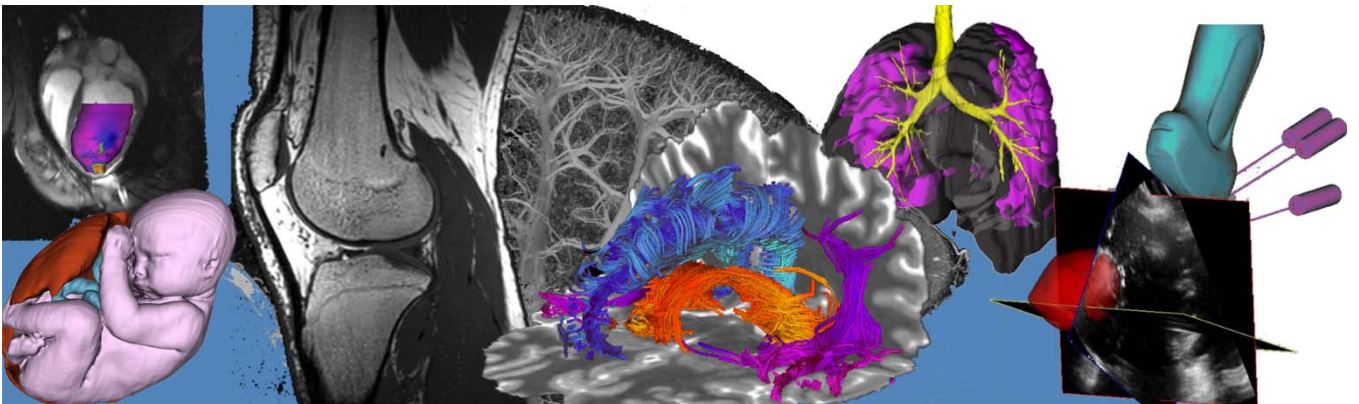
**References:** [1] Antel, Samson B., et al. "Automated detection of focal cortical dysplasia lesions using computational models of their MRI characteristics and texture analysis." *Neuroimage* 19.4 (2003): 1748-1759.

Table 1: Evaluating 2-Step Naive Bayes performances using T1, T2, and FLAIR on MRI-Positive and MRI-Negative cases

	MRI-Positive			MRI-Negative		
	T1	T2	FLAIR	T1	T2	FLAIR
Number of Incorrectly Rejected Cases of FCD	0/31	1/31	6/31	2/23	1/23	0/23
Subjectwise Specificity (%)	100	100	100	100	100	100
Subjectwise Sensitivity (%)	94	90	71	48	30	39
Lesional Specificity (%)	75	80	89	94	95	92
Lesional Sensitivity (%)	63	60	42	31	22	28

# Oral Presentation Abstracts

## Session 9: Lung Imaging



# Novel COPD Multi-parametric Response Map Phenotypes

Jonathan L. MacNeil<sup>1,2</sup>, Dante PI Capaldi<sup>3</sup>, Andrew R. Westcott<sup>1,4</sup>, David G. McCormack<sup>5</sup>, Grace Parraga<sup>1,2,4,5</sup>

<sup>1</sup>Robarts Research Institute, <sup>2</sup>School of Biomedical Engineering, The University of Western Ontario <sup>3</sup>Department of Radiation Oncology, Stanford University, Stanford, USA <sup>4</sup>Department of Medical Biophysics, <sup>5</sup>Department of Respirology, Department of Medicine, The University of Western Ontario, London, CANADA

**Introduction:** COPD is a multifaceted disease with both structural and functional components. Traditional imaging measurements include CT airway and parenchyma structural measurements that do not address lung functional abnormalities. Therefore, our objective was to develop a novel multi-parametric response mapping method that combined both magnetic resonance imaging (MRI) functional information and CT structural information in patients across a wide range of COPD severity.

**Method:** Participants were enrolled who provided written informed consent to an approved protocol and underwent spirometry for GOLD grade classification,<sup>1</sup> hyperpolarized MRI ventilation and diffusion-weighted images, and thoracic CT. CT and MRI segmentation<sup>2,3</sup> and co-registration methods were developed and applied<sup>4</sup> to generate multi-parametric response maps (mPRM)<sup>5</sup> that classified voxels into six categories of increasing lung abnormality/disease severity (Figure 1 bottom panel): 1) normal, 2) normal with microstructural abnormalities, 3) ventilated with CT evidence of emphysema and no microstructural abnormalities, 4) ventilated with CT evidence of emphysema, 5) poorly-ventilated but otherwise normal, and 6) poorly ventilated with CT evidence of emphysema. Kruskal-Wallis and Dunn-Bonferroni post-hoc tests were used to compare voxel distributions between COPD stages.

**Results:** We evaluated 36 participants including nine ex-smokers without COPD (67±13, 7M/2F), 10 COPD GOLD I (75±6, 7M/3F), nine COPD GOLD II (73±9, 6M/3F), and eight COPD GOLD III/IV (70±11, 7M/1F).

Figure 1 (top panel) shows representative mPRM for each group and mPRM voxel distributions revealed that normal lung voxels were significantly greater in ex-smokers compared to GOLD II and III/IV ( $p=.022$  and  $p<.001$  respectively). GOLD III/IV had significantly greater unventilated normal lung voxels compared to ex-smokers and GOLD I ( $p<.001$  and  $p=.011$  respectively). There were significantly greater unventilated emphysema lung voxels in GOLD III/IV compared to ex-smokers ( $p<.001$ ), and GOLD II compared to ex-smokers ( $p=.013$ ). GOLD II and III/IV had significantly greater ventilated emphysema lung voxels compared to ex-smokers ( $p=.009$  and  $p<.001$  respectively).

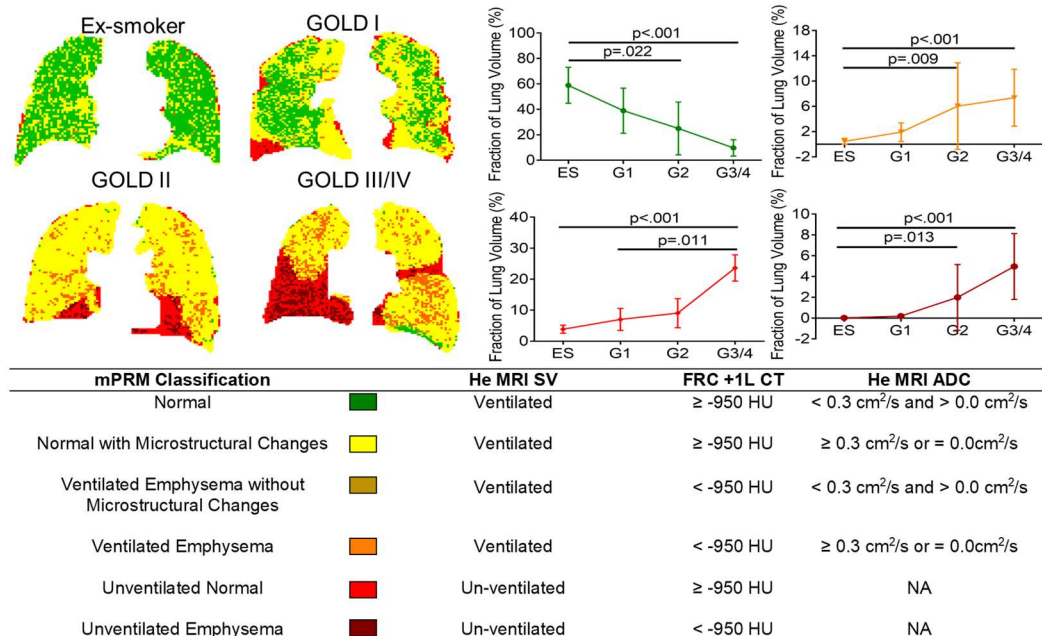


Figure 1: (top left) Representative mPRM for each stage of COPD. (top right) Distribution of normal, ventilated emphysema, unventilated normal, and unventilated emphysema lung voxels between COPD stages (mean  $\pm$  SD). (bottom) Definition of the mPRM classifications using CT Hounsfield units and age normalized ADC values. ES: ex-smokers, G1: GOLD I COPD, G2: GOLD II COPD, G3/4: GOLD III/IV COPD, FRC: lung functional residual capacity

GOLD II and III/IV had significantly greater ventilated emphysema lung voxels compared to ex-smokers ( $p=.009$  and  $p<.001$  respectively).

**Conclusion:** We generated novel COPD patient phenotypes using multi-parametric response maps (mPRM) to provide a more detailed understanding about how structural and functional abnormalities spatially and quantitatively correlate across GOLD grade COPD.

## References:

- 1) Vestbo, J. *et al.* AJRCCM (2013).;
- 2) Kirby, M. *et al.* AcadRadiol (2012).;
- 3) Hu, S. *et al.* IEEE TMI (2001).;
- 4) Heinrich, M.P. *et al.* MedIA (2012).;
- 5) Galban, C. J. *et al.* NatMed (2012).;

**Multi-scalar Perfusion and Ventilation Defects in Asthma**Alexander M Matheson<sup>1,2</sup>, Rachel L Eddy,<sup>1,2</sup> Dante PI Capaldi<sup>3</sup>, Fumin Guo<sup>4</sup>, David G McCormack<sup>5</sup> and Grace Parraga<sup>1,2,5</sup><sup>1</sup>Robarts Research Institute, <sup>2</sup>Department of Medical Biophysics, Western University <sup>3</sup>Division of Medical Physics, Department of Radiation Oncology, Stanford University, <sup>4</sup>Department of Medical Biophysics, University of Toronto, <sup>5</sup>Division of Respiriology, Department of Medicine, Western University

**INTRODUCTION:** To provide a deeper understanding of asthma pathogenesis, pulmonary imaging methods (including CT and MRI) have necessarily focussed on airway wall and lumen abnormalities using CT and more recently on ventilation abnormalities, using MRI. Recent results from the Severe Asthma Research Program (SARP) have revealed CT evidence of pulmonary vascular tree pruning<sup>1</sup> in patients with severe disease. Based on these surprising CT findings, we hypothesized that microvascular perfusion abnormalities would be present in severe asthmatics and that these would be spatially and quantitatively related to MRI and multi-breath washout ventilation heterogeneity measurements. Recent pulmonary functional MRI advancements include the development of Fourier-decomposition of free-breathing conventional <sup>1</sup>H magnetic resonance imaging (FDMRI) to simultaneously measure ventilation and perfusion, without ionizing radiation or exogenous contrast agents.<sup>2</sup> FDMRI ventilation measurements were previously shown to be significantly related to hyperpolarized gas MRI ventilation defects in asthma,<sup>3</sup> whereas FDMRI perfusion maps were also spatially and quantitatively correlated with dynamic contrast-enhanced perfusion MRI maps.<sup>4</sup> Our objective was directly compare FDMRI perfusion abnormalities with CT pulmonary vessel trees to test hypotheses about pulmonary and bronchial vascular abnormalities in patients with severe asthma.

**METHODS:** Patients enrolled with mild to severe asthma provided written informed consent to an approved protocol (NCT02351141) and underwent FDMRI,<sup>5</sup> pulmonary function tests and thoracic CT. FDMRI perfusion images were generated based on previously described methods<sup>5</sup> and segmented using hierarchical k-means clustering to produce maps, from which ventilation defect percent (VDP) and perfusion defect percent (QDP) were calculated. CT pulmonary vessel trees were generated using Pulmonary Workstation 2.0 (VIDA Diagnostics).

**RESULTS:** Demographic data for all asthmatics evaluated (n=23) are summarized in Figure 1. VDP and QDP measurements correlated ( $R^2=0.42$ ), although VDP was lower ( $2\pm 2\%$ ) or more normal as compared to QDP ( $6\pm 4\%$ ). Figure 1 also shows that MRI ventilation and perfusion abnormalities were spatially congruent, and these were also spatially-matched with CT evidence of vessel pruning.

**CONCLUSION:** We developed a way using MRI to measure lung perfusion and ventilation in asthmatics that show multi-scalar airway and vessel functional abnormalities.

**REFERENCES:**

1. Ash, S. *et al. Am J Respir Crit Care Med* **198** (2018).
2. Bauman, G. *et al. Magn Reson Med* **62** (2009).
3. Capaldi, D. P. I. *et al. Acad Radiol* **24** (2017).
4. Bauman, G. *et al. Eur J Radiol* **82** (2013).
5. Capaldi, D. P. *et al. Acad Radiol* **22** (2015).

Parameter ( $\pm$ SD)	
Age	48 $\pm$ 10
Sex, % Female	46
ACQ Score	1.4 $\pm$ 0.8
FEV <sub>1</sub>	2.51 $\pm$ 0.78
FEV <sub>1</sub> % <sub>pred</sub>	72 $\pm$ 17
FVC	3.85 $\pm$ 1.16
FVC % <sub>pred</sub>	86 $\pm$ 17
LCI	8.15 $\pm$ 1.33
LCI % <sub>pred</sub>	128 $\pm$ 19
VDP (%)	2 $\pm$ 2
QDP (%)	6 $\pm$ 4

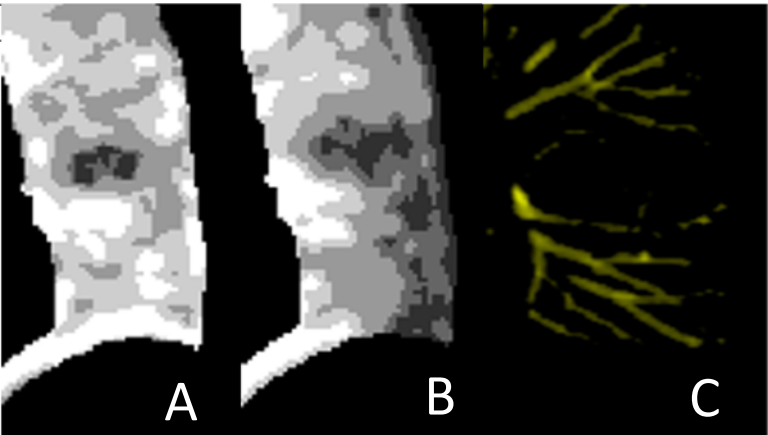


**Figure 1:** Demographics, pulmonary-function, and image-derived functional measurements in asthma patients. Defects were spatially and quantitatively related, as shown in insets. Defect maps were clustered into 5 grades, ranging from 1 (defect) to 5 (hyper-functional). Inset A: FDMRI ventilation of lower left lobe (defects indicated by arrows); Inset B: FDMRI perfusion of the same location; Inset C: CT vessel-mask of the same location. ACQ=Asthma Control Questionnaire; FEV<sub>1</sub>=Forced Expiratory Volume in 1 Second; FVC=Forced Vital Capacity; LCI=Lung Clearance Index; FDMRI=Fourier Decomposition of Free-breathing MRI; VDP=Ventilation Defect Percent; QDP=Perfusion Defect Percent

## Improved Tumor Motion Estimation by Incorporating Patho-physiology in Biomechanical Model of the Lung

Parya Jafari<sup>1</sup>, Douglas A Hoover<sup>2,3,7</sup>, Ali Sadeghi-Naini<sup>1,4,5,6</sup>, Abbas Samani<sup>1,6,7,8</sup>

<sup>1</sup>School of Biomedical Engineering, The University of Western Ontario, London, Ontario, Canada

<sup>2</sup>Department of Radiation Oncology, London Regional Cancer Program, London, Ontario, Canada

<sup>3</sup>Department of Oncology, Western University, London, Ontario, Canada

<sup>4</sup>Department of Radiation Oncology, Odette Cancer Centre, Sunnybrook Health Sciences Centre, Toronto, ON, Canada

<sup>5</sup>Department of Electrical Engineering and Computer Science, Lassonde School of Engineering, York University, Toronto, ON, Canada

<sup>6</sup>Department of Electrical and Computer Engineering, The University of Western Ontario, London, Ontario, Canada

<sup>7</sup>Department of Medical Biophysics, The University of Western Ontario, London, Ontario, Canada

<sup>8</sup>Imaging Research Laboratories, Robarts Research Institute, University of Western Ontario, London

**Introduction:** Radiation therapy (RT) with curative intent is a main component of the current standard treatment for inoperable non-small cell lung cancer (NSCLC). However, respiratory motion can cause inaccuracies and uncertainties in radiation dose distribution, resulting in substantial pulmonary toxicity in some patients. One possible solution to account for intrafraction and inter-fraction changes is using a lung biomechanical model capable of estimating the tumor's motion/deformation. About 60% of lung cancer patients also suffer from Chronic obstructive pulmonary disease (COPD), associated with extensive heterogeneity in lung parenchyma. Such heterogeneity may render lung biomechanical models developed based on lung parenchyma homogeneity assumption insufficient for tumor motion/deformation estimation. The purpose of this study is to improve tumor motion/deformation estimation accuracy by developing a patho-physiologically realistic lung finite element (FE) model.

**Methods:** Patient-specific FE models were developed using radiation therapy treatment planning 4D CTs. The geometry of the lung used for FE mesh was acquired from segmentation of the CT volume at end-exhalation (50%). The COPD phenotypes causing structural changes in the lung parenchyma, namely emphysema and small airways disease, were quantified using CT data before incorporation in the FE model through assigning different mechanical properties. Loadings were defined in terms of the transpulmonary pressure expanding the lungs. Boundary conditions consisted of the diaphragm motion and fixed points for each patient. Image information, including segmented lung and gross tumor volume (GTV), were used to find the pressure and mechanical properties of healthy and pathological tissue volumes of the lung through an optimization algorithm. This algorithm registers the lung image at end-exhalation to its counterparts at other phases using the FE model, optimizing for pressure and mechanical properties. Finite element models with and without COPD-induced heterogeneities in mechanical properties were built for each patient to compare the results of the heterogeneous model to the homogeneous counterparts.

**Results:** The tumor motion/deformation during 10 respiration phases was modeled for 3 patients. The average DICE similarity coefficient between the actual and simulated tumor volumes were  $0.824 \pm 0.050$  and  $0.765 \pm 0.045$  for heterogeneous and homogeneous models, respectively. The average volume similarity between actual and simulated tumor volumes were  $0.976 \pm 0.042$  and  $0.875 \pm 0.037$  for heterogeneous and homogeneous models, respectively.

**Conclusion:** A substantial improvement was observed in the accuracy of the tumor motion/deformation estimation when pathology induced heterogeneities in the lung tissue structure were incorporated in the model. Results show the benefit of more realistic lung biomechanical models, in addition to their potential in intra- and interfraction tumor motion compensation.

## Is Vascular Pruning Related to MRI Ventilation Defects in Bronchiectasis and COPD patients?

Andrea L Barker<sup>1,2</sup>, Rachel L Eddy<sup>1,2</sup>, Alexander M Matheson<sup>1,2</sup>, Andrew Westcott<sup>1,2</sup>, George R Washko<sup>3</sup> and Grace Parraga<sup>1,2,4</sup>

<sup>1</sup>Robarts Research Institute, <sup>2</sup>Department of Medical Biophysics, Western University, London, CANADA; <sup>3</sup>Division of Pulmonary and Critical Care Medicine, Brigham and Women's Hospital, Harvard Medical School, Boston, USA; <sup>4</sup>Division of Respiriology, Department of Medicine, Western University London CANADA

**INTRODUCTION:** In approximately 50% of COPD patients,<sup>1</sup> there is CT evidence of bronchiectasis characterized by abnormal airway dilatation, traction bronchiectasis, mucous plugging and signet ring findings that are believed to result from recurrent infection. Previous work showed that hyperpolarized gas magnetic resonance imaging (MRI) ventilation abnormalities were spatially related to abnormally remodelled airways in patients with bronchiectasis<sup>2</sup> and asthma.<sup>3</sup> Moreover, in COPD patients, the increased broncho-arterial (BA) ratio measured using thoracic computed tomography (CT) also appears to be driven by small artery abnormalities.<sup>4</sup> Accordingly, the objective of this study was to investigate potential relationships between CT pulmonary vascular tree measurements and MRI ventilation in patients with COPD and bronchiectasis. We hypothesized that vascular pruning (decreased pulmonary vessel volume) would be significantly different in patients as compared to age-matched health volunteers.

**METHODS:** Participants provided written informed consent to an ethics-board approved protocol (#NCT02282202) and underwent thoracic CT and hyperpolarized <sup>3</sup>He MRI as previously described.<sup>2</sup> MRI ventilation defect percent (VDP) and CT total blood vessel volume (TBV) were quantified using in-house algorithms. Lobe-specific vessel volume and ventilation defect volume were generated using a lobar CT mask (VIDA Diagnostics Inc., Coralville, IA, USA). Relationships were determined using linear regression and one-way ANOVA was used to determine significant subgroup differences (Graphpad Prism version 7, La Jolla, CA, USA).

**RESULTS:** We evaluated 44 participants (70±9 yrs) including 15 bronchiectasis (69±11yrs), 14 COPD chronic bronchitis (69±8yrs) and 15 never-smoker participants (72±7yrs). Figure 1 provides demographic and imaging findings and shows that VDP and TBV were significantly different between subgroups. VDP was significantly associated with FEV<sub>1</sub> (p<0.0001) as previously described<sup>3</sup> and significantly related to normalized TBV (p<0.0001).

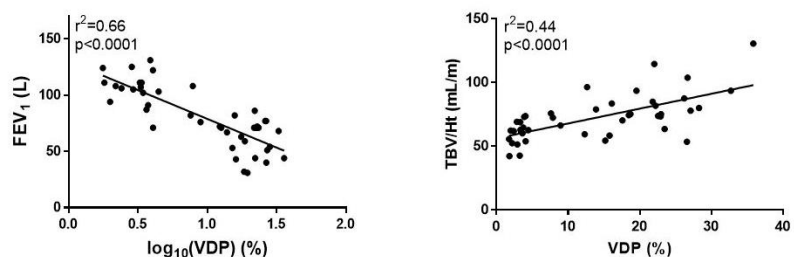
**CONCLUSIONS:** In a small group of healthy volunteers, COPD patients with mainly chronic bronchitis (small airways disease and not emphysema) and bronchiectasis patients, pulmonary vascular volume measured using CT was moderately related to ventilation abnormalities measured using MRI. There were significant differences between the age-matched healthy volunteers and patients. To forge a better understanding of the differences between patient subgroups, and of potential V/Q mismatch, regional analysis of the spatial correlations between ventilation abnormalities and vascular tree patency is required.

**REFERENCES:** 1. Patel, I. S. *et al. Am J Respir Crit Care Med* (2004); 2. Svenningsen, S. *et al. Acad Radiol* (2017); 3. Svenningsen, S. *et al. Thorax* (2014); 4. Diaz, A. A. *et al. Respiriology* (2017).

**Figure 1.** Demographic, imaging results and relationships

Parameters (±SD)	Healthy Volunteers (n=15)	Bronchiectasis (n=15)	COPD (n=14)	Significance p-value
Female %	73	66	43	
FEV <sub>1</sub> % <sub>pred</sub>	110 ± 11	68 ± 11	60 ± 21	<0.0001
FEV <sub>1</sub> /FVC	77 ± 4	70 ± 11	53 ± 9	<0.0001
VDP %	3.3 ± 1.5	17 ± 7.5	21 ± 9.1	<0.0001
TBV/Ht (mL/m)	61 ± 10	72 ± 15	87 ± 19	0.0002
TBV/TCV %	2.3 ± 0.2	2.6 ± 0.4	2.6 ± 0.4	0.4
TBV/TCV <sub>LLL</sub> %	2.3 ± 0.3	2.4 ± 0.5	2.5 ± 0.8	0.8
TBV/TCV <sub>LUL</sub> %	2.2 ± 0.3	2.4 ± 0.7	2.4 ± 0.7	0.7
TBV/TCV <sub>RLL</sub> %	2.4 ± 0.2	2.5 ± 0.4	2.6 ± 1.0	0.6
TBV/TCV <sub>RML</sub> %	2.0 ± 0.3	2.3 ± 0.4	2.2 ± 0.7	0.4
TBV/TCV <sub>RUL</sub> %	2.3 ± 0.2	2.6 ± 0.7	2.3 ± 0.8	0.5

FEV<sub>1</sub>=forced expiratory volume in 1 second, FVC=forced vital capacity, TBV=total blood volume, Ht=height, VDP=ventilation defect percent, VV=ventilated volume, total blood vessel volume=TBV, TVC=thoracic cavity volume, LLL=left lower lobe, LUL=left upper lobe, RLL=right lower lobe, RML=right middle lobe, RUL=right upper lobe.





## Can Oscillometry Explain Differences Between $^3\text{He}$ and $^{129}\text{Xe}$ Ventilation Heterogeneity?

Rachel L Eddy<sup>1,2</sup>, Andrew Westcott<sup>1,2</sup>, Geoffrey N Maksym,<sup>3</sup> David G McCormack<sup>4</sup> and Grace Parraga<sup>1-4</sup>

<sup>1</sup>Robarts Research Institute, <sup>2</sup>Department of Medical Biophysics, Western University, London, Canada <sup>3</sup>School of Biomedical Engineering, Dalhousie University, Halifax, Canada <sup>4</sup>Division of Respiriology, Department of Medicine, Western University, London, Canada

**INTRODUCTION:** To date, hyperpolarized noble gas magnetic resonance imaging (MRI) has been dominated by  $^3\text{He}$  because of its high gyromagnetic ratio and the high polarization levels that can be achieved, which results in excellent image quality with relatively small doses. The increased availability, decreased costs and advances in polarization physics have shifted most centres to  $^{129}\text{Xe}$ . Compared with  $^3\text{He}$ ,  $^{129}\text{Xe}$  ventilation was previously shown to be qualitatively more heterogeneous with larger and a greater number of ventilation abnormalities in both asthma<sup>1</sup> and chronic obstructive pulmonary disease (COPD).<sup>2,3</sup> Oscillometry probes lung mechanics related to ventilation heterogeneity by applying multi-frequency pressure oscillations at the mouth to measure respiratory impedance, consisting of respiratory resistance (R) and reactance (X).<sup>4</sup> Accordingly, the objective here was to investigate the relationships of  $^3\text{He}$  and  $^{129}\text{Xe}$  MRI with oscillometry to better understand the biomechanical factors that lead to different  $^3\text{He}$  and  $^{129}\text{Xe}$  ventilation heterogeneity.

**METHODS:** Participants with asthma and COPD provided written informed consent to ethics-board-approved protocols (NCT02351141, NCT02279329) and underwent MRI and oscillometry after administration of a bronchodilator during a single two-hour visit.  $^1\text{H}$ ,  $^3\text{He}$  and  $^{129}\text{Xe}$  MRI were performed within ten minutes of each other using a whole-body 3.0T Discovery MR750 system (General Electric Healthcare, USA) with broadband imaging capabilities as previously described.<sup>3</sup> Oscillometry was acquired using the tremoFlo C-100 Airwave Oscillometry System (Thorasys, Canada) to measure total respiratory system resistance at 5Hz ( $R_5$ ), frequency-dependence of resistance as R at 5Hz minus R at 19Hz ( $R_{5-19}$ ) which reflects small airways resistance, reactance at 5Hz ( $X_5$ ) and reactance area ( $A_X$ ) which is the area under the negative part of the reactance curve.  $^3\text{He}$  and  $^{129}\text{Xe}$  static ventilation images were segmented to generate ventilation defect percent (VDP) as previously described.<sup>5</sup> A Wilcoxon signed-rank test was performed to compare  $^3\text{He}$  and  $^{129}\text{Xe}$  VDP. Univariate relationships between MRI VDP and oscillometry measurements were assessed using Spearman correlation coefficients.

**RESULTS:** We evaluated 36 participants including 23 with COPD (75±8 years, 15M/8F) and 13 with asthma (44±9 years, 4M/9F). Figure 1 demonstrates qualitative differences between  $^3\text{He}$  and  $^{129}\text{Xe}$  ventilation heterogeneity for participants with COPD and asthma.  $^{129}\text{Xe}$  VDP was significantly greater than  $^3\text{He}$  VDP for participants with COPD (36±22% vs. 19±14%,  $p<0.0001$ ) but not for participants with asthma (8±11% vs. 6±7%,  $p=0.2$ ). For participants with COPD,  $^{129}\text{Xe}$  VDP was significantly correlated with  $R_5$ ,  $R_{5-19}$ ,  $X_5$  and  $A_X$ , whereas  $^3\text{He}$  VDP was significantly correlated with  $R_{5-19}$ ,  $X_5$  and  $A_X$  but not  $R_5$ . For asthmatics,  $^{129}\text{Xe}$  VDP was not significantly correlated with oscillometry measurements whereas  $^3\text{He}$  VDP was significantly correlated with  $X_5$  only.

**CONCLUSIONS:** Post-bronchodilator values of  $^{129}\text{Xe}$  VDP were significantly greater than  $^3\text{He}$  VDP for COPD but not asthma, in agreement with previous results.<sup>1-3</sup> Investigation of pre-bronchodilator relationships in asthma may be necessary to tease out differences with oscillometry. In participants with COPD,  $^{129}\text{Xe}$  VDP was significantly related to  $R_5$  whereas  $^3\text{He}$  was not.  $R_5$  reflects the resistance of the entire respiratory system and this may suggest that  $^{129}\text{Xe}$  is more sensitive to increased resistance throughout the entire airway tree.

**REFERENCES:** 1. Svenningsen, S. *et al. JMRI*, (2013). 2. Kirby, M. *et al. Radiology*, (2012). 3. Kirby, M. *et al. J Appl Physiol* (1985), (2013). 4. Oostveen, E. *et al. Eur Respir J*, (2003). 5. Kirby, M. *et al. Acad Radiol*, (2012).

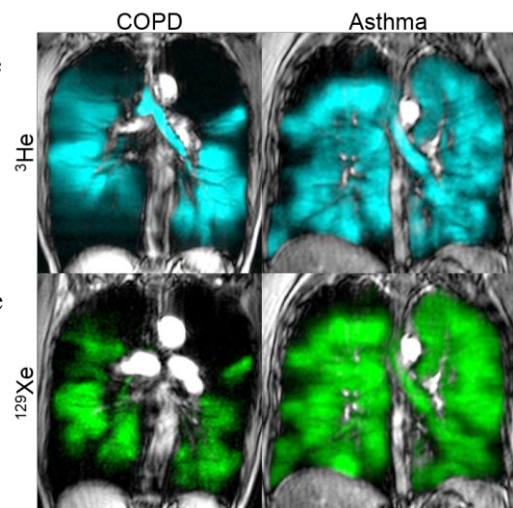
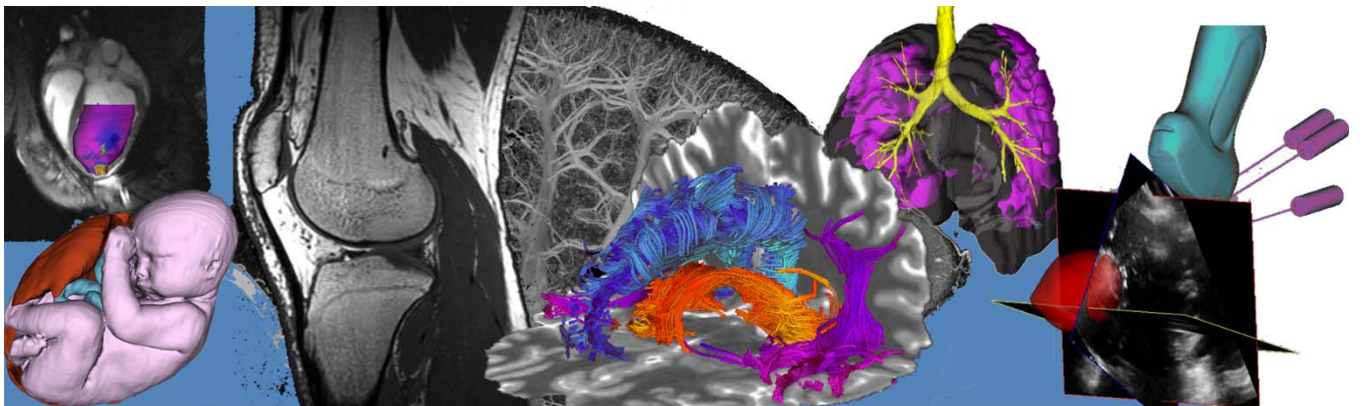


Figure 1. Centre slice  $^3\text{He}$  and  $^{129}\text{Xe}$  static ventilation images.

# Oral Presentation Abstracts

## Session 10: New Contrast Agents



**Safe harbor targeted CRISPR/Cas9 tools for molecular-genetic imaging of cells in living subjects**Veronica P. Dubois\*<sup>1,2</sup>, Darya Zotova\*<sup>2</sup>, Katie M. Parkins<sup>1,2</sup>, Connor Swick<sup>2</sup>, Amanda M. Hamilton<sup>2</sup>, John J. Kelly<sup>2</sup>, John A. Ronald<sup>1,2,3</sup>

1. The Department of Medical Biophysics, Western University, London, Ontario 2. Robarts Research Institute, London, Ontario 3. Lawson Health Research Institute, London, Ontario

**Introduction:** Noninvasive molecular-genetic imaging of cells expressing imaging reporter genes is an invaluable approach for longitudinal monitoring of the biodistribution and viability of cancer cells and cell-based therapies in preclinical models and patients. However, to label cells with reporter genes often relies on using gene transfer methods that randomly integrate the reporter genes into the genome, which may cause unwanted and serious detrimental effects. To overcome this, we have developed CRISPR/Cas9 tools to edit cells at the adeno-associated virus site 1 (AAVS1) safe harbour with a large donor construct (~6.3 kilobases) encoding an antibiotic resistance gene and reporter genes for bioluminescence (BLI) and fluorescence imaging (FLI).

**Methods:** HEK293T cells were transfected with a dual plasmid system encoding the Cas9 endonuclease and an AAVS1-targeted guide RNA in one plasmid, and a donor plasmid encoding a puromycin resistance gene, TdTomato and Firefly Luciferase flanked by AAVS1 homology arms. Following transfection, puromycin antibiotic (0.6  $\mu\text{g/ml}$ ) was added to the growth medium for puromycin selection of resistant clonal cells. AAVS1 integration of the donor construct was tested via PCR and sequencing of the PCR product. *In vitro* fluorescent microscopy and BLI were performed to test reporter gene function. After this confirmation, engineered cells ( $2.5 \times 10^6$ ) were injected into the left hind flank of nude mice and *in vivo* BLI was performed on days 0, 7, 14, 21, and 28. Endpoint histology was performed to test for firefly luciferase reporter gene expression in the HEK293T growth tissue.

**Results:** Transfection with our dual plasmid system resulted in puromycin-resistant clonal cells. PCR and sequencing of the PCR product confirmed AAVS1 integration of the donor construct. *In vitro* fluorescent microscopy showed expression of the tdTomato reporter gene. *In vitro* BLI signal correlated well to cell number ( $R^2=0.9988$ ;  $p<0.05$ ) and was stable over multiple passages. Following injection of the engineered cells into the left hind flank of nude mice, *in vivo* BLI showed signal at all imaging time points. BLI signal trended down from day 0 to day 7, but significantly increased by day 28 due to cell growth ( $p<0.05$ ). Endpoint histology showed firefly luciferase expression in the HEK293T growth tissue.

**Conclusions:** This describes the first CRISPR/Cas9 system for AAVS1 integration of large gene constructs for molecular-genetic imaging of cells *in vivo*. With further development, including improving editing efficiency, use of clinically-relevant reporters, and evaluation in other cell populations that can be readily expanded in culture (e.g., immortalized cells or T cells), this CRISPR/Cas9 reporter gene system could be broadly applied to a number of *in vivo* cell tracking studies.

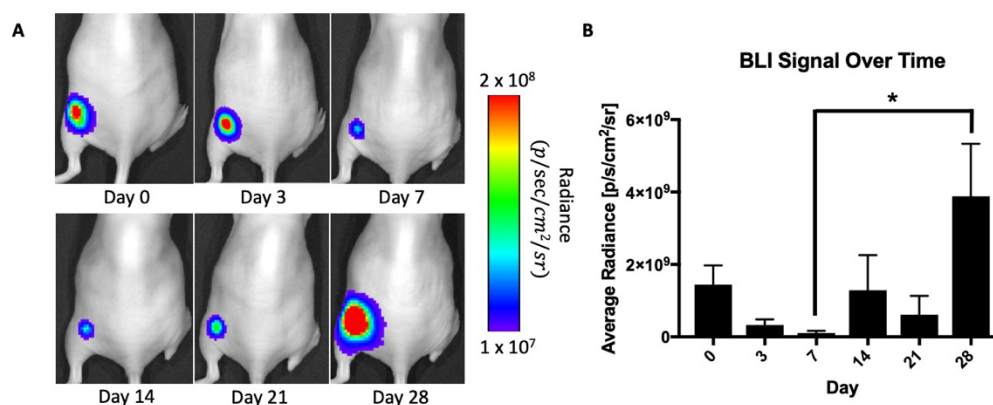


**Figure 1.** *In vivo* BLI of AAVS1-edited cells over time. (A) BLI of FLuc-expressing AAVS1-edited HEK293T cells implanted into the left hind flank of a representative mouse imaged on days 0, 3, 7, 14, 21, and 28 post-implantation. (B) Quantification of the average radiance in each image over time shows a significant increase in the BLI signal from day 7 to day 28 ( $p<0.05$ ;  $n=4$  mice).

## Multimodality organic contrast agents for ultrasound and photoacoustic imaging

Yohannes Soenjaya<sup>1</sup>, Samantha Slikboer<sup>2</sup>, Holly Bilton<sup>2</sup>, John Valliant<sup>2</sup>, Stuart Foster<sup>1,3</sup>, Christine Demore<sup>1,3</sup>

<sup>1</sup>Sunnybrook Research Institute, Physical Sciences, Toronto, Ontario, Canada

<sup>2</sup>Department of Chemistry and Chemical Biology, McMaster University, Hamilton, Ontario, Canada

<sup>3</sup>Department of Medical Biophysics, University of Toronto, Toronto, Ontario, Canada

### Introduction

Photoacoustic (PA) and contrast-enhanced ultrasound (CEUS) imaging are non-invasive imaging modalities that are used for visualization of the vasculature to diagnosis and monitor a variety of diseases in both clinical and pre-clinical settings. Currently, contrast in these imaging modalities arise from endogenous photo absorbers (i.e. blood) for PA, and microbubble contrast agents for CEUS, both of which are intravascular imaging agents due to their size. However, a wide range of diagnostic and therapeutic targets outside of the microvasculature could benefit from contrast-enhanced imaging to, for example, localize sites of disease, visualise distribution of therapeutic agents, or monitor response to treatment. These applications require nano-scale multimodality contrast agents (PA or US) with the potential to extravasate. Here, we introduce modified nano-scale gas vesicles (GVs) that have dual function as ultrasound contrast agent and photoacoustic imaging biosensor for molecular imaging.

### Method

The GV's are gas-filled protein nanostructures that are expressed in photosynthetic microorganisms as a mean to regulate buoyancy. They are harvested from *Halobacterium sp.* culture using previously published lysis and purification methods. In order to functionalize the GV's, a multi-step novel bioorthogonal chemistry method involving trans-cyclooctene (TCO) and tetrazines (Tz) conjugated with IR783 was utilized. First, the GV's are functionalized with TCO and then IR783 conjugated-Tz molecules are added to create the IR783-GV biomolecules. For all the photoacoustic *in vitro* experiment, a phantom platform with tubing channels is used. The tubes are filled with various contrast agents and then photoacoustic signals (680-980nm) are measured at three different locations along the tubes.

### Results

The phantom studies confirm that strong PA signals are observed at two absorption wavelengths (710 and 783 nm) for both IR783conjugated-GV and IR783-Tz control (0.5mM); whereas similar low background PA signal to that of PBS is observed in the TCO conjugated-GV control group. In addition, a clinically approved ICG dye, which has PA peak signals at approximately 735 and 815 nm wavelengths are also used for comparison. In spite of the difference in absorption wavelength peaks, at similar concentration of 0.5 mM, both ICG and IR783 conjugated-Tz showed similar PA signal intensity.

### Conclusions

These results provide essential information for the development and evaluation of a new nano-scale contrast agent. The IR-GVs will next be tested *in vivo* using proof-of-concept models of healthy mice and also as a potential targeting biosensor vector in diseased mice.

### KEYWORDS:

Acoustic nanostructures; Bioorthogonal chemistry; Gas vesicles; Photoacoustic; Ultrasound contrast agent

**Lanthanide nanoparticles as vascular contrast agents for *in vivo* dual energy microcomputed tomography**  
 Charmaine Cruje,<sup>1,2</sup> Eric Grolman,<sup>3</sup> Joy Dunmore-Buyze,<sup>1,2</sup> David W. Holdsworth,<sup>1,2</sup> Elizabeth R. Gillies,<sup>3,4</sup> and Maria Drangova<sup>1,2</sup>  
<sup>1</sup>Robarts Research Institute, <sup>2</sup>Department of Medical Biophysics, <sup>3</sup>Department of Chemical and Biochemical Engineering, and <sup>4</sup>Department of Chemistry, The University of Western Ontario, London, Ontario, Canada

**Introduction.** There have been recent technical advances in dual energy (DE) imaging during the last decade, both in clinical imaging by computed tomography (CT) and in pre-clinical research using micro-CT scanners. Since DE imaging takes advantage of the sharp differences in attenuation of x-rays below and above the k-edge of a selected material, it is important to achieve adequate spectral separation between low- and high-energy images, as well as sufficient photon flux.<sup>1</sup> In pre-clinical research in particular, *in vivo* imaging of the vasculature utilizes commercially available contrast agents, which are predominantly based on iodine. Some benefit is gained from DE imaging with an iodine agent, but the k-edge of iodine is too low (33.2 keV), which limits low-energy photon flux. While there are commercially available lead-based *ex vivo* agents, and more recently developed gold-based formulations for *in vivo* imaging, obtaining a sufficient photon flux above the k-edge of lead (88 keV) and gold (80.7 keV) requires high x-ray tube potential, which many micro-CT scanners are not capable of. It has been demonstrated *ex vivo* that combining a lanthanide-based contrast agent containing erbium (k-edge of 57.5 keV) with spectral shaping can optimize the performance of DE micro-CT in a large base of installed scanners.<sup>2</sup> Thus, the purpose of this work was to synthesize an *in vivo* analogue of a lanthanide-based vascular contrast agent for DE micro-CT. We applied advancements in nanotechnology by developing polymer-encapsulated erbium nanoparticles (ErNP) that remain in circulation for at least an hour in small animals. By utilizing spectral shaping techniques that were developed with an erbium-based *ex vivo* agent, DE images of a mouse that was injected with the ErNP were acquired. Although preliminary, this work presents promising results from the material decomposition of DE images.

**Methods. Contrast agent preparation and characterization-** A diblock copolymer containing poly(ethylene glycol) and poly(L-lactide) was synthesized and used to prepare ErNP encapsulations by nanoprecipitation.<sup>3</sup> The size and appearance of the nanoparticles were characterized using dynamic light scattering (DLS) and transmission electron microscopy (TEM). The suspension was then freeze-dried and stored at room temperature. The dried formulation was dissolved in normal saline immediately before injection at an erbium concentration of 100 mg/mL. ***In vivo* application and micro-CT imaging-** Using 0.2 mL of the contrast agent, male C57BL/6 mice (25-30 g) were injected intravenously ( $n=4$ ) via tail vein catheterization. Time-course micro-CT images were obtained over a one-hour period ( $n=3$ ) using the GE Locus Ultra (London, ON), where 1000 views (16 ms per view) were acquired at 80 kVp, 55 mA over 360° and reconstructed with a cone-beam reconstruction algorithm to a voxel size of (150  $\mu\text{m}$ )<sup>3</sup>. Images were rescaled into Hounsfield units (HU) using vials of water and air within the volume and were analyzed using MicroView (Parallax Innovations, London, ON). ***In vivo* DE micro-CT imaging and decomposition-** DE images were obtained ( $n=1$ ) using the GE Vision 120 (London, ON), where images were acquired by rapid filter switching. Low-energy images were acquired using 480  $\mu\text{m}$  of copper, while high-energy images were obtained with 64  $\mu\text{m}$  of erbium. Both scans were acquired with 90 kVp, 32 mA, 100  $\mu\text{m}$  isotropic voxel spacing, 220 projections over 192°, 4 frames averaged per projection, and 16 ms per frame. The complete DE scan was acquired over 12 minutes. Reconstructed three-dimensional images were rebinned 2 $\times$ 2, resulting in 100- $\mu\text{m}$  isotropic voxel spacing. Material decomposition of the volume image was performed by matrix factorization, as described by Granton et al.<sup>4</sup>

**Results. Physical characterization-** The polymer assemblies containing ErNP had an average hydrodynamic diameter of 171  $\pm$  3 nm, with low size dispersity as measured by DLS, and TEM results showed good agreement with the DLS-measured diameters. ***Single-energy in vivo imaging-*** In the blood pool of the animals that were intravenously injected, contrast enhancements of over 250 HU were observed for up to an hour (Figure 1). CT contrast enhancement in the blood pool decreased an hour post-injection, and negligible vascular contrast was observed after four hours. ***DE decomposition results-*** Thick slab projections (1-cm thick) of the DE images and decomposed volume images of bone and the contrast agent are shown in Figure 2. Although DE decomposition has yet to be optimized (as some contrast agent was misclassified as bone and conversely), the contrast agent image demonstrates the potential for bone removal.

**Conclusions.** Long-circulating erbium-based nanoparticles that can be used for *in vivo* imaging of the vasculature were synthesized. The preliminary results we present demonstrate the feasibility of DE material decomposition in live animals by using polymer-encapsulated ErNP with spectral shaping techniques.

**References.** [1] Krauss, B. *et al. Invest Radiol* **50**, 114-118 (2015). [2] Tse, J. J. *et al. Journal of medical imaging (Bellingham, Wash.)* **5**, 033503 (2018). [3] Cruje, C. *et al. Biomacromolecules* **19**, 896-905 (2018). [4] Granton, P. V. *et al. Med Phys* **35**, 5030-5042 (2008).

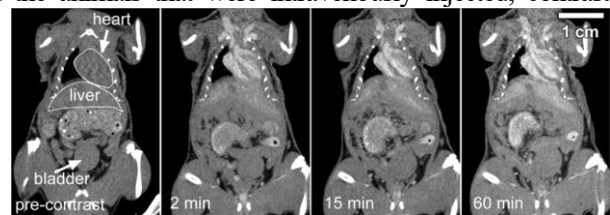


**Figure 1.** Time-course micro-CT images of a mouse that was intravenously injected with the contrast agent.

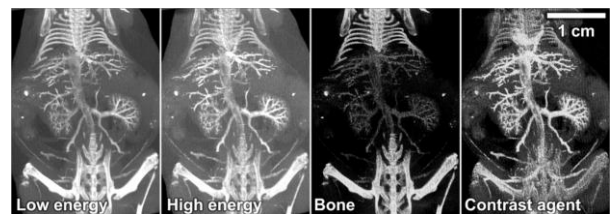


**Figure 2.** Low- and high-energy DE images, and decomposed bone and contrast agent images.

## Lymphatic Drainage from the Eye Quantified Non-Invasively by Photoacoustic Imaging Using a Near Infrared Tracer

Kirsten Cardinell<sup>1,2</sup>, Neeru Gupta<sup>2,4</sup>, Shireen Khattak<sup>1,3,4</sup>, Xun Zhou<sup>2</sup>, Michael Lapinski,<sup>1,2</sup> Fang Chen<sup>1,4</sup>, and Yeni Yücel<sup>1,4</sup>

<sup>1</sup>Keenan Research Centre for Biomedical Science, St. Michael's Hospital, Toronto, ON, Canada, <sup>2</sup>Ryerson University, Toronto, ON, Canada, <sup>3</sup>Department of Laboratory Medicine and Pathobiology, University of Toronto, Toronto, ON, Canada, <sup>4</sup>Department of Ophthalmology & Vision Sciences, University of Toronto, Toronto, ON, Canada

**Introduction:** Glaucoma is the leading cause of irreversible global blindness. All treatments lower intraocular pressure (IOP), mostly by increasing fluid drainage from the eye via two well known outflow pathways. We have recently discovered a third pathway that leads into the lymphatic system. Lymphatic vessels were observed within the human and sheep ciliary body<sup>1</sup> and lymphatic drainage from the eye was further evaluated in sheep using a radioactive tracer<sup>2</sup>. To date, a method to measure lymphatic outflow from the eye with nonionizing tracers is lacking. Here, for the first time, we detect and quantify lymphatic drainage from the mouse eye in the live state using photoacoustic tomography (PAT) and a near-infrared (NIR) tracer.

**Methods:** A NIR photoacoustic tracer was injected into the right eye anterior chamber of 10 mice under general anesthesia. Mice were imaged with PAT (MSOT 128, iThera Medical Inc. Germany) before and 20 minutes, 2, 4, and 6 hours after injection. Tracer signal intensity was measured in both right and left neck lymph nodes (LNs) at every time point and signal intensity slopes were calculated. Slope differences between right and left neck nodes were compared using paired t-test. Neck LNs were examined with fluorescence optical imaging and histologically for the presence of tracer, 4 hours and 2 hours post right eye injection of a NIR fluorescent tracer respectively.

**Results:** Following right eye tracer injection, increasing tracer signal was observed in the right neck LN from 20 minutes to 6 hours (Fig 1A). Slope differences of the signal intensity between right and left neck nodes were significant (Fig 1B,  $P = 0.0051$ ). Ex vivo in situ optical fluorescence imaging (Fig 1C) and histopathologic microscopic examination of neck nodes (Fig 1D) confirmed tracer presence within submandibular LNs.

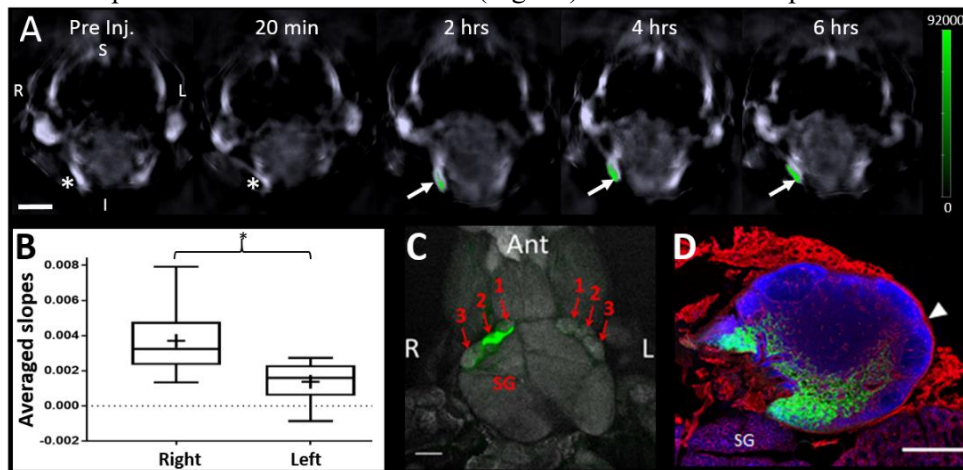


Fig 1. LN imaging of a mouse A) PAT at several time points after tracer injection into the right eye (scale bar = 3 mm), Arrows point to the tracer in the right neck LNs. Vertical scale in green. B) Average change in PAT tracer detection between right and left LNs, C) Fluorescence imaging 4 hours post injection. Arrows point to various neck LNs: 1 and 2 to submandibular LNs and 3 to parotid LNs, SG = submandibular gland (scale bar = 1 mm), D) Histopathologic examination 2 hours after injection shows tracer in green in the right submandibular LN surrounded by

Collagen IV-positive capsule (in red, white arrow head points to the capsule) (scale bar = 0.5 mm). Adapted from Yücel et al.<sup>3</sup>

**Conclusion:** Active lymphatic drainage of aqueous from the eye to cervical LNs was measured noninvasively by PAT of a NIR nanoparticles. This unique *in vivo* assay may help to uncover novel drugs that target alternative outflow routes to lower IOP in glaucoma and may provide new insights into lymphatic drainage in eye health and disease. Furthermore, this *in vivo* assay may be relevant to the study of lymphatic cancer spread

**References:** <sup>1</sup>Yücel, Y. H. *et al.* Identification of lymphatics in the ciliary body of the human eye: A novel 'uveolymphatic' outflow pathway. *Exp. Eye Res.* **89**, 810–819 (2009). <sup>2</sup>Kim, M., Johnston, M. G., Gupta, N., Moore, S. & Yücel, Y. H. A model to measure lymphatic drainage from the eye. *Exp. Eye Res.* **93**, 586–591 (2011). <sup>3</sup>Yücel, Y. H. *et al.* Active lymphatic drainage from the eye measured by noninvasive photoacoustic imaging of near-infrared nanoparticles. *Invest. Ophthalmol. Vis. Sci.* **59**, 2699–2707 (2018). **Acknowledgements:** We thank Barbara Thomson MSc, Hyacinth Irving MA, Clinton Hupple MSc, and Paola Luciani PhD, CHIR, NSERC, CFI-LOF, Glaucoma Research Society of Canada, Thor and Nicky Eaton Research Fund, and Henry Farrugia Research Fund.

## Ultrafast three-dimensional microbubble imaging for monitoring nonthermal brain ablation

Ryan M. Jones<sup>1</sup>, Dallan McMahon<sup>1,2</sup>, and Kullervo Hynynen<sup>1,2</sup>

<sup>1</sup>Physical Sciences Platform, Sunnybrook Research Institute, Toronto, ON, Canada  
<sup>2</sup>Department of Medical Biophysics, University of Toronto, Toronto, ON, Canada

**Introduction:** Nonthermal ablation via focused ultrasound and contrast agent microbubbles (MBs) is under pre-clinical investigation for non-invasive brain surgery. Existing sources of variability can lead to inconsistent treatment outcomes and bioeffect generation outside of the intended target volume(s), warranting the development of methods for online monitoring and control prior to clinical translation. Our group has shown that 3D MB imaging can be used to calibrate ultrasound exposure levels for inducing transient blood-brain barrier permeabilization without causing overt tissue damage [Jones *et al* 2018]. Here we investigate ultrafast 3D MB imaging for predicting the spatial distribution of tissue damage induced following nonthermal brain ablation.

**Methods:** Experiments were performed on craniotomized rabbits using a clinical-scale prototype ultrasound brain system [Jones *et al* 2018]. Pulsed ultrasound ( $f_0 = 612$  kHz, pulse length = 10 ms, pulse repetition frequency = 1 Hz, duration = 120 s) was electronically steered over a 2 x 2 point square grid (side length = 6 mm) starting concurrently with MB infusion (200  $\mu$ l/kg Definity™ over 90 s, 10 x maximum allowable clinical imaging dose) via 3D subharmonic ( $f_0/2 = 306$  kHz) imaging-based feedback control [Jones *et al* 2018]. Exposures were carried out at 0/50/100/150% of the peak negative pressure required to detect subharmonic activity *in vivo* ( $p_{\text{sub}}$ ) via multi-channel 3D beamforming. Short-time analysis of the acoustic emissions data (moving, non-overlapping 1  $\mu$ s beamforming windows) was performed offline. MRI was carried out at 3T to assess the induced tissue effects. Animals were sacrificed 48 hr post-treatment for histological examination.

**Results:** Multi-point exposure level calibration via 3D subharmonic imaging was feasible *in vivo* ( $p_{\text{sub}} = 0.67 \pm 0.19$  MPa).  $T_2^*$ w MR images acquired immediately post-sonication displayed regions of signal hypointensity induced by the exposures at 100%  $p_{\text{sub}}$  and 150%  $p_{\text{sub}}$ , but not at lower target levels (Fig. 1). Hematoxylin-eosin (H&E) stained tissue sections associated the  $T_2^*$ w MRI signal hypointensities with the presence of red blood cell (RBC) extravasations and regions of tissue necrosis, the spatial extent of which were both found to increase with increasing exposure level (Fig. 1). H&E histology also revealed small zones of RBC extravasations and tissue necrosis resulting from exposures at 50%  $p_{\text{sub}}$  that were not evident on  $T_2^*$ w MRI (Fig. 1). Ultrafast 3D MB imaging data correlated well with the spatial distribution of  $T_2^*$ w MRI signal hypointensities (Fig. 1).

**Conclusions:** Volumetric imaging of ultrasound contrast agents *in vivo* over microsecond timescales shows promise as a method for predicting the spatial morphology of tissue damage induced following nonthermal brain ablation. Ultrafast 3D MB imaging is expected to aid in the development of active exposure control strategies for bubble-mediated ultrasound treatments both in the brain and in other parts of the body.

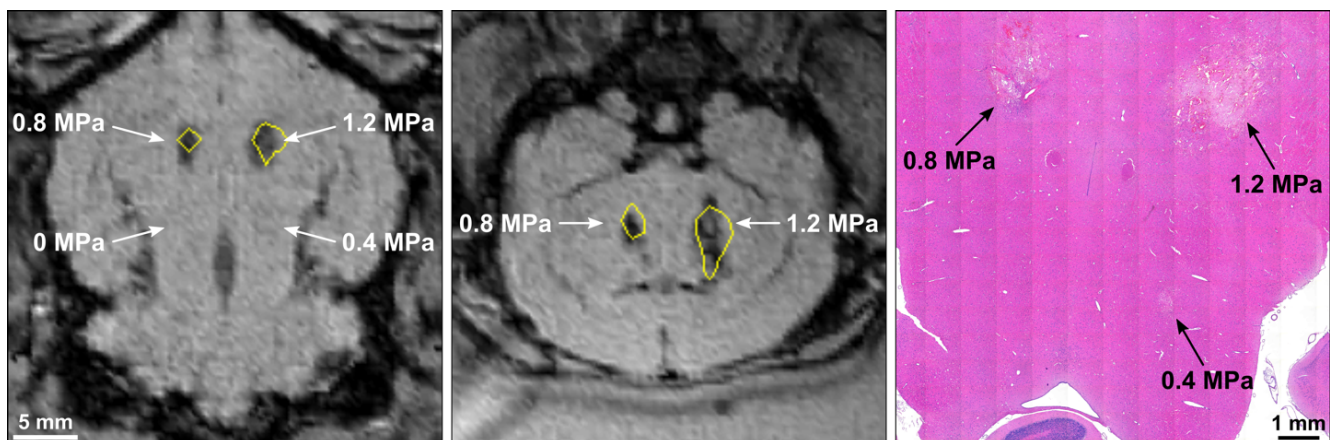
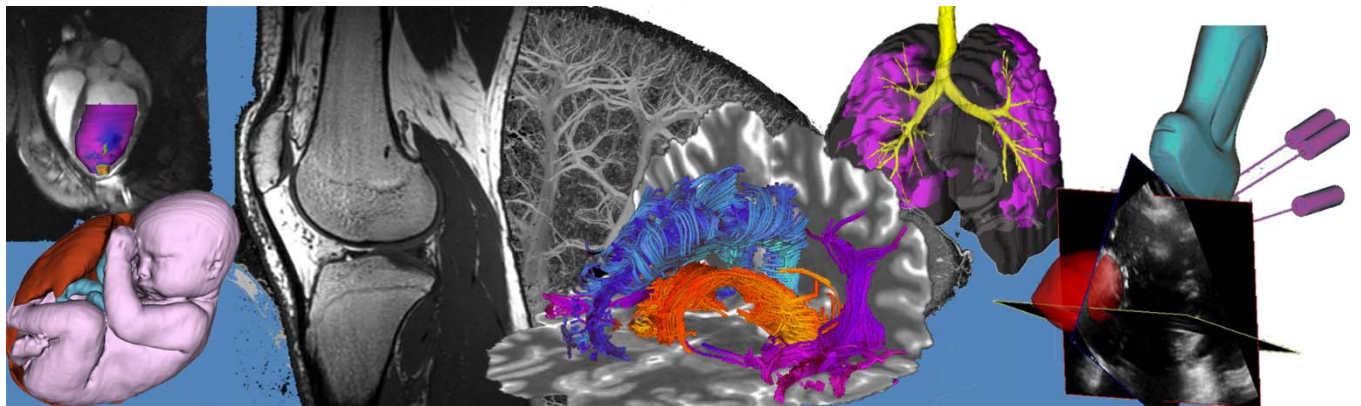


**Figure 1.** Axial (left) and coronal (middle)  $T_2^*$ w MR images demonstrate regions of signal hypointensity induced by the exposures at 0.8 MPa (100%  $p_{\text{sub}}$ ) and 1.2 MPa (150%  $p_{\text{sub}}$ ). Yellow contours: -8 dB source field intensity distributions from the corresponding anatomical plane (spatial-peak source field intensity location/magnitude integrated over each pulse for the full treatment duration). Axial H&E stained tissue section from the same animal (right) shows regions of RBC extravasations and lightly stained necrotic areas (arrows).

# Oral Presentation Abstracts

## Session 11: Neuroimaging





## ERROR ANALYSIS OF A NON-INVASIVE HYBRID PET/MRI METHOD FOR IMAGING CMRO<sub>2</sub>

Lucas Narciso<sup>1,2</sup>, Tracy Ssali<sup>1,2</sup>, Udunna Anazodo<sup>1,2</sup>, Hidehiro Iida<sup>3,4</sup>, Keith St Lawrence<sup>1,2</sup>

<sup>1</sup>Lawson Health Research Institute, London, Ontario

<sup>2</sup>Department of Medical Biophysics, Western University, London, Ontario

<sup>3</sup>University of Turku and Turku PET Centre, Turku, Finland

<sup>4</sup>National Cerebral and Cardiovascular Center, Osaka, Japan

**Introduction:** The gold standard for imaging the cerebral metabolic rate of oxygen (CMRO<sub>2</sub>) in humans is positron emission tomography (PET) using <sup>15</sup>O-labelled tracers: <sup>15</sup>O<sub>2</sub> to measure the oxygen extraction fraction ( $E$ ), H<sub>2</sub><sup>15</sup>O to measure cerebral blood flow ( $f$ ) and C<sup>15</sup>O to correct for activity from the cerebral blood volume ( $V_B$ ). Commonly referred as the three-step autoradiographic (ARG) method, this is a complex, lengthy, and invasive procedure that requires arterial blood sampling (Mintun *et al.*, 1984; Ohta *et al.*, 1992). The aim of this work was to conduct an error analysis of a non-invasive, reference-based method to image CMRO<sub>2</sub> on a hybrid PET/magnetic resonance imaging (MRI) scanner. With this approach, MRI techniques are used to image  $f$  as well as measure whole-brain CMRO<sub>2</sub>, which acts as a reference for PET <sup>15</sup>O<sub>2</sub> imaging (Wehrli *et al.*, 2014). This hybrid method avoids arterial sampling and reduces the PET to a single tracer.

**Methods:** The reference-based method is based on a simple one-compartment model of <sup>15</sup>O<sub>2</sub> uptake in brain tissue (Fig. 1A), which ignores two common sources of error with the standard PET-alone method: recirculating H<sub>2</sub><sup>15</sup>O (RW) created by metabolism and  $V_B$ . To assess the sensitivity to these potential errors, simulated time activity curves (TACs) that included RW and  $V_B$  (Fig. 1A) were generated over a range of  $f$  values (10 to 100 mL/100g/min) with whole-brain  $E$  and  $f$  fixed (0.40 and 50 mL/100g/min, respectively). These TACs were analyzed with the model solution for the reference-based method over scan times from 2 to 5 min. To demonstrate the feasibility of the hybrid method, it was applied to human <sup>15</sup>O<sub>2</sub> dataset ( $n = 11$ ) provided by Dr. H. Iida (Osaka, Japan).

**Results:** Simulations indicated that neglecting RW caused negligible error in the CMRO<sub>2</sub> estimates (0.03±0.16%), and any effects of a blood-borne activity could be substantially reduced using integration times greater than 3 min (Fig. 1B). Applying the hybrid method to the human dataset produced similar CMRO<sub>2</sub> images when compared to the ARG method (Fig. 1C), with mean whole-brain error of -2.7±14.9%. Regression analysis indicated a significant correlation between whole-brain CMRO<sub>2</sub> values from the hybrid and standard PET method ( $p < .05$ , slope = 0.97,  $R^2 = .99$ ).

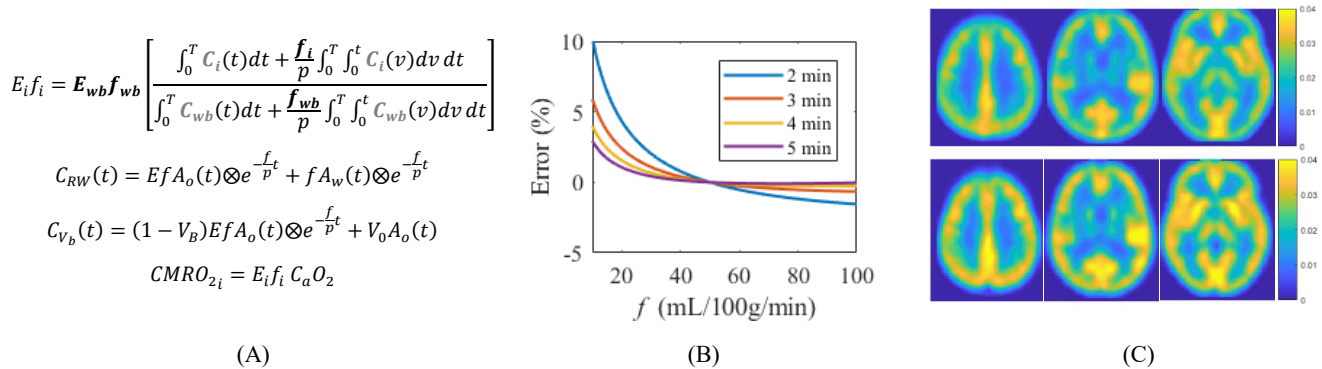


**Figure 1.** (A) Model solution for the reference-based method derived from a one-compartment <sup>15</sup>O<sub>2</sub> model. The quantities in grey come from <sup>15</sup>O<sub>2</sub>-PET and the bold from MRI. The subscripts  $i$  and  $wb$  refer to the  $i^{\text{th}}$  voxel and whole brain, respectively, and  $T$  is scan time. TACs were simulated including RW and  $V_B$  with the middle equations, where  $p$  is the blood-brain partition coefficient for water,  $\otimes$  represents convolution,  $V_0 = R_{Hct}(1 - EF_v)V_B$ ,  $R_{Hct} = 0.85$  is the small-to-large hematocrit ratio, and  $F_v = 0.835$  the effective venous fraction. CMRO<sub>2</sub> is computed from the bottom equation, where  $C_aO_2$  is the arterial content of oxygen. (B) Predicted error caused by excluding  $V_B$ . (C) CMRO<sub>2</sub> images obtained with the hybrid PET/MRI method (top) applied to <sup>15</sup>O<sub>2</sub>-PET data from healthy volunteers ( $n = 11$ ) compared to standard PET images (bottom, Kudomi *et al.*, 2013).

**Conclusions:** The insensitivity to RW and  $V_B$  showed from the simulations indicates the potential of the hybrid PET/MR method to non-invasively image CMRO<sub>2</sub>. This was confirmed by the good agreement between the CMRO<sub>2</sub> images obtained by the hybrid approach and by stand-alone PET. However, the accuracy of the approach will depend on the MRI techniques used to image  $f$  and whole-brain CMRO<sub>2</sub>. The next step is to validate the approach in an animal model.

## Empirical evaluation of a DTI tractography pipeline using whole-brain tractograms from a white matter phantom.

Stefan E Poirier<sup>1,2</sup>, Jonathan D Thiessen<sup>1,2</sup>, and Udunna C Anazodo<sup>1,2</sup>

<sup>1</sup>Lawson Health Research Institute, London, ON, Canada, <sup>2</sup>Medical Biophysics, Western University, London, ON, Canada

**INTRODUCTION:** Diffusion tensor imaging (DTI) tractography is a technique used to reconstruct white matter (WM) fiber pathways in the brain (Tournier et al., Int J Imaging Syst Technol 2012). In order to perform DTI tractography, diffusion images must first be preprocessed to remove noise, subject motion, and other image artifacts. There are different approaches for preprocessing diffusion images which can impact the accuracy of fiber tract reconstruction. In this study, we aim to empirically evaluate our DTI image preprocessing and tractography pipeline using the ground-truth phantom from the ISMRM 2015 Tractography Challenge (<http://www.tractometer.org/>). Whole-brain fiber tracts (tractograms) from both the artifact-free phantom and the challenge phantom dataset will be scored and compared to a database of other tractograms.

**METHODS:** The phantom diffusion data, which contained noise, motion, and image artifacts, were generated using Fiberfox (Neher et al., MRM 2014) from 25 computer-simulated WM bundles with the following parameters; in-plane resolution = 2 mm isotropic, 32 contiguous slices, b values = 0, 1000 s/mm<sup>2</sup> and 32 directions. All pipeline steps were performed using MRtrix3 ([mrtrix.org](http://mrtrix.org)). Image preprocessing steps included: subject motion, eddy current, and bias field corrections; and tensor-fitting to generate a fractional anisotropy (FA) map. DTI tractography steps included: single fiber response function estimation of DTI data using a spherical harmonics order of 8 and an FA threshold of 0.7; DTI upsampling to 1x1x1 mm<sup>3</sup>; fiber orientation distribution function calculation by constrained spherical deconvolution with a spherical harmonics order of 8; and deterministic streamlines tractography to generate the whole-brain tractogram using a step size of 1mm and a WM seed image. Tractograms were scored using the scoring system from the ISMRM 2015 Tractography Challenge, which compared streamlines to the ground-truth bundles and generated the following parameters; valid bundles (VB) – scored out of 25, invalid bundles (IB) – number of bundles that did not exist in ground-truth phantom, valid connections (VC), invalid connections (IC), and no connections (NC).

**RESULTS:** Scores from the artifact-free phantom: VB = 24, IB = 59, VC = 63.26%, IC = 24.22%, and NC = 12.52%. Scores from the challenge phantom data: VB = 23, IB = 58, VC = 36.56%, IC = 29.85%, and NC = 33.60%. Whole-brain and corpus callosum tractograms for the artifact-free and challenge phantom data are shown in the figure below.

**CONCLUSIONS:** In this study, we empirically evaluated our tractography pipeline using a diffusion phantom dataset. We found that our tractography pipeline performed well in all categories, except IC and NC where IC and NC should be as close to 0% as possible. We believe that our IC and NC results may be due to streamlines passing through WM-gray matter boundaries into non-WM regions. Next steps are to evaluate our pipeline performance after applying techniques to constrain fiber tracts within WM anatomy such as anatomically-constrained tractography (ACT) and spherical-deconvolution informed filtering of tractograms (SIFT). We aim to use this improved tractography pipeline for reconstruction of WM fibers in epilepsy patients.

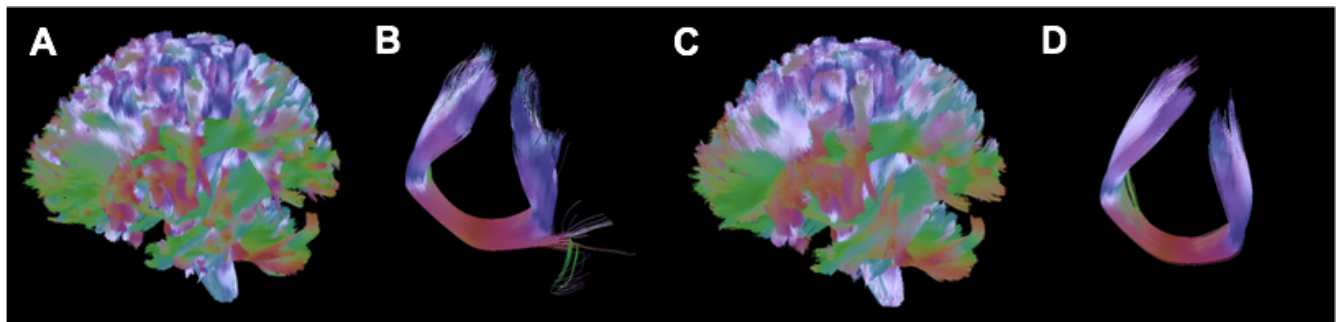


**Figure.** Tractograms from artifact-free phantom: (A) Whole-brain and (B) Corpus callosum. Tractograms from challenge phantom dataset: (C) Whole-brain and (D) Corpus callosum.

## Differentiating the substantia nigra pars compacta and ventral tegmental area in early-stage Parkinson's Disease using structural magnetic resonance imaging

Erind Alushaj<sup>1,2</sup>, Nicholas Handfield-Jones<sup>1,2</sup>, Dr. Nole Hiebert<sup>2,3</sup>, Dr. Adrian M. Owen<sup>3,4</sup>, Dr. Ali R. Khan<sup>5,6\*</sup>, and Dr. Penny A. MacDonald<sup>2,4,7\*</sup>

<sup>1</sup> Department of Neuroscience, Western University, <sup>2</sup> Brain and Mind Institute, Western University, <sup>3</sup> Department of Physiology and Pharmacology, Western University, <sup>4</sup> Department of Psychology, Western University, <sup>5</sup> Robarts Research Institute, Western University, <sup>6</sup> Department of Medical Biophysics, Western University, <sup>7</sup> Department of Clinical Neurological Sciences, Western University

**Introduction:** The midbrain dopaminergic system plays a major role in the pathology of Parkinson's disease (PD). Degeneration in the substantia nigra pars compacta (SNc) causes motor symptoms; whereas, neuronal loss in the lesser-affected ventral tegmental area (VTA) produces non-motor symptoms. Despite this knowledge, there are no validated biomarkers of PD, but magnetic resonance imaging has great potential for their discovery. Our lab found the caudal motor sub-region of the striatum is atrophied in PD, which makes this subregion a potential diagnostic biomarker (Khan et al., 2018). Striatum biomarkers, however, appear too late for improved diagnosis, and development of neuroprotective treatment. Biomarkers in the midbrain are a potential solution and could even uncover pre-clinical changes that predict the development of PD. Imaging the midbrain nuclei comes with several challenges due to their small size, close proximity, and often the requirement of higher field strengths. This study aimed to segment and parcellate the SNc and VTA at 3T and 7T to search for PD biomarkers. Based on our previous findings in the striatum, we hypothesized the caudal motor sub-region of the SNc is the first to degenerate in early-stage PD patients with sparing of the VTA.

**Methods:** Using probabilistic tractography from 3T and 7T diffusion weighted imaging data, we parcellated the striatum based on reciprocal connections to the cortex in twenty early-stage PD patients (Disease duration < 5 years and receiving dopamine therapy) and twenty age-matched healthy controls. We then parcellated the SNc and VTA based on their reciprocal connections with the striatum using similar methodology. This approach allows us to look at volume, surface displacement, and fractional anisotropy of the different midbrain sub-regions for comparison between patients and controls, as well as between field strengths. Quantitative susceptibility mapping was also conducted to measure iron content changes in the midbrain nuclei as a result of PD and assess for differences.

**Results:** From preliminary analysis, no significant differences were found in the volumes and fractional anisotropy of the parcellated sub-regions of the striatum. Marginal effects exist within the caudal motor subregion of the striatum due to the early-stage nature of our PD patients. While our current midbrain atlas shows no significant differences in volume, we will update our methodology to employ the CIT168 atlas which has improved midbrain segmentation (Pauli et al., 2018). Caudal motor subregion shown in blue (Fig. 1) is in the ventrolateral aspects of the SNc, which is the first region to degenerate in PD.

**Conclusions:** Preliminary findings suggest the SNc and VTA parcellation is feasible at 3T and 7T with potential indications of degeneration in the caudal motor sub-regions at the level of the striatum. Our recent adaptation of the CIT168 atlas developed by Pauli and colleagues (2018) shows promise for enhanced midbrain segmentation and parcellation at both field strengths with data analysis on-going.

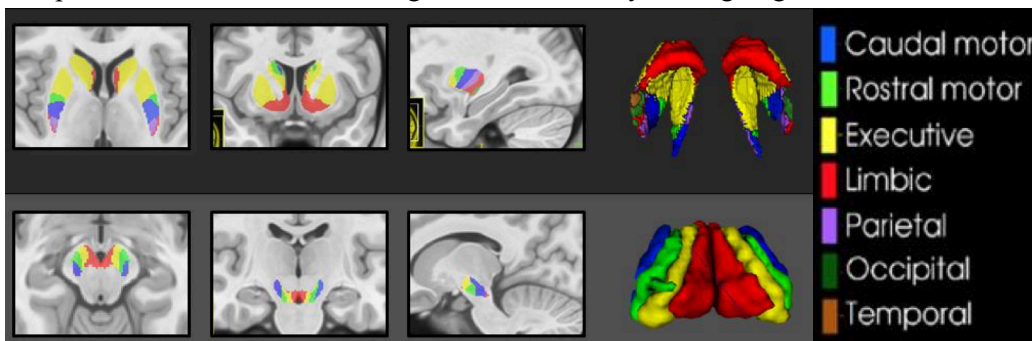


**Figure 1:** Averaged striatum (top), SNc and VTA (bottom) parcellations for healthy controls at 3T. Averaged control parcellations (n = 20) show overlap of limbic subregion with VTA and caudal motor subregion with ventrolateral aspects of SNc. Parcellation methodology adapted from Tziortzi and colleagues (2014).

**References:** Khan, AR, et al. (2018). *NeuroImage: Clinical*. <https://doi.org/10.1016/j.nicl.2018.11.007>  
Pauli, WM, Nili AN, & Tyszka, JM. (2018). *Scientific Data* 5: 180063. doi: 10.1038/sdata.2018.63  
Tziortzi, AC, et al. (2014). *Cerebral Cortex*, 24(5), 1165-1177. doi: 10.1093/cercor/bhs397

## Sub-millimeter blood flow mapping of cortical and hippocampal gray matter

Haast RAM<sup>1</sup>, Ivanov D<sup>2</sup>, DeKraker J<sup>1,3</sup>, Kashyap S<sup>2</sup>, Janssens S<sup>2</sup>, Poser BA<sup>2</sup>, Khan AR<sup>1,3,4</sup> and Uludağ K<sup>2,5</sup>

<sup>1</sup>Centre for Functional Metabolic Mapping, Robarts Research Institute, Western University, London, ON, Canada, <sup>2</sup>Department of Cognitive Neuroscience, Maastricht University, Maastricht, Netherlands, <sup>3</sup>Brain and Mind Institute, Western University, London, ON, Canada, <sup>4</sup>Department of Medical Biophysics, Schulich School of Medicine and Dentistry, Western University, London, ON, Canada, <sup>5</sup>Center for Neuroscience Imaging Research, Institute for Basic Science (IBS) & Department of Biomedical Engineering, Sungkyunkwan University, Suwon, Republic of Korea.

### Introduction

High-quality human whole-brain 0.7 mm isotropic resolution cerebral blood flow (CBF) mapping using arterial spin labeling (ASL) has been demonstrated using 7T MRI<sup>1</sup>. Here, we demonstrate the use of such high-fidelity CBF map for cortical surface mapping of perfusion and evaluate its utility with regards to detection of possible differences across subregions of the hippocampal formation using a recently published coordinate system<sup>2</sup>.

### Methods

Data were acquired on a whole-body 7T MRI scanner (Siemens Healthineers) with a 32-channel receive head-coil (Nova Medical) on one female volunteer (20 yr) during 12 sessions. Each session contained at least six ASL runs positioned at different locations across the brain to measure CBF in the most efficient manner. In addition, whole-brain 0.7 mm<sup>3</sup> MP2RAGE and IR-EPI T<sub>1</sub> data and B<sub>1</sub><sup>+</sup> maps were obtained. See Ivanov et al. (2018)<sup>1</sup> for further details. The B<sub>1</sub><sup>+</sup>-corrected MP2RAGE data<sup>3</sup> were used for cortical surfaces reconstruction using FreeSurfer (v6.0). A distortion-matched IR-EPI T<sub>1</sub> map was coregistered to the MP2RAGE T<sub>1</sub> map using ANTs<sup>4</sup> to subsequently transform the CBF map for mapping baseline perfusion onto the cortical surface and comparison across regions<sup>5</sup>. Finally, the hippocampal formation was manually segmented in the IR-EPI T<sub>1</sub> map, for unfolding and mapping of hippocampal CBF using an in-house developed coordinate system<sup>2</sup>.

### Results

Clear differences in baseline perfusion can be observed across the cortex, see Fig. 1A. The primary (i.e. highly myelinated) cortical areas, especially the somatosensory, motor and visual cortices, were characterized by higher baseline perfusion levels. Note that CBF was artificially low in the inferior parts of the temporal and frontal lobes, due to lower (temporal) SNR. After unfolding using manual hippocampal segmentation (see Fig. 1B), higher perfusion was especially observed in the subiculum (Sub) within the uncus and head portion of the hippocampus,

### Conclusions

The current results show that sub-millimeter CBF data can be used to discern between cortical regions, as well as for differentiation between subregions within more fine-scale structures. In general, higher baseline perfusion levels were observed in cortical and hippocampal regions that are highly myelinated (i.e. low T<sub>1</sub>)<sup>6</sup>. However, data from multiple subjects need to be acquired to carefully assess the correlation between CBF and myelination. Finally, for correct interpretation of the resulting cortical CBF maps, as well as potential fMRI data, additional data modalities to measure vascular density (e.g. time-of-flight and susceptibility-weighted imaging) should be used to rule out or correct for potential large vessel biases.

### References

<sup>1</sup>Ivanov et al. (2018) Proc. Intl. Soc. Mag. Reson. Med. 26 p. 2301. <sup>2</sup>DeKraker et al. Neuroimage. 2018 Feb 15;167:408-418. <sup>3</sup>Marques and Gruetter, PLoS One. 2013 Jul 16;8(7). <sup>4</sup>Avants et al. Neuroinformatics. 2011 Dec;9(4):381-400. <sup>5</sup>Glasser et al. Nature. 2016 Aug 11;536(7615):171-178. <sup>6</sup>Haast et al. Front Neuroanat. 2016 Nov 18;10:112.

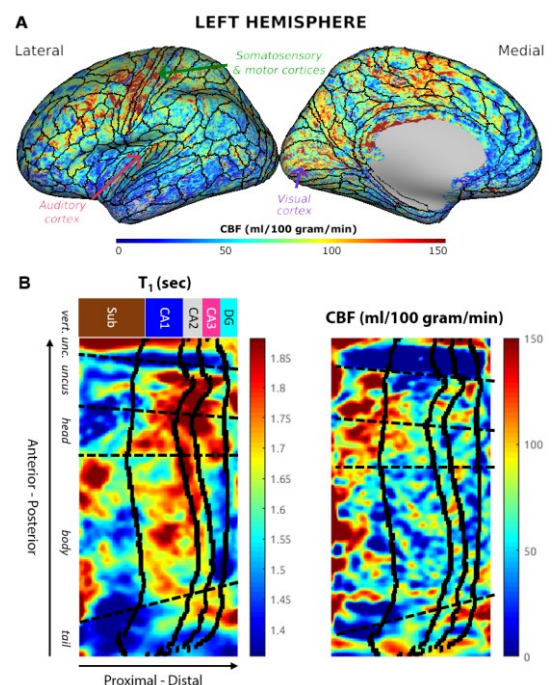


**Fig 1** - Cortical (A, left hemisphere only) and hippocampal subfield (B) CBF mapping.

## Optimization of Phase Contrast for CBF Quantification by a Non-Invasive Hybrid PET/MR-approach

Tracy Ssali<sup>1,2</sup>, Lucas Narciso<sup>1,2</sup>, Justin Hicks<sup>1,2</sup>, Udunna Anazodo<sup>1,2</sup>, Elizabeth Finger<sup>1,2</sup>, Frank Prato<sup>1,2</sup>, and Keith St Lawrence<sup>1,2</sup>

<sup>1</sup>Lawson Health Research Institute, London, Canada, <sup>2</sup>Western University, London, Canada

**Introduction:** While PET with radiolabeled water remains the gold standard for imaging CBF, widespread use is limited by the requirement of arterial sampling. Arterial spin labeling (ASL) MRI is non-invasive and quantitative; however, its sensitivity to the arterial transit time reduces its accuracy, making it challenging to image patients with cerebrovascular diseases (CVD). We previously proposed a non-invasive hybrid PET/MR approach that uses a measurement of global CBF (gCBF) by phase contrast (PC) MRI to convert PET activity into quantitative CBF images without the need for arterial sampling<sup>1</sup>. This PET/MR approach has the potential to provide a method of measuring regional CBF that is accessible to patients whom arterial sampling is not advisable and more importantly, can be used as a reference to optimize ASL. The technique was initially validated in a large animal model, and the next step is to adapt it to human studies. Although the PET imaging will be similar, the PC sequence needs to be optimized for measuring gCBF in humans. In this study, we assess the variability in gCBF due to slice location and gating, and as a proof of concept, we present the first CBF images from one participant obtained using this non-invasive hybrid PET/MR approach.

**Methods:** Data were acquired using the Siemens Biograph mMR in 6 healthy volunteers (age:  $31 \pm 10$ , 2 females). PC images (4 averages, VENC: 70 cm/s, retrospective-gating) were acquired at the level of the first/second cervical vertebrae ( $gCBF_{low}$ ) and basilar artery ( $gCBF_{high}$ ) (Fig.1). Global  $gCBF_{low}$  was repeated using a non-gated sequence. In 3 volunteers, PC data were acquired on 2 occasions separated by 1-2 months. Global CBF was quantified by scaling the blood velocity by vessel area and brain volume. For hybrid PET/MR-CBF<sup>1</sup>, 5 minutes of PET list-mode data were acquired after rapid intravenous bolus injection of <sup>15</sup>O-water (800 MBq). Raw PET data were reconstructed using an MR-based attenuation correction map.

**Results:** Global CBF, was  $53.9 \pm 7.4$  ( $gCBF_{low}$ ) and  $57.5 \pm 12.6$  ml/100g/min ( $gCBF_{high}$ ) (ns). Repeat measurements were within 9.0% ( $gCBF_{low}$ ) and 6.1% ( $gCBF_{high}$ ) of each other (Fig. 2). Non-gated  $gCBF$  was 24% lower than the gated sequence (ns). The CBF image obtained by PET/MR is shown in Figure 3.

**Conclusion:** The  $gCBF$  estimates were similar<sup>2</sup> but lower than previous studies<sup>3</sup>. Differences could be attributed to increased noise resulting from a high VENC<sup>4</sup>. The 6.5% difference between  $gCBF_{high}$  and  $gCBF_{low}$ , which may be significant with a larger sample size, could be related to partial volume errors due to contributions from stationary tissue<sup>5,6</sup>. PC-CBF measurements were reproducible, with <9% difference between measurements. The CBF map generated by the non-invasive PET/MR approach resembles a typical CBF map; with higher flow in grey matter. Future goals are to use this hybrid approach to image CBF in CVD patients to evaluate its ability to quantify perfusion abnormalities and subsequently, determine optimal parameters for imaging CBF in this population with ASL.

**References:** (1) Ssali, T. et al, JNM (2018). (2) Spilt, A. et al. JCBFM (2005). (3) Puig, O. et al. JCBFM (2018). (4) Lotz, J. et al. JMRI (2005). (5) Peng, S.-L. et al. JMRI (2015). (6) Tang, C et al. JMRI (1993).

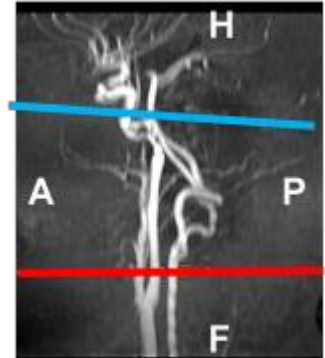


Figure 1: Time of flight image with high (blue) and low (red) imaging planes

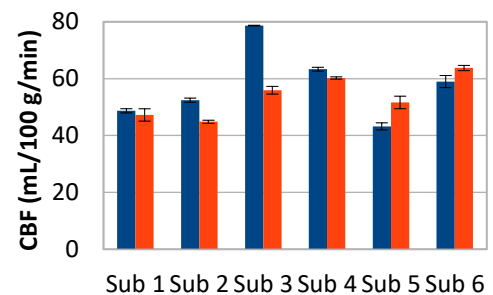


Figure 2: CBF measured at the high (blue) and low (orange) position

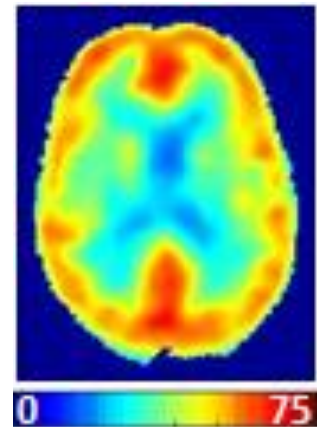


Figure 3: CBF map (ml/100g/min) generated by the non-invasive PET/MR approach.

## Assessing the reliability and reproducibility of NeuroBundle Extraction and Evaluation Resource, an automated tool for clustering diffusion tractography

Jason Kai<sup>1</sup>, Ali R. Khan<sup>1,2</sup>

<sup>1</sup>Dept. of Medical Biophysics, <sup>2</sup>Robarts Research Institute, Western University, London, ON, Canada

**Introduction:** Tractography offers a non-invasive technique for probing the white matter fibres which comprise the structural connections of the brain<sup>1</sup>. Many streamlines, often in the millions, are generated from tractography to infer the fibre projections. Unique pathways, comprising a group of streamlines, join different regions of the brain. Manual or automated techniques are used to identify these pathways from tractography<sup>2</sup>. Additionally, quantitative MRI can be used to further quantify identified pathways. With any technique, it is imperative to assess the reliability and reproducibility of the output. Here, we introduce the NeuroBundle Extraction and Evaluation Resource. This tool identifies fibre bundles based on geometric similarity and can extract short-ranged U-shaped bundles, which have been previously implicated in neurological conditions. We also assess output reproducibility of the tool.

**Methods:** Pre-processed diffusion MRI (dMRI) data (n=100) from the Human Connectome Project<sup>3</sup> was used to generate a whole-brain tractography template. Data was acquired on a customized Siemens Skyra 3T scanner<sup>4,5</sup> at 1.25mm isotropic resolution, b-values=1000, 2000, 3000 s/mm<sup>2</sup> and 270 total diffusion-encoding directions. Additionally, multiple sessions (n=15) of dMRI from a single male subject released from the MyConnectome Project<sup>6</sup> was used to assess the reliability of identified pathways. This data was collected on a separate Siemens Skyra 3T scanner at 1.74x1.74x1.7mm<sup>3</sup> resolution, b-values=1000, 2000 s/mm<sup>2</sup> and 60 total diffusion-encoding directions. Preprocessing was performed using in-house pipelines and whole-brain tractography was generated for each session. Unique fibre bundles were clustered using our developed tool. Reproducibility of outputs was assessed by computing average Euclidean distances between each session to the template. Intraclass correlation was also computed for fractional anisotropy (FA) measurements to identify reliability of quantitative measurements. Assessment was performed on five identical clusters in each hemisphere and five additional clusters along the corpus callosum (figure 1).

**Results:** Average Euclidean distance was computed between the identified session and template clusters from tracts identified using the NeuroBundle Extraction and Evaluation Resource. Computed distances between sessions and templates was found to be within 4.5mm. Intraclass correlations of FA ranged from 0.83 to 0.99 in corresponding clusters.

**Conclusions:** Reliability and reproducibility of results was assessed for our developed tool. Quantitative assessments show the tool's ability to identify similar tracts and extract reliable quantitative metrics. Future work includes creating a unique white matter atlas using the NeuroBundle Extraction and Evaluation Resource and to investigate structural connectivity of patient populations using the tool.

### References:

- |  |  |
|--|--|
| [1] Sotiropoulos and Zalesky. (2017). <i>NMR Biomed.</i> | [4] Van Essen et al. (2012). <i>NeuroImage.</i>    |
| [2] Tunc et al. (2014). <i>NeuroImage.</i>               | [5] Sotiropoulos et al. (2013). <i>NeuroImage.</i> |
| [3] Van Essen et al (2013). <i>NeuroImage.</i>           | [6] Poldrack et al. (2015). <i>Nat Commun.</i>     |

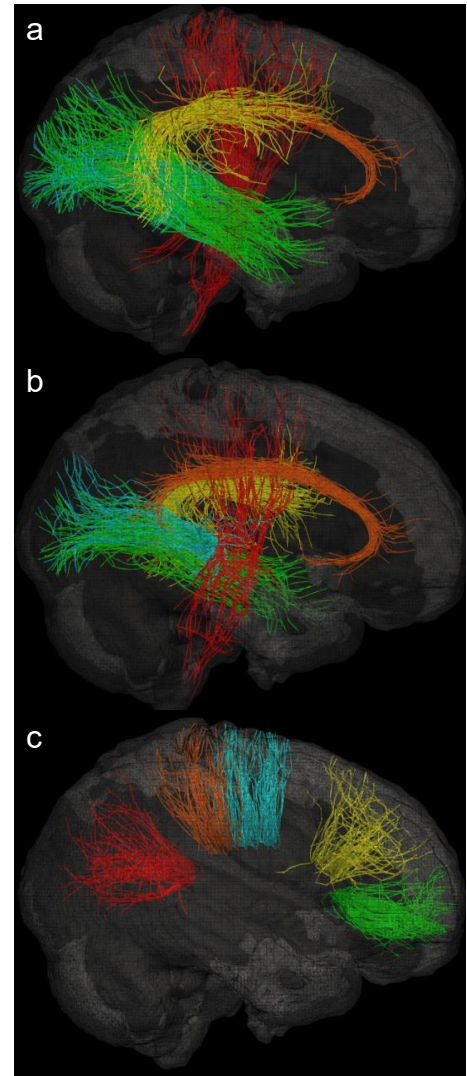
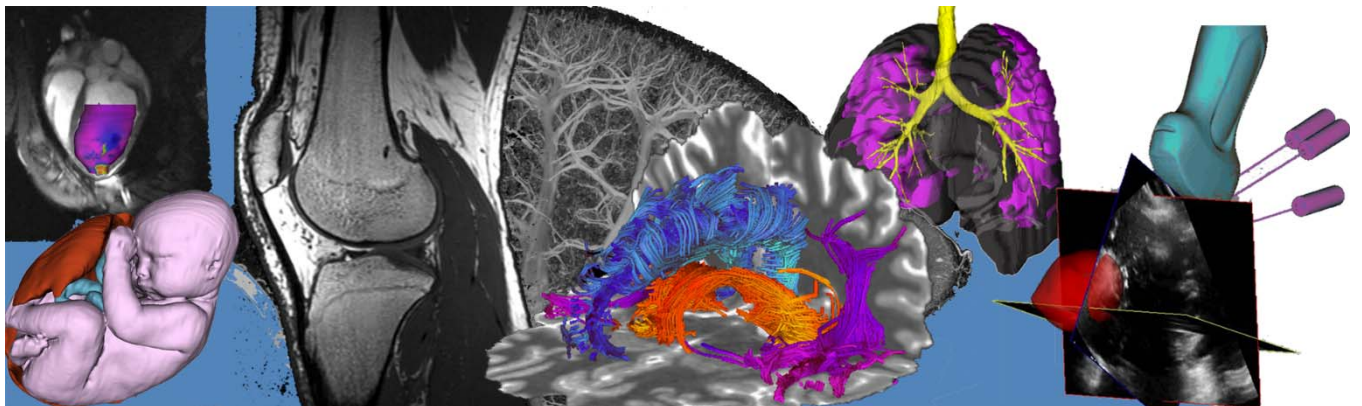


**Figure 1:** Sagittal display of investigated tracts in (a) right hemisphere, (b) left hemisphere, and, (c) along the corpus callosum.

# Oral Presentation Abstracts

## Session 12: Cardiac and Vascular Imaging



## Examining the effect of hepcidin on cardiac inflammation using THP-1 monocytes and MRI

P. Dassanayake<sup>1,2,3</sup>, N. Gelman<sup>1,2</sup>, R.T. Thompson<sup>1,2</sup>, F.S. Prato<sup>1,2,3</sup>, D.E. Goldhawk<sup>1,2,3</sup><sup>1</sup>Imaging Program, Lawson Health Research Institute; <sup>2</sup>Medical Biophysics and <sup>3</sup>Collaborative Graduate Program in Molecular Imaging, Western University; London, Ontario, Canada

**Introduction:** After an acute myocardial infarction (AMI), inflammatory responses stabilize the region of infarction by strengthening the heart muscle; however, an unrestricted inflammatory response leads to excessive left ventricular remodeling [1]. Differentiating between pro- and anti-inflammatory signaling may help establish when interventions should be introduced to curb unwanted tissue remodeling [1, 2]. Monocytes are the precursors of M1 (pro-inflammatory) and M2 (anti-inflammatory) macrophages. While there is a spectrum of macrophage phenotypes, M1 generally displays an iron storage phenotype while M2 exhibits an iron recycling phenotype [2]. Hepcidin, a hormone expressed post-AMI (unpublished results), is induced by pro-inflammatory signaling [3] and downregulates ferroportin (FPN), an iron export protein found on monocytes and macrophages [2, 3]. These features of iron metabolism may allow us to differentiate between pro- and anti-inflammatory responses post-AMI using magnetic resonance imaging (MRI). We used the human monocyte THP-1 cell line to examine the effect of hepcidin and extracellular iron on their cellular MRI signal.

**Hypothesis:** Changes in monocyte iron regulation are mediated by hepcidin and influence both cellular iron content and MR relaxation rates.

**Objectives:** 1. Measure MR relaxation rates in THP-1 monocytes and characterize the influence of hepcidin and extracellular iron on these measures. 2. Examine the expression of FPN in THP-1 monocytes/macrophages and determine the influence of hepcidin and extracellular iron on the regulation of iron export.

**Method:** THP-1 cells were cultured for 7 days in the absence (-Fe) and presence (+Fe) of iron-supplemented medium (25  $\mu$ M ferric nitrate). Upon withdrawal of iron supplement, cells were further cultured for 1, 2, 4 and 24 hours. In addition, all samples were treated with 200 ng/ml hepcidin for up to 24 hours of culture. At harvest, cells were either mounted in a gelatin phantom for MRI or lysed in buffer/protease inhibitors (Roche) for analysis of FPN. Protein was quantified using the BCA assay [4]. Expression of FPN was assessed by Western blot using primary rabbit  $\alpha$ -FPN (Invitrogen). Transverse relaxation rates were measured at 3T [4] using single-echo spin echo for R2 and multi-echo gradient echo for R2\* acquisitions. The reversible component (R2') was calculated from the difference (R2\* - R2).

**Results:** THP-1 monocytes express iron export protein and addition of hepcidin decreases this expression, as expected (data not shown). Interestingly, changes in extracellular iron also decrease iron export, producing a transient and significant increase in R2\* between 1-4 h after removal of iron supplement (Figure 1A). Addition of hepcidin (Figure 1B) narrows this window of MR detection to 2-4 h.

**Conclusion:** THP-1 monocytes display relatively high, baseline R2\* (-Fe), suggesting an iron storage phenotype. The activation of FPN degradation by hepcidin is consistent with the role of monocytes in hepcidin-mediated pro-inflammatory signaling [3]. While transient changes in monocyte iron export may also be regulated by extracellular iron, importantly, MRI may be used to detect these fluctuations.

**References:** [1] Fang et al. (2015) J Geriatric Cardiol 12: 305; [2] Alizadeh (2017) MSc thesis, Western University; [3]; Theurl et al. (2008) Blood 111: 4; [4] Sengupta et al. (2014) Front Microbiol 5: 29

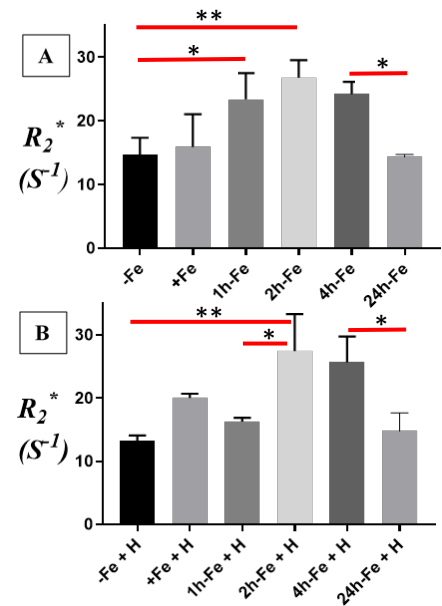


**Figure 1. Influence of extracellular iron and hepcidin on transverse relaxation rates in THP-1 monocytes.** Cells were cultured with (+Fe) or without (-Fe) iron-supplemented medium for 7 days, then harvested and scanned either immediately or 1 (1h-Fe), 2 (2h-Fe), 4 (4h-Fe) and 24 (24h-Fe) hours after the withdrawal of iron supplement. A) Transverse relaxation rates ( $R_2^*$ ) increase significantly hours after withdrawal of iron supplement, before returning to baseline. B) At 1h-Fe, exogenous hepcidin has a significant influence on  $R_2^*$ . n=3-4, \* p<0.05, \*\* p<0.01.



## Development of an *ex vivo* porcine model of coarctation of the aorta: Possible treatment applications with MR-guided HIFU using boiling histotripsy

Sergio Vegas Salas<sup>1</sup>, Aodhnait Fahy<sup>1</sup>, Karolina Piorkowska<sup>2</sup>, Adam Waspe<sup>2</sup>, Mandolin Bartling<sup>2</sup>, James Drake<sup>2</sup>, Christoph Haller<sup>3</sup>, Justin T Gerstle<sup>1</sup>.

<sup>1</sup> Division of General and Thoracic Surgery, The Hospital for Sick Children Toronto, ON, Canada.

<sup>2</sup> Centre for Image Guided Innovation & Therapeutic Intervention, The Hospital for Sick Children, Toronto, ON, Canada.

<sup>3</sup> Division of Cardiovascular Surgery, The Hospital for Sick Children, Toronto, ON, Canada.

**Introduction:** Coarctation of the aorta is one of the most common types of congenital heart defects in neonates and is characterized by a narrowing of the aorta caused by a shelf-like obstructive lesion that leads to hypertension and heart failure. Current treatment strategies include open chest surgery with resection and end-to-end anastomosis or balloon-based catheter dilatation of the coarcted segment. These treatments are associated with risks that could be potentially avoided via a non-invasive technique, such as MR-guided high-intensity focused ultrasound (MRgHIFU). The purpose of this study was to create an *ex vivo* porcine model of a coarctation of the aorta and then determine if it was amenable to HIFU treatment of boiling histotripsy as a proof of concept.

**Materials and Methods:** To create a model of aortic coarctation, abdominal aortas were harvested from pigs and divided into 3 cm segments. Skin porcine gelatin at a concentration of 7% was injected under the intima using ultrasound image guidance (1 ml of solution) in order to create a gelatin mass within the lumen that would narrow the aorta, simulating a coarctation. One gelatin mass per aortic segment. Two segments were embedded into a 15% gelatin phantom. A 3 Tesla MRI (Philips Achieva, Best, Netherlands) was used for guidance, and one segment was sonicated on a Sonalleve V1 HIFU table (Profound Medical, Toronto, Canada) and the other segment left as an untreated control. Four adjacent sonications (900 Watt, 51 seconds duration, 20 pulses, duty cycle 0.21%) were performed within each treated gelatin mass. Post-treatment imaging was performed, and the pre- and post-treatment imaging was analyzed.

**Results:** There were n= 8 aortic segments with a gelatin mass sonicated and n= 8 adjacent untreated gelatin mass controls. Longest diameter mean of the gelatin mass was 9.55 mm (13.8 mm to 6.6 mm). Post-treatment imaging revealed a smaller mass and wider lumen compared to pre-treatment imaging, with a mean reduction in the longest diameter of 11.4% (range from 5.2 to 28.4% with a standard deviation of 7.6), visualized on 2D in the T1w Vista. Boiling histotripsy did not grossly damage the endothelium nor adventitia.

**Conclusions:** We have developed a basic *ex vivo* porcine model for coarctation of the aorta that can be treated with MRgHIFU. It was possible to dissolve a portion of the narrowing that was simulating the coarctation without injuring the nearby adventitia nor the endothelium. This *ex vivo* porcine model as a proof of concept suggests that boiling histotripsy can be used to treat tissue narrowing the aorta without damaging the adjacent vessel. Future directions include evaluating the efficacy of histotripsy to dissolve the tissue normally found in the coarctation shelf, as well as to create an *ex vivo* pulsatile model of aortic coarctation.

## Soft Tissue and Vascular Visualization of Iodine-Enhanced Samples via Dual-Energy Computed Tomography

Justin J Tse,<sup>1,3</sup> Joy Dunmore-Buyze,<sup>1,3</sup> Charmainne Cruje,<sup>1,3</sup> Maria Drangova,<sup>1,3</sup> and David W Holdsworth<sup>1,3,4</sup>

<sup>1</sup>Robarts Research Institute, <sup>2</sup>Department of Physiology and Pharmacology, <sup>3</sup>Department of Medical Biophysics, <sup>4</sup>Department of Surgery  
Western University, London, Ontario, Canada

**Introduction:** To better understand disease progression and their impact in the local tissue environment (*i.e.* myocardial infarctions, ischemic injuries, etc), the visualization and quantification of all tissue types (*i.e.* soft tissue, bone, and vascular structures) is necessary. Computed tomography (CT) is often chosen as the ideal imaging technique due to its availability and non-destructiveness; however, differentiation of soft tissue and vessels with CT has been challenging due to the tissues' low x-ray attenuation. Perfusing and soaking samples in a contrast agent, most commonly iodine-based, can facilitate the visualization of the contrast-enhanced tissues with single-energy CT; however, the tissues are indistinguishable from neighbouring dense bone based on greyscale values alone. Recently, we have pre-clinically demonstrated the ability of dual-energy computed tomography (DECT) to provide 3D visualizations and quantification of individually segmented tissues (*i.e.* soft tissue, bone, and perfused microvessels)<sup>1</sup>. Our previous results were demonstrated using an erbium (Er) based contrast agent, custom Er x-ray filtration, and DECT protocols optimized with Er. Thus, optimizing iodine DECT will require further spectral shaping (*i.e.* iodine x-ray filter) and modifications to the scan protocols.

**Methods:** To fabricate a low-energy iodine x-ray filter, we 3D printed a cylindrical annular – with 3-mm thick hollow cavity, and fill and evacuation ports – via the fused deposition of polylactic acid (PLA). The cavity was filled with a 2% w/v iodine in distilled water, while avoiding air bubbles. The copper filter that was used for high-energy scans was comprised of three sheets of 80  $\mu\text{m}$  thick copper wrapped around an acrylic cylinder, providing a total pathlength of 480  $\mu\text{m}$  of Cu. The low-energy scan was acquired with 70 kVp, 50 mA, and the additional 3D-printed iodine filter. High-energy scans were acquired at 90 kVp, 40 mA, with the copper filter. Two samples were prepared: (1) a mouse perfused with an iodine-based contrast agent<sup>2</sup>; and (2) an expired skinned mouse submerged within an I<sub>2</sub>KI solution in distilled water (2.5% w/v KI and 1.3% w/v I<sub>2</sub>) for 24 hours. Iodine-enhanced samples were then DECT-scanned, co-registered, and decomposed into individually segmented and quantitative 3D volumes of iodine-enhanced soft tissue, bone, and non-contrast enhanced tissues.

**Results:** We have demonstrated the success of pre-clinical iodine DECT via the decomposition of both an iodine-perfused (Fig. 1AB) and iodine-soaked (Fig. 1C) sample into visually distinct and quantitative volumes of iodine-enhanced tissue (Fig. 1BC) and bone (Fig. 1A). We can observe coronary and intercostal arteries, in addition to the vascularized bone (Fig. 1B). From the iodine-soaked sample (Fig. 1C), we can distinguish between various muscles groups (*e.g.* pectoralis major). Samples were not formalin-fixed prior to DECT scanning; thus, slight motion artifacts can be observed in Fig. 1AB, present as misclassified voxels (*i.e.* bleed-over).

**Discussion:** While iodine-soaking samples limits this DECT implementation to pre-clinical studies, the capability to perform DECT with widely used iodine-based contrast agents provides researchers with the ability to visualize and potentially quantify changes to soft tissue, bone, and vessels impacted by disease, surgical interventions (*i.e.* myocardial infarction, ischemic injury, etc), and treatments.

**References:** 1. J. J. Tse, J. Dunmore-Buyze, M. Drangova, D. W. Holdsworth. (2018) *Journal of Medical Imaging*, vol. 5, pp. 10. 2. J. Dunmore-Buyze, C. Cruje, Z. Nong, J. J. Lee, J. A. Kiernan, J. G. Pickering, and M. Drangova. *Scientific Reports*, Received Sept 3, 2018, Accepted Nov 23, 2018.



Fig. 1. Results of iodine DECT. The iodine-perfused sample was decomposed into (A) bone- and (B) vessel-only images. (C) Represents the iodine-enhanced soft tissue-only image from iodine-soaked sample.

## Towards quantifying tissue perfusion with dynamic contrast-enhanced near-infrared imaging

Seva Ioussoufovitch<sup>1,2</sup> & Mamadou Diop<sup>1,2,3</sup>

<sup>1</sup> School of Biomedical Engineering, Collaborative Training Program in Musculoskeletal Health Research, Bone & Joint Institute, Western University, London, Ontario, N6A 5C1, Canada

<sup>2</sup> Imaging Program, Lawson Health Research Institute, London, Ontario, N6A 4V2, Canada

<sup>3</sup> Department of Medical Biophysics, Western University, London, Ontario, N6A 5C1, Canada

**Introduction:** Dynamic contrast-enhanced near-infrared spectroscopy (DCE NIRS) is a robust, quantitative technique used for measuring hemodynamic parameters of various tissue beds including brain and joint tissues [1,2]. Nevertheless, the method still relies on the use of emission and detection probes. As such, the technique remains impractical for use in clinical contexts where quick, multi-target monitoring is needed (e.g. monitoring treatment response of 20 hand joints in arthritis patients). Recent studies have shown that spatial encoding of detected light using a two-dimensional array of micro-mirrors (digital-micro-mirror device; DMD), can enable cost-efficient implementation of wide-field near-infrared imaging methods which have traditionally been limited by low frame rates and high cost approaches [3]; this development is based on the single-pixel camera (SPC) principle [4]. Building on these advancements, our current objective is to integrate an SPC into a typical DCE NIRS system with the goal of developing a novel wide-field near-infrared perfusion imaging technique. Furthermore, we seek to validate the system's performance by testing its ability to quantify absorption changes in tissue-mimicking phantoms and to image tissue perfusion in an animal limb.

**Methods:** A picosecond diode laser (780nm; 80MHz) was used to illuminate a 3x3 cm area (defined as the system's field of view; FOV) on an optically clear imaging stage. Light transmitted through the stage was projected onto a time-resolved single-pixel camera (TR-SPC) made up of a digital micro-mirror device (DMD) whose output was coupled to a photomultiplier detector connected to a time-correlated single photon counting module. In addition, a mirror was used to image the FOV onto a CCD camera which was used to acquire dynamic light intensity measurements. To test the system's ability to resolve changes in absorption, phantom experiments were conducted. Polypropylene test tubes (1mm wall thickness; 8mm inner diameter) were filled with various India Ink and Intralipid solutions; solutions had absorption coefficients within the 0.20 – 5.0cm<sup>-1</sup> range. During imaging, tubes were suspended in tissue-mimicking solution (0.5% Intralipid). Next, as a proof-of-concept, an animal experiment was conducted by imaging the right limb of an adult male Lewis rat. The rat was anesthetized, placed on the imaging stage, and its right leg was positioned within the system's FOV so that parts of the foot, ankle joint, and thigh were clearly visible. The TR-SPC was then used to acquire an estimate of optical pathlength through the limb. Next, the rat received an intravenous injection of Indocyanine green dye and the resulting light intensity modulations in the limb were recorded using the CCD camera.

**Results:** Tested absorbing inclusions were clearly visible in reconstructed TR-SPC intensity images. Absorption values were reconstructed at each image pixel and average absorption coefficients in the inclusions showed good agreement with expected values based on solution concentrations ( $R^2 = 0.93$ ; slope of 0.98). For animal experiments, temporal curves of tracer concentration were reconstructed at each image pixel. An overlay of peak tracer curve values onto a CCD image of the FOV revealed heterogeneity in tracer uptake throughout the limb.

**Conclusion:** An SPC was integrated into a DCE NIRS system to enable wide-field imaging capability. The system's ability to resolve changes in absorption was successfully demonstrated in tissue-mimicking phantoms. A preliminary animal experiment showed the system's ability to track tracer concentration throughout an animal limb which suggests the system is capable of quantifying wide-field perfusion. Future experiments will focus on conducting further phantom experiments and quantifying perfusion using acquired tracer concentration curves.

### References:

1. Rajaram et al., Biomed. Opt. Express **7**(10), 3843.
2. Elliott et al., J. Biomed. Opt. **15**(3), 037014.
3. Pian et al., Nat. Photonics **11**(7), 411–414.
4. Duarte et al., IEEE Signal Process. Mag. **25**(2), 83–91.

## Exploring the Effects of Standard and Cooled Hemodialysis on Renal Blood Flow using CT Perfusion

Raanan Marants<sup>1,3</sup>, Elena Qirjazi<sup>2</sup>, Claire J Grant<sup>2</sup>, Christopher W McIntyre<sup>1,2,3,4</sup>, Ting-Yim Lee<sup>1,3</sup>

<sup>1</sup>Department of Medical Biophysics, Western University, London, Canada

<sup>2</sup>Lilibeth Caberto Kidney Clinical Research Unit, London Health Sciences Centre, London,

<sup>3</sup>Canada Lawson Health Research Institute and Robarts Research Institute, London, Canada

<sup>4</sup>Division of Nephrology, London Health Sciences Centre, London, Canada

**Introduction:** Hemodialysis (HD) patients lose residual renal function (RRF) rapidly. The presence and preservation of RRF is linked to better clinical outcomes and improved survival. While clinical characteristics associated with RRF loss in HD patients have been identified, the mechanism behind this decline is still not clear. HD results in reduced myocardial and cerebral blood flow due to HD-induced circulatory stress, and several authors have postulated that recurrent renal ischemic insults may be responsible for HD-mediated RRF loss. Dialysate cooling (DC) effectively ameliorates intradialytic hypotension and helps to preserve myocardial and cerebral hemodynamics during HD. Recurrent HD-induced renal ischemic insults ('kidney stunning') may be the first step towards RRF decline, and DC may be a feasible solution. The aim of this work was to study how HD-induced circulatory stress affects renal hemodynamics in relation to RRF in end-stage renal disease patients under standard and cooled HD conditions using CT perfusion imaging.

**Methods:** 29 patients who have been on HD for >3 months with urine output <250 mL/day provided written informed consent for the study. 14 patients underwent standard (36.5°C) HD only while 15 patients were randomized to receive either standard or cooled (35.0°C) HD first in a 2-visit crossover study design. For each visit, CT perfusion imaging was performed at three timepoints (before, during and after HD) on a 256-slice CT scanner (GE Healthcare) without any interruption to HD treatment. Each scan was done without breath-hold for 2 minutes immediately following a bolus injection of iodinated contrast agent. During HD, perfusion imaging and echocardiography (assessment of myocardial stunning) were performed at peak stress (~3 hours into HD). Misalignment among CT perfusion images was minimized using non-rigid registration software, and parametric kidney perfusion maps were generated from the registered CT images. Statistical analysis was performed using non-parametric tests.

**Results:** Baseline renal perfusion was markedly reduced compared to normal (33.2 vs. >200 mL/min/100g) and was related to dialysis vintage ( $r = -0.35$ ,  $p < 0.01$ ). During standard HD, renal perfusion dropped 18.4% ( $p < 0.005$ ) ('kidney stunning') and was associated with myocardial injury ( $r = -0.33$ ,  $p < 0.05$ ) and mean HD ultrafiltration rate ( $r = -0.31$ ,  $p < 0.05$ ). With DC, perfusion dropped 10.6% and did not worsen myocardial stunning in two thirds of patients. In addition, myocardial stunning-free patients experienced milder kidney stunning during both standard and cooled HD. Additional stunning and HD stress factor data is presented below in Table 1.

	Standard HD 29 Patients, 57 Kidneys	Standard HD vs. Cooled HD 15 Patients, 30 Kidneys	
		Standard HD	Cooled HD
<b>Kidney Stunning</b>	65%	67%	50%
<b>Myocardial Stunning</b>	83%	87%	73%
<b>Correlation between Kidney and Myocardial Stunning</b>	$p < 0.05$	NS	$p < 0.05$
<b>Intradialytic Hypotension</b>	24%	20%	20%
<b>Systolic BP Drop &gt;20 mmHg</b>	59%	67%	53%

**Table 1:** Stunning and HD stress factor data for standard HD, and a comparison between standard and cooled HD.

**Conclusions:** This study is the first to demonstrate that HD-induced circulatory stress is associated with an acute reduction in renal perfusion and that DC can mitigate these effects. HD patients are exposed to recurrent circulatory stress, resulting in cumulative renal injury and thus provides an explanation for loss of RRF. These findings suggest that dialysis-based interventions aimed at improving hemodynamic tolerability, such as DC, may be effective in ameliorating RRF loss. Further studies are required to: (1) assess renal perfusion during standard and cooled HD in people with higher RRF (2) longitudinally follow incident HD patients with respect to declining RRF.

## Effects of the iron chelator deferiprone on porcine acute myocardial infarction and cardiac remodeling

Jill J Weyers<sup>1</sup>, Reuben Thomas<sup>1</sup>, Xiuling Qi<sup>1</sup>, Jennifer Barry<sup>1</sup>, Vraj Rabadia<sup>2</sup>, Dino Manca<sup>2</sup>, John Connelly<sup>2</sup>, Michael Spino<sup>2</sup>, Bradley H. Strauss<sup>3</sup>, Graham A. Wright<sup>1,3,4</sup>, Nilesh R. Ghugre<sup>1,3,4</sup>

<sup>1</sup> Physical Sciences Platform, Sunnybrook Research Institute, Toronto, ON, Canada; <sup>2</sup> ApoPharma Inc., Toronto, ON, Canada; <sup>3</sup> Schulich Heart Research Program, Sunnybrook Health Sciences Centre, Toronto, ON, Canada; <sup>4</sup> Department of Medical Biophysics, University of Toronto, Toronto, ON, Canada;

**Introduction:** Modern myocardial infarction (MI) treatments alleviate vascular occlusion to reperfuse the infarcted tissue. While reperfusion can salvage myocardium, it also increases damage to the unsalvageable tissue, one mechanism of which is hemorrhage: the resulting blood and iron deposits increase edema and inflammation. We hypothesize that removing these iron deposits using the iron chelating drug deferiprone (DFP) will lead to reduced inflammation and faster healing post-MI.

**Methods:** Swine underwent balloon-induced ischemia and reperfusion, and were given either DFP or saline for 4 weeks post-MI. Animals underwent cardiac MRI on a 3T scanner to observe heart function (steady-state-free-precession), infarct progression (late gadolinium enhancement, LGE), hemorrhage (multi-echo gradient-echo T2\*), and edema (T2-prepared spiral imaging) at baseline and 1 day, 1 week, and 4 weeks post-MI. Animals were then sacrificed and hearts were processed for histology.

**Results:** Treatment with DFP increased T2\* values in the infarct over that of saline by one week post-MI, indicating less iron was present (Fig. 1). DFP treatment also decreased end diastolic wall thickness, suggesting less swelling and inflammation post-MI. To support this, T2 values in remote myocardium trended lower with DFP than with saline, pointing to decreased remote edema. Ventricular remodeling, infarct size, and transmuralty were unaffected, but heart function did improve with DFP treatment: ejection fraction recovered faster, and wall thickening increased faster in the treatment group.

**Conclusions:** DFP treatment successfully reduced the presence of iron within the infarct as compared to the saline group, indicating a clearing of the hemorrhagic iron byproducts. Treatment also decreased wall thickness, suggesting reduced inflammation, and improved heart contractile function measured by ejection fraction and wall thickening. In the infarct, this faster decrease in wall thickness could be indicative of a faster resolution to scar. Overall, iron chelation appears to be a promising therapy that could reduce the negative effects of hemorrhage and speed the functional recovery of patients post-MI.

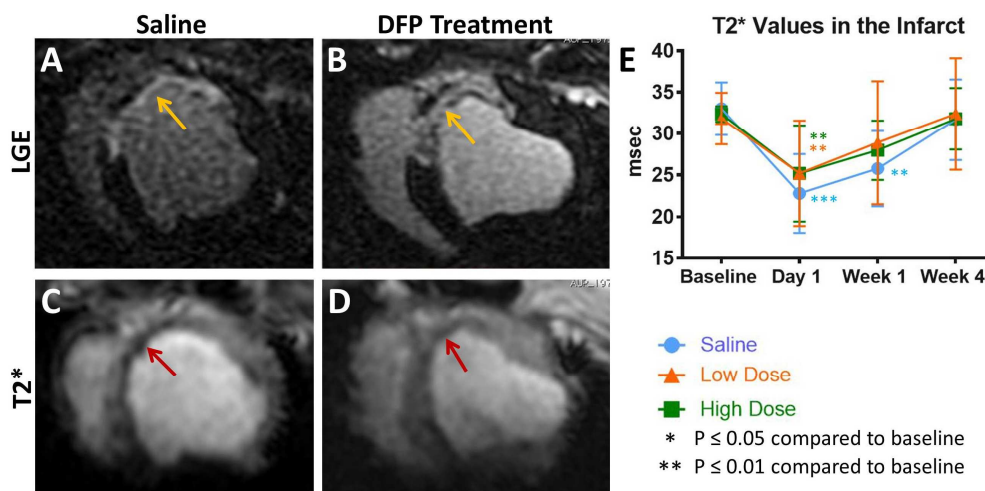
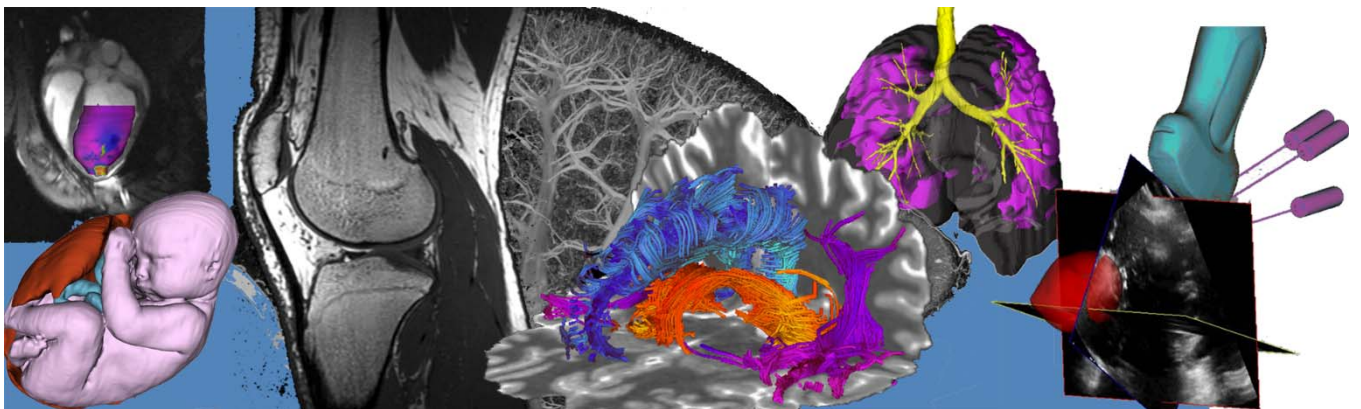


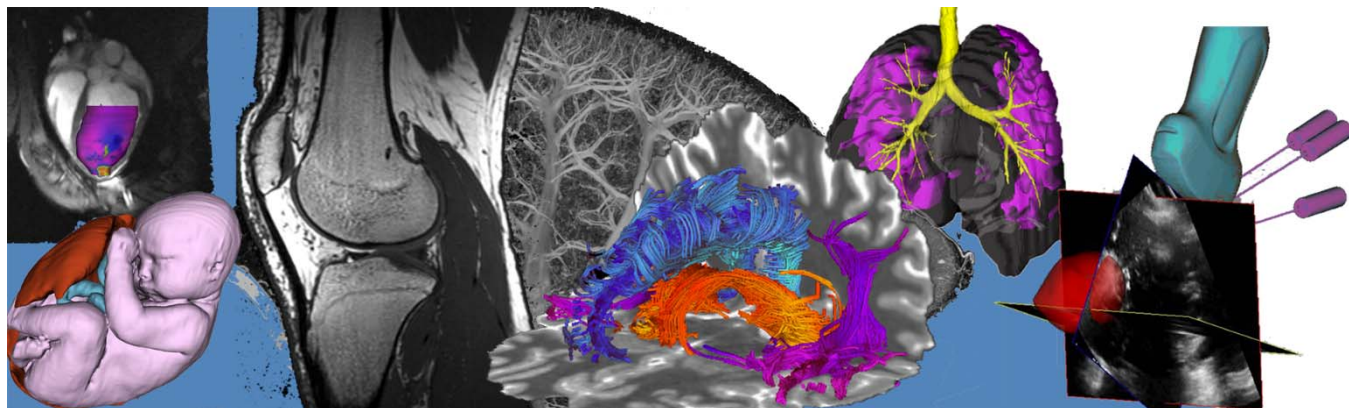
**Figure 1:** Representative MR images one week after infarction. **A,B**) LGE shows the infarct (bright regions in the heart wall, yellow arrows). **C,D**) T2\*-weighted (TE = 17 ms) images show hemorrhage (dark region in the heart wall, red arrows). **E**) T2\* values are higher in the DFP treated groups, indicating the presence of less iron.

# Poster Presentation Abstracts



# Poster Presentation Abstracts

## Session 1: Instrumentation and Technology Development



**Bowel safety margins with MRgHIFU thermal ablation in a preclinical porcine model****Sergio Vega<sup>1</sup>, Aodhnait Fahy<sup>1</sup>, Karolina Piorkowska<sup>2</sup>, Adam Waspe<sup>2</sup>, Mandolin Bartling<sup>2</sup>, James M Drake<sup>2</sup> and J. Ted Gerstle<sup>1</sup>**<sup>1</sup>Division of General and Thoracic Surgery, The Hospital for Sick Children, Toronto, ON, Canada<sup>2</sup>Centre for Image Guided Innovation & Therapeutic Intervention, The Hospital for Sick Children, Toronto, ON, Canada

**Introduction:** MRgHIFU is currently approved for thermally ablative treatments of uterine fibroids and bone metastasis in adults. Abdominal soft tissue masses, such as neuroblastoma and pelvic rhabdomyosarcoma, are under investigation as potential targets for thermally ablative HIFU. However, one of the significant potential risks of abdominal HIFU is thermal injury to nearby bowel (necrosis and/or perforation). To minimize the risk of injury to the bowel, current protocols for treating other pathologies using HIFU recommend maintaining a safety margin of 4 cm. However, the extent of this safety margin has not been scientifically delineated. In the pediatric abdomen, maintaining 4 cm from any edge of the bowel would significantly limit the amount of tumor tissue that could be treated or debulked, and practically, this type of margin would prevent a significant proportion of patients' tumors from being treated. The objective of this study was to create an *in vivo* porcine model to refine bowel safety margins for thermal ablation using MRgHIFU.

**Materials and Methods:** Pigs (n=2, mean weight of 22 kg) underwent a laparotomy under general anesthesia. A 4cm gel marker (Aquaflex®, Parker Labs) was placed in a pocket within the retroperitoneal muscle, lateral to the lower pole of the kidney and caudal to the rib cage. A 10 cm segment of small bowel was fixed to the retroperitoneal wall with a Penrose drain through the mesentery. The same procedure was performed on the contralateral side. Pigs were imaged with a 3 Tesla MRI (Philips Achieva, Best, Netherlands) which enabled localization of the gel markers. HIFU treatment was performed on a Sonalleve V1 HIFU table (Profound Medical, Toronto, Canada) using a soft tissue ablation protocol consisting of an acoustic power of 100 W for a sonication duration of 20s at 1.2MHz. Sonications on the gel marker within the muscular layer was 1.0 cm and 1.5 cm from the nearest bowel. After post-treatment imaging, bowel segments were collected for histological analysis.

**Results:** The Penrose drain allowed stable but not restrictive fixation of small bowel near to the fiducial marker, directly against the retroperitoneal wall. The distance from the fiducial marker and sonication to the bowel wall was quantifiable via MRI. This method simulated the naturally fixed duodenum, which could not be used due to its nearby relation with ribcage. Immediate necrosis on the bowel occurred at both 1.0 cm and 1.5 cm distance from HIFU therapy. Future experiments will also assess injury due to therapy, at 2 cm to 4 cm from the bowel.

**Conclusions:** This preclinical porcine model enables reproducible positioning of fixed bowel in relation to the abdominal wall, which will help to determine a safety margin to bowel with thermal ablation using MRgHIFU. Further investigations will vary the distance between the HIFU focus and the bowel in order to refine the proximity to bowel at which MRgHIFU thermal ablation can be safely used with various MRgHIFU treatment parameters.



## Color Coherent Endoscopic/Laparoscopic Image Enhancement with Noise Suppression

Wenyao Xia<sup>1,2</sup>, Elvis Chen<sup>1,2</sup>, Terry Peters<sup>1,2</sup>

1: Robarts Research Institute and 2: Medical Biophysics, Western University, London, Canada

**Introduction:** Stereoscopic endoscopes have been used increasingly in minimally invasive surgery to visualize the organ surface and manipulate various surgical tools. However, insufficient and irregular light sources present major challenges for endoscopic surgery. Not only would they hinder computer assisted algorithms, sometimes the surgical tools would be hardly visible when operating within low-light regions. In addition, the low-light regions tend to suffer from low signal to noise ratio and metrication artifacts due to quantization errors. As a result, the traditional image enhancement scheme often leads to heavy noise amplification in low-light region.

**Methods:** In this paper, we propose an effective endoscopic image enhancement scheme to improve the visibility of lowlight region during endoscopic surgery. The algorithm first identifies different illumination regions using thresholds. The image is then further decomposed into illumination and detail layer and the illumination and detail layers are enhanced separately to meet the enhancement design criteria for desired image quality. Finally, the saturation will be corrected based on the saturation information from the endoscopic image from the previous time frame.

**Results:** In our experiment, we tested our algorithm using 200 test endoscopic images and we use naturalness image quality evaluator (NIQE) and illumination index (LI) as our metrics to evaluate the enhanced image qualities. The NIQE is often used to measure the presence of image artifacts, such as noise and blur and in this study, the NIQE is used to measure noise amplification caused by the enhancement algorithms. The LI is defined as the standard deviation of the lightness and in this study, it is used to measure the uniformity of lighting distribution. For both NIQE and LI, the lower the scores, the higher the image qualities. In our experiment, our algorithm yielded an average NIQE of 2.46, which is better than the state-of-the-art approach with average NIQE of 2.91. For LI, our algorithm yielded an average of 0.22, which is considerably better than original images with an average of 0.28 and ties with the state-of-the-art approach with an average LI of 0.22.

**Discussion:** Through comparison, we can see visible image artifacts amplified by other algorithms, while our approach yields enhanced images with more natural appearances and higher image quality. All the results confirm that our method has superior performance than the other state-of-the-art algorithms, and can effectively enhance the endoscopic image without amplifying underlying noise/artifact in the low-light regions. In the future we will improve the computational speed of our algorithm and a blinded qualitative rating study will be carried out to learn surgeons' preferences on the enhanced images.

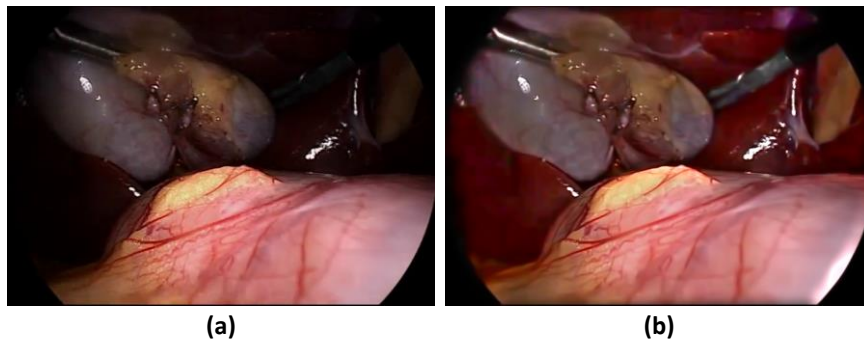


**Figure 1.** (a) Input image with low lighting (b) Output image with enhanced lighting and details

**Abstract: Evaluation of Cochlear Duct Length Measurements from a 3D Analytical Cochlear Model Using Synchrotron Radiation Phase-Contrast Imaging**

*\*Luke W. Helpard (BESc), †Seyed A. Rohani (PhD), \*†‡¶\Hanif M. Ladak (PhD), \*†‡¶\Sumit K. Agrawal (MD)*

*\*School of Biomedical Engineering; †Department of Otolaryngology—Head and Neck Surgery; ‡Department of Medical Biophysics; and ¶Department of Electrical and Computer Engineering, Western University, London, Ontario, Canada*

**Introduction:** Accurate cochlear duct length (CDL) determination can aid in cochlear implant sizing for full coverage and frequency map programming, which has the potential to improve hearing outcomes in patients. Many CDL measurement techniques have been well established and validated in a research setting, however are time consuming and require resources that exceed what is available in a standard clinical setting. The *A* value technique described in the literature is valuable in its ability to generate individual CDL estimates in a clinical setting, however does not capture apical variations in the cochlea and traditionally has not been used to model any geometric information aside from cochlear lengths. To overcome these problems, a 3D individualized cochlear model dependent on four basal turn distances was proposed in the literature. Initial validation of this model was done using corrosion casts of human cochlea. The objective of this work was to validate the 3D individualized cochlear model using Synchrotron Radiation Phase – Contrast Imaging (SR-PCI) data. Compared to corrosion casts, SR-PCI provides higher discernment of both bone and soft tissue, and the ability to view cross sections of the cochlea during point placement.

**Methods:** SR-PCI data from 11 cadaveric human cochleae were used to obtain reference measurements. For each sample, the reference CDL value, the reference number of cochlear turns (NCT), and the four model input distances were determined. CDL values generated by the 3D model were evaluated in two conditions: when the NCT were automatically predicted based on the input distances, and when the NCT were manually specified based on SR-PCI data.

**Results:** When the 3D model automatically predicted the NCT, the mean absolute error was  $2.6 \pm 1.6$  mm, with only 27% (3/11) of the samples having an error in the clinically acceptable range of  $\pm 1.5$  mm. When the NCT were manually specified based on SR-PCI data, the mean absolute error was reduced to  $1.0 \pm 0.6$  mm, with 73% (8/11) of the samples having a clinically acceptable error.

**Conclusions:** The 3D analytical model introduced in the literature is effective at modelling the 3D geometry of individual cochleae, however slight tuning in the cochlear turn estimation is required.

**Ultrasound Probe Calibration – The effect of imaging and tracking parameters on calibration robustness**L.A.Groves<sup>\*1</sup>, A.Rankin<sup>1</sup>, T.Peters<sup>1</sup>, E.C.S.Chen<sup>1</sup><sup>1</sup>Robarts Research Institute, School of Biomedical Engineering, Western University

**Purpose:** The use of ultrasound (US) to guide minimally invasive procedures is becoming increasingly more common [1]. Navigation can be further improved through the inclusion of augmented reality (AR) components, such that medical images and virtual models can be placed in a single field of view [1]. The fundamental requirement to integrate US images into AR environments is US probe calibration, which provides a transformation matrix that places images from a tracked US probe in the context of the spatial tracker's coordinate system [2]. To address the limitations associated with common US probe calibration methods, Chen *et al.* developed the guided ultrasound calibration or GUSC method [3]. The 3D Slicer GUSCal implementation will be the ultrasound probe calibration method used for this research. One focus of this research is to analyze the robustness of the GUSCal method for a group of novice users. The second focus is to understand how parameters that affect the image quality and tracking accuracy will affect the outcome of the novice users' calibrations.

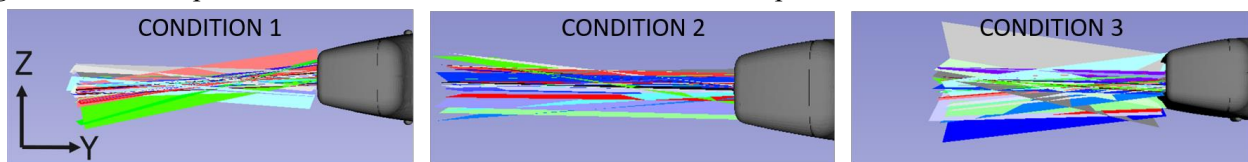
**Methods:** The US calibration is formulated as a point-line registration between homologous datasets; the user is required to insert a tracked needle (line) into the US beam, causing a hyperechoic reflection (point) [3]. As a registration problem, the accuracy of US calibration is influenced, among other things, by the location of the US reflections and needle orientations. The US reflection is segmented manually, requiring users to freeze the US and tracking streams, and select the needle centroid. Users repeated this process 14 times at various needle locations and orientations, performing the calibration under three different conditions: (1) free-hand with one focal depth, (2) free-hand with three focal depths, and (3) using a mechanical arm to fix the needle with one focal depth. All other settings on the US scanner remained consistent and a randomized order was assigned to each subject. The resultant transformation matrix for the calibration and the time were recorded per condition.

**Results:** The users' results were analyzed through applying the resultant transformation matrices to five pixel locations within the image to obtain locations in 3D space. These locations were normalized and the point reconstruction accuracy (PRA) was calculated through solving for the root mean squared distance (RMSD) from the average reconstructed locations these results are presented along with the average for each condition.

**Table 1.** Normalized PRA five pixels throughout the image and average time. Condition 1 is free-hand needle interaction with one focal depth, condition 2 is free-hand needle interaction with 3 foci, and condition 3 uses a mechanical arm to fix the needle with one focal depth.

Parameter	Condition 1	Condition 2	Condition 3
Normalized PRA RMSD for pixel (0,0,0) to the average (mm)	1.19	0.82	1.38
Normalized PRA RMSD for pixel (600,0,0) to the average (mm)	0.82	0.98	1.81
Normalized PRA RMSD for pixel (0,380,0) to the average (mm)	0.67	0.87	1.43
Normalized PRA RMSD for pixel (600,380,0) to the average (mm)	0.89	0.88	0.98
Normalized PRA RMSD for pixel (300,190,0) to the average (mm)	0.70	0.69	1.10
Time (min)	3.20 ± 0.90	3.8 ± 1.5	5.1 ± 2.5

**Figure 1.** Visual representation of users calibrations overlaid in 3D space for each condition



**Conclusions:** The qualitative and quantitative analysis shows that condition two is the most consistent between users and thus the most robust. The ability for novice users to successfully complete the calibration process under three conditions shows the usability of the GUSCal method. The low completion time for novice users is further indicative to the usability of this implementation. To achieve a sufficient calibration effectively performing it free-hand with foci at the top, bottom, and center of the image is recommended for any user. We believe that with practice the use of a mechanical arm to stabilize the needle would improve the calibration results. The GUSCAL, a 3D Slicer module for ultrasound calibration that can be performed by a user of any level, is publicly available as an open-source software.

**References:** [1] Nobel *et al.* Interface Focus (2011). [2] Mercier *et al.* Ultrasound Med Biol (2005). [3] Chen *et al.* SPIE (2017).

## Measuring 3D facial displacement of increasing smile expressions to inform facial paralysis reanimation

Z Fishman<sup>1,2</sup>, JA Fialkov<sup>3,4</sup>, CM Whyne<sup>1,2,3</sup>

1. Orthopaedic Biomechanics Laboratory, Sunnybrook Research Institute, Toronto, ON; 2. Institute of Biomaterials and Biomedical Engineering, University of Toronto, Toronto, ON; 3. Department of Surgery, University of Toronto, Toronto, ON; 4. Division of Plastic Surgery, Sunnybrook Health Sciences Center, Toronto, ON

**Introduction:** Facial paralysis greatly impacts a patient's social well-being by limiting emotional expression as well as their physical function by constraining eyelid closure. Facial paralysis can be caused by infection, tumor growth, trauma, stroke, congenital (Moebius syndrome), or spontaneous occurrence (Bell's palsy). In cases where surgical intervention is required, 'facial reanimation' can be performed to restore movement, either by using a nerve or muscle transfer within the face. This work aims to provide an improved understanding of a normal smile's lip and cheek movements to better inform facial reanimation surgery; for example, to better guide the length of muscle to cut and transfer and the points of insertion to create a functional, natural, and symmetrical smile. Previous efforts to measure the normal smile [1] have been limited by small sample sizes (~20 subjects) and only reported maximum smile displacement values. More importantly, these earlier measurements were based on front view 2D photography to measure 3D vectors. This new analysis will utilize a database of 3D face scans to measure smile movement in 3D and with an increasing extent of smiling. The facial movement analysis will also be valuable information for 3D face morphable models, where a patient's face shape is captured when smiling in a pre-trauma photograph but is then in a neutral expression under anesthetic.

**Methods:** The Binghamton University 3D facial expression (BU-3DFE) database [2] is composed of 3D scans for 100 multi-ethnic subjects' faces in a neutral and 4 increasing happiness intensity levels. In addition to the entire 3D face surface, the database includes 3D facial landmark points that have been labelled for each subject's mouth, tracking the upper and lower lip locations as the smile progresses from neutral to a happy expression. To compare the 3D geometries within the BU-3DFE database, the faces are spatially aligned with the nose tip at the axis origin and then are rigidly registered with an iterative closest point (ICP) algorithm. After registration, the displacement vectors and a per-vertex Euclidian distance transform are measured for each subject's 3D face & mouth landmarks between the neutral expression and the four increasing happy expressions. With these smile vectors, the magnitude (i.e. distance), azimuth and elevation angles are calculated and averaged for the 100 subjects.

**Results:** For the 100 subjects in the BU-3DFE database, the average lip commissure displacement is 9.2, 11.4, 13.5, and 16.0 mm for increasing happy levels 1 through 4, respectively. The standard deviations of these commissure displacement averages are approximately 4.0 mm. Similarly, the average lip's commissure azimuth angle is approximately  $44 \pm 21$  degrees in the posterior direction, and the elevation angle is  $37 \pm 15$  degrees in the superior direction. At its maximum displacement, the cheek moves from the neutral expression by 4.5, 5.7, 6.8, and 7.9 mm for the increasing happy levels 1 through 4, respectively. The cheek displacement vectors move outwards within ~10 degrees from the neutral expression's normal vectors.

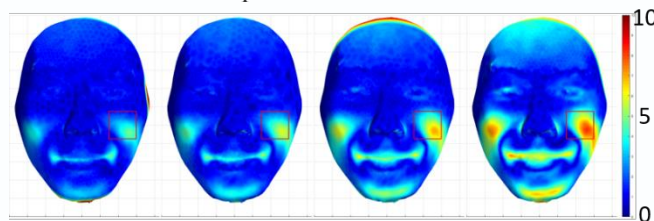


Figure 1. 3D facial displacements for top: Male #13 (East-Asian) from the BU-3DFE database by comparing the face shape at happiness levels 1-4 (left -> right) to the neutral expression. The colormap scalebar represents a range of 0 to 10 mm displacement.

**Conclusions:** Analysis of the BU-3DFE database yields average 3D displacement distance and angle measurements for plastic surgeons to better understand a baseline smile and inform clinical reanimation surgery. The smile displacement vectors at the lips and cheek improve on previous measurement efforts as well as evaluate the smile at increasing happiness levels, from a smirk to an exaggerated grin.

1. Paletz, J. L.; Manktelow, R. T.; Chaban, R. The shape of a normal smile: implications for facial paralysis reconstruction. *Plast. Reconstr. Surg.* 1994, 93, 784-9; discussion 790-1.

2. Yin, L.; Wei, X.; Sun, Y.; Wang, J.; Rosato, M. J. A 3D Facial Expression Database For Facial Behavior Research. *7th Int. Conf. Autom. Face Gesture Recognit.* 2006, 2006, 211-216.

## C-arm simulator for fluoroscopy-guided procedures

D.R.Allen, T.Peters, J.Moore, E.C.S.Chen

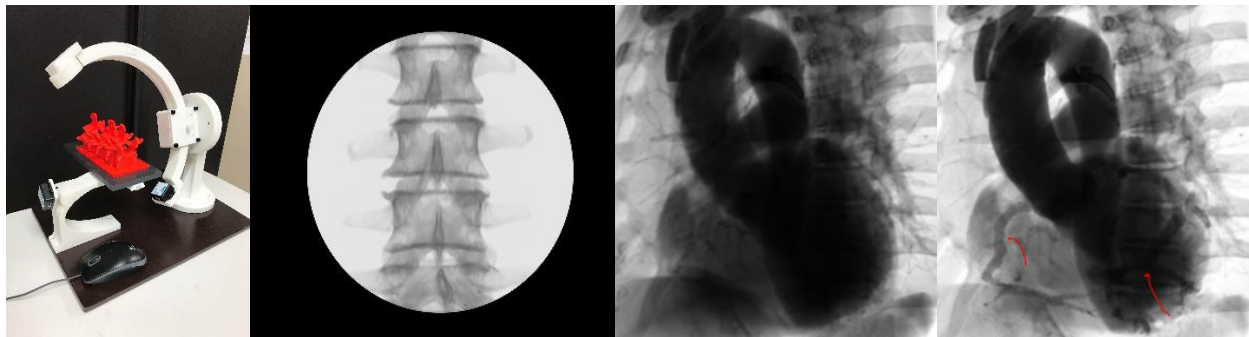
Robarts Research Institute, School of Biomedical Engineering, Western University

**Purpose:** A C-arm is a device capable of producing X-ray images at specific angles by operating along 5 or 6 Degrees of Freedom (DoF). It has enabled minimally-invasive procedures to be performed under real-time image guidance. The manipulation of the C-arm requires extensive training in order to produce the desired images and current training methods require physical access to a C-arm and exposure to radiation [1]. Therefore, a 3D-printed, bluetooth accelerometer-tracked C-arm training system is presented.

**Methods:** A miniature C-arm model was 3D-printed and fixed with wireless bluetooth accelerometers to track the orientation of the C-arm head (3 DoF) and position of the table (1 DoF). The Accelerometer was added as a new device to PlusLib which enabled easy integration with 3DSlicer and Visualization Tool Kit (VTK). The Digitally Reconstructed Radiographs (DRR's) were generated in real-time using a 1-dimensional transfer function applied to spine and heart CT data based on the tracked orientation of the C-arm head [2]. For DRR generation of the heart, a custom contrast enhancement algorithm was developed in order to modify the attenuation values for the coronary arteries in the heart CT. This was developed in order to simulate the effects of contrast dye.

**Results:** Qualitative analysis shows that the system can generate real-time spine and heart DRR's based on the position of the C-arm. Quantitative analysis needs to be performed in order to validate the accuracy of the DRR's against real X-ray images. The 3D-printed C-arm and top views of the spine DRR, non-contrast enhanced heart DRR, and contrast-enhanced heart DRR are shown in figure 1.

**Figure 1:** 3D printed C-arm and Bluetooth accelerometers (mouse shown for scale), Spine DRR, Heart DRR, Contrast-enhanced Heart DRR (red arrows point to coronary arteries)



**Conclusions:** A C-arm simulator program was developed consisting of a miniature 3D-printed C-arm, wireless bluetooth accelerometers, and software capable of generating real-time DRR's based on CT data and the tracked C-arm head. Future work includes quantitative analysis of the accuracy of the DRR's, incorporation of a 4D heart CT in order to generate DRR's simulating the movement of the beating heart and generating the contrast enhancement throughout the coronary arteries as a function of time.

**References:** [1] Wang, Lejing, et al. "Modeling kinematics of mobile C-arm and operating table as an integrated six degrees of freedom imaging system." *International Workshop on Medical Imaging and Virtual Reality*. Springer, Berlin, Heidelberg, 2010.

[2] Cai, Wenli, and Georgios Sakas. "DRR volume rendering using splatting in shear-warp context." *Nuclear Science Symposium Conference Record, 2000 IEEE*. Vol. 3. IEEE, 2000.

## Tracking, Calibration and Characterization of a Single-element Ultrasound

Hareem Nisar<sup>1</sup>, John Moore<sup>1</sup>, Natasha Alves-Kotzev<sup>2</sup>, Germain Hwang<sup>2</sup>, Terry Peters<sup>1</sup> and Elvis Chen<sup>1</sup>

<sup>1</sup>VASST Lab, Robarts Research Institute, Western University

<sup>2</sup>Sunnybrook Research Institute, Toronto

**Introduction:** Previously labelled as ‘the forgotten valve’, tricuspid valve (TV) and its repair surgeries are getting prominent recently. To reduce the risks and traumas involved with open heart surgeries, interventional methods for the right side of the heart are proposed. Typically transthoracic and transesophageal ultrasound imaging is used to view heart valves. However, posterior position of the right atrium and presence of the ribcage causes hindrance to image the TV properly. Intracardiac echocardiography (ICE) is often used to guide these minimally invasive cardiac procedures by advancing the probe inside the heart and providing real-time imaging of the heart anatomy. A recently introduced single-element transducer ICE probe, the Foresight ICE™ (Conavi Medical Inc., Toronto), provides a large, forward-looking field of view by spinning the transducer through 360 degrees and tilting the transducer forward, creating a conical surface. By changing the tilting angle, the Foresight system provides 3D imaging at the probe’s tip. Efforts are underway to integrate spatial tracking in the Foresight ICE system to expand its 3D field of view. In this study we investigate and validate a point-to-line method of spatial calibration as well as perform temporal calibration.

**Method:** Owing to the unique 2.5D conical configuration of the images taken by Foresight ICE system, standard cross-wire phantoms or Z-fiducial phantoms cannot be used as they are designed for conventional 2D planar images. Spatial calibration is done using a pre-calibrated needle as a phantom and modelling calibration as a point-to-line registration problem. A Foresight ICE probe was used with an electromagnetic tracking system (Aurora, NDI, Canada), with a 6 degree-of-freedom (DOF) magnetic tracking sensor rigidly attached to the outer sheath close to the probe tip. A water bath was scanned at room temperature using the tracked Foresight ICE probe. A pre-calibrated needle (Aurora Needle, 18G/150 mm, NDI, Canada) was used to model a line. The needle has a 5 DOF magnetic sensor built in. The needle was oriented at multiple positions and angles to produce point fiducials on the cone-shaped 2.5D images. For this initial assessment, the tilt angle  $\phi$  of the ICE transducer was kept constant at  $80^\circ$ . Clamps were used to minimize motion jitter and overcome inaccuracies caused by spatial misalignment. 15 point fiducials were recorded using screen-capture of the ICE images on the console, along with the pose of both the probe and the needle. For characterization of the probe, we will solve for angle calibration and anisotropic pixel spacing. We are currently working to perform temporal calibration to ensure that the tracker and image data is synchronized in real time.

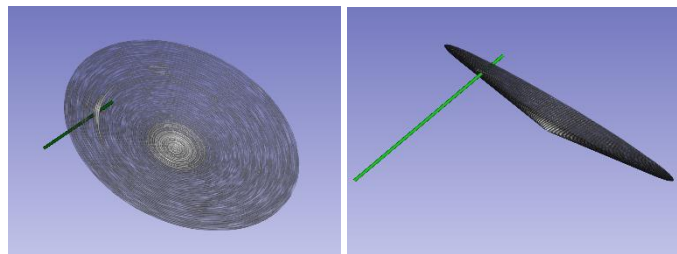


Fig 1. Qualitative validation for spatial calibration

**Result:** For initial validation, a qualitative assessment was performed. The 2.5D images were reconstructed from the screen captures. Figure 1 shows that the needle is passing through the needle intersection or point fiducial seen in the image, thus validating the calibration method. For quantitative results, we report a spatial calibration accuracy (Fiducial registration error, or FRE) of 1.74 mm.

**Conclusion:** This is preliminary study towards tracking a Foresight ICE probe. We will soon perform temporal calibration and system validation and indicate their results in the final version. Tracking the Foresight ICE probe will improve image guidance for the right side of the heart including procedures like tricuspid valve repair, pacemaker lead placement and closure device placement.

## Characterization of scalp signal contamination for noninvasive optical brain monitoring

Daniel Milej<sup>a,b\*</sup>, Ajay Rajaram<sup>b</sup>, Androu Abdalmalak<sup>b</sup>, Mahro Khalid<sup>b</sup>, Marwan Shahid<sup>b</sup>, Matthew Kewin<sup>b</sup>, Mamadou Diop<sup>a,b</sup> and Keith St. Lawrence<sup>a,b</sup>

<sup>a</sup>Lawson Health Research Institute, Imaging Program, London, Ontario, Canada

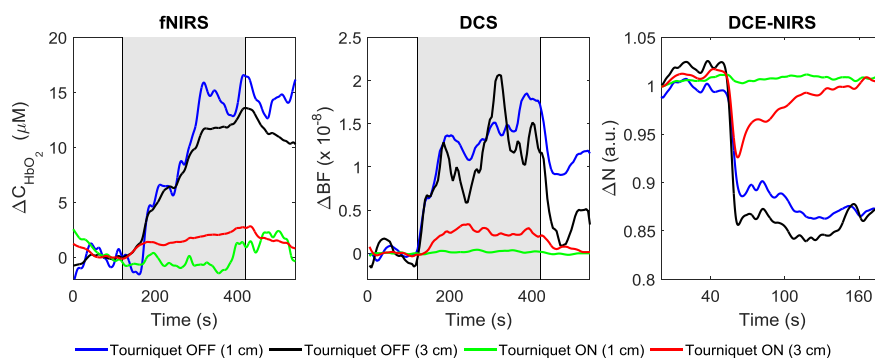
<sup>b</sup>Western University, Department of Medical Biophysics, London, Ontario, Canada

\*dmilej@uwo.ca

**Introduction:** Near-infrared spectroscopy (NIRS) and diffuse correlation spectroscopy (DCS) are convenient bedside neuromonitoring methods but suffer from signal contamination due to hemodynamic changes in extracerebral (EC) tissue. The *purpose* of this study was to assess the magnitude of this contamination using a computerized gas control system (RespirAct™) to generate a reproducible vasodilatory response and a pneumatic tourniquet wrapped around the head to eliminate scalp blood flow, which was confirmed by dynamic contrast-enhanced (DCE) NIRS.

**Methods:** Five healthy participants with no history of neurological conditions were recruited. NIRS data were acquired using a four-channel time-resolved system<sup>1,2</sup>, and DCS data with an in-house built software correlator<sup>3</sup>. Each experiment involved securing one emission and three detection fibers on the forehead at source-detector distances (SDDs) of 1 and 3 cm. Blood flow and oxygenation responses to 5-min hypercapnic challenges were recorded by NIRS and DCS, respectively. DCE-NIRS protocol involved an IV bolus injection of Indocyanine green (0.1 mg/kg), followed by 300 s of data collection to capture contrast kinetics. Two sets of data (with and without tourniquet inflation) were obtained from every subject.

**Results:** fNIRS and DCS data showed the expected increases in oxygenation and blood flow during hypercapnia. Signal changes recorded at SSD = 1 cm were negligible after inflating the tourniquet, demonstrating that scalp blood flow had been abolished. As expected results with and without tourniquet inflation for larger SSD = 3 cm showed smaller EC contamination. The BF changes measured by DCS at two SDD showed similar changes and sensitivity as fNIRS signals. In addition, DCE-NIRS data showed not only change in signal amplitude but also a faster outflow of the contrast agent for tourniquet inflated, which is typical for signals that are related mostly to the brain.



Example of the signals measured with and without a tourniquet. A grey area represents hypercapnia.

**Discussion:** Use of short and long SDDs in combination with a tourniquet helped to understand better and differentiate how EC signal contamination affects the different optical methods. All techniques clearly showed EC signal contaminations effects. Using a pumped tourniquet can potentially improve the sensitivity of optical techniques, based on the on the light intensity measurements, to the brain. It should be noted that for higher moments, especially recorded at larger SDD, the impact of the tourniquet was significantly smaller, or did not cause any changes to the signals (data not shown).

**References:** [1] A. Abdalmalak et al., Neurophotonics, 4(4), 040501, 2017; [2] D. Milej et al., 2018, Biomedical Optics Congress 2018, paper BF2C.2; [3] M. Khalid et al., Biomedical Optics Congress 2018, paper JTU3A.63

## Ultrahigh-resolution imaging of microcalcifications in mammography

Tomi F. Nano<sup>1</sup>, Karim S. Karim<sup>2</sup>, Muriel Brackstone<sup>3</sup> and Ian A. Cunningham<sup>1</sup>

1. Robarts Research Institute, Dept. of Medical Biophysics, Western University; 2. Dept. of Computer Engineering, University of Waterloo; 3. Dept. of Surgery, London Health Sciences Center, Western University

**Introduction:** Since the launch of mammography screening programs in early 1990s, there has been a 40% reduction in mortality rate of breast cancer.<sup>[1,2]</sup> However, not all mammography screenings result in the same benefit. The Ontario Breast Screening Program found 30% greater cancer detection at centers using x-ray detectors that produce images with higher SNR.<sup>[3]</sup> We are developing a novel x-ray detector design to improve SNR by using an ultrahigh-resolution sensor with smaller sensor element size (10-25 $\mu\text{m}$ ) than current mammography pixel size (50-100 $\mu\text{m}$ ).<sup>[4]</sup> Image SNR is tested clinically using phantoms (such as CDMAM) that allow for detectability scoring of disks in a uniform background. Our objective is to investigate SNR and detectability scoring in images from conventional and ultrahigh-resolution designs.

**Methods:** An x-ray detector prototype having selenium (Se) directly deposited on a complementary metal-oxide-semiconductor (CMOS) sensor with 7.8x7.8 $\mu\text{m}$  element size was used to acquire images of phantoms and microcalcification samples from breast biopsies. A 60kV x-ray beam from a tungsten tube with 2mm of aluminum filtration was used to acquire images at 85 $\mu\text{Gy}$  air-KERMA incident on the sensor. Conventional images were created using 6 x 6 binning to synthesize typical mammography pixel size (47 $\mu\text{m}$ ) and repositioning of the phantom was simulated using sub-pixel shifts. Variance map of each pixel was calculated and shows pixel value variability from phantom repositioning.

**Results:** High SNR images of microcalcifications were acquired using a Se/CMOS prototype with 7.8 $\mu\text{m}$  element size. Fig. 1 shows better visualization of calcification morphology at ultrahigh-resolution. Conventional x-ray images of a CDMAM phantom resulted in different scoring from sub-pixel repositioning. Fig. 2 shows a CDMAM image on the left and the pixel variance map (in red) on the right showing differences in pixel value.

**Conclusion:** We are designing an x-ray detector for mammography that can acquire ultrahigh-resolution images of microcalcification with high SNR. This design can also be used to removed signal aliasing artifacts in conventional images that would eliminate inconsistent image quality scoring used for clinical decision making.

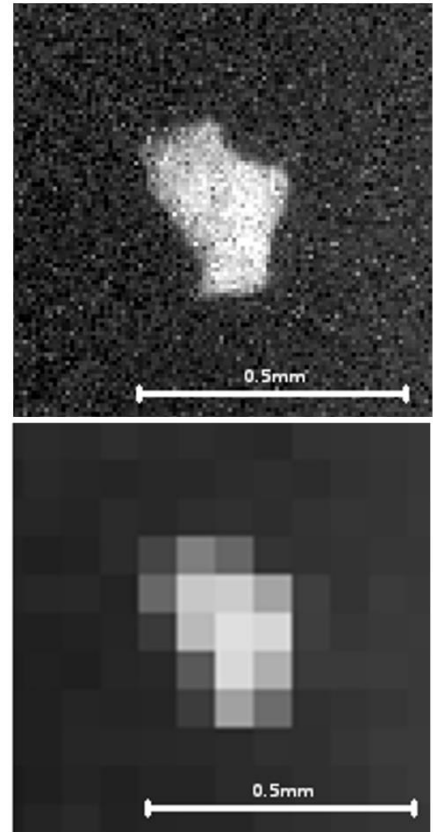


Fig. 1 Morphology of the  $\mu\text{Calc}$  is better visualized in the ultrahigh-resolution image (top) than in the conventional (bottom) image.

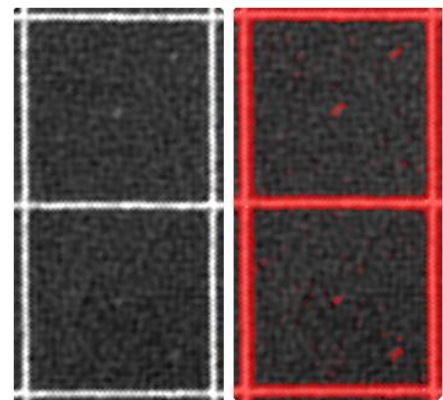


Fig. 2 Left: CDMAM image of two panels used for disk detection. Right: Pixel variance map (in red) showing inconsistencies due to phantom positioning that affect scoring.

[1] Canadian Cancer Statistics, 2018; [2] American Cancer Society, 2018; [3] Yaffe et. al., Med Phys, 40(12), 2013; [4] Nano et. al., Med Phys, 44(4), 2017



## Development of a non-contact holographic scanner for photoacoustic tomography of the breast

Hui Wang<sup>\*1,2</sup>, Parsa Omid<sup>1,2</sup>, Jeffrey Carson<sup>1,2,3</sup>, and Mamadou Diop<sup>1,2,3</sup>

<sup>1</sup>Imaging Program, Lawson Health Research Institute, London, Ontario, Canada

<sup>2</sup>School of Biomedical Engineering, The University of Western Ontario, London, Ontario, Canada

<sup>3</sup>Department of Medical Biophysics, The University of Western Ontario, London, Ontario, Canada

**Introduction:** Photoacoustic tomography (PAT) is a well-established optical modality for breast imaging<sup>1</sup>. Based on thermoelastic effect, tissues that absorbed energy from a near infrared short pulsed laser are transiently heated. The heating generates an instantaneous pressure wave that propagates in all directions, eventually reaching the detectors. The recorded ultrasound signals are then used to reconstruct 3D images of the distribution of light absorbers in the tissue. The conventional PAT breast imaging device requires efficient signal transmission between the tissue and the detectors by immersing both breast and transducer into a water tank, in which lead to a cumbersome sized device and limit the patients in a prone position. Therefore, if the water tank could be removed, then a non-contact PAT breast scanner can overcome the mentioned shortcomings as well as open up the possibility of PAT-guided biopsies.

**Hypothesis:** The topography of the skin surface can be converted into interferograms consist of fringe patterns by an interferometer<sup>2</sup>. We hypothesize that fringe patterns shifting induced by skin surface deformation due to photoacoustic sources inside the breast can be detected and recorded with a interferometer based holographic scanner. The data collected from measurement will provide estimates of tumor's location and profile after applying our developed 3-steps reconstruction algorithm.

**Materials and Methods:** The core of our non-contact holographic scanner is based on a modified off-axis Mach-Zehnder interferometer working with a He-Ne laser as the light source. To achieve fast acquisition speed, a time-gated intensified camera was implemented directly facing the object surface. By setting a short exposure time while increasing the intensifier gain, images with good contrast could be captured in 1 ns. Performance of the current setup was evaluated using a customized resolution target, aiming to determine the smallest height difference the system could distinguish. The target's surface equally divided into four quadrants, which etched with same patterns but different depth. The measured etch depths were 123 nm, 82 nm 33 nm, and 10 nm for the upper-left, upper-right, lower-right, and lower-left quadrant, respectively. Light reflected from the non-etched surface had a phase difference compared to light reflected from the etched areas. These phase information are coded intrinsically in the holographic fringes. After applying reconstruction algorithm to the acquired holograms, we assessed the surface displacement as well as evaluated the performance of the setup.

**Results:** The holograms of four target quadrants were imaged individually and acquired in single shot mode with a 1 ns camera gate time. The corresponding depth images were reconstructed by applying our 3-step algorithm. For better visualization of the surface profile, a portion of reconstructed image that acquired from the quadrant with 33nm etched depth is presented as a 3D depth map and its extracted 2D height profile. The height differences between the top and bottom of the bars 2D height profile were consistent with the etch depth.

**Discussion and Conclusions:** As an essential step toward completing the non-contact photoacoustic imaging system for breast, the high-speed holographic scanner was capable of measuring nanoscale surface displacement without contact in a 1 ns single exposure. Optimizations of the optical setup were essential for acquiring high quality holograms. A CCD with larger size and higher pixel count will improve the camera's field of view and depth resolution. Our next step includes replacing the object with tissue and assembling photoacoustic wave excitation unit into the system.

### Reference:

1. Zhou, Y., Yao, J. & Wang, L. V. Tutorial on photoacoustic tomography. *J. Biomed. Opt.* **21**, 061007 (2016).
2. Carp, S. A. Optoacoustic imaging based on the interferometric measurement of surface displacement. **12**, 1–9 (2007).

**Non-contact Imaging of Breast Surface for Breast Surgical Planning**

Olivia Tong\*<sup>1,2</sup>, Astrid Chamson-Reig<sup>1</sup>, Lawrence Yip<sup>1,3</sup>, Muriel Brackstone<sup>4,5</sup>, Mamadou Diop<sup>1,2,3</sup>,  
Jeffrey Carson<sup>1,2,3,5</sup>

<sup>1</sup>Imaging Program, Lawson Health Research Institute, London, Canada

<sup>2</sup>Biomedical Engineering Graduate Program, The University of Western Ontario, London, Canada

<sup>3</sup>Department of Medical Biophysics, The University of Western Ontario, London, Canada

<sup>4</sup>London Regional Cancer Program, London Health Sciences Centre, London, Canada

<sup>5</sup>Department of Surgery, The University of Western Ontario, London, Canada

**Introduction**

Objective and accurate surface measurements of the human breast are important for surgical planning. Traditionally, surgeons plan their procedures using radiographic images, but these images do not illustrate the breast in the same position as during surgery, i.e., the supine position<sup>1-3</sup>. As a result, surgeons need to account for differences in breast size and shape, and surgical outcome is largely dependent on the surgeon's experience. Previous studies have shown that scanning large-breasted patients in the standing position resulted in breast ptosis and high variability. A system capable of accurately scanning patients in the supine position is therefore desirable<sup>1,4,5</sup>. The aim of this work was to develop a non-contact imaging system that can provide 3D information of a breast surface from patients in the supine position.

**Methods**

Two structured-light surface scanners were combined using separate colour optical filters to minimize cross-talk between scanners. Scanning with blue and green filters simultaneously at two different angles eliminated shadowing artifacts compared to a single scanner reconstruction. Test scans were collected from a 3D printed breast phantom in both supine and standing positions. After scans were performed on breast phantom, we conducted a preliminary study on three human participants and they were scanned in three different positions: supine with hands behind the head, standing with hands at the waist, and standing with hands behind the head. System performance was evaluated through 1) accuracy of the scan results, and 2) usability of the system in the clinic. For accuracy, scan results were compared to the 3D breast model used to print the phantom. Usability of the system was evaluated based on the results of the human participants in terms of completeness of breast surface visualization as well as extracted breast volumes in various postures.

**Results**

We tested the system with breast phantoms, and the mean distance between the phantom model and point cloud measurements was  $0.13 \pm 0.02$  mm for the standing position and  $0.14 \pm 0.02$  mm for the supine position. Our system performed better than currently available commercial systems, which have accuracy of 0.5 - 1 mm. We also validated the system with human participants. Incomplete breast visualization was found in all participants when they were standing straight with hands at the waist. All the breast surface scans were also incomplete for one participant as a result of shadowing. We performed volume analysis for the other two participants. The volumes of both left and right breasts of these individuals at supine position were smaller than the ones at standing positions.

**Conclusions**

We have developed a 3D imaging system that can non-invasively scan 3D breast surfaces in both standing and supine position. The compact imaging system that we developed can scan patients with chest circumferences smaller than 90 cm and cup sizes of B or less. We were unable to draw any conclusive result with a sample size of two and we cannot determine if there would be any significance difference in terms of hand and body positions for breast morphology and breast volumes. We will implement the modifications, height and range of motion of the system, to overcome the limitations of the system to capture a wider population. Once the system is improved, a feasibility study on human participants will be conducted.

## Preliminary Study of Motion Artefact Reduction in Volumetric 4-dimensional Computed Tomography

Heather M Young<sup>1,2</sup>, Ting-Yim Lee<sup>1</sup> and Stewart Gaede<sup>1,2</sup>

<sup>1</sup>Department of Medical Biophysics, University of Western Ontario, <sup>2</sup>Department of Physics and Engineering, London Regional Cancer Program

**Introduction:** Conventional 4D-CT scans are susceptible to respiratory motion artefacts due to the narrow axial field of view (AFOV). The purpose of this study was to investigate the reduction of motion artefacts using a volumetric 4D-CT (v4D-CT) scanner.

**Methods:** The GE 256-slice Revolution CT scanner was used to acquire v4D-CT images of the Quasar Respiratory Motion Phantom (Modus Medical Devices, London, Canada) with a cedar insert containing three polystyrene spheres (30mm, 20mm, 10mm diameter) which moved in an irregular respiratory motion pattern. Gold markers were embedded within one of the spheres. Images were acquired in axial mode at a single bed position (140 mm AFOV, 0.28s/revolution, 0.88s between images, 52s scan time, 120kVp, 10mA, 2.5mm slices). The images were binned into 10 respiratory phases and averaged to recover the signal-to-noise ratio. The motion of the markers was tracked, their volumes determined, and mean CT number in the static acrylic portion of the phantom was calculated at each phase. v4D-CT images of a sedated and ventilated pig were also acquired (120mm AFOV, 0.5s/revolution, 5mm slice thickness) and analyzed for motion artefacts.

**Results:** Phantom motion was recovered for the entire 52s acquisition and was strongly correlated with the known motion trace using the Pearson Correlation Coefficient ( $r=0.912$ ,  $p<0.001$ ) as shown in Figure 1. The CT number measured in a single image was  $(124\pm 13)$  HU and after binning was  $(125\pm 4)$  HU, indicating a decrease in noise. Three spheres (30mm, 20mm and 10mm diameter) were contoured, and the measured diameter was in agreement within 5% of the known diameter for all phases:  $30.0\pm 0.4$ mm,  $20.6\pm 0.3$ mm, and  $10.5\pm 0.5$ mm, respectively, indicating that there were no motion artefacts. In the porcine images the lung, heart, diaphragm and liver were imaged though all phases of the breathing cycle in the 120mm AFOV with no visible motion artefacts.

**Conclusion:** v4D-CT may allow for fast acquisition of artefact-free 4D-CT images with accurate CT number, and for improved estimation of respiratory motion over time.

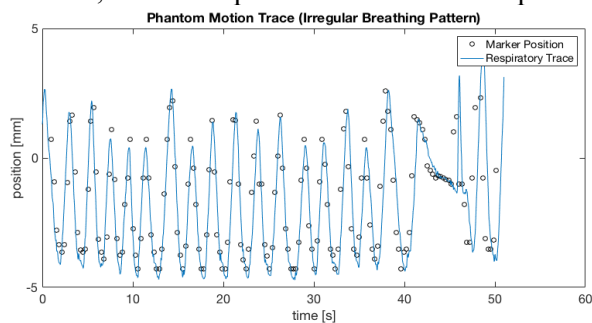


Figure 1. Known motion trace (blue) and imaged phantom position (black) over 52s of imaging.

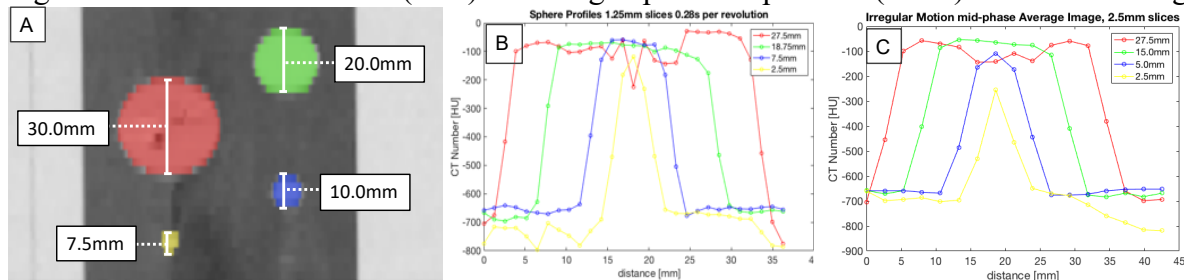


Figure 2. (A) Known diameter of the 4 imaged spheres. (B) Measured profiles of the spheres in a single image. (C) Measured profiles of the spheres in the averaged image.

## Developing a Non-Invasive Optical System for Monitoring Oxygenation and Blood Flow Dynamics in the Adult Brain

M. Shahid<sup>b\*</sup>, Daniel Milej<sup>a,b</sup>, Androu Abdalmalak<sup>a,b</sup>, Ajay Rajaram<sup>b</sup>, Mahro Khalid<sup>b</sup>, Mamadou Diop<sup>a,b</sup>, Keith St. Lawrence<sup>a,b</sup>.

<sup>a</sup>Lawson Health Research Institute, Imaging Program, London, Ontario, Canada

<sup>b</sup>Western University, Department of Medical Biophysics, London, Ontario, Canada

\**mshahi4@uwo.ca*

**Introduction:** Although cerebral blood flow (CBF) and oxygen delivery are tightly controlled to meet neuronal energy demands, studying dynamic neurovascular coupling in the human brain is challenging due to the lack of methods that can measure rapid changes in tissue oxygen saturation (StO<sub>2</sub>) and CBF. Optical techniques are promising as light absorption in tissue is oxygen dependent and can be monitored non-invasively by near-infrared spectroscopy (NIRS). In addition, CBF can be measured using an emerging technology known as diffuse correlation spectroscopy (DCS). As both technologies can provide sub-second temporal resolution, their combination provides a unique approach for simultaneous monitoring of StO<sub>2</sub> and CBF dynamics. However, a major challenge to applying these technologies to adults is removing signal contamination from the scalp. This study presents a hybrid system that incorporates techniques to enhance depth sensitivity: Time-resolved (TR) NIRS, since late-arriving photons travel deeper, and multi-distance DCS, since depth sensitivity increases with source-detector distance (SDD). Experiments were conducted using tissue-mimicking phantoms in order to evaluate the crosstalk between the two systems.

**Methods:** To measure StO<sub>2</sub>, the TR-NIRS system used two pulsed lasers, operating in the range of 0.3-0.5 mW, that are sensitive to changes in oxy- and deoxyhemoglobin (760 and 830 nm). A longer wavelength laser (850 nm) was chosen for the DCS laser to avoid crosstalk with the TR-NIRS measurements. This laser operated in continuous mode at a power of 89 mW. The DCS system collected signals at two SDDs: 1 cm, sensitive to scalp blood flow and 2.7 cm, which has greater sensitivity to the brain. Similarly, the TR-NIRS system collected data at distances of 1 and 3 cm. Low-pass interference filters (840 nm) were placed in front of the TR detectors to avoid contamination from the stronger DCS laser. The TR detector at an SDD of 1 cm also required neutral density filters because of the considerably higher count rate. Tests were performed on phantoms with optical properties similar to tissue. Signal contamination for each system was evaluated by acquiring data with and without the light source from the other system operating.

**Results:** The DCS system did not require any filtering, provided the distance between the TR-NIRS lasers and a DCS detector was  $\geq 2$  cm, which is due to the low power levels required for TR-NIRS compared to DCS. In contrast, the TR-NIRS system required a series of low-pass interference filters in front of each detector – three at an SDD of 3 cm and two at 1 cm – to reduce signal contamination from the stronger DCS laser to less than 5%. The overall loss of TR-NIRS signal was at worst 15% as each filter reduced light intensity by approximately 5%. In addition, three neutral density filters (OD = 4.0, 0.6, and 0.4) were required at SDD = 1cm and one (OD = 1.0) at SDD = 3 cm.

**Conclusion:** These results demonstrated that the two systems can be run simultaneously with minimal crosstalk. The immediate goal is to use this hybrid system to study cerebral hemodynamics in healthy participants. Experiments will be conducted using a computer-control gas delivery system (Respiract) to induce rapid changes in arterial carbon dioxide tension that will in turn lead to increases in cerebral oxygenation and blood flow. Our long-term goal is to use this technology to study cerebrovascular health, such as in the ageing brain.

### Assessment of CT-based strain measurement using embedded fiducial markers

Alexandra M. Blokker,<sup>a,b</sup> Timothy A. Burkhart, PhD,<sup>b,c,d</sup> Alan Getgood, MD,<sup>c,d</sup> David W. Holdsworth, PhD<sup>a,b,c</sup>

<sup>a</sup>Robarts Research Institute, <sup>b</sup>Department of Biomedical Engineering, <sup>c</sup>Department of Surgery and Medical Biophysics, <sup>d</sup>Fowler Kennedy Sports Medicine Clinic, all: Western University, London, ON, Canada

**Introduction.** Characterizing regional soft tissue strain under relevant joint loads is essential to understanding sub-optimal surgical outcomes such as instability and degenerative joint diseases.<sup>1</sup> Current strain measurement methods are invasive, low resolution, require image registration, or are unable to differentiate strain in different regions of the tissue.<sup>2</sup> Computed tomography (CT) imaging is often used to assess musculoskeletal disorders due to its high image resolution, bone contrast, and non-invasive nature. However, while bone tissue has high contrast, insufficient soft tissue contrast inhibits regional soft tissue strain calculation with current image correlation methods. Recent implementation of radiopaque fiducial markers and CT imaging in a cadaveric meniscus demonstrated potential for regional, high-resolution, minimally invasive soft tissue strain measurement.<sup>3</sup> This method has not yet been implemented to investigate regional ligament strains. The first step in implementing this method in pre-clinical studies is identifying the resolution of strain measurement using CT imaging. Therefore, the purpose of this work was to assess the resolution to which micro-CT and intra-operative resolution CT systems can quantify distances between fiducial markers.

**Methods.** The fiducial marker was selected based on CT compatibility and size considerations. Contrast with surrounding tissue structure was the most important material property. Marker diameter was minimized to avoid disrupting surrounding tissue while maintaining a sufficient diameter to be identified in an image. Twenty-two markers (Fig. 1) were cast in a silicone phantom (Fig. 2a), then imaged at ten random rotations and translations within the field of view of a micro-CT (GE Locus Ultra, 0.154 mm isotropic resolution), and an intra-operative CT (Medtronic O-Arm, 0.204×0.204×0.408 mm resolution) using a standard acquisition protocol (80 kVp, 50 mA). Two methods for identifying a repeatable point within the markers in an image were compared: a bounding box method which calculated the centroid of a box bounding isosurfaces in the image, and a weighted binary method which calculated a weighted centroid of all neighbouring voxels in a binary image (generated using a threshold). Each method was used to calculate the location of all beads in an image, then the Euclidian distance between neighbouring bead coordinates was calculated. The standard deviation in the inter-bead distance measurements from each of the marker position methods across the ten repeated trials was calculated for each marker identification method to provide a measure of the precision of the strain measurement with each scanner.

**Results.** Sufficient contrast with surrounding structures without image artifacts indicated that spherical 0.8 mm diameter zirconium dioxide beads (Fig. 1) best met the marker criteria. The imaging systems measured 3D distances between markers to within 0.007 mm and 0.028 mm in the micro-CT (Fig. 2b) and intra-operative CT (Fig. 2c) respectively using the bounding box method, and to within 0.011 mm and 0.040 mm in the micro-CT and intra-operative systems respectively using the weighted mask method.

**Conclusion.** The bounding box method was found to be the most repeatable, and is highly promising for applications in high resolution regional soft-tissue strain measurements. Future work will determine the bead's effects on soft-tissue material strength. By investigating two imaging systems, multiple study setups can be accommodated, with those requiring a higher resolution measurement using the micro-CT system, and those requiring a large bore diameter using the intra-operative CT system. The outcomes of this research will facilitate pre-clinical research aimed at improving the outcome of soft tissue injuries.

**References.** 1. D. Butler *et al.*, Surface Strain Variation in Human Patellar Tendon and Knee Cruciate Ligaments. *J Biomech Eng* (1990).

2. M. J. Anderson *et al.*, A Systematic Summary of Systematic Reviews on the Topic of the Anterior Cruciate Ligament. *Orthop J Sports Med* (2016).

3. S. Kolaczek *et al.*, Analysis of 3D strain in the human medial meniscus. *J Mech Behav Biomed Mater* (2016).

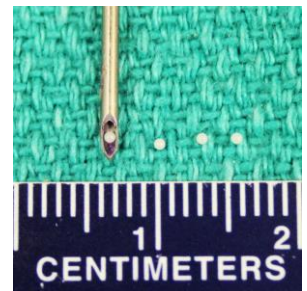


**Fig. 1:** Zirconium dioxide fiducial markers with needle (18 G) for minimally invasive tissue insertion.

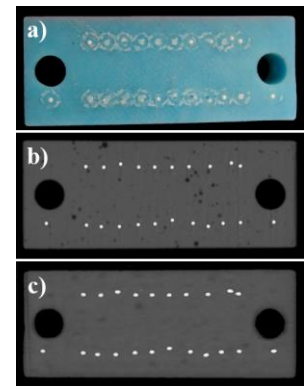


**Fig. 2:** a) Silicone phantom with embedded zirconium dioxide fiducial markers, and isosurfaces of markers generated from images of phantom acquired on a b) micro-CT, and c) intra-operative CT.

## Development of a high frequency photoacoustic imaging device for improved detection of esophageal neoplastic lesions

C.F. Roa<sup>1</sup>, J. Yin<sup>2</sup>, A. Boyes<sup>2</sup>, B. Motlagh<sup>2</sup>, E. Chérin<sup>2</sup>, N. Singh<sup>1</sup>, F.S. Foster<sup>1,2</sup>, C.E.M. Démore<sup>1,2</sup>

<sup>1</sup>Department of Medical Biophysics, University of Toronto, Toronto

<sup>2</sup>Sunnybrook Research Institute, Sunnybrook Health Sciences Centre, Toronto

### Introduction

Esophageal cancer is aggressive in nature, asymptomatic in early stages and has a 5-year survival rate of less than 20%. Intestinal metaplasia, usually detected with white light endoscopy, marks the beginning of progression towards adenocarcinoma. Early detection of foci of malignant disease, while contained in the superficial layers, is key for patient survival since minimally invasive endoscopic treatment is possible, avoiding surgical removal. Current diagnostic techniques have limitations in differentiating between benign and malignant regions and must rely on biopsies. This is restrictive in the amount of tissue that can be tested and introduces the risk of missing important diagnostic information. There is, therefore, a need for improved imaging techniques to differentiate between benign and malignant esophageal tissue and to determine the extent of invasion through the esophageal wall.

We have recently shown, in *ex vivo* tissue specimens, the feasibility of using a photoacoustic targeted contrast agent to visualize neoplastic lesions. We have also shown that photoacoustics and microultrasound ( $\mu$ US) can image microvasculature and tissue structure deeper than conventional optical endoscopic techniques. The combination of the ultrasound and photoacoustic images (PAI) could serve to characterize tissue and enable early stage treatment of disease.

This paper describes early efforts to develop a micro-ultrasound transducer that can be incorporated in a miniature endoscope and coupled with a laser to enable *in vivo* photoacoustic imaging. The planned 64-element transducer array is designed to operate at 50 MHz for imaging resolution on the order of 50  $\mu$ m, suitable for resolving the critical layers of the esophageal wall (mucosa, submucosa, muscularis). The dimensions of the designed transducer elements are on the order of 30  $\mu$ m, and the probe must fit within 6 mm diameter housing, posing challenges for conventional fabrication techniques and for creating the electrical connections to the driving electronics.

### Methods and Results

We demonstrate fabrication of an 8-element section of the array using laser machining of lead-zirconate-titanate (PZT) piezoelectric ceramic to achieve 5  $\mu$ m element separation. Flexible cabling was fabricated with copper polyimide using a tailored chemical etching technique that overcomes the strict requirements of photolithography. Electrical and acoustic characterization of the transducer shows consistency between elements and feasibility of attaining design parameters.

### Discussion and Conclusions

The functional prototype supports continuing work to optimize the design and manufacturing process for fabrication and packaging of a 64-element array to be used in combination with conventional endoscopy. Fiber optic cabling for transmitting laser pulses will need to be incorporated within the miniature endoscope to allow photoacoustic imaging. This device will be used to test our hypothesis that a photoacoustic targeted contrast agent can improve differentiation between benign and malignant lesions in the esophagus and help guide minimally invasive treatment of esophageal cancer.

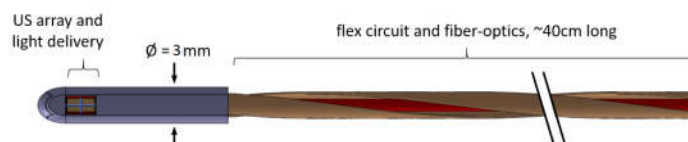


**Figure 1.** Miniature endoscopic probe integrating  $\mu$ US and PAI.

**Micro-CT Based Validation of Anatomical Geometry for 3D Printing**Jaques S. Milner<sup>1</sup>, Joseph U. Umoh<sup>1</sup>, Yara Hosein<sup>3</sup>, Matt Parkes<sup>3</sup>, David W. Holdsworth<sup>1,2</sup><sup>1</sup>Robarts Research Institute, Western University, London, Canada<sup>2</sup>Departments of Medical Biophysics and Surgery, Western University, London, Canada<sup>3</sup>ADEISS, Additive Design in Surgical Solutions, London, Canada

**Objectives:** 3D printing continues to gain strength as a potentially revolutionary step in medical technology. One area of growth with potential clinical impact is the capability to print metal components (i.e. surgical guides and implants) in medical-grade metal alloys. In this application, success in printing and implantation is typically linked to the conformity of the fabricated object with respect to existing bone anatomy. While it is obviously necessary for the printed part to be true and accurate to the geometric model it derives from, sometimes overlooked is the need for the geometric models themselves to be validated prior to printing, particularly those produced from medical image data (i.e. clinical CT). In this investigation, the precision of a grouped set of image-derived geometric models originating from separate micro-CT scans of a human cadaver mandible was evaluated, with the goal of producing 3D reference geometry.

**Methods:** The specimen was scanned five times (with repositioning) using micro-CT (Locus Ultra, GE Healthcare) at 120 kV and 20 mA with voxel spacing of 150  $\mu\text{m}$ . Isosurfaces were extracted from each image volume using an intensity value of 700 HU. No smoothing or decimation was applied. Surface models ( $n = 5$ ) averaged 7,240,656 triangles (COV = 0.080%) and 3,607,220 points (COV = 0.078%). Surfaces were imported into digital metrology software (Geomagic Control, 3D Systems, SC) for deviation analysis. One of the five surface models was chosen at random to act as the reference model (Reference) to which all others would be registered and analyzed (Tests). Model alignment was optimized using an iterative best-fit method by comparing the locations of 100,000 points on each of the Reference and Test surfaces at every step. Registration was halted when five successive iterations showed no improvement in residual alignment values. Deviations were computed as the shortest distance from the Test surface to any point on the Reference surface.

**Results:** Registration resulted in minimum and maximum mean deviation values of 0.0406 mm (RMSE = 0.0355) and 0.0421 mm (RMSE = 0.0389) respectively, evaluated over the 100K registration alignment points. Mean surface deviation per model across all  $\sim 3.6\text{M}$  model points, post-registration, ranged from 0.0432 mm (SD = 0.0557) to 0.0444 mm (SD = 0.0597). On average  $\sim 85\%$  (SD = 0.33) of Test surface points fell within a one-half voxel distance (0.075 mm) of the Reference surface,  $\sim 14\%$  (SD = 0.24) within one voxel (0.150 mm), and  $\sim 1.5\%$  (SD = 0.14) within two voxels (0.300 mm). Only 0.05% (SD = 0.001) of points exceeded a deviation greater than two voxels in distance, on average, from the Reference surface. Maximum deviation ranged from 0.932 mm to 3.547 mm (MEAN = 2.645 mm, SD = 0.607). Seemingly large maximum deviations were incidental and resulted from spurious unmatched isosurface islands located within the internal trabecular bone region of the lower mandible and had no impact on the geometry of the external surface. Deviation distances were symmetrically distributed about 0 mm deviation, where negative deviations correspond to points on the Test surface located along an inward direction relative to the Reference surface, and where positive deviations correspond to points on the Test surface located along an outward direction relative to the Reference surface.

**Conclusions:** This study has demonstrated the precision of geometric models reconstructed from separate micro-CT scans of the same anatomical geometry, as evidenced through the small overall differences between all surfaces when spatially registered and compared to one another. Based on previous geometric calibration of the scanner, we are confident that surface models reconstructed from micro-CT will be precise and accurate representations of the underlying anatomical geometry. The resulting 3D geometry should provide an accurate reference when evaluating the quality of human bone models produced from clinical CT scans.

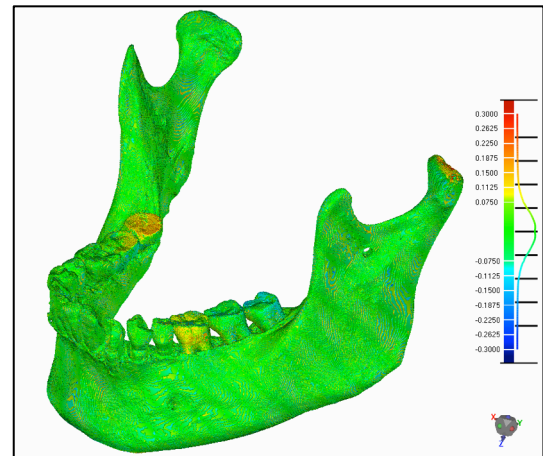


Fig 1. Surface deviation between a Test and Reference model. Qualitative histogram on scale bar highlights symmetric deviation distribution. Units in mm.

## Confirmation of Derivative Hyperspectral NIRS Methods to Measure Oxygen Saturation

Matt Kewin<sup>2</sup>, Ajay Rajaram<sup>1,2</sup>, Daniel Milej<sup>1,2</sup>, Mamadou Diop<sup>1,2</sup>, Sandrine de Ribaupierre<sup>2,3</sup>, Keith St. Lawrence<sup>1,2</sup>

<sup>1</sup>Department of Medical Biophysics, University of Western Ontario, London, ON, Canada

<sup>2</sup>Imaging Division, Lawson Health Research Institute, London, ON, Canada

<sup>3</sup>Department of Clinical Neurological Sciences, University of Western Ontario, LHSC, London, Ontario, Canada  
mkewin2@uwo.ca

### 1. Introduction

Brain injury during preterm-infancy can cause serious intellectual and behavioral disability. As such, reliable monitoring of cerebral health in the neonatal intensive care unit is needed. Near-infrared spectroscopy (NIRS) is considered an ideal candidate for this purpose because it is non-invasive, available at the bedside, and it can make deep tissue oxygenation and hemodynamic measurements. Historically, it has been difficult to obtain reliable estimates with commercially available NIRS systems, while gold-standard techniques are technically complex and are primarily research tools. In comparison, hyperspectral (HS) NIRS is technically simpler and less expensive. This technique also benefits from its ability to measure multiple chromophores, both endogenous and exogenous, because it acquires data across the whole NIR spectrum. Finally, quantitative measurements of light absorbers, most notably oxy and deoxyhemoglobin, can be obtained using spectral derivative methods to remove the confounding effects of light scattering. The aim of this study was to confirm the ability of HS-NIRS to measure changes in oxygen saturation (StO<sub>2</sub>). Experiments were conducted in a tissue-mimicking phantom and in piglets under different levels of hypoxia. For validation StO<sub>2</sub> was measured independently by time-resolved (TR) NIRS.

### 2. Methods

#### 2.1 In vitro demonstration of HS-NIRS system

In order to characterize the ability of HS-NIRS to measure changes in StO<sub>2</sub>, experiments were conducted using a liquid phantom containing 1% Intralipid, 2.3 %blood and the remainder water to mimic the optical properties of the human brain. Measurements were acquired with an in-house-developed system consisting of a halogen light source (Ocean Optics, Dunedin, Florida) and a custom-built spectrometer (P&P Optica, Waterloo, Ontario). Serial NIRS measurements were acquired after adding yeast to the phantom to consume oxygen, converting the oxyhemoglobin to deoxyhemoglobin.

#### 2.2 In vivo hypoxia challenges

The piglet experiments were performed at different arterial oxygen levels (hyperoxia to hypoxia). At each level, data were acquired by the HS-NIRS as well as the gold standard TR-NIRS systems. Data were acquired from probes fixed to the head at a source detector separation of 3 cm. In addition, arterial blood was withdrawn at each level to determine PaO<sub>2</sub>.

### 3. Results

Phantom experiments demonstrated the ability of HS-NIRS to measure the changes in the hemoglobin concentrations with the addition of respiring yeast. As expected, the concentration of oxyhemoglobin was reduced and there was a corresponding increase in deoxyhemoglobin as the yeast consumed the oxygen in the phantom as shown in figure 1. In the piglet experiments, there was a very strong average correlation ( $R^2 = 0.99$ ) between StO<sub>2</sub> measured by both NIRS systems across eight animals, the StO<sub>2</sub> measurements as a function of blood oxygen content are displayed in figure 2. Additionally, there was no significant effect between StO<sub>2</sub> measurements from the two techniques ( $F_{5,35} = 1.591$ ,  $p > 0.05$ ) tested by a two-factor repeated-measures ANOVA.

### 5. Conclusion

HS-NIRS can be used to monitor changes in cerebral oxygen saturation at the bedside for patients in the NICU and is a simpler alternative to gold-standard NIRS devices that are used.

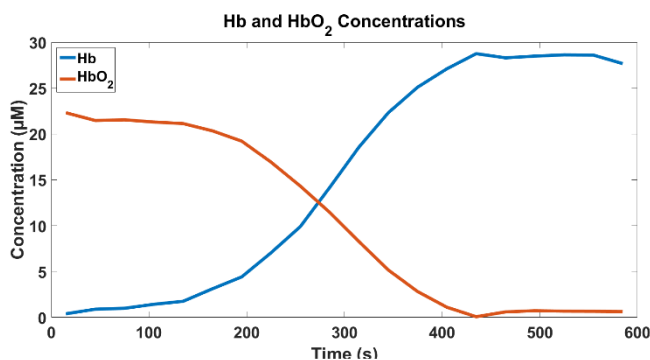


Figure 1: Change in hemoglobin concentrations with addition of yeast to an optical phantom.

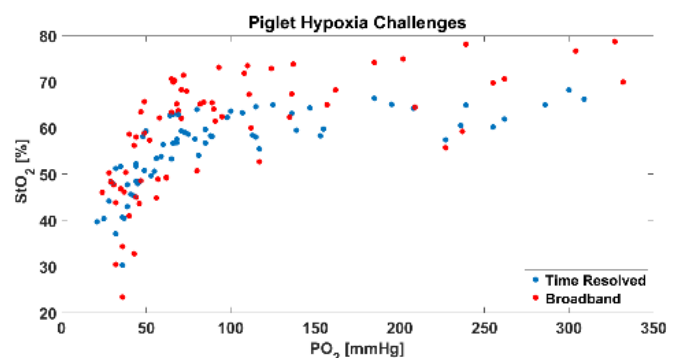


Figure 2: Comparison of oxygen saturation measurements between HS and TR NIRS.



## Development of a 3-French Photoacoustic Catheter for Imaging Mouse Colon

Rodrigo P. de Oliveira<sup>1,2</sup>, Nidhi Singh<sup>2</sup>, Chelsea E. Munding<sup>2</sup>, F. Stuart Foster<sup>2,3</sup>, João C. Machado<sup>1,4</sup>,  
Christine E.M. Demore<sup>2,3</sup>

<sup>1</sup> Biomedical Engineering Program - COPPE/UFRJ, Rio de Janeiro, Brazil

<sup>2</sup> Department of Medical Biophysics, University of Toronto, Toronto, Canada

<sup>3</sup> Sunnybrook Research Institute, Sunnybrook Health Sciences Center, Toronto, Canada

<sup>4</sup> Post-Graduation Program on Surgical Sciences - FM/UFRJ, Rio de Janeiro, Brazil

rpo@peb.ufrj.br

**Introduction:** Colon cancer is the third most common cancer in the world, if skin cancer is not considered. Despite the high incidence and high mortality rate, most of the outcomes could be prevented by using accurate techniques for early cancer detection to enable early treatment. In this context, it is important to conduct preclinical studies, using animal models of colon diseases, to test new diagnostic approaches including imaging instrumentation. Mice are commonly used as an animal model of colon cancer and therefore imaging devices to be used in studies of mouse models of colon disease must account for the small dimensions of the mouse colon lumen and must be able to accurately resolve and display the layers of the colon wall.

This paper describes the design of miniaturized instrumentation for micro-ultrasound (micro-US) and photoacoustic (PA) imaging of the mouse colon. We have previously used a 3-French ultrasound catheter normally used for intravascular ultrasound imaging (IVUS) to and image the layered structure in the mouse colon, detect polyps, and visualize their invasion through the colon wall [1]. We now want to add PA imaging to visualize the vasculature and PA contrast agents.

**Method and Results:** In order to fit within the 1.18 mm diameter working channel of a miniature endoscope for *in vivo* imaging of the mouse colon, the PA imaging device must fit within a 3-French catheter. The device includes both an optical fiber for pulsed laser illumination of tissue to generate the PA signal, and the ultrasound transducer for detecting the PA signal and generating a micro-US image. The single element a lead zirconate titanate (PZT) ceramic 40 MHz ultrasound transducer faces outwards and is rotated inside a low-density polyethylene (LDPE) sheath, to produce a cross-sectional image of the colon. Designed transducer dimensions 600  $\mu\text{m}$  x 600  $\mu\text{m}$  x 1500  $\mu\text{m}$  (width x thickness x length) include matching and backing layers. The transducer fabrication process uses micromachining processes to precisely define the transducer layers [2] and allows robust integration of a microcoaxial cable. The initial device design includes a single 500  $\mu\text{m}$  diameter optical fiber positioned at the center of the catheter. The system has been designed to work with a diode laser with a fast repetition rate (1000 pulses/second) that transmits at 810 nm. The fast repetition rate is needed to achieve real-time PA image frame rates since only a single image line is acquired at a time. The catheter system also includes a torque cable for rotating together the microcoaxial cable and the transducer while the optical fiber is static. Electrical impedance and pulse response simulated with finite element analysis will be shown. In further work, prototypes will be characterised using a hydrophone, and images of phantoms will be acquired. Previous transducers operating at this ultrasound frequency showed enough resolution to be used to image mice colons, and the cross-section imaging approach with pull-back to generate volumetric images has allowed visualization of the anatomic shape and lesions in the colon.

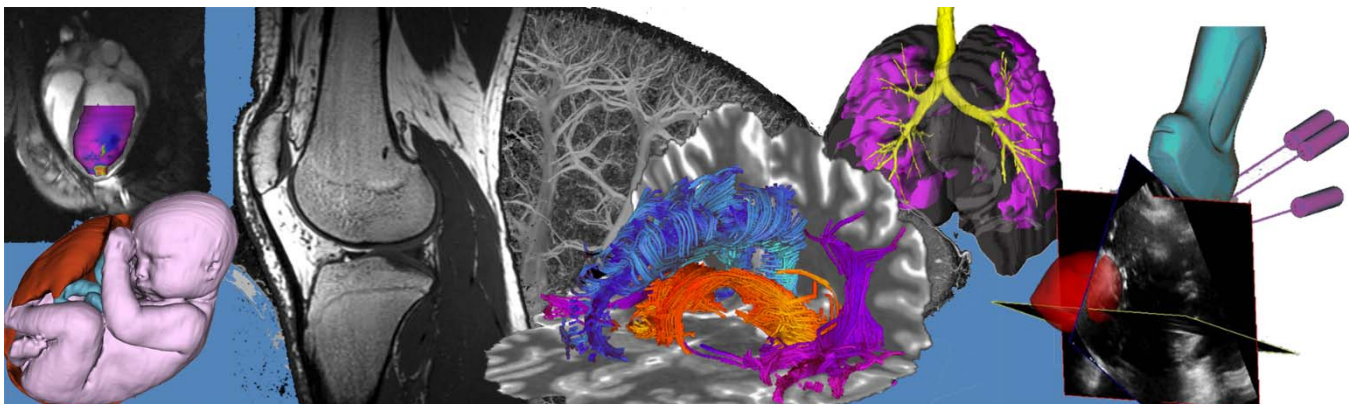
**Conclusion:** Miniature ultrasound and photoacoustic imaging devices are required for diagnostic imaging in the mouse colon, as part of preclinical studies of colorectal cancer or other diseases of the bowel. Like recently presented research, this work shows the possibility of developing a combined photoacoustic and micro-ultrasound catheter for imaging the mouse colon. These cross-section images can present an anatomic shape as well characteristics of the layers. Thus, with the combined PA and micro-US system in development can be suitable for imaging tumors in mice colon and acquiring images of tumor vascularization.

**Keywords:** Phantom, Photoacoustic, Colon Cancer, Mouse model of disease

- [1] Oliveira, R. P.; D'Agostini, J. G. ; Soletti, R.C.; MACHADO, J.C.. Geração de Imagens 3D de Biomicroscopia Ultrassônica Endoluminal do Cólon de Camundongo. In: Congresso Brasileiro de Engenharia Biomédica - CBEB2016, 2016, Foz do Iguaçu. Anais do XXV Congresso Brasileiro de Engenharia Biomédica - CBEB2016, 2016. v. 1. p. 1107-1110.
- [2] Chelsea E. Munding, Emmanuel Chérin, Issac Jourard, Jill J. Weyers, David E. Goertz, Brian K. Courtney F. Stuart Foster. Development of a 3 French dual frequency intravascular ultrasound catheter. *Ultrasound in Medicine & Biology*, Vol. 44. N.1, 2018.

# Poster Presentation Abstracts

## Session 2: Machine Learning



**Machine Learning for Lung Function Synthesis: Predicting MRI Ventilation from Thoracic CT**

Andrew Westcott BAsc<sup>1,2</sup>, Dante P.I. Capaldi PhD<sup>3</sup>, David G McCormack MD FRCPC<sup>4</sup>, Aaron Fenster PhD<sup>1,2</sup> and Grace Parraga PhD<sup>1,2,4</sup>

<sup>1</sup>Robarts Research Institute; <sup>2</sup>Department of Medical Biophysics, Western University London CANADA; Department of Radiation Oncology, Stanford University School of Medicine, Stanford, USA; <sup>4</sup>Division of Respiriology, Department of Medicine, Western University London CANADA

**Introduction:** Hyperpolarized noble gas magnetic resonance imaging (MRI) provides valuable insights on lung function, and yet is not widely available, whereas thoracic x-ray computed tomography (CT) protocols are nearly universally accessible. Our aim was to develop a texture analysis pipeline to train and test machine learning classifiers, predicting MRI-based ventilation metrics from single-volume thoracic CT.

**Methods:** Ten ex-smokers with chronic obstructive pulmonary disease (COPD) provided informed written consent to an ethics-board approved protocol (NCT02279329) and underwent spirometry, MRI and thoracic CT as previously described.<sup>1</sup> MR ventilation maps were generated and registered to thoracic CT datasets using an affine landmark based registration.<sup>2</sup> Images were segmented into volumes of interest (VOI) (15x15x15mm<sup>3</sup>), resulting in approximately 6,000 VOI per subject, as shown in Figure 1. 85 first-order and texture features were calculated to describe each volume, including a new 3-dimensional texture feature based on the size and occurrence of CT clusters (we called the cluster volume matrix), analogous to the run-length-matrix.<sup>3,4</sup> A logistic regression, linear support vector machine and quadratic support vector machine were trained using 5-fold cross-validation on a cohort of seven subjects. The highest performing classification model was then applied to a test cohort of three subjects.

**Results:** There was qualitative spatial agreement for the experimental MRI ventilation maps and the CT-predicted functional maps, as displayed in Figure 2 with yellow arrows. The training set was classified with 71% accuracy, while the test set was classified with 66% accuracy and area under the curve (AUC) of 0.72. To explore the predictive value of quantitative CT measures, and the additional value of texture features, we trained separate models on the same patient dataset, using only two traditional quantitative CT measures, previously been shown to spatially correlate with ventilation defects.<sup>5</sup> Logistic regression performed best in the training set when using only these two measurements, resulting in 61% accuracy and an AUC of 0.66. This trained model was applied to the test set, with an accuracy of 66% and AUC of 0.63.

**Conclusions:** In this proof-of-concept demonstration we developed a pipeline to generate a novel way to simulate functional information from single-volume thoracic CT. In a small training and test dataset of COPD patients this developed approach yielded an increased prediction success as compared to emphysema CT biomarkers alone. To our knowledge, this is the first demonstration of texture analysis and machine learning to predict ventilation abnormalities using single-volume thoracic CT. Novel insights will be used to optimize this approach with future application to a larger heterogeneous patient cohort.

**References:** [1] Parraga, G et al. Invest Radiol (2007); [2] Kirby, M et al. Acad Radiol (2012); [3] Tang, X et al. IEEE Trans Image Process (1998); [4] Haralick, RM et al. IEEE Trans Systems, Man, Cyber (1973); [5] Capaldi, DPI et al. Radiology (2016)

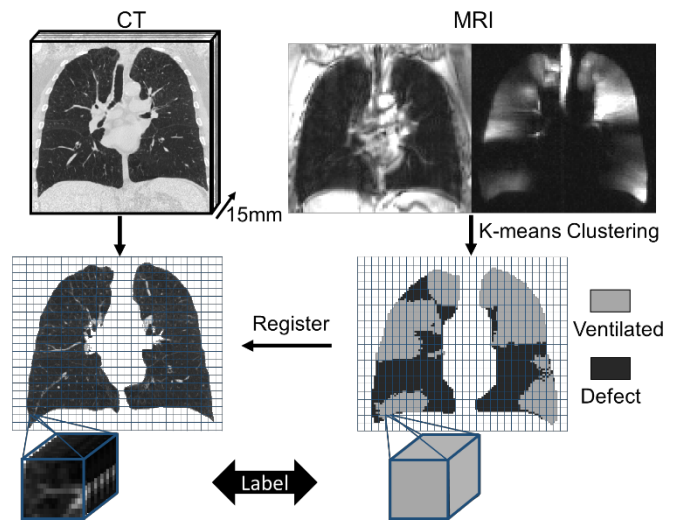


**Figure 1:** MRI to CT registration pipeline, showing the 3-dimensional grid used to define CT VOI and corresponding MR based ventilation label.

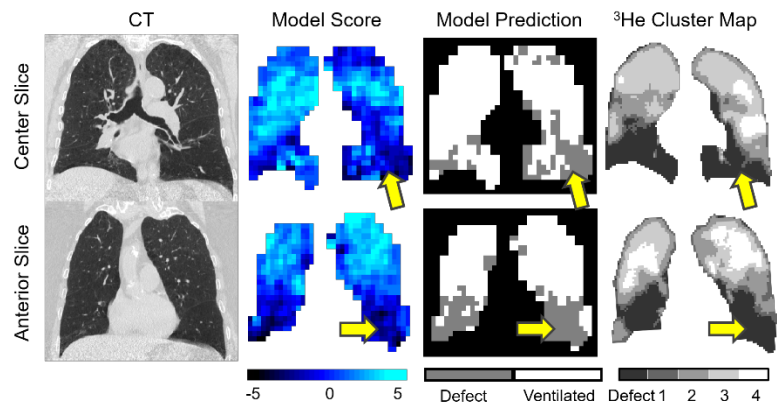


**Figure 2:** CT, Model predicted score, model binary prediction and <sup>3</sup>He cluster map for a test subject showing representative center and anterior slices.

## Comparison of convolutional neural networks for central venous catheterization tool detection

Rebecca Hisey<sup>1</sup>, Tamas Ungi<sup>1</sup>, Daenis Camire<sup>2</sup>, Jason Erb<sup>2</sup>, Daniel Howes<sup>2</sup>, Gabor Fichtinger<sup>2</sup>

<sup>1</sup>Laboratory for Percutaneous Surgery, School of Computing, Queen's University, Kingston, Canada

<sup>2</sup>Department of Critical Care Medicine, Queen's University, Kingston, Canada

**Introduction:** Central Line Tutor is a program for training ultrasound-guided central venous catheterization (CVC). The workflow for CVC contains many steps that use multiple different tools (Fig. 1). Feedback has been shown to be essential for trainee learning [1]. By recognizing which tool is being used Central Line Tutor is able to give trainees feedback about their compliance to proper procedure workflow in real-time. The purpose of this work is to evaluate the use of convolutional neural networks (CNN) to recognize the tools used in CVC compared to a previous colour based method [2].

**Methods:** Two different CNNs were evaluated for this work: Inception\_v3 and MobileNet. These networks were selected as they provide a balance between accuracy and size. MobileNet especially is designed to be run efficiently on mobile devices and embedded systems [3]. Each of these networks was pre-trained on the ImageNet dataset and used transfer learning to recognize the tools used in CVC. The final layer of each network is a fully connected layer that was retrained on a database of 100 000 images collected of the CVC tools using the Central Line Tutor setup. In order to evaluate these networks recordings were obtained of seven medical residents performing CVC on the Central Line Tutor setup. Each of these recordings is broken down into individual frames and we compared the frame-by-frame accuracy of each of these networks. None of these images were available while the networks were trained. We also compared these networks to a previous colour-based method which uses a sliding window to locate the region of the image that best matches a 30 pixel x 30 pixel image of the tool.

**Results:** Inception\_v3 achieved a frame-by-frame accuracy of 71% (Fig. 2). MobileNet had slightly worse performance, achieving only 69% accuracy. The colour-based approach was only able to achieve an accuracy of 16%. The guidewire casing was the best recognized tool by each of the CNNs. The syringe was the best recognized tool using the colour-based method.

**Conclusions:** Both CNNs substantially outperformed the colour-based method. This is due to the fact that CNNs recognize objects using multiple different features rather than just colour. There was very little difference in the accuracy of Inception\_v3 compared to MobileNet. Further work will be done to establish whether the efficiency of MobileNet's computation is worth the slight reduction in accuracy.

**Acknowledgements:** This work was funded, in part, by NIH/NIBIB and NIH/NIGMS (via grant 1R01EB021396-01A1), by CANARIE's Research Software Program, and is supported as a Collaborative Health Research Project (CHRP #127797) by the Natural Sciences and Engineering Research Council of Canada (NSERC) and the Canadian Institutes of Health Research (CIHR). R. Hisey is supported by the Canada Graduate Scholarship from NSERC. G. Fichtinger is supported as a Canada Research Chair.

### References:

- [1] Rogers DA, Regehr G, Howdieshell TR, Yeh KA, Palm E (2000) The impact of external feedback on computer-assisted learning for surgical technical skill training. *Am J Surg* 179(4):341-343.
- [2] Hisey R, Ungi T, Holden MS, Baum ZM, Keri Z, McCallum C, Howes DW, Fichtinger G (2018) Real-time Workflow Detection Using Webcam Video for Providing Real-time Feedback in Central Venous Catheterization Training. *SPIE Medical Imaging* 2018.
- [3] Howard AG, Zhu M, Chen B, Kalenichenko D, Wang W, Weyand T, Andreetto M, Adam H (2017) MobileNets: Efficient Convolutional Neural Networks for Mobile Vision Applications. *CoRR*, abs/1704.04861.

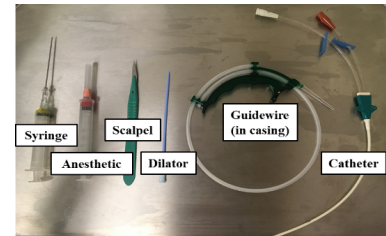


**Figure 1.** Tools used for central venous catheterization.

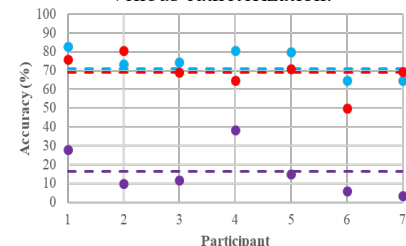


**Figure 2.** Accuracy of histogram (purple), Inception\_v3 (blue), and MobileNet (red). Dotted lines represent the average across all frames.

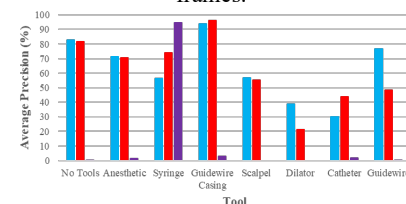


**Figure 3.** Average precision for each tool for histogram (purple), Inception\_v3 (blue) and MobileNet (red).

### Machine learning functional metrics for recovery path analysis following total knee replacement

\*Riley A Bloomfield<sup>1,4,5</sup>, Harley A Williams<sup>2,4,5</sup>, Brent A Lanting<sup>3</sup>, Kenneth A McIsaac<sup>1</sup>, Matthew G Teeter<sup>2-5</sup>  
<sup>1</sup>Dept. Electrical & Computer Engineering, <sup>2</sup>Dept. Medical Biophysics, <sup>3</sup>Dept. Surgery, <sup>4</sup>Robarts Research Institute, Western University; <sup>5</sup>Lawson Health Research Institute; Ontario, Canada

**Introduction:** Predicting surgical outcomes following total knee replacement (TKR) can be used to plan recovery resources and support for patients. If these outcomes can be accurately predicted, parameters determined earlier in surgical recovery can be used as indicators that further physio-therapeutic or surgical intervention will be required. Previous research has shown that functional performance before intervention is one of the strongest determinants of successful outcomes post-surgery, with stronger performing patients more likely to have positive outcomes [2]. Furthermore, the timed-up-and-go (TUG) functional test execution time can predict length of stay and short term functional performance following surgery when administered preoperatively [3]. The objective of this study is to apply machine learning to find patterns in functional performance data recorded from patients before and after their TKR surgery to identify key functional parameters that contribute to better outcomes.

**Methods:** Forty patients undergoing TKR as a treatment for knee osteoarthritis completed TUG tests while instrumented with a previously developed wearable sensor system to measure knee activity [1]. Each subject completed two or three trials depending on fatigue at their preoperative clinical appointment and at their six and twelve week follow-up visits. These tests were segmented into sub-activities and 52 temporal and angular knee motion metrics were extracted autonomously using custom software. Western Ontario and McMaster University Osteoarthritis Index (WOMAC) and Knee Society Score (KSS) patient reported outcome measures (PROM) were completed by patients at each clinical visit and were used to subjectively evaluate function and surgical satisfaction outcomes. KSS satisfaction reports were binned into binary categories and WOMAC function scores were binned into three categories representing low, medium, and high function. To evaluate effectiveness of the additional derived functional test metrics compared to using temporal metrics alone, two support vector machine (SVM) classifiers were trained and tested in MATLAB using all subjects' six week test samples and binned WOMAC function scores as ground truth labels. One classifier included only temporal metrics as feature vectors while the other included all 52 derived metrics. This time point was chosen for comparison because it offered the most balanced data set between satisfied and non-satisfied subjects. Classifier performance was evaluated using classification accuracy, recall, precision, and F-score.

**Results:** The percentage of samples from dissatisfied patients decreased at each of the test time points: preoperative (88.6%), six week (39.2%), and twelve week (22.6%) showing subjective improvement for most subjects following surgical intervention. Classification accuracy with all derived functional metrics was 87.9% with a recall of 0.95, a precision of 0.81 and an F-score of 0.875. Accuracy using only sub-activity completion times was 72.7% with a recall of 0.33, a precision of 0.24, and an F-score of 0.28.

**Conclusions:** Using additional derived functional metrics has increased the predictability of a classifier to predict labelled functional status'. The current work has only examined predicting a single subjective outcome measure. Although PROM metrics have been validated and shown useful for patient evaluation, they remain subjective and are heavily influenced by patient expectations and opinions. Predicting a single measure from data from the same time point is also less relevant to predicting overall patient outcomes since we have the final outcome labels at each point from PROM surveys. Future work will examine functional metrics across multiple time points to predict late time point outcomes and we hypothesize that metric changes over recovery will be more valuable than metrics from any single time point individually.

[1] R. Bloomfield et al. "Proposal and Validation of a Knee Measurement System for Patients with Osteoarthritis". In: *IEEE Transactions on Biomedical Engineering* (2018). [2] A. Judge et al. "Predictors of outcomes of total knee replacement surgery". In: *Rheumatology (Oxford)* 51.10 (Oct. 2012), pp. 1804–1813. [3] S. Poitras et al. "Predicting early clinical function after hip or knee arthroplasty". In: *Bone Joint Res* 4.9 (Sept. 2015), pp. 145–151.

## Automatic localization of anatomical fiducials using 3D intensity features and machine learning

Daniel J. Cao<sup>1</sup>, Dimuthu Hemachandra<sup>2</sup>, Jonathan C. Lau<sup>\*2</sup>, and Ali R. Khan<sup>\*1,2,3</sup>

<sup>1</sup>Dept. of Medical Biophysics, <sup>2</sup>School of Biomedical Engineering, <sup>3</sup>Robarts Research Institute, (\*co-senior)  
Western University, London, Ontario, Canada

**Introduction:** In neuroimaging, image registration is a critical process for establishing correct spatial correspondence between images. This permits a multitude of useful applications, such as the creation of population atlases for brain modelling or the delivery of stereotactic information for surgical planning. Landmark-based validation is a popular method of evaluating registration accuracy which involves placing anatomical fiducials on robust sets of anatomical features across image pairs and computing the distance error between these sets [1]. Currently, many landmark-based validation techniques require trained raters to place fiducial markers manually, which is an accurate but tedious process. Considering this, we propose an automated method that can efficiently complete the fiducial markup procedure, building a registration validator for brain images while maintaining the same level of accuracy as current validation tools. In this research we will implement linear support vector machines (SVM) that can identify a set of 32 anatomical landmarks found within all brains. We derive features for these landmarks by describing their surrounding voxel neighborhoods with modified scalar-invariant feature transform (SIFT) descriptors, which are subsequently fed into SVM classifiers as training data. Once classifiers are built, anatomical fiducials can be automatically placed in new patient brain volumes.

**Methods:** *Data collection:* We used T1-weighted MRI volumes from 25 adult patients for training and 7 for testing. All volumes were labelled with manually-placed fiducials in 32 key brain regions by trained raters, and these labels serve as the ground-truth. *Feature extraction:* In our algorithm, we created a 25x25x25 voxel space around each of the 32 fiducial locations for each brain volume in the training set. 3D-compatible SIFT descriptors [2] were extracted from each voxel in each local neighborhood. Positive class labels were assigned to all voxels in 3x3x3 boxes that surround the manually-placed fiducials, and negative class labels were assigned to the rest of the voxels in each of the 25x25x25 blocks. Voxels that were assigned to the negative class label were sampled so that the number of positive label descriptors roughly equals the number of negative class descriptors. *Training and classification:* Individual SVM classifiers were built for each of the 32 regions. In testing, we computed descriptors for all voxels in 25x25x25 search boxes in the new test volume, with each box corresponding to one of the 32 key brain regions and SVM classifiers. Because all the volumes in our dataset share the same pose, we used the average location of the landmarks in our training set as the center seed for the search box in our testing volumes.

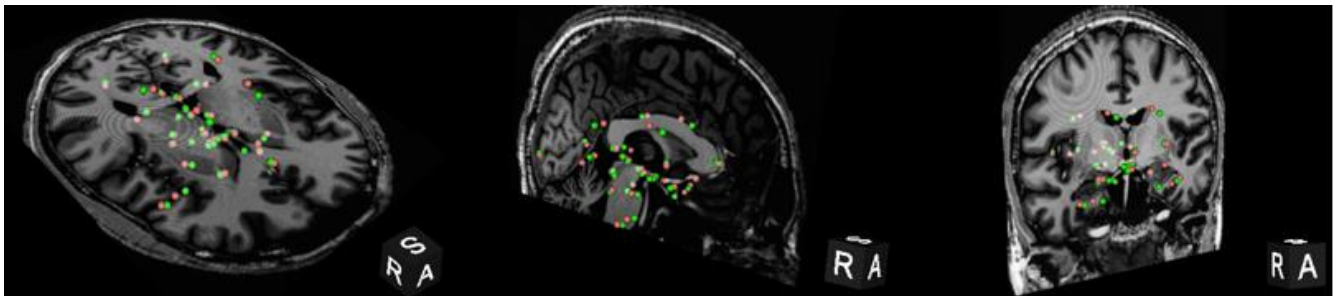


**Fig. 1.** Axial, sagittal, and coronal slices showing distribution of manually-labelled fiducials (green) and automatically-placed fiducials (red)

**Results:** Using Euclidean distance as the evaluation metric, our preliminary results indicate that fiducials placed through our automated method lie an average distance of  $1.28 \pm 0.52$  mm away from manually-placed, ground-truth locations. **Fig. 1** displays the distribution of our results for the 32 landmarks in one particular brain volume.

**Conclusion:** This research presents an automated method of identifying 32 key landmark positions using SVM classifiers, in which some but not all fiducials are placed with an accuracy comparable to that of raters' manually-placed labels. As such, some aspects of manual fiducial placement in the pipeline for landmark-based validation of image registration can be replaced. More robust classifiers will be needed to predict points more accurately.

**References:** [1] Lau et al BioRxiv.org 2018; doi: <https://doi.org/10.1101/460675>, [2] Rister et al IEEE Trans. Image Process. 2017; 26:4900-4910

## Automated Segmentation of Prostate Zonal Anatomy on T2-Weighted (T2W) and Apparent Diffusion Coefficient (ADC) Map MR Images Using Cascaded U-Nets

Fatemeh Zabihollahy, Nicola Schieda, Satheesh Krishna Jeyaraj, Eranga Ukwatta

**Introduction:** Accurate regional segmentation of the prostate boundaries on MR images is a fundamental requirement before automated prostate cancer diagnosis can be achieved. In this paper, we describe a novel methodology to segment prostate whole gland (WG), central gland (CG), and peripheral zone (PZ), where  $PZ+CG=WG$ , from T2W and ADC map prostate MR images.

**Methods:** We designed two similar models each made up of two cascaded U-nets to delineate the WG, CG, and PZ from T2W and ADC map MR images, separately. The U-net, which is a modified version of a fully convolutional neural network, includes contracting and expanding paths with convolutional, pooling and up-sampling layers. Pooling and up-sampling layers help to capture and localize image features with a high spatial consistency. We used a dataset consisted of 225 patients (combining 153 and 72 patients with and without clinically significant prostate cancer) imaged with multi-parametric MRI at 3 Tesla.

**Results:** Our proposed model for prostate zonal segmentation from T2W was trained and tested using 1154 and 1587 slices of 100 and 125 patients respectively. Median of Dice similarity coefficient (DSC) on test dataset for prostate WG, CG, and PZ were  $95.33 \pm 7.77\%$ ,  $93.75 \pm 8.91\%$ , and  $86.78 \pm 3.72\%$ , respectively. Designed model for regional prostate delineation from ADC map images was trained and validated using 812 and 917 slices from 100 and 125 patients. This model yielded a median DSC of  $92.09 \pm 8.89\%$ ,  $89.89 \pm 10.69\%$ , and  $86.1 \pm 9.56\%$  for prostate WG, CG, and PZ on test samples, respectively. Further investigation indicated that the proposed algorithm reported high DSC for prostate WG segmentation from both T2W and ADC map MR images irrespective of WG size. In addition, segmentation accuracy in terms of DSC does not significantly vary among patients with or without significant tumors. Figure 1 illustrates segmentation results for different image types in four patients (randomly selected from our test dataset).

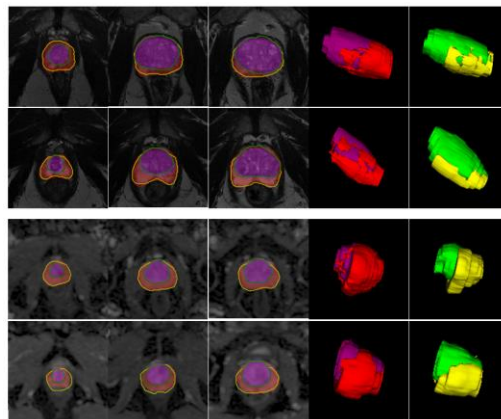


Fig. 1 Example results from segmented prostate WG, CG, and PZ using T2W and ADC map MR images (two top and two bottom rows) in four patients. On the source 2D images, the U-net-based method segmentation of the prostate CG and PZ for three slices presented from apex to base (left to right) extracted from MRI are shown in purple and red respectively and the contours computed from the expert manual are displayed in green and yellow. The fourth and fifth picture elements depict a 3D surface rendering of algorithm-generated and expert manual segmentation of prostate zones respectively.

**Significance:** We describe a method for automated prostate zonal segmentation using ADC map and T2W MR images independent of prostate size and presence or absence of tumor. Our results are important in terms of clinical perspective as fully automated methods for ADC map images, which are considered as one of the most important sequences for prostate cancer detection in the PZ and CG, have not been reported previously.

## Retraining MobileNet with highly variable data for tool detection in central venous catheterization

Jonah Isen, Rebecca Hisey, Tamas Ungi, Gabor Fichtinger

Laboratory for Percutaneous Surgery, School of Computing, Queen's University, Kingston, Canada

**Introduction:** Central venous catheterization (CVC) is a vital medical procedure with many possible complications. Complications that arise from improper technique can occur in as high as 12% of procedures [1]. As such, training to reduce complication rates is important. Central Line Tutor guides users through this process, providing real-time instructions and feedback [2]. Using MobileNet, a convolutional neural network, a tool in use is identified, indicating proper adherence to the procedure. The efficacy of the network is dependent on variation in training set images. This study evaluates the accuracy of a MobileNet that has been retrained using a high variation training set for identifying tools used in CVC.

**Methods:** To effectively retrain a neural network, numerous training images with high variation are needed. 17,500 images of each of the 7 tools used in CVC were gathered. Additionally, 25,000 images of the workspace without tools were collected, for a total of 147,500 images. To maximize variation, these images were taken in various tool positions, lighting conditions and camera angles. Furthermore, images were collected with and without medical gloves, and the tools were handled with different handedness. These variations are illustrated in 5 sample images from the scalpel training set (Fig. 1). The initial layers of a MobileNet network were then retrained on the ImageNet dataset, and the final layer was retrained on the collected training set using 100,000 training steps. To test the accuracy of the retrained network at identifying tools, 5 trials of the procedure were recorded using Central Line Tutor. These recordings were separated into frames, and classified manually and by the retrained network. The performance of the MobileNet was evaluated by comparing the manual and automatic classifications, measuring accuracy of the network across all frames, and its precision for each tool. The precision of classification is a percentage of correct classifications out of total classifications for a given tool. The accuracy of the network is the percentage of correct classifications from all of the recorded frames.

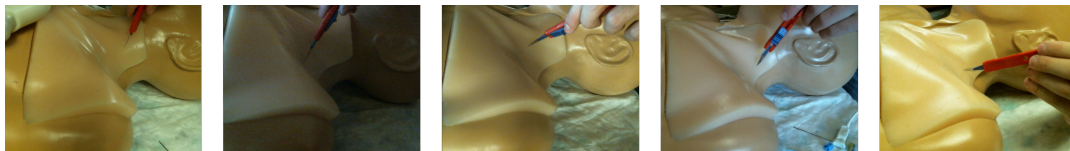


**Figure 1.** Sample images from scalpel training set

**Results:** On average, 62.4% of the 4,376 recorded frames were correctly classified. The best identified tool was the scalpel, with 95.7% precision. The least was the guidewire casing, with a precision of 21.7%. Tools fell into two distinct groups, and either had a high precision (70-100%) or a low precision (20-40%). High precision tools consisted of the scalpel, catheter, anesthetic and syringe, and low precision tools were the guidewire casing, guidewire and dilator.

**Conclusions:** These results indicate that the high variation training set was effective for identification of some tools used in CVC. Tools that were small in size with non-distinct colour, such as the guidewire or dilator, were classified less accurately. Tools with distinct shape and colour like the scalpel or catheter were reliably classified with the retrained network. A limitation may have stemmed from only one person gathering training images; multiple people would have introduced more variation. Further work can be done to improve the training set in order to better recognize those tools with low precision.

**Acknowledgements:** This work was funded, in part, by NIH/NIBIB and NIH/NIGMS (via grant 1R01EB021396-01A1 - Slicer+PLUS: Point-of-Care Ultrasound) and by CANARIE's Research Software Program.

1. Kornbau C, Lee KC, Hughes GD, Firstenberg MS. Central line complications. *Int J Crit Illn Inj Sci.* 2015 Sep; 5(3): 170–178.
2. Hisey R, Ungi T, Holden MS, Baum ZM, Keri Z, McCallum C, Howes DW, Fichtinger G (2018) Real-time Workflow Detection Using Webcam Video for Providing Real-time Feedback in Central Venous Catheterization Training. *SPIE Medical Imaging* 2018.



## Using Deep Learning for Transverse Process Detection in Spinal Ultrasounds

Victoria Wu, Tamas Ungi, Gabor Fichtinger

Laboratory for Percutaneous Surgery, School of Computing, Queen's University, Canada

**Introduction:** Adolescent idiopathic scoliosis is the most common form of scoliosis, affecting between 2-4% of the adolescent population [1]. However, screening and treatment require frequent x-ray procedures, which have been linked to health issues including an increased mortality rate for breast cancer in female patients [2]. This makes spinal ultrasounds an ideal substitute, as it does not expose them to those levels of radiation. However, one of the major issues associated with ultrasound images is the fuzzy border definitions, making it difficult to detect the presence of spinal processes. To overcome this difficulty, we employed a deep learning algorithm using a convolutional neural network to detect the presence of spinal processes. This detection is important as it shows that it is viable to perform an ultrasound scan on the spine.

**Methods:** Over 2000 ultrasound images were recorded from a spine phantom to train the convolutional neural network. Subsequently, another recording of around 750 images of the phantom was taken to be used as testing images. All the ultrasound images from the scans were then segmented manually, using 3D Slicer. In total, there were around 2000 images used for training, 750 used for validation, and 750 used for testing. Next, the images were fed through a convolutional neural network. The convolutional network used was a modified version of GoogLeNet (Inception v1), with 2 linearly stacked inception models. Typically, Inception can classify over 1000 different classes of images; the ultrasound images only belonged to 2 classes, so a simpler network was created based on the same premises. This network was chosen because it provided a balance between accurate performance, and time efficient computations.

**Results:** Deep learning classification using the Inception model achieved an accuracy of 84% for the phantom scan.

**Conclusions:** The classification model performs with considerable accuracy. Better accuracy needs to be achieved, possibly with more available data and improvements in the classification model.

**Acknowledgements:** G. Fichtinger is supported as a Canada Research Chair in Computer-Integrated Surgery. This work was funded, in part, by NIH/NIBIB and NIH/NIGMS (via grant 1R01EB021396-01A1 - Slicer+PLUS: Point-of-Care Ultrasound) and by CANARIE's Research Software Program.

### References:

- [1] Horne JP, Flannery R, Usman S. (2014). Adolescent idiopathic scoliosis: diagnosis and management. *Am Fam Physician* 89(3):193-8.
- [2] Ronckers CM, Land CE, Miller JS, Stovall M, Lonstein JE, Doody MM. (2010). Cancer mortality among women frequently exposed to radiographic examinations for spinal disorders. *Radiation Research* 174(1):83-90.

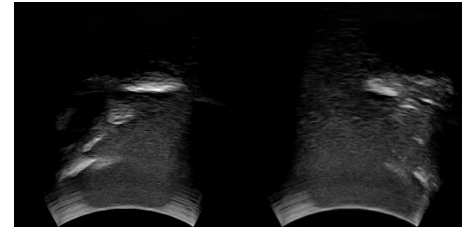


**Figure 1:** Ultrasound scan containing a transverse process (left), and ultrasound scan containing no transverse process (right)

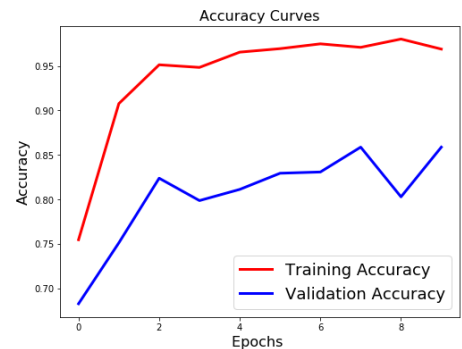
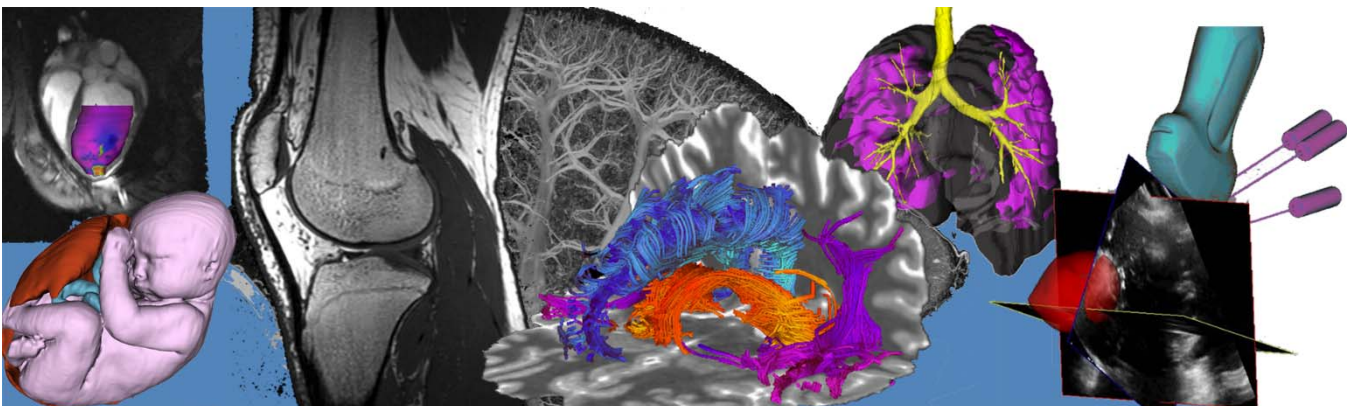


**Figure 2:** Accuracy of classification for training (red) and validation (blue)

# Poster Presentation Abstracts

## Session 3: Cellular and Molecular Imaging



## Phenotyping cells in the tumour and microenvironment using protein multiplexing and quantitative image analysis

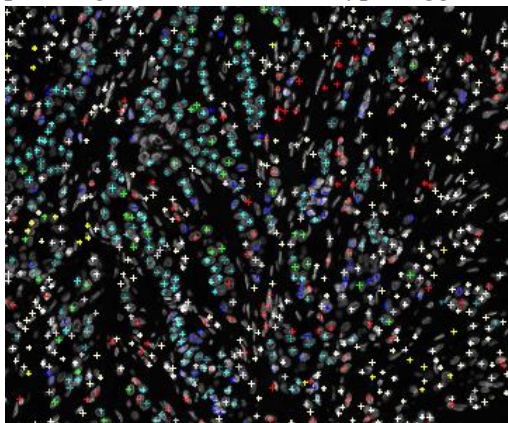
Alison M Cheung<sup>1</sup>, Dan Wang<sup>1</sup>, Kela Liu<sup>1</sup>, Tyna Hope<sup>1</sup>, Simone Stone<sup>2</sup>, Ben X. Wang<sup>2</sup>, Fiona Ginty<sup>3</sup>, Pam Ohashi<sup>2</sup> & Martin Yaffe<sup>1</sup>

<sup>1</sup>Biomarker Imaging Research Lab, Sunnybrook Research Institute, Toronto, ON

<sup>2</sup>Princess Margaret Cancer Centre, Toronto, ON

<sup>3</sup>Biosciences, General Electric Global Research Centre (GE GRC), Niskayuna, NY

**Introduction:** The effectiveness of targeted cancer regimen or immunotherapy could be limited due to the heterogeneous spatial distributions of cancer cells and infiltrating inflammatory cells. As such, development of a tool that can 1) distinguish sub-populations of cancer cells and immune infiltrates, and 2) that also enables visualization and measurement of their spatial distributions, will be invaluable for assessing and monitoring patients' immune and cancer profiles before and during therapy. **Methods:** Here we report the use of an *in situ* protein marker multiplexing immunofluorescence system (MxIF) to phenotype both cancer cells and tumour-infiltrating lymphocytes in breast cancer using single sections of formalin-fixed, paraffin-embedded (FFPE) tissue of a breast cancer tissue microarray (TMA). Quantitative analysis of protein expressions were performed using thresholding or kmeans clustering. **Results:** We imaged the staining of 9 markers (ER, PgR, HER2, KI67, P53, P21, P16, CD8, CD20) on a single FFPE section with 114 breast cancer TMA cores and quantified the protein expressions from 304,102 single cancer and immune cells. We have identified clusters of breast cancer cells based on co-expression signal intensities of ER, PgR and HER2 (called EPH clusters 1-8) and observed significant levels of cellular heterogeneities in a spectrum of breast cancer subtypes, particularly among the hormonal receptor-positive breast cancers. We did not observe any significant association of KI67-positive cells to individual cluster. However, certain clusters harbored higher levels of P53 and P16 expressions. Tumour-infiltrating lymphocytes CD8 T-cells and CD20 B-cells were quantified in each TMA core. Densities of CD8 T-cell were positively associated with EPH cluster 4 (cluster with low ER, low PgR and intermediate HER2)( $r=0.88$ ,  $p=0.05$ ) and negatively correlated with EPH cluster 1 (cluster with low ER, intermediate PgR and intermediate HER2)( $r=-0.64$ ,  $p=0.05$ ). Using visualization tools, each cell on the image was marked with colours corresponding to their cluster assignment, and the co-occurrence between clusters are quantified to study the potential functional relationship in cellular arrangement (Fig). **Conclusion:** We have demonstrated the application of this platform in phenotyping cancer and surrounding immune cells and quantified the co-expression relationships of cancer driver proteins. The spatial and cellular heterogeneity of cell clusters within each pathologic breast cancer subtype suggests "evolution" of the lesion during progression and therefore tools that can



more accurately characterize breast cancer is needed to improve diagnosis and therapy planning for each patient.

spot014	1	2	3	4	5	6	7	8
1	0.027671	0.003438	0.01295	0.003992	0.005115	0.017811	0.032259	0.025884
2	0.003438	0.003079	0.002731	0.002136	0.00339	0.009918	0.00667	0.009206
3	0.01295	0.002731	0.018086	0.000944	0.006897	0.019261	0.010398	0.015961
4	0.003992	0.002136	0.000944	0.013108	0.000622	0.004466	0.014152	0.010883
5	0.005115	0.00339	0.006897	0.000622	0.008679	0.016346	0.00619	0.010878
6	0.017811	0.009918	0.019261	0.004466	0.016346	0.046442	0.024466	0.042003
7	0.032259	0.00667	0.010398	0.014152	0.00619	0.024466	0.074663	0.044412
8	0.025884	0.009206	0.015961	0.010883	0.010878	0.042003	0.044412	0.081517

**Figure:** Representative image of a cancer with different cell clusters (colour of each cluster as indicated in table) and the co-occurrence matrix of clusters. Certain clusters exhibited higher likelihood of co-occurrence than others.

## A Genomic Safe Harbour Homology Independent Targeted Integration (HITI) CRISPR/Cas9 System for Efficient Tri-Modal Reporter Gene-Based *In Vivo* Cell Tracking.

J. J. Kelly\*<sup>1,2</sup>, N. N. Nyström<sup>1,2</sup>, M. Saeed-Marand<sup>2</sup>, Y. Chen<sup>2</sup>, A. M. Hamilton<sup>2</sup>, J. A. Ronald<sup>1,2</sup>.

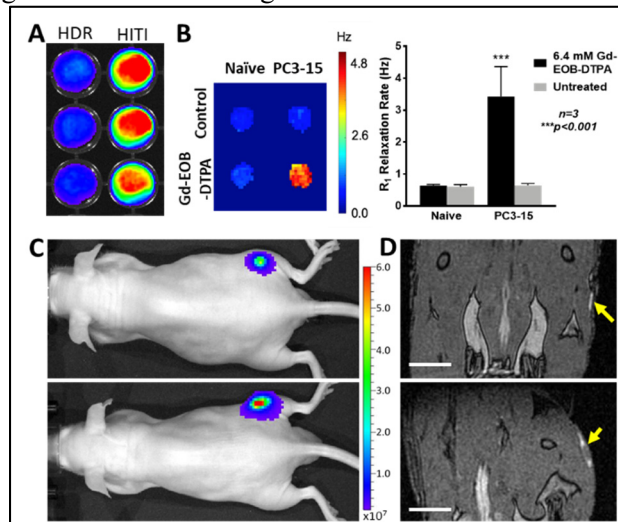
<sup>1</sup>Robarts Research Institute and <sup>2</sup>Dept. of Medical Biophysics, University of Western Ontario, London, ON

**Introduction:** Non-invasive tracking of cells with imaging reporter genes (RGs) can allow one to monitor the fates of implanted cells, providing vital quantitative information on treatment response. Engineering cells to express RGs often relies on gene transfer methods that lead to random integration of foreign DNA into the genome, which may cause unwanted and serious detrimental effects. To circumvent this, non-viral CRISPR/Cas9 homology directed repair (HDR) has been used to integrate genes into specific genomic loci, however it's inefficiency limits it's use for cell-based therapies. Thus, we have developed CRISPR/Cas9 minicircle (MC) constructs that utilize the Homology Independent Targeted Integration (HITI) strategy, which allows for safe and efficient genome editing of cells with RGs for non-invasive and longitudinal monitoring of transplanted cell fate. Here, we compared the efficiency of HDR and HITI CRISPR/Cas9 systems in their ability to correctly incorporate large donor DNA constructs encoding genes for fluorescent (FLI), bioluminescent (BLI) and magnetic resonance (MRI) imaging at the adeno-associated viral site 1 (AAVS1), or "safe harbour" locus.

**Methods:** 293T and PC3 cell lines were co-transfected with MCs expressing zsGreen and Cas9-guide or Cas9-scrambled RNA together with donor MCs encoding Fluc, tdTomato and OATP1A1 RGs. Donor MCs were also engineered to have the same Cas9-gRNA cut site for HITI as the AAVS1 site. Cells were FACS sorted twice before clonal selection. PCR analysis was performed to check for correct AAVS1 integration and BLI, FLI and MRI imaging modalities utilized to test for RG functionality *in vitro*. Finally, naïve and engineered PC3 cells were injected into nude mice (n=5) for *in vivo* tracking of tumour growth over time using BLI and MRI.

**Results:** PCR analysis revealed correct AAVS1 integration of the tri-modal RG constructs in cell lines co-transfected with Cas9-gRNA, but not for Cas9-scrambled controls, indicating successful integration. BLI signal was consistently higher in HITI engineered cells compared with HDR (A), suggesting higher integration efficiency. Clonal selection of tdTomato positive cells revealed a greater integration efficiency of RGs in 293T HITI clones, of which 36% (13/34) were positive compared with 11% (4/34) for HDR. Due to lower transfection efficiency of PC3 cells, 2/19 HITI clones were positive for HITI integration vs 0/14 for PC3 HDR clones. 3T MRI scans of 293T and PC3 HITI clones exposed to 6.4 mM of the gadolinium contrast agent Gd-EOB-DTPA (for OATP1A1) for 1 hour revealed an average  $R_1$  relaxation rate of 7.95 Hz ( $\pm 0.87$ , SD) for 293T and 3.43 Hz ( $\pm 0.22$ , SD) for PC3 cells, indicating successful OATP1A1-induced Gd-EOB-DTPA uptake (B). Engineered PC3 cells injected into nude mice revealed positive BLI signal at day 3, 7, 14 and 21 post injection (C). In addition, Gd-EOB-DTPA-enhanced MRI images of developing sub-cutaneous tumours after Gd-EOB-DTPA injection were noticeable after only 11 days post injection prior to them being palpable or readily visible on pre-contrast images (D).

**Conclusion:** This describes the first CRISPR/Cas9 HITI system for safe harbor integration of large tri-modal RG constructs, including the clinically-relevant OATP1 reporter, for multi-modal longitudinal imaging of cells *in vivo*. This work lays the foundation for an effective and safe genome editing tool for RG tracking of multiple cell types *in vivo*, including cell-based cancer immunotherapies.



A, BLI of HITI engineered PC3 cells vs HDR. B,  $R_1$  map and quantification of Gd-EOB-DTPA uptake in HITI PC3 cells expressing OATP1A1. C, BLI of mice injected subcutaneously with naïve (left flank) and HITI engineered PC3 cells (right flank) at day 14, scale = radiance (p/sec/cm<sup>2</sup>/sr). D, MRI scans 5hrs post Gd-EOB-DTPA injection at day 11 of tumour growth. Enhanced contrast indicated by arrows.

## Magnetic resonance imaging of commensal and pathogenic bacteria

<sup>1,2,3\*</sup> Donnelly, SC; <sup>1,4</sup> Thompson, RT; <sup>1,3,4</sup> Prato, FS; <sup>1,4</sup> Gelman, N; <sup>2,5,6</sup> Burton, JP; <sup>1,3,4</sup> Goldhawk, DE

<sup>1</sup> Imaging Program, Lawson Health Research Institute; <sup>2</sup> Microbiology & Immunology, <sup>3</sup> Collaborative Graduate Program in Molecular Imaging, <sup>4</sup> Medical Biophysics, <sup>5</sup> Surgery, Western University; <sup>6</sup> Human Microbiome & Probiotics Research Program, St. Joseph's Health Care; London, Ontario, Canada

**Introduction:** Magnetic resonance imaging (MRI) is a non-invasive imaging modality with superb resolution and penetration depth, ideal for examining soft tissues of the intestinal mucosa. Current methods to identify and characterize microbes in the gut microbiome involve *ex vivo* propagation, risking changes in bacterial behaviour and contamination<sup>1</sup>. While *in vivo* microbiome analyses are challenging<sup>2</sup>, imaging provides an alternative to *ex vivo* analyses and molecular imaging may be enhanced by contrast agents. For example, expression of magnetotactic bacterial genes like *maga*<sup>3</sup> increases long-term magnetic resonance (MR) contrast in mammalian cells<sup>4,5</sup>. To explore microbial behaviour, growth and dispersion *in vivo*, we hypothesize that MagA expression in *Escherichia coli* will increase cellular iron content and impart magnetic properties for cellular detection by MRI. Here, we examine MR relaxation rates in bacterial isolates using a gelatin phantom previously validated in mammalian systems<sup>4</sup>.

**Methods:** Bacterial isolates from the human gut and urinary tract were cultured overnight; washed and loaded into Ultem wells by centrifugation at 4500 x g; and mounted in a gelatin phantom for MRI at 3 Tesla<sup>4</sup>. Images were evaluated using custom MATLAB software. Longitudinal ( $R1 = 1/T1$ ) and transverse ( $R2^* = 1/T2^*$ ;  $R2 = 1/T2$ ) relaxation rates were acquired using inversion-recovery spin-echo (SE) for T1, single-echo SE for T2 and multi-echo gradient echo for T2\*. Statistical analyses were done in GraphPad Prism 7.03.

**Results:** Longitudinal relaxation rates did not vary between *E. coli* strains or different bacterial species (data not shown, range 0.23 – 2.74 s<sup>-1</sup>). However, in all bacterial species, the irreversible R2 component accounts for virtually the entire transverse relaxation rate (Figures 1 and 2,  $R2^* = R2 + R2'$ ), with little or no contribution from the reversible R2' component ( $R2^* - R2 \sim 0$ ). For *E. coli*, R2 differs significantly between strains (Figure 1); however, there is no consistent difference between strain characteristics or origin. *Lactobacillus gasseri* 33323, the dominant microbe of the healthy female urinary tract, shows significantly higher relaxation rates than any other bacterial species examined (Figure 2).

**Conclusions:** This is the first report of MR relaxation rates in human clinical *E. coli* isolates and urinary and gut-associated microbes. *E. coli* provide detectable MR contrast, with R2 values much higher than those of previously studied mammalian cells<sup>3,4</sup>. Given these results, the large MR signal observed in the mammalian gut<sup>5</sup> may potentially reflect an extensive contribution from bacteria. In addition, the high MR signal from *L. gasseri* raises the possibility of *in vivo* detection of dysbiosis in the urinary microbiota, where Lactobacilli levels are drastically reduced. Future work will examine cellular iron content in these bacterial species, using mass spectrometry, and explore the impact of *maga* expression on MRI of *E. coli*.

**References:** 1) Bao et al (2016) Ann Transl Med 5, 33. 2) Bron et al (2012) Nat Rev Microbiol 10, 66. 3) Goldhawk et al (2009) Mol Imaging 8, 129. 4) Sengupta et al (2014) Front Microbiol 5, 29. 5) Rohani et al (2014) Mol Imaging Biol 16, 63.

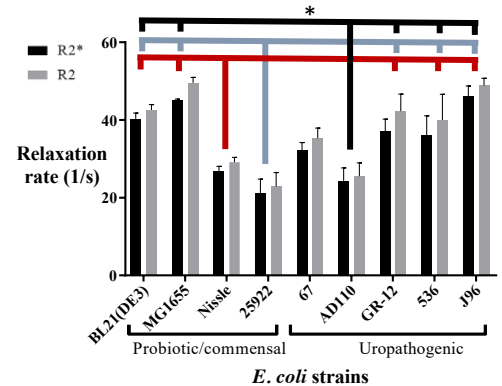


**Fig. 1. Transverse relaxation rates of commensal and uropathogenic *Escherichia coli* strains.** *E. coli* strains show high transverse relaxation rates. Bars represent mean  $\pm$  SEM ( $n=3-5$ ). One-way ANOVA and Tukey's test show that R2 and R2\* of Nissle (red line), 25922 (blue line) and AD110 (black line) are significantly lower than most other tested strains (\*  $p<0.05$ ). R1 ranged between 0.60 – 2.68 s<sup>-1</sup>.

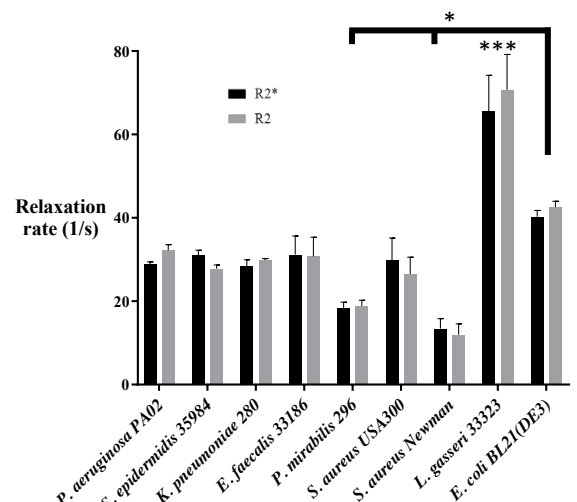
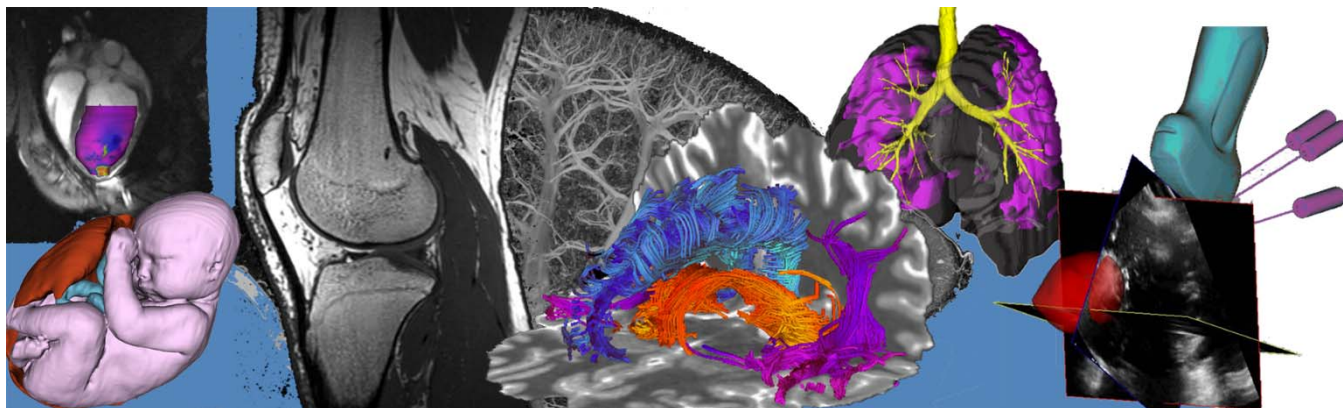


**Fig. 2. Transverse relaxation rates of various bacterial species.** Bacteria display high transverse relaxation rates. Bars show mean  $\pm$  SEM ( $n=3-5$ ). One-way ANOVA and Tukey's test show that *L. gasseri* 33323 displays significantly higher R2 and R2\* than any other species tested (\*\*\*)  $p<0.001$ . *E. coli* BL21(DE3) displays higher relaxivity than *P. mirabilis* 296 and *S. aureus* Newman (\*  $p<0.05$ ). R1 values ranged between 0.23 – 2.74 s<sup>-1</sup>.

# Poster Presentation Abstracts

## Session 4: New MRI Approaches / Magnetic Resonance Imaging



## Design Exploration for a Head and Neck Gradient Coil: Effect of Shoulder Cut-out Length on Performance

EJ Lessard<sup>1</sup>, WB Handler<sup>1</sup>, BA Chronik<sup>1</sup>

<sup>1</sup>The xMR Labs, Physics and Astronomy, University of Western Ontario, Canada.

**INTRODUCTION:** Head and neck imaging account for the majority of all diagnostic MRI scans performed worldwide. However, due to the cylindrical design of traditional compact head-only gradients the neck is situated outside of the imaging region which provides challenges in imaging the neck and cervical spine. This can be alleviated by lengthening and adding cut-outs to the gradient coil to accommodate the patient's shoulders while moving the extent of the gradient coil into the cut-out region. However, the benefits and trade-offs of adding shoulder cut-outs to the gradient coil on performance is not well explored. In this work, our objective was to perform a design study on an actively shielded shoulder cut-out design while exploring the effect of cut-out length on coil performance.

**METHODS:** Triangular element meshes were designed in, and exported from, COMSOL Multiphysics (COMSOL, Burlington, MA) for analysis in MATLAB (Mathworks, Natick, MA). The exported meshes composed of a primary surface (length = 0.55 - 0.76 m, radius = 0.22 m), a shield surface (length = 1.00 m, radius = 0.26 m) and a bore surface (length = 1.00 m, radius = 0.325 m). The cut-out height (y-direction) was held constant at 0.15 m and the cut-out length (z-direction) was varied for the control coil (no cut-out, length = 0.55 m) and three gradient coils with varying cut out lengths (7 cm (length = 0.62 m), 14 cm (length = 0.69 m), and 21 cm (length = 0.76 m). The boundary element method was implemented using custom built MATLAB software aiming for control of field uniformity and minimum wire spacing<sup>1</sup> by performing a grid search of weighting parameters. The imaging region was shifted from the isocenter by 0.07 cm and 0.14 cm (along Z) for the control and shoulder cut-out coils, respectively.

**RESULTS:** Examples of X-, Y-, and Z-gradients with shifted imaging regions are shown in **Figure 1**.

**CONCLUSIONS:** In this initial explorative design study we have demonstrated that by allowing shoulder cut-outs the imaging region can be shifted providing imaging of the cervical spine in addition to the brain with acceptable impact on system performance. Although the designs presented here provide fields suitable for imaging and have effective shielding, before a design is chosen for manufacturing there are many things that must be considered. A final design must be balanced for forces and torque within the realistic field it will be subjected to. Furthermore, the effect of cut-out height on performance parameters must be evaluated as well as broadening the design study to explore the effects of coil efficiency, imaging region size, and imaging region offset on the designs. In summary, we have performed a preliminary design study on an actively shielded shoulder cut-out head and neck gradient coil and demonstrated that regions of cut-out can be added to the gradient surface to allow a shifted imaging region which can facilitate improved imaging of the neck and cervical spine.

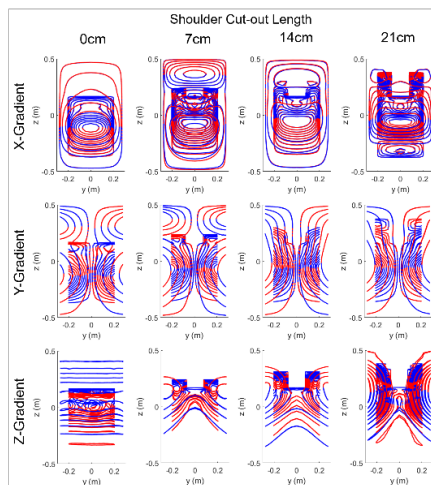


**Figure 1.** Example wire patterns for X-, Y-, and Z-gradient shoulder cut-out. Colour indicates current direction with respect to azimuthal direction. Wire patterns for illustration given for 0.10 mT/m/A

### REFERENCES:

1. CT Harris, WB Handler and BA Chronik. Electromagnet Design Allowing Explicit and Simultaneous Control of Minimum Wire Spacing and Field Uniformity. *Concepts Magn. Reson.*, 41B: 120-129 (2012)

## Gradient dB/dt Heating Measurements of Copper, Steel, and Titanium Annuli: Assessment of Measurement Repeatability, and Identification of a Potential Reference Standard

Joel Crane, Christine Wawrzyn, William B. Handler, Blaine A. Chronik

The xMR Labs, Department of Physics and Astronomy, University of Western Ontario, London ON, Canada

**INTRODUCTION:** Changes in magnetic field through time (dB/dt, measured in T/s) induce eddy currents on conductive materials, and this is of particular significance for both passive and active implantable devices (AIMDs). The purpose of this work is to develop a simple reference standard to be used for gradient-induced heating tests to verify test system operation, alongside provide data on measurement repeatability of heating in these reference objects.

**METHODS:** The gelled hydroxyethyl cellulose (HEC) phantom material was prepared in accordance with [1]. The gelled HEC serves to simulate human tissue, sharing similar conductive and thermal properties, alongside limiting internal conduction and minimizing thermal convection. Four copper annuli, two stainless-steel annuli, and two titanium annuli were measured for temperature change when subjected to gradient field exposure. All annuli had a 5-cm outer diameter with varying thickness and varying inner diameters. Two different dB/dt exposures were used: a continuous 270 Hz sinusoidal wave (dB/dt value of 42 T/s rms [root mean square]), and a continuous 1000 Hz sinusoidal wave (dB/dt value of 42 T/s). Temperature was measured by two fiber optic temperature probes (Neoptix Inc., TIC-15548A) placed in 1-mm holes on the outer edges of each annuli. The metal annuli underwent three repeated exposures, each involving a 20-second gradient exposure followed by 160-seconds of cool-down time. Two fiber optic probes collected temperature readings of the annulus during each trial, totaling six temperature readings per three trials for each condition.

**RESULTS AND DISCUSSION:** Heating is greatest when the metal annulus is oriented orthogonally to the vector of the gradient field and positioned at the radial centre of the phantom [2]. Of the 3 metals tested, the copper annuli heated up the greatest due its conductive properties (**Table 1**). A larger inner diameter, i.e., Copper Annulus #2 and #4, heated up greater than copper annuli of lesser inner diameter. The ratio of heating at 270 Hz to that at 1 kHz is geometry dependent, with the greatest difference for the annuli with the most cross-sectional area. We believe that the Copper Annulus #4 represents the best single candidate for a reference standard object for these tests, since the heating is significant across the frequency range of interest gradient dB/dt in MRI (300 to 1200 Hz [1]), allowing for temperature measurements to be made with an SNR of at least 20 across the range. The copper annulus is also practical, readily available, easy to manufacture, and low-cost.

Disk	Thickness (mm)	Inner Diameter (mm)	Outer Diameter (mm)	Mean of $\Delta T$ ( $^{\circ}\text{C}$ ) $\pm$ SE	
				(270 Hz)	(1000 Hz)
Copper Annulus #1	3.1	29.9	50.1	10.32 $\pm$ 0.10	1.79 $\pm$ 0.02
Copper Annulus #2	3.1	39.9	50.0	14.96 $\pm$ 0.15	3.27 $\pm$ 0.03
Copper Annulus #3	1.5	30.0	50.1	12.24 $\pm$ 0.12	3.49 $\pm$ 0.04
Copper Annulus #4	1.5	39.8	50.2	13.98 $\pm$ 0.25	5.79 $\pm$ 0.07
Steel Annulus #1	2.9	30.0	50.0	0.62 $\pm$ 0.03	/
Steel Annulus #2	2.9	40.0	50.0	0.50 $\pm$ 0.03	/
Titanium Annulus #1	3.1	29.8	50.2	0.34 $\pm$ 0.02	/
Titanium Annulus #2	3.1	29.8	50.1	0.28 $\pm$ 0.02	/

**Table 1:** Summary of Results and Disk Dimensions

**CONCLUSION:** The gradient-induced temperature rise of three MRI compatible metals was measured using a laboratory dB/dt exposure system. Based on the temperature rise, Copper Annulus #4 would likely be most suitable as a dB/dt heating standard across the frequency range of interest as defined in [2].

**REFERENCES:** [1] ASTM F2182-11a, 2016, 3-5. [2] ISO/TS 10974, 2018, 40-41. [3] K. E. Bannan, et al., 2013, J. Magn. Reson. Imaging 38:411-416.



## Uncertainty Analysis of Torque Measurement Methods Described in ASTM F2213-17

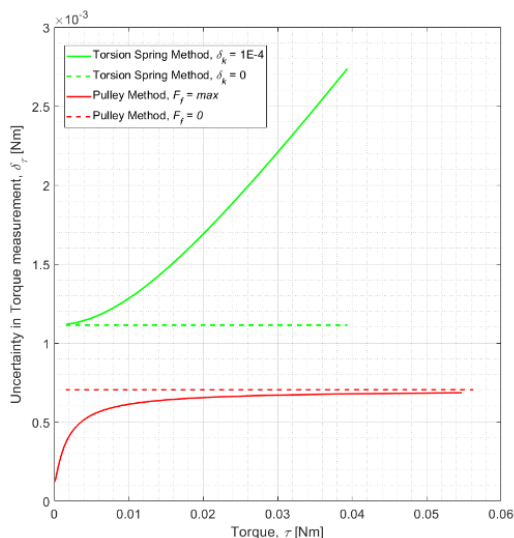
Xiao Fan Ding <sup>1</sup>, William B. Handler <sup>1</sup>, and Blaine A. Chronik <sup>1</sup>

<sup>1</sup> The xMR Labs, Department of Physics and Astronomy, University of Western Ontario, London, ON, Canada

**Introduction:** The number of people with permanent or semi-permanent medical implants has seen annual growth in parallel with the growth of MRI as a diagnostic tool not only in Canada and abroad. There is a need to know whether patients with medical implants that cannot be readily removed, can receive a scan without complications, one of which is the possibility of torque on the implant. The current test standard for measuring magnetically induced torque in medical implants is the ASTM F2213-17 [1] which lists five methods. Three of the methods are pass/fail criteria. The remaining two methods, the ones under consideration in this abstract, are the ‘torsional spring’ and the ‘pulley’ methods, which aim to measure a quantitative torque value. The purpose of this work is to identify and compare the measurement uncertainties in the methods published by ASTM International, and thereby aid in the selection of the appropriate method for any device or system.

**Methods:** In the torsional spring method, there are errors in reading the angular deflection, likely the dominant source of error, and in calibrating the torsion spring constant. In the pulley method, there are errors in the force sensor and measurement of the apparatus radius. There is also an error in the torque required to overcome static friction. To find the error in static friction, measurements are made using the pulley method apparatus. A lightweight thread was extended from the apparatus and placed over a secondary pulley and attached to a hanging mass. The surface was divided into 30° sections. The mass suspended was incrementally increased until the weight was enough to set each section of the surface in motion. The method of changing the mass was to place staples into a small basket. Staples were chosen because individually, the mass is insignificant, but multiple staples have a noticeable change in torque in a tangible quantity allowing for reproducibility. For a function,  $x$ , such that  $x = f(u_1, u_2, \dots, u_n)$ , the uncertainty,  $\delta_x$ , based on known sources of error is propagated by,  $\delta_x^2 = \sum_{i=1}^n \delta_{u_i}^2 \left(\frac{\partial x}{\partial u_i}\right)^2$ . This equation is true when all independent variables are uncorrelated. An expression for measurement uncertainty of each method can be calculated and propagated to see how uncertainty changes with torque.

**Results:** The standard deviation of masses required to set the surface in motion came to 1.394 g or a torque of 0.693 mNm.  $\delta_{F_s} = 0.693$  mNm was used in the error propagation of torque and measurement uncertainty starting from the smallest observed torque, 1.574 mNm, as shown in **Figure 1**. The calibration report of the force sensor used listed a capacity of 1.11 N and an uncertainty of 1.668E-3 N. Measurements using a digital caliper yielded a radius apparatus of  $50.72 \pm 0.01$  mm. The torsional spring method required a spring constant capable of measuring 1° intervals which yielded  $\delta_\theta = 0.5^\circ$ . For  $\tau = 1.574$  mNm,  $k = 1.574$  mNm with an arbitrarily chosen  $\delta_k$ .



**Conclusions:** As was anticipated, the dominant source of error in the torsional spring method was the instrument uncertainty of the protractor. The dominant source of error in the pulley method was the error due to static friction. For comparable measurements of torque, the pulley method, while considering all sources of error, fared better than the torsion spring method.

### References:

[1] ASTM International, “F2213-17 Standard Test Method for Measurement of Magnetically Induced Torque on Medical Devices in the Magnetic Resonance Environment”

**Figure 1:** Propagation of errors for ASTM methods, starting from 1.574 mNm until a deflection of 25° for the torsional spring method and 1.11 N force sensor reading for the pulley method.

## Evaluation of blood clot MR relaxivity and susceptibility preservation using room temperature, refrigerator and cryogenic storage *in vitro* at 3T

Spencer D. Christiansen,<sup>1,2</sup> Junmin Liu,<sup>1</sup> Michael B. Boffa,<sup>3</sup> and Maria Drangova<sup>1,2</sup>

<sup>1</sup>Robarts Research Institute, <sup>2</sup>Dept. of Medical Biophysics, <sup>3</sup>Dept. of Biochemistry  
Western University, London, Ontario, Canada

**Introduction:** Thrombus (blood clot) MR imaging has the potential to provide valuable information towards the treatment of acute stroke including predicating thrombus composition,<sup>1</sup> etiology<sup>2</sup> and treatment response,<sup>3</sup> however technique validation is challenging to perform *in vivo*. Mechanical thrombectomy therapy provides an opportunity to perform imaging studies of retrieved stroke thrombi without patient burden. However, delays between thrombus retrieval and scanning may lead to altered MR characteristics. To assess the scope of these effects, we investigated whether *in vitro* clot  $R_2^*$  and quantitative susceptibility (QS) values, previously shown indicators of clot composition and age,<sup>4</sup> change over periods of up to 48 hours using simple storage strategies, and whether cryogenic freezing is a viable alternative for preserving thrombus imaging characteristics.

**Methods: Phantom-** Porcine whole blood was used to create blood clots with a Chandler loop device.<sup>5</sup> Samples were spun in 3 mm tubing at 30 rpm for 90 min, removed and deoxygenated under vacuum before transfer into plasma-filled tubes inside an agar phantom. The phantom was scanned and clots were then divided into 5 storage groups (G1-5); G1: room temperature, G2: refrigerator, G3: frozen in dimethyl sulfoxide (DMSO), G4: frozen in vacuumed DMSO, G5: frozen in vacuumed DMSO and thawed in saline bath. G1 and G2 were scanned after 24 and 48 hours of storage, while G3-5 were frozen at -80 °C for 40 h and then scanned immediately after thawing.

**Imaging-** Scans were performed at 3T with a 32-channel receive head-coil using a custom dual echo-train 3D GRE sequence ( $TE1/\Delta TE/TE5 = 3.20/1.46/9.04$  ms,  $TE6/\Delta TE/TE10 = 16.75/7.15/45.35$  ms, TR: 47.6 ms, resolution:  $0.94 \times 0.94 \times 1$  mm<sup>3</sup>, matrix:  $192 \times 192 \times 50$ , BW: 142.86 kHz, flip angle: 10°, scan time = 7 min 41 sec). A co-registered steady-state free precession (SSFP) scan with identical resolution was also acquired.

**Image post-processing-** Channel-combined complex data were processed using the non-iterative B0-NICE algorithm<sup>6</sup> to calculate  $R_2^*$  maps and the MEDI QS algorithm<sup>7</sup> to calculate QS maps.

**Analysis-** Clots were segmented using SSFP images and ROIs were used to calculate  $R_2^*$  and QS values.

**Results:** Clot  $R_2^*$  and QS values throughout storage are shown for G1-2 and G3-5 in Figs 1 and 2, respectively; mean group changes are listed in Table 1.  $R_2^*$  and QS values decreased slightly in room-temperature clots (G1) after 24h but increased by 48h, while in refrigerated clots (G2)  $R_2^*$  and QS dropped within 24h and remained low at 48h. Clot  $R_2^*$  and QS values decreased in each of G3-5 after freezing; the smallest decrease occurred in G4, which was still larger than the changes observed in G1 after 24h. Decreasing  $R_2^*$  and QS is likely due to red blood cell (RBC) hemoglobin re-oxygenation;<sup>8</sup> G4 decreased the least suggesting DMSO vacuuming limited re-oxygenation. However,  $R_2^*$  and QS values still fell in this group compared to baseline; RBC lysis may be responsible.

**Conclusions:** Refrigeration of deoxygenated clots leads to large decreases in  $R_2^*$  and QS within 24 hours, while room temperature storage provides moderate preservation up to 24 hours. Tested cryogenic strategies were less successful than room temperature storage, but may prove superior if RBC lysis is mitigated; further investigation is ongoing.

**References:** [1] Kim, S et al. Am J Neuroradiol 2015. [2] Yamamoto, N et al. Stroke 2015. [3] Bourcier, R et al. J Neuroradiol 2017 [4] Christiansen, S et al. IMNO 2018 [5] Robbie, L et al. Thromb Haemost 1997. [6] Liu, J et al. Magn Reson Med 2015. [7] Liu, J et al. NeuroImage 2012. [8] Jain, V et al. Magn Reson Med 2012.

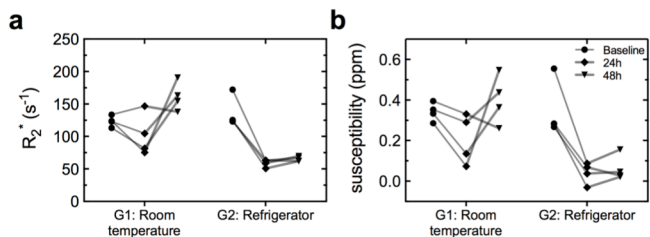


**Fig. 1:**  $R_2^*$  and QS values of G1&2 clots throughout storage.

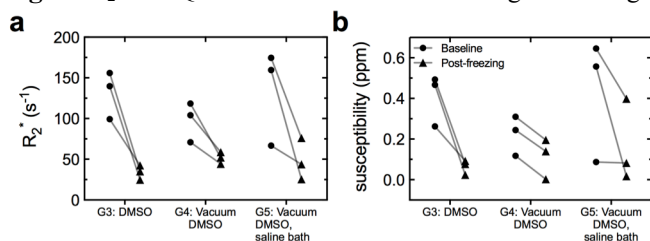


**Fig. 2:**  $R_2^*$  and QS values of G3-5 clots throughout storage.

**Table 1:** Mean group  $R_2^*$  and QS change from baseline

Storage group (n)	$\Delta R_2^*$ (s <sup>-1</sup> )	$\Delta$ QS (ppm)	Imaging time post baseline
G1 (4)	-21 ± 26	-0.13 ± 0.08	24 h
	38 ± 26	0.06 ± 0.16	48 h
G2 (4)	-77 ± 22	-0.31 ± 0.12	24 h
	-71 ± 23	-0.28 ± 0.08	48 h
G3 (3)	-98 ± 35	-0.34 ± 0.15	post-freezing
G4 (3)	-46 ± 20	-0.11 ± 0.01	post-freezing
G5 (3)	-85 ± 57	-0.26 ± 0.27	post-freezing

**$^{23}\text{Na}$  MRI: Measurement of point-spread functions in resolution phantoms with 3D radial projections**Paul Polak<sup>1,2</sup>, Rolf Schulte<sup>3</sup>, and Michael Noseworthy<sup>1,2</sup><sup>1</sup>School of Biomedical Engineering, McMaster University, Hamilton, ON, Canada,<sup>2</sup>Imaging Research Centre, St. Joseph's Healthcare, Hamilton, ON, Canada, <sup>3</sup>GE Global Research, Munich, Germany

**Introduction:** In vivo  $^{23}\text{Na}$  MRI is desirable due to sodium's essential role human metabolism,<sup>1,2</sup> but its acquisition suffers from many inherent technical challenges.<sup>3</sup> Ultrashort echo time (UTE) sequences are preferred in order to capture the signal from the short T2 times, and among these is 3D radial projection (3DRP) imaging.<sup>4</sup> Brain  $^{23}\text{Na}$  concentrations range from 15 to 150 mM, thereby necessitating the imaging and reconstruction methods to be sensitive to a broad signal range. We present here quantitative measurements of point-spread functions (PSFs) for saline concentrations in a resolution phantom with 3DRP pulse sequences.

**Methods:** The experiments were conducted using a GE 3T MR750 using a custom built birdcage head coil (33.7 MHz). A phantom (Figure 1a) was filled with different concentrations of NaCl and distilled water (150, 60, and 30 mM), and a single healthy volunteer was scanned in order to qualitatively assess the performance for neuroimaging.

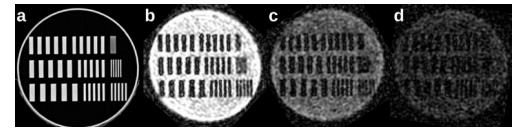


Figure 1: (a): CT image of phantom, split into 9 regions with negative and positive contrasts ranging from 1-9 mm. (b-d):  $^{23}\text{Na}$  MRI images for saline phantom windowed identically for concentrations of 150 mM (b), 60 mM (c), and 30 mM (d).

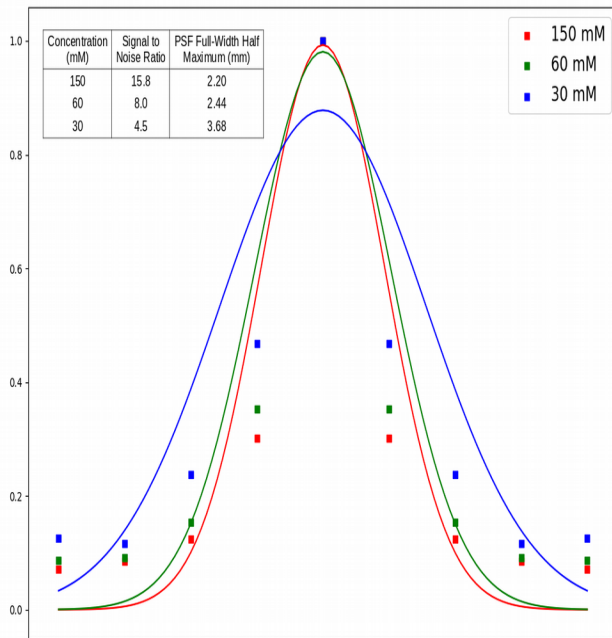


Figure 2: Calculated PSFs from the 3 concentrations. Measured data (squares) normalized before being fitted with Gaussian functions (solid lines). R-squared values for fits were 0.78, 0.77, 0.70 respectively for 150, 60, and 30 mM phantom data. The upper-left corner has SNR and FWHM data presented as an embedded table.

phantom, which is akin to unbound sodium in vivo – bound intracellular sodium is of more use diagnostically, although the techniques sensitive to it exclusively cause a further signal reduction.<sup>6,7</sup> Low signal in the in vivo image (Figure 5) is in evidence by the lower  $^{23}\text{Na}$  concentrations in the white and grey matter contributing to reduced image quality as compared to cerebrospinal fluid. Compressed sensing techniques<sup>8</sup> provide a potential opportunity to increase signal without an increase in scan time. This work examined the performance of a 3DRP UTE sequence in the context of varying levels of  $^{23}\text{Na}$  concentration in a resolution phantom, and demonstrate some of the difficulties with sodium imaging. Future research will examine the performance of different pulse sequence trajectories and reconstruction techniques with this phantom.

References: 1. Rose AM, Valdes R. Understanding the sodium pump and its relevance to disease. Clin Chem 1994;40:1674–1685. 2. Skout JC, Esmann M. The Na, K-ATPase. J Bioenerg Biomembr 1992;24:249–261. 3. Madelin G et al, Sodium MRI: Methods and applications. Prog Nucl Magn Reson Spectrosc 2014;79:14–47. 4. Nagel AM et al, Sodium MRI using a density-adapted 3D radial acquisition technique. Magn Reson Med 2009;62:1565–1573. 5. Martin Uecker et al, Annual Meeting ISMRM, Toronto 2015, In Proc. Intl. Soc. Mag. Reson. Med. 23:2486. 6. Ooms KJ et al,  $^{23}\text{Na}$  TQF NMR imaging for the study of spinal disc tissue. J Magn Reson. 2008 Nov;195(1):112–115. 7. Stobbe R, Beaulieu C. In vivo sodium magnetic resonance imaging of the human brain using soft inversion recovery fluid attenuation. Magn Reson Med. 2005;54(5):1305–1310. 8. Lustig M et al, Sparse MRI: The application of compressed sensing for rapid MR imaging. Magn Reson Med. 2007 Dec;58(6):1182–95.

3DRP UTE gradients were designed to sample k-space at  $1/r$ , with 16380 spokes, TR/TE of 30/0.5 ms, FOV of 240 mm, and acquisition time of 8:11. 3D polar coordinate angles were calculated from points distributed on a sphere. Reconstructions used the non-uniform fast fourier transform from the Berkeley Advanced Reconstruction Toolbox,<sup>5</sup> and these were converted into 160x160x160 NIFTI files for analysis by Mango (<http://ric.uthscsa.edu/mango/>). The PSFs were calculated under the assumption they were Gaussian distributions. Signal to noise ratios (SNR) were also calculated with Mango.

**Results:** Figure 1b-d has representative slices from the 3 phantom concentrations. Images are progressively noisier as the concentration of saline decreases in the phantom. Figure 2 displays the calculated PSF data and fitted Gaussian functions for the phantom concentrations. SNR and full-width half maximum (FWHM) results can also be found in Figure 2. Figure 3 displays a representative sagittal slice from the volunteer.

**Conclusions:** In vivo  $^{23}\text{Na}$  MRI is challenging because of the scarcity of available signal. As the signal is proportional to the concentration of  $^{23}\text{Na}$ , and the performance of the imaging system is correlated with signal (Figure 2), it is expected that any further reduction of signal will negatively impact image resolution. This work examined performance in a saline

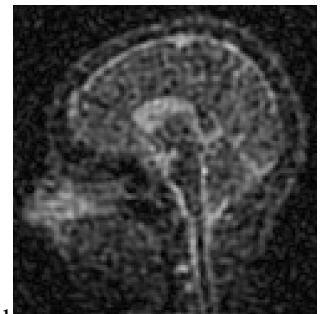


Figure 3: Representative  $^{23}\text{Na}$  image from a healthy human volunteer. Reconstruction applied with a moderate amount of l2-normalization.

## RF heating of an intracranial pressure sensor in a 64 MHz head-only RF coil: a simulation study

S Batebi<sup>1</sup>, BA Chronik<sup>1</sup>

<sup>1</sup>The xMR Labs, Physics and Astronomy, University of Western Ontario, Canada.

**Introduction:** Heating of implanted medical devices is a well-known hazard in MRI. A first stage in the evaluation of any device system for RF heating is to determine, via computer simulations or other means, what the worst-case configuration(s) of the device(s) are. One class of device that is particularly difficult to evaluate is a device that has only a portion of a lead implanted, and the remainder outside the body. In this study, we evaluated a simplified device which represents an intracranial pressure sensor device, in which a catheter would be inserted into the cranium while the remainder of the catheter and device would be outside the skull, possibly under the skin. The simple question we sought to answer was: for a fixed lead length and exposure to a 64 MHz head-only RF coil, what the worst-case configuration is?

**Methods:** The head was modeled as a three-component spherical structure. The brain was approximated as a uniform sphere of 80 mm radius, mass density of 1050 kg/m<sup>3</sup>, electrical conductivity of 0.72 S/m, and relative permittivity of 116. The layer surrounding the brain was “bone” with thickness of 5 mm, mass density of 1180 kg/m<sup>3</sup>, electric conductivity of 0.082 S/m, relative permittivity of 16.7. The outermost layer was “skin” with thickness of 3 mm, mass density of 1109 kg/m<sup>3</sup>, electric conductivity of 0.436 S/m, relative permittivity of 92. The device was modeled as a 0.75 mm diameter PEC that had a total fixed length of 200 mm with insulation thickness of 0.5 mm, exposed end of 2 mm, relative permittivity of 3 and was positioned with a variable amount of the lead within the brain (6 different cases, with between 2 mm and 160 mm within the brain) and the remaining portion running under the skin but outside the skull (bone). The RF coil was modeled as a shielded, Circularly-polarized head-only 64 MHz cylindrical RF coil, with 16 equally spaced rungs, radius of 145 mm, and length of 384mm. The diameter of shield was 400 mm with a length of 500 mm. The current in the rungs was set such that B<sub>1</sub> in the center volume of the brain would be 1 μT when no device was present.

**Results:** The results for 0.1 g spatial averaged SAR along aYZ slice at the location of the wire is shown in Figure 1. As expected, the heating increased (in all regions) as more of the wire was positioned along the outside of the skull, underneath the skin.

**Conclusion:** This simulation study suggests that for devices with a portion of the lead within the brain and the other portion implanted outside the skull but under the skin, the heating is highest when the amount within the brain is minimized. This can help to guide more complicated simulations and possibly guide the simulation parameter space, enabling more simulation efforts to be directed to other parameters where the effects are less clear. Expansion of this study to 128 MHz (3 T) head-only RF coils is also an obvious avenue for future work.

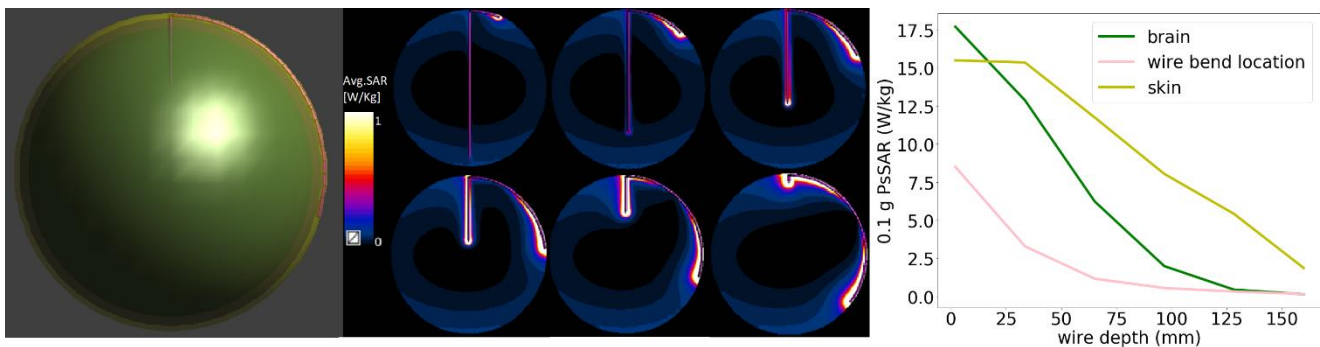


**Figure 1:** Left: The schematic of the simulation with brain, skull, skin, and device. Middle: Spatial Average SAR over 0.1 g of tissue for different length of the lead in the brain. The z-direction is vertical. Right: The Peak spatial averaged SAR over 0.1 g of tissue at three different regions (tip of the wire in the brain, the end of the wire under the skin, and the wire bend location).

## Metabolite Levels Differ in Contact and Non-Contact Sport Female Varsity Athletes

Amy Schranz<sup>1,2</sup>, Gregory A. Dekaban<sup>1</sup>, Lisa Fischer<sup>2</sup>, Kevin Blackney<sup>1</sup>, Christy Barreira<sup>1</sup>, Timothy J. Doherty<sup>2</sup>, Douglas D. Fraser<sup>3</sup>, Arthur Brown<sup>1,2</sup>, Jeff Holmes<sup>2</sup>, Ravi S. Menon<sup>1,2</sup>, and Robert Bartha<sup>1,2</sup>

1. Robarts Research Institute 2. University of Western Ontario 3. London Health Sciences Centre

**Introduction:** Athletes participating in contact sports have a high risk of sustaining a concussion, which can lead to structural and metabolic changes in the brain. Our group previously found reduced glutamine levels in the prefrontal white matter of female varsity rugby athletes at the end of a sports season and after concussion.<sup>[1]</sup> However, this study was limited by the absence of a non-contact control group to rule out exercise as a cause for the observed metabolite level change. Therefore, the purpose of this study was to quantify changes in brain metabolite levels in female athletes engaged in non-contact sports over the course of a sports season to compare to female athletes who participate in contact sports. It was hypothesized that MRI brain metabolite levels would not significantly change in the non-contact group over the course of a season.

**Methods:** All participants in this study were athletes between the ages of 16 and 22 recruited from women's varsity rugby, rowing and swim teams. Non-contact (rowers and swimmers, n=31) athletes were scanned at the beginning of the season (in-season) and followed up at the end of the season (off-season) using a Siemens 3T MRI scanner (Erlangen, Germany) using the identical methodology to that previously used for the contact (rugby, n=54) group.<sup>[1]</sup> <sup>1</sup>H magnetic resonance spectroscopy was acquired (TE/TR=135/2000 ms, dwell time = 833  $\mu$ s, number of points = 1024, number of averages suppressed/unsuppressed = 192/8) in the left prefrontal white matter. Spectra were lineshape corrected by QUECC<sup>[3]</sup> then fitted in the time domain using a Levenberg-Marquardt minimization routine, using a prior knowledge template that models the metabolite lineshapes acquired from *in vitro* spectra obtained from aqueous solutions of all metabolites at pH=7.0 prior to the study.<sup>[2]</sup> All data analysis was performed using GraphPad Prism version 7.0 for Mac OS X (San Diego, CA). A repeated-measures two-way ANOVA,  $\alpha = 0.05$ , was used to compare metabolite levels between the in-season and off-season time points between the rowers and swimmers prior to combining both teams into the non-contact group. Then a repeated-measures two-way ANOVA,  $\alpha = 0.05$ , was used to analyze the contact and non-contact groups comparing the in-season and off-season values.

**Results:** No significant differences were found between the rowers and swimmers so these data were combined into a single non-contact group. Furthermore, there were no metabolite levels including glutamine that significantly changed between the in-season and off-season in the non-contact athletes. However, significant differences between the contact and non-contact groups ( $p < 0.05$ ) were observed for *N*-acetyl aspartate, creatine, *myo*-inositol, glutamate and glutamine. Additionally, a significant interaction ( $p = 0.019$ ) was observed with *myo*-inositol. Further analysis revealed a significant difference ( $p = 0.014$ ) between the change in *myo*-inositol from in-season to off-season between the contact and non-contact athletes.

**Discussion and Conclusion:** The current study did not find any change in glutamine levels in non-contact athletes over a season. Therefore, the previously reported reduced glutamine levels in the prefrontal white matter of female varsity rugby athletes at the end of a sports season<sup>[1]</sup> is unlikely due to an exercise effect since this group of non-contact athletes were matched for activity level. Ruling out exercise, the previous findings in contact-athletes could be interpreted to be the result of concussion history or cumulative sub-concussive impacts over the course of the season. Reduced *N*-acetyl aspartate and glutamate in the contact group are in line with previous reports of reduced NAA/Cr in non-concussed female hockey players<sup>[4]</sup> and reduced glutamate levels in former athletes with a history of concussion.<sup>[5]</sup> Future work includes obtaining data from a non-athlete group to further aid in interpretation of these results. With the comparison of a sedentary group to our non-contact and contact athletes, it may be possible to further elucidate the benefits of activity level on brain biochemistry, as well as the potential negative effects of concussion history and cumulative impacts from contact sports.

[1] Schranz AL *et al.* Hum Brain Mapp. 2018;39(4):1489-1499. [2] Bartha R *et al.* NMR Biomed. 1999;12: 205-216. [3] Bartha R *et al.* Magn Reson Med. 2000;44: 641-645. [4] Chamard E *et al.* Neurosurg. Focus. 2012;33(E4): 1-7. [5] De Beaumont L *et al.* BMC Neurol. 2013;13:109. [6] Tremblay S *et al.* Cereb. Cortex 2012;23

## A study of flip-angle effects in simultaneous quantification of fat fraction, susceptibility and R2\*

Junmin Liu,<sup>1</sup> Spencer Christiansen,<sup>1,2</sup> and Maria Drangova<sup>1,2</sup>

<sup>1</sup>Imaging Research Laboratories, Robarts Research Institute, Schulich School of Medicine & Dentistry, University of Western Ontario, London, Ontario, Canada

<sup>2</sup>Department of Medical Biophysics, Schulich School of Medicine & Dentistry, University of Western Ontario, London, Ontario, Canada

**INTRODUCTION:** Simultaneous quantification of fat (e.g., proton density fat-fraction (FF)) and iron levels (e.g., R2\* and the quantitative susceptibility mapping (QSM)-derived tissue susceptibility ( $\chi$ )) in the human body from a single multi-echo gradient echo (mGRE) scan has potential to become highly valuable in the clinic. A few mGRE-based Dixon-QSM techniques have been developed to jointly estimate B0 inhomogeneity, FF, R2\* and  $\chi$ , however effect of flip angle (FA) has only been evaluated with respect to the accuracy of the FF and not  $\chi$ .<sup>1</sup> To mitigate the T1 effect on FF accuracy, the typical FA prescribed in most multi-echo Dixon protocols ranges from 3° to 5°. Meanwhile, the accuracy of  $\chi$  estimation, has only been evaluated at larger FAs, *i.e.* ranging from 15° to 30°. In this work, we performed a systematic phantom study to investigate FA effects in the quantification of FF,  $\chi$  and R2\* from a single mGRE acquisition with echo times (TEs) optimized to quantify both fat-water chemical shift and  $\chi$  effects.

**METHODS: Phantom construction:** A 14 cm diameter cylindrical phantom containing 13 vials (polystyrene; 1 cm diameter, 5 mL volume) was constructed: one filled with water, one with peanut oil, six with oil-water emulsions of varying true fat volume percentages (three each of 10 and 20 vol%) stabilized with agar and five with aqueous Gadolinium (Gd) solutions of 0.5, 1, 1.5, 2 and 2.5% of Magnevist (0.5 mmol Gd), yielding susceptibility shifts of 0.81, 1.63, 2.45, 3.26 and 4.08 ppm at room temperature. All vials were embedded in agar gel prior to scanning.

**Protocol and data acquisition:** A dual-echo-train bipolar mGRE protocol was developed on a 3 T scanner (Siemens Prisma) to cover the whole head in approximately 5 minutes.<sup>2</sup> The phantom was scanned in the coronal plane with five different FAs (1°, 3°, 5°, 8° and 15°).

**Processing and analysis:** A detailed description of the processing algorithm was presented in a previous publication.<sup>2</sup> Regions of interest (ROIs) were manually drawn on the 1<sup>st</sup> echo magnitude image for each vial at the central coronal slice; mean and standard deviation over each ROI (~ 36 pixels) were calculated for the FF,  $\chi$  and R2\* maps; the water vial was chosen as the reference for the susceptibility value.

**RESULTS:** Results from the phantom experiments show that the FF of the oil-water emulsions was overestimated with FA = 15° (mean estimated FF is 19% for the three 10 vol% vials and 33% for the 20 vol% vials). The results also show that in the presence of Gd, fat is artificially detected, with values as high as 5% at FA = 5°. Further, the results show that estimated  $\chi$  was most sensitive to FA in vials with Gd concentration >1.0%; in these vials estimated  $\chi$  was lower than expected, and this effect increased/decreased with higher FA. As expected, the results show that both FF and  $\chi$  affect R2\*, with a decrease in estimated R2\* with increasing FA.

**DISCUSSION:** When using a small FA (< 5°) in the presence of fat and high Gd concentration, both FF and  $\chi$  will be erroneously calculated due to FA effects. When a FA = 8° is used, fat will not appear artifactually in FF maps where Gd content is high and will suffer an overestimation of FF of approximately 7%. At the highest FA (15°) T1 correction for FF estimation should be applied as severe FF overestimation occurs (12%). Therefore, our phantom results suggest that a FA of 8° is an optimal tradeoff, but future work with *in vivo* data is required.

**CONCLUSION:** A single mGRE scan has the potential to accurately estimate FF,  $\chi$  and R2\* if FA-dependent biases are understood and accounted for.

**References:** 1. Liu CY, McKenzie CA, Yu H, Brittain JH, Reeder SB. Fat quantification with IDEAL gradient echo imaging: correction of bias from T1 and noise. *Magn Reson Med* 2007;58(2):354-364.

2. Liu J, Christiansen SD, Drangova M. Single multi-echo GRE acquisition with short and long echo spacing for simultaneous quantitative mapping of fat fraction, B0 inhomogeneity, and susceptibility. *Neuroimage* 2018;172:703-717.

## Comparison of Robotically Mapped and Simulated RF Fields in 64 and 128 MHz Medical Implant Test Systems

Krzysztof Wawrzyn, Jack Hendriks, Dereck Gignac, William B. Handler, Blaine A. Chronik  
The xMR Labs, Department of Physics and Astronomy, Western University, London ON, Canada

**Introduction:** Automated robotic mapping of RF exposure in device test platforms is of great value within an ISO 17025-compliant test facility for both verification and validation processes<sup>[1-2]</sup>. Establishing and evaluating consistence between measured and simulated fields is critical when either is used as part of a medical device testing procedure. In this study, we show results from proof-of-concept work that demonstrates a procedure for the use of a custom-built, semi-automated robotic positioning system to map electromagnetic fields within and around RF exposure systems and quantitatively compare the results against detailed simulation of those same systems.

**Methods:** All measurements were performed on two different RF bench top exposure systems, commercially available as “Medical Implant Testing Systems”, or MITS 1.5 and 3.0, corresponding to frequencies of 64 and 128 MHz<sup>[3]</sup>. The RF exposure parameters for the MITS 1.5 and 3.0 were (respectively): pulse type = sinc $2\pi$ , duty cycle = 40 %, pulse repetition rate = 1 kHz, polarization = circular 270 & 90 °, frequency = 63.8 & 127.7 MHz, input power = 50 dBm. All field measurements were obtained independently with either a calibrated E-field (EX3DV4) or H-field (H3DV7) RMS probe (EASY4MRI standalone data acquisition system<sup>[3]</sup>). The field probes and data collection were fully integrated into a custom built automated robotics system. A 3-axis stepper motor driven gantry robotic field mapping system built in-house was used to gather data. Data collection was taken at points in the unloaded MITS bore at constant spatial increments (3.0 cm) along all directions. Labview was used to pursue arbitrary motion objectives and integration with the data acquisition system for data collection. Finite difference time domain (FDTD) computations were carried out using commercially available EMPro 3D EM simulation software<sup>[4]</sup>. The model was based on the geometry of the physical coils, without lumped elements, using 48 generic ports with sinusoidal excitation at corresponding frequencies. The phase of the signal feeding the source was equal to its azimuthal position and the ports at the same azimuthal position in the two rings were 180-degree out of phase. The simulated field was normalized using a scaling factor determined from a fixed reference H-field location. MATLAB was used to linearly interpolate 3D data onto a 1 mm grid and measured data was compared to simulated data using a linear regression model.

**Results and Discussion:** Figure 1 shows a 2D profile of collected measured and simulated data for MITS 3.0, with percent difference of 4 %. To better quantify the variation of measured to simulated values, a linear regression fit was applied. Reported R-squared values for all cases range from 0.83 to 0.97. Lower R-squared values are associated higher variation and may be due to uncertainties in systematic measurement and inaccuracies in the simulation model. Future work will (1) investigate the effect of correcting the correlation with a rigid body transform (2) analyze the accuracy of this method using uncertainty propagation and budgeting, (3) optimize the workflow, (4) compare mapped SAR values within an ASTM phantom<sup>[5]</sup>, and (5) validate the methods against those described in ISO DTS10974<sup>[2]</sup>.

**Conclusion:** In this work, we have presented a protocol and results from work showing that a semi-automated robotic system can effectively operate within the complicated EM environment of the RF exposure platforms with good agreement between simulated and measured results.

**Acknowledgements:** This work was funded by NSERC, Ontario Research Fund, and the Canadian Foundation for Innovation.

**References:** [1] ISO/IEC 17025:2017 [2] ISO/TS 10974:2018 [3] ZMT/Spag, Zurich, Switzerland [4] Keysight, Santa Rosa, CA [5] ASTM F2182-11a.

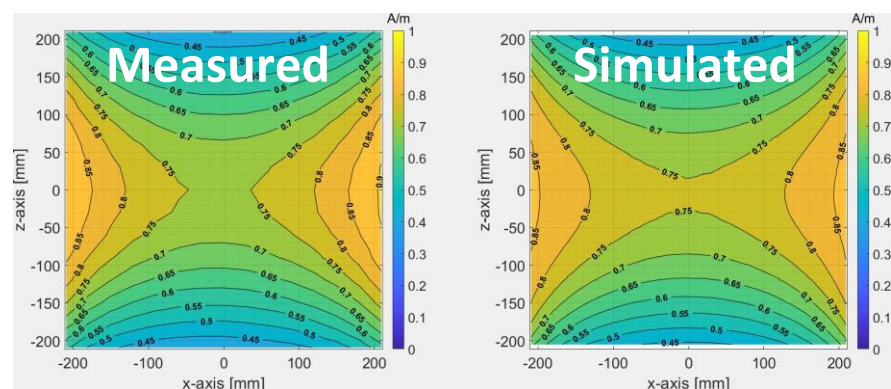


**Figure 1:** Representative MITS 3.0 2D planes for XZ-axis showing data collected at the geometric coil isocenter in air ( $Z$ -axis = 0 cm). Measured (left) and scaled simulated (right) total vector magnitude H-field (RMS).

## Design and initial evaluation of a 64 MHz RF head coil for testing of implanted medical devices

K. J. Davieau<sup>1</sup>, A. Attaran<sup>1</sup>, B. A. Chronik<sup>1</sup>

<sup>1</sup>The xMR Labs, Department of Physics and Astronomy, Western University, London, Ontario, Canada.

**INTRODUCTION:** Testing of active implantable medical devices (AIMDs) is guided by the requirements described in ISO 10974:2018(E) [1]. Interactions between AIMDs and the radiofrequency (RF) fields of the MRI system are of paramount importance, and the most common RF environment for testing is that of a whole-body transmit (TX) RF coil. Whole-body-size RF exposure systems designed for testing of devices are commercially available [2]; however, there is not a validated head-only RF exposure system available for either 64 or 128 MHz, even though head-only TX/RCV coils are available on MRI scanners. Not all devices require separate testing within a head-only exposure system; however, devices implanted in the head and neck experience a significantly different local electric field environment when the patient is in a head-only transmit coil as compared to a whole-body coil. To adequately evaluate the safety of these devices in that environment, head-only RF exposure systems are needed. In this abstract we summarize our initial work in the development and validation of a head-only 64 MHz RF exposure system for testing of implanted medical devices.

**METHODS:** The RF transmit head coil was designed to be like those currently used in 1.5 T clinical systems. The coil was a high-pass, 14.5 cm radius, 16-rung birdcage coil 36.8 cm in length. The distributed model for the birdcage coil was designed in EMPro (EMPro, Keysight Technologies) and simulated in an ADS EM-cosimulation (ADS, Keysight Technologies) to determine the capacitor values required for resonance. The S-parameter was extracted from the simulation and was used for tuning the elements to resonate at 64 MHz center frequency and matching to 50  $\Omega$ . The 3-D step file for the birdcage coil was implemented in SolidWorks (SolidWorks, Dassault Systèmes) for use in FDTD simulations. The coil was fabricated on a copper clad G10 sheet and wrapped to form a cylinder. Capacitor values determined from the simulations were applied to the coil with additional variable tuning capacitors applied in a parallel-to-series configuration at the ports. A built-in house 3D E-field probe is going to be used to measure the electric field [3]. A directional coupler, was used to monitor the signal generated from signal generator. This is followed by a power splitter to divide the signal power to equal half for the I and Q ports. A 90 degrees phase shifter was added to the Q port to generate a circularly polarized field. The schematic and experimental diagram for the configuration is shown in **Figure 1**.

**RESULTS and Discussion:** The simulated results for x, y, and z components of the E-field along a XZ slice at  $y = 0$  show the field measurements for an ideal case where the current was forced through each rung. The E-field was shown to decrease towards the center of the coil and increase towards the rungs of the coil. When 20 mA currents was applied to the rungs of the coil, the maximum recorded E-field in the simulations was 16.20 V/m closest to the rung. At the time of writing, after using correction variable capacitors for tuning, matching and isolation, empty coil S-parameter measurement results indicated a return loss of better than -27 dB and -12 dB for port one and two while isolation was better than -8 dB.

**CONCLUSION:** Verified and validated head-only RF exposure systems are needed to allow for testing of implantable medical devices per the requirements of ISO 10974, and this abstract marks our initial efforts in this direction. The coil described here is not intended for MRI or imaging of any kind, but is part of a dedicated effort to establish improved test platforms for evaluation of implanted devices.

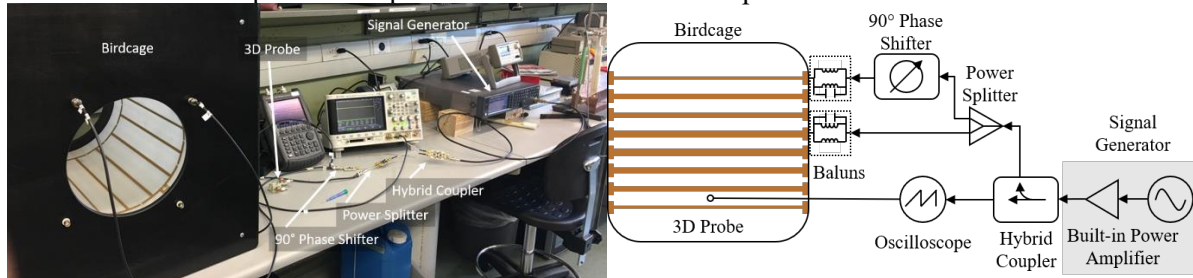


**Figure 1.** Schematic diagram for the experimental setup of the RF transmit head coil.

### REFERENCES:

1. ISO 10974:2018(E), Assessment of the safety of magnetic resonance imaging for patients with an active implantable medical device, ISO International Organization of Standardization, Switzerland, ISO/TC 150/SC 6(2), 2018, [www.iso.org](http://www.iso.org)
2. Medical Implant Test Systems, Zurich MedTech AG, Zurich, Switzerland
3. Attaran A, Handler W B, Wawrzyn K, Menon R S, and Chronik B A. Reliable RF B/E-Field Probes for Time Domain Monitoring of EM Exposure During Medical Device Testing. IEEE Transactions on Antennas and Propagation, vol. 65, no. 9, pp. 4815-4823, Sep. 2017.



## Evaluation of Diffusion MRI Fibre Reconstruction with a 3D Printed Phantom

Tristan K. Kuehn, Farah N. Mushtaha, John Moore, Corey A. Baron, Ali R. Khan  
*Robarts Research Institute, Western University, London, Canada*

**Introduction:** Diffusion MRI (dMRI) models of brain microstructure are hard to validate because there is no “ground truth” for comparison. We use a phantom produced using fused deposition modeling with a composite material (Poro-Lay) made of an elastomer and PVA. The PVA dissolves in water, leaving anisotropic pores that mimic diffusion characteristics of axons.<sup>1</sup> Here, we investigate the ability of constrained spherical deconvolution (CSD) to describe pores in Poro-Lay phantoms from dMRI scans with different numbers of acquisitions.

**Methods:** Four cylindrical phantoms (radius 11 mm) were 3D printed with 100  $\mu\text{m}$  layers of parallel lines with alternating orientations. The crossing angles were 0°, 30°, 60°, and 90°. The phantoms were immersed in water for 168 hrs then imaged in a test tube with distilled water. Diffusion MRI was implemented at 9.4 T using 0, 60 and 120 directions at  $b=0$ , 1000, and 2000  $\text{s}/\text{mm}^2$ , respectively.

MRtrix was used to compute CSD<sup>2</sup> representations by estimating a response function<sup>3</sup> from the 0° phantom then segmenting a fibre orientation distribution (FOD) for each phantom to identify two fibre populations.<sup>4</sup> Dispersion, peak FOD magnitude, and apparent fibre density (AFD)<sup>5</sup> were estimated for each fibre population, and the crossing angle was estimated at each voxel. This analysis was repeated using 50 (5  $b_0$ , 15  $b_{1000}$ , 30  $b_{2000}$ ) and 20 (2  $b_0$ , 6  $b_{1000}$ , 12  $b_{2000}$ ) acquisitions, approximately maintaining isotropic spatial sampling of directions.

**Results:** The estimated crossing angles for the 60° phantoms had a bias of about 10°, while the crossing angles of the 90° phantoms were estimated correctly.

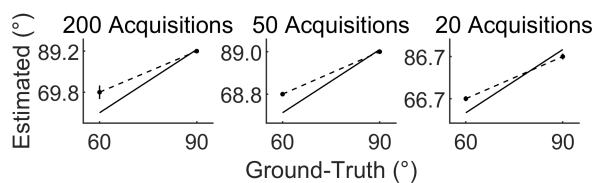


Figure 1: Estimated crossing angle vs. ground-truth crossing angle and number of dMRI acquisitions.

CSD metrics in the fibre populations converged for crossing angles greater than 30°, and changed with crossing angle in the dominant fibre population.

With fewer acquisitions, peak FOD amplitude and AFD decreased, while dispersion increased.

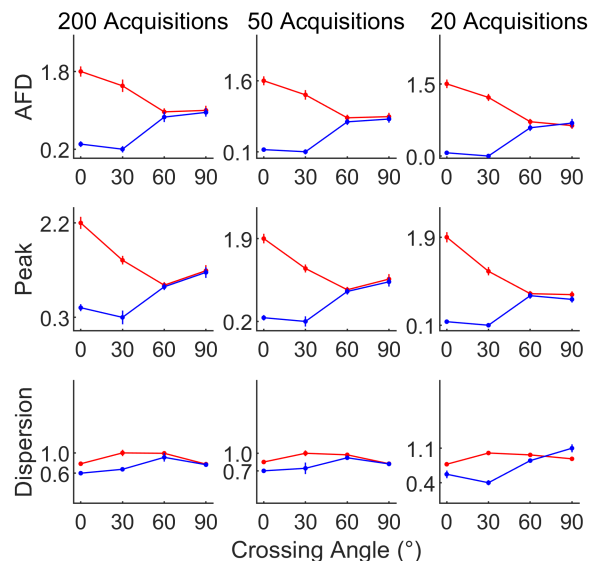


Figure 2: CSD metrics vs. crossing angle and number of dMRI acquisitions. Dominant fibre population in red, secondary in blue.

**Conclusions:** The inability of CSD to resolve 30° crossings supports simulation findings.<sup>2</sup> The bias in estimated crossing angle and CSD metrics under different conditions shows that these phantoms can uncover issues. Future work will produce phantoms with more complex brain-mimetic geometries.

**Acknowledgements:** This work was supported by the Canada First Research Excellence Fund, Brain Canada, and NSERC Discovery Grants.

**References:** [1] Abu-Sardana SO et al. In: Proc. SPIE 10573. International Society for Optics and Photonics; 2018. [2] Tournier J-D et al. NeuroImage. 2007;35(4):1459-1472. [3] Tournier J-D et al. NMR in Biomedicine. 2013;26(12):1775-1786. [4] Smith RE et al. NeuroImage. 2013;67:298-312. [5] Raffelt D et al. NeuroImage. 2012;59(4):3976-3994.

## Modelling electric field near medical devices within a gradient dB/dt exposure system

Arjama Halder, William B. Handler, Blaine A. Chronik

The xMR Labs, Department of Physics and Astronomy, Western University, London, ON, Canada.

**INTRODUCTION:** Time-varying gradient magnetic fields cause time-varying electric fields, and within human tissues, the most well-known consequence of this is peripheral nerve stimulation. However, with the increased use of medical implants, it is also necessary to understand, model, and test for the effects of gradient-induced electric fields on active implantable medical devices (AIMDs). ISO/TS 10974:2018(E) [1] identifies and describes testing of AIMDs for gradient-induced electric field effects (Clauses 13 and 16 in particular). A key step in the process of conducting those tests is to be able to simulate gradient induced electric fields for realistic gradient coils, in realistic patient geometries, in the presence of realistic implanted devices. This abstract describes first steps in the development and validation of a simulation pipeline for this purpose.

**METHOD:** A finite difference simulation tool was implemented in MATLAB to solve Laplace's equation by applying boundary conditions. It was used to simulate a time varying device testing coil, essentially a Helmholtz pair, driving at 100 T/s, which contained a conducting phantom configured as a half cylinder. The simulation relied on the quasi-static approximation [2]. A uniform grid with voxel size 2 mm isotropic was used for the object and the surrounding region. The scalar potential for each voxel was calculated. Chebyshev acceleration using successive over-relaxation was used to converge the scalar potential at all voxels to idealized solutions. Upon completion, the electric fields were calculated. For the validation of these simulated results measurements will be performed with electric field probes operating at low frequencies inside the device testing coil.

**RESULTS:** The electric field produced by the coil in air on the xy plane at the center of the coil is shown in Figure 1. Figure 2 shows the resultant total electric field caused by the charge built up on the conducting cylinder when placed in the coil.

**CONCLUSION:** As suggested in Figure 1 a circulating electric field is created on the xy plane at the center of the device testing coil. There is no z contribution in this circulating electric field. However, with a conducting half cylinder the circulating electric field was perturbed by charge accumulation near the boundaries as shown in Figure 2. The ability to accurately simulate the total induced electric field within the human body and in the vicinity of an AIMD is required in order to guide the physical testing currently required in ISO 10974, as well as to support verification and validation processes for dB/dt exposure systems used in physical testing. The simulation capability described in this abstract is one step in our program to implement and validate a comprehensive capacity to model, measure, and test devices for the complete MRI system electromagnetic environment.

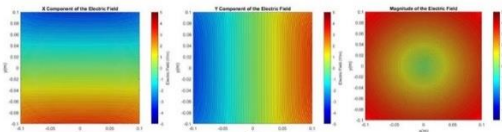


Figure 1: Shows the circulating electric field inside an empty coil.

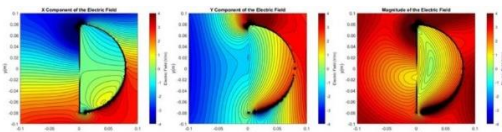


Figure 2: Shows the total electric field with the object inside the coil.

### REFERENCE:

1. International Organization for Standardization. Assessment of the safety of magnetic resonance imaging for patients with an active implantable medical device. *ISO/TS 10974*. 2018;4.
2. Roth BJ, Cohen LG, Hallett M. The Electric Field Induced During Magnetic Stimulation. *Magn Mot Stimul Basic Princ Clin Exp*. 1991;43:268-278.

## An adjustable susceptibility phantom for evaluating effects of foreign objects on field mapping and fat fraction estimation algorithms.

Paul A. Picot, Junmin Liu, and Maria Drangova. *Robarts Research Institute, London, ON, Canada*

### Introduction

MRI requires high local  $B_0$  magnetic field homogeneity, which may be difficult to achieve with implanted devices and other objects in the magnet bore, so there is interest in methods to measure and compensate for local  $B_0$  inhomogeneity. It is difficult to quantify the performance of these  $B_0$  field-mapping algorithms, in part due to the lack of ways to generate controlled inhomogeneities. To test these algorithms we have developed a method to produce controlled arbitrary  $B_0$  field distortions, simulating the presence of objects of differing susceptibilities. Quantifying field mapping algorithm performance against known inhomogeneity will inform models of its effects, with the ultimate goal of enabling more effective correction of their effects.

### Methods

**Variable susceptibility object:** A cylinder with a magnetic susceptibility different from its surroundings was simulated by a coil of insulated copper wire, 75 mm in diameter and 100 mm long. The resulting short solenoid was oriented with its axis parallel to  $B_0$ . The apparent susceptibility of the cylindrical region of the solenoid is adjusted by varying the current through it between 0 and 2 amperes, producing a field shift within the solenoid of up to 2 mT, an apparent susceptibility of 667 ppm at 3T. **Phantom:** A test phantom of a series of peanut oil-water emulsions in agar and doped with  $GdCl_3$  was made. Fat fractions of 100, 72, 53, 33, 17, 7.4, 2.5 and 0 percent were sealed in 50 mL centrifuge tubes, and suspended in a 2-litre fat-free outer volume of 2% agar. The susceptibility-simulating coil was secured to the exterior of the phantom (Fig.1). **Imaging:** The technique was tested on two clinical 3T scanners, using a dual echo-train 3D GRE sequence (e.g.  $TE_1/\Delta TE/TE_5 = 3.20/1.46/9.04$  ms,  $TE_6/\Delta TE/TE_{10} = 16.75/7.15/45.35$  ms) optimized for fat fraction and  $R2^*$  measurements<sup>1</sup>. Imaging was performed with several coil currents from 0 to 2000 mA. Data were processed offline by the PUROR algorithm<sup>2</sup> and  $B_0$ -NICE<sup>3</sup> to generate  $B_0$  and fat fraction maps.

### Results

The field perturbation from the solenoid winding, evidenced by the phase maps (Fig.2), appears qualitatively as expected, and is of sufficient magnitude to simulate materials of relatively large susceptibility. The method can generate susceptibilities sufficient to exercise the limits of the algorithms, evidenced by discontinuities in the field map and fat fraction maps (Fig.3).

### Conclusion

We have demonstrated it is practical to produce a simple shape with adjustable apparent susceptibility in a magnet. We expect to use this approach to test methods to compensate for local susceptibility differences in a magnet bore. Arbitrary volumes of susceptibility distribution, with some constraints, might be designed with modeling and optimization tools used in gradient coil design

**References:** 1. Liu J, Christiansen SD, Drangova M. *Neuroimage* 2018;172:703-717. 2. Liu J, Drangova M. *Magn Reson Med* 2012;68:1303-1316. 3. Liu J, and Drangova M.. *Magn Reson Med* 2015;74:1177-1188.

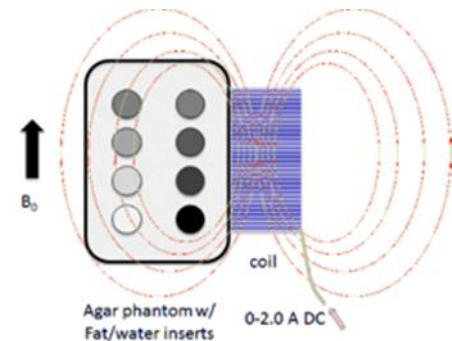


Fig. 1 Schematic of coil next to phantom.

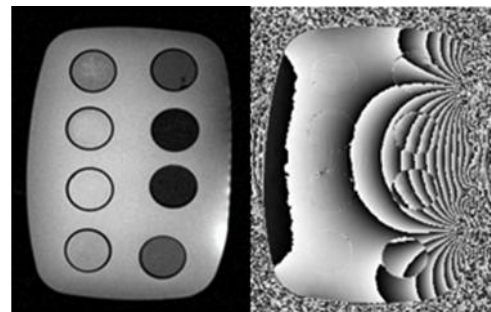


Fig. 2 Magnitude (L) and phase (R) images.

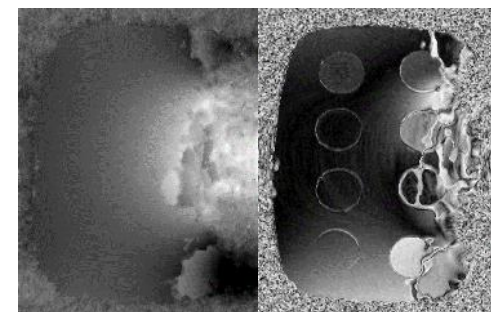


Fig. 3 Magnitude (L) and phase (R) images.

## The effect of spatial averaging on dB/dt exposure values for implanted medical device

C. A. P. Brown<sup>1</sup>, B. A. Chronik<sup>1</sup>

<sup>1</sup>The xMR Labs, Physics and Astronomy, University of Western Ontario, Canada.

**INTRODUCTION:** The objective of this investigation was to determine the effect that spatial averaging would have on predicted dB/dt values within realistic MRI gradient systems. ISO 10974:2018(E) [1] contains simulated data describing the peak dB/dt values that active implantable medical devices (deep brain stimulators, pacemakers, etc.) could be exposed to when within varying compliance volumes within the bore of the MRI scanner. But for devices with realistic spatial extent, the effective dB/dt relevant for testing would be the spatial average dB/dt value. Clearly the average dB/dt value will be smaller than the peaks, but by how much? Basing safety compliance on the spatial averages would allow more devices to be considered safe.

**METHODS:** The interactions of the example device were investigated over the range of MRI gradient coils described in Annex A of 10974, which were designed to represent most possible gradient coil designs in clinical systems. Three-axis coil sets which corresponded to both 60 cm and 70 cm inner diameter MRI systems were modeled using previously developed and validated methods [2]. They were designed with lengths of: 140, 150, 160, and 170 cm, and for each length, the size of the imaging region varied over: 35, 40, 45, and 50 cm. For each of these designs, the field produced by all seven axis combinations were evaluated:  $G_x$ ,  $G_y$ ,  $G_z$ ,  $G_{xy}$ ,  $G_{xz}$ ,  $G_{yz}$  and  $G_{xyz}$ . Thus, a total of 224 gradient coils were considered. For each gradient, the local dB/dt produced was calculated over a device on the surface of a compliance volume within the coil. The grid used was a cylinder composed of 777 points inside the bore. The radius of the cylinder was such that when the device was positioned on it, its edge would be at some ‘compliance radius’: 10, 15, 20, 25, and 30 cm. The device was simulated as a 5 cm diameter sphere. Its interior was discretized in a 5 mm rectangular grid with 552 points, and its surface was subdivided into 552 equally spaced points. The magnetic field was calculated over the device using Biot-Savart methods and the average and peak fields were determined for each location and for each coil.

**RESULTS:** The results obtained across the five different compliance radii are shown in table 1. For a 5 cm diameter spherical device, across a range of compliance radii from 10 cm to 30 cm, the highest spatially-averaged dB/dt value that could realistically be experienced across all the combinations of device location and gradient coil design at a slew rate of 200 T/m/s is 116 T/s X SR.

**CONCLUSIONS:** The maximum dB/dt the device experiences increases with compliance radius. From table 1, when we add spatial averaging, the difference between the mean and peak values increases monotonically between 2 and 17%. If basing the MR compatibility of a device on the mean rather than the peak, this would allow more devices to be classified as MR safe or conditional. In the future, differences between peak and mean values will be investigated over a range of different devices.

### REFERENCES:

[1] ISO/TS 10974:2018, Assessment of the safety of magnetic resonance imaging for patients with an active implantable medical device

[2] CT Harris, WB Handler and BA Chronik. Electromagnet Design Allowing Explicit and Simultaneous Control of Minimum Wire Spacing and Field Uniformity. Concepts Magn. Reson., 41B: 120-129 (2012)

### FIGURES:

Compliance Radius [m]	Spatially-averaged dB/dt				Peak dB/dt			
	X	Y	Z	Mag.	X	Y	Z	Mag.
0.10	59.4	59.2	60.8	63.0	61.6	61.4	62.2	65.2
0.15	64.6	64.2	64.2	68.0	68.6	68.0	66.8	72.0
0.20	73.6	72.8	69.8	77.2	80.6	79.2	74.6	83.6
0.25	89.0	87.2	82.8	91.6	101	98.0	92.4	102.0
0.30	114	110	104	116	132	126	117	134.8

**Table 1:** The maximum dB/dt by compliance radius for the family of coils at a slew rate of 200 T/m/s. The component labels indicate the components of the dB/dt vector. The right-most three columns list the peak (no spatial averaging) obtained for the individual dB/dt components. The magnitude column is the peak of all the magnitudes in the calculation region.

## Correction of Respiration-Induced Magnetic Field ( $B_0$ ) Fluctuations in the Spinal Cord

Alicia Cronin\*, BSc,<sup>1,2</sup> Neil Duggal, MD, MSc, FRCS(C),<sup>1,3</sup> and Robert Bartha, PhD<sup>1,2</sup>

<sup>1</sup>Department of Medical Biophysics; <sup>2</sup>Centre for Functional and Metabolic Mapping, Robarts Research Institute, The University of Western Ontario; and <sup>3</sup>Department of Clinical Neurological Sciences, University Hospital, London Health Sciences Centre, London, ON, Canada

**Introduction:** Magnetic resonance spectroscopy (MRS) is a non-invasive method used to measure metabolite concentrations in a region of interest based on principles of nuclear magnetic resonance.<sup>1</sup> This approach assumes the external static magnetic field ( $B_0$ ) remains stable during acquisition. This condition is violated when acquiring MRS data from the spinal cord because of the proximity to the lungs, which changes magnetic susceptibility during data acquisition,<sup>1,3,4</sup> causing distortions in spectral line shapes, line broadening, and reducing the signal-to-noise ratio (SNR).<sup>1</sup> Although spectroscopy in the spinal cord could have widespread applications for understanding disease processes, there is currently no method to overcome this artefact. The objective of this study is to develop a correction algorithm to reduce the line shape distortion in the  $^1\text{H}$  spectrum caused by fluctuations of the applied  $B_0$  magnetic field within the spinal cord. Since  $B_0$  varies periodically, aligning with the respiratory cycle,<sup>2</sup> we hypothesize that a retrospective correction algorithm based on *a priori* knowledge of the  $B_0$  fluctuations in the cord due to respiration, combined with real time monitoring of respiration during the scan, could improve line shape and spectral quality.

**Methods:** The correction algorithm uses the phase of a time domain signal acquired using  $^1\text{H}_2\text{O}$  from within the tissue of interest during respiration. The following steps are used: 1) the phase changes over time are unwrapped, 2) the frequency shift of the signal is determined by calculating the slope of the unwrapped phase signal, 3) this frequency shift is removed, 4) remaining phase offsets represent temporal  $B_0$  variations and are subtracted from metabolite time domain signals prior to Fourier transform to the frequency domain. This retrospective correction algorithm was implemented in the MATLAB programming language. The proper phase correction to apply to a metabolite spectrum will be determined using a calibration stage that involves acquiring a series of  $^1\text{H}_2\text{O}$  time domain signals during normal respiration and relating these to the respiration pattern observed during metabolite acquisition. Preliminary water unsuppressed data were acquired in one subject on a 3 Tesla Siemens Prisma scanner using a PRESS localization sequence (TR = 6000 ms, TE = 145 ms, number of averages = 1).

**Results and Discussion:** Preliminary results obtained from the spine of one volunteer shows that the Lorentzian line shape and line width of the acquired water spectrum improved when applying the retrospective correction algorithm, as demonstrated in Figure 1. The line width measured at 50% of the maximum height demonstrated a decreased width of 40.2 Hz to 35.6 Hz when the correction algorithm was applied. Future work includes collection of metabolite and water spectra to determine the reproducibility of the line width improvement. In addition, line shape correction based on respiration pattern will be tested to determine improvement of the SNR of the metabolite spectra collected.

**References:** [1] Hock, A *et al.* *Am J Neuroradiol*, 34: 1682–1689, 2013. [2] Vannesjo, SJ *et al.* *NeuroImage*, 167: 191–202, 2018. [3] Wilm, BJ *et al.* *Magn Reson Med*, 71: 1657–1662, 2014. [4] Topfer, R, Foias, A, Stikov, N, & Cohen-Adad, J. *Magn Reson Med*, 80: 935–946, 2018.

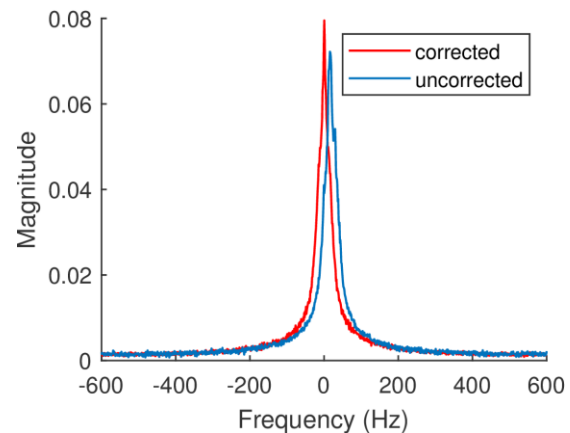
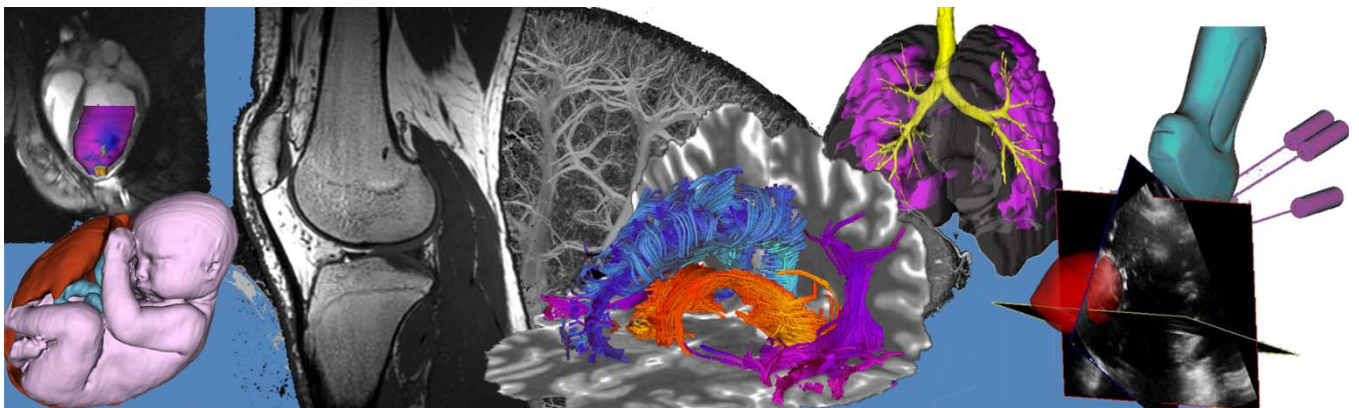


**Figure 1:** Corrected and uncorrected water signal acquired from the spine of a healthy volunteer, collected on a 3T Siemens

# Poster Presentation Abstracts

## Session 5: Image Guided Intervention and Augmented Reality



## Development of an MRI-guided robotic platform for focused ultrasound induced sonothrombolysis of brain intraventricular blood clots

N. Soucier, S. Pichardo, W. Chu-Kwan, K. Piorowska, T. Looi, A. Waspe, and J. Drake

Institute of Biomaterials and Biomedical Engineering: Neural, Sensory Systems and Rehabilitation  
The Hospital for Sick Children (SickKids): Neuroscience and Mental Health

**Introduction:** One in every ten babies are born premature and many with a low-birthweight. Nearly 50% of low-birthweight premature babies develop an intraventricular hemorrhage. This can lead to an intraventricular blood clot, which obstructs the flow of cerebrospinal fluid leading to hydrocephalus. This is characterized by increased pressure and enlarged ventricles resulting in secondary brain injury if untreated. Currently, minimally invasive neurosurgery is the only available therapy for these infants, which aims to care for the symptoms of hydrocephalus long-term, instead of treating the actual underlying condition. Our aim is to provide a non-invasive method of treatment by dissolving the blood clot directly in the ventricles, thereby eliminating the need for shunt surgery and reducing the effects caused by hydrocephalus. This proposed treatment platform is composed of a focused ultrasound (FUS) transducer to perform thrombolysis and the development of a robotic platform to target the blood clot using real-time MRI.

**Methods:** A 256-element FUS transducer is mounted on an MRI-safe robot that operates in the bore of a clinical 3T MRI scanner to achieve precise image-guided targeting. This is a five degree-of-freedom robot that was designed using MR-safe materials and integrated into existing Sonalleve electronics (Profound Medical) and software interfaces. Fiducial markers are placed on the transducer which are imaged by the MRI and transferred as DICOM's to the robot software so that its location can be determined. The robot software has an interface that allows for its maneuverability, initiation of sonication and monitoring the treatment. Once the FUS parameters are set, the sonication is initiated and thermal map images are displayed. These images are initially planned and captured on the MR software, then continually pushed to the robot software to provide real-time feedback of the sonication. When sonicating a clot, the volume reduction and targeting accuracy will be assessed with a goal of more than 50% decrease in volume with targeting capabilities within  $\pm 2$ mm. This will initially be tested using in-vitro phantom models and porcine cadaver heads, followed by in-vivo animal tests using an established piglet model of an intraventricular hemorrhage.

**Results:** The robot software has been developed to import the DICOM files that are pushed from the MRI and provide a graphical user interface that allows for control of the robot and FUS. The 1.2MHz FUS transducer will be tested with power values ranging between 375-450W, duty cycles of 0.1-1.0% and treatment durations from 25-60 seconds. These different parameters will allow for the analysis of the most efficient method of thrombolysis. The blood clots will be synthesized using fresh porcine blood and a mixture of a calcium chloride solution to promote clotting in a 3D printed tray with cavities of 2 cm<sup>3</sup>. The blood clots will be assessed pre and post sonication comparing the volume change in the blood clots structure. Additionally, the platform will also monitor the treatment in real-time as MR thermal images are continually streamed to the robot user interface.

**Conclusions:** The results from this work will provide a method of treating premature babies with intraventricular clots that is non-invasive, thus eliminating the need for shunt surgery.

## Benefits of personalized gel pads for magnetic resonance-guided focused ultrasound

William Chu Kwan<sup>1</sup>, Adam Waspe<sup>1</sup>, Michael Temple<sup>1</sup>, James Drake<sup>1</sup>

<sup>1</sup> The Hospital for Sick Children, Toronto, ON, Canada

**Introduction:** To minimize the attenuation and reflection of ultrasound energy emitted by a transducer, coupling mediums are employed. Existing coupling agents include mineral oils, degassed water, and hydrogels such as agar. During Magnetic Resonance-guided Focused Ultrasound (MRgFUS) treatments, standard discoid gel pads (Aquaflex, Parker Labs) coated with diluted ultrasound gel are typically used between transducers and patients. Of concern is the ultrasound energy reflection due air and coupling at the skin-gel interface. Energy is absorbed by the medium and converted into heat, leading to skin necrosis. Other drawbacks include decreased surface area contact on smaller patients, and positional changes throughout treatment. Ultimately, these factors diminish the overall effectiveness of treatment and increase treatment time and cost.

Our goal is to determine the benefits of using personalized agar gel pads. The aim is to analyze if there is an increased effectiveness of ultrasound energy coupling, and to explore if it is both practical and advantageous to construct these personalized agar gel pads.

**Methods:** We prepared 2 personalized agar gel pads and compared them to 3 control setups consisting of the standard Aquaflex pads. A total of 5 porcine leg specimens were harvested. The mould consisted of a permanent section designed to fit in the HIFU sonication window encompassing the complete conical sonication beam. For the personalized section, a modular piece was 3D-printed based on anatomic MRI scans (Figure1). After mould assembly, the gel pads were prepared with a mixture of 2% purified agar in water (Figure2).

For testing, the specimens were sonicated using a V1 Sonalleve HIFU table (Profound Medical). For each specimen, 10 treatment cells of 2mm were ablated at a power of 100W for 20 seconds. Near-field temperature mapping at the skin-gel interface was obtained with an Achieva 3T MRI (Philips Healthcare). The distance between the sonication plane and the temperature mapping plane were comparable.

**Results:** Visual inspection of the near field temperature map demonstrated a significant decrease in energy scattering in the personalized gel pad when compared to the standard gel pad (Figure3 and Figure4). The maximum temperature recorded on the personalized gel pad ranged from 45.7°C to 56.3°C with a maximal area of 90.1 mm<sup>2</sup> at a distance of 14 mm from the treatment plane. In contrast, the maximum temperature recorded on the standard gel pad ranged from 45.9°C to 67.7°C with an area of 205.98 mm<sup>2</sup> at an average distance of 14 mm from the treatment plane. Other notable differences were the ease of sample positioning on the personalized gel pad and the lack of motion or shifting of the sample throughout testing.

**Conclusions:** Our results demonstrate a reproducible and feasible method of preparing patient-specific personalized agar gel pads for MRgFUS treatment. The benefits of these personalized gel pads include greater acoustic coupling and effective energy delivery, which translates into improved patient safety. Additionally, the ease of positioning and the lack of motion provide a shorter treatment time and reduced therapy cost.



## Improved Intraoperative Needle Tip Identification Using Power Doppler Ultrasound

Nathan Orlando<sup>1,2</sup>, Jonatan Snir<sup>3</sup>, Kevin Barker<sup>2</sup>, Douglas Hoover<sup>4</sup>, Aaron Fenster<sup>1,2</sup>

<sup>1</sup>Department of Medical Biophysics, <sup>2</sup>Robarts Research Institute, Western University; <sup>4</sup>London Regional Cancer Program; London, Ontario, Canada; <sup>3</sup>Tom Baker Cancer Centre, Calgary, Alberta, Canada

**Introduction:** Ultrasound (US)-guided high-dose-rate (HDR) brachytherapy (BT) is a common treatment technique for intermediate and high-risk localized prostate cancer.<sup>1</sup> This minimally invasive procedure uses a radioactive source passed through multiple hollow needles inserted through a rigid grid of evenly spaced holes (needle template) to deliver radiation. Accurate identification of needle tips is a key component of both patient safety and treatment effectiveness for HDR-BT. Unfortunately, image artifacts from nearby needles and the surrounding tissue often limit the accuracy of needle tip identification when using standard 2D brightness (B)-mode US guidance.<sup>2</sup> To overcome these limitations and improve the accuracy of intraoperative needle tip identification, we propose the use of power Doppler (pD) US imaging while a mechanical perturbation is applied to the needle of interest.

**Methods:** A mock HDR-BT procedure was completed in a tissue-mimicking agar phantom.<sup>3</sup> In total, 13 plastic needles were inserted in the phantom. The chosen implant pattern, insertion depth, and number of needles were representative of what might be seen in a real HDR-BT procedure. Following the standard clinical procedure, needles were inserted from left to right and from the top of the needle template to the bottom to limit shadowing artifacts. For each needle, the tip location was selected by two observers using in-house software, first using B-mode US and then using pD US while the needle in question was vibrated. Needle vibration was accomplished using a mechanical oscillator developed in our laboratory, capable of oscillating at a fixed and controllable frequency. To test each tip identification method in the presence of shadowing artifacts, this procedure was repeated after all needles were inserted, ensuring there were needles present between the US probe and the needle in question to provide shadowing artifacts. Accuracy of each tip identification method was evaluated by calculating insertion depth error (IDE). This metric compares the needle tip's apparent location in the image to the physical needle length and insertion depth.

**Results:** Mean  $\pm$  standard deviation IDE, averaged for the two observers, was  $2.0 \pm 0.5$  mm and  $1.0 \pm 0.5$  mm for unobstructed needles, and  $1.7 \pm 0.6$  mm and  $1.1 \pm 0.6$  mm for shadowed needles, imaged using B-mode and pD US respectively. Correlation of IDE between observers was found to be  $r=0.607$ , with a paired t-test showing no statistically significant difference ( $n=26$ ). A two-way ANOVA showed no statistically significant interaction between US imaging method and shadowing artifact presence. There was a statistically significant main effect for US imaging method on IDE ( $p < .0001$ ), but no statistically significant main effect was observed for the presence of shadowing artifacts. No significant correlation was observed between IDE and needle insertion depth, and no statistically significant differences in IDE were found for needles inserted at different distances from the US probe.

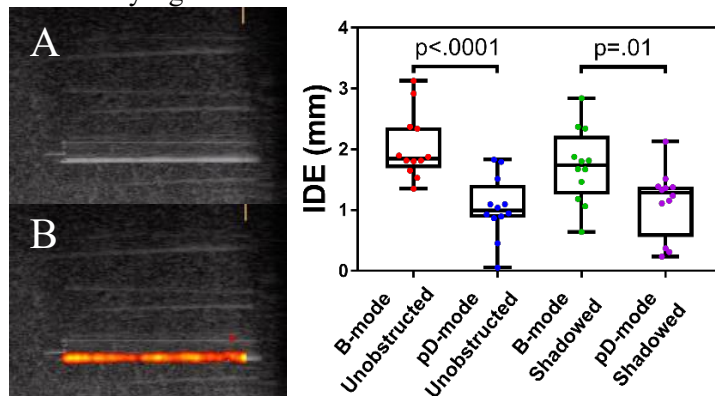


**Fig 2:** Example of an inserted needle in a phantom as seen in (A) B-mode US, and in (B) pD US while the needle was vibrated. On the right is a plot showing mean IDE for unobstructed and shadowed needles imaged using B-mode and pD US.



**Fig 1:** Image of our mechanical oscillator.

**Conclusions:** Our pD US based tip identification method significantly reduced IDE when compared to B-mode US for both unobstructed and shadowed needles. Our method showed no inter-observer variability and performed independently of needle insertion depth and distance from the US probe. These results were observed in a phantom where needle visualization is ideal compared to what is seen in patients, suggesting that our technique may be useful in reducing tip identification error in clinical HDR-BT procedures, potentially improving patient safety and treatment effectiveness. Future work includes improving our gold standard using CT and assessing trajectory error, with the goal being translation to the clinic.

**References:** [1] Yamada et al. *Brachytherapy* **11**(1), 20-32 (2012). [2] Hamper et al. *Am. J. Roentgenol.* **156**(2), 401-402 (1991). [3] Rickey et al. *Ultrasound Med. Biol.* **21**(9), 1163-1176 (1995).

## Usability and accuracy of an electromagnetically tracked partial nephrectomy navigation system

Hillary Lia<sup>1</sup>, Zachary Baum<sup>1</sup>, Thomas Vaughan<sup>1</sup>, Tamas Ungi<sup>1</sup>, Thomas McGregor<sup>2</sup>, Gabor Fichtinger<sup>1</sup>

1. Laboratory for Percutaneous Surgery, Queen's University, Kingston, Canada
2. Department of Urology, Queen's University, Kingston Canada

**INTRODUCTION:** Laparoscopic partial nephrectomy is increasing in popularity as the preferred method for managing small renal masses. The nephron-sparing technique preserves renal function and has comparable outcomes to radical nephrectomy. However, laparoscopic partial nephrectomy is challenging due to the lack of tactile feedback and risk of incomplete tumor resection and damage to surrounding calyces and vasculature. We propose an electromagnetically tracked navigation system that displays real-time three-dimensional anatomical models.

**METHODS:** The partial nephrectomy navigation system was configured using the SlicerIGT extension ([www.slicerigt.org](http://www.slicerigt.org)) of 3D Slicer ([www.slicer.org](http://www.slicer.org)). The experimental setup (Figure 1) consists of a laptop running the software, a TelemedMicrUS portable US machine with a linear transducer (Telemed Medical Systems, Lithuania), and an Ascension TrakSTAR electromagnetic position tracker (Northern Digital Inc., Waterloo, ON). Electromagnetic sensors are attached to the ultrasound probe and hooked needle. A reference sensor is placed inside the calyces of the kidney phantom, where a catheter would reside during surgery. The kidney phantom is placed in a laparoscopic box trainer and a sensor is attached to the laparoscopic scissors.

On the laptop screen, the three-dimensional view displays the laparoscopic scissors, tumor model, and a model of combined kidney calyces and vasculature. The tumor model is generated by placing points around the tumor boundary on live ultrasound images, as described by Ungi *et al* [1]. The model of combined kidney calyces and vasculature is segmented from live ultrasound reconstruction images generated using the Plus Remote module of SlicerIGT. The position of the laparoscopic scissors is displayed in relation to the anatomical models.

The navigation system was assessed for usability and accuracy. The usability of the system was assessed using a System Usability Survey administered to ten participants who were instructed to use the laparoscopic scissors to trace the tumor border of a kidney phantom. Furthermore, the lag of the navigation display was measured. The navigation screen and laparoscopic scissors were video-recorded. Frame-by-frame analysis was used to determine the time difference between the change in direction of the physical laparoscopic scissors and the model of the laparoscopic scissors. The accuracy of the system was measured using fiducial registration by placing the tip of the laparoscopic scissors on each corner of a box of known dimensions. The RMS error was recorded.

**RESULTS:** The mean calculated System Usability Survey was 82.8, with a standard deviation of 7.2. Using frame-by-frame analysis, it was found that the navigation view showed 5 frames per second. Average lag was 243 milliseconds with a standard deviation of 61 milliseconds. The RMS error was 2.84 mm.

**CONCLUSION:** An electromagnetically tracked partial nephrectomy navigation system was developed. The results of the study indicate that this navigation system is both usable and accurate. In future studies, this navigation system will be modified and validated for both clinical and educational use.

**REFERENCES:** [1] Ungi *et al.*, *IEEE Trans Biomed Eng.*, 2016.

**ACKNOWLEDGEMENTS:** This work was funded, in part, by NIH/NIBIB and NIH/NIGMS and by CANARIE's Research Software Program. G. Fichtinger is supported as a Canada Research Chair. H. Lia was supported by NSERC USRA.

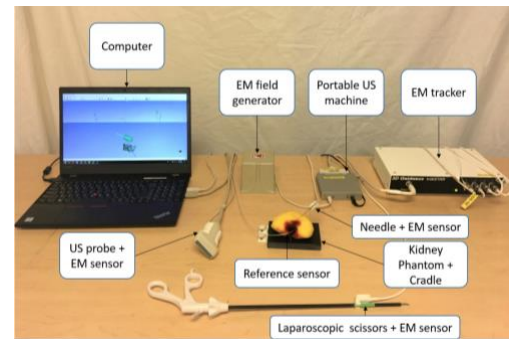


**Figure 1.** Experimental setup.

## MRI Driven Augmented Reality Image-Guidance Platform for Myocardial Cell Delivery

Mitchell Doughty<sup>1,2</sup>, Jill Weyers<sup>2</sup>, Xiuling Qi<sup>2</sup>, Graham Wright<sup>1,2</sup>, Michael Laflamme<sup>3</sup>, Nilesh R. Ghugre<sup>1,2</sup>

<sup>1</sup>Department of Medical Biophysics, University of Toronto, <sup>2</sup>Schulich Heart Research Program, Sunnybrook Research Institute, <sup>3</sup>McEwen Centre for Regenerative Medicine, University Health Network

**Introduction:** Myocardial infarction (MI) remains the leading cause of heart failure (HF), a condition with a 5-year mortality rate of ~50%<sup>1</sup>. Current HF management techniques focus on slowing disease progression rather than improving contractile function. Cardiac regenerative medicine (CRM) using cell-based approaches, offers the potential to repopulate non-contractile scar tissue and overcome the limited regenerative capacity of the human heart<sup>2,3</sup>. However, regions of scar are not well delineated during surgical delivery procedures, and accurate cell placement is vital to maximize outcomes<sup>5</sup>. MRI is considered the gold standard for cardiac function and scar imaging post MI<sup>4</sup>. We aim to develop a novel integrative solution to guide cell injections using late gadolinium enhancement (LGE) cardiac MRI to generate 3D scar roadmaps and augmented reality (AR) guidance through an optical see-through head-mounted display (OST-HMD) to visualize critical MR imaging information intraoperatively.

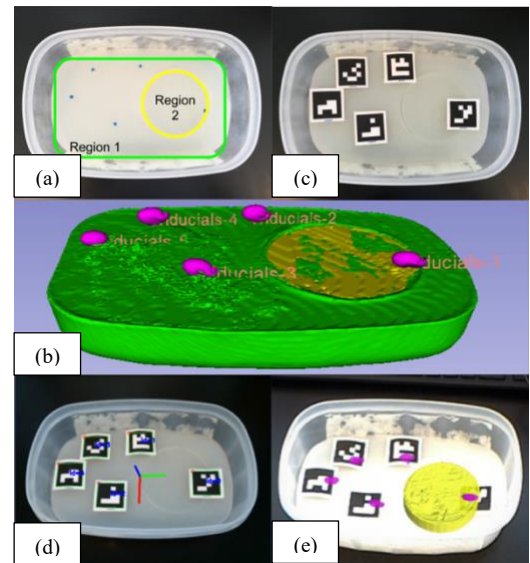
**Methods:** Device: We have utilized the Microsoft HoloLens OST-HMD for initial experiments due to its class leading performance in contrast perception, task load and frame rate<sup>5</sup>. Our initial implementation leverages the HoloLens front facing sensor capabilities for pose estimation through robust square-based fiducial tracking<sup>6</sup>. Display errors common to OST-HMDs<sup>5</sup> were minimized through a homography to align the tracking camera and user vision coordinate frames. A modified version of the single-point active alignment method was implemented to compute this transform<sup>7</sup>. Phantom study: An agar phantom was prepared to provide a substrate for future mock injection studies (Figure 1a). The phantom is comprised of two regions with differing T1 contrast, representing the organ and an embedded target. Vitamin E tablets within the agar gel served as MRI-visible fiducial markers, which are later aligned with custom square-based fiducial landmarks to enable registration between AR projections of the MRI volumes and the real scene.

Animal study: Using a porcine MI model (N=3), infarcts were characterized through LGE MRI and infarcts were segmented using a full width half maximum algorithm to semi-automatically quantify infarcted areas<sup>8</sup>.

**Results:** Phantom study: 3D MRI of phantom and subsequent segmentation and model creation was performed (Figure 1b). Square fiducial markers are aligned with the MRI fiducial locations on the phantom (Figure 1c), creating consistent landmarks between preoperative and intraoperative image space. Robust visual tracking of the custom marker configuration using the front-facing sensors on the HoloLens permitted virtual model alignment with the intraoperative scene with reasonable accuracy (Figure 1d, e).

Animal study: 3D MRI models of the heart and scar anatomy were displayed to the user through the HoloLens device alongside interfaces for interaction, providing the means for future studies evaluating accuracy of cell-delivery in a blind versus guided scenario. **Conclusion:** Our study offers the first proof-of-concept MRI-guidance solution for accurate surgical delivery of cell-based therapies to the heart. Initial results of OST-HMD guidance are promising; however, more work is necessary to ensure consistent virtual content registration stability and accuracy. Our system could improve on a challenging aspect of cell delivery, potentially leading to improved management of HF.

**References:** 1. H&S. *Heart and Stroke* (2016). 2. Gerbin, K. A. & Murry, C. E. *Cardiovascular Pathology* (2015). 3. Chong, J. J. H. *et al. Nature* (2014). 4. Pop, M. *et al. PMB* (2013). 5. Qian, L. *et al. IJCARS* (2017). 6. Garrido-Jurado, S., *et al. PR* (2014). 7. Azimi, E., *et al.* (2017). 8. Pop, M. *et al. IEEE TBE* (2014). 9. Kikinis, R., Pieper, S. D. & Vosburgh, K. G. *IIIGT*.



## An optical brain-computer interface for establishing rudimentary communication with patients with brain injuries

A. Abdalmalak<sup>a,b\*</sup>, D. Milej<sup>a,b</sup>, M. Diop<sup>a,b</sup>, A. M. Owen<sup>c</sup> and K. St. Lawrence<sup>a,b</sup>

<sup>a</sup> Department of Medical Biophysics, Western University, London, ON, Canada <sup>b</sup> Imaging Program, Lawson Health Research Institute, London, ON, Canada <sup>c</sup>Brain and Mind Institute, Western University, London, ON, Canada

\*aabdalma@uwo.ca

**Introduction:** Brain-computer interfaces (BCIs) are devices that can be used to bridge the gap between thoughts and actions, allowing patients who cannot physically or verbally communicate the ability to establish rudimentary 'mental communication'. Optical technologies such as functional near-infrared spectroscopy (fNIRS) are ideal for this purpose, since the systems are portable and inexpensive. Motor imagery (MI) is a commonly used BCI task that involves actively imagining coordinated movements in response to questions and detecting the corresponding brain activity in motor planning regions. Our team used this approach in combination with fNIRS to communicate with a locked-in patient under intensive care<sup>1</sup>. Although promising, the accuracy of this approach should be assessed on a larger cohort, which is the **purpose** of the current study, if it is to be used a reliable BCI.

**Methods:** 21 healthy participants with no history of neurological conditions were recruited. A four-channel fNIRS system ( $\lambda = 760$  and 830 nm) developed in house was used. One emission and four detection fibers were secured onto the head and centered over the supplementary motor area and premotor cortex. Each participant was asked four questions (factual and open-ended) in a block design with an overall time of 5:30 minutes per question. The order of the questions was randomized between participants. Participants were instructed to imagine playing tennis to answer 'yes', otherwise to remain relaxed if the answer was 'no'. The change in concentration of oxyhemoglobin was calculated and averaged across all channels.

Forward feature selection was used to select the optimal temporal features to train and test the classifiers, based on the leave-one-out cross validation method. Two classifiers were tested: a support vector machine (SVM) and a linear discriminant analysis (LDA). Each participant answered the same questions after the study and these responses were used as the ground truth for calculating accuracy.

**Results:** 2 subjects were excluded from the analysis due to motion artifacts and overall low quality of the data. Results showed that the highest accuracy was achieved using the LDA classifier with an overall value of 75% (five participants had an accuracy of 100%, nine had an accuracy of 75% and five had an accuracy of 50%).

**Discussion and Conclusion:** These results demonstrated that the fNIRS approach achieved good accuracy compared to previous studies<sup>2</sup>. On-going work is to evaluate how the accuracy would be affected by reducing the number times each question was asked. In conclusion, this work highlights the potential of MI-based fNIRS as a BCI. Future work will focus on translating this research to patients with severe brain injuries.

**References:** [1] A. Abdalmalak et al., *Neurophotonics*, 4(4), 040501, 2017. [2] N. Nasser and KS. Hong, *Frontiers in Human Neuroscience*, 9(3), 2015.

**Development of a 3D ultrasound guidance system for high-dose-rate interstitial gynecologic brachytherapy**

Jessica R. Rodgers<sup>1,2</sup>, Jeffrey Bax<sup>2</sup>, Kathleen Surry<sup>3</sup>, W. Thomas Hrinivich<sup>4</sup>, Eric Leung<sup>5</sup>, Vikram Velker<sup>3</sup>,  
David D'Souza<sup>3</sup>, Aaron Fenster<sup>1,2</sup>

<sup>1</sup>Biomedical Engineering Graduate Program, Western University, London, Ontario, Canada; <sup>2</sup>Robarts Research Institute, Western University, London, Ontario, Canada; <sup>3</sup>London Regional Cancer Program, London, Ontario, Canada; <sup>4</sup>Johns Hopkins Hospital, Baltimore, Maryland, USA; <sup>5</sup>Odette Cancer Centre, Toronto, Ontario, Canada

**Introduction:** High-dose-rate (HDR) interstitial brachytherapy (ISBT) may be used during treatment for gynecologic malignancies to increase the tumor dose relative to nearby healthy tissues. The procedure requires precise insertion of multiple hollow needles (typically about 14 needles) through a perineal template to optimize dose distributions and avoid overexposing organs-at-risk (OAR), such as the bladder, rectum, and bowel. Currently, there is no standard method to visualize the needles intraoperatively, which would allow needle positions to be verified and facilitate image guidance for the implant, with the potential to improve implant quality and avoid OAR. This study describes the implementation of an accessible intraoperative system for verifying needle positions using a 3D ultrasound (US) system for implant assessment during gynecologic ISBT.

**Methods:** The system includes both 3D transrectal US (TRUS) and 360° 3D transvaginal (US) scanning modes to account for the individual patients' anatomical and tumor geometries, using a clinical 2D side-fire endocavity US probe. The probe is rotated using a stepper motor system to acquire 3D fan-shaped TRUS or ring-shaped TVUS (*Fig. 1a*) images in 12 s and 20 s, respectively, with a hollow sonolucent vaginal cylinder compatible with perineal template used for TVUS scanning to maintain the implant stability. TRUS and TVUS scans were acquired for five (58 needles) and six (54 needles) patients undergoing HDR ISBT, respectively, and needle positions compared to the clinical post-insertion x-ray computed tomography (CT) images. To improve the clinical utility of the system, an automatic needle segmentation algorithm leveraging the randomized 3D Hough transform to simultaneously identify multiple needles was tested on one TVUS image (8 needles) as a proof-of-concept.

**Results:** The mean  $\pm$  standard deviation difference in needle tips identified in the 3D TRUS images was  $3.82 \pm 1.86$  mm with a mean angular difference of  $3.04 \pm 1.63$ °. The mean maximum position difference was  $2.36 \pm 0.97$  mm and mean angular difference was  $1.95 \pm 0.70$ ° for the needles in the 3D TVUS images. Nearby OAR were visible in most images, in addition to needles, particularly the rectum in TVUS images and bladder with Foley catheter in the TRUS and TVUS images (*Fig. 1a*). All needles were also identified by the algorithm (*Fig. 1b*) with a mean maximum difference in needle positions compared to manually segmented needles of  $0.78 \pm 0.17$  mm and mean angular difference of  $0.44 \pm 0.19$ °.

**Conclusions:** The proposed 3D US system provides the potential for a versatile method to visualize and localize needles and OAR intraoperatively during HDR gynecologic ISBT, allowing implants to be immediately assessed using two acquisition modes, depending on the particular patient's presentation. This may provide the ability for 3D image guidance during needle insertion procedures for HDR ISBT of gynecologic malignancies.

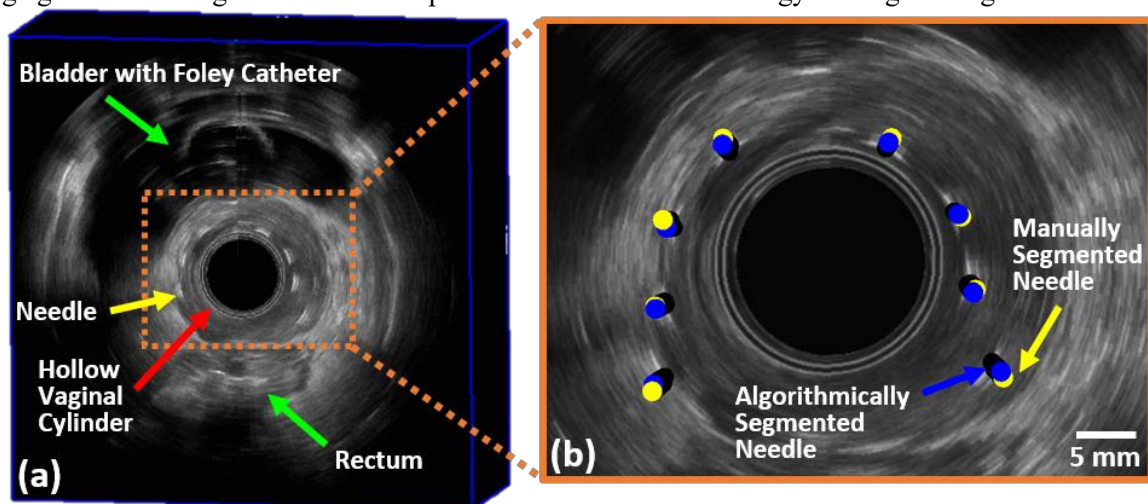


Figure 1: (a) Reconstructed axial view of a patient 360° 3D TVUS image with key features indicated and (b) cropped image region showing manually (yellow) and algorithmically (blue) segmented needle trajectories.

## Assessment of immersive medical virtual reality visualization using 3D Slicer

Salah Choueib<sup>1</sup>, Csaba Pinter<sup>1</sup>, Andras Lasso<sup>1</sup>, Jean-Christophe Fillion-Robin<sup>2</sup>, Jean-Baptiste Vimort<sup>2</sup>, Ken Martin<sup>2</sup>, Gabor Fichtinger<sup>1</sup>

1. Laboratory for Percutaneous Surgery, School of Computing, Queen's University, Kingston, Canada
2. Kitware Incorporated, Carrboro, North Carolina, USA

**INTRODUCTION:** Virtual reality (VR) systems typically consist of a tracked head-mounted-display (HMD), tracking stations, and tracked controllers, which immerses users in a virtual environment. The applications for these systems range from simulation training to entertainment. Recently, applications in the medical field have also been explored. For instance, VR systems are showing promise as training simulators for complex medical procedures [1]. Our aim was to extend 3D slicer, an open-source medical image analysis and visualization platform, with VR capabilities and to evaluate 3D Slicer as a VR platform as well as the feasibility of using VR for the medical field.

**METHODS:** The requirements for the VR extension are: intuitive controls for seamless navigation of virtual environments, maintaining high performance rendering to prevent motion sickness, convenient import and visualization of medical imaging data, and the platform must be open-source with a permissive license. The platform extends 3D Slicer which provides many tools for medical imaging and visualization such as image segmentation, surface modeling, and volume rendering [2]. We propose to assess the feasibility of using VR for navigating and comprehending 3D renderings by having participants complete tasks that require them to maneuver within complex virtual scenes. In this experiment, we will compare the stereoscopic display of VR to viewing 3D renderings on a 2D monitor. Participants must complete two tasks using both VR and mouse-monitor navigation. Each scene is designed to require constant reorientation. The first task consists of 8 hollow cubes with coloured integers, 1 to 8, inside the cube. The cubes have a small hole in one of the sides, which participants will navigate to, in order to identify the integer. The task is complete once they identify the colour of each of the 8 integers. The second task is a rendering of a brachytherapy phantom with just the catheters displayed. The catheters, on one side, are labeled with letters A to E, and on the other side, integers 1-5. The goal of this task is to correctly map each letter to the corresponding integer. This task was designed users to navigate the scene to find better angles of view, as the catheter renderings intertwine at some sections, making it hard to follow from just one angle. Each task is done twice – once using mouse-monitor navigation, and once using VR navigation with the HTC Vive HMD and controllers. For each task, we created slightly modified scenes for the two modalities to avoid bias in the results. We had participants complete one task with both modalities before introducing the next task. The tasks are timed until completion.

**RESULTS:** 5 participants conducted our experiments. Results show a significant decrease in total time needed to complete the tasks using VR. For the box task, the mean completion time using mouse-monitor was 7 minutes and 52 seconds—compared to 4 minutes and 24 seconds using VR. Furthermore, the mean number of revisits (where participants navigated to a cube they had already identified) for mouse-monitor navigation was greater than VR navigation – 11.6 revisits vs 5, respectively. This result is corroborated in the catheter task. The mean completion time using mouse-monitor was 3 minutes and 57 seconds, compared to VR's 2 minutes and 37 seconds.

**CONCLUSION:** Our work extended 3D Slicer with VR capabilities. Users are able to create 3D medical scenes and visualize them with ease. Further, our experiment results demonstrate the usefulness of the intuitive controls of VR navigation for medical scenes in comparison to mouse-monitor navigation.

**REFERENCES:** [1] N. E. Seymour et al., *Annals of Surgery*, 2002 [2] A. Fedorov et al., *Magnetic Resonance Imaging*, 2012

**ACKNOWLEDGEMENTS:** G. Fichtinger is supported as a Canada Research Chair.

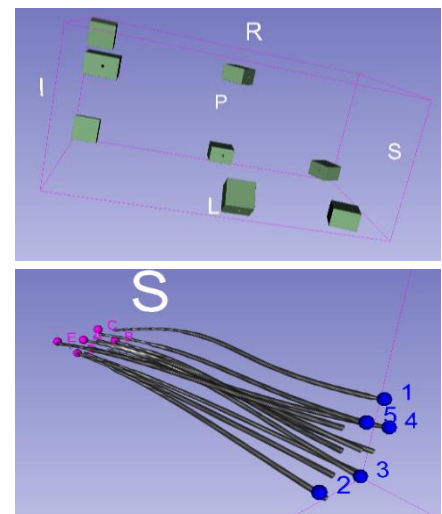


**Figure 1.** *Top:* The integer eight in pink found inside one of the eight cubes. *Center:* Eight cubes created by the Segment Editor tool in 3D Slicer. *Bottom:* Volume renderings of brachytherapy phantom using the Volume Rendering tool in 3D Slicer with only the catheters visualized.

## Quantifying the effect of patient position on the curvature of colons

Jacob Laframboise<sup>1</sup>, Tamas Ungi<sup>1</sup>, Andras Lasso<sup>1</sup>, Mark Asselin<sup>1</sup>,

Matthew S. Holden<sup>1</sup>, Pearl Tan<sup>2</sup>, Lawrence Hookey<sup>2</sup>, Gabor Fichtinger<sup>1</sup>

<sup>1</sup>Laboratory for Percutaneous Surgery, School of Computing, Queen's University, Kingston, Canada

<sup>2</sup>Gastrointestinal Diseases Research Unit, Department of Medicine, Queen's University, Kingston, Canada

**INTRODUCTION:** Colonoscopy is a complex procedure with considerable variation among patients, requiring years of experience to become proficient. Understanding the curvature of colons could enable practitioners to be more effective. Position change for extubation has been found to increase the rate of adenoma detection, while adding just 44 seconds to the procedure and being cost neutral[1]. Therefore, positional recommendations could be made during intubation to increase patient comfort and ease of operation. The purpose of this research is to develop methods to analyze the curvature of patients' colons, and compare key segments of colons between supine and prone positions.

**METHODS:** The colon lumen in CT scans of ten patients are segmented. The following steps are automated by Python scripts in the 3D Slicer application: generate centerline points of the colon, fit a curve to the center points, and compute the curvature at every point along the curve. With point curvature data, we can identify the maximums and minimums in curvature. Curves are defined between two local curvature minimums. Angle of curves is calculated over the distance of curves by the angle between the vectors from local curvature minimum to curve maximum, and from the maximum to the next minimum.

**RESULTS:** This automated process identifies curves on the colon centerline for quantitative analysis in different patient positions. On average, there are  $4.6 \pm 3.8$  more curves in supine position than prone. In the descending colon, there is a mean of  $3.7 \pm 3.7$  curves more in the supine position. In the descending colon, prone curves turn a mean of  $6.2 \pm 8.8$  degrees more than supine curves.

**CONCLUSION:** Our process identified and quantified curves in the colons of ten patients' CT scans to reveal more curves in patients' colons in the supine position, especially in patients' descending and sigmoid colons. It is also observed that curves in the descending colon are of a higher degree in the prone position. With the data provided in this study, and with the future data collected from a study with a larger sample size, physicians will have a better idea of the typical curvatures of colons, to aid them in colonoscopy.

**ACKNOWLEDGEMENTS:** G. Fichtinger is supported as a Canada Research Chair. This work was funded, in part, by CANARIE's Research Software Program.

### REFERENCES:

- [1] A. Wilson MRCP and B. P. Saunders FRCP, "Position change during colonoscopy: the oldest and best trick in the book," *Gastrointest. Endosc.*, vol. 82, pp. 495–496, 2015.

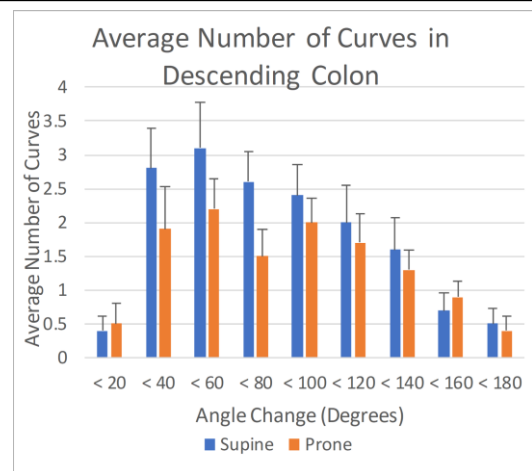


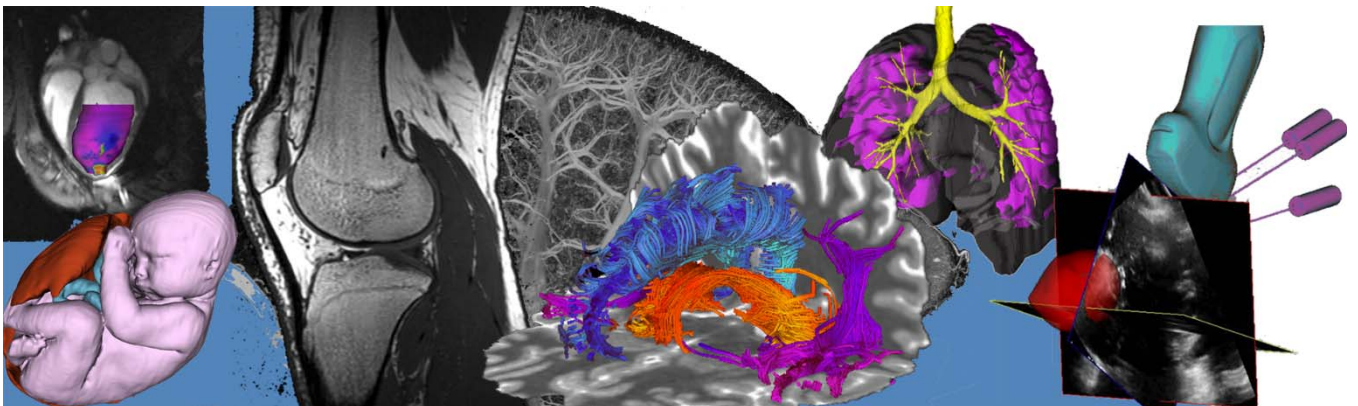
Figure 1. Histogram of the average number of curves ( $\pm$ SEM) in the descending colon per degree interval, with degree intervals of 20 degrees.

Table 1. Mean ( $\pm$ SEM) Number of Curves in Each Segment by Position.

Mean Number of Curves	Supine	Prone
Whole Colon	$33.5 \pm 2.1$	$28.9 \pm 1.7$
Ascending Colon	$2.6 \pm 0.3$	$3.0 \pm 0.7$
Transverse Colon	$14.8 \pm 1.5$	$13.5 \pm 1.2$
Descending Colon	$16.1 \pm 2.0$	$12.4 \pm 1.7$

# Poster Presentation Abstracts

## Session 6: Bone and Joint Imaging





## Total Hip Arthroplasty Surgical Approach and Implant Design: Effects on Patient Function, Patient Activity, and Implant Migration

Maxwell E. Perelgut<sup>1,2,5</sup>, E.M. Vasarhelyi<sup>3</sup>, B.A. Lanting<sup>3</sup>, M.G. Teeter<sup>2-5</sup>

<sup>1</sup>School of Biomedical Engineering, <sup>2</sup>Robarts Research Institute, <sup>3</sup>Dept. Surgery, <sup>4</sup>Dept. Medical Biophysics, Western University; <sup>5</sup>Lawson Health Research Institute; London, Canada

**Introduction:** Total hip arthroplasty (THA) is a common procedure to treat end-stage hip osteoarthritis (OA). Increasing pressure for rapid recovery care pathways following THA is pushing for new ways to measure patient functionality. A variety of surgical changes have been made to facilitate these pathways. The increasing adaptation of the muscle sparing Direct Anterior (DA) approach relative to the more invasive Direct Lateral (DL) approach can be seen as a response to these changes. Femoral implants have been designed with the intention of enhancing patient function and implant stability. It is believed that collared femoral stems, in comparison with collarless femoral stems, provide earlier implant stability, resulting in increased early patient activity and a decreased risk of implant revision. This study aims to evaluate the effects surgical approach and implant design have on patient function and implant migration.

**Methods:** Patients (n=100) with unilateral hip OA who were undergoing primary THA surgery were recruited pre-operatively to participate in this prospective randomized clinical trial. Selection for surgical approach was expertise based (DA/DL=50/50) and all patients were randomized to receive either a collared (n=50) or collarless (n=50) cementless femoral stem. Patients will be seen at nine-appointments (pre-operative, <24 hours post-operation, two-, four-, six-weeks, three-, six-months, one-, and two-years). Patients completed an instrumented timed-up-and-go (TUG) test using wearable sensors at each visit, excluding the day of their surgery. Participants logged their steps using Fitbit activity trackers and a seven-day average prior to each visit was recorded. Patients also underwent supine radiostereometric imaging <24 hours post-operation prior to leaving the hospital, and at all follow-up appointments.

**Results:** Significant differences in implant subsidence were seen within the first two-weeks post operatively. The collared implant migrates into the femur less than the collarless implant ( $p=0.045$ ), while both stems have similar migration patterns from two-weeks onward (Fig. 1). Patients that underwent the DA approach experience more implant migration than patients that received the DL approach regardless of stem design ( $p=0.002$ ). This migration trend continued beyond two-weeks (Fig. 1). The DA patients experience faster recovery early post-operatively for both function and activity compared to the DL patients. Significant differences in patient function were observed at two-weeks ( $p<0.001$ ) and four-weeks ( $p=0.025$ ) (Fig. 2). Significant differences in patient activity were observed at 6-weeks ( $p=0.035$ ) and 3-months ( $p=0.011$ ) (Fig. 3).

**Conclusions:** Early results suggest that the collared femoral stem migrates less than the collarless stem which could result in a decreased risk of revision in the future. These results also suggest that the DA surgical approach results in earlier patient functional recovery and activity compared to the DL surgical approach, but this does not come without the cost of more implant migration.

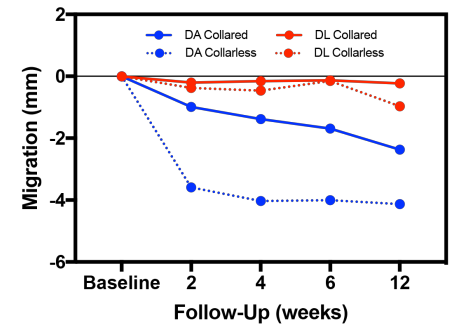


Figure 1: Total implant subsidence for collared and collarless stems in Direct Anterior and Direct Lateral patients.

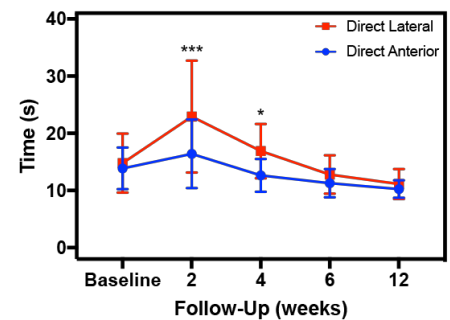


Figure 2: Time to complete the TUG test for Direct Anterior and Direct Lateral patients throughout recovery.

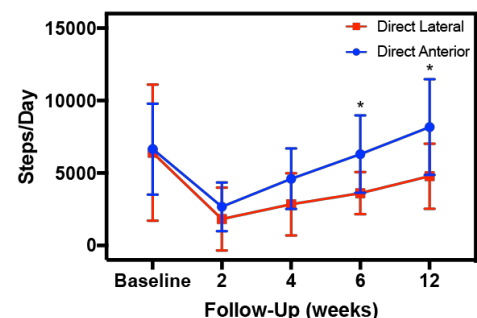


Figure 3: Number of steps per day for Direct Anterior and Direct Lateral patients throughout recovery.

## Does an Anatomically Designed Total Knee Replacement Improve Knee Joint Kinematics?

Jordan S. Broberg<sup>1,3</sup>, J.L. Howard<sup>4</sup>, B.A. Lanting<sup>4</sup>, E.M. Vasarhelyi<sup>4</sup>, X. Yuan<sup>2</sup>,

R.W. McCalden<sup>4</sup>, D.D.R. Naudie<sup>4</sup>, and M.G. Teeter<sup>1-4</sup>

<sup>1</sup>Department of Medical Biophysics, Schulich School of Medicine & Dentistry, Western University, London, Canada;

<sup>2</sup>Robarts Research Institute, London Canada; <sup>3</sup>Lawson Health Research Institute, London, Canada;

<sup>4</sup>Department of Surgery, Schulich School of Medicine & Dentistry, Western University, London, Canada

**Introduction:** Arthritis is a serious health issue affecting one in five Canadians and causes significant joint pain and loss of function<sup>1</sup>. For end stage arthritis of the knee, the only treatment currently available is total knee replacement (TKR). Even though TKR has improved over the years, with implants having greater longevity, patient satisfaction following TKR has not improved, with approximately 20% of patients recording dissatisfaction with their new knee joint<sup>2</sup>. It is unclear why many patients feel this way, but it may relate in part to implant designs that do not provide a “natural” feeling knee. Implant manufacturers continue to introduce new concepts for implant design, which are essential for reaching the goal of a “normal” knee after TKR surgery. The Journey II TKR (Smith & Nephew) was developed with this goal in mind. Its anatomical design attempts to mimic the normal knee joint structure to return more natural kinematics to the joint, with emphasis on preserving femoral rollback posteriorly and eliminating paradoxical anterior motion. Our objective is to examine patients receiving the Journey II TKR to measure the knee joint contact kinematics of the Journey II TKR compared to a non-anatomically designed implant by the same manufacturer. We hypothesize that the Journey II TKR will have more natural contact kinematics that differ from the non-anatomically designed implant.

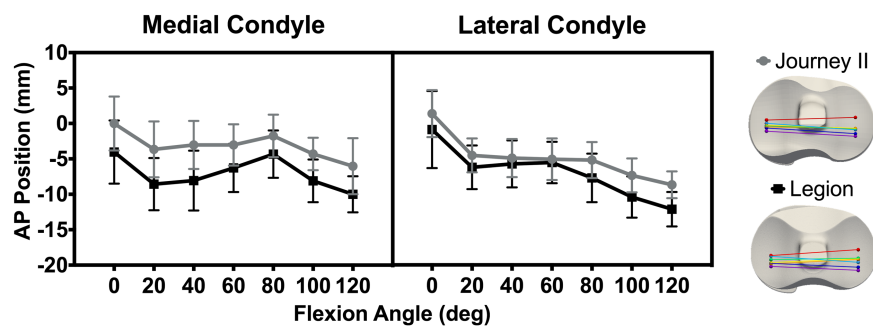


**Figure 1.** Average anterior-posterior (AP) tibiofemoral contact locations from 0° to 120° of flexion on the medial and lateral condyles for patients in the anatomically designed Journey II TKR group and the non-anatomically designed Legion TKR group. On the right are maps of the tibiofemoral contact locations for each group. Both display similar femoral rollback posteriorly. The Legion TKR group experiences more paradoxical anterior motion on the medial condyle than the Journey II TKR group.

**Methods:** A total of 56 individuals will be recruited to receive a Journey II TKR, matching an existing prior cohort with a non-anatomically designed TKR (Legion TKR, Smith & Nephew). For the Journey II TKR group, a series of radiostereometric analysis (RSA) images were acquired at 3-months post-operatively at different knee flexion angles, ranging in 20° increments from 0° to 120°. Model-based RSA software (RSACore, Leiden, Netherlands) was used to obtain the 3D positions and orientations of the femoral and tibial implant components. Results from the model-based RSA software were used to attain kinematic measures (contact locations and magnitude of excursion) for each condyle. Results from the Journey II TKR group were compared to the 2-year post-operative measurements from the Legion TKR group. Statistical analyses (t-test and Mann-Whitney test) were performed for comparisons between the groups.

**Results:** Preliminary results from 65 patients (21 Journey II TKR, 44 Legion TKR) found that for contact locations on the medial condyle (Fig. 1), there were significant differences at all angles of flexion ( $p < 0.01$ ). For contact locations on the lateral condyle (Fig. 1), there were significant differences for 0°, 20°, 80°, 100°, and 120° of flexion ( $p < 0.05$ ). There was no significant difference between groups with respect to magnitude of excursion on both medial (mean difference=0.20 mm,  $p=0.83$ ) and lateral (mean difference=1.97 mm,  $p=0.13$ ) condyles.

**Conclusions:** Early results suggest that the anatomically designed Journey II TKR provides significantly different knee kinematics from the non-anatomically designed Legion TKR. The decrease in the unnatural paradoxical anterior motion and similar femoral rollback in the Journey II TKR group suggests that an anatomically designed implant provides more natural knee joint kinematics than a non-anatomically designed implant.

**References:** <sup>1</sup>Canadian Community Health Survey (2016). <sup>2</sup>Bourne et al. (2010). *Clin. Orthop. Relat. Res.* 468, 57-63.

## In vivo polyethylene wear measurement in reverse total shoulder arthroplasty

Madeleine Van de Kleut<sup>1,2,5</sup>, George S. Athwal<sup>4,5</sup>, Xunhua Yuan<sup>1</sup>, Matthew G. Teeter<sup>1,3,4,5</sup>

<sup>1</sup>Robarts Research Institute, The University of Western Ontario, London, Canada

<sup>2</sup>Graduate Program in Biomedical Engineering, The University of Western Ontario, London, Canada

Depts. <sup>3</sup>Medical Biophysics and <sup>4</sup>Surgery, The University of Western Ontario, London, Canada

<sup>5</sup>Lawson Health Research Institute, London, Canada

### Introduction:

Reverse total shoulder arthroplasty (RTSA) features a cobalt-chrome glenosphere articulating against an ultra-high molecular weight polyethylene humeral liner. A number of studies have evaluated the wear of this configuration through retrieval analysis and simulation studies, though no study has quantified the material loss of well-functioning RTSA implants in vivo. The purpose of this study was to validate the use of a calibrated stereo x-ray technique known as radiostereometric analysis (RSA) for in vivo RTSA wear measurement at a single time point using a phantom setup.

### Methods:

Six additively manufactured polyethylene inserts were fabricated, one unworn control and five to represent known wear patterns (Figure 1), and individually fit within RTSA components. Each insert was imaged using standard radiostereometric techniques and analyzed using proprietary software. From the position and orientation estimation provided by the software, a micro-computed tomography model of the control insert was virtually placed within the metaphyseal tray. The apparent intersection of the glenosphere into the insert was recorded as wear. Both volumetric and linear wear depth were recorded.

### Results:

Our method of measuring in vivo polyethylene wear using radiostereometric analysis provided a linear wear depth precision of 0.19 mm and bias of  $0.5 \pm 0.22$  mm, and volumetric precision of  $47.0 \text{ mm}^3$ , with a bias of  $46.6 \pm 20.4 \text{ mm}^3$ . Preliminary results from our in vivo study applying the measurement methodology indicate a volumetric wear rate  $40 \text{ mm}^3/\text{year}$  and maximum linear wear of 0.1 mm/year. Wear was distributed throughout the articular surface, with slight localization to the inferior aspect of the polyethylene insert (Figure 2).

### Conclusion:

This technique allows for the in vivo measurement of polyethylene wear without the requirement of marker beads or baseline radiographs, expanding the potential for in vivo wear measurements to larger populations and retrospective analysis. Measured in vivo wear for implants that are well-functioning in the mid-term is in line with estimates provided by in vitro and in silico simulation studies and below the threshold for osteolysis leading to inflammation and aseptic loosening.

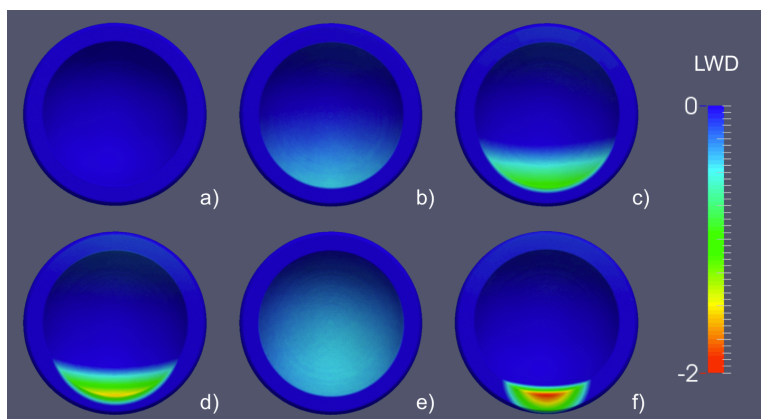


**Figure 1.** Deviation maps representing the linear wear depth (LWD) of each additively manufactured worn insert, using the unworn insert (a) as reference. Insert 1 (b) simulates inferior articular wear, Insert 2 (c) inferior articular and rim wear, Insert 3 (d) inferior rim wear, Insert 4 (e) large articular wear, and Insert 5 (f) simulating small inferior rim notching.

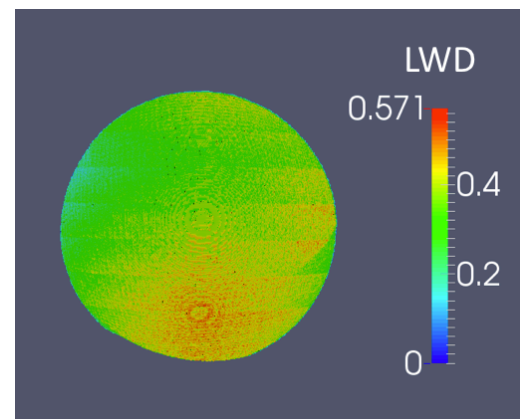


**Figure 2.** Example wear map from in vivo wear measurement. Volumetric wear of  $271 \text{ mm}^3$  and maximum linear wear of 0.571 mm was recorded at 6.7 years following surgery.

**Cementless Total Knee Arthroplasty: Does surgical technique impact implant migration?**H.A. Williams<sup>1,2,5</sup>, R.A. Bloomfield<sup>1,3</sup>, X. Yuan<sup>1</sup>, J.L. Howard<sup>4</sup>, B.A. Lanting<sup>4</sup>, M.G. Teeter<sup>1,2,4,5</sup><sup>1</sup>Robarts Research Institute; Depts of <sup>2</sup>Medical Biophysics; <sup>3</sup>Electrical and Computer Engineering; <sup>4</sup>Surgery, Western University, London, Canada; <sup>5</sup>Lawson Health Research Institute, London, Canada

**Introduction:** A total knee arthroplasty (TKA) is the standard of care treatment for end-stage osteoarthritis (OA) of the knee. Historically, bone cement (a grout-like substance) has been used to establish fixation between the implant and bone, resulting in two interfaces where component loosening may occur. With an increasingly younger cohort requiring TKA's alongside prosthetic design and instrumentation advancements, cement durability is of increasing concern. Cementless implant systems are press fit implants coated with an osteoconductive component surface and rely on bone ingrowth for fixation. It is currently unknown whether the surgical technique used to implant the cementless prostheses impacts the longevity of the implant. Two different surgical techniques are commonly used by surgeons and may result in different load distribution across the joint, which will affect bone ingrowth. The overall objective of the study is to assess implant migration and functional ability after cementless TKA.

**Methods:** Thirty-nine patients undergoing a primary unilateral TKA as a result of OA were recruited prior to surgery and randomized to a surgical technique based on surgeon referral. In the gap balancing surgical technique (GB) soft tissues are first released from bone to restore neutral limb alignment followed by bone cuts (resection) to balance the joint space in flexion and extension. In the measured resection surgical technique (MR) bone cuts are made based on pre-determined anatomical landmarks and soft tissue releases are made with implant components *in-situ* following bone resection. Patients returned 2 weeks, 6 weeks, 12 weeks, and 24 weeks following surgery for radiographic evaluation, the Timed-Up-and-Go (TUG) functional performance assessment, and to complete a series of questionnaires.

**Results:** There were no significant differences between the groups at baseline in terms of age, sex, body mass index, operative limb, patient reported outcome measure, total time to complete the TUG test, or any other temporal or flexion metrics ( $p > 0.05$ ). Regardless of technique, all temporal and flexion metrics improved over the follow up period ( $p < 0.0001$ ). No significant differences in migration were observed between the two approach groups at any time in any axial direction for the femoral and tibial components.

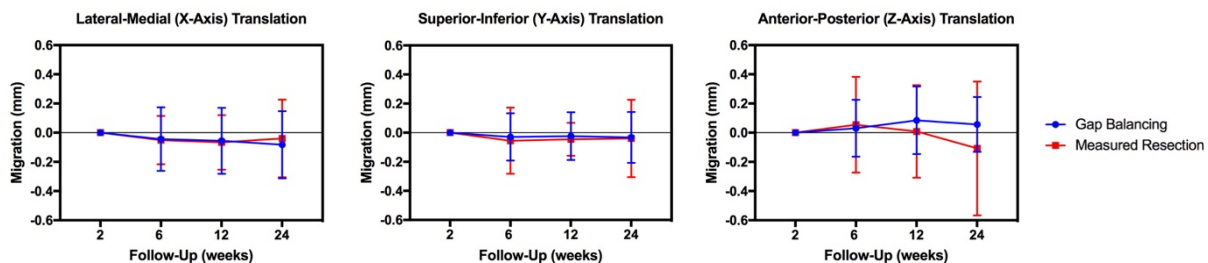


**Figure 1.** Implant migration of the tibial component.

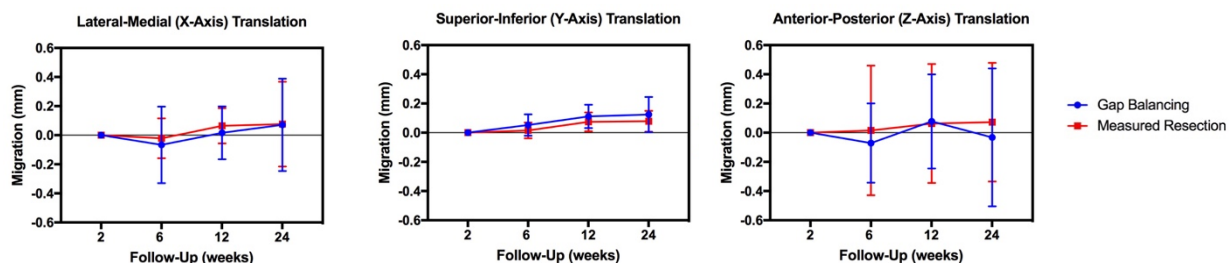


**Figure 2.** Implant migration of the femoral component.

**Conclusion:** Including functional performance assessments provides a new perspective to functional restoration. No differences in migratory patterns were observed in the early post-operative period between the surgical techniques. Once all patients return for their 24 week follow up's migration data will be compared to established thresholds which can predict long-term implant failure.

**Biomechanical changes of porcine tendons following high-intensity focused ultrasound ablation**William Chu Kwan<sup>1</sup>, Adam Waspe<sup>1</sup>, Unni Narayanan<sup>1</sup>, James Drake<sup>1</sup><sup>1</sup>The Hospital for Sick Children, Toronto, ON, Canada

**Introduction:** Diabetic foot ulcer, pediatric toe-walking, and cerebral palsy are musculoskeletal conditions that can be corrected with surgical resection of tendons. Given current trends towards non-invasive procedures, Magnetic Resonance-guided Focused Ultrasound Surgery (MRgFUS) is an ablation technique that has the potential to provide an incisionless non-invasive treatment for these conditions. This could translate into less exposure to anesthetics, less prophylactic antibiotics use, better pain management medication, reduced hospitalization time, and ability to perform conservative treatments with retreatments.

Our goal in this study is to perform a quantitative analysis of biomechanical changes in tendons after MRgFUS ablation. Understanding these effects sets the foundation for future studies in non-invasive MRgFUS tendon transection.

**Methods:** To standardized this experiment, 4 agar phantoms were prepared. Each phantom contained 4 pairs of matching porcine deep digital flexor tendons. One tendon in each pair would be treated with MRgFUS ablation while the other tendon would serve as a control. Physical properties such as temperature, length, and diameter were recorded during preparation, verified to be consistent between control and treatment tendons, and used for analysis.

Ablation treatment was performed using a V1 Sonalleve (Profound Medical). The treated tendon from each pair was randomly assigned to one of four groups based on ablation parameters. Group 1 did not receive any treatment serving as an additional control. Group 2 had 1 treatment with a power of 50W for 20 seconds. Group 3 had 1 treatment with a power of 100W for 20 seconds. Group 4 had 2 treatments of 100W for 20 seconds each. MR imaging and temperature maps were performed throughout the experiment.

Following ablation, the tendon biomechanical properties were analyzed using an Instron MicroTester. This machine applied a tensile force on the tendon and generated a stress versus strain curve, yielding the Young's modulus.

**Results:** Overall, there was a decrease in Young's modulus as more power was used to ablate the tendon. Treated tendons from Group 3 and 4 experienced a rupture while subjected to the Instron tester. The treated tendons in Group 2 had a decrease of 16.07% in Young's modulus and no tendon rupture observed. The tendons in Group 3 had a decrease of 41.97% in Young's modulus and a maximum tensile stress of 6.59 MPa. Finally, the tendons in Group 4 had a decrease of 73.01% in Young's modulus and a maximum tensile stress of 4.48 MPa.

Given the Instron's tensile force maximum of 500N, there was no data to report Young's modulus or fracture strain for all the untreated controls. These tendons did not rupture during testing and remained intact.

**Conclusions:** Our results demonstrate that MRgFUS ablation changes the biomechanical properties of tendon by decreasing the Young's modulus and its elasticity. As more power is delivered on a treatment cell, the maximum tensile stress required to rupture the tendon decreased. This demonstrates that MRgFUS ablation could be a feasible intervention for non-invasive tendon transection for many musculoskeletal conditions.

## 4DCT to Examine Wrist Contact Mechanics

Michael Riddle<sup>1</sup>, Puneet Ronota<sup>1,2,3</sup>, Rob Gray<sup>1,2,3</sup>, Nina Suh<sup>6,7,8</sup>, Ting-Yim Lee<sup>4,5,6</sup>, Emily Lalone<sup>1,2,3,6,8</sup>

<sup>1</sup>School of Biomedical Engineering, <sup>2</sup>Department of Mechanical and Materials Engineering, <sup>3</sup>Faculty of Engineering, <sup>4</sup>Medical Biophysics, <sup>5</sup>Robarts Research Institute, <sup>6</sup>Lawson Health Research Institute, <sup>7</sup>Roth|McFarlane Hand and Upper Limb Center, <sup>8</sup>Department of Surgery, The University of Western Ontario

### Introduction

Distal radius fractures (DRF) are a common occurring nearly twice the frequency of hip/femur fractures and nearly five times that of vertebral/spine fractures(1). Radiographic and degenerative changes are frequently reported in patients who have suffered a DRF, but the long-term clinical impact of these changes has not been clearly defined. Some studies have indicated that mal-alignment is associated with higher arm-related disability and other studies have indicated that a large amount of radiographic deformity is required before function is lost(2–4). Four-dimensional CT (4DCT) is an imaging technique whereby joint motion is acquired using a dynamic sequential scanning model. The images are acquired while the joint is moving and allows kinematic assessment of the joint motion. In this study, we propose to employ a 4DCT approach for quantifying wrist motion.

### Methods

A single healthy participant underwent unilateral imaging of a left wrist using the 4DCT Scanner (GE Revolution). The wrists were scanned for 15 second as the patient moved their wrist in a cyclical, and repeatable motion (pronation-supination) (1 motion= 5 seconds, repeated 3 time) using a non-gated 4DCT technique. The 4DCT images obtained from the individual case were reconstructed and segmented using Mimics Materialise Software. Three-dimensional reconstructions were created and used to assess the proximity between the distal radius and lunate and scaphoid, during the wrist motion using a previously developed, automatic an inter-bone distance algorithm(5). Briefly, the algorithm calculates minimum inter-bone distances between opposing bone surfaces using a point-to-point distance measurement. Six phases of the kinematic scan were analyzed separately.

### Results

Qualitative comparison of a single patient for 6 static phases throughout the 24 second scan (pronation to supination) is shown below. This figure shows the greater sigmoid notch of the distal radius (distal ulna not shown).

Preliminary results indicate that the ulna tracks from the volar to the dorso-medial region of the greater sigmoid notch during rotation.

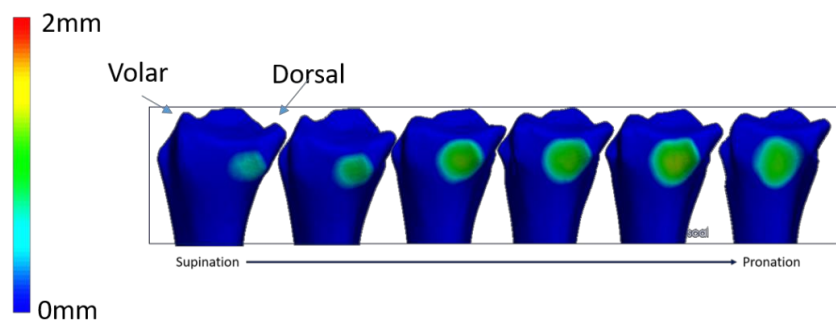


Figure 1: Proximity Maps of Joint Congruency of Left Wrist

**Conclusions:** Previous studies have also documented the volar to dorsal shift during forearm rotation. Early results indicate that while using the 4DCT continuous scanning technique, it is possible to examine wrist motion dynamically without blurring and compromising spatial resolution. Future work will be to examine the effect wrist fracture and joint mal-alignment on the underlying joint mechanics.

1. Nellans KW, Kowalski E, Chung KC. The Epidemiology of Distal Radius Fractures. Vol. 28, Hand Clinics. 2012. p. 113–25.
2. Jaremko JL, Lambert RGW, Rowe BH, Johnson JA, Majumdar SR. Do radiographic indices of distal radius fracture reduction predict outcomes in older adults receiving conservative treatment? Clin Radiol. 2007 Jan;62(1):65–72.
3. Anzarut A, Johnson JA, Rowe BH, Lambert RGW, Blitz S, Majumdar SR. Radiologic and patient-reported functional outcomes in an elderly cohort with conservatively treated distal radius fractures. J Hand Surg Am. 2004 Nov;29(6):1121–7.
4. Grewal R, MacDermid JC. The risk of adverse outcomes in extra-articular distal radius fractures is increased with malalignment in patients of all ages but mitigated in older patients. J Hand Surg Am [Internet]. 2007 Sep [cited 2018 Jul 30];32(7):962–70. Available from: <http://www.ncbi.nlm.nih.gov/pubmed/17826547>
5. Lalone EA, McDonald CP, Ferreira LM, Peters TM, King GW, Johnson J a. Development of an image-based technique to examine joint congruency at the elbow. Comput Methods Biomech Biomed Engin. 2013 Mar;16(3):280–90.

## Validating Three-Dimensional Ultrasound Measurements of the Synovium for Diagnosis of Rheumatoid Arthritis

Sam Papernick<sup>1,2</sup>, Derek J Gillies<sup>1,2</sup>, Kevin Barker<sup>2</sup>, Lori Gardi<sup>2</sup>, Aaron Fenster<sup>1,2</sup>

<sup>1</sup>Department of Medical Biophysics, <sup>2</sup>Robarts Research Institute, Western University, London, Ontario, Canada

**Introduction:** Rheumatoid arthritis (RA) is an autoimmune disease that is associated with disability, early death, pain, and socioeconomic costs. There is currently no definitive test to confirm the diagnosis of RA, and the exact causes of the disease are unknown. Current diagnostic methods for RA involve x-ray, magnetic resonance imaging (MRI), or two-dimensional (2D) ultrasound (US) imaging to look for joint damage, such as thickened synovial tissues or articular cartilage degradation. Unfortunately, x-ray and 2D US can be limited when trying to interpret the three-dimensional (3D) anatomical environment, and MRI is costly, associated with long wait times in Canada, and may be inaccessible to certain patients. 3D US devices acquire images by tilting a conventional US transducer around a center of rotation point in contact with the object, or by linearly translating the transducer while scanning is active. Previously, our lab has demonstrated the capabilities of 3D US to acquire images at high frame rates and measure volumes of tissues in the body accurately. Since an inflamed synovium is seen in almost all patients with RA, it is possible that comparing synovium volume measurements from RA patients and healthy patients can provide a definitive, fast, and reliable metric for diagnosis. We have developed a handheld 3D US device that acquires images by linearly translating a 2D US transducer with the aim of improving the quality of 3D US images and thus increasing diagnostic efficiency and reliability for patients with RA.

**Methods:** The handheld 3D US acquisition device must have its linear and volumetric measurement capabilities validated before it can be used in a clinical setting. Linear measurements were validated using a string phantom containing a grid of wires separated by known distances (i.e. 10 mm) that was submersed in an isopropyl alcohol solution to approximately match the speed of sound of tissues. This phantom was imaged with a Phillips iU22 ultrasound system using an L12-5 50 mm linear transducer, which are both typically used clinically. Volumetric measurements were then validated using 3D US images of a fabricated agar synovial tissue phantom (Fig. 1(A) and (B)). A mold with a known volume (i.e. 9840 mm<sup>3</sup>) was filled with agar and cooled prior to being embedded in an agar background that contained cellulose for acoustic scattering and contrast. The images of the phantom were manually segmented using itk-SNAP and compared to the known mold volume. After the device was validated, a healthy volunteer was imaged by a collaborating rheumatologist to assess clinical applicability (Fig. 1(C)).

**Results:** The linear measurement phantom images resulted in mean distances of 9.87 mm in the reconstruction plane and 9.99 mm in the acquisition plane. This corresponds to percent errors of 1.32% and 0.095% for the reconstruction and acquisition planes respectively. The segmentation volume of the simulated tissue phantom was measured to be 9802.64 mm<sup>3</sup>, resulting in a percent error of 0.38%. The volunteer image was able to depict and reconstruct tissues in the knee without many image artifacts due to motion or other sources, providing additional support for clinical applicability.

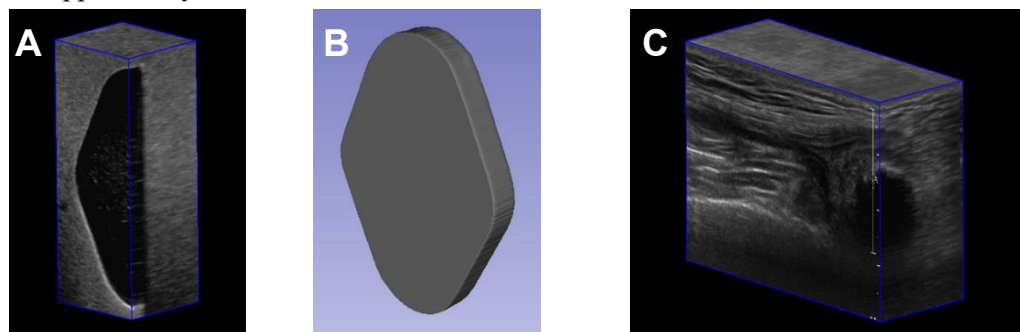


**Figure 1.** Scan of synovium phantom (A) and segmentation (B), and a 3D US image of the knee (C).

**Conclusions:** The handheld 3D US device demonstrated clinically acceptable linear and volumetric measurements with all errors less than 1.5%. Future work will focus on scanning volunteers with 3D US and MRI to demonstrate the accuracy of volumetric measurements of the knee synovium. The 3D US scans will be conducted by a rheumatologist to ensure that the synovium is correctly identified and analyzed. This will build the foundation for a study comparing the synovial tissue volumes in patients with RA versus healthy patients that may provide a definitive diagnostic metric with the potential of providing insight into the disease pathology.

## Wireless Telemetry Load Sensor for Orthopaedic Applications

William Anderson<sup>1,2</sup>, Sydney Wilson<sup>2</sup>, David W Holdsworth<sup>3</sup>

<sup>1</sup>School of Biomedical Engineering, Western University, <sup>2</sup>Faculty of Engineering, Western University, <sup>3</sup>Robarts Research Institute, Western University, London, Ontario, Canada

**Introduction:** Recording real time in-vivo load data has long been a challenge due to requirements in size, data transmission, and power management of load sensors<sup>1</sup>. Load data can allow scientists and clinicians to quantify the forces acting on structures within the human body. This information can improve orthopaedic implant design and patient rehabilitation practices. The objective of this study is to convert a commercially available wireless telemetric tire pressure sensor into a compact, ultra-low power load sensor for use in orthopaedic applications.

**Methods:** The tire pressure sensor (FXTH87, NXP) deforms approximately 600 microns over the full range of its pressure measurement capability (100-450 kPa). A deformation calibration from 0-600 microns was performed to determine the signal value corresponding to the deformation of the sensor. Two tire pressure sensors were used, and five trials were performed for each sensor. Compressive extension was applied to the sensor enclosure using an Instron 3343 and a 3D printed indenter at a rate of 600 microns/min. Compressive load (internal sensor resistance) was recorded using a 50 N load cell. Compressive load and extension were obtained using Instron Bluehill Software. Sensor signal data was recorded using an FRDM KW019032 RF receiver and plotted in real time in a graphical user interface (GUI) developed by NXP Semiconductors. Signal values and internal sensor resistance were plotted against compressive extension in Prism. Sensor dimensions and weight were obtained using a caliper and analytical balance, respectively. RF transmission range through air was determined by extending the sensor from the RF receiver until no signal values were observed in the sensor GUI. The average power draw and battery lifetime were calculated using the average current draw of the sensor package during continuous transmission, powered by a 3V, 130mAh CR1632 lithium coin battery. The average current draw of a single transmission was determined using an oscilloscope and a multimeter current adapter.

**Results:** The sensitivity of the signal vs extension plot is 1.25 microns/signal unit over the linear region of the graph. The average standard deviation of internal sensor resistance and pressure signal over the linear region of the graph was 0.05 N and 5.35 signal units, respectively. This corresponds to an uncertainty in position of  $\pm 8.04$  microns. The maximum internal sensor resistance/compressive load applied to the sensor was  $6.34 \pm 0.20$  N (mean  $\pm$  SD). The dimensions of the tire pressure sensor were 7 mm x 7 mm x 2 mm and weighed 0.3 g. The dimensions of the commercially available sensor package used for testing had a diameter of 17.4 mm, a height of 7.4 mm, and weight of 3.5 g. The mean RF transmission range was  $4.71 \pm 0.49$  m. The average power draw during continuous transmission (the highest power consumption state) was 10.3 mW. The average current draw during a single transmission was 3.46 mA. The lifetime of the sensor package during continuous transmission was 37.6 hours.

**Conclusions:** The results of this study show that a commercially available tire pressure sensor can be converted into a functioning load cell, as there is a relationship between reported signal and deformation over a range of 0-600 microns. The load sensor can be configured into an ultra-miniature package with sophisticated power management and RF transmission capabilities. To the best of our knowledge, this is the smallest system in the world with the capability of wireless transmission of applied deformation, making it an ideal candidate for implantation within orthopaedic components. This sensor package can also be configured within custom mechanical enclosures that are designed to transduce compression, tension, flexure, and torque into compressive extension. This package could be embedded within intervertebral disc replacements, spinal fusion cages, fracture fixation plates, high tibial osteotomy implants, and more.

**References:** 1. D'Lima, D., Fregly, B. and Colwell, C. (2013). Implantable sensor technology: measuring bone and joint biomechanics of daily life in vivo. *Arthritis Research & Therapy*, 15(1), p.203.

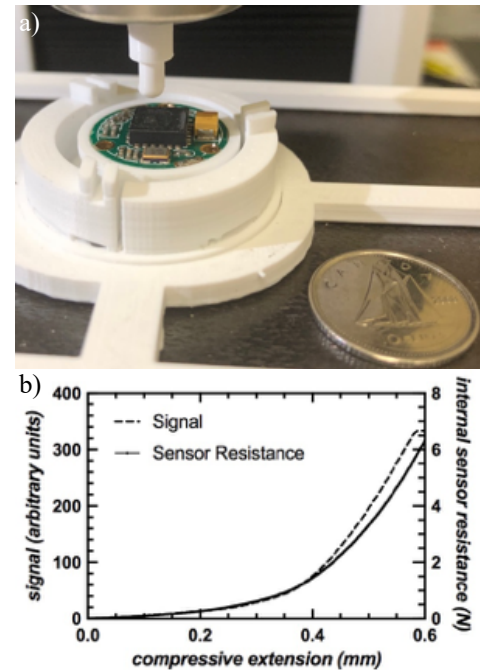


**Fig. 1:** (a) Experimental Instron testing apparatus. (b) Results of compressive extension testing, sensor signal and sensor resistance vs. compressive extension.



## Characterization of a Temperature Sensor for Implementation in Instrumented Orthopaedics

M. K. Lavdas<sup>1,2</sup>, D. W. Holdsworth<sup>1</sup>, M. Teeter<sup>1,3</sup>

<sup>1</sup>Robarts Research Institute; <sup>2</sup>School of Biomedical Engineering; <sup>3</sup>Department of Medical Biophysics, Western University, London, Canada

**Introduction:** Infections affect 1-2% of Total Knee Arthroplasty (TKA) patients with severe ramifications to mobility. One common treatment strategy is removal of the infected implants and installation of a temporary “spacer” while the infection is treated before implanting a revision TKA after the infection has subsided. Our solution involves the development of a novel instrumented tibial spacer to provide the physician with telemetry. The context of this abstract relates to a subset of the overall design challenge: Temperature sensing from within the knee. Specifically, the tuning of a TMP235A2DCKR (Texas Instruments (TI), Dallas, USA) analog temperature the commercially validated D1 (Kestrel Meters, Boothwyn, USA) data logger. The goal of this paper is to show that similar (mean  $\leq 5\%$  error) sensing performance can be attained with  $0.1^\circ\text{C}$  resolution, while using a package more suitable for implantation than the D1 and that it can be refined further through calibration.

**Methods:** The TI TMP235A2DCKR was selected for theoretically infinite (analog) resolution, stated linear  $\pm 0.02^\circ\text{C}$  (typ) response over a  $-40$  to  $150^\circ\text{C}$  range, low ( $9\ \mu\text{A}$ ) current draw and compact DBZ package. Based upon resolution and dynamic range it was determined that the analog/digital converter must be a minimum of 11 bits to deliver competitive ( $0.1^\circ\text{C}$ ) resolution. A 12 bit ADC equipped microcontroller was selected. The D1 delivers discrete output but is certified to  $\pm 0.5^\circ\text{C}$  accuracy with  $0.1^\circ\text{C}$  resolution over a range of  $-10$  to  $55^\circ\text{C}$  with no specification of latency. The data from both modalities can be exported as comma delimited text files. In a thermally insulated chamber with a resistive heating element, the following experiments were conducted: First, a shorter temperature cycle (12 min) over a range of thermal values spanning beyond what might be collected in body ( $35$  to  $42^\circ\text{C}$ ) was conducted. Profile was referenced at the TI sensor and compared with D1 output. Several iterations of changes were made to the calibration of the TI manufacturer linear characteristic equation before performing a longer (90 minute) trial over a wider range ( $26$  to  $42^\circ\text{C}$ ). Outputs were compared in Prism 7 and the percentage error between sensors was used to ascertain similarity and improvement in profile.

**Results:** Upon initial testing, inconsistencies were identified between the validated Kestrel sensor and the TI sensor as characterized by the manufacturer’s equation. A mean  $7.6\%$  error was observed with a standard deviation of  $5.7\%$ . With the altered characteristic equation and a linear chronological shift to account for the D1’s slower response, a mean  $4.0\%$  error with  $2.5\%$  standard deviation was achieved.

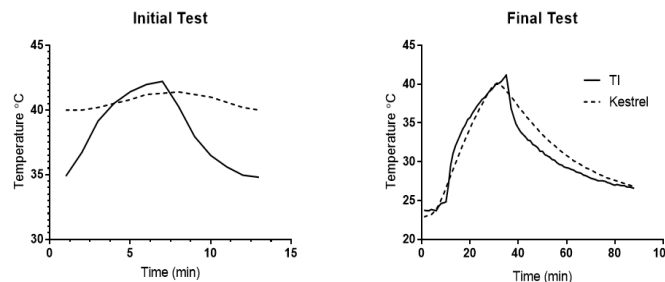


Fig 1 - Initial thermal cycle output (left). Final thermal cycle output (right)

**Conclusion:** Infection is a devastating complication of joint arthroplasty, with an ongoing call for better treatments. This study highlights the thermal sensing component tuning of a novel personalized healthcare solution to provide physicians crucial information. Following an iterative calibration process it has been shown that the Texas Instruments TMP235A2DCKR sensor has been characterized to deliver temperature measurements over the range of temperatures required for tibial implant applications with a resolution of below  $0.1^\circ\text{C}$  at a mean percentage error of less than  $5$  ( $4.0$ ) as compared to the Kestrel D1 while satisfying the other design constraints of the instrumented tibial spacer.

## The effect of region of interest size on subchondral bone measurements in an ovine post traumatic osteoarthritis model.

Omar Turk BSc<sup>1</sup>, Alan Getgood, MD<sup>2</sup>, Timothy A. Burkhart PhD<sup>2,3</sup>,

<sup>1</sup>Department of Kinesiology, <sup>2</sup>Fowler Kennedy Sport Medicine Clinic, <sup>3</sup>Department of Mechanical Materials and Engineering  
Western University, London, ON, Canada

**INTRODUCTION:** The severity of post-traumatic osteoarthritis (PTOA) and the effectiveness of treatments aimed at mitigating its effects can be assessed by analyzing the condition of the subchondral bone (SCB) via micro-CT imaging. Parameters such as bone mineral density, bone volume fraction, and bone volume/total volume can be calculated within a standardized region of interest (ROI). This ROI must be optimized to ensure that the area of the injury is being sampled without introducing unwanted noise to the signal. However, there is currently no consensus regarding the size of the ROI or what effect this might have on the measurements of interest from the SCB. Therefore, the purpose of this investigation was to determine the effect of different SCB ROI widths and depths on the SCB parameters most commonly used to assess PTOA.

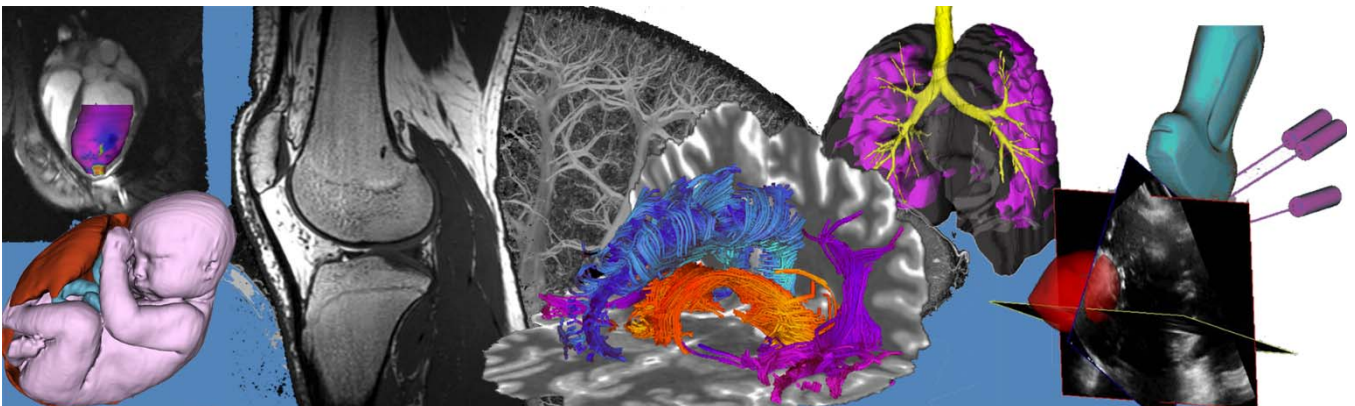
**METHODS:** Twelve skeletally mature female sheep underwent a surgical procedure to expose the medial femoral condyle (MFC) of both hind stifle (knee) joints. Once exposed the left and right side were randomized to either: i) an impact injury group – a 30MPa impact was applied to the weight bearing surface of the MFC; or ii) an arthrotomy only group - the joint was immediately closed with no injury initiated. After 3 months at pasture, the animals were euthanized, the hind limbs disarticulated at the hip and the knee joints micro-CT scanned (GE Locus Ultra; 80 kVp, 50 mA, 16s; 0.154 mm isotropic resolution). The micro-CT images were analysed in micro-view image analysis software by selecting ROIs that differed in widths (3,6, and 9mm) and depths (0.5, 1, and 2mm) all through the mid-articular surface in the sagittal plane. Total volume (TV), bone volume (BV), bone mineral content (BMC), bone mineral density (BMD), bone volume fraction (BVF), bone volume/total volume (BV/TV), bone surface/bone volume (BS/BV), trabecular thickness (Tb. Th), trabecular number (Tb. N), and trabecular spacing (Tb. Sp) were output for analysis. A two-way (3 widths by 3 depths) ANOVA ( $\alpha=0.05$ ) was used to assess the effect of the ROI parameters on the measures of SCB. A Bonferroni adjustment was used for all post-hoc analyses.

**RESULTS:** There were significant differences between all three SCB ROI widths in TV, BV, BMC, BMD, and BV/TV ( $p<0.01$ ). There were significant differences between all three SCB ROI depths in TV, BV, BMC, BMD, BVF, BV/TV, and Tb. Sp ( $p<0.01$ ). Interclass Correlation Coefficients were greater than 0.75 for all ten SCB parameters analysed.

**CONCLUSION:** Based on the evidence provided in this study, the widths and depths of the SCB ROIs significantly affects the SCB parameters. Therefore, careful attention should be paid to the selection of these parameters to ensure accurate SCB measurements. In the current investigation, the diameter of the impactor used to initiate the injury was 6mm and therefore, an ROI based on this dimension would be adequate to accurately assess the localized effect on the SCB.

# Poster Presentation Abstracts

## Session 7: Cancer Imaging



## Feasibility of micro-CT imaging for direct assessment of surgical resection margins during breast conserving surgery

Natasja Janssen<sup>1\*</sup>, Maartje van Seijen<sup>2</sup>, Claudette Loo<sup>3</sup>, Marie-Jeanne Vrancken Peeters<sup>4</sup>, Tara Hankel<sup>5</sup>, Jan-Jakob Sonke<sup>1</sup>, Jasper Nijkamp<sup>1,4</sup>

<sup>1</sup> Department of Radiation Oncology, Netherlands Cancer Institute, Amsterdam, the Netherlands, <sup>2</sup> Department of Molecular Pathology, <sup>3</sup> Department of Radiology, <sup>4</sup> Department of Surgical Oncology, <sup>5</sup> Department of Technical Medicine, University of Twente, Enschede, the Netherlands

\*The first author is currently working at the Laboratory for Percutaneous Surgery, School of Computing, Queen's University, Kingston, Canada

**Introduction:** Early-stage breast tumors are increasingly detected, due to the introduction of effective screening programs. The preferred treatment is often breast-conserving surgery (BCS), aiming to resect the whole tumor while sparing as much healthy tissue as possible. However, complete removal of such tumors can be difficult since the surgeon often can't see or palpate the tumor borders. The surgical resection margins of the excision specimen are analyzed by the pathologist, in which results are available a few days after surgery. In a considerable amount of the patients positive resection margins are found, requiring a re-operation to remove the remaining tumor. With micro-CT imaging ( $\mu$ CT) the whole excision specimen can be imaged shortly after the operation, allowing direct and 3-D analysis of surgical resection margins [1]. This study analyzed the feasibility and accuracy of  $\mu$ CT for surgical margin assessment in breast excision specimen.

**Methods:** Sixty excision specimen were imaged on  $\mu$ CT after surgery and retrospectively evaluated for positive resection margins by 4 observers in 2 phases. Resection margins were considered positive in case a solid tumor mass or malignant calcifications were found in the excision borders on  $\mu$ CT (red dot in Fig 1C-F). Pathology was used as ground truth for determining the accuracy, sensitivity, specificity, and positive predictive value (PPV) of  $\mu$ CT for determining margin status. Kappa was also calculated to determine inter-observer agreement. Additionally, 40 excision specimen were prospectively imaged inside a specific scan container (Fig 1A-B) on  $\mu$ CT and directly evaluated for positive resection margins by 1 observer. The 3-D rendering of the  $\mu$ CT allowed the observer to localize a suspect positive margin onto the specimen (red dot in Fig 1F), which was subsequently annotated onto the specimen with black ink. This location was evaluated for presence of tumor by pathology, serving as ground truth.

**Results:** Average accuracy, sensitivity, specificity, and PPV for the 4 observers were 63%, 38%, 70%, and 22%. The inter-observer agreement was fair (Kappa (range): 0.31 (0.12 – 0.80)). In the prospective study 70% of the surgical resection margins were correctly evaluated on  $\mu$ CT. Ten specimen had suspect positive margins on  $\mu$ CT, which were annotated onto the specimen by the observer. These correlated with 3 positive and 3 close margins (tumor within 1 mm of excision border) on pathology. Sensitivity, specificity, and PPV were 38%, 78% and 30%.

**Conclusions:**  $\mu$ CT imaging of breast excision specimen has moderate accuracy and considerable inter-observer variation for analysis of surgical resection margins. Especially sensitivity and PPV need to be improved before  $\mu$ CT-based margin assessment can be introduced in clinical practice.

**Acknowledgements:** this work was funded by Dutch Cancer Society (grant number NKI 2012-5716).

### References:

[1] R. Tang *et al.*, "Intraoperative micro-computed tomography (micro-CT): a novel method for determination of primary tumour dimensions in breast cancer specimens.," *Br. J. Radiol.*, vol. 89, no. 1058, p. 20150581, Feb. 2016.

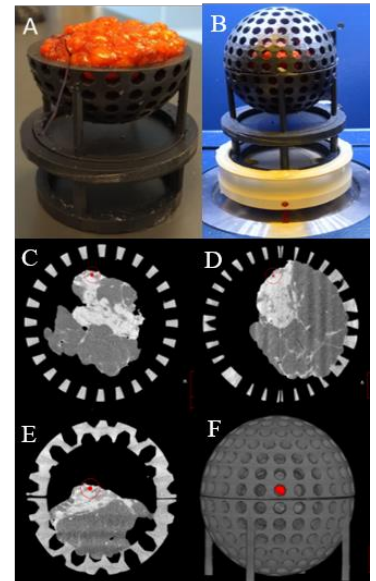


**Fig. 1:** The excision specimen was positioned inside the scan container (A) and scanned (B). Axial (C), sagittal (D), coronal (E) and 3-D volume render view (F) of the specimen. The location of a suspect positive resection margin was annotated in the 3D volume render in order to ink the specimen accordingly (D).

***Investigating the arrest, retention, and proliferative potential of iron-labeled breast cancer cells in NSG and nude mice using MRI***

Natasha Knier<sup>1,2</sup>, Amanda M. Hamilton<sup>1</sup>, Ashley V. Makela<sup>1,2</sup>, Paula J. Foster<sup>1,2</sup>

<sup>1</sup>Robarts Research Institute, The University of Western Ontario, London, Ontario, Canada

<sup>2</sup>Department of Medical Biophysics, The University of Western Ontario, London, Ontario, Canada

**Introduction:** Metastasis is the leading cause of mortality in breast cancer patients, with brain metastasis occurring in up to 30% of cases<sup>1</sup>. Our group has developed imaging technologies to track metastasis from the arrest of cells to tumour progression and cell dormancy in the brain through iron nanoparticle retention. Previously, our studies have focused on human brain metastatic breast cancer cell lines (such as 231BR) in nude mice, however, there is momentum towards use of patient derived xenografts (PDX) to allow for better representation of the tumour heterogeneity seen clinically<sup>2</sup>. NOD/SCID/IL2Rg<sup>-/-</sup> (NSG) mice are necessary for successful engraftment of these PDX models<sup>3</sup>, however studies characterizing brain metastases in NSG mice are scarce. To transition from cell lines to PDX models, it is necessary to understand differences that may exist in NSG mice, first with human cell lines. Here, we use cellular magnetic resonance imaging (MRI) to characterize the arrest, retention, and metastasis of a human brain metastatic breast cancer cell line in NSG mice and compare these findings to nude mice.

**Methods:** NSG mice (n=8) received intracardiac injections of  $1.5 \times 10^5$  iron-labeled GFP+ brain-seeking breast cancer cells (231BR). Images of the brain and body were acquired at 3T using a high-performance gradient coil insert, custom-built mouse RF coils, and a 3D balanced steady state free precession (bSSFP) sequence. Day 0 images were assessed for black signal voids, representing iron labeled 231BR cells arrested in the brain; the number of black pixels was determined. Day 21 images were assessed for retained signal voids and brain metastases. Brain metastases were counted and body images were assessed for lung, liver and lymph node metastases. Data was compared to previous studies in our lab using the 231BR cell line in nude mice.

**Results:** On day 0, iron labeled cells were visualized throughout the brain, revealing arrested cells in all NSG mice. Over time the number of signal voids declined as cancer cells die and are cleared from the brain. Signal voids were quantified by calculating the % of black pixels. This value decreased significantly between day 0 and 21. This is consistent with our previous data on nude mice, indicating that the retention of non-proliferating cells is similar in both strains. On day 21 brain metastases were evident in all NSG mice as regions of signal hyperintensity. Significantly more 231BR brain metastases were counted in NSG mice at day 21 compared to nudes. Unlike nude mice, NSG mice had numerous body metastases, including in liver, lung, and lymph nodes. The higher brain tumour burden and additional body tumour burden led to an early endpoint for NSG mice based on signs of weakness and weight loss.

**Conclusion:** Successful implementation of PDX models for studying brain metastases due to breast cancer requires that the NSG mouse as a preclinical platform must be fully characterized. Here we showed that the 231BR cell line grew differently in NSG mice compared to nude mice. While both are immune-compromised strains, the NSG is more severely deficient; nudes have no T cells, NSG have no T, B or NK cells, which may explain the more aggressive growth of brain metastases. Although the 231BR cells were selected *in vivo* to only grow in the brain, in NSG mice we found that liver and lung metastases were frequent, numerous, and contributed to a shorter disease model. Ultrasound revealed that the myocardium of NSG mice was much thicker than in nude mice, making intracardiac cell injections more challenging. Our work demonstrates the valuable role that imaging can play in the progress toward credentialing these important models.

#### References

1. Cheng, X., & Hung, M. C. (2007). Breast cancer brain metastases. *Cancer and Metastasis Reviews*, 26(3-4), 635-643.
2. Cassidy, J. W., Caldas, C., & Bruna, A. (2015). Maintaining tumor heterogeneity in patient-derived tumor xenografts. *Cancer research*, 75(15), 2963-2968.
3. Hidalgo, M., Amant, F., Biankin, A. V., Budinská, E., Byrne, A. T., Caldas, C., ... & Roman-Roman, S. (2014). Patient-derived xenograft models: an emerging platform for translational cancer research. *Cancer discovery*, 4(9), 998-1013.

**Photoacoustic tomography for intraoperative tumour margin assessment during breast-conserving surgery**Lawrence CM Yip<sup>1,3</sup>, Parsa Omid<sup>1,2</sup>, Ivan Kosik<sup>1</sup>, Astrid Chamson-Reig<sup>1</sup>, Muriel Brackstone<sup>4,5</sup>, Jeffrey JL Carson<sup>1,2,3,5</sup><sup>1</sup> Imaging Program, Lawson Health Research Institute, London, Canada<sup>2</sup> Department of Biomedical Engineering, Western University, London, Canada<sup>3</sup> Department of Medical Biophysics, Western University, London, Canada<sup>4</sup> London Regional Cancer Program, London Health Sciences Centre, London, Canada<sup>5</sup> Department of Surgery, Western University, London, Canada

**Introduction:** Breast cancer accounts for 25% of all cancer cases among women. In many early stage cases, breast-conserving surgery (BCS) is recommended, where the tumour is excised with a thin margin of healthy tissue. While several techniques for tumour localization exist, margin detection can still be difficult. Recent changes in surgical standards for acceptable margins have dropped re-excision rates to ~10% in London; however, this is still a significant number of re-excision surgeries.

Photoacoustic tomography (PAT) is an imaging technique with advantages of both optical imaging and ultrasound. Pulsed laser light is used to safely irradiate tissue, producing acoustic waves, which are then reconstructed into 3D images. PAT can image hemoglobin, lipid, or contrast agents such as indocyanine green, allowing functional and anatomical imaging. This is particularly useful when imaging cancerous tissues; PAT can detect differences between tumour and healthy tissue using their corresponding wavelengths. Our lab previously developed a PAT system with sensitivity of 85% for positive margins, which could provide up to 75% reduction in re-excision surgeries. However, limited sensitivity to high frequency acoustic waves and detector coverage of the specimens, which led to a limited spatial resolution (~2.5 mm), resulted in high occurrence of false positives. The objective of this project was to develop a clinical PAT system with improved spatial resolution, capable of >90% sensitivity and specificity for tumour margin assessment.

**Methods:** A detector array was constructed with 41 circular transducers positioned on two concentric circular rings with a single focal point. The imaging area was illuminated via an optical window located at the center of the transducer rings. The array was tested on a phantom consisting of polyester monofilament (110  $\mu\text{m}$  diameter) arranged in parallel lines separated by increasing distances from 1 mm to 9 mm. The detectors were positioned above and perpendicular to the threads and raster scanned across a 40 mm x 40 mm grid with 1 mm steps. Ten signals were averaged at each position and images were reconstructed with universal back projection.

**Results:** A high-resolution PAT system was developed. Image analysis shows monofilament diameter to be  $200 \pm 50 \mu\text{m}$  full width at half max (FWHM) and each pair of lines were resolved down to the smallest spacing tested (Fig. 1). This translated to a 10-fold increase in spatial resolution compared to the previous version of the system.

**Conclusions:** Photoacoustic tomography provides high contrast between tumour and healthy tissue and has potential to decrease re-excision rates in BCS. We present a PAT system capable of sub-millimeter resolution. With the excellent soft tissue contrast provided by this imaging modality, it has the potential to drastically lower patient burden and healthcare costs.

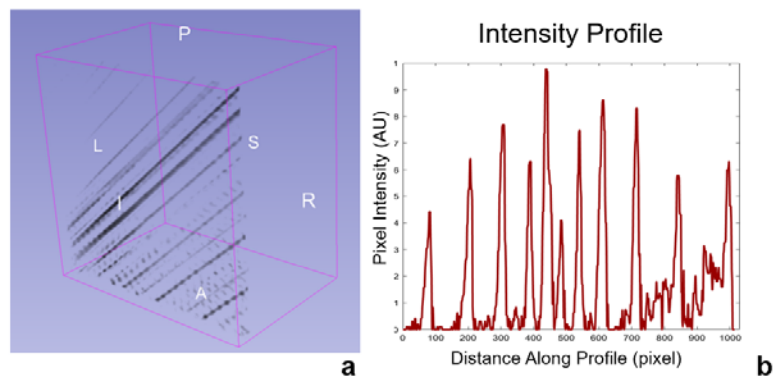


**Fig. 1:** 3D rendering of the imaging phantom using 3D Slicer (a). Intensity profile demonstrating signal peaks at each sewing thread (b). The FWHM of each peak is ~200-250  $\mu\text{m}$ , and a clear separation between threads can be seen.

## Polarized light imaging of human breast cancer

Jared Westreich<sup>1</sup>, Mohammadali Khorasani<sup>2</sup>, Adam Gribble<sup>1</sup>, Blake Jones<sup>1</sup>, and I. Alex Vitkin<sup>1,3,4</sup>

<sup>1</sup>Department of Medical Biophysics, University of Toronto; <sup>2</sup>Department of Surgery; <sup>3</sup>Department of Radiation Oncology

<sup>4</sup>Division of Biophysics and Bioimaging, Princess Margaret Cancer Centre

**Introduction:** Polarimetry is a promising optical method to rapidly and noninvasively assess biophysical characteristics of tissues. As polarized light propagates through tissue, its polarization state is altered by heterogeneous scattering bio-structures. Tissue properties of interest are contained within the Mueller matrix (MM), a complete mathematical description of its interaction with polarized light. Biophysical quantities derived from the MM, such as depolarization (a measure of heterogeneity) and linear retardance (a measure of anisotropy) can help differentiate tumor from surrounding healthy tissue. [2] Our objective is to use polarimetry images and machine learning to automatically differentiate invasive breast cancer from normal breast fat and connective tissues in unstained human surgical specimens. Our ultimate aim is constructing a rapid and accurate intra-operative tool to assess surgical margins in breast cancer surgery. This could help reduce the number of re-operations needed to address inadequate surgical margins in breast conserving surgery (currently ~20%). [1]

**Methods:** For our first study, we used unstained formalin-fixed paraffin-embedded pathology slides (5  $\mu\text{m}$ ) obtained from human lumpectomy surgical specimens containing invasive breast cancer (various grades and receptor status) and surrounding normal breast tissue. A subset of slides ( $n=4$ ) were imaged with a Mueller matrix transmission mode polarimetry system to obtain depolarization, linear retardance, diattenuation, and cross-polarization images. Adjacent slides were stained with Haematoxylin and Eosin (H&E), scanned, and segmented by a pathologist into fat, connective tissue and tumor, to be used as the ground truth for polarimetric image analysis. Features for classification were measured independently on  $200\mu\text{m} \times 200\mu\text{m}$  regions of interests (ROIs, ~57,000 in total) into which each image was subdivided. First and second order statistical features were extracted from all polarimetry ROIs, which were then classified using a random forest algorithm. Leave-one-patient-out cross validation was performed (each slide was tested using a classifier which was trained on all other slides).

**Results:** The classifier was able to identify tumor with a sensitivity and specificity of 78% and 83% respectively. We anticipate improved performance with a larger dataset, as the classifier will generalize better after being trained on more samples. The classifier can also be adjusted to improve sensitivity at the expense of specificity or *vice versa*. For example, if the clinical goal is guiding the surgeon to regions of suspected pathology, high sensitivity is more important.

**Conclusions:** The encouraging initial classification accuracy of breast cancer slides with polarized light motivates further work in developing this method as a potential intra-operative margin assessment tool during breast conserving surgery. Sensitivity and specificity will determine whether polarimetry contains sufficient information for definitive positive tumor margin detection, or whether using polarimetry as a guidance mechanism (e.g., for more accurate but slow point-sensing classification via mass spectrometry) is more appropriate.

### References:

[1] E. R. St John, *et al.* Annals of Surgery, 2017

[2] A. Tata, *et al.* Chemical Science, 2016

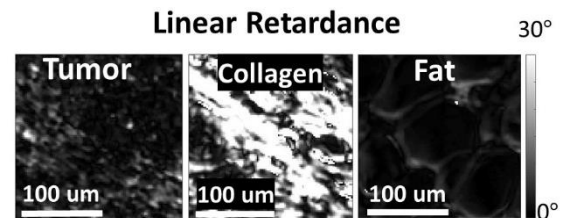


Figure 1 Typical  $200\mu\text{m} \times 200\mu\text{m}$  ROIs of linear retardance showing the three types of breast tissue.

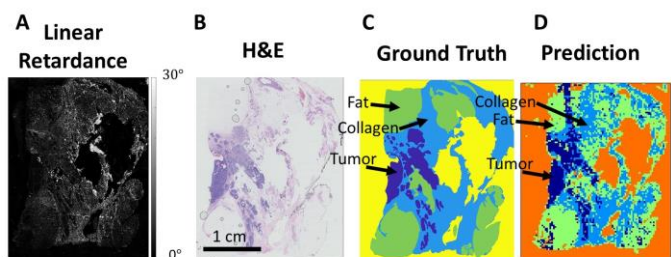


Figure 2 A) Linear retardance image; B) H&E of adjacent slide; C) Pathologist-labeled regions based on B); D) Polarimetry-based predictions

## Photoacoustic Technology for Imaging Prostate Cancer

Nidhi Singh<sup>1,2</sup>, Y. Soenjaya<sup>2</sup>, Felipe Roa<sup>1,2</sup>, Carl Fisher<sup>3</sup>, Aaron Boyes<sup>2</sup>, Gang Zheng<sup>1,3</sup>, Brain C. Wilson<sup>1,3</sup>, Brian Wodlinger<sup>4</sup>, Stuart Foster<sup>1,2</sup>, Christine Demore<sup>1,2</sup>

<sup>1</sup>Department of Medical Biophysics, University of Toronto, Toronto, <sup>2</sup>Sunnybrook Research Institute, Sunnybrook Health Sciences Centre, Toronto, <sup>3</sup>Princess Margaret Cancer Centre, University Health Network, Toronto, <sup>4</sup>Exact Imaging Inc., Toronto.

### Introduction:

Prostate cancer (PCa) in most cases, is a multifocal disease but several studies have suggested that the largest, or 'Index Lesion' contributes to most of the volume of the disease and predominantly determines the progression of disease, including likelihood of metastasis. Photothermal Therapy (PTT), a focal therapy that uses optical fibers inserted into the prostate to selectively ablate index lesions while sparing majority of the prostate gland, delicate neurovascular bundles and urinary sphincter, offers an effective alternative to radical prostatectomy. While multiparametric-MRI is used to localize and delineate lesions to identify the target tissue volume, technical limitations, such as difficulty in accurately delineating sparse tumors and weak correlation between 3D MRI estimation of tumor volume and histological volume estimates, have been identified. Also, MRI is not used in real time during treatment, so displacement of the prostate while placing treatment fibers causes misalignment relative to pre-treatment target localization, which can affect the therapy outcome. Hence, there is a need for a real-time, high-contrast imaging modality for pre-treatment lesion localization. Photoacoustic (PA) imaging combined with transrectal high resolution micro-ultrasound (micro-US) offers a new opportunity in real-time tissue visualization of the prostate. PA imaging yields an image of the optical absorbers, e.g. blood, usually overlaid on an ultrasound image of tissue structures. It has the potential to provide high contrast lesion localisation when combined with contrast agents such as organic porphyrins (PS), nanoparticles that are strong optical absorbers, produce a strong PAI signal, are preferentially taken up by tumours, and can be used in PTT for spatial confinement of thermal damage. **The objective of the project is development of a combined transrectal micro-US and PA imaging system, used alone or in combination with PS contrast agents, to enable accurate index lesion localization and image guidance for PTT in patients with prostate cancer.**

### Methods and Results:

We conducted a preliminary study by imaging healthy dog prostate *in vivo* using a commercial PAI system (Vevo LAZR X, FUJIFILM VisualSonics Inc.) which showed that we can image 12-15 mm deep in the prostate. Dogs were injected with ACE-1 prostate cancer cell line and tumor growth was monitored with MRI. *Ex vivo* imaging of excised prostate with tumor and metastatic lymph nodes showed localization of PS contrast agents and PA signal in the suspected tumor region.

For the combined PA and micro-US imaging system, we demonstrate the design and early prototype of a transurethral light delivery system to be used with a transrectal 20 MHz micro-US probe which will detect acoustic signal. A commercialized transrectal ultrasound system (ExactVu, Exact Imaging Inc.), has been successfully modified for synchronized laser illumination of the tissue and data acquisition for PA image reconstruction.

### Discussion and Conclusion:

Preliminary evaluation of PA imaging of PS contrast agents in the prostate yields images with acceptable depth of penetration. Further development of transurethral light delivery for combined transrectal micro-US and PA imaging will improve the useful imaging depth. These PA technologies, alone and in combination with PS contrast agents have the potential to enable accurate pre-treatment index lesion localization for PTT in patients with prostate cancer.



## Optimization of pH MRI for Cancer Detection

Maryam Mozaffari<sup>1,2</sup>, Alex Li<sup>2</sup>, Miranda Bellyou<sup>2</sup>, Robert Bartha<sup>1,2</sup>

1. Department of Medical Biophysics 2. Robarts Research Institute, University of Western Ontario

**Introduction:** In pathological tissue, pH is a fundamental marker of disease progression. It has been shown that for many cellular functions the regulation of intracellular pH ( $\text{pH}_i$ ) is crucial, and that  $\text{pH}_i$  regulation is altered in cancer cells. Specifically, cancer cells generate a large amount of acid metabolites, which are efficiently extruded, and as a result have  $\text{pH}_i > 7.2$ . A previous study found that tumor response to radiation therapy within a couple of days of treatment was traceable using the  $^1\text{H}$  MRI contrast mechanism called chemical exchange saturation transfer (CEST). Dilute proteins can be selectively irradiated at their absorption frequency and detected through the transfer of magnetization to bulk water [1-3]. The rate of transfer of magnetization is pH dependent. Adopting CEST MRI, our group has previously developed a technique to measure absolute tissue pH that is heavily weighted to the intracellular compartment. The technique called amine and amide concentration-independent detection (AACID) utilizes the ratio of endogenous amine and amide protons to measure pH [4,5]. Previous work was performed mostly in mouse U87 tumours on an Agilent 9.4T MRI. The purpose of the current study was to examine the change in  $\text{pH}_i$  over time in a rat C6 glioma model on a Bruker 9.4T MRI.

**Methods:** C6 GBM cells ( $8\mu\text{L}$ ) were injected at a rate of  $0.5\mu\text{L}/\text{min}$ , into the right frontal lobe of thirteen 8-week old Wistar rats using a Hamilton (Reno, NV, USA) syringe with a 27-gauge needle attached. CEST MRI was performed on a 9.4 Tesla small animal MRI scanner at the Robarts Research Institute. Images were acquired for the slice of interest using an echo-planar-imaging pulse sequence with parameters:  $\text{TR}=10\text{ s}$ ,  $\text{TE}=25\text{ ms}$ ,  $\text{FOV}=38.4\times 38.4\text{ mm}^2$ , slice thickness= $1\text{ mm}$ , acquisition time $\approx 19\text{ min}$ , preceded by a continuous wave RF pulse with amplitude of  $1.5\mu\text{T}$  and duration of  $4\text{ s}$ . CEST images were acquired at saturation frequencies between  $1.2\text{ ppm}$  to  $6.6\text{ ppm}$  with step size of  $0.1\text{ ppm}$  and analyzed in Matlab. The pH was estimated using the following calibration equation:  $\text{pH} = -4 \times \text{AACID} + 12.8$  [4,5].

**Results:** Preliminary results are presented for a single animal. Figures 1 and 2 show the pH maps from one animal at day 7 and day 14 after tumor implantation respectively. The average tumour  $\text{pH}_i$  at day 7 was 7.54 and the average contralateral  $\text{pH}_i$  was 7.62. On day 14, the average  $\text{pH}_i$  within the tumour was 7.90 and on the contralateral side was 7.62.

**Discussion and Conclusion:** Tumour pH measured by CEST on the 9.4T Bruker MRI was consistent with previous measurements made on our previous system. We hypothesized that pH measured by CEST would change over time while the tumor develops. Based on the preliminary results presented here, tumor  $\text{pH}_i$  did increase as the tumour increased volume. In the future, data from all thirteen animals included in this study will be pooled to examine trends in tumour pH over time.

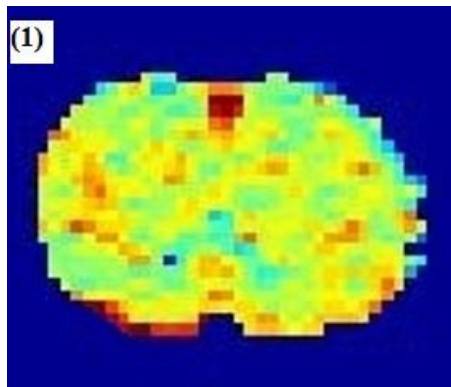


Figure 1. pH map at day 7

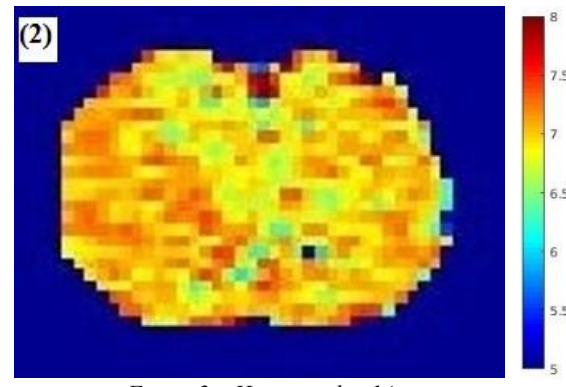
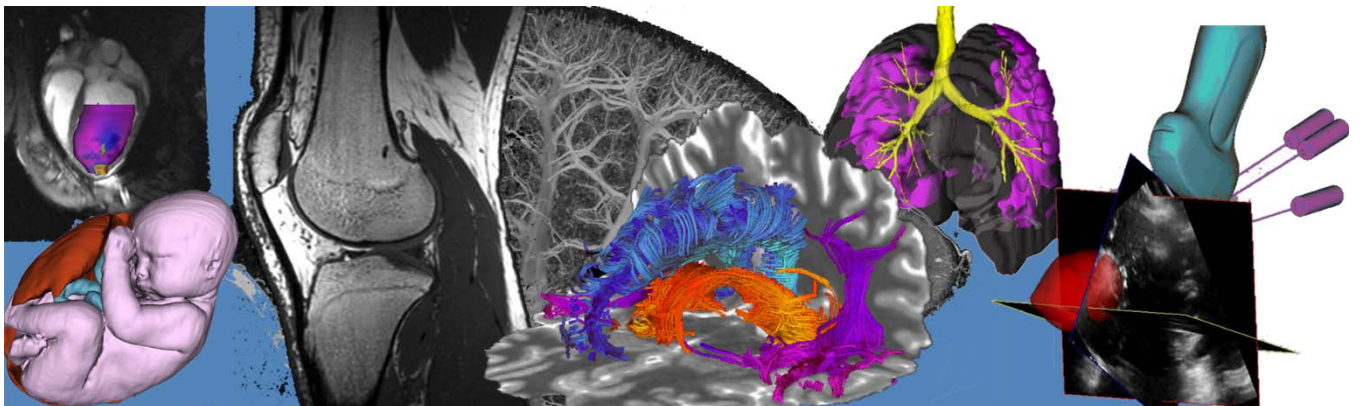


Figure 2. pH map at day 14

[1] Zhou *et. al.* Progress in Nuclear Magnetic Resonance Spectroscopy 2006;48:109–136. [2] Ward *et. al.*; Magnetic Resonance in Medicine 2000;44:799–802. [3] Wu *et. al.*; EJNMMI Physics,2016; 3(19):1-21. [4] Bartha *et. al.*; Journal of Cerebral Blood Flow & Metabolism 2014;34:690–698. [5] Bartha *et. al.*; NMR Biomed. 2015;28(5):566-575.

# Poster Presentation Abstracts

## Session 8: Lung Imaging



## Why Are Chronic Hemodialysis Patients Short of Breath? A Novel Symptom-Centered Study

Fabio R. Salerno<sup>1-3</sup>, Alireza Akbari<sup>2,4</sup>, Grace Parraga<sup>1,4</sup> and Christopher W. McIntyre<sup>1-3</sup>.

<sup>1</sup>Department of Medical Biophysics, Western University, London, ON, Canada,

<sup>2</sup>The Lilibeth Caberto Kidney Clinical Research Unit, London, ON, Canada,

<sup>3</sup>Division of Nephrology, Department of Medicine, Western University, London, ON, Canada,

<sup>4</sup>Robarts Research Institute, London, ON, Canada.

**INTRODUCTION:** The prevalence of dyspnea in patients with end-stage renal disease (ESRD) has been shown to be as high as 60%, improving only partially after commencing hemodialysis (HD).<sup>1</sup> However, research on dyspnea is limited to few studies. Autopsy and computed tomography studies have revealed a very high prevalence of lung disease in this patient population.<sup>2,3</sup> ESRD facilitates the development of many different lung parenchymal abnormalities, such as edema, fibrosis and calcifications. Sodium overload due to ESRD is also associated with airway hyperresponsiveness. Furthermore, HD also contributes to recurrent lung inflammatory damage and air microembolism.

The purpose of this exploratory study is to investigate the prevalence, pathophysiology, etiology and progression of dyspnea in a sample of chronic HD patients, by using state-of-the-art functional and imaging tests.

**METHODS:** This is an exploratory, prospective, observational study. Recruitment of 20 chronic HD patients 18 years of age and older and on HD for at least three months is currently underway from the prevalent HD population in a tertiary care center in London, Canada. We will evaluate the prevalence and severity of dyspnea and undiagnosed lung disease, one-year changes and the relationship between soft tissue sodium content and airway function using multi-spectral (<sup>1</sup>H, <sup>23</sup>Na, <sup>129</sup>Xe) magnetic resonance imaging (MRI) and clinical measurements.

Each patient will undergo study visits at baseline and one-year follow-up on a non-HD day. Study visits will include self-administered dyspnea questionnaires and lung disease assessment with functional tests (spirometry, six-minute walk test and fractional exhaled nitric oxide), high-resolution thoracic computed tomography for quantitative evaluation of lung parenchyma, airway and vascular tree, hyperpolarized <sup>129</sup>Xe MRI to evaluate ventilation and perfusion abnormalities and sodium MRI to measure soft tissue sodium content.

Linear regression and Pearson correlation coefficients will be used to assess the relationship between quantitative imaging data, soft tissue sodium content and dyspnea scores.

**RESULTS:** Based on our clinical experience, we expect to observe a high prevalence of lung disease in the HD population, with the severity of lung abnormalities increasing with time on HD; we also expect to uncover a strong, positive correlation between soft tissue sodium content and airway functional and pulmonary vascular abnormalities.

**CONCLUSIONS:** This will be, to our knowledge, the first symptom-centered study in HD patients aimed at explaining the pathogenesis of chronic dyspnea.

### REFERENCES:

1. Murtagh FE et al. *AdvChronicKidnDis*, 2007.
2. Fairshter RD et al. *IntJArtifOrgans*, 1982.
3. Coskun et al. *ActaRadiol*, 1999.

## Assessing Risk of Accelerated COPD Progression using MRI and Machine Learning

Cathy Ong-Ly<sup>1,2</sup>, Andrew Westcott<sup>1,2</sup>, Inderdeep Dhaliwal<sup>3</sup>, Aaron Fenster<sup>1,2</sup>, Miranda Kirby<sup>4</sup> and Grace Parraga<sup>1-3</sup>

<sup>1</sup>Robarts Research Institute, <sup>2</sup>Department of Medical Biophysics, <sup>3</sup>Division of Respiriology, Department of Medicine, Western University, London, Canada; <sup>4</sup>Department of Physics, Ryerson University, Toronto Canada

**INTRODUCTION:** In patients with chronic obstructive pulmonary disease (COPD), progressively worse expiratory airflow occurs over time and is believed to stem from progressively worse airway wall and lumen microstructure, or airway remodeling and emphysematous abnormalities in the lung parenchyma.<sup>1</sup> While FEV<sub>1</sub> measurements are straightforward and cost-efficient to implement, these cannot provide spatial nor functional information about the small airways, which are believed to drive COPD pathogenesis. Hyperpolarized noble-gas magnetic-resonance-imaging (MRI) quantifies ventilation abnormalities that stem from abnormalities in the large and small airways as well as emphysema.<sup>2</sup> We previously showed that such measurements progressively worsen in FEV<sub>1</sub>-stable patients and predict worse outcomes over short time-periods.<sup>3,4</sup> Supervised machine-learning provides new ways to understand and explain our previous findings about accelerated disease progression in COPD patients. We hypothesized that functional MRI measurements, machine-learning and multivariate modelling could be combined to sensitively and specifically predict COPD patients at risk of accelerated disease-progression over short time-periods.

**METHODS:** Spirometry and hyperpolarized <sup>3</sup>He MRI were performed at baseline and 31±8-months later in participants with a clinical diagnosis of COPD enrolled in an approved study (NCT02723474).<sup>5</sup> Ground-truth disease progression was defined as a change in GOLD grade at follow-up. We evaluated 15 different MRI parameters, including: ventilation-defect-percent, ventilation-defect-cluster-percent (VDCP), low-ventilation-clusters, cluster defect diameter voxel size one (CDD1), first-order-texture, run-length-matrix and gray-level-co-occurrence-matrix (GLCM) measurements as inputs for machine-learning algorithms: 1) decision tree, and 2) RUSBoosted tree. Performance of machine-learning algorithms was evaluated by receiver-operator characteristic-curve ROC area-under-the-curve (AUC), sensitivity and specificity. Patient demographics and features were evaluated using parametric and non-parametric t-tests with Holm-Bonferroni correction and multivariate analyses.

**RESULTS:** Table 1 shows measurements for 52 participants at baseline (71±8yr) and follow-up classified by change in GOLD grade. Using the training dataset, the RUSBoosted/decision tree accuracy was 81%/76% while test data accuracy was 75%/68%, respectively. AUC were 0.73 and 0.44 for RUSBoosted and decision trees respectively. Sensitivity/specificity was 50%/87% for RUSboosted compared to 17%/87% for decision trees for predicting clinically-relevant progression based on GOLD. Multi-variate statistical modelling revealed that baseline age (p=0.03) and three MRI parameters (VDCP p=0.0004, CDD1 p=0.0001, RLN p=0.045) significantly predicted disease progression.

### CONCLUSIONS:

Supervised machine-learning algorithms and multi-variate models provide a way to reveal the determinants of accelerated COPD progression using MRI-derived ventilation texture-based measurements.

### REFERENCES:

- Hogg JC, *et al.* NEJM (2004).
- Saam BT, *et al.* Magn Reson Med (2000)
- Kirby M, *et al.* Radiology (2010)
- Kirby M, *et al.* Thorax (2017)
- Kirby M, *et al.* Acad Radiol (2012).

Table 1. Subject demographics and machine-learning/multivariate model results.

Parameter Mean (±SD)	Stable COPD (n=44)	COPD Progression (n=8)	Sig. Diff. (p-value)	Holm-Bonferroni Corrected (p)
Age Baseline	71 (8)	69 (7)	0.38 <sup>#</sup>	1.0
ΔAge at follow-up	2.3 (0.7)	2.8 (0.7)	<b>0.049</b>	0.43
Female %	27	37	ND	ND
FEV <sub>1</sub> % <sub>pred</sub> Baseline	72 (23)	68 (32)	0.25	1.0
ΔFEV <sub>1</sub> % <sub>pred</sub> at follow-up	-1.4 (10)	11 (12)	ND	ND
<sup>3</sup> He VDP %	14 (9)	22 (8)	<b>0.02</b>	0.26
VDCP %	13 (10)	17 (6)	0.14	0.98
LVC	-4.0 (0.3)	-4.0 (0.4)	0.85	1.0
CDD1	5000 (3000)	9000 (1000)	<b>0.0005</b>	<b>0.009</b>
FO-Mean	4.8 (0.9)	3.9 (0.6)	<b>0.009<sup>#</sup></b>	0.14
FO-Standard Deviation	2.8 (0.3)	2.5 (0.5)	<b>0.02<sup>#</sup></b>	0.26
FO-Skewness	0.7 (0.4)	1.0 (0.2)	<b>0.048<sup>#</sup></b>	0.43
RLM-SRE	0.6 (0.06)	0.5 (0.06)	<b>0.007<sup>#</sup></b>	0.12
RLM-LRE	11 (4)	15 (3)	<b>0.01</b>	0.15
RLM-GLN	154 (26)	160 (31)	0.52 <sup>#</sup>	1.0
RLM-RLN	400 (100)	300 (100)	<b>0.03</b>	0.33
RLN-Run Percentage	0.45 (0.05)	0.40 (0.05)	<b>0.01<sup>#</sup></b>	0.15
GLCM-Entropy	1.0 (0.2)	1.0 (0.08)	0.99	1.0
GLCM-Correlation	0.19 (0.0008)	0.96 (0.00005)	<b>0.03<sup>#</sup></b>	0.33
GLCM-Homogeneity	0.95 (0.008)	0.96 (0.005)	0.14 <sup>#</sup>	0.98

ΔAge =change in age years at follow-up; FEV<sub>1</sub>=Forced Expiratory Volume in 1 second; ΔFEV<sub>1</sub> %<sub>pred</sub> =change in FEV<sub>1</sub> %<sub>pred</sub> at follow-up; <sup>3</sup>He VDP=ventilation defect percent; FO=First-order texture measurements of gray-level MRI-histogram; RLM-SRE=Run-length-matrix-short run emphasis; RLM-LRE=Run-length-matrix long run emphasis; RLM-GLN=Run-length-matrix gray-level non-uniformity; RLM-RLN=Run-length-matrix run-length non-uniformity.

## Longitudinal Emphysema Measurements in Patients using $^3\text{He}$ and $^{129}\text{Xe}$ MRI

Alexei Ouriadov<sup>1</sup>, Andrew Westcott<sup>2,3</sup>, David G. McCormack<sup>4</sup> and Grace Parraga<sup>2-4</sup>

<sup>1</sup>Department of Physics and Astronomy;

<sup>2</sup>Robarts Research Institute; <sup>3</sup>Department of Medical Biophysics;

<sup>4</sup>Division of Respiriology, Department of Medicine,  
The University of Western Ontario, London, Canada.

**RATIONALE:** For patients with emphysema stemming from COPD and Alpha-1 Antitrypsin Deficiency (AATD) there are few biomarkers that sensitively measure changes in emphysema over time. However, hyperpolarized  $^3\text{He}/^{129}\text{Xe}$  MRI provides direct measurements of acinar duct geometry, non-invasively and without radiation-burden.<sup>1</sup> We previously developed an accelerated MRI method that allows for a high-resolution measurement of the acinar ducts in a single breath-hold.<sup>2</sup> We hypothesize that regional  $^3\text{He}/^{129}\text{Xe}$  MRI estimates of alveolar microstructure are sensitive to emphysematous destruction and will sensitively detect emphysema progression in patients longitudinally when CT evidence is either not detected or not acquired.

**METHODS:** Participants provided written informed consent to an ethics-board-approved protocol (NCT02279329) and underwent two visits, four-years-apart that included CT, spirometry, plethysmography, DL<sub>CO</sub> and MRI including anatomical  $^1\text{H}$ ,  $^3\text{He}$  (2014) and  $^{129}\text{Xe}$  (2018) diffusion-weighted and static-ventilation imaging. MRI was performed at 3.0T as previously described.<sup>3</sup> MRI apparent-diffusion-coefficients (ADC) were generated and  $^3\text{He}/^{129}\text{Xe}$  lung morphometry maps were estimated using the stretched-exponential-method<sup>4</sup> which was extended and adapted for both  $^3\text{He}/^{129}\text{Xe}$  to provide clinically-relevant biomarkers of emphysema.<sup>5,6</sup> Ventilation-defect-percent (VDP),<sup>3</sup> the CT relative-area-of-the-lung-with-attenuation $\leq$ -950HU (RA<sub>950</sub>) were measured using custom-built software.

**RESULTS:** Four AATD patients (58 $\pm$ 5yr) and a single COPD patient (76yr) were evaluated at baseline and 4 years later. Figure-1 shows CT,<sup>3</sup>  $^3\text{He}/^{129}\text{Xe}$  MRI ADC, mean-linear-intercept ( $L_m$ ) maps and ADC/ $L_m$  values for both gases in all participants. CT low attenuating areas reflected moderate to severe emphysema (RA<sub>950</sub>=8%, 14% and 31%) in 2014 but CT was not acquired in 2018. Mean ADC<sup>He</sup>/ADC<sup>Xe</sup> estimates were evaluated using linear-regression<sup>3</sup> to generate ADC<sup>He</sup> values for the follow-up visit. Mean ADC estimates were not significantly different at follow-up (0.46cm<sup>2</sup>s<sup>-1</sup>/0.44cm<sup>2</sup>s<sup>-1</sup>; p>.80). Mean  $L_m^{\text{He}}$  estimates were not significantly different from corresponding mean  $L_m^{\text{Xe}}$  estimates (590 $\mu\text{m}$ /610 $\mu\text{m}$ ; p>.84; 2014/2018).

**DISCUSSION:** In the COPD patients,  $L_m$  estimates confirmed emphysema progression in the absence of confirmatory CT evidence. For the AATD-1 patient, regions at visit-1 with abnormally high ADC<sup>He</sup>/ $L_m^{\text{He}}$  values were not ventilated at the visit-2 with the result being apparently improved ADC<sup>Xe</sup>/ $L_m^{\text{Xe}}$  values. More AATD will be scanned with  $^{129}\text{Xe}$  MRI to increase a number of subjects.

**CONCLUSIONS:** MRI morphometry is sensitive to regional emphysema and may be considered instead of CT for detecting disease progression. However, as ventilation worsens over time, ADC/ $L_m$  values require normalization to ventilation volume.<sup>7</sup>

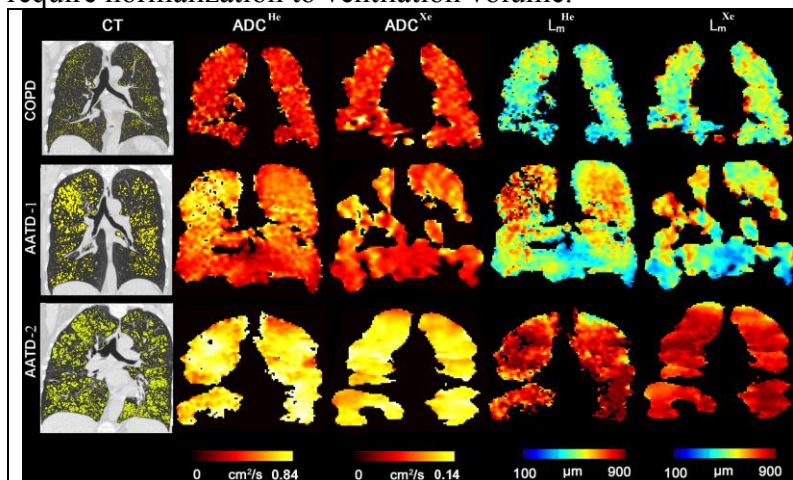


**Figure 1.** Representative CT and  $^3\text{He}/^{129}\text{Xe}$  MRI Maps and imaging measurements

### References

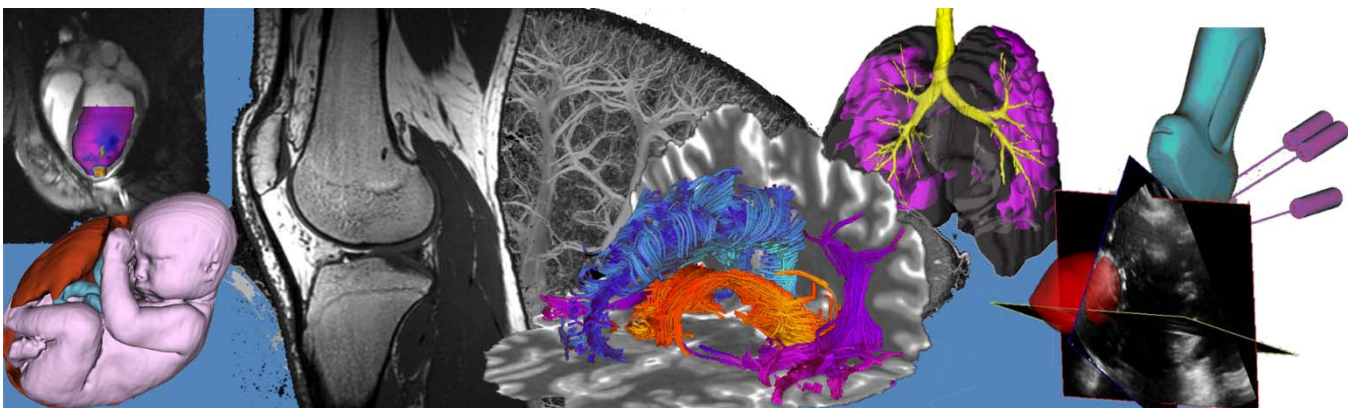
1. Yablonskiy DA et al J Appl Physiol (2009).
2. Ouriadov A et al ISMRM (2018).
3. Kirby M et al Radiol (2012).
4. Abascal JFPJ et al ArXiv (2017).
5. Ouriadov A et al MRM (2017).
6. Westcott A et al JMRI (2018).
7. Westcott A et al JMRI (2018).

### Acknowledgments

**A. Ouriadov was funded in part by the Alpha-1 Foundation (USA).**

# Poster Presentation Abstracts

## Session 9: New Contrast Agents



**Earlier detection of spontaneous breast cancer lung metastases using an improved bioluminescence reporter**Amanda M Hamilton<sup>1</sup>, Paula J Foster<sup>1,2</sup> and John A Ronald<sup>1-3</sup><sup>1</sup>Imaging Research Laboratories, Robarts Research Institute, London, ON, Canada, <sup>2</sup>Medical Biophysics, University of Western Ontario, London, ON, Canada, <sup>3</sup>Lawson Health Research Institute, London, ON, Canada

**Introduction:** Breast cancer-associated mortality is most often due to late-stage metastasis rather than the presence of a primary tumour, thus there is a continuing need for metastatic models to further our understanding and permit the evaluation of novel therapies against breast cancer metastasis.<sup>1</sup> In metastatic modeling, cells can be tagged with markers that enable the detection of systemic metastasis and overall tumour burden over time. Bioluminescence imaging (BLI) is based on the detection of light produced by an enzyme-catalyzed oxidation reaction of a substrate and has been used extensively for the evaluation of preclinical cancer models. Very recently an evolved novel BLI reporter (Akaluc) has been developed that demonstrates 7-fold higher catalytic efficiency than its parental reporter Firefly luciferase.<sup>2</sup> It also utilizes an optimized substrate (Akalumine) with greater tissue permeability and a shifted emission spectrum enabling greater light penetrance. In this study we transduced triple negative breast cancer cells to express either the conventional codon-optimized (luciferase2) or advanced (Akaluc) BLI reporter and evaluated differences in spontaneous lung metastasis detection from experimental orthotopic breast cancer in mice.

**Methods:** Third generation lentiviral vectors conferring tdTomato (fluorescent; tdT) and either luciferase2 or Akaluc (bioluminescent) imaging genes were produced in house. Triple negative breast cancer cells (MDA-MB-231; 231) were transduced at a multiplicity of infection of 5 and matched for tdT expression by fluorescence activated cell sorting. Akaluc and luciferase2-expressing 231 cells were analyzed *in vitro* by fluorescence microscopy and BLI. In an *in vivo* pilot study,  $3 \times 10^5$  tdT luciferase2+ or tdT Akaluc+ 231 cells were implanted into mammary fat pad (MFP) of female NSG mice (n=2 per group). Fluorescence signal and BLI activity in the MFP were assessed weekly using an *in vivo* optical imaging system for approximately 2 months. Four weeks post-cell implantation mice were also evaluated for indications of spontaneous thoracic metastases by shielding the primary tumour and assessing BLI activity in the chest cavity.

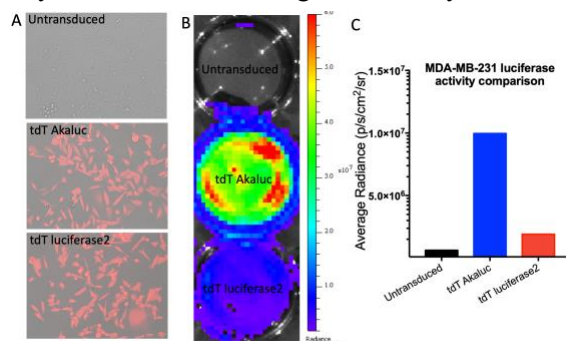


**Figure 1:** *In vitro* analysis of tdT luciferase2+ and tdT Akaluc+ 231 cells by fluorescence microscopy (A) and BLI (B&C).

MFP of all injected mice from the day of implantation through endpoint. By day 35 post-MFP implantation, BLI activity was evident in the thoracic region of tdT Akaluc+ 231 bearing mice (Fig 2A&B), however, discernable BLI activity was not noted in the chest region of tdT luciferase2+ 231 mice until day 49.

**Conclusions:** In this work we compared the activity of two BLI reporters and evaluated their ability to discern spontaneous lung metastasis in an orthotopic mouse model of breast cancer. The favourable distribution of the Akaluc substrate coupled with the improved catalytic activity of the Akaluc enzyme resulted in enhanced detection of lung metastases to a time point 2 weeks sooner than that detected by the conventional system. Our *in vitro* and *in vivo* findings were particularly notable as 20-fold less enzyme substrate was used to detect Akaluc activity compared to the conventional luciferase2 system. Our future work will expand this imaging strategy to evaluate spontaneous and experimental metastases at other sites including the brain. We believe the improved sensitivity evident in this imaging approach will prove incredibly useful in the advancement of our understanding of metastatic cancer and in our assessment of novel treatments.

**References:** 1) Kerbel RS. *Cancer J.* 2015, 21(4):274-283. 2) Iwano S *et al.* *Science.* 2018, 359:935-939.

**Results:** Matched tdT luciferase2+ and tdT Akaluc+ 231 cells showed similar tdT fluorescence after sorting (Fig 1A) with a geometric mean fluorescence of 4497 and 4480, respectively. *In vitro* analysis of BLI activity revealed a 5-fold greater average radiance (Fig 1B&C) of tdT Akaluc+ 231 cells compared to their luciferase2+ counterparts, despite the use of 20-fold less substrate (0.01 $\mu$ mol vs 0.2 $\mu$ mol, respectively). 231 cells were detectable in the

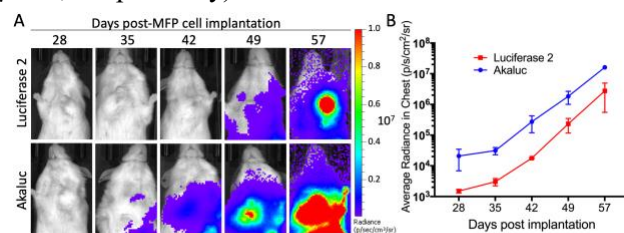


**Figure 2:** Akaluc expression permits earlier detection of breast cancer lung metastases than conventional luciferase 2, despite the use of 20-fold less substrate (0.5 $\mu$ mol vs 10 $\mu$ mol).

## Urinary-based prostate cancer detection using tumour-activatable minicircles

TianDuo Wang<sup>1,2</sup>, Yuanxin Chen<sup>1</sup>, John A. Ronald<sup>1,2,3</sup>

1. Robarts Research Institute – Imaging; 2. Department of Medical Biophysics, University of Western Ontario;  
3. Lawson Health Research Institute, London, ON, Canada.

**INTRODUCTION:** The holy grail for cancer detection is finding cancer-specific biomarkers which can detect tumours early and predict patient prognosis. Our group has previously developed non-viral gene vectors called tumour-activatable minicircles<sup>1</sup> (TA-MCs), shortened plasmids that possess superior potency and safety<sup>2</sup>, which can produce an exogenous blood reporter in cancers cells but not healthy cells. These TA-MCs were able to identify mice with prostate tumours, and notably produced more blood reporter in more aggressive tumours. To improve upon these initial construct designs, we have replaced the blood reporter gene on our TA-MCs with *Gussia luciferase* (GLuc), a sensitive reporter detectable in urine, allowing for non-invasive urine-based assay development<sup>3</sup>. Use of the tumour-specific survivin promoter (pSurv) to mediate transcription allows us to express GLuc exclusively in prostate cancer (PCa) cells, titrating biomarker output to tumour aggression, as more aggressive PCa tumours express more survivin in patients<sup>4</sup>. Our goal is to assess the ability of these GLuc-expressing TA-MCs to detect and determine PCa aggression through a urine test in mice.

**METHODS:** We constructed parental plasmids, precursors to minicircles, that expressed GLuc downstream of pSurv. TA-MCs were then made from these parental plasmids using a previously described production system<sup>5</sup>. Next, we validated these TA-MCs via transfection of PCa cell lines (Du145, LNCaP, PC3, PC3MLN4) of varying aggressiveness and normal prostate epithelial cells. Cell media was collected at 2 and 5 days post-transfection and GLuc levels were quantified using a commercial kit. We also measured the survivin expression in cell lysates using immunoblotting. We then assessed TA-MCs in nude mice with subcutaneous PC3MLN4 PCa tumours of ~150 mm<sup>3</sup>. TA-MCs complexed with a polyethylenimine transfection agent were injected intratumourally, then GLuc levels were measured in urine samples collected pre- and 2, 5 and 7 days post-MC injection.

**RESULTS:** GLuc levels were significantly higher in PCa cell lines than primary prostate epithelium (Fig. 1C). Between PCa cell lines, GLuc expression was highest in PC3MLN4 and lowest in LNCaP cells, showing a similar trend to that of survivin expression (Fig 1B). Tumour-bearing mice exhibited no detectable levels of urine GLuc initially, but showed significantly increased urine GLuc soon after administration of TA-MCs (Fig 1D).

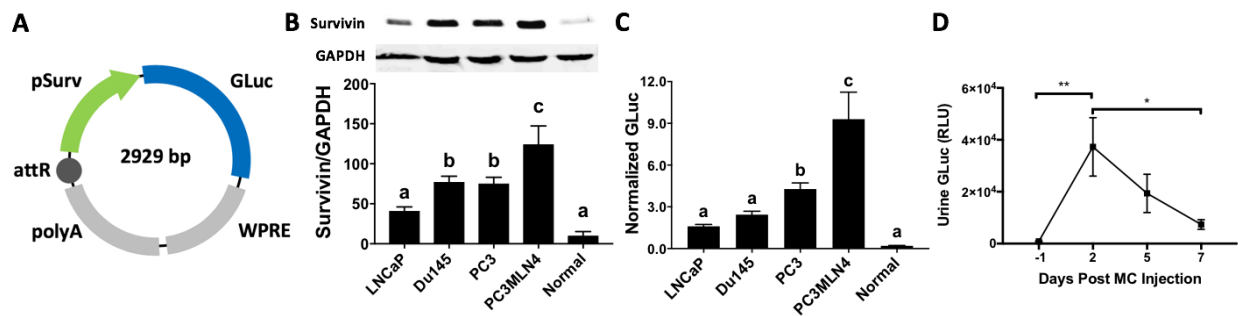


**Figure 1.** (A) Vector map of TA-MC. (B) Western blot analysis of survivin expression relative to GAPDH in cell lysates (n=4). (C) *In vitro* secreted GLuc normalized for Renilla luciferase co-expression two days after transfection (n=6). (D) Urine GLuc in mice with PC3MLN4 tumours post-MC administration (n=5). Data are presented as mean ± SD. Letters represent significant differences between groups (p<0.05). \*, p<0.05, \*\*, p<0.01.

**DISCUSSION:** Our TA-MCs were able to effectively produce GLuc related to pSurv activity, allowing for differentiation of low and high survivin PCa cells from healthy prostate cells *in vitro*. GLuc exhibited minimal background *in vivo* and is detectable in urine of tumour-bearing mice after TA-MC injection. Future work is focused on testing TA-MCs in mice with non-aggressiveness LNCaP tumours to validate our system's ability to discern PCa aggressiveness. These TA-MCs represent a novel diagnostic tool that offers more comprehensive information regarding PCa, which can ultimately help patients more confidently choose the appropriate care.

**REFERENCES:** [1] Ronald J. et al., PNAS, 2015, 112(10): 3068–3073. [2] Chen Z. et al., Mol Ther, 2003, 8(3): 495–500. [3] Tannous B. et al., Mol Ther, 2005, 11(5): 435–443. [4] Shariat S. et al., Cancer, 2004, 100(4): 751–757. [5] Kay M. et al., Nat Biotechnol, 2010, 28(12): 1287–1289.



**3D micro CT vessel-wall virtual histology: A novel tri-element stain and whole-body perfusion**P. Joy Dunmore-Buyze,<sup>a</sup> Charmainne Cruje,<sup>a,b</sup> Zengxuan Nong,<sup>a</sup> Jason J. Lee,<sup>a,b</sup> John A Kiernan,<sup>c</sup>  
J. Geoffrey Pickering,<sup>a,c,d</sup> and Maria Drangova<sup>a,b</sup><sup>a</sup>Robarts Research Institute, <sup>b</sup>Department of Medical Biophysics, <sup>c</sup>Departments of Medicine and Biochemistry,  
<sup>d</sup>Department of Physiology and Pharmacology, <sup>e</sup>Department of Anatomy and Cell Biology, University of Western  
Ontario, London ON, Canada

**Introduction.** Vascular research relies on histological techniques to characterize rodent models of disease. While histology can provide information on the microanatomy of the vasculature and organs of mice, it requires the excision of tissue from mice, followed by multi-step preparation protocols. Recently, a strategy of using x-ray attenuating histological stains that mark specific tissue components combined with microcomputed tomography (micro-CT) has been applied in “virtual histology” – a technique that can be used to study the microstructure of tissues without disturbing the morphology of an organ or tissue of interest.<sup>1,2</sup> While existing histological stains such as I<sub>2</sub>KI, PTA, and OsO<sub>4</sub> are useful in studying the vessel wall as a whole unit, no micro-CT stain that highlights individual wall components has been demonstrated. In this work, we describe a novel, tri-element x-ray attenuating stain derived from the Verhoeff’s stain that provides micro-CT contrast of the entire vasculature of an intact mouse. We deliver our novel stain *via* a whole-body rapid perfusion technique that our group has developed, which obviates the need to extract and soak individual organs or tissues.<sup>3</sup> Corresponding histological sections localized the heavy elements within the vessel wall. To our knowledge, no other CT staining technique localizes contrast within the structural components of the vessel wall, thereby producing whole-mouse vasculature-specific images using 3D micro-CT, following a perfusion procedure under 30 minutes.

**Methods. Preparation of perfusion solutions-** A modified version of the Verhoeff’s stain was prepared using 56% v/v aluminum (Harris) heamatoxylin, 2.2% w/v FeCl<sub>3</sub>•6H<sub>2</sub>O, 0.6% w/v KI and 0.3% w/v I<sub>2</sub> in distilled water (AlumHemFeI). In a 0.9% normal saline solution, 0.1% v/v heparin and 0.03% v/v Triton™ X-100 – a non-ionic detergent that permeabilizes the vessel wall – was prepared; when this solution is used prior to AlumHemFeI as opposed to normal saline, the perfusion is referred to as AlumHemFeI-T. **Perfusion protocol-** Male C57BL/6 mice (25-30 g) were perfused *via* retrograde perfusion of the abdominal aorta at physiological pressure (110 mm Hg). The vessels were cleared of blood by perfusing the vasculature with normal saline or Triton™ X-100- and heparin-containing saline for 10 minutes. The AlumHemFeI stain was delivered for 10 minutes, followed by a 5-minute flush with normal saline. **Micro-CT and histology of organs-** Immediately following perfusion, whole animal micro-CT scans were obtained using an eXplore specCZT scanner (5-minute acquisition, 90 kVp, reconstructed to 50 or 100 μm isotropic voxels). To verify the localization of the stain in tissue, organs were harvested for histology. The samples were fixed in formalin, paraffin-embedded and sectioned at 10 μm. Using Perls’ prussian blue, which is known to bind to iron, sectioned tissues were stained and viewed using the Olympus BX51.

**Results.** The AlumHemFeI and AlumHemFeI-T perfusions provide excellent visualization of the vasculature of mice, as shown in Figure 1. More specifically, the vessel walls demonstrate high CT attenuation, while the lumen in the major vessels appears void of any stain. Comparing the micro-CT results from both perfusions show sharper delineation of the vessel walls in the AlumHemFeI-T images than AlumHemFeI. Histological analysis of the Prussian blue-stained sections shows the presence of iron in the interlamellar units of the aorta, with a high concentration in the endothelium and in the endothelial-cell nuclei (Figure 2); in the coronary vessels, the stained sections demonstrate the presence of iron in the endothelial and medial layers and in the endothelial cells. The histology results confirm the presence of the iron from both perfusions in the vessel walls, which verifies 3D micro-CT imaging results. The AlumHemFeI-T sections demonstrate a substantial amount of iron localized within the vessel walls only, while the AlumHemFeI sections show an uneven distribution of some iron in the myocardium, which is consistent with the micro-CT results.

**Conclusion.** The novel, non-toxic stain, AlumHemFeI-T we developed provides excellent visualization of the vasculature of mice for virtual histology with 3D micro-CT. It provides increased contrast to the components of blood vessel walls, with a unique sensitivity to endothelial nuclei and the extracellular matrix in the media of medium and large sized vessel. The new stain that we presented can potentially benefit the study of normal and diseased vasculature in rodent models.

**References.** [1] Pauwels, E. *et al. Journal of microscopy* **250**, 21-31, doi:10.1111/jmi.12013 (2013). [2] Pai, V. M. *et al. Journal of anatomy* **220**, 514-524, doi:10.1111/j.1469-7580.2012.01483.x (2012). [3] Dunmore-Buyze, P. J. *et al. Contrast media & molecular imaging* **9**, 383-390, doi:10.1002/cmim.1588 (2014).

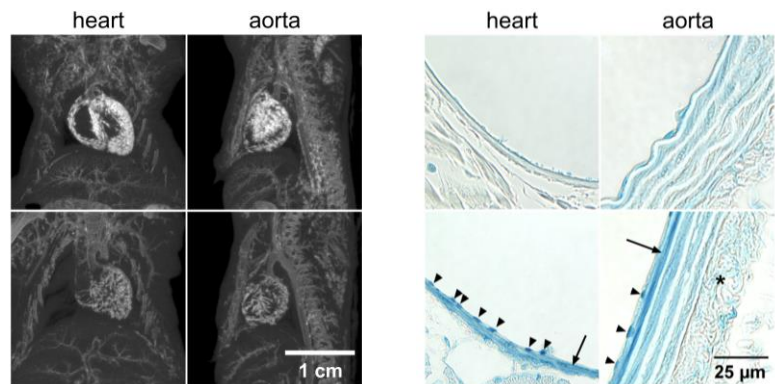


Figure 1. Micro-CT images of mice perfused with AlumHemFeI (top) and AlumHemFeI-T (bottom). Vessel walls appear sharper in the AlumHemFeI-T images.

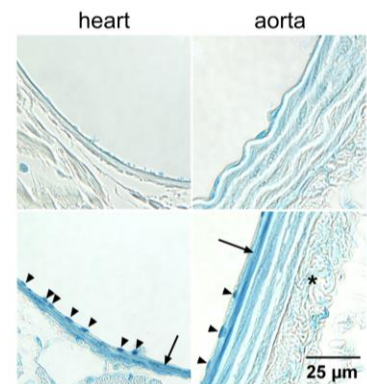


Figure 2. Tissue sections of mice perfused with AlumHemFeI (top) and AlumHemFeI-T (bottom). Endothelial-cell nuclei are indicated by the arrowheads, and the interlamellar units by the arrows.

### Small gadolinium nanoparticles for preclinical computed tomography

Eric Grolman,<sup>1</sup> Charmainne Cruje,<sup>2,3</sup> Maria Drangova,<sup>2,3</sup> and Elizabeth R. Gillies<sup>1,4</sup>

<sup>1</sup>Department of Chemical and Biochemical Engineering, <sup>2</sup>Imaging Research Laboratories, Robarts Research Institute,

<sup>3</sup>Department of Medical Biophysics, <sup>4</sup>Department of Chemistry, Western University, London, Ontario, Canada

**Introduction.** Microcomputed tomography (micro-CT) is used in pre-clinical research of the vasculature to study small animals at high resolutions. Micro-CT can be used to non-invasively acquire three-dimensional images of live animals in tens of minutes.<sup>1</sup> Since soft tissues have poor inherent contrast to x-rays due to their similar endogenous densities, contrast agents are used to differentiate the vasculature of mice in micro-CT. There are micro-CT contrast agents that are available for use *in vivo* in small animal,<sup>2,3</sup> and these are predominantly composed of iodine. However, lanthanide-based contrast agents can provide higher contrast than iodine.<sup>4</sup> Previously, our group successfully synthesized a long-circulating contrast agent containing 100 mg/mL of lanthanide for micro-CT imaging through the polymer encapsulation of erbium nanoparticles. Although this contrast agent had a long circulation time that meets micro-CT requirements, the viability of the animals that were injected needs improvement, which could be attributed to the accumulation of the nanoparticles in the hepatobiliary clearance organs. Previous reports have shown that polymer-encapsulated nanoparticles smaller than 10 nm can be cleared through the kidneys after circulating during micro-CT imaging, which could potentially increase subject viability. Hence, the purpose of this work was to synthesize lanthanide nanoparticles smaller than 10 nm. By varying the amount of time of the nanoparticle growth phase during synthesis, we demonstrate a method of fabricating different sizes of lanthanide nanoparticles. While the encapsulation technique of the small nanoparticles has yet to be optimized, this work presents a reproducible means of changing lanthanide nanoparticle size.

**Methods. Nanoparticle preparation-** The solvothermal synthesis method previously utilized by our group was slightly modified to produce smaller nanoparticles.<sup>5</sup> During the last step of nanoparticle synthesis – which is the nanoparticle growth phase – aliquots were removed at 30, 60, 90 and 120 minutes to confirm the relationship between time and nanoparticle size.

**Preparation of contrast agent-** A diblock copolymer of poly(L-lactide) and poly(ethylene glycol) was synthesized and utilized for encapsulation of the gadolinium nanoparticles (<10 nm in size) to form assemblies *via* nanoprecipitation, where equal mass of polymers and nanoparticles were used.<sup>5</sup> The nanoparticles and assemblies were characterized using dynamic light scattering (DLS) to measure size, and were visualized by transmission electron microscopy (TEM). The assemblies were then lyophilized and stored at room temperature. Dried samples were dissolved in saline before injection at a lanthanide concentration of 100 mg/mL. ***In vivo* injection and micro-CT imaging-** 0.2 mL of contrast agent was injected subcutaneously into C57BL/6 mice (n=2) and imaged by micro-CT over the course of two weeks to observe the biodistribution of gadolinium in the subjects. Images were acquired at 80 kVp, 55 mA over 360° and reconstructed using a cone-beam reconstruction algorithm (150  $\mu\text{m}^3$  voxel size). Images were rescaled into Hounsfield units (HU) and analyzed using MicroView (Parallax Innovations, London, ON). The subjects were sacrificed and dissected to observe the gross anatomy of subcutaneous tissue.

**Results. Physical characterization-** DLS results showed that limiting the growth phase step to within 30 minutes produced nanoparticles that are smaller than 10 nm in size. When analyzed by DLS, the nanoparticles that were grown in 30 minutes had a volume size distribution peak at  $7 \pm 1$  nm, with a polydispersity index (PDI) of  $0.15 \pm 0.04$ , while the encapsulated assemblies had a volume size distribution peak of  $135 \pm 1$  nm, with a PDI of  $0.10 \pm 0.01$  (Figure 1). The TEM images in Figure 2 are in good agreement with DLS results. ***In vitro* and *in vivo* characterization-** Upon redispersal in saline, serum and water, the contrast agent demonstrated colloidal stability in DLS for up to an hour. However, the solution was highly viscous and was difficult to inject *via* 30G needles at 100 mg/mL of gadolinium. Results from subcutaneous injection showed a redistribution of the contrast agent within the tissue (Figure 3), while subcutaneous tissue and skin near the injection site appear healthy.

**Conclusion.** We have shown that by varying the time of nanoparticle growth phase, the size of the synthesized Gd nanoparticles can be modified. Although the encapsulation technique and viscosity has yet to be optimized, this work demonstrates that small nanoparticles – which may be desirable for having higher chances of kidney clearance after a micro-CT scan of the vasculature – can achieve *in vitro* colloidal stability and inert properties in subcutaneous tissue when encapsulated within polymers.

**References.** [1] Badea CT et al. *Phys. Med. Biol.* **2008**, 53, R319–350. [2] Detombe SA et al. *Invest. Radiol.* **2008**, 43, 520–529. [3] Willekens I et al. *Mol. Imaging Biol.* **2009**, 11, 128–135. [4] Cardinal HN et al. *Med. Phys.* **1993**, Jan-Feb;20(1): 15-31. [5] Cruje C et al. *Biomacromolecules*, **2018**, 19(3), 896–905.

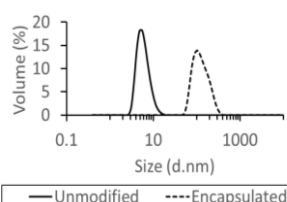


**Fig. 1.** Volume distribution of individual nanoparticles and assemblies.

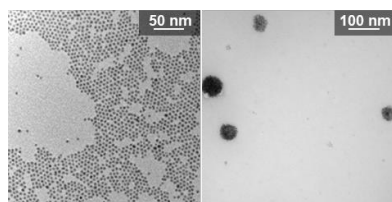


**Fig 2.** TEM images of individual (left) and encapsulated (right) nanoparticles.

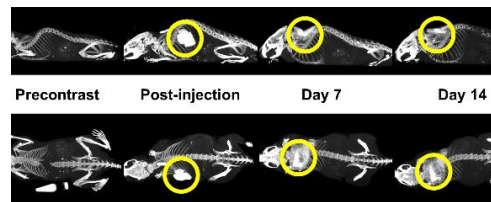


**Fig 3.** Time-course micro-CT images of a mouse injected with the agent (circled) subcutaneously.

## Using Essential Magnetosomal Proteins to Refine Gene-Based Iron Contrast for Magnetic Resonance Imaging

Q. Sun<sup>1,2,3</sup>, C. Fradin<sup>4</sup>, R.T. Thompson<sup>1,2</sup>, F.S. Prato<sup>1,2,3</sup>, D.E. Goldhawk<sup>1,2,3</sup>

<sup>1</sup>Imaging Program, Lawson Health Research Institute, <sup>2</sup>Medical Biophysics & <sup>3</sup>Collaborative Graduate Program in Molecular Imaging, Western University, London, Canada; <sup>4</sup>Physics & Astronomy, McMaster University, Hamilton, Canada

**Introduction:** With its superb spatial and temporal resolution, magnetic resonance imaging (MRI) has great potential to track cellular activities that define early stages of disease [1]. To improve molecular imaging techniques, we are developing MRI reporter gene expression based on the magnetosome. In magnetotactic bacteria (MTB), magnetosome formation allows cells to concentrate and compartmentalize iron biominerals in membrane-enclosed vesicles [2]. While the entire process is regulated by numerous genes, we have selected a subset of genes, *mamI*, *mamL*, *mamB*, and *mamE*, deemed essential for initial stages of magnetosome formation [1]. While *mamI*, *mamL*, and *mamB* have roles in designating the magnetosome vesicle, they may also provide docking site(s) for additional proteins, such as *mamE*, that facilitate biomineralization [1-3]. Refining the development of magnetosome-like nanoparticles will provide an endogenous magnetic resonance (MR) label for long-term molecular imaging throughout the cell's life cycle.

**Hypothesis:** In mammalian cells, MamI and MamL co-localize on an intracellular membrane and interact to initiate formation of a rudimentary magnetosome-like nanoparticle.

**Methods:** MTB genes *mamI* and *mamL* were isolated from the *M. magneticum* sp. AMB-1 genome and cloned into vectors with fluorescent protein tags (GFP and Tomato, respectively) to create Mam fusion proteins [4]. Human MDA-MB-435 melanoma cells were transfected with each hybrid construct to develop stable expression systems. Subcellular location and co-localization of fusion proteins were examined with confocal microscopy and fluorescence correlation spectroscopy (FCS) [4], respectively. FCS also estimated size and mobility of fusion proteins and their associated structures.

**Results:** When expressed alone, GFP-MamI formed a net-like fluorescence pattern, while Tomato-MamL showed punctate fluorescence that exhibited motion in live cells (Figure 1A). When Tomato-MamL and GFP-MamI were co-expressed, their fluorescence signal co-localized (Figure 1B) and, unexpectedly, also exhibited motion similar to Tomato-MamL alone. FCS data indicate that Tomato-MamL is associated with larger intracellular structures when it is co-expressed with GFP-MamI than when it is expressed alone.

**Conclusions:** We have shown that over-expression of MTB proteins MamI and MamL are compatible with mammalian cell system biology. Confocal fluorescence microscopy and FCS demonstrated that these membrane proteins co-localize in an intracellular compartment. Future work will use MR cell phantoms to examine the potential of these Mam proteins to modulate MR relaxation rates when expressed alone or in combination.

### References:

- [1] Goldhawk *et al.* (2017) Design and Applications of Nanoparticles in Biomedical Imaging, pp 187-203
- [2] Uebe & Schuler (2016) Nat Rev Microbiol 14:621
- [3] Quinlan *et al.* (2011) Mol Microbiol 80:1075
- [4] Sun *et al.* (2018) 6<sup>th</sup> international MTB meeting, Kanazawa, Japan

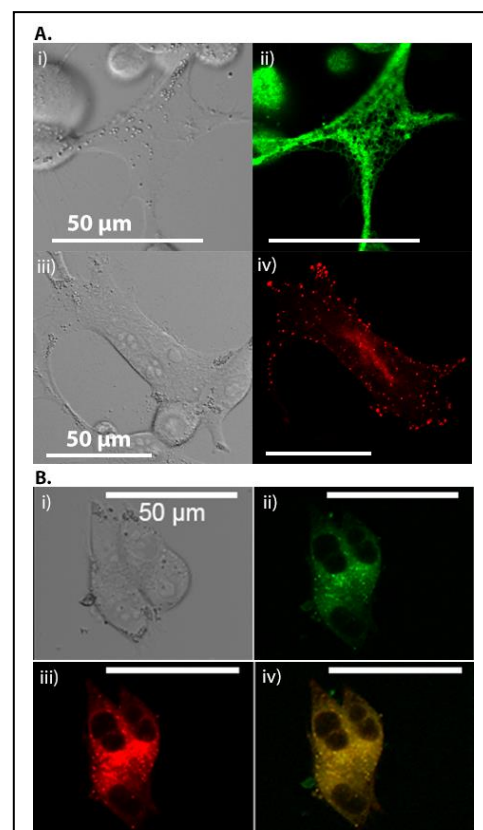
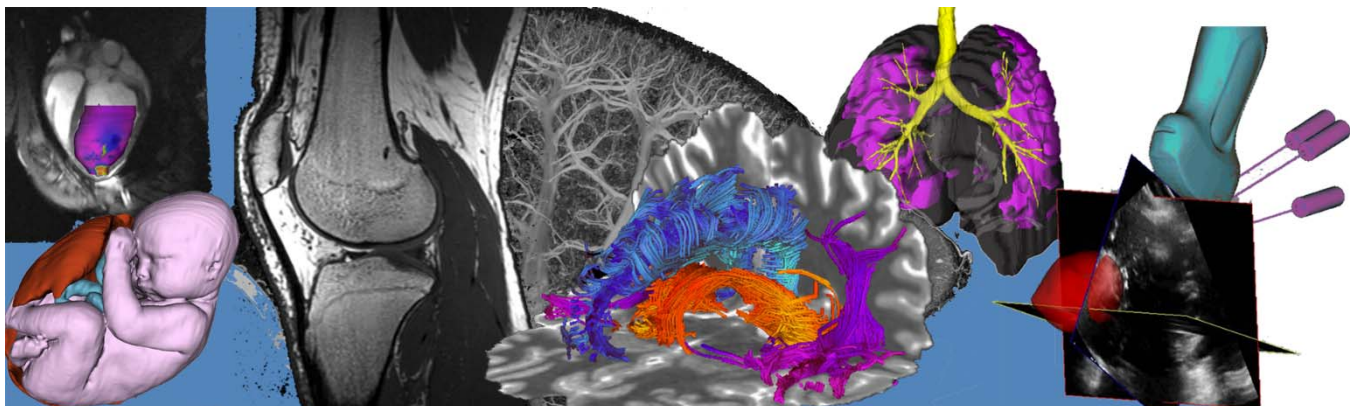


**Figure 1. Confocal fluorescence images of MDA-MB-435 cells stably expressing MTB genes. A.** Single expression of GFP-MamI (ii) and Tomato-MamL (iv) show two different patterns of expression. **B.** Co-expression of GFP-MamI (ii) and Tomato-MamL (iii) indicate co-localization of these proteins (iv).

# Poster Presentation Abstracts

## Session 10: Neuroimaging



## Short Diffusion Time Microscopic Anisotropy to Detect Neurite Pathology in Grey Matter

Jake J Valsamis, Corey A Baron

Centre for Functional and Metabolic Mapping, The University of Western Ontario, London, Ontario, Canada

Robarts Research Institute, The University of Western Ontario, London, Ontario, Canada

Department of Medical Biophysics, The University of Western Ontario, London, Ontario, Canada

**Introduction.** Neurological disorders represent a significant health burden, but their physiological underpinnings are generally still poorly understood. The brain is primarily made up of neurons, and the integrity of axons and dendrites (“neurites”) is essential for normal brain function.

Diffusion MRI (dMRI) is sensitive to the microstructural characteristics of tissue via sensitivity to the random motion of water molecules. Fractional anisotropy (FA) has been used in many studies, but due to its artificial decrease in regions of crossing fibres, it is not a sensitive measurement in grey matter. Microscopic anisotropy ( $\mu A$ ) is a new parameter that reflects the anisotropy if all axons were aligned [1].

$$\mu A^2 = \frac{\ln(S_{lin}) - \ln(S_{iso})}{b^2}$$

where  $S_{lin}$  is the mean signal when diffusion is encoded linearly along 15 directions,  $S_{iso}$  is the signal measured with isotropic encoding, and  $b$  is the b-value.

$\mu A$  has the potential to probe neurites in grey matter; however, signal from cell bodies will reduce its ability to probe anisotropy of dendrites. Oscillating gradient spin-echo (OGSE) diffusion encoding enables access to much shorter diffusion times, lowering sensitivity to larger cavities [2]. Combining these two approaches could lead to improved sensitivity to neurites. We test this using a beading model of neurite damage, which has been implicated in many neurological conditions [3].

**Methods.** This project utilized the Camino Monte-Carlo diffusion simulator [4] to perform *in silico* dMRI experiments in a substrate mimicking the properties of neurites. Simulated environments were comprised of 50% neuron cell bodies by volume, while varying amounts of healthy and beaded neurites constituted the other 50%. Figure 1 displays the cellular structures used in simulation. dMRI parameters like OGSE, isotropic encoding, and linear encoding can be defined with “scheme files” in simulation. A b-value of 2500 s/mm<sup>2</sup>, and OGSE frequencies ranging from 0-100 Hz were used.

**Results.** Figure 2 displays the large  $\mu A$  measurements in healthy voxels (0% beading), and the rapid decrease in  $\mu A$  as the percentage of beading increases.

**Conclusion.** The large decrease in  $\mu A$  with just 10% volume filled by beaded neurites emphasizes the technique’s sensitivity to small changes in microstructure. Higher OGSE frequencies yield increased sensitivity to beading.

**References.** [1] Shemesh N, et al. (2016) *MRM*, 75:82–87. [2] Baron & Beaulieu (2014) *MRM*, 72: 726. [3] Ochs S, et al. (1997) *PNB*, 391:426. [4] Hall & Alexander (2009) *IEEE TMI*, 28:1354.

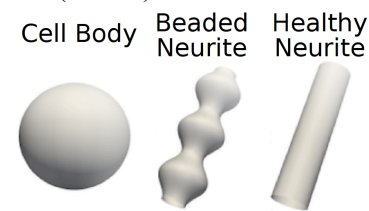


FIG 1: Cellular structures used in simulation.

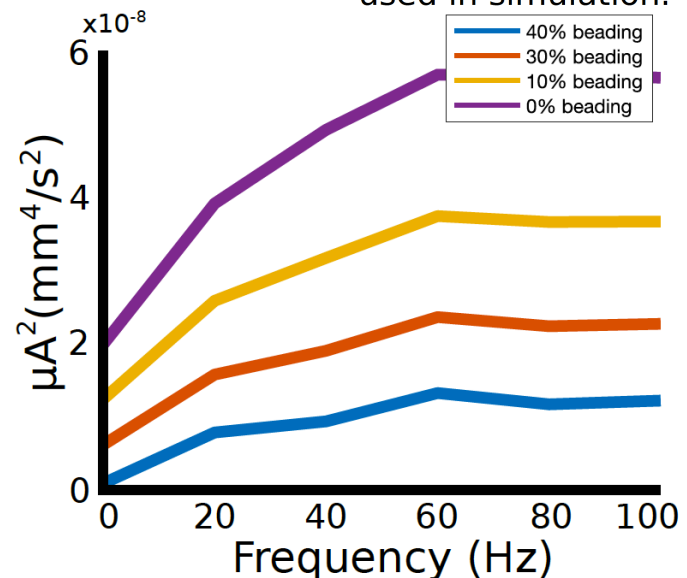


FIG 2: Change in  $\mu A^2$  with increasing frequency,  $b=2500\text{s/mm}^2$

## Mapping Diffusion Dispersion in the In Vivo Human Brain

Arbabi, Aidin<sup>1</sup> and Baron, Corey A.<sup>1</sup>

<sup>1</sup>Robarts Research Institute, Western University, London, ON, Canada

**Introduction.** Oscillating gradient spin-echo (OGSE) diffusion MRI allows measurement of the frequency dependence of the apparent diffusion coefficient (ADC), which gives insight into tissue microstructure [1]. An *in vivo* parameterization that allows visualization of maps of the frequency dependence of ADC throughout the human brain has thus far not been demonstrated. In this work, we define the diffusion dispersion (DD), which can be acquired efficiently with no need for non-diffusion weighted images. This comes with several advantages, including reduced scan time, reduced Gibbs ringing, and low sensitivity to perfusion. Here, we demonstrate full-brain DD mapping *in vivo* at 7T.

**Methods.** OGSE diffusion encoding with single shot EPI was implemented in a healthy volunteer on a 7T head-only system (80 mT/m strength and 350 T/m/s slew rate). PGSE (0 Hz; diffusion time 55 ms) and cosine-modulated trapezoidal OGSE with 30Hz and 60Hz frequencies were implemented ( $b=565 \text{ s/mm}^2$ , 4 direction tetrahedral encoding with 10 averages each, 15  $b_0$  acquisitions, TE/TR=111/5500 ms, FOV=200x200 mm<sup>2</sup>, 2.5 mm isotropic in-plane resolution, 32 slices (3 mm), scan time 15 min). In animal models, ADC has been observed to vary linearly with  $\sqrt{f}$  [2] and, accordingly, DD is defined as the linear regression of ADC with  $\sqrt{f}$ .

**Results.** Fig. 1 shows sample PGSE and OGSE ADC maps and DD maps, with uniform DD values observed throughout the brain tissue. ADC increases approximately linearly with  $\sqrt{f}$  (Fig. 2a-c).

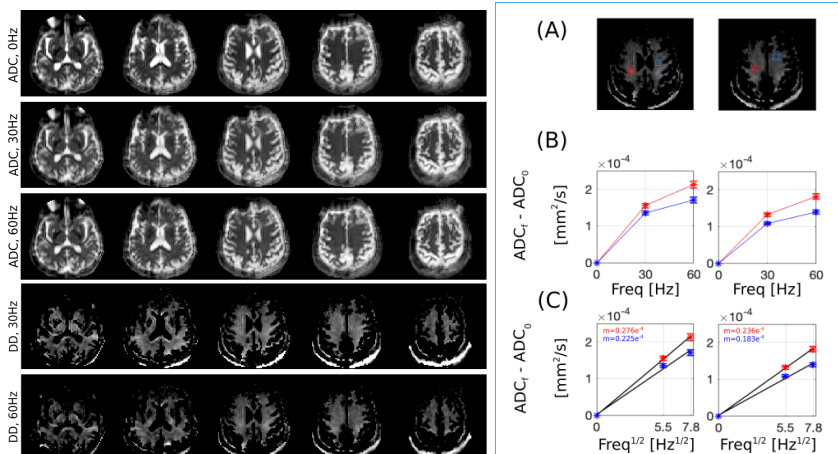


Fig. 1. Sample ADC and DD maps

Fig. 2. ADC versus  $f$  and  $\sqrt{f}$

**Conclusion.** Maps of diffusion dispersion (DD) were demonstrated for the first time in the *in vivo* human brain, with  $b=565 \text{ s/mm}^2$  at the peak frequency of 60Hz. New clinical systems come equipped with 80mT/m gradients, and SNR advantages of 7T were modest at TE=111ms; accordingly, similar quality DD maps may be feasible on clinical systems. The minimum scan time required to create the 60Hz DD maps would have been only 7 minutes (no  $b=0$  or 30Hz acquisitions used for those maps). The obtained results demonstrate the feasibility of robust, time-efficient acquisition of parameter maps characterizing OGSE frequency dependence of ADC.

**References.**[1] Schachter et al., *J. Magn. Reson.*, 147, 232–237 (2000). [2] Novikov et al., *Proc. Natl. Acad. Sci. U. S. A.*, 111, 5088–5093 (2014).

## CORTICAL LAYER ALIGNMENT IN SURGICALLY-RESECTED NEOCORTEX HISTOLOGY

Hossein Rejali<sup>1,3</sup>, Jordan DeKraker<sup>1,4</sup>, Uzair Hussain<sup>1</sup> and Ali R. Khan<sup>1-3</sup>

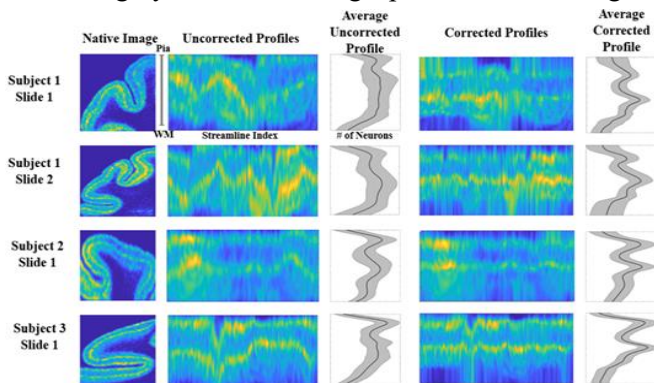
<sup>1</sup>Robarts Research Institute, <sup>2</sup>Dept. of Medical Biophysics, <sup>3</sup>Biomedical Engineering Graduate Program, <sup>4</sup>Neuroscience Graduate Program

Western University, London, Ontario, Canada

**Introduction:** Focal cortical dysplasias (FCD) are localized regions of malformed cerebral cortex that are frequently associated with epilepsy. Objective and quantitative characterization of FCDs is challenging, even in histology, and improving this quantification can aid in understanding the pathology and also provide a reference for MRI-histology studies. Cortical tissue is arranged in layers, or lamina, which optimally need to be taken into account when performing quantification. However, detecting cortical laminae is challenging due to the complex morphological structure and folding pattern of the cortex, combined with limited 2D sampling. These issues result in laminar profiles that appear distorted in different areas. Once aligned, quantitative laminar comparisons within slides, and across multiple slides and multiple subjects can be made without compromise.

**Methods:** *Data acquisition:* Histological processing was performed on tissue samples obtained from the surgically resected temporal lobe of patients with temporal lobe epilepsy (TLE). Coronal, 8-um thick sections of formalin fixed, paraffin-embedded tissue was processed with a NeuN staining. Following staining, the resulting histology slides were digitized on a ScanScope GL (Aperio Technologies, Vista, CA, USA) bright field slide scanning system in BigTIFF file format, using a pixel resolution of 0.5  $\mu\text{m}$ . *Preprocessing:* We began with whole slide images of brain slices, we then performed neuron cell body segmentation to extract feature maps from the histological images, describing the neuron density and average size, using a patch-based analysis. Subsequently, we extracted profiles which were obtained using equi-potential cortical laminae modeling. Finally, we corrected for the cortical layer distortion by applying a technique, referred to as iso-area correction, that leverages anatomical observation about how laminae become displaced, which is a 2D implementation of the Iso-volume model [2]. In addition, an iterative warping technique was applied which makes use of correlation optimized warping algorithm [3], effectively stretching and compressing profiles to reach alignment with a global reference.

**Results:** We performed this approach on 4 slides from 3 subjects and evaluated our ability to effectively align the cortical gray matter. Average profiles in the aligned and uncorrected space were used to assess quality of alignment. A summary of results is shown in **Figure 1**.



In general, the alignment of the cortical layers seemed to provide more detail and less variation in the average profiles. The corrected averages profiles more prominently show peaks corresponding to layers 2 and layer 4.

**Conclusion:** In this work, we have presented a method for aligning cortical lamina in histology, by first deriving features from histological slides, creating a coordinate system, using the equi-potential model, to sample along the cortical depth, and aligning the profiles using the iso-area correction and an iterative warping technique. The distortions seen in the uncorrected profiles contribute to a greater variance in the average profile, this ultimately leads to smoothing of characteristic profile shape features, such as smoothing of peaks corresponding to layers with high density neurons. The results showed relative decrease in variation in the average profiles across multiple subjects and slides, indicating better alignment with cortical

**Figure 1:** Alignment correction results across multiple slides and subjects. Native Images represent density feature maps extracted from NeuN stain histology slides.

**References:** [1] Bok 1929, [2] Waehnert et al Neuroimage 2014; 2:210-20, [3] Nielsen et al J. Chromatogr 1998 805:17-35

## Investigation of microstructural differences in the nigrosome-1 region of the substantia nigra between healthy and Parkinson's disease subjects at 7T

Yiming. Xiao<sup>1</sup>, Jonathan.C. Lau<sup>1,3</sup>, Terry Peters<sup>1,2,3</sup>, and Ali R. Khan<sup>1,2,3,4</sup>

<sup>1</sup>Imaging Research Laboratories, Robarts Research Institute, Western University, Canada

<sup>2</sup>Department of Medical Biophysics, Schulich School of Medicine and Dentistry, Western University, Canada

<sup>3</sup>School of Biomedical Engineering, Western University, Canada

<sup>4</sup>The Brain and Mind Institute, Western University, Canada

**Introduction:** The nigrosome-1 region undergoes the greatest and earliest cellular changes within the substantia nigra (SN) in Parkinson's disease (PD). Typically observed in T2\*w MRI in the axial view, the healthy hyperintense nigrosome-1 divides the SN to form a “swallow tail” shape, which disappears in PD patients, and this phenomenon is currently being investigated as a biomarker for the disorder<sup>1</sup>. With the high sensitivity and increased resolution of 7T MRI, we are able to study, for the first time, microstructural changes in the nigrosome-1 region due to PD using quantitative MRI measurements.

**Methods:** Five PD patients (age = 61±3y) and six healthy subjects (age = 47±11y) were scanned on the 7T Siemens Magnetom MRI scanner with MP2RAGE (0.7x0.7x0.7mm<sup>3</sup>), 3D T2w SPACE (0.7x0.7x0.7mm<sup>3</sup>), 3D four-echo GRE (0.8x0.8x0.8mm<sup>3</sup>), and 2D EPI DWI (1.5x1.5x1.5mm<sup>3</sup>) protocols. T1w MRIs and T1 maps were obtained from the MP2RAGE sequence. T2\*w images were generated by averaging the last 3 echoes of the GRE sequence to improve the contrast-to-noise ratio, and R2\* maps were computed from the same sequence.

Finally, the DTI-related metrics, including fractional anisotropy (FA), mean diffusivity (MD), and mode of anisotropy (MO) were derived from the DWI scans. All images were rigidly registered and resampled to the space of the individual's T1w MRI for analysis. To obtain the regions of interest (ROIs) for comparison, averaged brain templates were created with deformation fields obtained from a multi-contrast group-wise nonlinear registration using all subjects' T1w MRI, T2w MRI, and FA maps to ensure structural correspondence. The nigrosome-1 ROI was manually segmented in addition to the inner side of the “swallow tail” (medioposterior SN), which has a distinct feature on T2\*w MRI, and the rest of the SN bilaterally based on the T2\*w sub-group template of healthy subjects (see **Fig.1**). Then, the labels were propagated back to the individual T1w images. Finally, the mean values of the quantitative MRI measures were taken for both healthy and patient groups within the ROIs, and compared using one-tail two-sample t-tests.

**Results:** Statistical analysis demonstrated that in the nigrosome-1 of the PD cohort, T1 and MO are lower, and R2\* is higher bilaterally (p<0.05) while increased FA (p<0.05) is only present on the right-hand side. For both the left and right medioposterior SN, T1 values are significantly higher (p<0.05) for the healthy subjects. The observed higher R2\* in nigrosome-1 for PD implies elevated iron content, and the iron deposition varies more notably among patients than healthy subjects. The T1 shortening of the same region in PD may come from iron content increase and a decrease in free water, possibly due to cellular death. Notably, the reduced MO suggests less “organization” of fibers in the nigrosome-1 among PD patients, with potential selective degeneration in certain pathways of the fiber crossing, as suggested by the increased FA on the right-hand side.

**Conclusions:** We measured the underlying microstructural differences within the nigrosome-1 regions of the SN using quantitative MRI techniques, and report significant changes in T1, R2\*, MO, and FA within this sub-region in PD patients. Future investigation with a larger cohort will help further disclose the physiological changes within the SN to better understand PD and its progression.

### References

1. Schwarz *et al.* The ‘Swallow Tail’ Appearance of the Healthy Nigrosome – A New Accurate Test of Parkinson's Disease: A Case-Control and Retrospective Cross-Sectional MRI Study at 3T. *PloS one.* 2014;9(4): e93814.

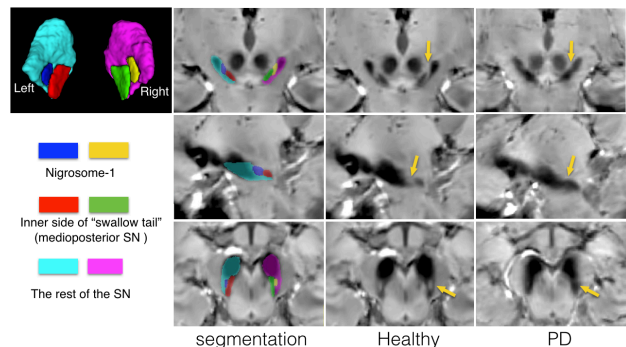


Figure 1. Segmentations of substantia nigra (SN) sub-regions and comparison of T2\*w group-averaged templates of healthy and Parkinson's disease (PD) cohorts. Yellow arrows highlight the difference.



## CLARIFYING DOPAMINERGIC PROJECTIONS OF THE VENTRAL TEGMENTAL AREA AND SUBSTANTIA NIGRA IN HUMAN USING STRUCTURAL MAGNETIC IMAGING

Nicholas Handfield-Jones<sup>1,2</sup>, Erind Alushaj<sup>1,2</sup>, Nole M. Hiebert<sup>2,3</sup>, Adrian M. Owen<sup>2,4</sup>, Ali R. Khan<sup>5,6</sup>, Penny A. MacDonald<sup>2,4,7</sup>

<sup>1</sup>Department of Neuroscience, Western University, <sup>2</sup>Brain and Mind Institute, Western University,

<sup>3</sup>Department of Physiology and Pharmacology, Western University, <sup>4</sup>Department of Psychology, Western University, <sup>5</sup>Department of Medical Biophysics, Western University, <sup>6</sup>Robarts Research Institute, Western University, <sup>7</sup>Department of Clinical Neurological Sciences, Western University

**Introduction:** Substantia nigra pars compacta (SNc) and ventral tegmental area (VTA) are the two primary dopaminergic (DAergic) producing nuclei of the midbrain, which, through projections to the striatum and cortex, mediate movement and cognitive processes.<sup>1</sup> Classically, these projections have been divided into the nigrostriatal and mesolimbic pathways: in the nigrostriatal pathway, the SNc innervates the dorsal striatum (DS), and in the mesolimbic pathway, the VTA innervates the ventral striatum (VS).<sup>2</sup> However, recent human magnetic resonance imaging (MRI) studies suggest that projections from both the SNc and the VTA target DS, VS, and multiple cortical regions, irrespectively.<sup>3</sup> Here, we aim to clarify these projections in humans using ultra-high field MRI.

**Methods:** 20 healthy, elderly participants ( $65.60 \pm 6.56$  years) were scanned in 7-Tesla (7T) field strength. Anatomical MP2RAGE T1 (TR=6000 ms, TE=2.73 ms, 0.7mm<sup>3</sup> iso) and diffusion weighted imaging (b=2000 s/mm<sup>2</sup>, TR=5500 ms, TE=60.8 ms, 95 directions, 1.5 mm<sup>3</sup> iso) sequences were performed on each participant. Scans were first converted to MNI152 stereotaxic space. The cortex, striatum, and midbrain were segmented from each participant's T1 image. FSL BEDPOST probabilistic multi-fibre ball and stick tractography (BST) was employed to parcellate the SNc and the VTA into functionally-derived sub-regions based on their maximal connectivity to an in-house parcellated striatum (figure 1), itself parcellated by maximal connectivity to the cortex.<sup>4</sup> To measure the extent to which each midbrain sub-region connected with the other brain sub-regions, whole-brain probabilistic BST was performed with seeds originating in each midbrain sub-region voxel and with streamlines targeting the striatum and cortex. Connectivity was defined as the proportion of streamlines that travelled from a sub-region origin to a sub-region target.

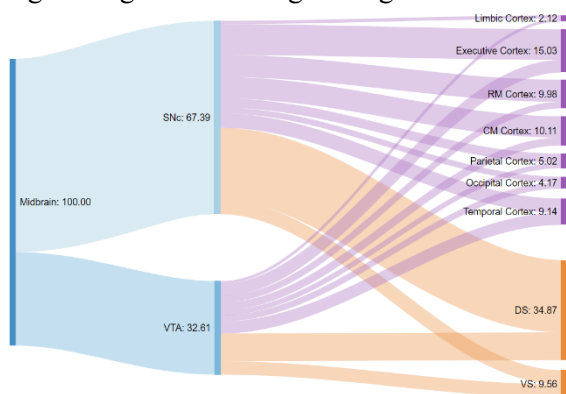


Figure 2: Sankey diagram of relative sizes of SNc and VTA (blue). From each, projections target cortex (purple) and striatum (orange)

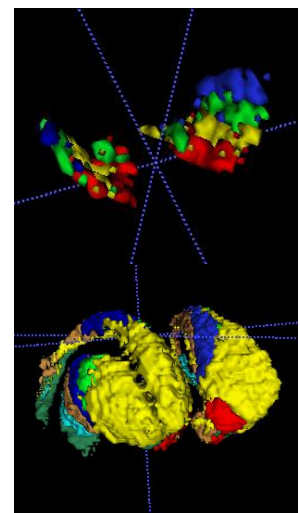


Figure 1: Parcellation of midbrain (above) and striatum (below). Both are parcellated into the limbic, executive, rostral motor, & caudal motor sub-regions. Striatum also contains parietal, occipital, & temporal sub-regions

**Results:** Of all streamlines that emerged from the midbrain, 34.87% and 9.56% targeted the DS and the VS, respectively. A significant amount also targeted the sub-regions of the cortex, to varying degrees. Considering midbrain DAergic connections to the striatum only, 83.70% of SNc projections were to the DS compared to 16.30% to the VS. In contrast, 67.48% of VTA projections targeted the DS while 32.52% targeted the VS (figure 2). These data are, however, preliminary. Notably, given that this method of connectivity mapping employs the same use of probabilistic BST as was used to parcellate the midbrain, it will be necessary for future analyses to use a midbrain parcellation template from

a different set of participants to avoid data double-dipping. Though this will avoid circular analysis, we expect no significant changes between this and the preliminary results.

**Conclusion:** In preliminary data analysis, we found that both the SNc and the VTA project to all striatal and cortical sub-regions. Midbrain DAergic circuits result in many behavioural sequelae; clarifying their anatomical networks may provide further clarification as to how they produce such complex outputs. Additionally, they have been implicated in a number of disease states. Should this experiment succeed in healthy controls, it could be replicated in patients with disease states to assess how these networks change pathologically. **References:** [1] Gonzalez KK. Ann NY Acad Sci. 1349(1): 1-45. [2] Düzel et al. Trends Neurosci. 32(6):321-328. [3] Kwon et al. Front Hum Neurosci. 6: 2014. [4] Tziortzi et al. Cereb Cortex. 24(5): 1165-1177.

**PET-guided DTI tractography reveals white matter abnormalities in medically refractory epilepsy: applications to epilepsy surgical planning.**

**Stefan E Poirier<sup>1,2</sup>, Benjamin Y Kwan<sup>3</sup>, Michael Jurkiewicz<sup>4</sup>, David Steven<sup>5</sup>, William Pavlosky<sup>4</sup>, Jonathan Romsa<sup>4</sup>, Frank S Prato<sup>1,2</sup>, Terry R Thompson<sup>1,2</sup>, Jorge Burneo<sup>5</sup>, Jonathan D Thiessen<sup>1,2</sup>, and Udunna C Anazodo<sup>1,2</sup>**

<sup>1</sup>Lawson Health Research Institute, London, ON, Canada, <sup>2</sup>Medical Biophysics, Western University, London, ON, Canada, <sup>3</sup>Department of Diagnostic Radiology, School of Medicine, Queens University, Kingston, ON, Canada, <sup>4</sup>Department of Medical Imaging, Western University, London, ON, Canada, <sup>5</sup>Clinical Neurological Sciences, Western University, London, ON, Canada

**INTRODUCTION:** Medically refractory epilepsy (MRE) is a condition that occurs when seizures cannot be controlled by medication and is often treated by surgically removing the brain tissue responsible for seizures called the epileptic focus (EF). Surgery fails to prevent seizures when EF and its relationships with surrounding brain regions are poorly characterized. Removing EF that is connected to surrounding neural networks can cause patients to develop debilitating conditions, such as memory, speech, or motor impairments (Helmstaedter et al., *Ann Neurol* 2003). Better, non-invasive methods are therefore needed to improve epilepsy surgical planning. Diffusion tensor imaging (DTI) is an advanced magnetic resonance imaging (MRI) technique that can effectively characterize EF and its relationships with surrounding brain regions (Jiang et al., *Neuroradiology* 2017). However, one in three MRE patients have non-structural EF (non-lesional) that cannot be detected by MRI (Knowlton, *Epilepsy & Behavior* 2006). <sup>18</sup>F-Fluorodeoxyglucose (FDG) positron emission tomography (PET) can detect non-structural EF as brain areas showing decreased activity, also known as glucose hypometabolism (Aparicio et al., *NeuroImage* 2016). In this study, we aim to use FDG-PET to guide DTI tracking of white matter (WM) pathways in non-lesional MRE patients to better understand how EF affects surrounding brain regions.

**METHODS:** FDG-PET and DTI scans were acquired simultaneously on 20 non-lesional MRE patients using a 3T PET/MRI scanner (Biograph mMR, Siemens Healthineers, Erlangen, Germany). DTI acquisition protocol: single-shot EPI with 64 diffusion encoding directions; b-values = 0 and 1000 s/mm<sup>2</sup>; 2x2x2 mm<sup>3</sup> isotropic voxels. Image preprocessing steps included: denoising with an optimized non-local means filter (ONLM) (Coupé et al., *Ieee Med Imaging* 2008); subject motion, eddy current, and bias field corrections; and tensor-fitting to generate fractional anisotropy (FA), mean diffusivity (MD), axial diffusivity (AD), and radial diffusivity (RD) maps. Areas of decreased glucose activity on PET images served as regions of interest (ROIs). WM integrity around the EF was assessed by calculating mean FA, MD, AD, and RD in the temporal WM adjacent and contralateral to these ROIs. ROIs served as seed regions to initiate neural fiber bundle tracking using Fibernavigator (Chamberland et al., *Front Neuro* 2015), a novel tractography visualization tool. Fibernavigator was also used to perform fiber statistics to measure total fiber bundle count and mean fiber length (mm).

**RESULTS:** Data from five non-lesional MRE patients revealed visual differences as well as lower fiber count and mean fiber length in temporal WM tracts adjacent to PET ROIs compared to the contralateral side. FA was reduced in the posterior thalamic radiation ipsilateral to PET ROIs. There were no differences in mean MD, AD, or RD. WM tracts around a PET ROI are shown for one patient in the figure below. Mean and standard deviation FA, fiber count and mean fiber length are also included as quantitative measurements of WM integrity.

**CONCLUSIONS:** In this study, we showed the feasibility of combining FDG-PET and DTI to investigate WM integrity in MRE patients. PET-guided DTI tractography revealed fiber tract differences between ipsilateral and contralateral WM around EF identified by PET ROIs. Preliminary results are promising but need to be further validated in a larger patient population. In general, PET-guided DTI tractography will shed new insight into WM altered in MRE and can be used to further improve epilepsy surgical planning.

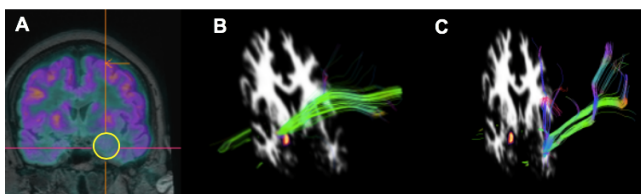


**Figure.** (A) PET showing glucose hypometabolism (circle). Streamlined WM tracts (coloured lines) going through: temporal WM (B) adjacent and (C) contralateral to the PET ROI (orange), FA (right/left) =  $0.16 \pm 0.03/0.21 \pm 0.05$ , count = 282/166, length = 105.91/91.68.

## Investigating the added value of Diffusion Kurtosis Imaging in Temporal Lobe Epilepsy

Loxlan W. Kasa<sup>a, b</sup>, Terry M Peters<sup>a, b, c</sup>, Seyed M. Mirsattari<sup>c, d</sup>, Ali R. Khan<sup>a, b, c</sup><sup>a</sup>Imaging Research Laboratories, Robarts Research Institute, <sup>b</sup>School of Biomedical Engineering, <sup>c</sup>Department of Medical Biophysics,<sup>d</sup>Departments of CNS, Medical Imaging and Psychology, Western University, London, Ontario, Canada

**Introduction:** Patients exhibiting no structural abnormalities in their MRI scans, present a challenge during pre-surgical investigations in temporal lobe epilepsy (TLE). The diffusion tensor model (DTI) (Tournier et al.), based on unrestricted water diffusion, is the simplest way to quantify brain microstructure of TLE patients *in vivo* non-invasively, but still often fails to detect subtle pathology. Therefore, diffusion kurtosis imaging (DKI), extension of DTI could better characterize water diffusion properties (Jensen et al.). Investigations of DKI on left TLE patients have demonstrated DKI to be more sensitive compared to DTI. To assess DKI ability in characterizing left and right TLE, we performed feature selection and multiclass classification to identify regional abnormalities (Fig 1).

**Methods:** Patients with TLE (n=17) eight left and nine right with healthy controls (n=21) were recruited for this study. All subjects underwent the same imaging protocol performed on a 3T MRI scanner. Diffusion-weighted images (DWI) were obtained by using multiband echo-planar sequence with 3 diffusion weightings ( $b = 0, 1300,$  and  $2600 \text{ s/mm}^2$ ) along 130 diffusion-encoding directions acquired twice with left-right, right-left phase encoding directions. The acquired DWIs were corrected for echo planar imaging and eddy current distortion using topup and eddy (Andersson et al.) from FSL. Gibbs' ringing artefact was corrected by determining optimal sub-voxel shifts within the neighbourhood of sharp edges including noise reduction (Veraart et al.). Diffusion and kurtosis measurements were obtained using the diffusion kurtosis estimator tool (<http://www.nitrc.org/projects/dke>). The following maps were generated: fractional anisotropy (FA), mean diffusivity (MD), axial diffusivity (AD) and radial diffusivity (RD) from DTI. And FA with kurtosis FA (FA+Kfa), MD with mean kurtosis (MD+MK), AD with axial kurtosis (AD+AK) and RD with radial kurtosis (RD+RK) from DKI. For WM analysis, the pre-processed data were registered to JHU-white-matter labels atlas in MNI space and grey-matter (GM) analysis we used Freesurfer to parcellate cortical and subcortical region of interest (ROI) in each of these parametric maps. Mean values from white matter (WM) and GM ROIs were extracted as our features.

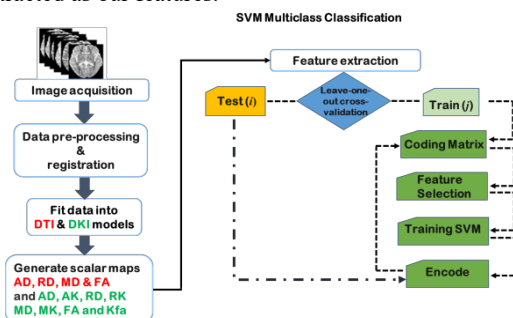


Fig. 1. General work-flow SVM multiclass classification.

We performed multiclass classification by training multiple binary support vector machine (SVM) classifiers after performing forward sequential feature selection for

individual classifiers. The output of each binary classifier was then combined using an error-correcting output code technique (Ali et al.) and were cross-validated and tested using leave-one-out cross validation strategy.

**Results:** The classification performance was evaluated as follows; MD vs MD+MK, AD vs AD+AK and RD vs RD+RK. In WM both DTI and DKI classifiers (MD, MD+MK, AD and RD+RK) scored the highest overall accuracy of 92.1% while DTI had greater number of classifiers with highest accuracy with FA scoring 89.5%. In GM DKI classifiers out-performed DTI scoring highest overall accuracy of 92.1% across while MD and AD scored 89.5% and RD scored 86.8%. Feature selection identified the discriminative regions between the classes (example Fig.2). For WM areas DTI detected mostly the single-fiber voxels bundles such as the commissure fibers including some large clusters with two fiber orientation such as parts of cerebral peduncle and superior longitudinal fasciculus. DKI was able to detect more of the major associative fiber bundles consistently, which are known to have higher fiber crossings. This difference could be due to the known short-coming of DTI due to its single fiber per voxel assumption. In GM, DTI generally selected parts of: temporal lobe regions including amygdala, cingulate cortex, frontal lobe, basal ganglia and cuneus. Again we note that most of these regions were also detected with DKI in addition to fusiform and precuneus gyrus. DKI compared to DTI, was more prominent in the right temporal lobe structures especially entorhinal cortex (EC).

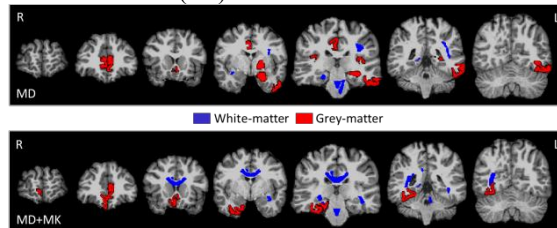


Fig.2. Shows the features selected consistently > 50% of time. For illustration only MD vs MD<sub>2</sub>MK is shown.

**Conclusion:** DKI detection of extrahippocampal areas: EC, fusiform and the precuneus gyrus supports the notion of TLE as a network disorder. EC sometimes have seizures originating from it which have contributed to lower seizure-freedom following surgery (Bonilha et al.). Fusiform abnormalities had been known to associate with face processing complications (Riley et al.) and changes in precuneus functional connectivity had been related to grey matter atrophy in TLE (Morgan et al.). The DKI detection of major associative WM bundles is parallel to previous findings (Winston et al.). In addition DKI was prominent in detecting right temporal lobe regions compared to DTI, this could be due to subtle changes DTI is not able to detect. The water diffusion abnormalities in these regions could be due to gliosis, demyelination, axonal and dendritic reorganization in TLE (Rodríguez et al.). Therefore DKI has potential to increase the ability of traditional DTI in accurately detecting brain microstructural changes in TLE patients and could improve the diagnosis of temporal lobe epilepsy.

## Diffusion in the unfolded hippocampus

Uzair Hussain<sup>a</sup>, Jordan DeKraker<sup>a</sup>, Corey Baron<sup>a,b</sup> and Ali R. Khan<sup>a,b</sup>

<sup>a</sup>Robarts Research Institute, <sup>b</sup>Departments of Medical Biophysics and Medical Imaging Western University, London, ON, Canada

**Introduction:** The ability to detect subtle hippocampal abnormalities early can significantly improve treatment for numerous neurological disorders. Ex vivo studies with ultra-high field have revealed that diffusion MRI (dMRI) can reveal microstructural variations in the hippocampus [1]. However, in vivo dMRI studies are challenging due to the complicated geometry and small size of the hippocampus. One novel way to overcome this is by transforming the usual cartesian coordinates in a MRI image to curvilinear coordinates [2]. This allows us to virtually flatten the hippocampus into a thin sheet. A particularly unique aspect of our proposed approach is to project the diffusion data onto this sheet. **Methods:** We manually segment both hippocampi from four participants in the Human Connectome Project (HCP) Young Adult 3T study [3]. This is followed by solving Laplace's equation,  $\nabla^2\phi = 0$ , to provide three new anatomical coordinates  $u$ ,  $v$  and  $w$ , allowing us to 'unfold' the hippocampus by going in to the domain of the new coordinates. We also map diffusion vector data to the unfolded space with the Jacobian encoding the unfolding transformation. Several existing tools for fitting can make use of a Jacobian to account for gradient non-linearities and can be used directly for fitting and tractography in the unfolded space. We utilized the inherent correspondence across subjects in the unfolded space to define subfield labels in our participants using average labels defined previously at 7T [2]. We used these to perform probabilistic tractography (FSL PROBTRACKX [4]). **Results:** The visualizations of fibre orientation maps in Fig. 1 demonstrates how unfolding provides a holistic visualization of the entire extent of the hippocampus and reveals patterns in fibre orientation and anisotropy that are difficult to discern in the native space. A validation of the ability of the unfolding approach to preserve orientation information is shown in Fig. 2, with angle errors from fits in the native space compared to fits performed in unfolded space and mapped back to the native space. We found that fractional anisotropy has some subfield specificity, with subiculum significantly different than all other subfields. Fig. 3 shows the intra-hippocampal connectivity for a hippocampus, revealing patterns that are consistent with connections related to the tri-synaptic pathway. **Conclusion:** A benefit of the unfolded space is that the orthogonal axes now represent anatomically relevant axes: longitudinal (anterior to posterior), laminar (deep to superficial), and lamellar (proximal to distal). These are notably the axes in which axonal projections generally follow anatomically, so tractography in this space could be constrained more effectively. This advantage could also be employed to inform novel microstructural models of cortical tissue, which future work will explore. One limitation of the current work is the need for manual segmentations, and thus was limited to a small number of subjects, however, semi-automated methods are currently in development, and this technique can also be applied more generally to any cortical structure.

**References:** [1] Beaujoin, J. et. al., Post-mortem inference of the human hippocampal connectivity and microstructure using ultra-high field diffusion MRI at 11.7 T. *Brain Struct. Funct.* 223, 2157–2179 (2018). [2] DeKraker, J. et. al., Unfolding the hippocampus: An intrinsic coordinate system for subfield segmentations and quantitative mapping. *Neuroimage* 167, 408–418 (2018). [3] Van Essen, D. C., et. al., The WU-Minn Human Connectome Project: an overview. *Neuroimage* 80, 62–79 (2013). [4] Behrens, T. E. J. et. al., Probabilistic diffusion tractography with multiple fibre orientations: What can we gain? *Neuroimage* 34, 144–155 (2007).

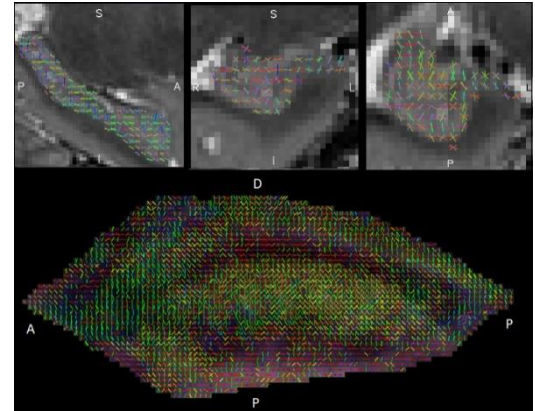


Fig. 1: Top panels show the hippocampus in the native space and below we see the unfolded hippocampus. The colored sticks show the diffusion direction.

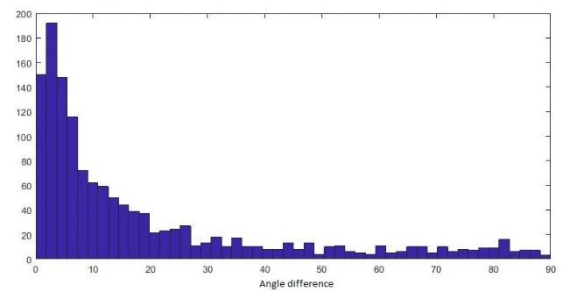


Fig. 2: The angle difference between sticks fit from BEDPOST in unfolded space with sticks fit in native space.

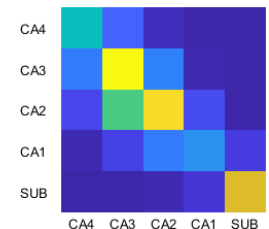


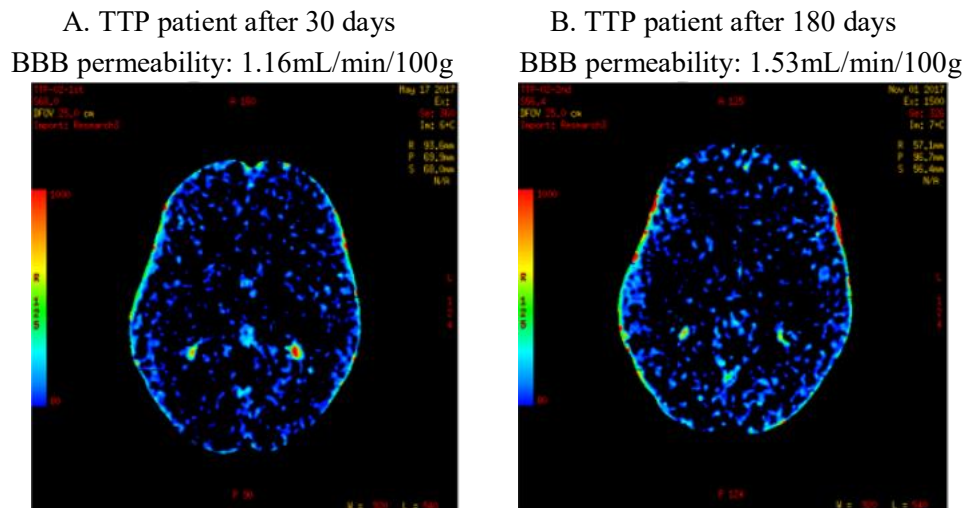
Fig. 3: Intra and inter connectivity of the subfields

**Compromised blood brain barrier in patients with TTP by CT motivates further investigation using MRI**JG Hamilton<sup>1</sup>, TY Lee<sup>1,2,3</sup>, JD Thiessen<sup>1,2</sup>, SHS Huang<sup>1,4,5</sup><sup>1</sup>Department of Medical Biophysics, Western University, London, Ontario, Canada<sup>2</sup>Lawson Health Research Institute, London, Ontario, Canada<sup>3</sup>Imaging Research Labs, Robarts Research Institute, London, Ontario Canada<sup>4</sup>Department of Medicine, Schulich School of Medicine & Dentistry, London, Ontario, Canada<sup>5</sup>The Lilibeth Caberto Kidney Clinical Research Unit, London, Ontario, Canada

**Introduction:** Thrombotic thrombocytopenic purpura (TTP) is a life-threatening disease that affects approximately 5 people per million per year (Joly et al, 2017). The disease is characterized by insufficient activity in ADAMTS13 (A Disintegrin-like And Metalloprotease with Thrombospondin type 1 repeats 13) which is an enzyme important for preventing blood clotting. The five predominant symptoms of TTP are fever, anemia, thrombosis, kidney failure, and neurological changes (which may include confusion, seizures, and decreased level of consciousness). Plasma exchange is the most common treatment and though it significantly reduces mortality rate there have yet to be improvements in understanding the pathology in such neurological changes. The study aims to better understand the neurological changes in patients with TTP. We hypothesized that blood brain barrier (BBB) permeability will temporarily increase after a patient experiences TTP but will improve over time.

**Methods:** Using computed tomography angiography (CTA) on a 256-slice CT scanner (GE Healthcare, Revolution) we measured brain perfusion in in TTP patients 30 and 180 days after hematological remission of TTP. This was using an iodinated contrast dose of 0.7 mL/kg of body weight and the radiation dose was 6 mSv. This was a preliminary study on a small sample size.

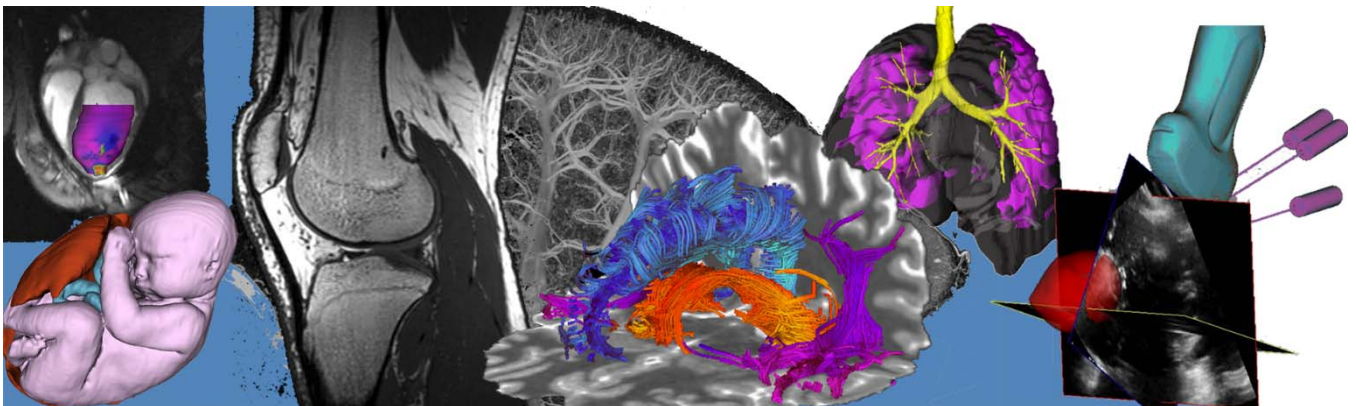
**Results:** Figures A and B show the same axial slice from a CT scan of a TTP patient at the timepoints of 30 days (increase in BBB permeability) and 180 days (a further increase in BBB permeability) after hematological remission. Because of this further increase, these findings do not follow our hypothesis.



**Conclusion:** In normal tissue the expected permeability is 0mL/min/100g. In these results there is an initial increase in BBB permeability after 30 days and after 180 days the permeability has worsened even further. This motivates further investigation where we intend to use quantitative magnetic resonance imaging (MRI) to measure longitudinal changes in white matter integrity relative to healthy controls. Our current direction is to use quantitative MRI to assess myelin water fraction (Deoni et al, 2008) where we hypothesize that brain white matter will deteriorate over time in patients with TTP.

# Poster Presentation Abstracts

## Session 11: Cardiac and Vascular Imaging



## CT Perfusion Imaging following a Wrist Fracture

Michael Riddle<sup>1</sup>, Nina Suh<sup>6,7,8</sup>, Ting-Yim Lee<sup>4,5,6</sup>, Emily Lalone<sup>1,2,3,6,8</sup>

<sup>1</sup>School of Biomedical Engineering, <sup>2</sup>Department of Mechanical and Materials Engineering, <sup>3</sup>Faculty of Engineering, <sup>4</sup>Medical Biophysics, <sup>5</sup>Robarts Research Institute, <sup>6</sup>Lawson Health Research Institute, <sup>7</sup>Roth|McFarlane Hand and Upper Limb Center, <sup>8</sup>Department of Surgery, The University of Western Ontario

### Introduction

Osteoarthritis is a disease of the global joint, originating from a combination of susceptibility and an abnormal mechanical environment (joint geometry/structure). Mounting research suggests that inflammation may mechanically accelerate disease progression in post-traumatic arthritis(1,2)(3,4). Inflammation associated with arthritis can be imaged using contrast-enhanced CT imaging. Intravenously administered iodinated contrast material can be used to measure capillary perfusion and permeability surface (PS). 4DCT scanners measure, over time, the wash-in and wash-out of inert contrast in the vasculature and soft tissues from the dual processes of blood flow and permeation of the blood-tissue barrier. We hypothesize that permeability surface can act as a biomarker of inflammation and help identify osteoarthritis in the wrist.

### Methods

A CT Perfusion (CTP) scan was acquired six weeks post fracture in a single patient to image capillary perfusion and PS. Regular CT contrast (Iovue 370) was injected via an antecubital vein in the contralateral arm at a dose of 0.7 mL/kg body weight (30% less than a regular contrast enhanced CT scan) and an injection rate of 3-4 mL/s. The whole affected wrist was scanned using 80 kV and 80 mAs continuously over the first 40 s and then once every 15 s for the remaining 180 s. Acquired data was reconstructed with the detail algorithm (spatial resolution of 10 lp/cm) in volumes at 1 s intervals. The 52 (40+12) dynamic reconstruction volumes will be analyzed with the CT Perfusion software (GE Healthcare) to determine soft tissue perfusion and vessel permeability in the wrist joint.

### Results

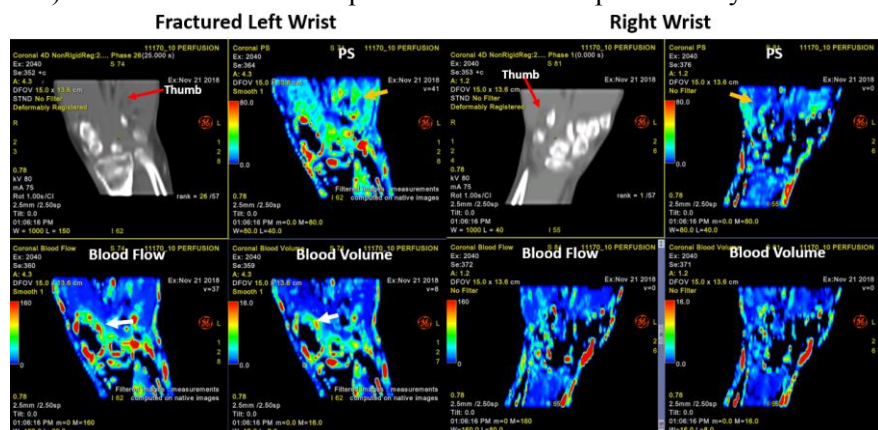
Qualitative comparisons of a single patient (6 weeks post-fracture) indicate asymmetric differences in the CTP maps between the fractured (left) and non-fractured (right) wrist. PS was increased in the affected wrist (yellow arrow) and blood flow and volume (white arrow) were also elevated.

### Conclusions:

Preliminary results suggest inflammation in the fractured wrist occurring 6 weeks following fracture when bone healing has already occurred. Low-grade inflammation may contribute to stiffness and limited mobility, and potentially an acceleration of degenerative changes in the joint that may lead to the development of post-traumatic arthritis in the fractured wrist. Inflammatory cytokines could potentially increase the capillary permeability independent of perfusion and may lead to elevated PS. Our preliminary results indicate that CTP maps may be able to monitor for inflammation post wrist fracture and therefore response to treatment to limit its deleterious effect.

### References:

- Ashford S, Williard J. Osteoarthritis: A review. Nurse Practitioner. 2014.
- Laulan J, Marteau E, Bacle G. Wrist osteoarthritis. Orthop Traumatol Surg Res [Internet]. 2015 Feb [cited 2019 Jan 23];101(1):S1–9. Available from: <http://www.ncbi.nlm.nih.gov/pubmed/25596986>
- Haugen I. Hand osteoarthritis: current knowledge and new ideas. Scandinavian Journal of Rheumatology. 2016.
- Bruyn GA, Naredo E, Damjanov N, Bacht A, Baudoin P, Hammer HB, et al. An OMERACT reliability exercise of inflammatory and structural abnormalities in patients with knee osteoarthritis using ultrasound assessment. Ann Rheum Dis [Internet]. 2016 May 1 [cited 2019 Jan 23];75(5):842–6. Available from: <http://www.ncbi.nlm.nih.gov/pubmed/25902788>



## A Carotid Artery Image-Derived Input Function for Pre-Clinical Simultaneous PET/MRI

Van Ginkel, MJ<sup>1</sup>; Fox, MS<sup>2</sup>; Qi, Q<sup>1,2</sup>; Smailovic, H<sup>2</sup>; Prato, FS<sup>1,2</sup>; Thiessen, JD<sup>1,2</sup>

1. Medical Biophysics, Western University, London, Ontario, Canada
2. Lawson Imaging, Lawson Health Research Institute, London, Ontario, Canada

### Introduction:

A dynamic positron emission tomography (PET) acquisition enables quantitative kinetic modelling. Often, an arterial input function (AIF) needs to be measured to perform kinetic modeling<sup>1</sup>. Blood sampling in small animals is difficult due to the limited amount of blood that can be drawn without compromising its health, necessitating an image-derived AIF (IDIF). The left ventricle is a convenient region of interest to extract the IDIF due to the size of the blood pool in this area<sup>2</sup>.

There are an increasing number of pre-clinical PET scanners available that are capable of simultaneous use inside an MRI scanner (e.g., Cubresa NuPET<sup>TM</sup>). Often, these inserts have axial field of views (FOVs) that are not large enough to include both the head and heart of a large rodent in a single bed position. Thus, dynamic PET imaging of the head cannot be done if one wants to use the left ventricle to extract an IDIF. Our objective is to develop a method for the extraction of an IDIF from the carotid arteries (cIDIF) of rats. This will enable dynamic PET imaging to be done on dedicated PET systems and PET inserts for simultaneous PET/MRI which have short axial FOVs.

### Methods:

Dynamic PET data was acquired in 4 rats for 60-90 minutes (Siemens Inveon). Injection of [<sup>18</sup>F]-FDG (~60 MBq) occurred 30 seconds after the start of the scan. Dynamic data was reconstructed using a 3D ordered subset expectation maximization (OSEM3D) reconstruction algorithm. 3T MRI (Siemens Biograph mMR) were acquired with a head coil developed for small animal imaging (Cubresa). An isotropic T<sub>1</sub>-weighted volumetric interpolated brain examination (VIBE) sequence was used with an isotropic resolution of 0.3 mm. 3D Slicer was used for manual co-registration of the PET and MR images followed by segmentation and extraction of the input functions. The cIDIF was extracted by using the MR images to create segmentation, which includes both carotid arteries. To get the input function from the left ventricle of the heart, the last frame of the PET image was used to create the segmentation. These segmentations were then used to measure the average diameter of each area. The appropriate recovery coefficient based on these size measurements were used to correct each input function.

### Results:

The co-registered data allowed for easy segmentation of the carotids in the rat images. Because of this, input functions from both the heart and the carotid arteries were successfully extracted. The input functions from both the heart and the carotid artery follow similar trends following correction of the time activity curves by the corresponding recovery coefficients.

### Conclusions:

The carotid arteries may become a useful site to extract an IDIF for PET systems possessing short axial FOVs. This will allow the users of small animal dedicated PET scanners as well as PET inserts for simultaneous PET/MRI to perform quantitative kinetic modeling in the brain using a cIDIF with their systems. In the future, we hope to refine our extraction and correction methods to further enhance the similarity between the input functions and finally validate the method of using cIDIF for kinetic modelling.

### References:

1. Morris, E. D., Endres, C. J., Schmidt, K. C., Christian, B. T., Muzic, R. F., & Fisher, R.E. (2004). Kinetic Modeling in Positron Emission Tomography. In *Emission Tomography: The Fundamentals of PET and SPECT* (pp. 499–540).
2. Fang, Y.-H. D., & Muzic, R. F. (2008). Spillover and partial-volume correction for image-derived input functions for small-animal F-18-FDG PET studies. *Journal of Nuclear Medicine*, 49(4), 606–614.



## Mapping Out the Average Fiber Architecture from Diffusion Tensor MR Images Of *Ex-Vivo* Porcine Hearts

Mia Mojica<sup>(\*)</sup>, Mihaela Pop<sup>(\*\*)</sup>, Maxime Sermesant<sup>(\*\*\*)</sup>, and Mehran Ebrahimi<sup>(\*)</sup>

<sup>(\*)</sup> Faculty of Science, University of Ontario Institute of Technology, Oshawa, ON, Canada

<sup>(\*\*)</sup> Department of Medical Biophysics, University of Toronto, Sunnybrook Research Inst., Toronto, ON, Canada

<sup>(\*\*\*)</sup> Asclepios Team, INRIA Sophia Antipolis, France

**Introduction:** Myocardial fiber directions play an important role in the electro-mechanical function of the heart, which is often impaired in cardiovascular disease (CVD). Fiber directions in healthy state can be determined via diffusion tensor DT MRI and then integrated into predictive image-based heart models and statistical atlases to help in diagnosis and therapy planning of CVD. However, such information is difficult to obtain *in-vivo*; thus, here, we present a pipeline for constructing a statistical fiber atlas from *ex-vivo* DT images of porcine hearts (with size similar to human hearts). We hypothesize that normalizing the cardiac geometries and reorienting local directional information on diffusion would yield an average DT field that preserves diffusion tensor and fiber orientations.

**Methods:** The diffusion-weighted (DW) MRI studies were performed on a dedicated 1.5T GE Signa Excite scanner using a small database of N=8 explanted healthy pig hearts, with approval from our institute. In the current study, we used the following MR parameters: TE=35 ms, TR=700 ms, ETL=2, b=0 for the unweighted MR images, and b=500 s/mm<sup>2</sup> when the seven diffusion gradients were applied, respectively [2]. Image resolution was ~0.5x0.5x1.6 mm. Notably, the total MR imaging time is ~10 hours/heart, which is not feasible for *in-vivo* patient studies.

A mean cardiac volume was generated by normalizing the anatomical structures of the eight subjects. This was done through an iterative groupwise registration scheme that converges to a stable average cardiac geometry. Every groupwise step was initialized by registering each subject to a current reference volume. The transformations from the pairwise alignments were used to compute updates to the reference geometries at each iteration.

We then projected the diffusion tensor (DT) field of each subject to a common reference frame using the final set of transformations from the groupwise step. This allowed us to compute the average DT field and visualize the preferential direction of diffusion at every voxel in the mean cardiac volume. Finally, the end-to-end pathway of diffusion given by the primary eigenvectors of the transformed diffusion tensors was tracked using MedInria (<http://med.inria.fr>).

**Results and Conclusions:** Pairwise alignments of the subjects to the reference geometries were performed via multilevel elastic registration. The groupwise scheme converged (after 7 iterations) to the mean volume shown in Fig. 1, along with the evolution of the reference geometries. The reoriented diffusion tensors were calculated using the Finite Strain method,

and we found that the local orientation of the tensors were indeed preserved, as shown in the comparison between the magnified areas selected from the septum of the original and transformed tensors of one of the hearts (Fig. 2). In Fig. 3, we present the associated average cardiac fiber architecture obtained from the reoriented DT fields.

Future work will focus on assessing the accuracy of fiber atlas using a leave-one-out validation method. Prior to clinical translation, we will also validate the output of 3D MR-based computer heart models that will integrate DTI fibers (as in [3]) vs. atlas fibers.

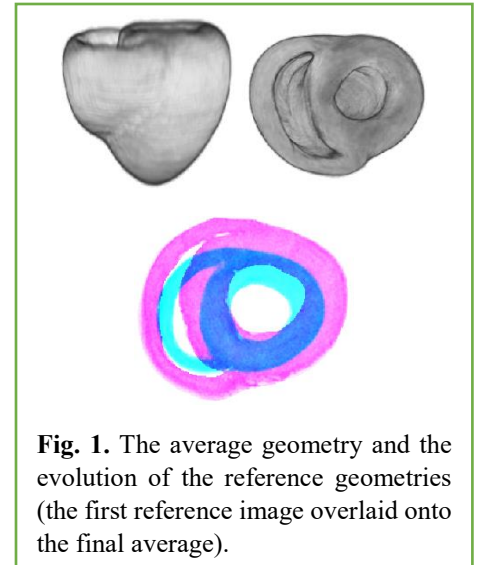


**Fig. 1.** The average geometry and the evolution of the reference geometries (the first reference image overlaid onto the final average).

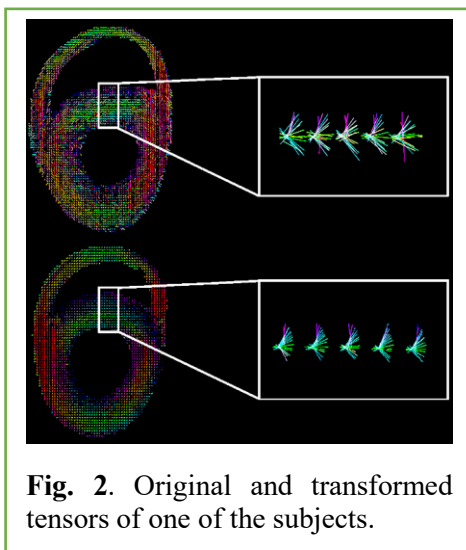


**Fig. 2.** Original and transformed tensors of one of the subjects.

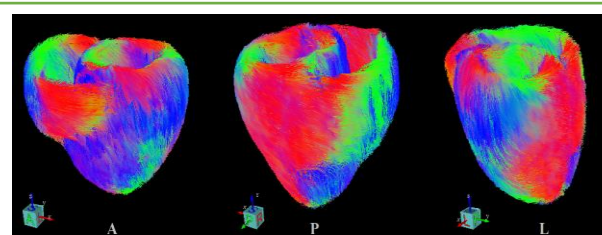


**Fig. 3. Fiber Tractography.** Cardiac fiber atlas obtained by tracking the end-to-end pathway of the principal direction of diffusion at every voxel.

**References:** [1] Peyrat, J.M., Sermesant, M., et al., IEEE Trans. Med. Imag. 26, 1500-14 (2007), [2] Pop, M., et al., Physics in Medicine and Biology. 58 (15), 5009-28 (2013), [3] Pop, M., et al., IEEE TBME 58(12) 3483 (2011)

## Interactive-Automatic Ultrasound Segmentation for Mitral Valve Modelling

P.Carnahan<sup>\*1</sup>, W.Xia<sup>1</sup>, O.Ginty<sup>1</sup>, J.Moore<sup>1</sup>, T.Peters<sup>1</sup>

<sup>1</sup>Robarts Research Institute, School of Biomedical Engineering, Western University

**Introduction:** Recently, developments have been made towards modelling patient-specific deformable mitral valves from transesophageal echocardiography (TEE) [2]. Thus far, a major limitation in the workflow has been the manual process of segmentation and model profile definition. Completing a manual segmentation from 3D TEE can take upwards of two hours, and fully automatic mitral valve segmentation techniques often struggle with inter-operator image variability and correcting for signal dropout. Streamlining the process of segmenting the valve and generating a surface mold is important for the scalability of patient-specific mitral valve modelling. We present an interactive-automatic mitral valve segmentation algorithm implemented in 3D Slicer.

**Methods:** Our segmentation technique is designed to be used on end-diastole images for high quality images and for use in mold creation. The algorithm works as follows: First, the user defines the mitral annulus by placing a series of points using the SlicerHeart Annulus Analysis module [2]. Second, the annulus definition is used to initialize a fast-marching segmentation of the blood pool above the valve, which is passed into a 3D geodesic active contour biased to grow. Third, once the blood pool segmentation is complete, the region bordering the surface of the blood pool segmentation is taken as the initialization for a second 3D geodesic active contour pass, this time biased to shrink. Both the blood pool and leaflet segmentation phases are interactive as the user advances the segmentation in increments until satisfied with the results. Evaluation of our proposed algorithm was performed using manual segmentations performed by a clinician as a gold-standard. The metrics used were Dice similarity coefficient, mean surface distance for the overall segmentation and mean surface distance for the proximal surfaces. We also recorded the time taken to complete each segmentation with each method. Since the manual segmentations do not include the atrial wall, we removed this region from our automatic segmentations. Thus far, analysis has been completed on one image set, however a total of sixteen are planned.

**Results:** Our preliminary results indicate that our segmentation algorithm can achieve a Dice similarity coefficient of 0.62. The unsigned mean surface distance was  $0.88 \pm 0.74\text{mm}$ , and the signed distance was  $0.2 \pm 1.04\text{mm}$ . When comparing only the proximal surfaces, we found an unsigned distance of  $1.01 \pm 0.64\text{mm}$ , and a signed distance of  $0.93 \pm 0.76\text{mm}$ . The times to complete the segmentations were 86 minutes for manual, and 13 minutes for our automatic method.

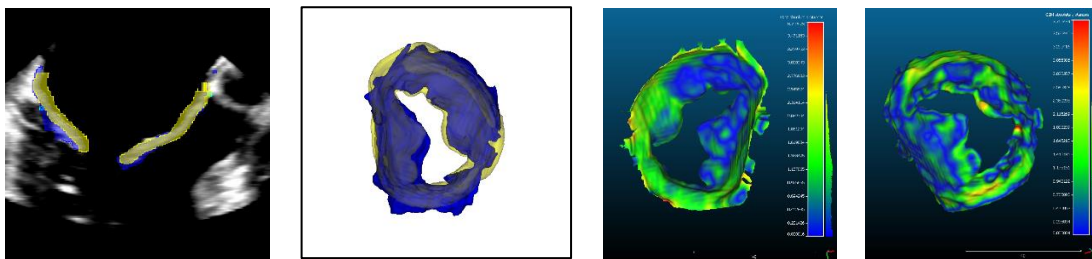


**Figure 1.** From left to right: 1. Cross section of manual (blue) and automatic (yellow) segmentations. 2. 3D representation of manual (blue) and automatic (yellow) segmentations. 3. Distance map for proximal surfaces. 4. Distance map for complete segmentations.

**Conclusions:** The resulting segmentations from our software successfully replicate the gold-standard segmentations within reasonable tolerance. The overall mean surface distance analysis demonstrated sub-millimeter accuracy for the automatic segmentation. The Dice similarity coefficient was only 0.62, however this is largely explained by noise on the distal leaflet surfaces. For the purposes of creating 3D printed molds only the proximal surface is used. Our results show that our software can extract the proximal surface within roughly one millimeter, indicating that it is suitable for use in patient-specific mitral valve modelling. This segmentation software reduces the time required for completing an accurate mitral valve segmentation and improves the workflow of the mitral valve modelling process.

**References:** [1] Ginty *et al.* J Cardiothorac Vasc Anesth (2018). [2] Scanlan *et al.* Pediatr Cardiol (2018)

## Pulse inversion increases sensitivity to transvertebral acoustic emissions from microbubbles sonicated with short burst, phase shift keying focused ultrasound exposures

Stecia-Marie Fletcher<sup>1,2</sup> and Meaghan O'Reilly<sup>1,2</sup>

<sup>1</sup>Physical Sciences Platform, Sunnybrook Research Institute, <sup>2</sup>Department of Medical Biophysics, University of Toronto.

**Introduction:** A key advantage of microbubble (MB)-mediated focused ultrasound (FUS) therapies, such as blood-brain and blood-spinal cord barrier opening, is the ability to passively monitor acoustic emissions from oscillating MBs in real time and control treatments [1]. When using long exposures (~10ms), bioeffects associated with acoustic signatures, like the presence of frequency harmonics and broadband noise (associated with stable and inertial MB behaviour respectively), have been well characterized [2]. Recently, our group has shown that a dual-aperture approach and a pulse train of short bursts (2 cycles at 514kHz) with random phase shift keying (PSK) can reduce the focal size and minimize standing wave formation in *ex vivo* human vertebrae, to enable a uniform focus for clinical-scale blood-spinal cord barrier opening [3]. However, emissions from MBs exposed to these pulses are complex and require advanced methods of analysis compared with conventional exposures. Additionally, emissions from MBs within the vertebral canal are small compared with strong ultrasound reflections at the bone interface and can be difficult to detect. Pulse inversion (PI) is an established technique used in ultrasound contrast-enhanced imaging to minimize linear tissue signals and amplify non-linear MB signals by summing reflections from consecutive, inverted pulses [4]. The aim of this study is to identify methods of analysis for MB emissions from short burst, PSK exposures, including the incorporation of PI to increase sensitivity to detecting transvertebral emissions.

**Methods:** FUS was generated using two confocal, single element transducers. Separate pulse trains for each transducer consisting of PSK and inverted pulse pairs at 514kHz (20 pairs, pulse repetition period = 54 $\mu$ s) were generated in MATLAB and programmed to an arbitrary function generator. In a water tank, a tube phantom (inner diameter = 1.07mm, wall thickness = 0.31mm) to accommodate circulating MBs was aligned with the focus. Baseline and MB (1:5000 solution Definity in deionized water) measurements were performed for comparison. A narrowband receiver (250kHz) was used to detect acoustic emissions. Measurements were performed with and without vertebrae at increasing peak negative pressure (PNP) between 60 and 600kPa. Analysis was performed by taking the Fourier Transform of short time windows (54 $\mu$ s) of the received signals and then averaging over the entire signal. For PI, the sum of consecutive time-domain windows containing inverted pulses was used.

**Results:** Through quantifying the ratio of the magnitude of frequency spectra between received MB and baseline signals, in the absence of vertebrae, the subharmonic (257kHz) was detected above PNPs of 200kPa. The threshold for detecting the 2<sup>nd</sup> harmonic (1028kHz) was below 60kPa. PI increased sensitivity to detecting these signals by up to 230%. Similar results were obtained when focusing into the canal of the 1<sup>st</sup> thoracic vertebrae (Fig. 1). The threshold for detecting the subharmonic was unchanged, while the threshold for detecting the 2<sup>nd</sup> harmonic was increased to 170kPa, indicating attenuation of high frequency components as MB emissions propagate through bone on the path to the receiver. At higher PNPs the MB/baseline signal ratio behaved non-linearly with increasing pressure, indicating the transfer of energy to other frequency bands and the presence of inertial MB behaviour.

**Conclusions and Future Work:** This study has confirmed that MBs targeted with short burst, PSK ultrasound pulses produce acoustic signals at subharmonic and 2<sup>nd</sup> harmonic frequencies and that PI can increase sensitivity to detecting small signals. Future work will include improved characterization of inertial behaviour. The bioeffects associated with MB emissions will be investigated *in vivo* for FUS-induced blood-spinal cord barrier opening. This work will contribute to clinical-scale advancements for targeted, therapeutic delivery to the spinal cord.

**References:** [1] O'Reilly and Hynynen, *Radiology*, 263(1), 2012. [2] McDannold, Vykhodtseva and Hynynen, *Phys. Med. Biol.*, 51(4), 2006. [3] Fletcher and O'Reilly, *IEEE Trans. UFFC*, 2018. [4] Simpson et al., *IEEE Trans. UFFC*, 46(2), 1999.

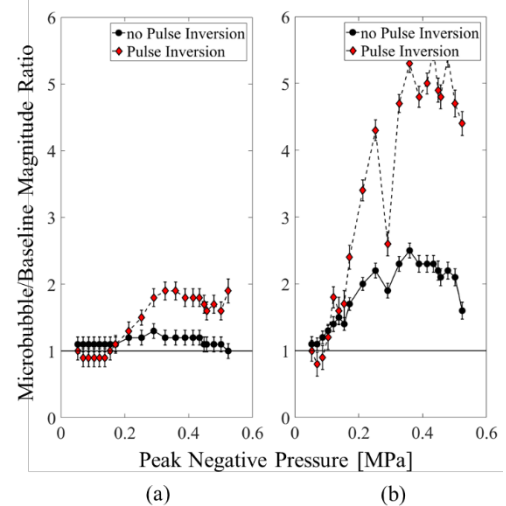


**Fig. 1** Ratio of microbubble to baseline (a) subharmonic and (b) 2<sup>nd</sup> harmonic spectral activity using dual aperture short burst and phase shift keying exposures (514kHz) with and without pulse inversion, measured in the *ex vivo*, human 1<sup>st</sup> thoracic vertebra.

## Catheter-Based Imaging Tools for Characterization of Cardiac Ablation Lesions

Charlene Leung, MEng (1); Natasha Alves-Kotzev, PhD (1); Atul Verma, MD (2); Graham Wright, (1); Brian Courtney, MD (1,3) PhD  
 1 - Sunnybrook Research Institute  
 2 - Southlake Regional Health Centre  
 3 - Dept. of Cardiology, Sunnybrook Health Sciences Centre

### Introduction

Atrial fibrillation (AF) is the most common cardiac arrhythmia and has a substantial impact on Canadian health outcomes. Catheter-based radiofrequency ablation (RFA) aims to create transmural lesions to electrically isolate the arrhythmogenic tissue, but this resource demanding process results in 25%-50% of patients requiring follow-up procedures. The efficacy of RFA could be improved with real-time monitoring of lesion size and continuity. Intracardiac echocardiography (ICE) has been used in human studies to characterize RFA lesions by assessing changes in tissue wall thickness and motion, and signal intensities and heterogeneity.

### Methods

We demonstrated similar findings using 21MHz and 40MHz linear-array ultrasound systems and Conavi Medical's 9MHz Foresight ICE catheter (Figure 1), where lesions were identified by an increase in image intensity and tissue cavitation. Utilizing the Foresight ICE system as the imaging platform, the project seeks to develop a system for real-time lesion visualization by adding hybrid imaging capabilities and developing custom ultrasound transducers. The project will evaluate imaging modalities (ultrasound, photo-acoustics, and optical coherence tomography) and configurations to visualize RFA lesions *ex-vivo*, and will prototype an intracardiac imaging probe for *in-vivo* lesion assessment. Image processing and visualization tools will be developed for real-time lesion assessment. The developed system will be tested in porcine models and validated against EAM-generated maps, MR-based lesion characterizations, and histology.

### Results and Conclusions

The project will produce a proof-of-concept imaging catheter and visualization software for real-time ablation lesion characterization. Providing a reliable method to facilitate the recognition of gaps in RFA lesions intraoperatively could improve the efficiency and efficacy of AF ablation procedures.

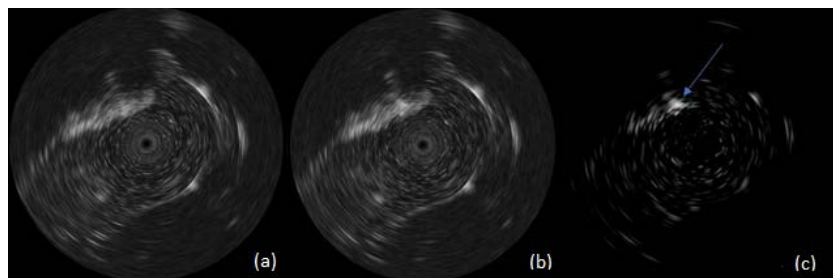


Figure 1: Images acquired from an *ex vivo* chicken breast using Conavi's Foresight ICE system. Images were captured (a) before RFA and (b) after RFA. The intensity difference between the pre-ablation and post-ablation ICE image is shown in (c).

## Penetration With Time of Gd-DTPA Into Infarcted and Microvascular Obstructed Myocardium During a Constant Infusion

**Authors:** Benjamin Wilk<sup>1,2</sup>, Jonathan D. Thiessen<sup>1,2</sup>, Heather Biernaski<sup>1</sup>, John Butler<sup>1</sup>, Jane Sykes<sup>1</sup>, Gerald Wisenberg<sup>1,2</sup>, Frank S. Prato<sup>1,2</sup> <sup>1</sup>Lawson Health Research Institute, London, ON, Canada.

<sup>2</sup>Western University, London, ON, Canada.

**Background:** In patients with a myocardial infarction (MI) the presence of a microvascular obstruction (MO), an area of extremely low flow, leads to worse cardiac functional outcome.<sup>1</sup> When performing MRI after a myocardial infarction, gadolinium contrast agents such as Gd-DTPA are used to enhance the contrast between infarcted and healthy tissue. The MO is then operationally defined on the MR images. In positron emission tomography (PET), there is the additional problem that the resolution of PET is not enough to separate the MO and infarct regions. This causes the presence of an

MO to artificially lower the intensity of PET signal in the infarct. As suggested by Prato et al<sup>2</sup>, a constant infusion may be used to penetrate this MO. The purpose of this experiment is to show that it is possible to penetrate this region and to determine the rate at which contrast agents may enter it if delivered as a slow constant infusion. **Methods:** Five canine subjects were imaged with simultaneous

PET/MRI (Siemens biograph mMR) five days post-MI, two of which exhibited a microvascular obstruction. Only animals with an MO were used for this experiment. MI was achieved through permanent occlusion of the left anterior descending coronary artery by snare ligation. Gd-DTPA was administered via a constant infusion of 0.004 mmol/kg/min for 150 minutes (delivering a total of 0.6 mmol/kg Gd-DTPA). T1 maps were acquired on a breath-hold with a modified Look-Locker inversion recovery method (MOLLI) in 2-chamber, 4-chamber and mid-ventricle axial views every 10 minutes. Free-breathing, navigator-gated T1-weighted 3D images were also acquired every 10 minutes.

These 3D datasets were analysed using 3D Slicer with regions of interest drawn over the MO and infarcted regions, to quantify apparent MO and infarct volume.

**Results:** This research shows a decreasing trend in apparent MO volume over the course of the 150-minute constant infusion demonstrating the rate at which Gd-DTPA is entering the MO tissue. The final MO size was measured to be less than 10% of the initial measurement in one animal and less than 5% in the other. For these two dogs it is shown that approximately 80% of the MO is penetrated by a 107 min CI and 90% after 147 min. Total infarct size did not change significantly over time.

**Discussion:** The decrease in apparent MO size may correspond to the contrast agent being delivered very slowly through existing vasculature or by diffusion through damaged tissue. Using a constant infusion, it is possible to determine the rate of diffusion into the MO. Since the apparent MO size is changing over time the size of the MO will vary when a constant infusion is used rather than an estimate based on delayed enhancement following a bolus injection. However, to fully penetrate the area of MO a prolonged constant infusion may be needed.

**Conclusion and Future Work:** Future work combining both a constant infusion of Gd-DTPA and 18FDG will be needed to determine if the penetration dynamics of 18FDG can be derived from the Gd-DTPA data. If that is possible then the 18FDG images could be corrected for partial volume and a more accurate estimate the extent of inflammation within the region of MO determined. Future work includes histological analysis of the tissue samples collected immediately after this experiment as well as comparison with the PET signal. In order to achieve an accurate measurement of inflammation through PET, it is important to penetrate the MO by reducing partial volumes. Alternate methods of tracer delivery such as a bolus injection followed by a constant infusion may allow penetration of the MO in a more clinically relevant time.

<sup>1</sup>Ito H, Tomooka T, Sakai N, et al. (1992) Lack of myocardial perfusion immediately after successful thrombolysis. *Circulation* 85:1699–1705.

<sup>2</sup>Prato, F. S. et al. (2015) Can the Inflammatory Response Be Evaluated Using 18F-FDG Within Zones of Microvascular Obstruction After Myocardial Infarction? *J. Nucl. Med.* 56, 299–304.

## Assessing Myocardial Perfusion after Cardiac Irradiation using Dynamic Contrast Enhanced Hybrid PET/MRI

Oi Wai Chau (Western University)\*; Stewart Gaede (Western University)

**INTRODUCTION:** Breast cancer accounts for 25% of total yearly female cancer mortalities. Adjuvant radiation therapy of the breast plays a vital role to breast cancer treatment and has shown to improve both local control and overall survival. However, patients with left-sided breast cancer are at an increased risk of coronary artery disease due to the proximity of the heart to the high radiation dose. Using hybrid PET/MR imaging, cardiac abnormalities, changes in myocardial viability, and coronary artery disease can be assessed noninvasively. A previous canine study done in our lab demonstrated that hybrid PET/MRI detected an increase in PET  $^{13}\text{N-NH}_3$  myocardial perfusion and was associated with a global inflammatory response after a low radiation dose exposure. However, the rest and adenosine induced stress  $^{13}\text{N-NH}_3$  myocardial blood flow (MBF) propagated in different trends starting from 1 month onwards after cardiac irradiation. Hence, further investigation was done in the dynamic contrast enhanced MR (DCE-MR) imaging data acquired simultaneously in our canine model to assess the change in myocardial perfusion.

**HYPOTHESIS:** We believe DCE-MR imaging acquired would detect changes in myocardial perfusion in our canine model after cardiac irradiation.

**METHOD:** 5 canines performed dual bolus Gd-DTPA DCE-MR imaging at baseline, 1 week, 1 month, 3 months, 6 months and 1 year after cardiac external beam irradiation. Rest and adenosine induced stress scan were conducted utilizing the fast gradient echo sequence on the 3T hybrid PET/MR scanner at St. Joseph's hospital. Axial slices of the myocardium were contoured on ITK-snap according to 17 segment cardiac model. With left ventricle selected as the arterial input function (AIF), myocardial tissue curves were fitted using MATLAB with Toft's model to determine volume transfer constant  $K_{\text{trans}}$ .  $K_{\text{trans}}$  data were sorted into regions supplied with respective coronary arteries (LAD, LCX or Both arteries). Since  $K_{\text{trans}} = \text{extraction fraction} * \text{MBF}$ , paired T-tests were performed with  $^{13}\text{N-NH}_3$  MBF versus  $K_{\text{trans}}$  divided by extraction fraction (assumed 0.5) determined from separated bolus curve fittings.

**RESULT:** P-values obtained from paired sample T-tests of  $^{13}\text{N-NH}_3$  MBF vs 1st MR Gd-DTPA bolus  $K_{\text{trans}} / 0.5$  and that of  $^{13}\text{N-NH}_3$  MBF vs 2nd MR Gd-DTPA bolus  $K_{\text{trans}} / 0.5$  for all coronary artery supplied regions under rest and stress scans were less than 0.05. This proved the presence of AIF signal saturation from left ventricle blood pool. DCE-MR  $K_{\text{trans}}$  rest and stress data propagated in different trends starting from 1 month post radiotherapy.

**CONCLUSION:** Dual peaks Toft's model curved fitting instead of separated peaks curve fitting for determining myocardial  $K_{\text{trans}}$  values was necessary for accurate myocardial perfusion quantification especially for dual bolus GD-DTPA injection scans due to signal saturation in the AIF. In this animal model study, we were not able to acquire same propagating trends in both PET MBF and MR  $K_{\text{trans}}$  imaging.

## Cardiac left ventricle segmentation and indices quantification using U-net and continuous max-flow

Fumin Guo<sup>1,2</sup>, Matthew Ng<sup>1,2</sup>, and Graham Wright<sup>1,2</sup>

<sup>1</sup>Sunnybrook Research Institute; <sup>2</sup>Medical Biophysics, University of Toronto, Canada

**Introduction:** Cardiac magnetic resonance imaging (MRI) is the method-of-choice for cardiovascular disease care [1] and segmentation of cardiac structures is typically required as a first step for quantification of cardiac MRI biomarkers. Recently, deep convolutional neural network (CNN) has achieved remarkable success in medical image segmentation but this method provides only suboptimal results with non-sharp edges and spatial/appearance inconsistencies [2]. On the other hand, graphical models provide well-defined segmentation formulation that encourages segmentation edge-alignment and spatial consistency. Therefore, the objective of this work was to combine the strengths of CNN and graphical models for improved cardiac MRI left ventricle (LV) segmentation, and LV biomarker quantification.

**Methods:** Eighty patients with five categories of cardiovascular pathologies were used to test our approach. For each patient, 20 frames of short axis MR images were acquired at the mid-cavity plane using a cine bSSFP sequence across the entire cardiac cycle. These images were post-processed as previously described [3], and the resulting image stacks with a matrix size of 80x80x20 were entered into our segmentation pipeline. Our segmentation framework consists of a 2D plain U-net and a three-class continuous max-flow module. The U-net was trained using 10 patients with cross entropy loss and the optimal model was selected based on the highest DSC in another 10 subjects. The U-net-derived segmentation probability maps  $\rho_l(x) \in [0,1], l \in \{LV, Myo.\}$  for the remaining 60 subjects were entered into a continuous min-cut segmentation module. In particular, the pixel-wise labeling cost was formulated as  $-\log(\rho_l(x))$  and the segmentation was regularized based on image edges to encourage edge alignment and segmentation consistency. The final algorithm segmentation was compared with expert manual output using Dice similarity coefficient (DSC [0,1]), average symmetric surface distance (ASSD [mm]), and Hausdorff distance (HD [mm]). In addition, the derived segmentation was used to generate LV cavity and Myo. area ( $A_{cav}, A_{myo}$  [mm<sup>2</sup>]), LV cavity dimensions (mm) in inferoseptal (IS)-anterolateral (AL) (D1), inferior (I)-anterior (A) (D2), and inferolateral (IL)-anteroseptal (AS) (D3) directions, and the regional wall thickness (mm) in IS ( $R_{IS}$ ), I ( $R_I$ ), IL ( $R_{IL}$ ), AL ( $R_{AL}$ ), A ( $R_A$ ), and AS ( $R_{AS}$ ) directions, as illustrated in Fig. 1. Our algorithm indices measurements were compared with manual results using Mean Absolute Error (MAE) and Pearson correlation ( $r$ ).

**Results:** As shown in Table 1, we achieved improved segmentation accuracy with a mean DSC of {0.888, 0.959}, ASSD of {0.957, 0.909} mm, and HD of {3.68, 2.58} mm for {Myo, LV} for 60 subjects. We also obtained excellent agreement with expert manual LV indices measurements as indicated by the low MAE and high Pearson  $r$  in Table 2.

**Conclusions:** Our approach provides high LV segmentation and indices quantification accuracy.

**Ref:** [1] Peng et al., MAGMA, 2016; [2] Zheng et al., ICCV, 2015; [3] Xue et al., MedIA, 2018

**Table 1.** LV segmentation accuracy

	Myo.		LV	
DSC [0,1]	0.882	<b>0.888</b>	0.957	<b>0.959</b>
ASSD (mm)	1.12	<b>0.96</b>	1.22	<b>0.91</b>
HD (mm)	9.65	<b>3.68</b>	6.59	<b>2.58</b>

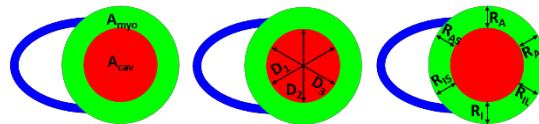


**Figure 1.** Illustration LV indices.

**Table 2.** LV indices quantification accuracy for 60 subjects.

	Methods	$A_{cav}$	$A_{myo}$	D1	D2	D3	$R_{IS}$	$R_I$	$R_{IL}$	$R_{AL}$	$R_A$	$R_{AS}$
MAE	Xue [3]	172	189	2.59	2.48	2.47	<b>1.26</b>	<b>1.40</b>	1.59	1.57	1.32	<b>1.25</b>
	Ours	<b>115</b>	<b>169</b>	<b>1.72</b>	<b>1.87</b>	<b>1.72</b>	1.55	1.43	<b>1.47</b>	<b>1.38</b>	<b>1.17</b>	1.36
$r$	Xue [3]	.943	.947	.894	.943	.957	.856	.747	.693	.659	.777	.877
	Ours	<b>.984</b>	<b>.949</b>	<b>.983</b>	<b>.972</b>	<b>.976</b>	<b>.958</b>	<b>.840</b>	<b>.809</b>	<b>.792</b>	<b>.871</b>	<b>.889</b>

## Microvessel Detection in Power Doppler Ultrasound Using Adaptive Singular Value Decomposition Clutter Filtering

Mahsa Bataghva and James C. Lacefield

School of Biomedical Engineering and Robarts Research Institute,  
Western University, London, Ontario, Canada

**Introduction:** Ultrasonic power Doppler imaging is used to visualize blood flow in the interior of tissues without injected contrast media. However, it is difficult to detect microvessels due to the existence of non-stationary echoes from tissue and transducer motion. Singular value decomposition (SVD) clutter filtering has shown the potential to adaptively suppress tissue clutter signals to achieve robust flow detection [1]. SVD filters decompose the signal into a set of mutually orthogonal and statistically independent eigen components in which low-rank and high-rank components represent clutter and noise, respectively, while mid-rank components are blood signals. Standard SVD filters use fixed thresholds for the rank of the clutter components; however, finding the right thresholds is challenging because the bounds on the blood signal highly depend on the application, equipment used and other factors [2]. Thus, the objective of this study is to develop a method to adaptively and automatically choose a variable threshold for blood-clutter separation. We also introduce a new approach of setting non-zero weights to low-rank components containing a mixture of tissue and blood signals.

**Methods:** Two-dimensional power Doppler cine loops of three preclinical applications (patient-derived tumors implanted in an *ex ovo* chick CAM model, a mouse model of hindlimb ischemia and placental circulation in rat model of fetal development) were acquired using a VisualSonics Vevo 2100 ultrasound system equipped with 20 and 40 MHz linear arrays. Digital quadrature-demodulated images were exported to MATLAB for offline processing. To reject tissue signals, a low-rank singular value cutoff was determined by identifying an inflection point in the singular value curve at which the curve began to flatten. Noise components were eliminated by removing singular values for which the slope of the singular value curve was approximately zero and the Doppler frequency was near the maximum frequency. The weights of the low-rank components were set equal to the mean power of the blood components to account for the overlap of tissue and blood signals. Filtered images were assessed qualitatively by visual inspection. Images reconstructed using the proposed adaptive SVD filter were compared to images processed using conventional filters with fixed thresholds.

**Results and Conclusion:** The proposed SVD clutter filter outperformed conventional high-pass clutter filters and standard fixed-threshold SVD filters in terms of detection of smaller vessels and visualization of microvessel branching. These improvements were the result of reduced false-positive flow detection using SVD clutter filtering, which permitted display of lower Doppler power (i.e., smaller) vessels (Fig. 1). Each application required different low- and high-rank cutoffs for clutter and noise singular values, respectively.

### References:

- [1] C. Demené *et al.*, "Spatiotemporal Clutter Filtering of Ultrafast Ultrasound Data Highly Increases Doppler and fUltrasound Sensitivity," *IEEE Trans. Med. Imaging*, vol. 34, no. 11, pp. 2271–2285, 2015.
- [2] M. Kim *et al.*, "Expanding Acquisition and Clutter Filter Dimensions for Improved Perfusion Sensitivity," *IEEE Trans. Ultrason. Ferroelectr. Freq. Control*, vol. 64, no. 10, pp. 1429–1438, 2017.

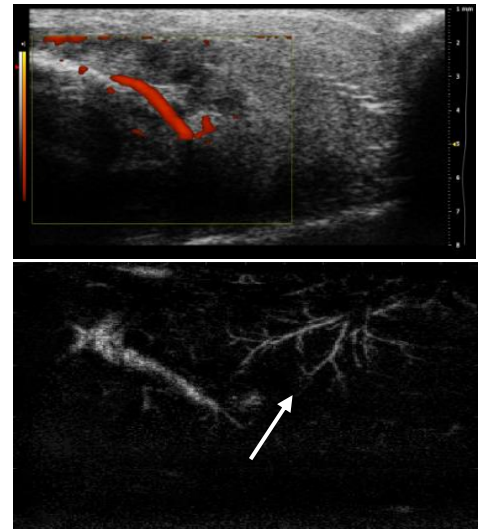


**Fig. 1.** Power Doppler images of mouse hind limb. The color map in (a) and the gray scale in (b) reflect the power of the blood signal. a) Infinite impulse response-filtered image produced by the ultrasound system. b) Image of the same animal after adaptive SVD clutter filtering and displayed with tissue background suppressed.



**PET Imaging of the Cardiac Growth Hormone Secretagogue Receptor in a Large Animal Model of Heart Failure**

Rebecca Sullivan<sup>1</sup>, Lihai Yu<sup>2</sup>, Jinqiang Hou<sup>2</sup>, Justin Hicks<sup>5,7</sup>, Jane Sykes<sup>3</sup>, John Butler<sup>4</sup>, Heather Biernaski<sup>4</sup>, Leonard Luyt<sup>2,5,6</sup>, Frank Prato<sup>5,7</sup>, Jonathan D. Thiessen<sup>5,7</sup>, Gerald Wisenberg<sup>5,7</sup>, and Savita Dhanvantari<sup>1,5,7,8</sup>

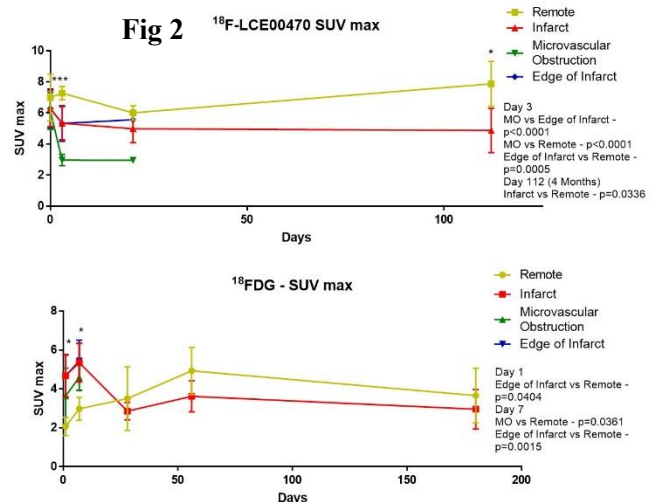
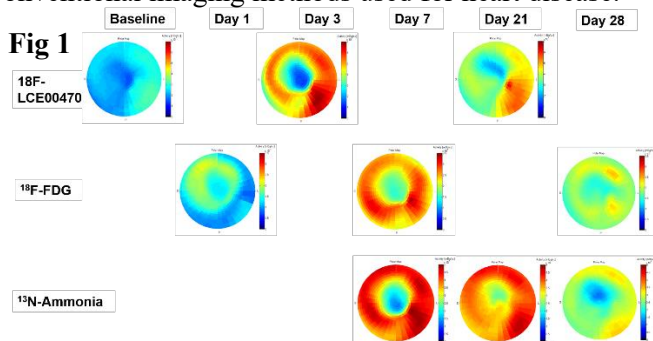
1. Pathology and Laboratory Medicine, Western University, London, Canada; 2. Chemistry, Western University, London, Canada; 3. Thames Valley Veterinary Services, Lawson Health Research Institute, London, Canada; 4. Radiology Department, Lawson Health Research Institute, London, Canada; 5. Imaging Program, Lawson Health Research Institute, London, Canada; 6. Department of Oncology, London Regional Cancer Program, Western University, London, Canada; 7. Medical Biophysics, Western University, London, Canada; 8. Metabolism and Diabetes, Lawson Health Research Institute, London, Canada

**Introduction** Cardiac imaging technologies, such as echocardiography and cardiac magnetic resonance imaging (cMRI), enable the non-invasive detection of changes in heart function that may indicate disease progression. These modalities detect changes in structure and anatomy, and thus there is a critical need for the detection of the biochemical and molecular changes that precede gross structural changes. The development of imaging agents that target these molecular changes, combined with hybrid imaging technology, will be a powerful means to address this need. My work has shown that the cardiac growth hormone secretagogue receptor (GHSR) could be a potential molecular imaging target. Our lab is currently characterizing an array of imaging agents designed for detecting myocardial GHSR by positron emission tomography (PET) *in vivo* in preclinical studies. With one of these novel agents, termed <sup>18</sup>F-LCE00470, I will be using the emerging technology of hybrid PET and MRI (PET/MRI) to detect and quantify changes in the regional distribution of myocardial GHSR in a canine model of heart failure.

**Methods** Female hounds (11-12 months of age) were used in this study. A myocardial infarct was generated by a 2-hour occlusion of the left descending coronary artery, followed by reperfusion. Dogs (n=4) were imaged with a combination of PET tracers at specific timepoints: <sup>18</sup>F-LCE00470 for GHSR (baseline, day 3, 21, 4 months post infarct); <sup>18</sup>F-FDG for inflammation (day 1, 7, 28, 6 months post infarct); and <sup>13</sup>N-ammonia for perfusion (day 7, 21, 28, 4 months post infarct). At these time points, there are marked regional changes in inflammation and perfusion [Lim, H. *et al* (2014)]. At each timepoint, dogs were scanned with simultaneous PET/MRI, as follows: dogs were injected with 100-150 MBq of <sup>18</sup>F-LCE00470, <sup>18</sup>F-FDG or <sup>13</sup>N-ammonia, immediately followed by a 1-hour (<sup>18</sup>F-LCE00470 and <sup>18</sup>F-FDG) or 30 min (<sup>13</sup>N-ammonia) dynamic PET scan. FlowQuant software (Ottawa Heart) was used to generate polar maps representing a 3D version of the entire left ventricle myocardium. These polar maps were used to determine regional changes in tracer uptake at each timepoint. Slicer software was used to quantify the standardized uptake value (SUV) for each tracer to determine regional analysis of tracers [Fig 2].

**Results** FlowQuant analysis initially showed differences in the patterns of regional distribution between tracers at all timepoints after surgery, indicating that uptake of <sup>18</sup>F-LCE00470 does not simply reflect changes in cardiac perfusion or inflammation [representative image n=1 Fig 1]. SUVmax analysis showed a significantly lower activity in the middle of the infarct (microvascular obstruction or MVO, usually only present until 14-21 days) when compared to other areas of the heart at days 1 and 7 with <sup>18</sup>F-FDG (p<0.05); and day 3 (p<0.001) and 112 (p<0.01) with <sup>18</sup>F-LCE00470 [Fig 2, n=4].

**Conclusions** We have used a novel small molecule PET tracer, <sup>18</sup>F-LCE00470, to detect changes in the regional distribution of GHSR in the canine heart after a heart attack. We have shown differences in the patterns of regional uptake compared to known tracers of perfusion and inflammation. The next steps of this work are to analyze this data using compartmental modeling to better understand the function of this tracer. This tool can be applied to many other cardiac diseases. This work will help to improve the knowledge of molecular changes in the heart prior to conventional imaging methods used for heart disease.



## Post-stroke Changes in T2-weighted Signal, Inflammation, and Perfusion

Al-Khishman N.<sup>1,3</sup>, Fox M.S.<sup>3</sup>, Qi Q.<sup>1,3</sup>, Roseborough A.<sup>2</sup>, Levit A.<sup>2</sup>, Hachinski V.<sup>4</sup>, Whitehead S.N.<sup>2</sup>, and Thiessen J.D.<sup>1,3</sup>

<sup>1</sup>Medical Biophysics and <sup>2</sup>Anatomy & Cell Biology, University of Western Ontario

<sup>3</sup>Lawson Health Research Institute, <sup>4</sup>Clinical Neurological Sciences, University Campus

**Introduction:** Recent brain studies show that T<sub>2</sub>-weighted hyperintensities, representing edema, measured by magnetic resonance imaging (MRI) correlate to translocator protein positron emission tomography (TSPO PET) signals (Unterrainer et al., 2018). This could have practical applications in stroke because the latter is associated with inflammation as activation of resident macrophages in the brain, microglia, which repair then damage the brain after a stroke (Iadecola & Anrather, 2011). Another factor that contributes to post-stroke damage is a reduction in perfusion. To date, no studies have monitored the relationship between T<sub>2</sub>-weighted hyperintensities, inflammation, and perfusion over time and after a stroke.

**Methods:** Ischemic stroke was induced in the left dorsal striatum of rats (n = 5). We scanned at baseline, 7-days-post-stroke, and 30-days-post-stroke. T<sub>2</sub>-weighted signal to noise ratios (SNR) was quantified using a scan with a flip angle of 150°, repetition time of 3900 ms, echo time of 97 ms, echo train length of 11, and 4 averages (3T Biograph mMR). To quantify inflammation, blood was sampled during a 90-minute dynamic 22.6-37.0 MBq [<sup>18</sup>F]-FEPPA PET scan (Siemens Inveon). These images were processed, using a model that assumes [<sup>18</sup>F]-FEPPA could be in the region of interest or circulation, into distribution volumes (DV). Perfusion was quantified as its inverse, mean transit time, using computed tomography enhanced by Isovue at a concentration of 300 mg/mL and a rate of 0.8 mL/s (revolution CT). For each rat, we manually co-registered and extracted parameters from all images using regions of interest defined, on the 7-days-post-stroke T<sub>2</sub>-weighted image, as hyperintensity and a contralateral control. Pearson correlation coefficients were calculated. **Results:** Qualitatively, T<sub>2</sub>-weighted hyperintensities appear to progress into hypointensities (figure 1, green arrows). There were no correlations between T<sub>2</sub>-weighted SNR and inflammatory DV (r = 0.30, P = 0.10) or T<sub>2</sub>-weighted SNR and perfusion mean transit time (r = 0.25, P = 0.20). Inflammatory DV and perfusion mean transit time correlated significantly (r = 0.59, P < 0.05).

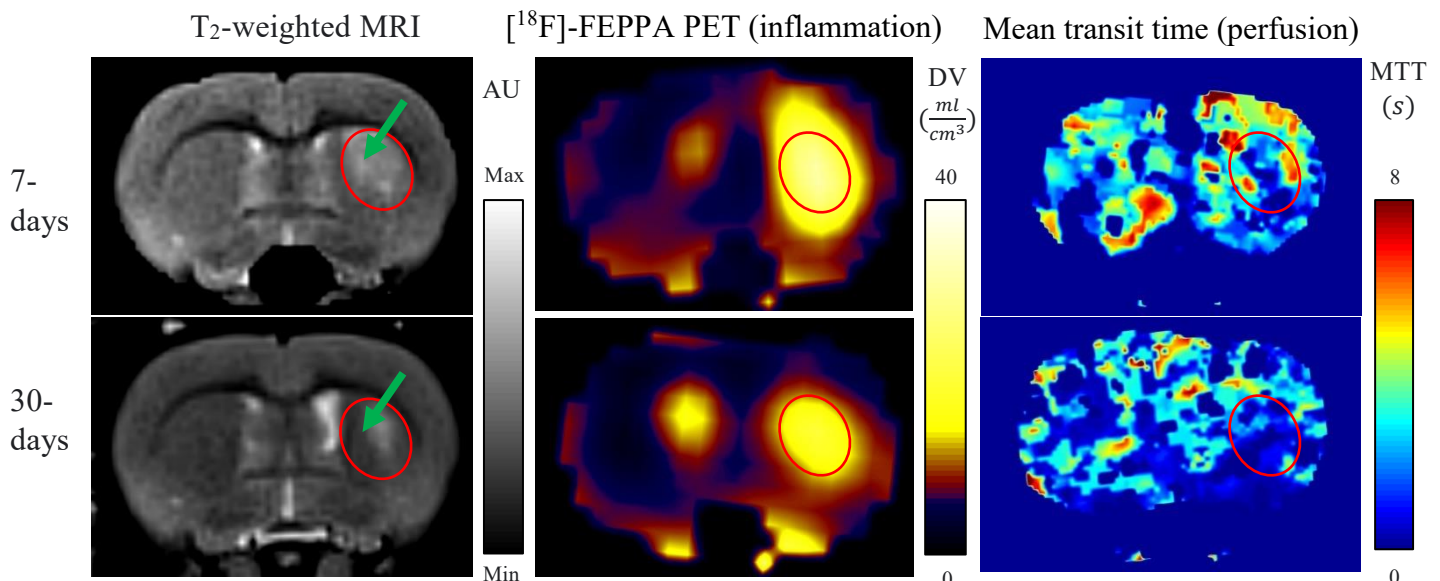


**Figure 1.** Post-stroke Relationship Between T<sub>2</sub>-weighted Hyperintensity, Inflammation, and Perfusion. T<sub>2</sub>-weighted hyperintensity (red outline) is proportional to inflammation and inversely proportional to perfusion.

**Conclusion:** T<sub>2</sub>-weighted hyperintensities may not be a sufficient proxy for inflammation. An increase in inflammation might correlate with a reduction in perfusion. In the future, a larger sample size will be analyzed to confirm these conclusions. Future studies should continue to investigate the relationship between T<sub>2</sub>-weighted hyperintensities and translocator protein PET inflammation in addition to the interaction between translocator protein PET inflammation and perfusion.

**Comparison of of post contrast 2 dimensional double inversion recovery fast spin-echo imaging black blood compared with Spoiled Gradient Echo sequence for visualizing sub-endocardium, papillary muscles, trabeculae, and right ventricular fibrosis**

**Akhavein Farhad MD.** Cardiologist; Cardiovascular MRI fellowship. Behsaz Teb Imaging Center, Mashhad, Iran

**Shiae Ali Emad BS,** Msc. of Medical Imaging. Behsaz Teb Imaging Center, Mashhad, Iran

**Shoraka Zohreh MD.** Aria Hospital, Mashhad, Iran.

**Introduction:** Myocardial fibrosis is the final common sequel in a broad variety of cardiac disorders that can directly lead to adverse consequences such as ventricular dysfunction, arrhythmias, and exercise intolerance. Cardiac Magnetic Resonance Imaging (CMRI) is a standard imaging modality that characterizes the distribution, extent, and pattern of fibrosis after intravenous (IV) injection of gadolinium (G) through Spoiled Gradient Echo (SPGR) sequence. In this sequence, myocardial delayed enhancement (i.e. Late Gadolinium Enhancement, LGE), may be inconspicuous in sub-endocardial (SE), papillary muscles (PM), and right ventricle (RV) areas due to poor contrast with the adjacent bright blood pool. In this study, we evaluate the diagnostic value of post-Gadolinium black blood 2 dimensional double inversion recovery fast spin-echo imaging (2D-T1-DIR-FSE; new test) against SPGR (non-reference standard) in detecting location of myocardial fibrosis.

**Methods:** CMRI (GE 1.5 T scanner) was performed in 122 consecutive patients with variety of heart diseases including non-compaction cardiomyopathy (NC.CM) ( N=56), dilated cardiomyopathy (DCM) (N=18), hypertrophic cardiomyopathy (HCM) (N=13), myocardial infarction (MI) (N=11), Arrhythmogenic right ventricular dysplasia (ARVD) (N=8), myocarditis (N=8), congenital heart diseases (CHD) (N=4), and others (N=7) . In all patients, 2D T1 DIR FSE was acquired with breath holding and ECG-gated through contiguous short axis slices to cover the entire left ventricle. The test was repeated 12 minutes after a bolus IV injection of 1 mmol/kg G. The SPGR sequence was also imaged 17 to 22 minutes after G injection. In both sequences, an appropriate inversion time and trigger delay were selected. The capability of the two sequences to visualize LGE or fibrosis tissue in prominent trabecula tissue of the NC myocardium, PM, septal insertion sites, and RV wall was examined. Data was analyzed through overall, positive, and negative percentage agreement.

**Results:** The following table is summarized capability of each sequence in visualizing fibrosis in the SE, prominent trabecula tissue of the NC myocardium, PM, septal insertion sites, and RV wall regions in different diseases, separately.

		Number of cases by SPGR				Total	
		Fibrosis +		Fibrosis -			
Number of cases by 2D-T1-DIR-FSE	Fibrosis +	A	59	B	16	A+B	75
	Fibrosis -	C	2	D	45	C+D	47
		A+C	61	B+D	61		122

Quantitatively, the overall, positive, and negative percent agreement between the two tests were 85% (104/122), 96.7% (59/61), and 73.7% (45/61), respectively.

**Conclusions:** 2D-T1-DIR-FSE has shown to have a very good agreement with SPGR and was superior in delineating small, thin, and fine regions of myocardial fibrosis in sub-endocardial border, PM, RV, trabeculae tissue, septal insertion sites, and RV wall.

## Imaging Network Ontario (ImNO) Code of Conduct

All attendees, speakers, sponsors and volunteers at ImNO are required to agree with the following code of conduct. Organisers will enforce this code throughout the event. We expect cooperation from all participants to help ensure a safe environment for everybody.

### Need Help?

If you are being harassed, notice that someone else is being harassed, or have any other concerns, speak to ImNO staff or send an email to [ombudsperson@ImNO.ca](mailto:ombudsperson@ImNO.ca) or [chair@ImNO.ca](mailto:chair@ImNO.ca)

### Overview

Imaging Network Ontario is committed to providing a harassment-free conference experience for everyone, regardless of gender, gender identity and expression, age, sexual orientation, disability, physical appearance, body size, race, ethnicity, religion (or lack thereof), or technology choices. We do not tolerate harassment of conference participants in any form. Use of sexualised language and imagery that does not convey a scientific message is not appropriate. We expect participants and sponsors to follow these rules for the duration of the conference in any conference venue, including talks, workshops, parties, Twitter and other online media. Conference participants violating these rules may be sanctioned or expelled from the conference without a refund at the discretion of the conference organisers.

### Details

All attendees, speakers, sponsors and volunteers at ImNO are subject to the anti-harassment policy.

Harassment includes offensive verbal comments related to gender, gender identity and expression, age, sexual orientation, disability, physical appearance, body size, race, ethnicity, religion, technology choices, sexual images in public spaces, deliberate intimidation, stalking, following, harassing photography or recording, sustained disruption of talks or other events, inappropriate physical contact, and unwelcome sexual attention. Use of images, activities, uniforms/costumes or other materials that create a sexualised environment will not be tolerated.

Anyone asked to stop any harassing behavior is expected to comply immediately.

If anyone engages in harassing behavior, the conference organisers may take any action they deem appropriate, including warning the offender or expulsion from the conference with no refund.

If you are being harassed, notice that someone else is being harassed, or have any other concerns, please contact a member of conference staff immediately. Conference staff can be identified as they'll be wearing clearly marked badges saying "ImNO staff". You can also send an email to the ImNO ombudsperson, Dr. Maria Drangova, at [ombudsperson@ImNO.ca](mailto:ombudsperson@ImNO.ca) or the ImNO 2019 Chair, Dr. Charles McKenzie, at [chair@ImNO.ca](mailto:chair@ImNO.ca)

Conference staff will be happy to help participants contact hotel/venue security or local law enforcement, provide escorts, or otherwise assist those experiencing harassment to feel safe for the duration of the conference. We value your attendance.

We expect everyone to follow these rules for the duration of the conference within and outside conference venues, including but not limited to conference-related talks, workshops, and social events involving ImNO attendees, and in all conference related communications, including social media.

## Author Index

Author	Presentation	Page	Author	Presentation	Page
Abdalmalak, Androu	Poster 1-8	103	Bartha, Robert	Oral 2-2	25
	Poster 1-13	108		Poster 4-7	133
	Poster 5-6	148		Poster 4-15	141
		Poster 7-6		169	
Admano, S	Oral 2-2	25	Bartling, Mandolin	Oral 12-2	89
Agrawal, Sumit	Poster 1-3	98		Poster 1-1	96
Akbari, Alireza	Poster 8-1	171	Barzda, Virginijus	Oral 6-4	53
Akens, Margarete	Oral 6-1	50	Bastian-Jordan, Matthew	Oral 7-3	59
	Oral 6-4	53	Bataghva, Mahsa	Poster 11-10	200
Akhavein, Farhad	Poster 11-13	203	Batebi, Saghar	Poster 4-6	132
Akhavein, H	Oral 2-2	25	Baum, Zachary	Oral 5-1	43
Alam, Faiyza	Oral 6-4	53		Poster 5-4	146
Alfano, Ryan M	Oral 2-1	24	Bauman, Glenn	Oral 2-1	24
Al-Khishman, Nassir UN	Poster 11-12	202		Oral 2-3	26
Allen, Daniel	Poster 1-6	101		Oral 7-2	58
Alushaj, Erind	Oral 11-3	83		Oral 7-3	59
	Poster 10-5	185	Bax, Jeffrey	Oral 5-4	46
Alves-Kotzev, Natasha	Poster 1-7	102		Oral 5-6	48
	Poster 11-6	196		Poster 5-7	149
Aminpour, Azad	Oral 8-5	67	Bellyou, Miranda	Poster 7-6	169
Anazodo, Udunna	Oral 11-1	81	Bhattacharya, Soume	Oral 8-2	64
	Oral 11-2	82		Oral 8-4	66
	Oral 11-5	85	Biernaski, Heather	Poster 11-7	197
	Poster 10-6	186		Poster 11-11	201
Anderson, William	Poster 6-8	160	Bilton, Holly	Oral 10-2	76
Arbabi, Aidin	Oral 4-1	37	Biswas, Labonny	Oral 5-5	47
	Poster 10-2	182	Black, SE	Oral 2-2	25
Arezza, Nico JJ	Oral 4-1	37	Blackney, Kevin	Poster 4-7	133
Asselin, Mark	Oral 5-3	45	Blake, Jones	Poster 7-4	167
	Poster 5-9	151	Blokker, Alexandra M	Poster 1-14	109
Athwal, George	Poster 6-3	155	Bloomfield, Riley A	Poster 2-3	117
Attaran, Ali	Poster 4-10	136		Poster 6-4	156
Barker, Andrea L	Oral 9-4	72	Boffa, Michael	Poster 4-4	130
Barker, Kevin	Oral 5-6	48	Boyes, Aaron	Poster 1-15	110
	Poster 5-3	145		Poster 7-5	168
	Poster 6-7	159	Brackstone, Muriel	Poster 1-9	104
Baron, Corey	Oral 1-3	19		Poster 1-11	106
	Oral 4-1	37		Poster 7-3	166
	Poster 4-11	137	Bragagnolo, Nadia	Oral 4-2	38
	Poster 10-1	181		Oral 7-4	60
	Poster 10-2	182	Broberg, Jordan	Poster 6-2	154
	Poster 10-8	188	Brown, Arthur	Poster 4-7	133
Baronette, Rudy	Oral 6-5	54	Brown, Christopher AP	Poster 4-14	140
Barreira, Christy	Poster 4-7	133			
Barry, Jennifer	Oral 12-6	93			

<b>Author</b>	<b>Presentation</b>	<b>Page</b>	<b>Author</b>	<b>Presentation</b>	<b>Page</b>	
Burkhart, Tim	Oral 4-5	41	Chronik, Blaine	Oral 1-2	18	
	Poster 1-14	109		Oral 4-5	41	
	Poster 6-10	162		Poster 4-1	127	
Burneo, Jorge	Poster 10-6	186		Poster 4-2	128	
Burns, David	Oral 6-6	55		Poster 4-3	129	
Burton, Jeremy	Poster 3-3	125		Poster 4-6	132	
Butler, John	Poster 11-7	197		Poster 4-9	135	
	Poster 11-11	201		Poster 4-10	136	
Camire, Daenis	Poster 2-2	116		Poster 4-12	138	
Cao, Daniel J	Poster 2-4	118		Poster 4-14	140	
Capaldi, Dante	Oral 9-1	69		Clement, Allison J	Oral 6-1	50
	Oral 9-2	70		Cobos, Santiago F	Oral 1-5	21
	Poster 2-1	115		Connelly, John	Oral 12-6	93
Cardinell, Kirsten	Oral 10-4	78		Cool, Derek	Oral 7-3	59
Carnahan, Patrick	Poster 11-4	194	Courtney, Brian	Poster 11-6	196	
Carson, Jeffrey	Oral 3-5	35	Crane, Joel	Poster 4-2	128	
	Poster 1-10	105	Cronin, Alicia	Poster 4-15	141	
	Poster 1-11	106	Cruje, Charmainne	Oral 10-3	77	
	Poster 7-3	166		Oral 12-3	90	
Cassidy, Kailas	Oral 6-4	53		Poster 9-3	177	
Chamson-Reig, Astrid	Poster 1-11	106		Poster 9-4	178	
	Poster 7-3	166	Cunningham, Charles H	Oral 4-2	38	
Chau, Oi Wai	Poster 11-8	198		Oral 7-4	60	
Chen, Albert	Oral 7-4	60	Cunningham, Ian	Poster 1-9	104	
Chen, Elvis	Poster 1-2	97	Dammak, Salma	Oral 7-1	57	
	Poster 1-4	99	Danko, Anna	Oral 2-4	27	
	Poster 1-6	101	Dassanayake, Praveen Sankajith B	Oral 12-1	88	
	Poster 1-7	102	Davieau, Kieffer J	Poster 4-10	136	
Chen, Fang	Oral 10-4	78	de Bruyn, John R	Oral 1-6	22	
Chen, Yuanxin	Oral 3-4	34	de Oliveira, Rodrigo	Poster 1-18	113	
	Oral 7-5	61	de Ribaupierre, Sandrine	Oral 8-2	64	
	Poster 3-2	124		Oral 8-3	65	
	Poster 9-2	176		Poster 1-17	112	
Cherin, Emmanuel	Poster 1-15	110	de Vrijer, Barbra	Oral 8-1	63	
Cheung, Alison	Poster 3-1	123		Oral 8-3	65	
Chin, Joseph	Oral 2-1	24	Dekaban, Gregory	Poster 4-7	133	
	Oral 2-3	26	DeKraker, Jordan	Oral 11-4	84	
	Oral 7-2	58		Poster 10-3	183	
Choueib, Saleh	Poster 5-8	150		Poster 10-8	188	
Christiansen, Spencer	Poster 4-3	130	Demidov, Valentin	Oral 6-4	53	
	Poster 4-8	134	Demore, Christine	Oral 10-2	76	
		Poster 1-15		110		
		Poster 1-18		113		
		Poster 7-5		168		
			Dhaliwal, Inderdeep	Poster 8-2	172	

<b>Author</b>	<b>Presentation</b>	<b>Page</b>	<b>Author</b>	<b>Presentation</b>	<b>Page</b>
Dhanvantari, Savita	Poster 11-11	201	El-Warrak, Alexander	Oral 6-2	51
Ding, Xiao Fan	Poster 4-3	129	Empey, Mary-Ellen	Oral 8-1	63
Diop, Mamadou	Oral 8-4	66	Erb, Jason	Poster 2-2	116
	Oral 12-4	91	Fahy, Ady	Oral 12-2	89
	Poster 1-8	103	Fahy, Aodhnait	Poster 1-1	96
	Poster 1-10	105	Fashandi, Homa	Oral 2-5	28
	Poster 1-11	106	Fenster, Aaron	Oral 5-4	46
	Poster 1-13	108		Oral 5-6	48
	Poster 1-17	112		Oral 8-2	64
	Poster 5-6	148		Poster 2-1	115
Dixon, S Jeffrey	Oral 1-6	22		Poster 5-3	145
Doherty, Timothy	Poster 4-7	133		Poster 5-7	149
Donnelly, Sarah C	Poster 3-3	125		Poster 6-7	159
Doughty, Mitchell	Poster 5-5	147		Poster 8-2	172
Dowlatshahi, D	Oral 2-2	25	Ferguson, Sebastian	Oral 5-5	47
Drake, James M	Oral 12-2	89	Fernando, Ann	Oral 3-1	31
	Poster 1-1	96	Fialkov, Jeff	Poster 1-5	100
	Poster 5-1	143	Fichtinger, Gabor	Oral 5-1	43
	Poster 5-2	144		Oral 5-3	45
	Poster 6-5	157		Poster 2-2	116
Drangova, Maria	Oral 4-4	40		Poster 2-6	120
	Oral 10-3	77		Poster 2-7	121
	Oral 12-3	90		Poster 5-4	146
	Poster 4-4	130		Poster 5-8	150
	Poster 4-8	134		Poster 5-9	151
	Poster 4-13	139	Fillion-Robin, Jean-Christophe	Poster 5-8	150
	Poster 9-3	177	Finger, Elizabeth	Oral 11-5	85
	Poster 9-4	178	Fischer, Lisa	Poster 4-7	133
Driscoll, Brandon	Oral 1-4	20	Fisher, Carl	Poster 7-5	168
D'Souza, David	Oral 7-3	59	Fishman, Zachary	Poster 1-5	100
	Poster 5-7	149	Fletcher, Stecia-Marie P	Poster 11-5	195
Dubois, Veronica	Oral 7-5	61	Foster, Paula	Oral 3-2	32
	Oral 10-1	75		Oral 7-5	61
Duggal, Neil	Poster 4-15	141		Poster 7-2	165
Dunmore-Buyze, Joy	Oral 10-3	77		Poster 9-1	175
	Oral 12-3	90	Foster, Stuart	Oral 10-2	76
	Poster 9-3	177		Poster 1-15	110
Dybner, Elena	Oral 6-4	53		Poster 1-18	113
Dzelzainis, Tom	Oral 6-4	53		Poster 7-5	168
Eagleson, Roy	Oral 8-2	64	Fox, Matthew	Poster 11-2	192
	Oral 8-3	65		Poster 11-12	202
Ebrahimi, Mehran	Oral 8-5	67	Fradin, Cecile	Poster 9-5	179
	Poster 11-3	193	Fraser, Douglas	Poster 4-7	133
Eddy, Rachel L	Oral 9-2	70	Frayne, Richard	Oral 2-4	27
	Oral 9-4	72	Gaed, Mena	Oral 2-1	24
	Oral 9-5	73		Oral 2-3	26

<b>Author</b>	<b>Presentation</b>	<b>Page</b>	<b>Author</b>	<b>Presentation</b>	<b>Page</b>
Gaede, Stewart	Poster 1-12	107	Hamilton, Amanda	Oral 3-2	32
	Poster 11-8	198		Oral 10-1	75
Gao, F	Oral 2-2	25		Poster 3-2	124
Gardi, Lori	Oral 5-6	48		Poster 7-2	165
	Poster 6-7	159		Poster 9-1	175
Gariepy, Jean	Oral 3-1	31	Hamilton, Jeffrey G	Poster 10-9	189
Gelman, Neil	Oral 12-1	88	Hammouti, Sabrina	Oral 6-4	53
	Poster 3-3	125	Han, Victor	Oral 8-4	66
Geraghty, Benjamin	Oral 4-2	38	Han, Wenchao	Oral 2-3	26
	Oral 7-4	60	Handfield-Jones, Nicholas	Oral 11-3	83
Gerstle, J Ted	Oral 12-2	89		Poster 10-5	185
	Poster 1-1	96	Handler, William	Oral 1-2	18
Getgood, Alan	Oral 4-5	41		Oral 4-5	41
	Poster 1-14	109		Poster 4-1	127
	Poster 6-10	162		Poster 4-2	128
Ghugre, Nilesh	Oral 12-6	93		Poster 4-3	129
	Poster 5-5	147		Poster 4-9	135
Gignac, Dereck	Poster 4-9	135		Poster 4-12	138
Gillies, Derek J	Oral 5-6	48	Hankel, Tara	Poster 7-1	164
	Poster 6-7	159	Hardisty, Michael	Oral 2-6	29
Gillies, Elizabeth R	Oral 10-3	77		Oral 6-1	50
	Poster 9-4	178	Hedley, David	Oral 3-3	33
Ginty, Fiona	Poster 3-1	123	Helpard, Luke	Poster 1-3	98
Ginty, Olivia	Poster 11-4	194	Hemachandra, Dimuthu	Poster 2-4	118
Giza, Stephanie A	Oral 8-1	63	Hendriks, Jack	Poster 4-9	135
Golaraei, Ahmad	Oral 6-4	53	Hicks, Justin	Oral 11-5	85
Goldberg, Estee	Oral 8-3	65		Poster 11-11	201
Goldhawk, Donna	Oral 12-1	88	Hiebert, Nole	Oral 11-3	83
	Poster 3-3	125		Poster 10-5	185
	Poster 9-5	179	Hisey, Rebecca	Poster 2-2	116
Gomez-Lemus, Jose	Oral 2-1	24		Poster 2-6	120
	Oral 2-3	26	Holden, Matthew	Poster 5-9	151
Goubran, Maged	Oral 2-2	25	Holdsworth, David W	Oral 1-5	21
Grant, Claire	Oral 12-5	92		Oral 1-6	22
Gray, Rob	Poster 6-6	158		Oral 4-4	40
Gribble, Adam	Poster 7-4	167		Oral 6-2	51
Grolman, Eric	Oral 10-3	77		Oral 6-3	52
	Poster 9-4	178		Oral 6-5	54
Groves, Leah	Poster 1-4	99		Oral 10-3	77
Guo, Fumin	Oral 9-2	70		Oral 12-3	90
	Poster 11-9	199		Poster 1-14	109
Gupta, Neeru	Oral 10-4	78		Poster 1-16	111
Haast, Roy AM	Oral 11-4	84		Poster 6-8	160
Hachinski, Vladimir	Poster 11-12	202		Poster 6-9	161
Halder, Arjama	Poster 4-12	138	Holmes, Jeff	Poster 4-7	133
Haller, Cristoph	Oral 12-2	89	Holmes, M	Oral 2-2	25



<b>Author</b>	<b>Presentation</b>	<b>Page</b>	<b>Author</b>	<b>Presentation</b>	<b>Page</b>
Hong, Gregory	Oral 4-4	40	Kewin, Matthew D	Oral 8-4	66
Hookey, Lawrence	Poster 5-9	151		Poster 1-8	103
Hoover, Douglas A	Oral 7-3	59		Poster 1-17	112
	Oral 9-3	71	Khalid, Mahro	Poster 1-8	103
	Poster 5-3	145		Poster 1-13	108
Hope, Tyna	Poster 3-1	123	Khan, Ali R	Oral 1-3	19
Hosein, Yara	Poster 1-16	111		Oral 11-3	83
Hou, Jinqiang	Poster 11-11	201		Oral 11-4	84
Howard, James	Poster 6-2	154		Oral 11-6	86
	Poster 6-4	156		Poster 2-4	118
Howes, Daniel	Poster 2-2	116		Poster 4-11	137
Hrinivich, William	Poster 5-7	149		Poster 10-3	183
Huang, Susan	Poster 10-9	189		Poster 10-4	184
Hussain, Uzair	Poster 10-3	183		Poster 10-5	185
	Poster 10-8	188		Poster 10-7	187
Hwang, Germain Yong Sin	Poster 1-7	102		Poster 10-8	188
Hynynen, Kullervo	Oral 10-5	79	Khattak, Shireen	Oral 10-4	78
Iida, Hidehiro	Oral 11-1	81	Khorasani, Mohammadali	Poster 7-4	167
Ilday, Omer	Oral 6-4	53	Kiernan, John A	Poster 9-3	177
Ioussoufovitch, Seva	Oral 12-4	91	Kirby, Miranda	Poster 8-2	172
Isen, Jonah	Poster 2-6	120	Klassen, Martyn	Oral 4-3	39
Ivanov, D	Oral 11-4	84	Klein, Geoff	Oral 2-6	29
Jafari, Parya	Oral 9-3	71	Knier, Natasha	Poster 7-2	165
Jaffray, David	Oral 1-4	20	Kosik, Ivan	Poster 7-3	166
	Oral 3-3	33	Krahn, Philippa	Oral 5-5	47
Janssen, Natasja	Oral 5-3	45	Kuehn, Tristan K	Oral 1-3	19
	Poster 7-1	164		Poster 4-11	137
Janssens, S	Oral 11-4	84	Kulaseharan, Sancgeetha	Oral 8-5	67
Jeyaraj, Satheesh Krishna	Poster 2-5	119	Kuling, Gregory C	Oral 2-5	28
Johnson, Carol	Oral 2-3	26	Kwan, Benjamin	Poster 10-6	186
Jones, Blake	Poster 7-4	167	Kwan, D	Oral 2-2	25
Jones, Ryan M	Oral 10-5	79	Kwan, William Chu	Poster 5-1	143
Jurkiewicz, Michael	Poster 10-6	186		Poster 5-2	144
Kai, Jason	Oral 11-6	86		Poster 6-5	157
Kakani, Nirmal	Oral 5-6	48	Lacefield, James	Poster 11-10	200
Kalaycıoğlu, Seydi Yavas Hamit	Oral 6-4	53	Ladak, Hanif M	Poster 1-3	98
Karim, Karim	Poster 1-9	104	Laflamme, Michael	Poster 5-5	147
Kasa, Loxlan W	Poster 10-7	187	Laframboise, Jacob R	Poster 5-9	151
Kashyap, S	Oral 11-4	84	Lalone, Emily	Poster 6-6	158
Kassam, Zahra	Oral 7-3	59		Poster 11-1	191
Kasuya, Hidetoshi	Oral 5-2	44	Lang, T	Oral 2-2	25
Kaufmann, Martin	Oral 5-3	45	Lanting, Brent	Poster 2-3	117
Kebaya, Lilian	Oral 8-4	66		Poster 6-1	153
Kelly, John	Oral 7-5	61		Poster 6-2	154
	Oral 10-1	75		Poster 6-4	156
	Poster 3-2	124			

<b>Author</b>	<b>Presentation</b>	<b>Page</b>	<b>Author</b>	<b>Presentation</b>	<b>Page</b>
Lapinski, Michael	Oral 10-4	78	Mak, Helium	Oral 6-3	52
Lasso, Andras	Oral 5-1	43	Makela, Ashley	Oral 3-2	32
	Oral 5-3	45		Poster 7-2	165
	Poster 5-8	150	Maksym, Geoffrey	Oral 9-5	73
	Poster 5-9	151	Manca, Dino	Oral 12-6	93
Lau, Jonathan C	Poster 2-4	118	Marants, Raanan	Oral 12-5	92
	Poster 10-4	184	Marjoribanks, Robin	Oral 6-4	53
Lavdas, Michael K	Poster 6-9	161	Marras, C	Oral 2-2	25
Lawrence-Dewar, J	Oral 2-2	25	Martel, Anne	Oral 2-5	28
Lee, Casey Y	Oral 4-2	38		Oral 2-6	29
	Oral 7-4	60	Martin, Ken	Poster 5-8	150
Lee, Jason J	Poster 9-3	177	Martire, Daniel	Oral 1-2	18
Lee, Ting	Oral 3-3	33	Matheson, Alexander M	Oral 9-2	70
	Oral 7-2	58		Oral 9-4	72
	Oral 12-5	92	Mattonen, Sarah	Oral 7-1	57
	Poster 1-12	107	McCalden, Richard	Poster 6-2	154
	Poster 6-6	158	McCormack, David	Oral 9-1	69
	Poster 10-9	189		Oral 9-2	70
	Poster 11-1	191		Oral 9-5	73
Lessard, Eric J	Poster 4-1	127		Poster 2-1	115
Leung, Charlene	Poster 11-6	196		Poster 8-3	173
Leung, Eric	Poster 5-7	149	McCurdy, Colin	Oral 1-2	18
Levit, Alexander	Poster 11-12	202	McGregor, Thomas	Poster 5-4	146
Levy, Ron	Oral 5-1	43	McIntyre, Christopher	Oral 12-5	92
Li, Alex	Poster 7-6	169		Poster 8-1	171
Li, Fiona	Oral 3-3	33	Mclsaac, Kenneth A	Poster 2-3	117
Lia, Hillary	Poster 5-4	146	McKenzie, Charles	Oral 8-1	63
Lilge, Lothar	Oral 6-4	53		Oral 8-3	65
Liu, Junmin	Oral 4-4	40	McMahon, Dallan	Oral 10-5	79
	Poster 4-4	130	Menon, Ravi	Oral 4-3	39
	Poster 4-8	134		Poster 4-7	133
	Poster 4-13	139	Milej, Daniel	Poster 1-8	103
Liu, Kela	Poster 3-1	123		Poster 1-13	108
Lo, Benjamin WY	Oral 5-2	44		Poster 1-17	112
Lo, Marcus	Oral 8-2	64		Poster 5-6	148
Loo, Claudette	Poster 7-1	164	Milner, Jacques S	Oral 1-6	22
Looi, Thomas	Poster 5-1	143		Poster 1-16	111
Lorusso, Daniel	Oral 1-6	22	Mirsattari, Seyed M	Poster 10-7	187
Louka, Amgad	Oral 4-5	41	Mojica, Mia	Poster 11-3	193
Lu, YingLi	Oral 2-5	28	Moody, A	Oral 2-2	25
Luyt, Leonard	Poster 11-11	201	Moore, John	Oral 1-3	19
MacDonald, Penny	Oral 11-3	83		Poster 1-6	101
	Poster 10-5	185		Poster 1-7	102
Machado, João	Poster 1-18	113		Poster 4-11	137
MacIntosh, B	Oral 2-2	25		Poster 11-4	194
MacNeil, Jonathan	Oral 9-1	69	Motlagh, Bahar	Poster 1-15	110

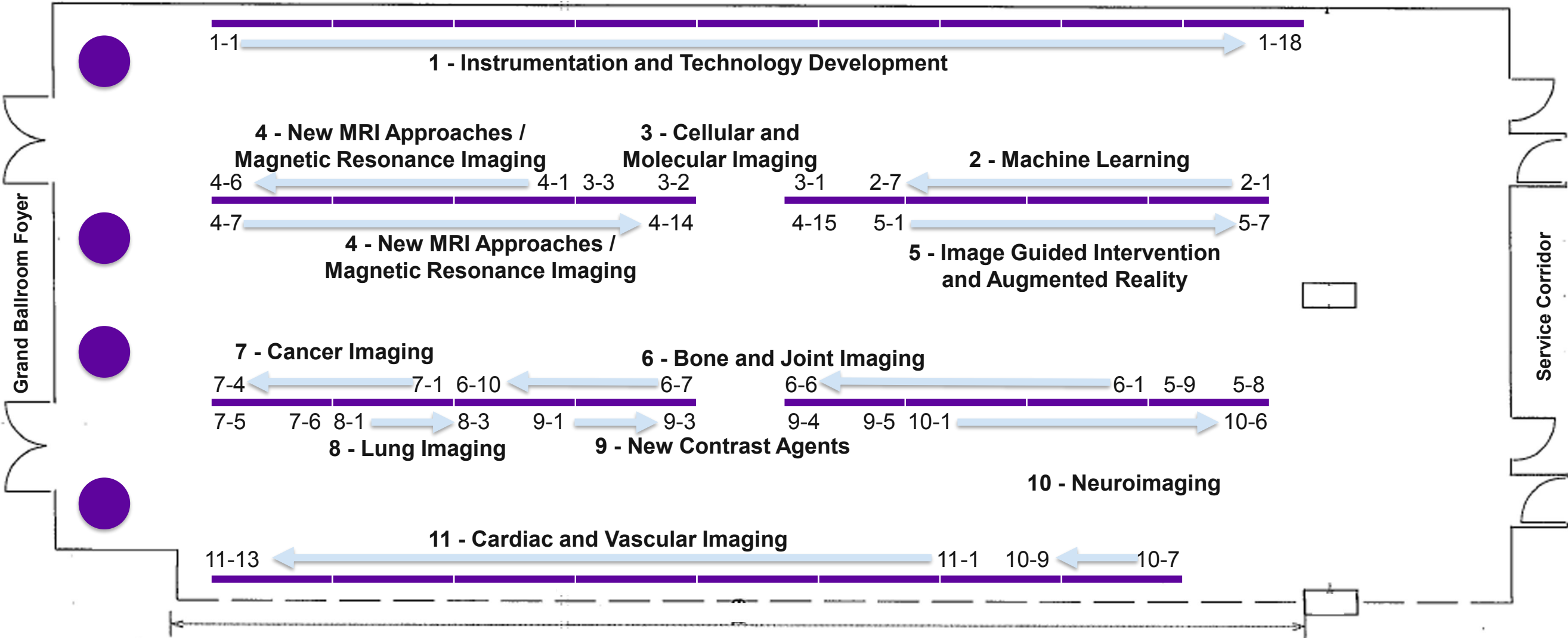
<b>Author</b>	<b>Presentation</b>	<b>Page</b>	<b>Author</b>	<b>Presentation</b>	<b>Page</b>
Moussa, Madeleine	Oral 2-1	24	Parraga, Grace	Oral 9-1	69
	Oral 2-3	26		Oral 9-2	70
Mozaffari, Maryam	Poster 7-6	169		Oral 9-4	72
Munding, Chelsea E	Poster 1-18	113		Oral 9-5	73
Mushtaha, Farah N	Oral 1-3	19		Poster 2-1	115
	Poster 4-11	137	Poster 8-1	171	
Nano, Tomi	Poster 1-9	104	Poster 8-2	172	
Narayanan, Unni	Poster 6-5	157	Poster 8-3	173	
Narciso, Lucas DL	Oral 11-1	81	Pautler, Stephen	Oral 2-1	24
	Oral 11-5	85		Oral 2-3	26
Naudie, Douglas	Oral 6-2	51		Oral 7-2	58
	Poster 6-2	154	Pavlosky, William	Poster 10-6	186
Nemirovsky, Idan	Oral 1-2	18	Peeters, Marie-Jeanne Vrancken	Poster 7-1	164
Ng, Matthew	Poster 11-9	199	Perelgut, Maxwell E	Poster 6-1	153
Nijkamp, Jasper	Poster 7-1	164	Perks, William	Oral 7-4	60
Nikolov, Hristo N	Oral 1-5	21	Peters, Terry M	Oral 5-2	44
	Oral 1-6	22		Poster 1-2	97
	Oral 6-2	51		Poster 1-4	99
Nisar, Hareem	Poster 1-7	102		Poster 1-6	101
Nong, Zengxuan	Poster 9-3	177		Poster 1-7	102
Noseworthy, Michael	Poster 4-5	131	Poster 10-4	184	
Ntiri, Emmanuel Edward	Oral 2-2	25	Poster 10-7	187	
Nyström, Nivin N	Oral 3-5	35	Poster 11-4	194	
	Poster 3-2	124	Pichardo, Samuel	Poster 5-1	143
Ohashi, Pam	Poster 3-1	123	Pickering, J Geoffrey	Oral 1-6	22
Omid, Parsa	Poster 1-10	105		Poster 9-3	177
		Poster 7-3	166	Picot, Paul	Poster 4-13
Ong-Ly, Cathy	Poster 8-2	172	Pinter, Csaba	Poster 5-8	150
O'Reilly, Meaghan	Oral 1-1	17	Piorkowska, Karolina	Oral 12-2	89
	Poster 11-5	195		Poster 1-1	96
Orlando, Nathan	Poster 5-3	145		Poster 5-1	143
Ouriadov, Alexei	Poster 8-3	173	Poepping, Tamie	Oral 1-6	22
Owen, Adrian M	Oral 11-3	83	Poirier, Stefan E	Oral 11-2	82
	Poster 5-6	148		Poster 10-6	186
	Poster 10-5	185	Polak, Paul	Poster 4-5	131
Ozzude, M	Oral 2-2	25	Pollmann, Steven I	Oral 1-5	21
Paish, Adam DM	Oral 6-2	51		Oral 6-5	54
Palma, David	Oral 7-1	57	Pop, Mihaela	Poster 11-3	193
Papernick, Sam	Poster 6-7	159	Poser, BA	Oral 11-4	84
Park, Claire K	Oral 5-4	46			
Parkes, Matt	Poster 1-16	111			
Parkins, Katie M	Oral 7-5	61			
	Oral 10-1	75			

Author	Presentation	Page	Author	Presentation	Page
Prato, Frank	Oral 11-5	85	Sahgal, Arjun	Oral 2-6	29
	Oral 12-1	88	Salerno, Fabio R	Poster 8-1	171
	Poster 3-3	125	Samani, Abbas	Oral 9-3	71
	Poster 9-5	179	Schieda, Nicola	Poster 2-5	119
	Poster 10-6	186	Scholl, Tim	Oral 3-5	35
	Poster 11-2	192	Schranz, Amy L	Poster 4-7	133
	Poster 11-7	197	Schulte, Rolf F	Poster 4-5	131
Prickaerts, Melissa J	Poster 11-11	201	Scott, C	Oral 2-2	25
	Oral 6-4	53	Sehl, Olivia C	Oral 3-2	32
Qi, Qi	Poster 11-2	192	Senan, Suresh	Oral 7-1	57
	Poster 11-12	202	Sermesant, Maxime	Poster 11-3	193
Qi, Xiuling	Oral 12-6	93	Sethi, Simran	Oral 8-1	63
	Poster 5-5	147	Shahid, Marwan	Poster 1-8	103
Qirjazi, Elena	Oral 12-5	92		Poster 1-13	108
Rabadia, Vraj	Oral 12-6	93	Shiae, Emad	Poster 11-13	203
Rae, Emily	Oral 5-1	43	Shoraka, Zohreh	Poster 11-13	203
Rajaram, Ajay	Oral 8-4	66	Singh, Nidhi	Poster 1-15	110
	Poster 1-8	103		Poster 1-18	113
	Poster 1-13	108		Poster 7-5	168
	Poster 1-17	112	Slikboer, Samantha	Oral 10-2	76
Ramirez, J	Oral 2-2	25	Smailovic, Haris	Poster 11-2	192
Rankin, Adam	Poster 1-4	99	Smith, Christopher W	Oral 7-3	59
Ranota, Puneet	Poster 6-6	158	Smith, E	Oral 2-2	25
Rejali, Hossein	Poster 10-3	183	Snir, Jonatan	Poster 5-3	145
Richards, Robin	Oral 6-6	55	Soenjaya, Yohannes	Oral 10-2	76
Riddle, Michael	Poster 6-6	158		Poster 7-5	168
	Poster 11-1	191	Soetemans, Derek	Oral 2-1	24
Roa, Felipe	Poster 1-15	110	Soliman, Hany	Oral 7-4	60
	Poster 7-5	168	Soni, Jay B	Oral 5-5	47
Rodgers, Jessica R	Poster 5-7	149	Sonke, Jan-Jakob	Poster 7-1	164
Rohani, Seyed Alireza	Poster 1-3	98	Soon, Kayla	Oral 1-6	22
Romanet, Cameron	Oral 6-4	53	Soucier, Nathan	Poster 5-1	143
Romsa, Jonathan	Poster 10-6	186	Souza, Roberto	Oral 2-4	27
Ronald, John	Oral 3-4	34	Spino, Michael	Oral 12-6	93
	Oral 3-5	35	Ssali, Tracy	Oral 11-1	81
	Oral 7-5	61		Oral 11-5	85
	Oral 10-1	75	St. Lawrence, Keith	Oral 8-4	66
	Poster 3-2	124		Oral 11-1	81
	Poster 9-1	175		Oral 11-5	85
	Poster 9-2	176		Poster 1-8	103
Roseborough, Austyn	Poster 11-12	202		Poster 1-13	108
Roy, Priyanka	Oral 8-2	64		Poster 1-17	112
Rudan, John	Oral 5-3	45		Poster 5-6	148
Ryan, Sarah	Oral 5-1	43	Stanley, Olivia W	Oral 4-3	39
Sadeghi-Naini, Ali	Oral 9-3	71	Steven, David	Poster 10-6	186
Saeed-Marand, Moe	Poster 3-2	124	Stone, Simone	Poster 3-1	123

<b>Author</b>	<b>Presentation</b>	<b>Page</b>	<b>Author</b>	<b>Presentation</b>	<b>Page</b>
Strauss, Bradley	Oral 12-6	93	Umoh, Joseph U	Oral 6-3	52
Strother, S	Oral 2-2	25		Poster 1-16	111
Suh, Nina	Poster 6-6	158	Ungi, Tamas	Oral 5-1	43
	Poster 11-1	191		Oral 5-3	45
Sullivan, Rebecca	Poster 11-11	201		Poster 2-2	116
Sun, Qin	Poster 9-5	179		Poster 2-6	120
Sunderland, Kyle	Oral 5-3	45		Poster 2-7	121
Surry, Kathleen	Oral 7-3	59		Poster 5-4	146
	Poster 5-7	149		Poster 5-9	151
Swartz, R	Oral 2-2	25	Valliant, John	Oral 10-2	76
Swick, Connor	Oral 10-1	75	Valsamis, Jake J	Poster 10-1	181
Sykes, Jane	Poster 11-7	197	Van de Kleut, Madeleine	Poster 6-3	155
	Poster 11-11	201	Van Ginkel, Michael J	Poster 11-2	192
Symons, S	Oral 2-2	25	van Seijen, Maartje	Poster 7-1	164
Tan, Pearl	Poster 5-9	151	Vasarhelyi, Edward	Poster 6-1	153
Tavallaei, Ali	Oral 5-5	47		Poster 6-2	154
Taylor, Edward	Oral 3-3	33	Vassallo, Reid	Oral 5-2	44
Teeter, Matthew	Oral 6-2	51	Vaughan, Thomas	Poster 5-4	146
	Oral 6-5	54	Vega, Sergio A	Oral 12-2	89
	Poster 2-3	117		Poster 1-1	96
	Poster 6-1	153	Velker, Vikram	Poster 5-7	149
	Poster 6-2	154	Verma, Atul	Poster 11-6	196
	Poster 6-3	155	Vimort, Jean-Baptiste	Poster 5-8	150
	Poster 6-4	156	Vitkin, I Alex	Oral 6-4	53
	Poster 6-9	161		Poster 7-4	167
Temple, Michael	Poster 5-2	144	Wan, Wankei	Oral 6-3	52
Tessier, David	Oral 5-6	48	Wang, Ben X	Poster 3-1	123
Thiessen, Jonathan D	Oral 11-2	82	Wang, Dan	Poster 3-1	123
	Poster 10-6	186	Wang, Hui	Poster 1-10	105
	Poster 10-9	189	Wang, TianDuo	Oral 3-4	34
	Poster 11-2	192		Poster 9-2	176
	Poster 11-7	197	Ward, Aaron	Oral 2-1	24
	Poster 11-11	201		Oral 2-3	26
	Poster 11-12	202		Oral 7-1	57
Thomas, Reuben	Oral 12-6	93		Oral 7-3	59
Thompson, R Terry	Oral 12-1	88	Washko, George R	Oral 9-4	72
	Poster 3-3	125	Waspe, Adam	Oral 12-2	89
	Poster 9-5	179		Poster 1-1	96
	Poster 10-6	186		Poster 5-1	143
Tong, Olivia	Poster 1-11	106		Poster 5-2	144
Truscott, Emily	Oral 6-2	51		Poster 6-5	157
Tse, Justin J	Oral 12-3	90	Wawrzyn, Christine	Oral 1-2	18
Turk, Omar	Poster 6-10	162		Poster 4-2	128
Ukwatta, Eranga	Poster 2-5	119	Wawrzyn, Krzysztof	Oral 4-5	41
Uludag, Kamil	Oral 11-4	84		Poster 4-9	135

<b>Author</b>	<b>Presentation</b>	<b>Page</b>	<b>Author</b>	<b>Presentation</b>	<b>Page</b>
Welch, Ian	Oral 6-2	51	Wu, Hongbo	Oral 2-5	28
Westcott, Andrew	Oral 9-1	69	Wu, Victoria	Poster 2-7	121
	Oral 9-4	72	Xia, Wenyao	Poster 1-2	97
	Oral 9-5	73		Poster 11-4	194
	Poster 2-1	115	Xiao, Yiming	Oral 5-2	44
	Poster 8-2	172		Poster 10-4	184
	Poster 8-3	173	Xu, Rui	Oral 1-1	17
Westreich, Jared	Poster 7-4	167	Yaffe, Martin	Poster 3-1	123
Weyers, Jill J	Oral 12-6	93	Yang, Dae-Myoung	Oral 7-2	58
	Poster 5-5	147	Yavas, Seydi	Oral 6-4	53
Whitehead, Shawn	Poster 11-12	202	Yee, Albert	Oral 6-1	50
Whyne, Cari	Oral 2-6	29	Yeung, Ivan	Oral 1-4	20
	Oral 6-1	50		Oral 3-3	33
	Oral 6-6	55	Yin, Jianhua	Poster 1-15	110
	Poster 1-5	100	Yip, Lawrence CM	Oral 3-5	35
Widjaja, Elysa	Oral 8-5	67		Oral 8-4	66
Wiercigroch, Julia	Oral 5-3	45		Poster 1-11	106
Wilk, Benjamin	Poster 11-7	197		Poster 7-3	166
Wilkie, Phoenix	Oral 6-1	50	Young, Heather M	Poster 1-12	107
Williams, Harley A	Poster 2-3	117	Yu, Lihai	Poster 11-11	201
	Poster 6-4	156	Yuan, Xunhua	Poster 6-2	154
Wilson, Brian	Poster 7-5	168		Poster 6-3	155
Wilson, Sydney	Poster 6-8	160		Poster 6-4	156
Wisenberg, Gerald	Poster 11-7	197	Yucel, Yeni	Oral 10-4	78
	Poster 11-11	201	Zabihollahy, Fatemeh	Poster 2-5	119
Wodlinger, Brian	Poster 7-5	168	Zheng, Gang	Poster 7-5	168
Wright, Graham	Oral 5-5	47	Zhou, Xun	Oral 10-4	78
	Oral 12-6	93	Zotova, Darya	Oral 10-1	75
	Poster 5-5	147			
	Poster 11-6	196			
	Poster 11-9	199			

# Poster Layout – Grand Ballroom West



The Scientific and Organizing Committee for the ImNO 2019 Annual Symposium would like to thank you for attending and acknowledge our supporting consortia and sponsors.

We invite you to attend the 18<sup>th</sup> ImNO Annual Symposium in March 2020 in Toronto, Ontario.



**Western**  
Biomedical Imaging  
Research Centre



**Accuracy. Confidence.™**

S H E L L E Y



M E D I C A L  
I M A G I N G  
T E C H N O L O G I E S



*Eunice Kennedy Shriver* National Institute  
of Child Health and Human Development



**Ontario**  
Research Fund

